

Zircon behaviour in low temperature environments

Duncan Charles Hay

Thesis presented for the degree of Doctor of Philosophy (Ph.D)

University of Glasgow

Department of Geographical & Earth Sciences

August 2007

Abstract

Zircon in mudstones, sandstones and greenschist facies metasediments has been investigated using conventional SEM techniques (BSE, CL and SE imaging) and reveals highly variable microstructures and textures. In these rocks, zircon readily responds to low temperature events due to radiation damage in its crystal lattice while crystalline zircon remains unmodified. Zircon that alters as a result of metamictization has a low BSE intensity (dark BSE zircon) and electron microprobe measurements show an enrichment of Mg, Al, Ca, Fe, Y and a loss of Si and Zr, while Hf appears to remain relatively constant between the unmodified parent and the resulting modified phase. Dark BSE zircon forms via two main mechanisms. The dominant dark BSE zircon form (Group 1) has a microstructure containing an abundance of pores, cavities and inclusions forming as a result of a coupled dissolution-reprecipitation mechanism. Electron backscattered diffraction (EBSD) analyses suggests that the structure is composed of randomly orientated nanocrystalline zircon. The other form of dark BSE zircon (Group 2) is produced by a solid-state diffusion-driven cation-exchange process in which structural recovery occurs (as determined by EBSD) and where inclusions or pores are absent in the microstructure of the product phase. The different forms of altered zircon are chemically indistinct.

Zircon outgrowths (*c.*1 μ m thick) on the margins of detrital unmodified zircon in clay-rich sandstones indicate Zr was transported from altered grains. These zircons crystallised below 100°C. The upper temperature at which metamict zircon may be dissolved is constrained by the annealing temperature of the zircon lattice whereby metamict areas are repaired above *c.*250°C. Zircon outgrowths are larger (*c.*3 μ m thick) and in much greater abundance in slates that have experienced deformation and temperatures *c.*350°C. They have a complex microstructure, partly as a result of interactions with xenotime that also forms outgrowths upto 12 μ m thick on zircon. Xenotime inclusions and zircon-xenotime complexes have been identified within zircon outgrowths

using TEM and LV-STEM. Electron transparent foils of the outgrowth were prepared using the FIB microscope. Zircon outgrowths have similar chemical characteristics to dark BSE zircon but have distinctly different substitution relationships. There are also differences between the chemistry of dark BSE zircon from sedimentary and greenschist facies rocks where the latter is considerably more enriched in Al, Y and Ca. The implications of this are that zircon chemistry is strongly influenced by the local conditions in which it formed.

Sedimentary processing causes considerable bias in the zircon population. Fine-grained sediment is a sink for high U and Th, heavily radiation damaged, old zircon in comparison to mature sediment that is likely to contain an abundance of low U and Th zircon or young zircon upon deposition. Small metamict zircon fragments are prone to dissolution and can be readily stripped from the matrix of fine-grained sediments. The concentration of zircon outgrowths in fine-grained sedimentary and metasedimentary rocks is primarily the result of sedimentological processes.

The findings of this work illustrate the importance of studying minerals in-situ and within their petrological context. The wide-spread and abundant nature of low temperature zircon is a major consideration for geochronology, sedimentary provenance studies, the interpretation of zoning in zircon and has significant implications for the long-term storage of radioactive material.

Table of contents

Abstract	i
Table of contents	iii
List of figures	viii
List of tables	xi
Glossary	xii
Acknowledgements	xiii
Declaration	xiv
Introduction	1
1.1 Introduction.....	1
1.2 Zircon composition and applications.....	2
1.3 Metamictization.....	4
1.4 Zircons response to metamorphism.....	6
1.5 Thesis.....	8
Methods & techniques	9
2.1 Imaging techniques.....	9
2.2 Chemical analysis.....	10
2.3 Determining crystallinity.....	11
2.4 High-resolution imaging.....	13
2.5 Calculating zircon populations in thin section.....	14
Zircon and xenotime behaviour in greenschist facies conditions	16
3.1 Introduction.....	16
3.2 Regional setting and samples.....	17
3.3 Groups within the zircon population.....	20
3.4 General zircon distribution and character.....	21
3.5 Dark BSE zircon.....	25
3.5.1 Dark BSE zircon adjacent to matrix in slates, phyllites and psammities.....	30
3.5.2 Dark BSE zircon in contact with quartzite matrix.....	30
3.5.3 Fractures related to dark BSE zircon.....	33
3.5.4 Crushed zircon.....	38

3.5.5 Dark veins.....	38
3.5.6 Xenotime and other high BSE contrast minerals.....	38
3.6 Porous zones in zircon.....	40
3.7 Features on the margins of unmodified zircon	42
3.7.1 Zircon outgrowths on unmodified zircon.....	42
3.7.2 Xenotime outgrowths on zircon.....	51
3.7.3 The relationship between of zircon and xenotime outgrowths	57
3.8 Other occurrences of xenotime	58
3.8.1 Overgrowths on detrital xenotime	58
3.8.2 Discrete xenotime within the matrix.....	58
3.9 Chemistry, CL and EBSD of zircon and xenotime.....	60
3.9.1 Light BSE zircon	60
3.9.2 Dark BSE zircon	67
3.9.2.1 Anomalous data points	68
3.9.2.2 Chemical analyses.....	76
3.9.2.3 EBSD, CL and BSE	88
3.9.2.4 Zircon Dh4zr14.....	89
3.9.2.5 Zircon KL05hxr16	92
3.9.3 Light BSE, low EBSD IQ zircon.....	97
3.9.4 Porous zones in zircon.....	99
3.9.5 Zircon Outgrowths	107
3.9.5.1 Anomalous points	107
3.9.5.2 Zircon outgrowth chemistry.....	115
3.9.5.3 CL and EBSD	124
3.9.6 Chemical comparison of zircon microstructures.....	124
3.9.7 Xenotime	132
3.10 Interpretation	134
3.10.1 General zircon character.....	134
3.10.2 Dark BSE zircon	134
3.10.2.1 Metamictization.....	135
3.10.2.2 Process of dark BSE zircon formation.....	135
3.10.2.3 Variation in microstructure	137
3.10.2.4 Crystallinity	138
3.10.2.5 Protection	140
3.10.2.6 Crushed and fragmented zircon.....	142
3.10.2.7 Shape of dark BSE zircon margins	142
3.10.3 Metamict zircon.....	143
3.10.4 Porous zones in zircon.....	144
3.10.5 Zircon and xenotime outgrowths	145

3.10.5.1 Zircon outgrowths	145
3.10.5.2 Xenotime outgrowths	146
3.10.5.3 Interactions of zircon and xenotime outgrowths	148
3.10.6 Xenotime and dark BSE zircon	148
3.10.7 Linking zircon features and behaviour.....	149
3.10.8 U, Th and Pb concentration in low temperature zircon.....	149
3.11 Summary	150
Zircon and xenotime behaviour during diagenesis.....	152
4.1 Introduction.....	152
4.2 Methods, regional setting and samples.....	153
4.3 General zircon distribution and character.....	157
4.4 Dark BSE zircon	159
4.4.1 Group 1 dark BSE zircon	159
4.4.1.1 Internal features and macrostructure of Group 1 dark BSE zircon.	168
4.4.2 Group 2 dark BSE zircon	172
4.5 Porous zones in light BSE zircon	175
4.6 Outgrowths on the margins zircon	175
4.6.1 Zircon outgrowths	175
4.6.2 Xenotime outgrowths	182
4.7 Chemistry and EBSD and their correlation with CL & BSE intensity in zircon..	187
4.7.1 Light BSE zircon	187
4.7.2 EPMA analysis and results	187
4.7.2.1 EPMA strategy.....	187
4.7.2.2 Anomalous points in EPMA data.....	189
4.7.2.3 Overall chemistry and trends	193
4.7.3 Group 1 dark BSE zircon individual grain study	205
4.7.3.1 Zircon KULM3zr7.....	205
4.7.3.2 Zircon KULM3zr6.....	209
4.7.3.3 Group 2 dark BSE zircon individual grain study	214
4.7.4 Group 1 and 2 dark BSE zircon	219
4.7.5 Chemical comparison of Group 1 & 2 dark BSE zircon	228
4.7.6 Pores in zircon.....	229
4.8 Interpretation	231
4.8.1 Group 1 Dark BSE zircon.....	231
4.8.1.1 Discontinuities in the grain microstructure.....	231
4.8.1.2 Volume loss in Group 1 dark BSE zircon and Zr mobility	232
4.8.2 Group 2 Dark BSE zircon.....	233
4.8.2.1 Character.....	233

4.8.2.2 Process of Group 2 dark BSE zircon formation.....	233
4.8.2.3 Metamict zircon in Group 2 dark BSE zircon.....	236
4.8.2.4 Discontinuities in the grain microstructure.....	236
4.8.3 Dark BSE zircon – summary and general comments.....	237
4.8.4 Segmented rims on Group 1 dark BSE zircon.....	238
4.8.5 Porous zones in zircon.....	239
4.8.6 The effect of chemical zoning on zircon behaviour.....	240
4.8.7 Outgrowths on zircon.....	241
4.9 Minimum reaction temperature of metamict zircon.....	242
4.10 Summary.....	243
Anatomy of zircon outgrowths.....	244
5.1 Introduction.....	244
5.2 Method technique and sample characterisation.....	245
5.3 FIB-prepared foil.....	249
5.3.1 Method.....	249
5.3.2 Foil morphology.....	251
5.3.3 Host zircon.....	251
5.3.4 Outgrowth.....	255
5.3.4.1 Zircon outgrowth.....	255
5.3.4.2 Xenotime outgrowth.....	256
5.3.4.3 Zircon-xenotime complex.....	257
5.3.5 Matrix grains.....	258
5.3.6 SAED.....	260
5.4 Interpretation.....	260
5.4.1 Zircon outgrowth.....	260
5.4.2 Xenotime phases in outgrowth.....	262
5.4.3 Sub-domains in quartz and mechanisms accommodating zircon and xenotime growth.....	262
5.5 Model for outgrowth formation.....	264
5.6 Summary.....	267
Zircon behaviour in shallow crustal environments.....	268
6.1 Metamorphic grade.....	268
6.1.1 Textural comparison.....	268
6.1.2 Chemical comparison.....	270
6.2 Depositional environment.....	278
6.3 Fluids.....	280
6.3.1 Fluid permeability.....	280
6.3.2 Fluid composition.....	280
6.4 Modelling zircon behaviour in the crustal environment.....	283

6.5 Low temperature pseudomorph	288
6.6 Dark BSE zircon and zircon outgrowths in higher grade rocks	289
Conclusions, implications and further work.....	292
7.1 Conclusions	292
7.1.1 Dark BSE zircon	292
7.1.2 Zircon outgrowths	293
7.1.3 Xenotime	294
7.1.4 Zircon provenance	294
7.1.5 Techniques	295
7.1.6 Suitability of dark BSE zircon and zircon outgrowths for geochronology	296
7.1.6.1 Dark BSE zircon	297
7.1.6.2 Zircon outgrowths	297
7.2 Further work	298
7.3 Summary	299
Thin section descriptions of metasediments.....	300
EPMA analyses in weight percent	304
Thin section descriptions of sedimentary rocks	309
EPMA analyses in weight percent	312
References	314

List of figures

Figure 1 High and low image quality kikuch patterns from EBSD zircon analysis.....	13
Figure 2 Geological map of Scottish Dalradian with sample localities.	18
Figure 3 Photo micrographs.....	20
Figure 4 Images depicting the textural variation in zircon.....	22
Figure 5 Distribution of zircon textures with respect to lithology.	24
Figure 6. Images of zircon containing dark BSE zircon	28
Figure 7. Images of dark BSE zircon in slates.....	31
Figure 8. BSE images of Fig. 6b showing margins of dark BSE zircon.....	32
Figure 9. BSE images of zircon containing dark BSE zircon in quartzites.	34
Figure 10. Crushed zircon in quartzites.....	36
Figure 11. BSE image of veined and fragmented dark BSE zircon	37
Figure 12. BSE images of zircon containing high mean atomic number inclusions.	39
Figure 13. Images of porous zones in zircon.....	41
Figure 14. Images zircon and xenotime outgrowths on the margins of zircon.	43
Figure 15. Images zircon and xenotime outgrowths on the margins of zircon.	46
Figure 16. BSE images of zircon and xenotime outgrowths on the margins of zircon.....	49
Figure 17. Images of zircon with zircon outgrowths.....	50
Figure 18. Images of xenotime outgrowths on zircon	54
Figure 19. Images showing examples of xenotime outgrowths on zircon	56
Figure 20. Xenotime overgrowths on xenotime	59
Figure 21. BSE image displaying discrete xenotimes (arrows) adjacent to quartz.....	59
Figure 22. CL emission spectra	61
Figure 23. Characterisation of concentric light BSE and dark BSE zoned zircon.	62
Figure 24. Characterisation of zircon containing dark BSE zircon.....	64
Figure 25. Characterisation of dark BSE zircon containing laths of light BSE zircon	66

Figure 26. BSE images of zircons analysed by EPMA	69
Figure 27. Element plots from dark BSE zircon EPMA analysis and weeding of anomalous data points. Units are c.p.f.u.....	70
Figure 28. Element plots from dark BSE zircon EPMA analysis and weeding of anomalous data points, round 2. Units are c.p.f.u.....	73
Figure 29. Element plots of data presented in Table 2 from dark BSE zircon EPMA analysis	81
Figure 30. Element plots for zircon Dh4zr14. Units are c.p.f.u.....	84
Figure 31. Element plots for zircon KL05hzh16. Units are c.p.f.u.....	86
Figure 32. Detailed analysis of EPMA traverse area of zircon Dh4zr14	90
Figure 33. Characterisation of zircon KL05hzh16	94
Figure 34. Detailed analysis of EPMA traverse of zircon KL05hzh16.....	95
Figure 35. Characterisation of zircon KL05zr22	98
Figure 36. Characterisation of zircon dh4zr17.....	106
Figure 37. Plots of EPMA data of zircon outgrowths showing anomalous data points....	108
Figure 38. Element plots of EPMA data of zircon outgrowths showing anomalous data points from second stage in the “weeding” process. Units are in c.p.f.u.....	110
Figure 39. Element plots of EPMA data of zircon outgrowths showing anomalous data points. Third stage of the “weeding” process. Units are in c.p.f.u.....	112
Figure 40. Element plots of EPMA analyses of zircon outgrowth data from Table 5.....	121
Figure 41. Non-formula element profile and element plots of zircon outgrowths	123
Figure 42. Character of zircon outgrowths	127
Figure 43. Chemical comparison of zircon textures in greenschist facies rocks.	128
Figure 44. Image with zircon and xenotime outgrowth on detrital zircon	133
Figure 45 Geological map of the Fife area.	154
Figure 46 BSE images of zircon in sandstone.....	158
Figure 47 Images of the varying microstructure of dark BSE zircon	163
Figure 48 Grains containing predominantly dark BSE zircon	165
Figure 49 Images of zircon containing dark BSE zircon.	167
Figure 50 High magnification images of porous microstructure in dark BSE zircon	171
Figure 51 BSE images of dark BSE zircon cemented by xenotime for images.....	171
Figure 52 BSE images of Group 2 dark BSE zircon	174

Figure 53 Images of porous zones in zircon.....	178
Figure 54 Zircon outgrowths on zircon	181
Figure 55 Pyramidal xenotime outgrowths on zircon.....	183
Figure 56 Xenotime outgrowths on zircons	186
Figure 57 BSE images of zircons analysed by EPMA	188
Figure 58 C.p.f.u. element plots from EPMA analysis of sedimentary zircons. Points highlighted are considered to be contaminated or anomalous analyses.	190
Figure 59 C.p.f.u. element plots from EPMA analysis identifying anomalous analyses after first round of “weeding”.....	194
Figure 60 Element plots of dark BSE zircon EPMA analyses with all anomalous points removed. Units are c.p.f.u.	200
Figure 61 Distribution of non-formula elements (c.p.f.u.) in sedimentary dark BSE zircon	203
Figure 62 Detailed analysis of zircon KULM3zr7.....	208
Figure 63 Detailed analysis of zircon KULM3zr6.....	213
Figure 64 Detailed analysis of Group 2 dark BSE zircon.....	217
Figure 65 Detailed analysis of zircon with both Group 1 & Group 2 dark BSE zircon.	220
Figure 66 Detailed analysis of porous zone in zircon.	229
Figure 67 Characterisation of zircon BAL1bzc8.....	246
Figure 68 High magnification images of zircon outgrowth microstructure.....	248
Figure 69 Foils prepared using the FIB microscope	250
Figure 70 Characterisation of the FIB-prepared foil.....	253
Figure 71 Dark-field TEM diffraction contrast images of areas defined in figure 70a.	254
Figure 72. Images revealing the tiled microstructure of zircon outgrowths.	256
Figure 73. Images identifying microstructural in the outgrowth.....	257
Figure 74 TEM SAED patterns from host zircon, zircon outgrowth & xenotime.	260
Figure 75 Model of zircon outgrowth formation	266
Figure 76 Element plots of zircon textures in sedimentary & greenschist facies rocks ...	275
Figure 77 Schematic illustration of zircon grain breakup due to metamictization	278
Figure 78 Modelling zircon behaviour through a metamorphic cycle.	285

List of tables

Table 1 Rock types and the relative proportion of zircon textures in greenschist facies rocks. *number has been calculated (see text). n.a. – not analysed.	23
Table 2 EPMA analyses from zircon containing dark BSE zircon. Data is in c.p.f.u. calculated to 4(O)	78
Table 3 Estimated substitution relationships in dark BSE zircon. NFE = Non-formula elements.....	96
Table 4 EPMA analyses of porous zircon with values presented in c.p.f.u. calculated to 4(O).....	101
Table 5 EPMA analyses of zircon outgrowths and the zircon hosts to those outgrowths. Presented in c.p.f.u. calculated to 4(O).....	117
Table 6 Summary of greenschist zircon textures.....	131
Table 7 The age at which a zircon with a given actinide content will reach the 1 st percolation point ($D_{\alpha} = 3.5 \times 10^{18}$ from Salje et al. (1999)).	140
Table 8 Rock types and associated zircon textures in sedimentary rocks. *number has been calculated (see 2.5)	156
Table 9 EPMA analyses of sedimentary zircon containing dark BSE zircon. Presented in c.p.f.u. calculated to 4(O).	196
Table 10 Chemical substitutions in Group 1 and Group 2 dark BSE zircons	228
Table 11 Summary of dark BSE zircon properties.....	237
Table 12 Comparison of element trends in low temperature zircon.	271

Glossary

BSE – Backscattered electrons

C.p.f.u. – Cations per formula unit

CI – Confidence index

CL – Cathodoluminescence

EBSD – Electron backscattered diffraction

EMP – Electron microprobe

EDX – Energy dispersive x-rays

FIB – Focused ion beam microscopy

IPF – Inverse pole figure

IQ – Image quality

LV-STEM – Low voltage scanning transmission microscopy

SE – Secondary electrons

SAED – Selected area electron diffraction

SEM – Scanning electron microscopy

SIMS – Secondary ion mass spectrometry

TEM – Transmission electron microscopy

Acknowledgements

There are many people I would like to thank that have made this research possible. Firstly John Gilleece for the preparation of thin sections, Peter Chung for carbon coating of samples, Paul Edwards at Strathclyde for probe time and Robert Macdonald for his tremendous help in all the EPMA work I attempted. I have to express an enormous amount of gratitude to Martin Lee and David Brown for FIB-TEM work, without their help considerable sections of this thesis would not be possible. I also have to thank Martin Lee for advice on all things SEM related. Thank you to Kenny Roberts who provided endless amounts of assistance with computer related issues. Nigel Kelly and Brian Bluck always provided thought provoking discussion and helped me in developing my ideas. Tim Dempster has been a great mentor, deserving incredible amounts praise and thanks for his endless energy in this project, putting up with my writing, helping develop ideas and generally coping with me. Kate Dobson has been brilliant in the production part of the thesis so many thanks.

The postgrads in the Gregory Building, past and present, have helped to amuse and distract me over the years. A special mention to Jamie, Graham, Paul, Sally, Aisling and to Dan for his insatiable thirst for coffee. but also Jeff Harris, who, although is not a postgrad, did consistently acted as one. The Glasgow crew have made my life a joy- Paul, Pearce, Martin, Vics to name but a few - thank you all. Don, Kate, Naiomh, Colin and Steve for providing endless amusement all things Geology related and to Mr & Mrs Chambers, Cal, Ewen, Sandy, Laura, Kenny, Lee, Rab, Gilies, Robbie, Rowan and Mambo for being great friends. Mr Moon – adventures?! I think so.

Merle has been an absolute god send over the last half year and without her i'm sure my emotional condition would have deteriorated to greater depths. You have been a great distraction, brightening up many a grey Glasgow day and thank you for putting up with me. Lastly I would like to thank Fo, Mum and Dad. You are the best family any one could possibly ask for and I love you all very much. Also Mum and Dad, thank you so much for encouraging me in anything I took an interest in and for your never ending support.

Declaration

The material presented in this thesis is the result of the independent research undertaken by myself between October 2003 and August 2007. This work was supervised by Tim Dempster and Brian Bluck. All work by other researchers that is quoted in this thesis is given full acknowledgement in the text.

Duncan C. Hay

August 2007

1

Introduction

“Zr is not only mobile but zircon can readily crystallise at temperatures <350 °C”
from Dempster et al. (2004).

The above quote was the significant finding of a study into zircon in metasediments. This thesis sets out to explore the implications of this finding by investigating zircon behaviour in low temperature rocks. This is significant not only for the meaningful use of zircon as a geochronometer but also for the safe storage of nuclear waste in zircon ceramic containers that has been proposed.

1.1 Introduction

The Earth's crust has experienced billions of years of reworking through melting, weathering, erosion and metamorphism as a result of tectonic movements. As a consequence, little information remains in the rock record that can be used to interpret conditions on early Earth (>4.0Ga). During these crustal processes most minerals breakdown, either mechanically or chemically, and can experience dissolution, alteration, recrystallisation or replacement, thereby erasing information that could help interpret its condition of formation. However, some minerals are rather more resistant, persisting throughout a wide range of environments and able to survive multiple phases of tectonism, partial melting and erosion.

Zircon (ZrSiO_4) is a mineral considered to be particularly resistant. Zircon genesis typically occurs in felsic magmas and zircons perceived resistance to alteration is owed to its persistence in a wide range of environments including its ability to endure high grade metamorphic conditions and

survive partial melting events. The discovery of zircons upto 4.4 Gyr old (Foude et al., 1983; Compston and Pidgeon, 1986; Mojzsis et al., 2001; Wilde et al., 2001; Utsunomiya et al., 2004; Nemchin et al., 2006) is also testament to the remarkable durability of crystalline zircon. This durability has allowed earth scientists an insight into conditions on early Earth by examining isotopic information stored within it. This suggests tectonics was established by at least 4.3Ga ago (Cavosie et al., 2005; Valley et al., 2005; Watson and Harrison, 2005). Zircon's most common use in earth science has been in U-Pb isotopic age dating where it has played an extremely important role in advancing our understanding of the timescales of the Earth. This is both important culturally as well as scientifically in that it has given a context for human history.

The durability of zircon has more recently led to it being proposed as a suitable container for the safe storage of nuclear waste (Ewing et al., 1988). Zircon could therefore not only play a potentially important role in dealing with nuclear waste but could also contribute to global efforts in seeking to reduce CO₂ emissions. Such pertinent issues beg the perceived unreactive nature of zircon to be questioned. As zircon appears to be of such great importance to us, this thesis sets out to ask is zircon really as refractory and stable as it is considered to be?

1.2 Zircon composition and applications

Zircon is the main sink for Zr in most rocks and is also host to Hf, U, Th, Y, Ti and REE at trace to weight percent levels (Sawka, 1988; Bea, 1996; O'Hara et al., 2001; Hoskin and Schaltegger, 2003). However, without these elements that substitute into the zircon crystal structure, zircon would be of little use to Earth Scientists. Zircon's ability to exclude common Pb from the crystal lattice upon formation (Watson et al., 1997), combined with the sluggish diffusion rates of these geochronologically important isotopes in crystalline zircon (Cherniak and Watson, 2001) are properties that have led to zircon being the premier U-Pb geochronometer (Davis et al., 2003). Moreover, zircon's use as a geochronometer is linked to crystalline zircon being a highly refractory mineral at the Earth's surface. Zircon has the ability to record multiple stages of growth, dissolution and resorption (Scharer et al., 1997; Corfu et al., 2003; Tichomirowa et al., 2005; Aleinikoff et al., 2006; Harley et al., 2007) that can be revealed when examined using CL and BSE

imaging (e.g. Nasdala et al., 2006). The preservation of these features provide isotopic and geochemical insights into thermal histories and past environments (e.g. Cherniak and Watson, 2003; Hoskin and Schaltegger, 2003).

Zircon is a vitally important mineral for several reasons. U-Pb dates from zircon helped establish the framework of the first geological timescales (Holmes, 1911; see Davis et al., 2003 for review). The zircon detrital record has been routinely used to determine the maximum age of sedimentary sequences, provenance age and composition, but also helped to reconstruct the palaeogeography and tectonic evolution of sedimentary basins and continents (Fedo et al., 2003 and references therein).

The discovery of detrital zircon upto 4.4 Gyr old (Foude et al., 1983; Compston and Pidgeon, 1986; Mojzsis et al., 2001; Wilde et al., 2001; Utsunomiya et al., 2004; Nemchin et al., 2006) is testament to the remarkable durability of crystalline zircon. The interpretation of the $\delta^{18}\text{O}$ isotopic signature of these ancient zircons has led some to believe that the Earth had settled into a pattern of crust formation, erosion, and sediment recycling within the first 200 Ma of its history (Watson and Harrison, 2005). However some earth scientists debate that such a hypothesis is necessary to explain the $\delta^{18}\text{O}$ isotopic signature of these zircons arguing instead that such a signature may be due to early stage alteration of magmatic zircon (Hoskin, 2005; Nemchin et al., 2006). As a consequence of zircons durability and stability in its crystalline state at surface conditions, it has also been proposed as a potential storage material for weapons-grade plutonium from dismantled weapons (Ewing et al., 1988; Ewing et al., 1995). As such, understanding the effects of radiation damage on the zircon crystal lattice is crucial for determining its suitability as a nuclear waste container but is also critically important for understanding its behaviour from a geochronological view point. Arising from these issues, a large body of work now exists which has studied how radiation damage accumulates within the crystal lattice (e.g. Farnan et al., 2003) and the effect this has had on the properties of zircon (e.g. Geisler et al., 2007).

1.3 Metamictization

The decay of radioactive elements in the zircon lattice causes the crystal structure to breakdown and this process has been termed metamictization. The main cause of radiation damage in zircon is via α -decay events where a He nucleus (α -particle) is emitted from the nucleus of the radioactive parent atom (Murakami et al., 1991). In response to the α -decay, the daughter nucleus recoils causing severe damage to the crystal structure and an amorphous collision cascade *c.*5nm in diameter develops (Geisler et al., 2007). Molecular-dynamic simulations have revealed the amorphous collision cascade consists of a matter-depleted core *c.*2nm in diameter surrounded by a zone of increased density (Trachenko et al., 2002, , 2003; Trachenko et al., 2004). Subsequent α -recoil events from the decay of the radioactive nuclide cause areas of depleted matter to overlap and become interconnected (Geisler et al., 2003b).

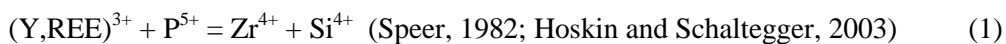
The self-irradiation by actinide elements in U- and Th-rich zircon causes metamict areas to accumulate on a mesoscopic scale. The point at which amorphous clusters overlap and connect up over macroscopic scales has been termed the 1st percolation point (Salje et al., 1999; Farnan and Salje, 2001; Geisler et al., 2003c; Trachenko et al., 2003; Trachenko et al., 2004). A 2nd percolation point occurs when the crystalline domains cease to be connected and islands of crystalline zircon exist within an amorphous matrix (Palenik et al., 2003). Consequently, metamictization in zircon creates a unique structure of amorphous and crystalline domains within the damaged zone.

Isolated amorphous clusters in crystalline zircon may remain unaltered in a fluid phase and therefore communication between amorphous clusters is considered necessary to enabling a fluid phase to migrate through the damaged zone. As such, when damage in zircon reaches the 1st percolation point, it experiences a significant increase in the solubility and uptake of non-formula elements. When the extent of damage in the zircon lattice reaches the 2nd percolation point, it is marked by another increase in both zircon solubility and the uptake of non-formula elements (Geisler et al., 2003c; Trachenko et al., 2004). In a heterogeneously metamict zoned zircon, the swelling of radiation damage areas (upto 18%) caused by metamictization can result in self-induced fracture generation of the crystalline zones. These fractures provide pathways for fluids

that enable alteration of metamict domains that would otherwise remain protected (Lee and Tromp, 1995).

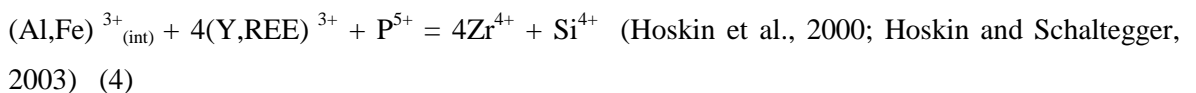
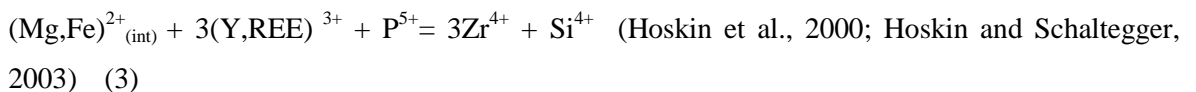
The resulting metamict zircon is less chemically and physically stable than its crystalline equivalent causing enhanced susceptibility to alteration by hydrothermal aqueous fluids (Pidgeon et al., 1966; Trocellier and Delmas, 2001; Geisler et al., 2003c; Hoskin, 2005; Geisler et al., 2007). Hydrothermal alteration of metamict zircon results in the structural recovery of amorphous areas and the enrichment of hydrous species and non-formula elements (according to Goldschmidt's rules) Al, Mg, Ca, Fe, Mn, Y and P (Speer, 1982; Geisler et al., 2003a; Geisler et al., 2003b; Geisler et al., 2007; Schmidt et al., 2007) with Ce also noted in altered areas (Utsunomiya et al., 2007). Metamict areas also experience significant amounts of Pb loss (Geisler et al., 2002) although there are conflicting reports of considerable U and Th loss (Geisler et al., 2002; Geisler et al., 2003a; Geisler et al., 2003d) compared to an almost complete retention of U and Th and even slight enrichment (Geisler et al., 2003b; Utsunomiya et al., 2007). Non-formula elements may substitute into zircon via the following mechanisms:

Substituting at two structural sites:



$M^{n+} + n(OH)^{-} + (4-n)H_2O = Zr^{4+} + (SiO_4)^{4-}$ (Caruba and Iacconi, 1983; Hoskin and Schaltegger, 2003) Where M is a metal cation and n is an integer. (2)

Substituting at an interstitial site:



Geisler et al. (2002) demonstrated that the structural recovery of metamict zircon was a result of water diffusion driving ion exchange and, when treated at higher temperatures, included solid-state recrystallization of the amorphous phase. Following on from this work, Geisler et al. (2003a & b) showed that these processes were capable of causing recrystallization at temperatures as low as

200°C and with the first structural changes occurring as low as 75°C (Geisler et al., 2003d). However Putnis (2002) disputes a solid state, diffusion-driven cation-exchange mechanism described by Geisler et al. (2002) and favours a simultaneous dissolution-reprecipitation approach that results in the development of a porous product phase but “still preserves the external shape of the parent”. Recrystallisation of metamict zircon at high temperatures can result in decomposition to ZrO₂ and SiO₂ in heavily damaged samples (Zhang et al., 2000). However, lower temperature alteration of metamict zircon results in a nanocrystalline structure of randomly orientated crystals (Schmidt et al., 2006; Utsunomiya et al., 2007).

It has been argued that over geological time, metamict zircon may be partly annealed at temperatures below 200°C (Nasdala et al., 2001) and possibly at Earth surface temperature (Meldrum et al., 1998). Fission tracks in zircon are known to anneal around 200-250°C (Garver, 2002; Yamada et al., 2003; Rahn et al., 2004) and this may suggest that α -event damage in zircon can be annealed over similarly low temperatures (Nasdala et al., 2001). However, more work is required to fully understand both the mechanics and kinetics involved in zircon annealing (Zhang et al., 2000; Nasdala et al., 2004).

1.4 Zircons response to metamorphism

The great majority of studies on the behaviour of zircon have been conducted on zircon mineral separates without regard to their in-situ petrological context. Investigations of zircon within thin sections of high metamorphic grade rock routinely provide evidence that it responds to metamorphic processes (Vavra et al., 1996; Rubatto et al., 2001; Kelly and Harley, 2005; Harley et al., 2007) and Zr mobilisation in hydrothermal settings suggests that zircon can be taken into solution and precipitated from such fluids (Fraser et al., 1997; Tomaschek et al., 2003).

Investigations of zircon in greenschist facies metasediments (Dempster et al., 2004) and prehnite-pumpellyite metasediments (Rasmussen, 2005b) revealed zircon outgrowths that project <3 μ m from the margins of detrital grains and were considered to be metamorphic in origin. Although metamorphic zircon described by Dempster et al. (2004) and Rasmussen (2005b) is on a scale of an

order of magnitude smaller than zircon overgrowths in equivalent higher-grade rocks, it demonstrates that Zr can be mobilised and form new zircon at temperatures and pressures considerably lower than previously believed possible. This notion was also considered over 70 years ago when the discovery of large outgrowths with similar optical properties to the detrital zircon onto which it had formed, was made in sedimentary rocks from Yorkshire, England (Butterfield, 1936). Multiple papers describing similar observations were published soon after, continuing until the late 1960's but these discoveries also prompted debate and considerable scepticism (for details see Rasmussen (2005b) and references therein). Thereafter, the idea of low temperature Zr mobility and zircon formation was almost completely forgotten. This is most likely due to "zirconologists" turning their attentions to age-determination, as zircons potential as a geochronological tool was beginning to be realised due to technological advances at the time. However, early studies on zircon outgrowths failed to provide evidence for a source of Zr. Dempster et al. (2004) provided such proof, observing significant dissolution of metamict zircon, although Rasmussen (2005b) stated he found no such evidence in his study. Yet despite these studies, very little is known about the response zircon has to low temperature and pressure events in geological conditions.

Understanding the low temperature behaviour of zircon at geological conditions is vital for providing a suitable container for nuclear waste storage but also has major implications for the interpretation of high temperature features in zircon as they will all have experienced a low temperature history. Alteration of zircon at low temperatures causes significant disruption to the concentration of geochronologically important radiogenic isotopes but also affects REE concentrations and can incorporate hydrous species, which may have a profound effect on $\delta^{18}\text{O}$ isotopic signature. Understanding alteration mechanisms and new growth may also provide earth scientists with potential age constraints on low temperatures events.

Xenotime (YPO_4) is a common diagenetic- or low grade metamorphic- overgrowth on zircon (Rasmussen and Glover, 1994; Rasmussen, 1996; McNaughton et al., 1999; Fletcher et al., 2000; Vallini et al., 2002; Kositcin et al., 2003; Rasmussen, 2005a; Rasmussen et al., 2005; Vallini et al.,

2005). The crystallisation of xenotime on zircon is well established and linked to the isomorphic relationship between the two minerals (Spear and Pyle, 2002). However, no study to date has described the complex interaction between low temperature zircon and xenotime.

1.5 Thesis

This thesis sets out to document the wide range of textures and microstructures in zircon from both sedimentary rocks and greenschist facies metasedimentary rocks. It is also the purpose of this thesis to provide evidence for the origins of these features and propose mechanisms for their formation. The thesis has been structured as follows. The methods and techniques used in this study will be documented in Chapter 2 and where necessary, any procedures in the sample preparation. Chapter 3 documents and characterises dissolution and precipitation features observed in- and associated with- zircon from greenschist facies rocks. The objective of Chapter 4 is similar to Chapter 3 but details the behaviour of zircon in sedimentary rocks. A high-resolution study of the microstructure of zircon outgrowths is undertaken in Chapter 5. The main results of the earlier chapters will be integrated in Chapter 6 with conclusions and suggestions for further work presented in Chapter 7.

2

Methods & techniques

To characterise the behaviour of zircon, and minerals associated with its behaviour, a wide range of imaging, chemical and crystallographic analytical techniques have been used. This chapter details the instruments employed and conditions of use.

2.1 Imaging techniques

Zircon behaviour was documented using a FEI Quanta 200F field-emission environmental scanning electron microscope (FEG-ESEM, simplified to SEM from hereon) operated at an accelerating voltage of 20 kV and moderate beam currents. Using SEM backscattered electrons, zircon can be easily identified in thin section due to its high mean atomic number, as can xenotime, which has a slightly higher BSE intensity than zircon due to a higher mean atomic number. Secondary electron (SE) images have also been used so that the textural relationship between zircon, xenotime and the rock matrix can be examined. Occasional BSE images were also obtained using a Cambridge Instruments S360 analytical SEM and is stated in the figure caption where this is the case. Cathodoluminescence (CL) images of zircon were obtained using a K.E. Developments Centaurus CL detector attached to the Quanta SEM. The CL is fitted with a bialkali type tube, responding to wavelengths in the range 300-650nm, peaking in the blue spectrum. CL is sensitive to rare earth elements (REE), U and Th contents and is suppressed by lattice defects (e.g. radiation

damage) (Rubatto and Gebaurer, 2000). CL can therefore reveal extremely intricate and detailed zonation patterns not identifiable in BSE.

2.2 Chemical analysis

The Quanta SEM is equipped with an EDAX Pegasus 2000 energy dispersive X-ray microanalyser (EDX) for qualitative element analysis. Spot analysis was operated using 20kV and moderate beam currents. Setup conditions for EDX scanned maps varied between individual grains and have therefore been stated in the appropriate figure captions where it is different from the above conditions. EDX scanned maps were typically obtained at 512x400 resolution.

The electron probe microanalyser (EPMA) was used for quantitative element analysis of zircon. This was conducted on two machines, a Cameca SX-50 at University of Glasgow and a Cameca SX-100 at University of Strathclyde. The Cameca SX-50 was used to analyse the host zircon and zircon outgrowths and the Cameca SX-100 for zircon grains containing dark BSE zircon. The setup conditions for both were 20kV and 20nA with a 30 second count time on peaks Al K α (Kyanite), Mg K α (Periclase), Ca K α (Wollastonite), Fe K α (FeS), Hf L α (Hafnium), Si K α (CaSiO₄), Y L α (Yttrium), Zr L α (Zircon) and Na K α (NaCl). All standards are given in brackets. Na was subsequently removed from the data set as it was not present in any of the zircon studied. Mg was not analysed during zircon outgrowths analysis and due to human error. The Hf standard was polished and recoated between the batches of analysis of zircon outgrowths and dark BSE zircon due to problems with the carbon coat. As a result it is possible that there is deviation between the number of counts for same the Hf standard. This issue may be amplified due to these analyses being conducted on different EPMA's. The effect this has on the data will be assessed in Chapter 6 of the thesis.

The detection limits for EPMA analysis on the elements analysed are as follows: Mg 100ppm, Al 100ppm, Si 150ppm, Ca 70ppm, Fe 300ppm, Y 300ppm, Hf 1000ppm and Zr 500ppm.

EPMA data has been converted from weight percent (wt%) into cations per formula unit (c.p.f.u.) so that chemical substitutions may be identified within the zircon phase. However, low temperature zircon may contain variable amounts of hydrous species and it is not clear whether this is structurally bound into the zircon lattice or located along grain boundaries within pore-rich or nanocrystalline domains. It is unlikely that the presence of hydrous species will significantly affect the relative trends that element substitution relationships follow but may cause slight changes in the absolute nature of that relationship. Substitution relationships in element plots have been judged by eye. This has been done because within plots showing data multiple grains, individual zircons may follow slightly different substitution relationships and in some element plots there can remain significant scatter in the data.

The Cameca SX100 EPMA has been modified so that full CL spectra may be obtained during analysis (see Edwards et al., 2007 for details).

2.3 Determining crystallinity

Crystallographic information of zircon and xenotime has been obtained through electron backscattered diffraction (EBSD). The EBSD detector is part of an integrated system with the EDAX Pegasus EDX on the Quanta SEM. Samples are given a final polish with colloidal silica for 10 minutes that greatly improves the quality of EBSD pattern. EBSD analysis of zircon grains in thin section have been carried out in the Quanta SEM using both environmental mode (low vacuum), where the sample is uncoated, and in high vacuum mode, with a very thin carbon coat applied to the sample (c.10nm thick). Both were successful. Analysis of zircon with no carbon coat produces a high detector signal pattern. The high detector signal pattern allows for more rapid scans and usually results in high quality patterns but these advantages are offset by problems caused by charging. To minimise the charging effect but to still obtain a high detector signal and high quality pattern, samples are coated with a very thin carbon coat and silver dag is painted around the site of interest. Samples in the Quanta SEM are then tilted to 70°. The effective resolution for SEM EBSD analysis is considered to be c.50nm (Humphreys, 2001).

The EBSD technique operates by focusing an electron beam on a crystalline material that diffracts electrons from crystallographic planes in the material. This produces a pattern of intersecting bands called EBSD patterns. The arrangement of these bands is a function of the crystallographic makeup of the material and the orientation of the crystal. This information is converted into an image by a process known as the Hough transform which allows the EBSD software to automatically detect the bands in a diffraction pattern. The position of these bands can then be used to determine the crystallographic properties of the diffracted volume that include phase, crystal orientation and crystal quality. A voting scheme is then used to determine the phase and orientation of the material analysed, also termed “indexing”. This is achieved by comparing all possible solutions from the structural information of the EBSD pattern obtained with a predetermined file containing structural information about that phase. For a given diffraction pattern several possible orientations may be found which satisfy the diffraction bands detected by the image analysis software. The software ranks these orientations (also known as solutions) using a voting scheme. The solution from the structure file that closely matches the pattern obtained from diffracted volume receives many votes while those that do not receive very few votes. This voting scheme is also used to calculate the confidence index (CI) which is done by subtracting the solution that received the second highest number of votes from the solution with the highest number of votes. This value is then divided by the total number of votes that is possible from the detected bands.

The use of EBSD in this study is two fold. EBSD is typically used to determine the orientation of crystals and therefore EBSD has been used to examine the crystallographic relationship between zircon and xenotime outgrowths and the host zircon. This is achieved through plotting the inverse pole figures (IPF) of the kikuchi patterns produced. An IPF shows the position of a sample direction relative to the crystal reference frame. However, EBSD is also sensitive to distortions or imperfections in the crystal lattice of the diffracting volume. As such EBSD can determine crystal quality by analysing the Image Quality (IQ) of the EBSD pattern. IQ is defined as the average height of the detected peaks that is a direct function of the intensity of the pixel on the Hough transform. A high density of distortions or imperfections in the crystal lattice will act to reduce

EBSI IQ producing diffraction patterns that are more diffuse than a crystal lattice with few (Fig.1). Therefore analysing EBSI IQ has the potential to determine the degree of radiation damage within crystalline zircon or “crystallinity”. Determining radiation damage in zircon is typically achieved using RAMAN spectroscopy (e.g. Nasdala et al., 2003). The application of EBSI to determining crystallinity in zircon has been very limited (Hoskin and Black, 2000 and N.J. Cayzer, personal communication) and it is therefore one aim of this thesis to assess its suitability for determining the degree of radiation damage in zircon crystals.

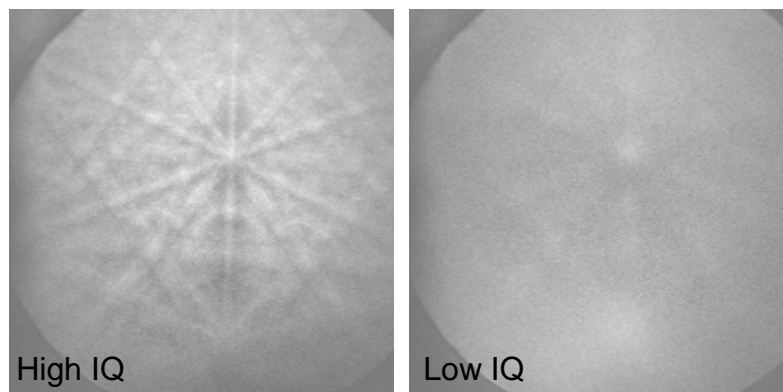


Figure 1 High and low image quality kikuch patterns from EBSD zircon analysis

2.4 High-resolution imaging

Many of the features of the zircon microstructure are too small to be resolved through conventional SEM BSE and SE image analysis. Transmission electron microscopy (TEM) and low voltage-scanning transmission microscopy (LV-STEM) are high-resolution imaging techniques that have been used to examine the microstructural features of zircon outgrowths. The application of TEM to study radiation damage in zircon dates back over forty years (Bursill and McLaren, 1966) and is now an established method for earth scientists studying sub-micron sized features in minerals. Despite the limited use of LV-STEM in the earth sciences (see Lee and Smith, In press), it has been shown to produce images comparable to those from a TEM. A brief outline as to how the two instruments function and form images is covered in Chapter 5 but for a more detailed

understanding of how these machines operate, see Lee and Smith (In press).

To use TEM and LV-STEM, an electron transparent film had to be prepared which was achieved using an FEI 200TEM Focused Ion Beam microscope (FIB). The sample (BAL1B) was coated with 120nm of Au in order to protect the area of interest from the effects of any potential damage by the 30kV Ga⁺ ion beam (Lee et al., In press). The sample was milled in the FIB microscope by bombarding the desired area with Ga⁺ ions. Milling in this way allows very precise shapes to be cut. Firstly, two crosses were milled 20µm apart on the surface of the thin section, either side of the proposed site. These act as reference points during milling. Then, a 1µm thick layer of Pt was deposited on the surface of the area of interest, ensuring it remains protected from the bombarding Ga⁺ ions. Two parallel trenches were then excavated, leaving a thin slice between them, which was then milled down to a thickness of <100nm to produce a c.15 by 5µm electron transparent foil. The foil was then detached at the base and extracted using an *ex-situ* micromanipulator and placed on a holey carbon film in the centre of the Cu supporting TEM grid. For further details on the preparation of TEM foils using a FIB microscope, see (Stroud et al., 2000; Heaney et al., 2001; Wirth, 2004, , 2005; Lee et al., In press; Lee and Smith, In press).

The foil was studied using a TEM FEI T20 instrument operated using 200kV and then using a LV-STEM that was conducted in the Quanta SEM at 20kV and a low beam current. Very high spatial resolution can also be obtained (c.50nm spot) by chemical analysis of the foil in the SEM due to the small interaction volume as a consequence of the thickness of the foil (Coyne, 2004).

2.5 Calculating zircon populations in thin section

To assess the relative proportions of the zircon populations in these rocks (e.g. **Table 1**), zircon in thin sections have been point counted using the SEM allowing them to be categorised based on their morphology and texture they preserved. To achieve this, a transect was made perpendicular to layering in each thin section at x50 magnification and the zircons in this transect were categorised. The total number of zircons in each thin section was then extrapolated from the data from single transect by multiplying it by the width of the thin section at x50 magnification. For

example at x50 magnification, a thin section may be 12 screen shot long and 5 wide. Therefore, for a transect along the length of the thin section, the total number of zircons in the thin section would be multiplied by the width of the thin section, in this instance 5.

Zircon was categorised in following way. Any zircon with internal modification (i.e. dark BSE zircon or abundance of cavities due to dissolution) has been categorised as dark BSE zircon. Light BSE zircon is zircon that is entirely unmodified within the context of the rock. The percentage of zircon and xenotime outgrowths is does not take into consideration of internal textures of the grain and only relates to grains that have zircon or xenotime outgrowths on their margin. Thus a grain may be marked as a dark BSE zircon if, internally, it has layers that are modified but it may also be marked as a zircon outgrowth if one is present on the outermost margin of the grain.

3

Zircon and xenotime behaviour in greenschist facies conditions

3.1 Introduction

Radiation damage that accumulates in zircon makes it considerably more susceptible to alteration and dissolution by fluids (Ewing et al., 2003). This is a primary concern to Earth scientists due to zircons extensive use in geochronology. It may also have consequences for the safe storage of nuclear waste where temperatures can reach similar to those experienced during low-grade greenschist facies metamorphism. This chapter therefore investigates the stability of zircon in low-grade greenschist facies metasediments. It shows that far from zircon being refractory in low-temperature rocks, zircon has a wide and varied response to metamorphism. This chapter reveals that radiation-damaged zircon may experience in-situ dissolution and reprecipitation that prompt a variety of textures and microstructures to develop in response to interactions with metamorphic fluids. In slates Zr is readily mobilised by fluids, from zircon that experiences dissolution, to detrital zircon where it crystallises as outgrowths on its margins. Xenotime also forms outgrowths on detrital zircon and may form intricate structures with zircon outgrowths. These features allow insights into fluid behaviour in the shallow crust during low temperature metamorphism.

3.2 Regional setting and samples

A series of typical, regionally metamorphosed low-grade greenschist facies metasediments were collected from various horizons in the Scottish Dalradian Supergroup for investigation (Fig.2). Localities and rock types were chosen for the following reasons: the rock being a typical example of that lithology at that metamorphic grade; a lack of any obvious late hydrothermal alteration (Rubin et al., 1993); each group of samples covers a range of different lithologies in a continuous sequence of metasediments.

Well constrained ages for the Dalradian have proved enigmatic, placing the whole sequence between *c.*800 Ma – 470 Ma. The Port Askaig Tillite is close to the base of the Supergroup and dated *c.*720-760 Ma (Brasier and Shields, 2000). The Tayvallich volcanics are thought to be around 600 Ma (Dempster et al., 2002) with the absolute top limit for the Dalradian sequence *c.*470 Ma, taken from basic intrusions that metamorphose the Southern Highland Group (Dempster et al., 2002).

A series of slates, phyllites, psammites and quartzites were collected from various horizons in the Dalradian that include Ballachulish slate from the Appin Group and Cowal slates from the Southern Highland Group. These units are interpreted to have formed from significant basin faulting and phases of rapid subsidence creating anoxic basin deposits (Ballachulish slate) and deep turbidite deposits (Cowal slates) (Trewin and Rollin, 2002). Most of these units have subsequently experienced low-grade greenschist facies metamorphism and several phases of deformation.

For detailed descriptions and locations of the following samples please see Appendix A. Samples KL01-KL06 are a sequence of quartzites and psammites from the Appin Group (Grid Ref. NN 152 618). The Appin Group is the oldest group sampled in this study and predates the Port Askaig Tillite (*c.*720-760 Ma). Samples were collected from the transitional boundaries of the Eilde Quartzite/Schist (KL01&KL02), Binnein Quartzite/Schist (KL03&KL04) and the Binnein Schist/Glencoe Quartzite (KL05, KL05h, KL05L & KL06) formations within the Lochaber Subgroup.

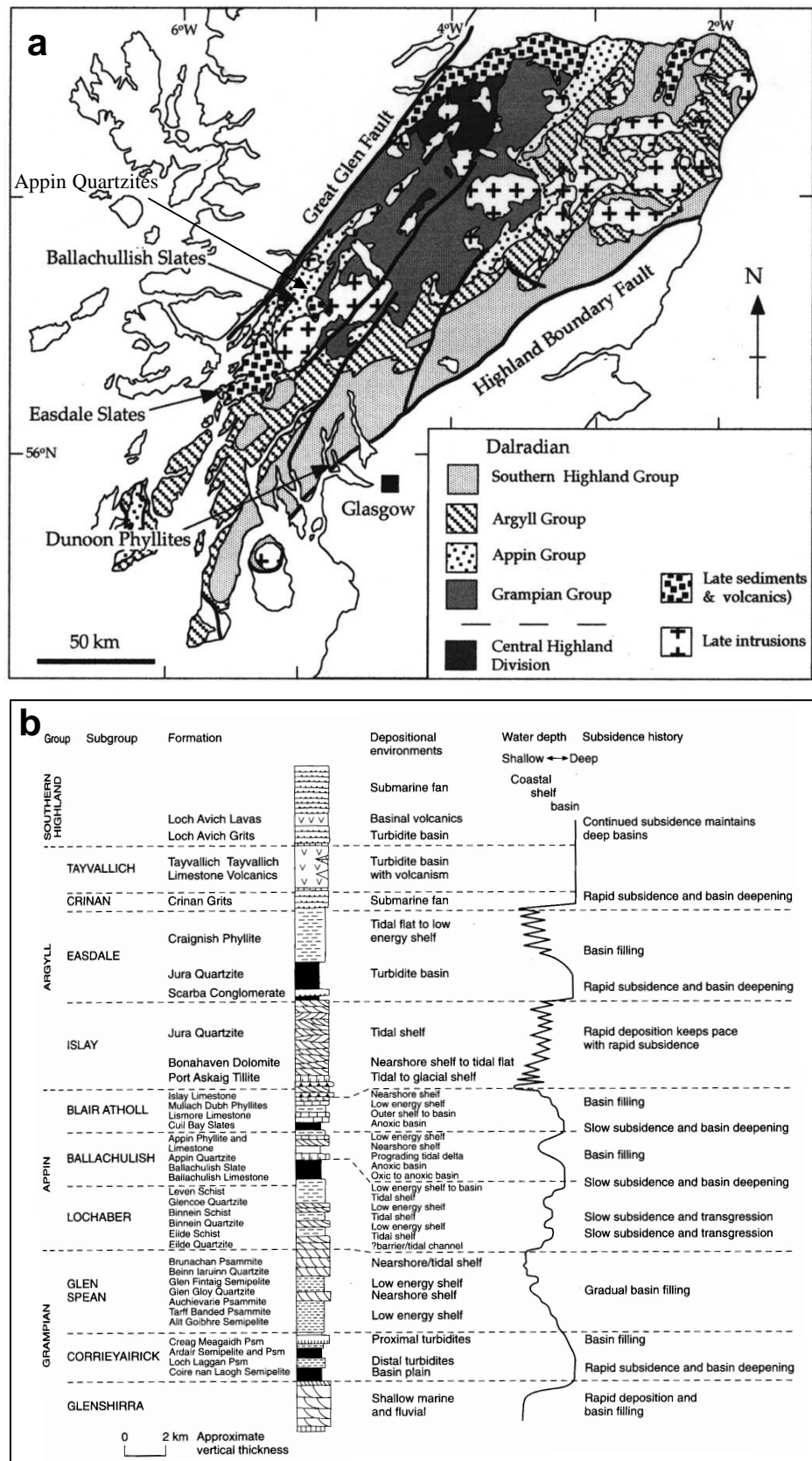


Figure 2. a Geological map of Scottish Dalradian with sample localities. b Stratigraphical column of the Scottish Dalradian

These deposits formed in a low energy shelf to tidally-dominated sequence and represent lithologies deposited during a period of slow subsidence and transgression (Glover et al., 1995). Some rocks contain biotite (upto 700 μ m) are found within weakly defined cleavage planes (Fig. 3a) and the presence of occasional very small (*c.*0.5mm across) garnet porphyroblasts suggest these units experienced greenschist facies metamorphism at temperatures *c.*450°C.

Bal1(a-d) are samples collected from the Ballachulish Slate Formation (Grid Ref. NN 085 583) within the Appin Group and sample Bal3 is a phyllite collected from near the base of the same formation. Ballachulish samples are dark and very graphitic and most contain small pyrites that reveal an anoxic depositional environment (Anderton, 1985). The appearance of occasional small biotites in Bal3 would suggest metamorphic temperatures of *c.*400°C although most Ballachulish samples (Bal1(a-d)) are dominated by a muscovite and chlorite mineral assemblage which implies that metamorphic may have been lower, *c.*300-350°C.

E1 and EAS1 are samples from the Easdale Slates (Grid Ref. NS 218 831) in the Argyll Group. E1 is a black graphitic slate with a fine but relatively well-defined cleavage (Fig.3b) and EAS1 is a carbonate cemented slate with a poorly defined cleavage. These slates are composed of muscovite, chlorite, quartz and plagioclase with occasional pyrites (upto 3mm across). These slates represent turbiditic muds and carbonate turbidites respectively, deposited as a result of rapid subsidence controlled by basin faulting (Anderton, 1985). Samples with the prefix Dh1-4, were collected from the Cove area on the Rosneath peninsula (Grid Ref. NS 218 831) and are part of a sequence from the Dunoon Phyllites, a unit within the Southern Highland Group (Harris et al., 1994). Dh1-Dh3(a-c) are a series of pale to dark graphitic slates with Dh4 a coarser psammitic bed sampled directly above Dh3. Dh1-Dh3(a-c) have a penetrative and strongly defined cleavage that can be weakly crenulated (Dh2) and are predominately composed of muscovite, chlorite and quartz. Dh4 contains quartz (polycrystalline (80%) and monocrystalline (20%)), occasional albite grains and rounded felsic clasts (upto 2mm). A weak cleavage is defined by muscovite with patches of carbonate cement also present. They are part of a sequence that are thought to represent a *c.*4km thick pile of turbiditic sedimentary and volcanoclastic strata (Harris et al., 1994). The Southern Highland Group

is the youngest of Dalradian groups and lies immediately above the Tayvallich volcanics making its deposition younger than 600Ma. Based on the muscovite and chlorite dominated mineral assemblage of the Dunoon Phyllites and Easdale slates, they have experienced low-grade greenschist facies metamorphism that is unlikely to have exceeded 300-350°C. There is no evidence of late veining in any of the rocks studied.

A total of 22 polished sections of these rocks were prepared and examined for SEM analysis. All the following images have been taken within the thin sections unless otherwise stated. In-situ analysis has been carried out so that the relationships of zircon and associated minerals can be determined.

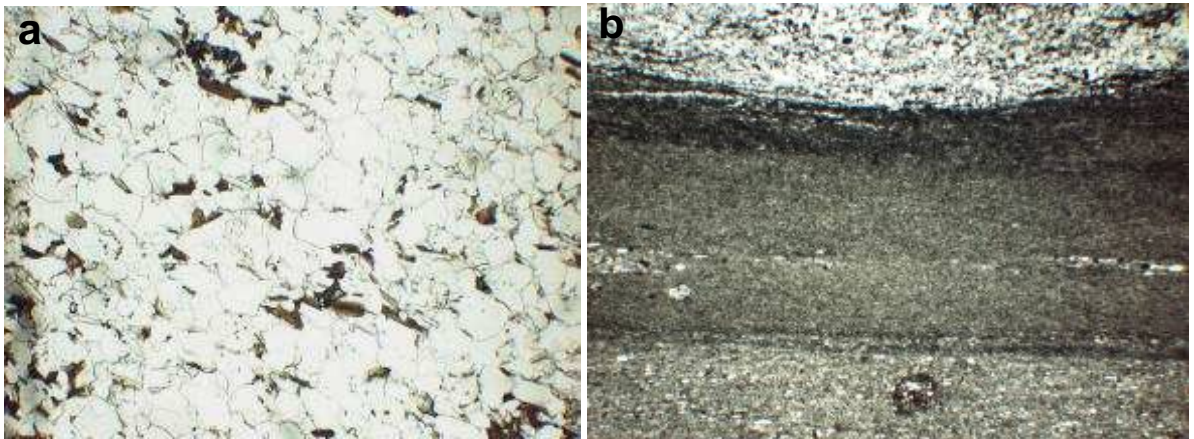


Figure 3 Photo micrographs of (a) quartzite KL02 and (b) banded graphitic slate E1. Field of view in both is 3 x 1mm.

3.3 Groups within the zircon population

Zircon has been characterised on the basis of shape, BSE signal intensity and microstructure of the grain. A wide variety of zircon types are observed in greenschist facies metasediments. Zircon that has a typical high BSE signal intensity, regardless of zoning variations will be referred to as “light BSE zircon” from hereon. However, many zircons have areas with a distinctive lower BSE signal intensity than that of a typical, light BSE zircon. From hereon, lower BSE signal intensity zircon will be referred to as “dark BSE zircon”.

Zircon in greenschist facies rocks can be split into the following groups:

- Light BSE zircon
- Fractured zircon
- Dark BSE zircon
- Porous zones in zircon
- Zircon with outgrowths of zircon and xenotime



The following examples are essentially a representation of the wide variety of textures and microstructures observed in and associated with zircon in the rocks studied.

3.4 General zircon distribution and character

Zircon grains are easily distinguished from the matrix in BSE by their high mean atomic number. The great majority of zircons found in the greenschist facies metasediments represent originally detrital grains. Grains composed entirely of light BSE zircon indicate that the grain is essentially unmodified since it was incorporated into the sediment during deposition. Zircon either has a random distribution or is concentrated in heavy mineral bands and therefore represents the original sedimentary layering of the rock (Fig. 4a&b). This is testament to detrital origin of the zircon in these rocks. The characteristics of the zircons in each of the groups of rocks studied is summarised in Table 1 and Figure 5.

Slates and phyllites contain an average of 700 zircons per thin section (Table 1). Zircon ranges from 2-40 μm in diameter and average 5-10 μm . Individual zircons in quartzites and psammities, are not as abundant (*c.*200 grains per thin section) but are generally larger with an average diameter of *c.*30 μm but ranging 5-120 μm . Larger zircons (>30 μm) are typically subhedral to well-rounded with occasional euhedral grains (Fig. 4c) with some zircons found as inclusions in large (>100 μm)

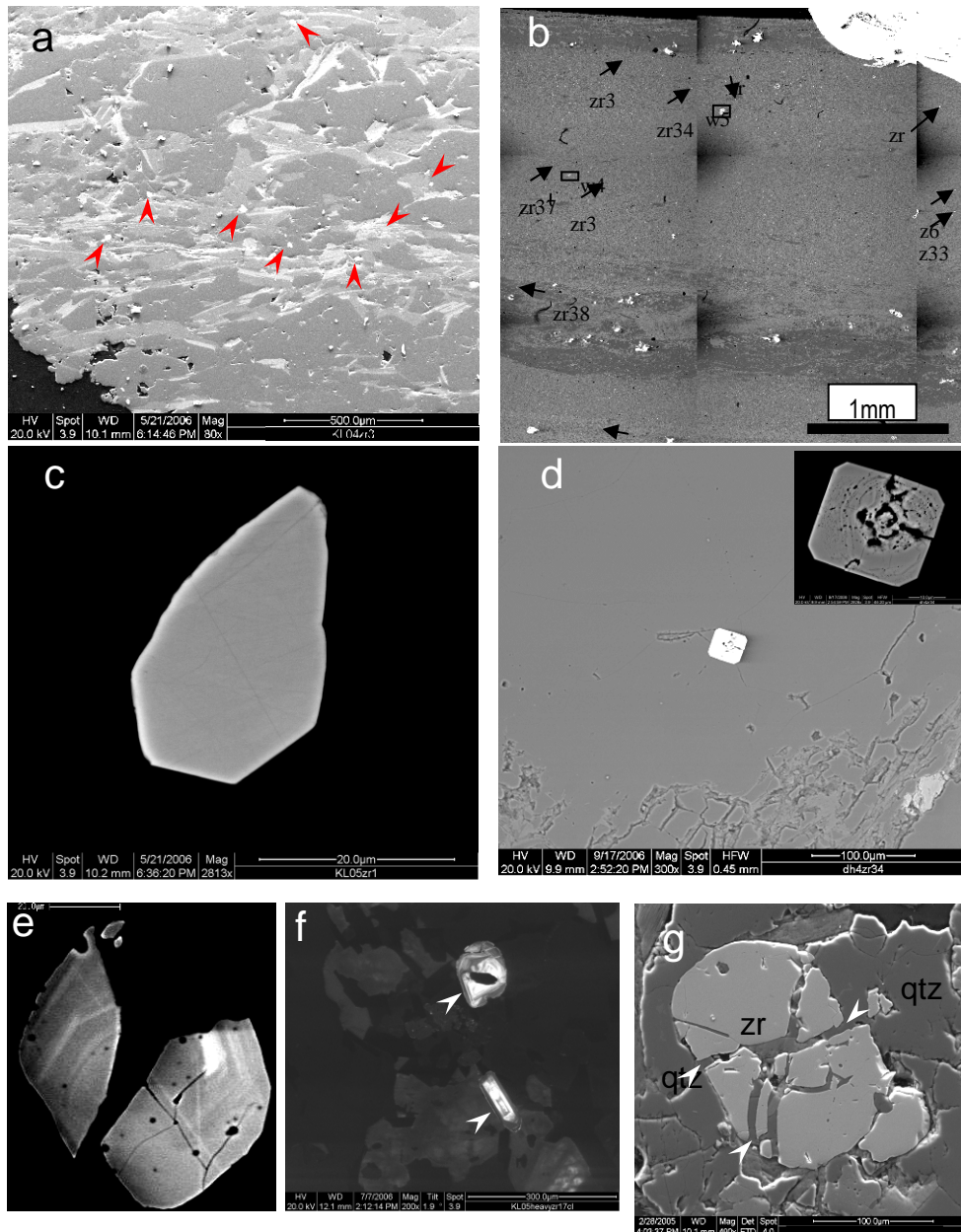


Figure 4. Images depicting the textural variation in zircon and its distribution in greenschist facies rocks

a SE image of heavy mineral layer. Arrow points to zircons (KL04). **b** BSE image of thin section BAL1B showing zircon distribution. **c** BSE image of zircon euhedral margins (KL05). **d** BSE image of euhedral zircon inclusion in quartz. Inset is high contrast, low brightness image of same zircon showing small concentric holes and large irregular holes within the interior (Dh4). **e** CL image showing oscillatory zoning that has been truncated by fracturing (KL05). **f** CL image. Arrows point to zircon. Lower zircon showing euhedral zoning and upper zircon showing complex internal zoning with outer sector zoning (KL05h). **g** SE image of zircon with fractures in-filled with quartz (KL05).

Sample	Rock type & grain size	Total no. of zircons per section*	Zircon size distribution	Completely unmodified zircon	Fragmented zircon	Dark BSE zircon	%age of zircon with zircon outgrowths	%age of zircon with xenotime outgrowths
KL-01	Quartzite, c.50-100µm	236	5-50µm, Av=20µm	83%	7%	10%	Absent	Absent
KL-02	Quartzite, 100-200µm	92	10-50µm, Av=40µm	87%	4%	9%	Absent	Absent
KL-03	Quartzite, 100-300µm	63	5-100µm, Av = 40µm	76%	5%	19%	Absent	Absent
KL-04	Quartzite, 30-300µm	424	5-50µm, Av=30µm	78%	7%	15%	1%	Absent
KL-05	Quartzite, 100-300µm	100	10-100µm, Av=40µm	43%	21%	36%	3%	Absent
KL-05 heavy	Quartzite, 100-300µm	n.a.						
KL-05 light	Quartzite, 100-300µm	63	5-120µm, Av=20µm	45%	17%	38%	4%	Absent
KL-06	Quartzite, <50-300µm	73	10-30µm, Av=20µm	62%	4%	34%	Absent	Absent
DH4	Psammite, 0.1 - 3mm	350	10-110µm, Av = 30µm	37%	18%	45%	18%	5%
BAL 3	Phyllite, 5-100µm	900	5-70µm, Av = 20µm	69%	13%	18%	3%	40%
E1	Slate, <5-10µm	1591	10-40, Av = 20µm	23%	2%	74%	42%	7%
EAS1	Slate, <5µm	n.a.						
BAL 1	Slate, <5-10µm	608	<5-30µm, Av = 10µm	42%	Absent	58%	58%	63%
BAL 1a	Slate, <5-10µm	805	<5-30µm, Av = 5µm	43%	Absent	57%	48%	61%
BAL 1b	Slate, <5-10µm	n.a.						
BAL 1c	Slate, <5-10µm	600	<5-20µm, Av = 5µm	0%	Absent	100%	17%	42%
BAL 1d	Slate, <5-10µm	627	<5-30µm, Av = 10µm	37%	Absent	63%	53%	47%
DH1	Slate, <5µm	684	<5-30µm, Av = 5µm	39%	5%	56%	67%	Absent
DH2	Slate, <5-10µm	1050	<5-30µm, Av = 10µm	63%	Absent	37%	73%	3%
DH3	Slate, <5-10µm	n.a.						
DH3A	Slate, <5-10µm	n.a.						
DH3B	Slate, <5-10µm	750	5-40µm, Av = 10µm	53%	Absent	44%	33%	6%
DH3C	Slate, <5-10µm	n.a.						

Table 1 Rock types and the relative proportion of zircon textures in greenschist facies rocks. *number has been calculated (see text). n.a. – not analysed.

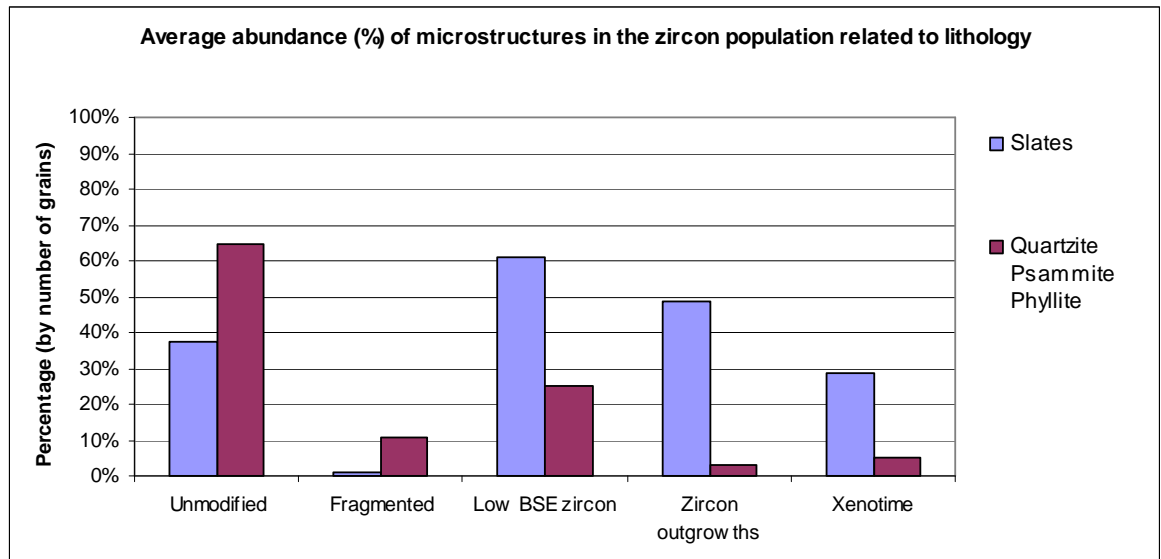


Figure 5 Distribution of zircon textures with respect to lithology.

quartz grains (Fig. 4d). Smaller zircons (<30 μ m) have a greater variety of shapes from well-rounded oval grains to those with sharp, angular margins.

At least 10% of the zircons examined are characterised by being partly composed of dark BSE zircon (Fig. 6). Zircon containing dark BSE zircon represents on average *c.*25% of the population by number, in quartzites and psammities and *c.*60% in slates and phyllites. Slates have a much lower percentage of zircon that is completely unmodified (av.35%) i.e. composed entirely of light BSE, than quartzite, psammite and phyllite samples (av.65%). Zircon outgrowths are present on average around 50% of the zircon in slates and xenotime outgrowths are commonly found in association with these. Xenotime outgrowths can be particularly abundant on the margins of zircon (over 60% of zircon) in some slates (Fig. 18a-c) and are occasionally found on the irregular surfaces of dark BSE zircon (Fig. 18d). Xenotime outgrowths are found on an average of 30% of the zircons in slates (Table 1) and, although less common, on an average of *c.*5% of zircons in quartzites. Xenotime can be relatively abundant in psammities, forming large outgrowths (upto 12 μ m) on upto 40% of zircons (Fig. 18e).

In rocks where dark BSE zircon dominates the zircon population (BAL1c, Table 1), zircon outgrowths are not particularly common. However, when dark BSE zircon is found in more modest amounts e.g. samples E1, BAL1, Dh1, Dh2, zircon outgrowths are found in much greater abundance. In a few rocks with particularly high numbers of zircon outgrowths, xenotime is scarce or absent.

Around 10% of zircon grains in quartzites and psammities are fractured. Fractures cross-cut the internal zoning (Fig. 4e) and are generally found associated with larger ($>30\mu\text{m}$) zircon. Fractures can be multiple, sometimes forming at $c.60^\circ$ and 120° to one another (Fig. 4g), or isolated single cracks (Fig. 4e). Such fractures are often filled with quartz (Fig. 4g). Zircon grains in slates and phyllites rarely contain fractures.

BSE and CL images of zircon in both quartzite and slate reveal a range of zoning types including completely homogeneous grains, those with simple sector zoning, concentric and oscillatory zoning and zircon with discrete cores and thick homogeneous rims (Fig. 4c, 4e&f).

3.5 Dark BSE zircon

Areas of zircon that emit a low BSE signal equate to a lower mean atomic number and are easily identified from unmodified zircon using high contrast, low brightness BSE images. The boundary between light and dark BSE zircon is typically well defined. These boundaries can be straight and follow the euhedral zoning patterns of the grain (Fig. 6e&6f) but curved boundaries (Fig. 6a) or slightly irregular boundaries with thin laths ($c.1\mu\text{m}$ thick) of light BSE zircon fingering between dark BSE zircon (Fig. 6d) are also observed. Light BSE zircon in association with dark BSE zircon is typically fractured perpendicular to the grain edge (Fig. 6b&d). SE images show that there is a topographic difference between light and dark BSE zircon on the polished surface with light BSE zircon standing slightly proud. This is most evident when the stage in the SEM is tilted to 70° (Fig. 6g). The difference in topography is too small to accurately measure but estimated at $c.<100\text{nm}$.

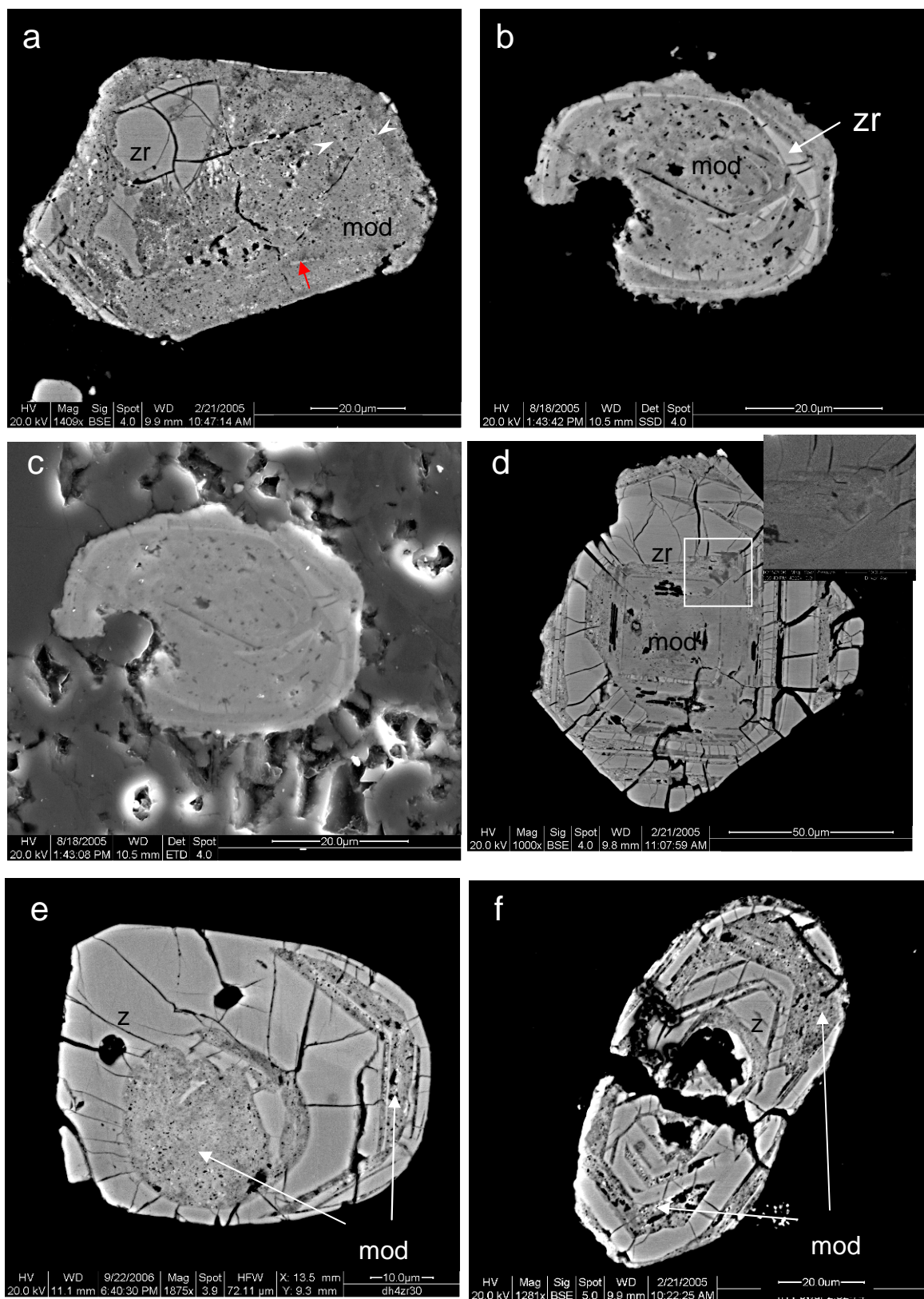


Figure 6 For caption see page 28

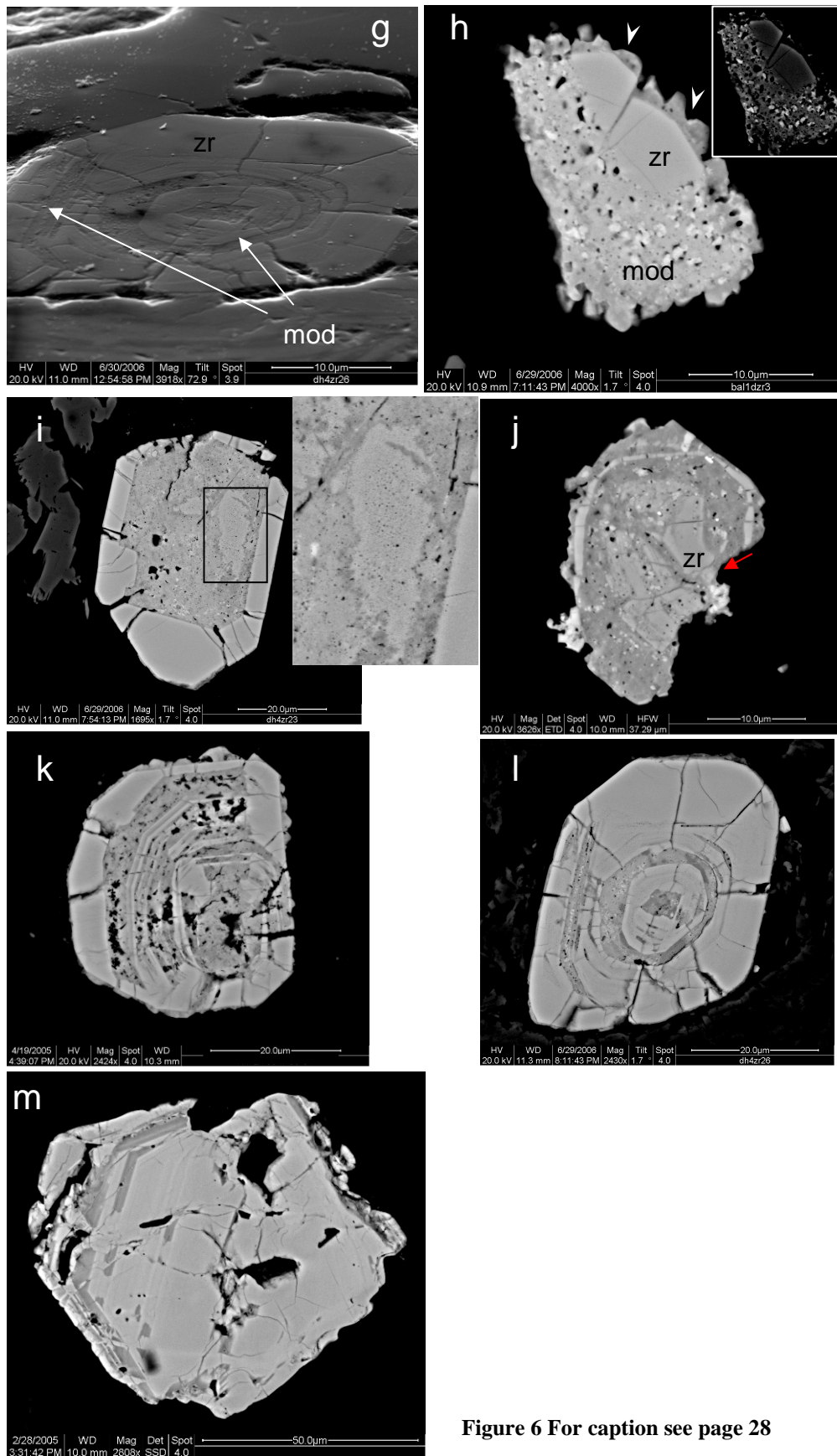


Figure 6 For caption see page 28

Figure 6. Images of zircon containing dark BSE zircon

All BSE images unless stated otherwise. Mod = dark BSE zircon, zr = light BSE zircon. **a** Zircon shows weak zoning (arrowed) parallel to grain edge within dark BSE area. Dark BSE zircon has significant variation in BSE intensity. There are fractured domains of unmodified zircon with some margins that have very fine irregularities. High BSE intensity inclusion is xenotime. The grain has light BSE segment margin (Dh4). **b** Dark BSE zircon with thin laths of concentric light BSE zircon that follow roughly the outline of the grain shape. Dark BSE zircon has highly irregular margins with the matrix and internally has irregularly shaped pores and contains inclusions (EAS1). **c** SE image of **b** illustrating irregular margins with matrix and inclusion and pore-rich microstructure. **d** Concentric zoned zircon with dark BSE core and outer layer of radially fractured light BSE zircon. Inset is an enlarged SE image of defined areas showing fingers of light BSE zircon within dark BSE core (Dh4). **e** Dark BSE core with concentric outer radially fractured light BSE zircon zoned. Dark BSE zircon zones on the outer margin of the grain are absent of radial fractures. Dark BSE core has patches of variable BSE intensity and very fine pores. Outer dark BSE layer has larger pores and contains very thin laths of light BSE zircon (Dh4). **f** Oscillatory dark BSE/light BSE zoned zircon. Central core has experienced significant dissolution with large crack into the centre of the grain. Dark BSE zircon has pore-rich microstructure also containing xenotime inclusions (Dh4). **g** SE image of **6l** of zoned light and dark BSE zircon with SEM stage tilted to 70°. This reveals that dark BSE zircon is topographically polished down in with respect to dark BSE zircon (Dh4). **h** Light BSE zircon encased by dark BSE zircon and zircon outgrowth (arrows). Inset is high contrast, low brightness image showing xenotime inclusion in dark BSE zircon microstructure (BAL1D). **i** Outer light BSE radially fractured zone with dark BSE interior. Within dark BSE interior is frilly edged higher BSE intensity area that is unmodified (as determined by EDX analysis). Inset shows pores in light BSE and dark BSE domains (Dh4). **j** Dark BSE zircon with thin concentric bands of light BSE zircon and a light BSE domain in the core. Arrow points to rounded bay in margin. Margins are also very irregular on the left side of the grain with but a euhedral boundary on the top of the image. High BSE intensity inclusions are xenotime (BAL 1B). **k** Concentric zones of light BSE/dark BSE zircon with zircon outgrowths on the margin. Dark BSE areas have large cavities as a result of dissolution. (E1). **l** Oscillatory light BSE/dark BSE zones zircon with radial fractures in light BSE zones. Porous zircon bands in light BSE zircon. Dark BSE zircon contains xenotime inclusions (Dh4). **m** light BSE zircon containing thin bands of dark BSE zircon that follow a euhedral shape. Dark BSE zircon has a microstructure completely absent of holes, cavities or inclusions. Light BSE zircon constrains large irregular features that are the result of dissolution. Irregular margins around the edge of the grain are a result of dissolution (KL05h).

Dark BSE zircon characteristically has a mottled BSE contrast or contain blotches or patches of higher BSE contrast material (Fig. 6a,b,d,e,g). Variations in the BSE intensity of dark BSE zircon is also observed as higher BSE intensity bands that run parallel to the edges of the grain (Fig. 6a). Zircon with slightly higher BSE signal intensity in these areas form irregularly-shaped frilly edged domains several μm 's across (Fig. 6i) but thin streaks (Fig. 6a) or nm-sized specks and blotches (Fig. 6f, 6h, 6j) are also observed.

Dark BSE zircon can contain an abundance of spherical to oval shaped pores ($<0.3\mu\text{m}$, after Rouquerol et al. (1994)), isolated cavities and inclusions (Fig. 6). Inclusions range from $0.3\mu\text{m}$ upto $12\mu\text{m}$ long and vary greatly in shape from regular and rounded to angular and highly irregular shaped grains (e.g. Fig. 6a, 6h, 6j,7b). Holes, irregular elongate openings and long thin cracks to large, very irregular voids have all been in filled. Where these minerals are large enough to be identified (i.e. $>2\mu\text{m}$), quartz, mica and FeO have been found. Other inclusions are also present as but due to their size, they cannot be easily identified. High BSE contrast grains (on average $<0.5\mu\text{m}$) are common inclusions found within dark BSE zircon (e.g. Fig. 6a, 6h, 6j) (see section 3.5.4). Generally, cavities are more irregular in shape with increasing size. Very occasionally greenschist facies rocks contain dark BSE zircon that completely lacks inclusions and any other microstructural discontinuities (Fig. 6m). Dark BSE zircon such as this has been categorised as Group 2 dark BSE zircon in sedimentary rocks with inclusion-rich dark BSE zircon referred to as Group 1 dark BSE zircon. This is explored further in Chapter 4. However for the purpose of this chapter, it will simply be referred to as dark BSE zircon.

Dark BSE zircon is most commonly found in the cores of zircon grains or particular growth layers or between zones of otherwise unmodified zircon (Fig. 6d, 6e, 6f, 6i, 6k, 6l). In such instances, dark BSE zircon is usually enclosed within unmodified zircon and has an overall shape typical of any other detrital unmodified zircon in that thin section. However where dark BSE zircon is in contact with the matrix, it can be found in a range of shapes and microstructures.

3.5.1 Dark BSE zircon adjacent to matrix in slates, phyllites and psammites

Dark BSE zircon displays small irregularities on its margin where in contact with the matrix in slates and phyllites (Fig. 7a-d & 6b,c,f,h,j). Unmodified zircon can be found within or partly surrounded by irregularly formed dark BSE zircon (Fig. 7c & 6h). Higher magnification images of the margins of dark BSE zircon reveal that the edges are a succession of very small ($<0.1\text{-}3\mu\text{m}$) jagged undulations, bays or frills (Fig. 8). Bays ($<0.5\text{-}3\mu\text{m}$ deep) can be U-shaped (Fig. 7a), rounded crescents (Fig. 6j), angular (Fig. 7d & 8) or irregular elongate inlets upto $2\mu\text{m}$ deep (Fig. 7b). Curved or irregularly shaped spines (upto $3\mu\text{m}$ long, $<0.2\mu\text{m}$ wide), sharp serrations ($<0.5\mu\text{m}$ deep), delicate bulbous ($<0.2\mu\text{m}$ deep) margins and $<0.1\mu\text{m}$ thin wisps of dark BSE zircon finger between matrix grains (Fig. 3a,d & Fig.8). Incomplete half hexagons, pyramids and sub-cubic shapes are also found along the margins with minute ($<200\text{nm}$) undulations on them (Fig. 6a, 6b & 7b). Occasional large ($10\mu\text{m}$) horseshoe-like bays (Fig. 6b) are also observed where the grain contains predominantly dark BSE zircon. However, occasionally margins of dark BSE zircon preserve euhedral edges (Fig. 7d). Despite the irregular features on the margins of dark BSE zircon, most still maintain a similar shape to that of unmodified detrital zircons in the rock (Fig. 6a, 6b, 6j).

3.5.2 Dark BSE zircon in contact with quartzite matrix

In quartzites, margins of dark BSE zircon are anhedral but more rounded than those in phyllosilicate-rich lithologies (Fig. 9). They are punctuated by a series of $<0.5\mu\text{m}$ deep nicks, slightly deeper ($0.5\text{-}5\mu\text{m}$) U-shaped notches (Fig. 9d) and cove-like bays ($2\text{-}5\mu\text{m}$ wide and deep) (Fig. 9c, 9d). Commonly, the contact between light and dark BSE zircon does not follow the internal zoning of the grain (Fig. 9a-c) which is in contrast to those in phyllosilicate-rich lithologies. Zircon containing dark BSE domains is observed in close proximity to entirely unmodified zircons with little or no difference in the surrounding mineralogy (Fig. 9a). Some grains preserve rounded $2\mu\text{m}$ domains of light BSE zircon within a matrix of dark BSE zircon inducing a mottled contrast (Fig. 9e) or a patchwork-like texture (Fig. 9f).

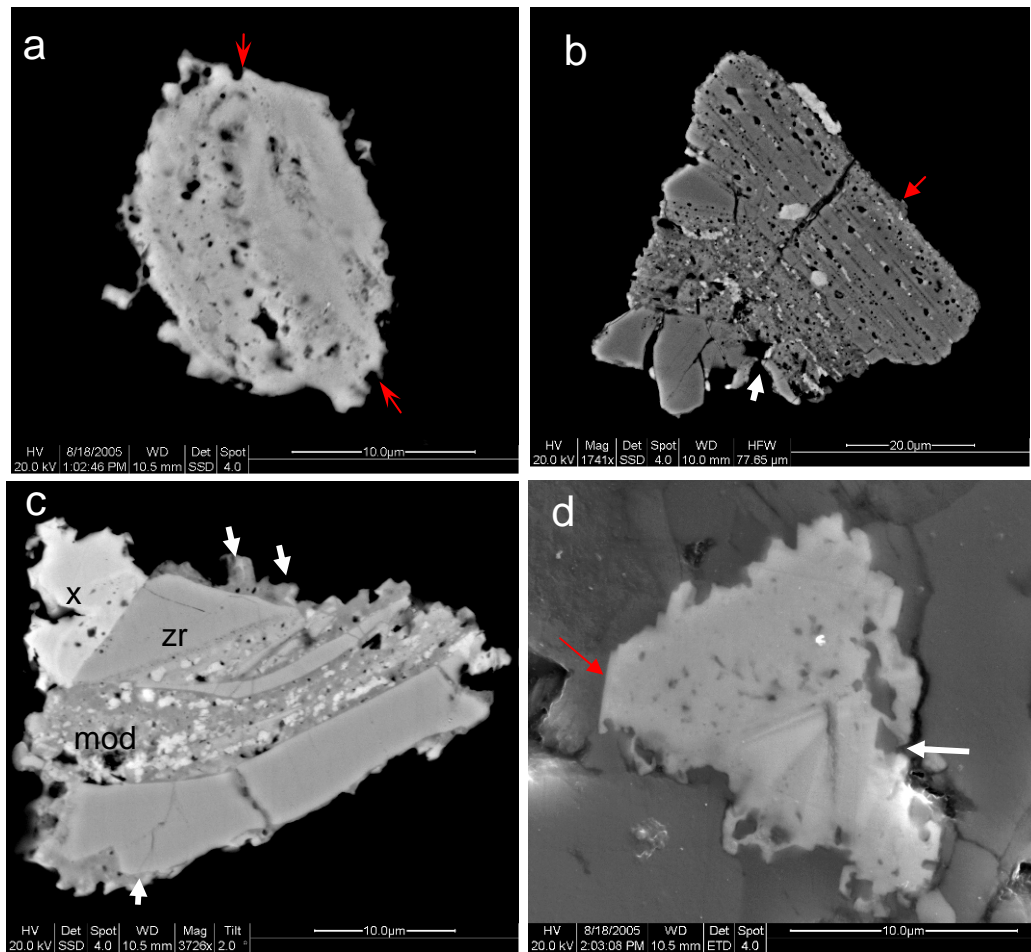


Figure 7. Images of dark BSE zircon in slates

All BSE images unless stated otherwise. **a** Almost completely dark BSE zircon with irregular notched margins (arrow) but also very fine and delicate outgrowth like feature from the margin. Domains of holes and pores and domains free of pores or inclusions (EAS1). **b** Zircon fragment showing alternate zoning of dark BSE/light BSE zircon. Dark BSE zones contain elongate holes aligned to zoning pattern. Bright inclusions of xenotime ranging from <1-10 μ m. Red arrow – sub-hexagonal margin with minute undulations, white arrow – angular bay into margin (BAL3). **c** Zircon fragment with xenotime (x) outgrowth, light BSE and dark BSE zircon and zircon outgrowths (arrows). Dark BSE zircon has grown out of original growth layer that has apparently “spilled out” and partly engulfed light BSE laths and forming outgrowth-like features on the margins of light BSE zircon (arrows). Dark BSE zircon contains xenotime inclusions (BAL1A). **d** SE image of dark BSE zircon with irregular margins and angular bays (white arrow). Microstructure contains an abundance of inclusions and pores. Red arrows show preserved euhedral margin (EAS1).

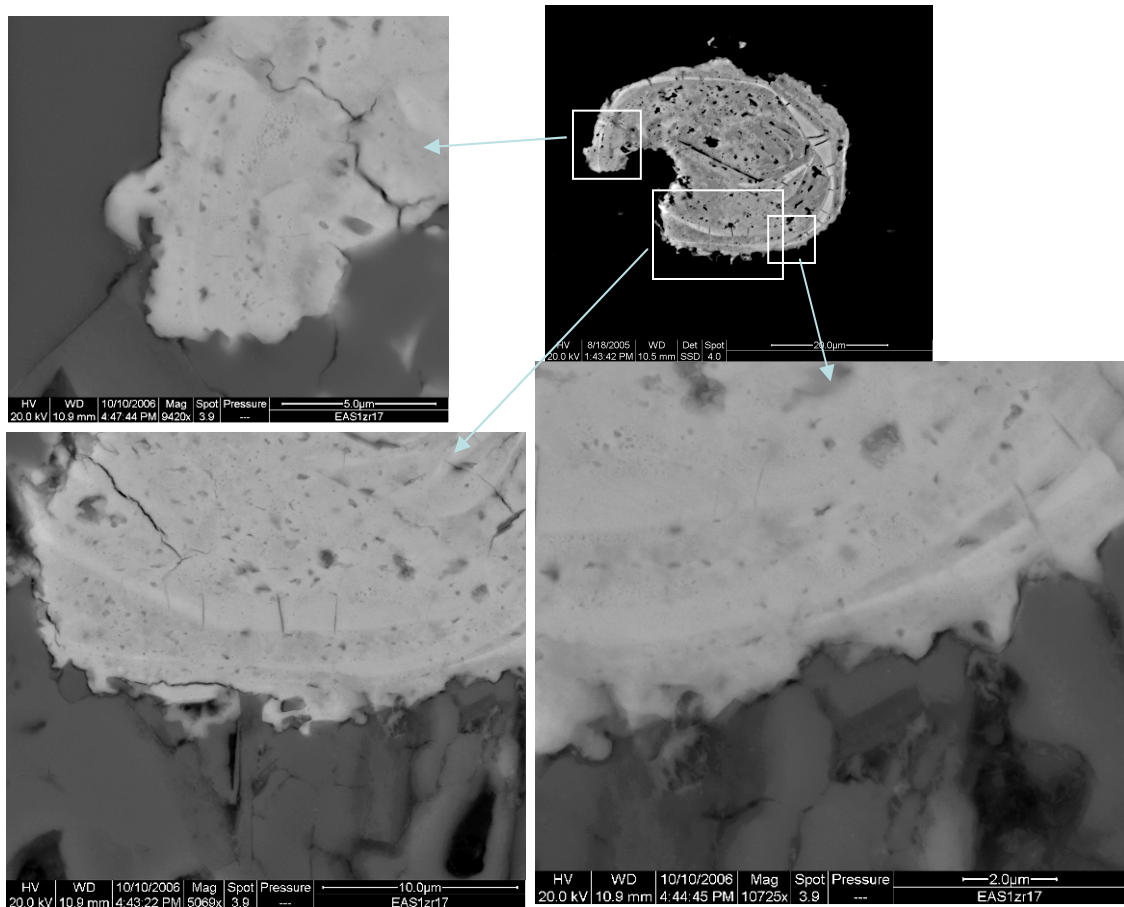


Figure 8. Higher magnification BSE images of Fig. 6b showing the delicate and irregular nature of the margins of dark BSE zircon inter fingering with the matrix. Microstructure contains minute inclusions and pores (EAS1).

Large irregular channels extend between some dark BSE zircon grains and can form elaborate and extensive networks through what were probably once single and complete grains (Fig. 9c). These channels can be long ($c.25\mu\text{m}$) and narrow ($<2\mu\text{m}$) and run between dark and light BSE zircon (Fig. 9b). Channel margins are generally smooth and rounded with occasional angular v-shaped (red arrows, Fig. 9e) or blocky (white arrow, Fig. 9e) clefts. Matrix minerals, most commonly quartz, muscovite, biotite and chlorite (Fig. 9c), are identified in these areas. The size of openings and bays are typically more pronounced, and the margins of dark BSE zircon grains more rounded with the increasing grain-size of the matrix and decreasing phyllosilicate content in the host rock. Often grains appear to have broken up along these channels between light and dark BSE zircon, becoming dispersed within a localised area in the matrix (most commonly quartz) (Fig. 9a-c). Islands of light BSE zircon are typically rounded in such instances (Fig. 9e&f). As with dark BSE zircon in phyllosilicate-rich rocks, these zircons typically retain a rough outline of an original detrital zircon and can occasionally exhibit euhedral grain edges when adjacent to phyllosilicate minerals (Fig. 9c).

3.5.3 Fractures related to dark BSE zircon

Fractures in unmodified light BSE zircon are often spatially associated with areas or zones of dark BSE zircon in the same grain. Multiple fractures frequently radiate from the boundary between dark BSE zircon and light BSE zircon and to the edge of the light BSE zircon (Fig. 6b-f, 6i-l). Such fractures are generally perpendicular to the light - dark BSE zircon boundary and are absent from zones with dark BSE zircon (Fig. 6b-f, 6i-l). Concentric fractures (Fig. 6d) also occur along the boundary between the dark BSE zircon layer and the next outermost light BSE growth zone. Multiple radial fractures, very similar to those described in section 3.5.3, are typically found in light BSE zircon adjacent to porous zones. Fractures are roughly perpendicular to the light BSE zircon-porous layer boundary and often reach the grain edge. Very dark BSE zircon is often located in the porous growth zone near the tip of the fracture. Where this occurs, small zircon outgrowths (see section 3.7.1) may be found at the point where the fracture meets the outer edge of the grain (Fig. 13a).

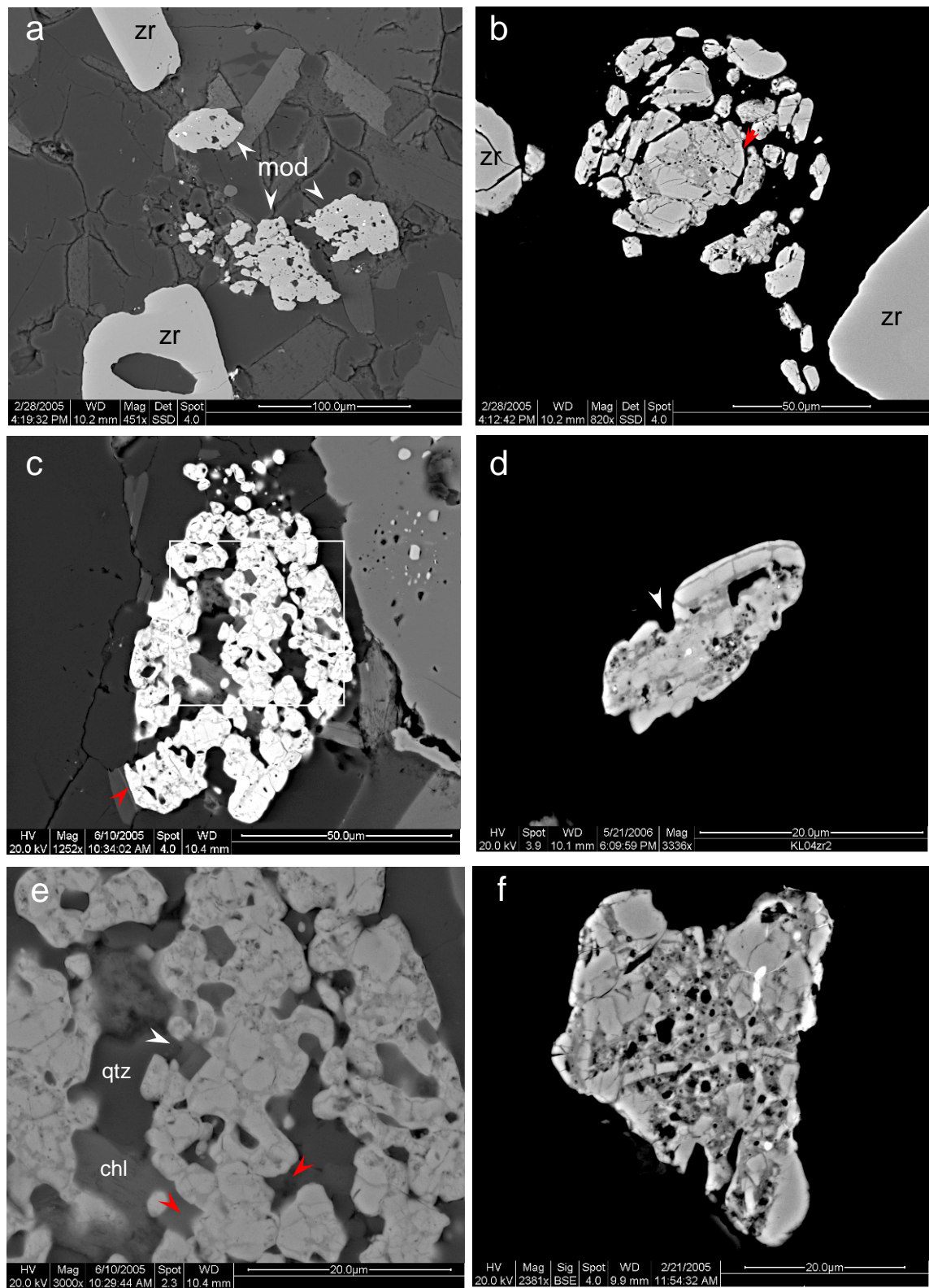


Figure 9. BSE images of zircon containing dark BSE zircon in quartzites. Caption is on next page.

Figure 9. cont.

a Disintegrated dark BSE zircon with abundant inclusions and cavities (mod) with unmodified zircon (zr) in close proximity (KL05h). **b** Central zircon contains dark BSE and light BSE areas with individual rounded zircon fragments. Unmodified light BSE zircons on left and right of image. Arrow points to quartz-fill along grain discontinuities (KL05h). **c** Dark BSE zircon with large matrix filled cavities as a result of dissolution. All margins are rounded and with small rounded grains extending from grain margin at the top of the image. Arrow points to euhedral grain edge preserved (KL05). **d** Dark BSE-light BSE zircon grain with U-shaped notch (arrow). Internally cavities and inclusions the have formed as a result of dissolution (KL04). **e** Enlarged area of c. Shows complex relationship between rounded light BSE zircon domains and dark BSE zircon domains. Red arrow shows v-shaped clefts, white arrow points to blocky shaped bays. Note matrix filled cavities (KL05). **f** Zircon with light BSE and dark BSE complex. Microstructure of light and dark BSE zircon complex is inclusion and pore –rich. High BSE intensity inclusion is xenotime that is also present as an outgrowth (KL05).

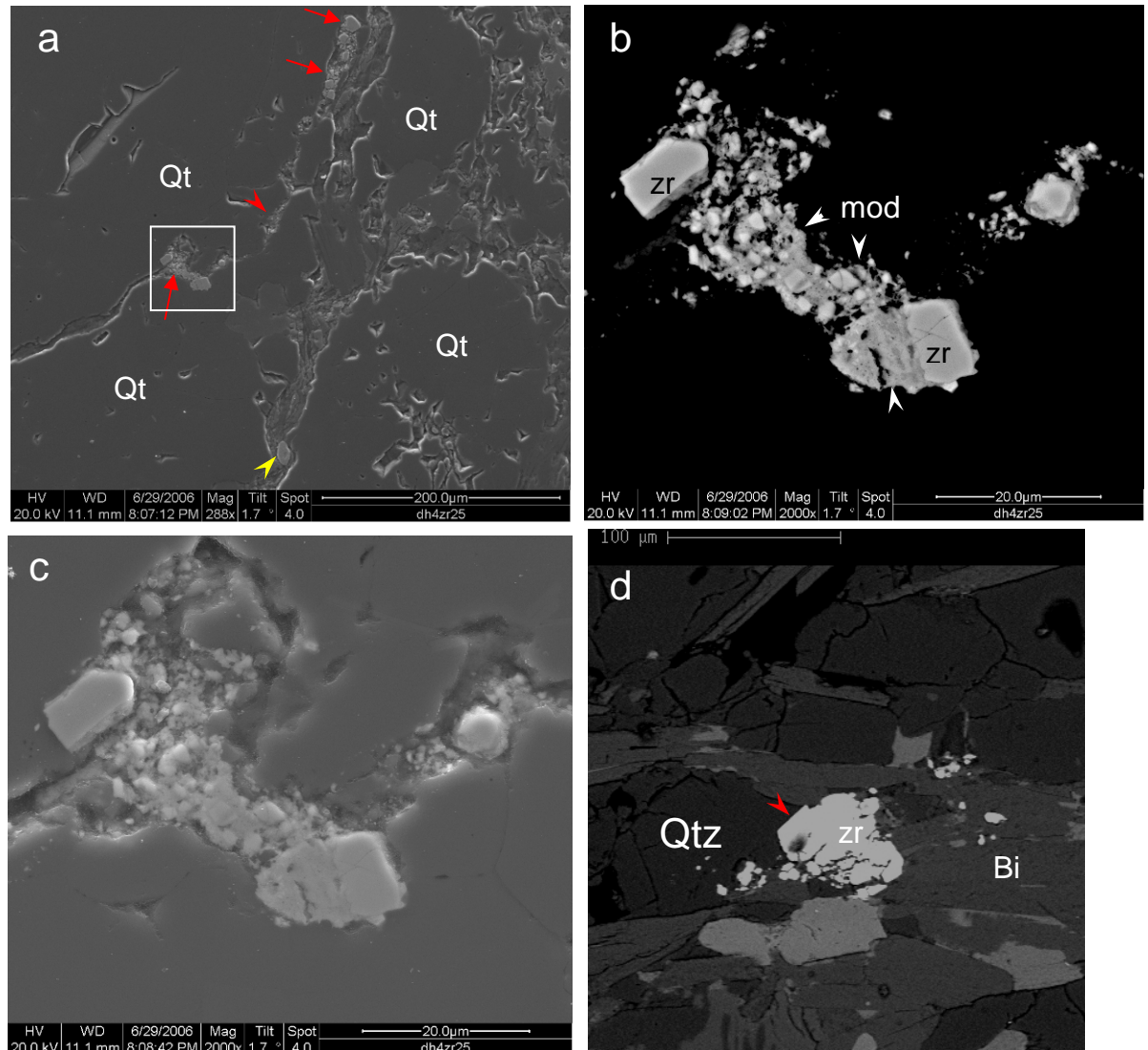


Figure 10. Crushed zircon in quartzites

a SE image with red arrows pointing to dark BSE zircons crushed along quartz grain boundaries. Yellow arrow indicates complete, unmodified light BSE zircon (Dh4). **b** Higher magnification image of area defined in **a**. Crushed dark BSE zircon that is partly surrounding blocks of light BSE zircon with **c** an SE image of the same area. Image shows crushed dark BSE zircon is found between the quartz grain boundaries. **d** BSE image of crushed dark BSE zircon biotite-rich zone of quartzite KL05. Red arrow points to euhedral grain edge preserved against quartz grain. Zircon is anchored in quartz grain with trail of zircon fragments from the parent grain.

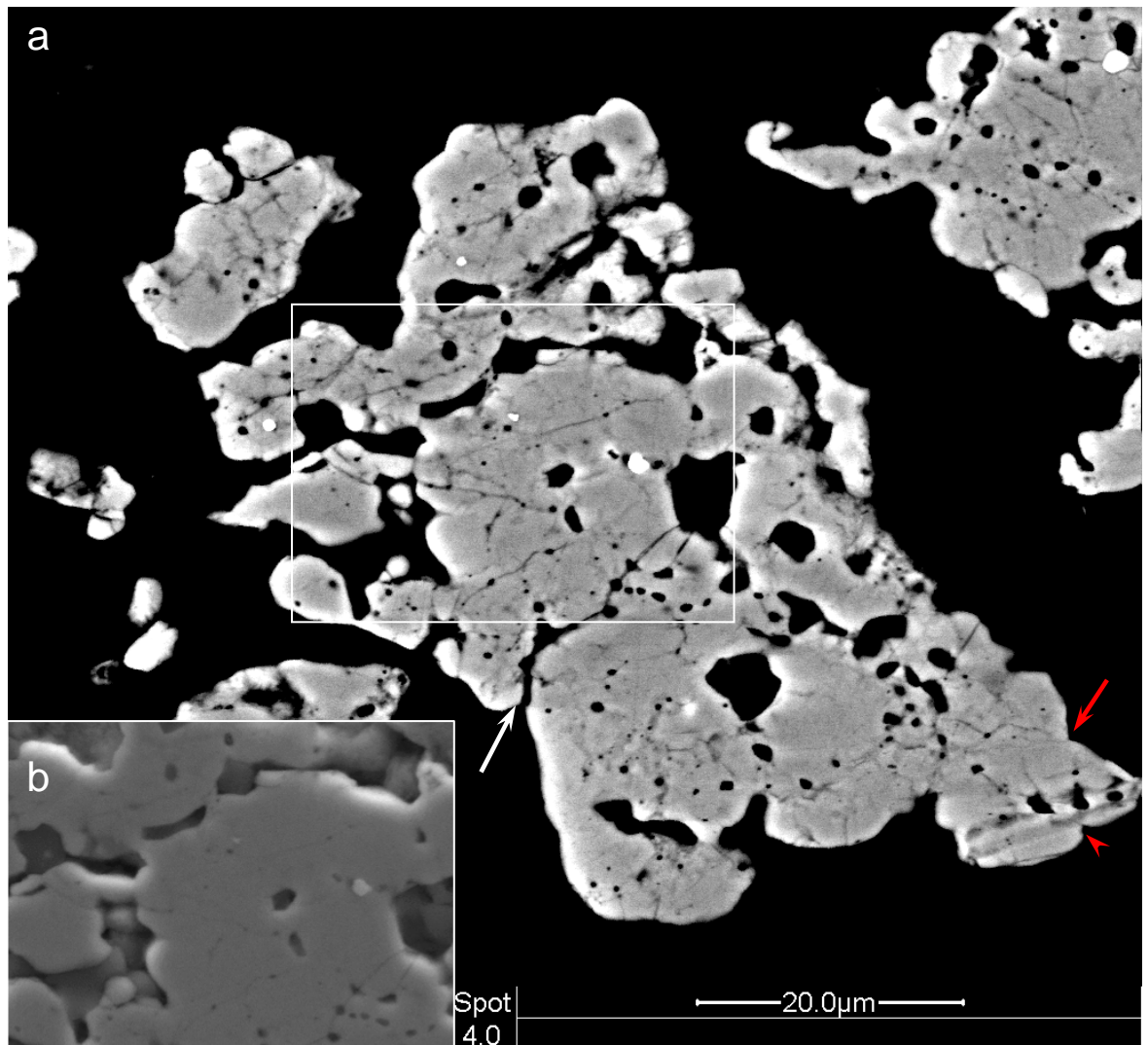


Figure 11. a BSE image of veined and fragmented dark BSE zircon with irregular edges and cavities. Red arrow points to preserved zoning and angular grain edge. Grain has been partly broken up. White arrow points to thin, vein-like inlet (KL05h). High BSE intensity inclusions are of thorite ((Th,U)SiO₄). **b** SE image of a showing veins are filled.

3.5.4 Crushed zircon

Crushed grains of dark BSE zircon are found between the grain boundaries of quartz and in cleavage domains of psammites and quartzites. Crushed, dark BSE zircon often surrounds small (<5 μm), subhedral or equant grains of light BSE zircon. Particles of dark BSE zircon may trail from larger (>10 μm) light BSE zircon cores (Fig. 10). Some light BSE zircon cores have irregular broken grain edges and occasionally preserve euhedral grain edges (Fig. 10d).

3.5.5 Dark veins

Occasionally dark BSE zircon in quartzite displays even darker, thin cross-cutting veins (100-400nm wide) (Fig. 11). Within these veins are a series of interconnected pores (<1 μm) and elongate holes (upto 2 μm long). Veins have a low BSE intensity than the zircon and are in filled (Fig. 11b) although with what cannot be identified. Veining in such zircon is also associated with numerous, slightly irregular shaped cavities 1-10 μm wide. Occasional zoned bands are observed (Fig. 11). Dark veined zircons typically have an anhedral shape with smooth and rounded margins punctuated by notches and inlets similar to those described in section 3.5.2. Around the margins occasional straight and angular grain edges are preserved.

3.5.6 Xenotime and other high BSE contrast minerals

Xenotime is abundant in some of the rocks studied (Table 1) and is commonly found in the pores and cracks within dark BSE zircon (Fig. 12, Fig. 7b,c, Fig.6a,h,j Fig. 9f). Xenotime inclusions are typically 0.2-1 μm in size but have been found upto 8 μm long (Fig. 7b). Inclusions of xenotime generally have highly irregular shapes, often with minute (<100nm) frilly edges (Fig. 3b&7c) and are concentrated in thin linear bands, often aligned parallel to zoning in light BSE zircon. Larger (>3 μm) xenotimes can be more rounded and blotchy in shape and may apparently fill cavities (Fig. 18k).

Some dark BSE zircon contains finer xenotime inclusions towards the rim of the grain (Fig. 12a)

but generally, xenotime size (within 0.2-1 μ m limits) and distribution appears to be random in dark BSE zircon. However, even where xenotime is abundant in dark BSE zircon, holes and cavities may remain empty (Fig. 6h). Zircon with marginal xenotime outgrowths (see section 3.7.2) is also likely to contain xenotime inclusions within dark BSE zircon areas. In xenotime-poor rocks, the cavities and holes in dark BSE zircon are typically empty (Fig. 6k, 7d & 8). No xenotime has been observed as inclusions within unmodified zircon.

Inclusions of thorite (ThSiO₄) and coffinite (USiO₄) are rare but have also been found within dark BSE zircon (Fig. 9g, 11, 12a) from slates as well as psammites and quartzites.

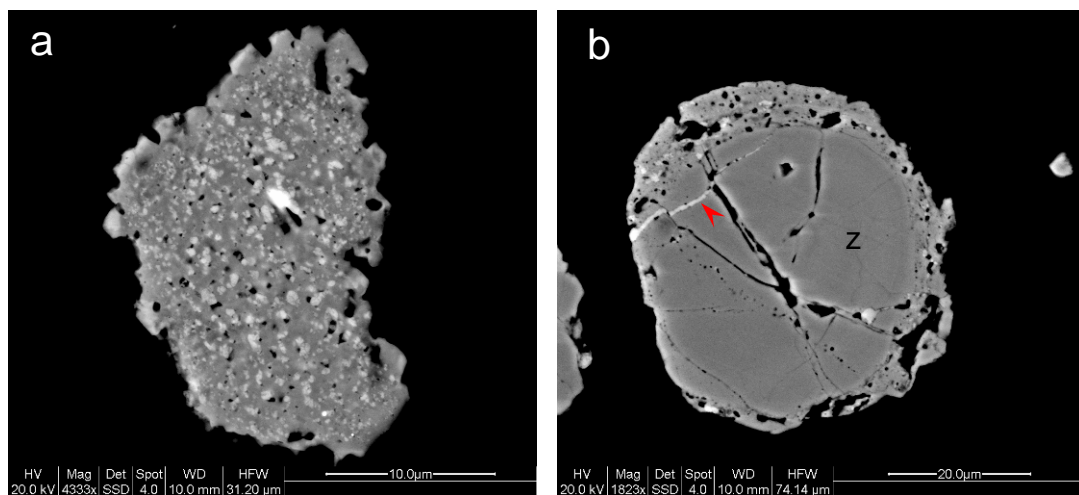


Figure 12. BSE images of zircon containing high mean atomic number inclusions.

a Dark BSE zircon with abundance of pores and inclusions in the microstructure and highly irregular margins. Bright inclusions are of xenotime with very bright central inclusion of coffinite (BAL1C). **b** Light BSE zircon grain with fractures and outer dark BSE zircon rim. Dark BSE zircon margins are irregular in shape and contain inclusions and holes. Red arrow points to xenotime-filled fracture. Note that fractures do not continue in dark BSE zircon (BAL3).

3.6 Porous zones in zircon

A small proportion of zircons (<3%) have particular light BSE zones or domains that contain dark BSE spots (Fig. 13) and these areas are often found in multiple zones of the same grain. Spots are generally spherical to oval in shape and upto 300nm wide. Spots typically have a relatively constant size within the same growth layer. However, occasional grading in the spot size has been observed in some zones, typically coarsening in the direction of the grain edge (Fig. 13a). Spots are normally relatively evenly distributed but the abundance of individual spots does vary from very high concentrations where they are almost touching to very few, sparsely distributed spots (Fig. 13a & 6l). The slightly higher contrast around the edge of these spots in SE images (Fig. 13c) would suggest that these may be pores within the zircon.

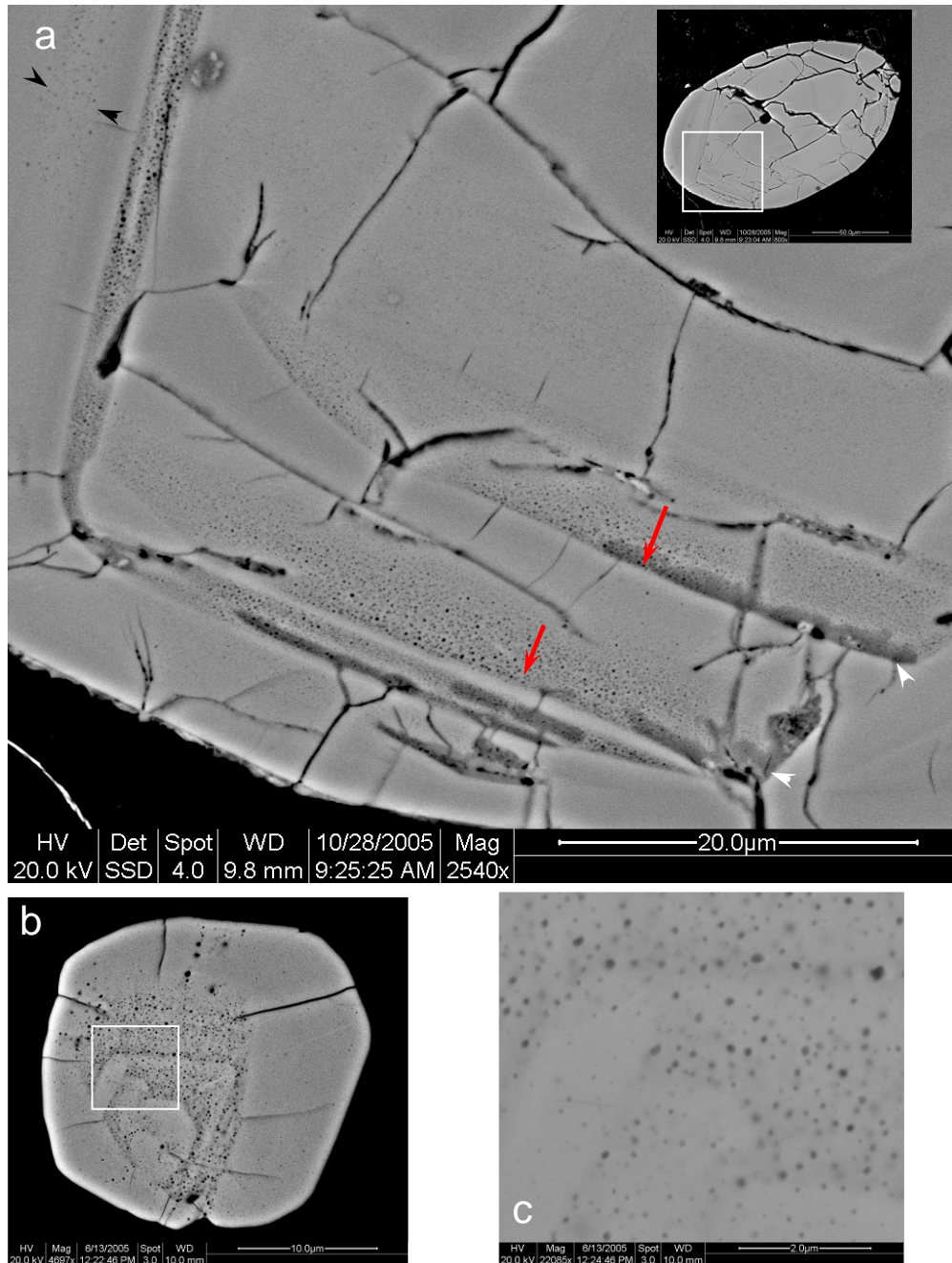


Figure 13. Images of porous zones in zircon

a BSE image of zoned zircon with porous zones that show size grading (red arrow, coarsening in direction of arrow) and band with sparsely distributed pores (black arrow). White arrows show light BSE areas that are linked to fractures. Inset shows whole grain with enlarged area. Note zircon outgrowths on the edge of the zircon grain that are spatially linked with dark BSE zircon (Dh4). **b** BSE image of zoned zircon with porous zones and radial fractures related to porous zones (KL05). **c** Higher magnification SE image of area defined in b.

3.7 Features on the margins of unmodified zircon

3.7.1 Zircon outgrowths on unmodified zircon

In phyllosilicate-rich rocks, zircon outgrowths (Fig. 14) are found on the grain margins of about 50% of the zircons (by number) in the rock. Zircon outgrowths cut across the internal zoning patterns of the host (Fig. 14a) and also found on the surfaces of broken detrital zircon grains that have been fractured in-situ (Fig. 14c). Zircon outgrowths typically protrude 2-3 μm into the matrix but range from <1 μm to 5 μm . They can be found as isolated, individual crystals (Fig. 14g-i) or in clusters (Fig. 14a, d-g, j-l). The latter take the form of either an engulfing crust when the host grain is completely surrounded (Fig. 15a&b) or a partially enclosing crust where outgrowths appear only on parts of the host (Fig. 15c, 14e-g). Zircon outgrowths also have a wide range of habits: rounded sub-hexagonal blocks (Fig. 15d, 14g); bulbous (Fig. 14a); jagged, saw-tooth serrations (Fig. 14c,d,h,j); individual euhedral prisms (Fig. 14a&14h); wispy and frilly shaped (Fig. 15b, 15e, 14k). A great variety of these forms may occur on the same zircon. Only zircon that entirely encloses the host zircon grain should be referred to as overgrowths (Dempster et al., 2004), with all other instances described as outgrowths (Rasmussen, 2005b).

Fingers of zircon within outgrowths often project into matrix grains of muscovite, chlorite and quartz (Fig. 15b, 15c, 15e & 14b, 14d, 14g, 14l). Outgrowths of zircon with euhedral grain edges have only been observed when adjacent to phyllosilicate minerals (Fig. 15e, 14b). Although identification is difficult due to the size of inclusions, zircon outgrowths do contain inclusions of quartz and phyllosilicate (Fig. 14b) and can occasionally be very inclusion-rich (Fig. 15a&b). Zircon outgrowths are notably absent in some instances when the host grain is adjacent to large (>30 μm) quartz grains (Fig. 14g, 15c). However, in other instances zircon outgrowths form adjacent to quartz in preference to other surrounding grains (Fig. 17). Zircon outgrowths are not orientated in the direction of the fabric in the rock and show no preference for a particular face or location on the host crystal, irrespective of where grain boundaries occur in the matrix surrounding the zircon. High magnification SE images of zircon outgrowths reveal as well as an inclusion-rich microstructure, they also contain an intricate network of pores (Fig. 15f).

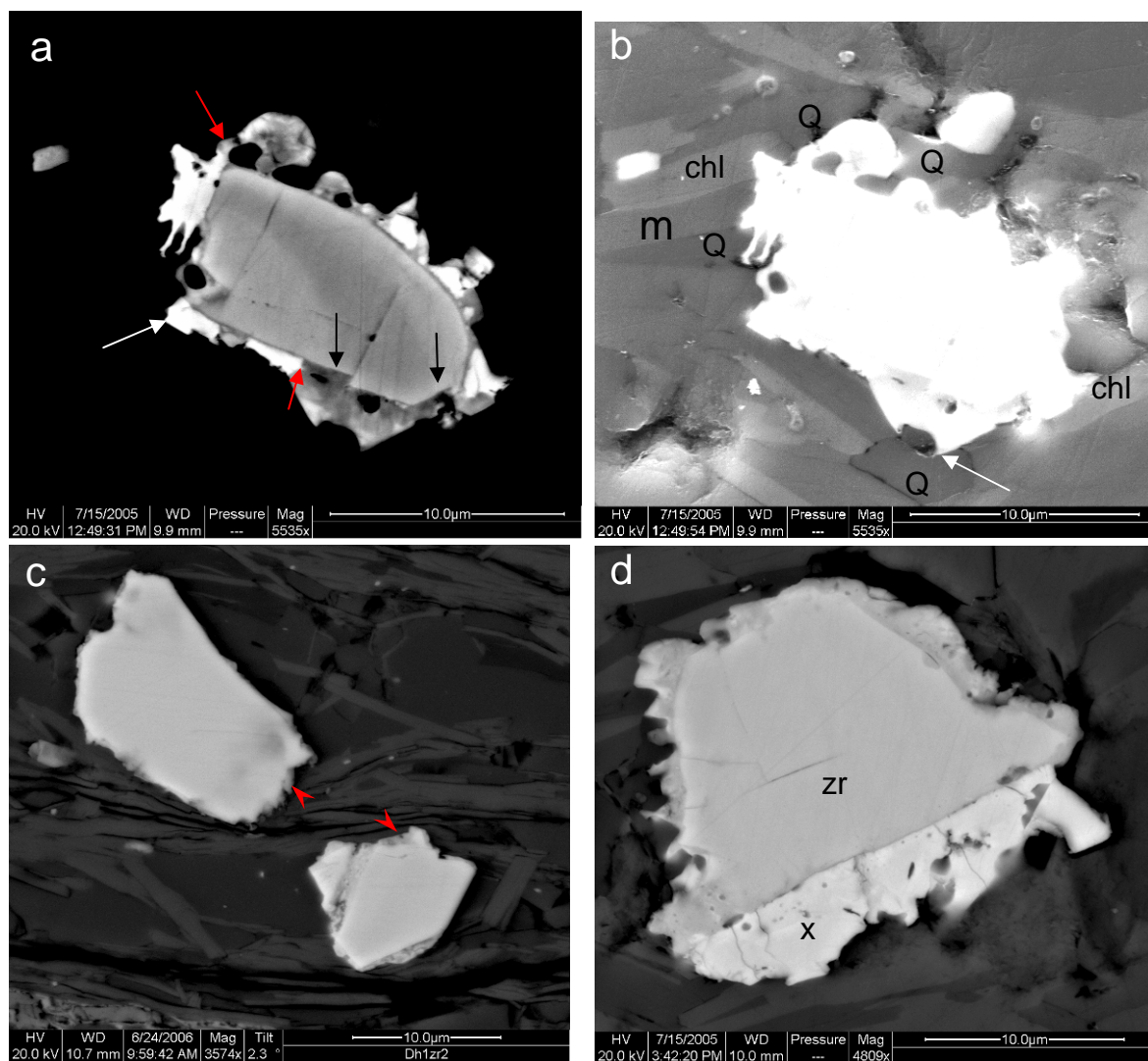


Figure 14. Images zircon and xenotime outgrowths on the margins of zircon. Caption is on page 45.

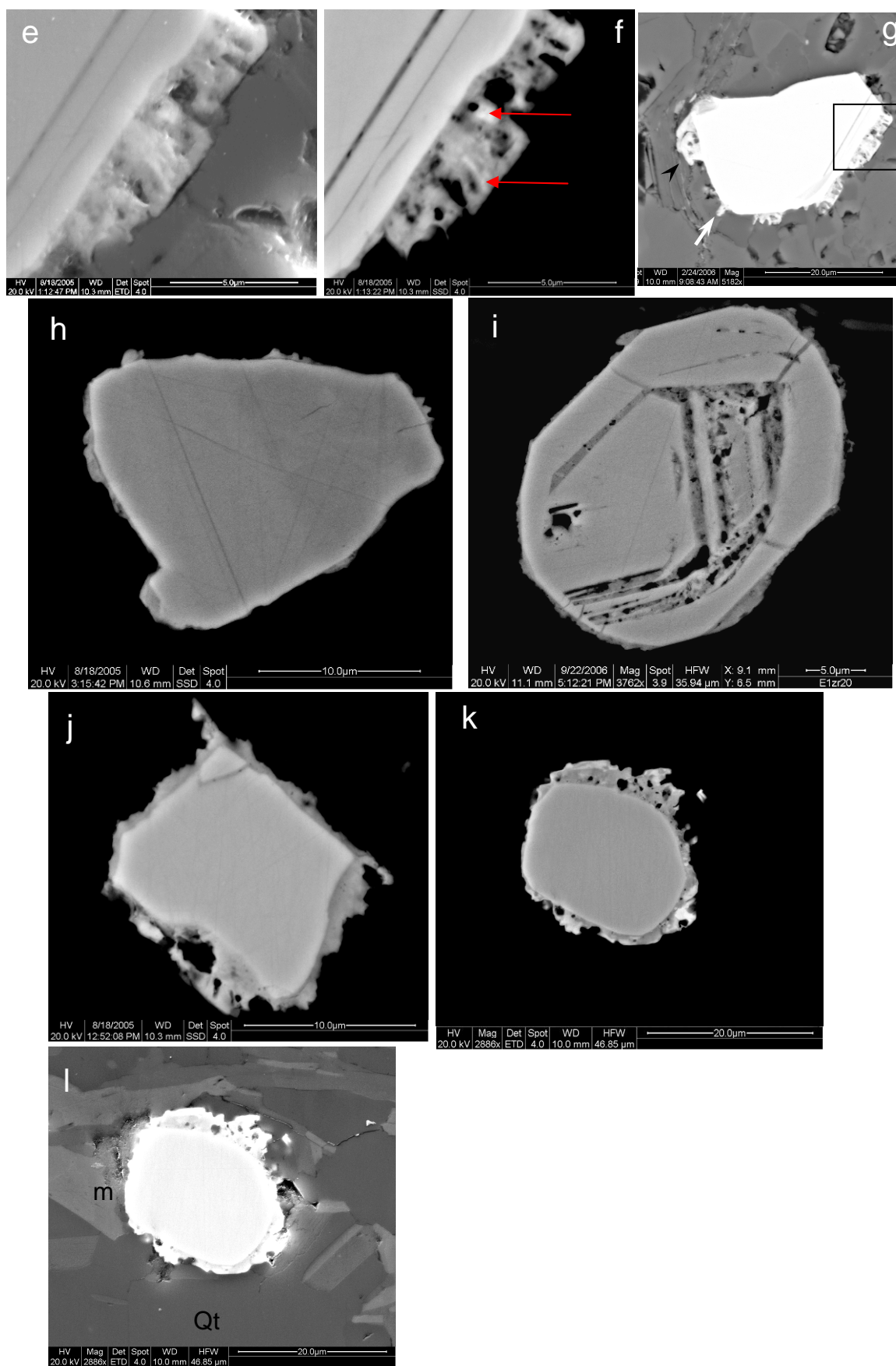


Figure 14. Images zircon and xenotime outgrowths on the margins of zircon. Caption is on page 45.

Figure 14. Images zircon and xenotime outgrowths on the margins of zircon.

All images BSE unless stated otherwise. **a** Rounded host zircon with zircon and xenotime outgrowths (xenotime – white arrow). Black arrow shows where host zoning is truncated by outgrowth. Red arrow points to interactions of zircon and xenotime outgrowths (top is transitional boundary and lower a spike of xenotime points into zircon outgrowth) (BAL1B). **b** SE image of **a** displaying outgrowth interactions with surrounding mineralogy. White arrow shows zircon outgrowth enclosing quartz grain. **c** Very fine zircon outgrowths on the broken margins of a fractured zircon grain (Dh1). **d** Zircon with zircon and xenotime outgrowth. Zircon outgrowths are pyramidal on left hand side of the grain while the right hand side has more rounded appearance (BAL1C). **e** and **f** are enlarged complementary SE and BSE images respectively of area in **g** (EAS1). **e** shows topographic variations within outgrowths and also inclusions within the microstructure, arrows in **f** show xenotime grains in zircon outgrowths while **g** shows sub-hexagonal outgrowths (black arrow) and lobe like outgrowths (white arrow) and relationship to surrounding mineralogy. **h** Host zircon with isolated jagged (top and right margins) and blocky (left hand side) outgrowths (Dh2). **i** Sub-hedral zircon grain with frilly outgrowths (top of grain) and sub-hexagonal outgrowth (bottom right margin) on the margin of zircon that has light BSE –dark BSE zone interior. Dark BSE zircon has cavity-rich microstructure and occasional fractures in light BSE zircon that have been sealed by dark BSE zircon (EAS). **j** Zircon with homogeneous frilly and jagged zircon outgrowths (EAS1). **k** Rounded detrital zircon with variable BSE intensity zircon outgrowths. Bright mineral in outgrowths is xenotime (BAL1B). **l** SE image of **k** showing outgrowth interactions with surrounding mineralogy, m=mica qtz=quartz and inclusions in the zircon outgrowth microstructure.

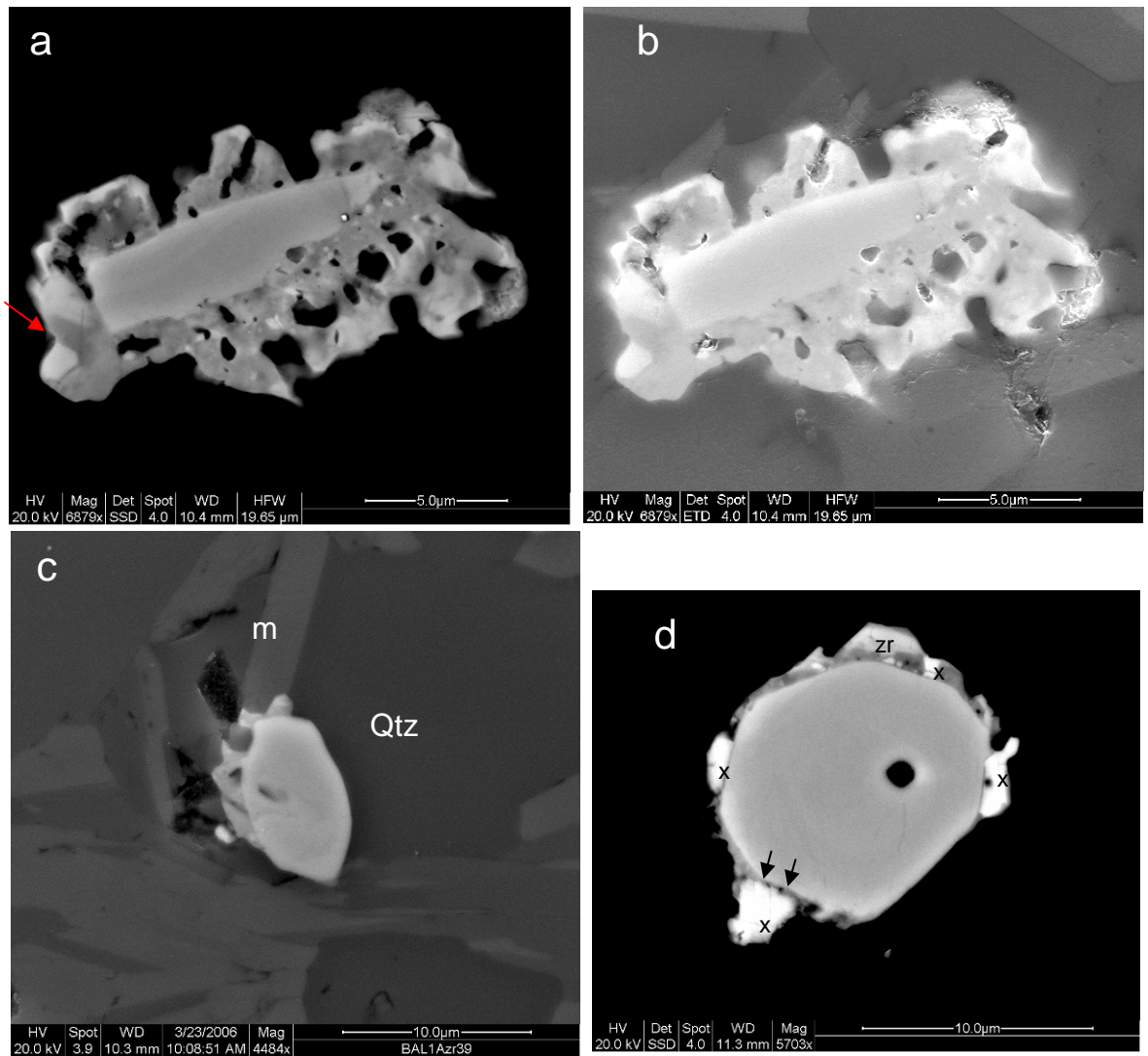


Figure 15. Images zircon and xenotime outgrowths on the margins of zircon.

All BSE images unless stated otherwise. **a** Host zircon with inclusion-rich, patchy BSE intensity zircon overgrowths. Arrow points to coherent higher BSE intensity zircon block in overgrowth (BAL1D). **b** SE image of **a** showing charging effects and overgrowth interaction with surrounding matrix. **c** Zircon outgrowth on host zircon adjacent to muscovite (m) (BAL1A). **d** Sub-euhedral detrital zircon host with zircon and xenotime outgrowths. Outgrowths show blocks of xenotime within zircon and higher BSE intensity zircon blocks. Arrow points to dark BSE zircon between host and outgrowth (BAL1). **e** SE image of zircon with zircon and xenotime outgrowth with surrounding matrix. Red arrow points to xenotime on zircon outgrowth tip. Inset is high contrast BSE image and shows xenotime on tip (BAL1D). **f** High magnification SE image showing intricate microstructure of inclusions and pores in zircon outgrowth (BAL1B). **g** Rounded detrital zircon with zircon and xenotime outgrowth. Arrows point to mottled texture in zircon outgrowth with **h** an SE image of **g** showing mottled appearance is due to charging (BAL1B). Figures 15e-h are on the follow page.

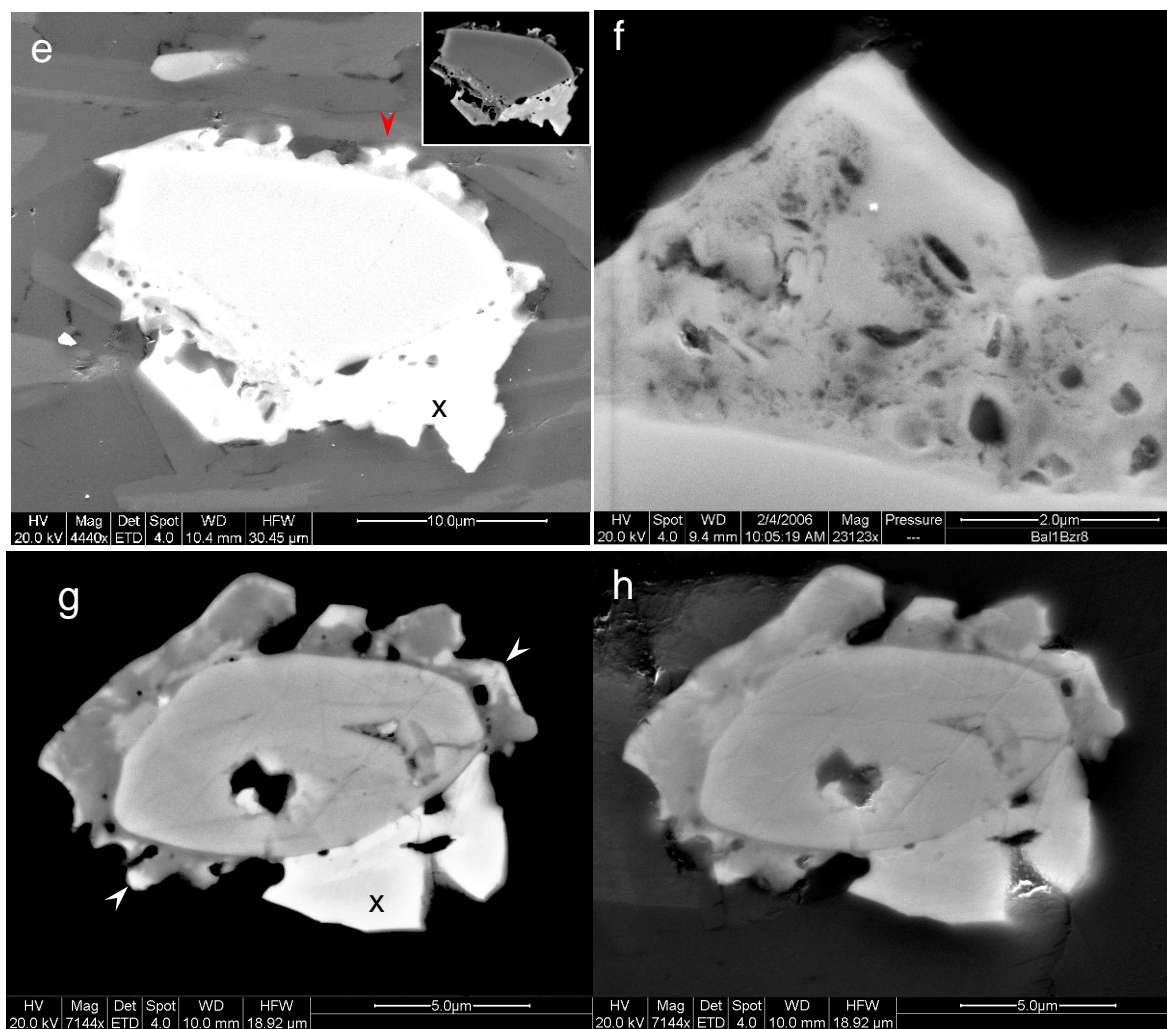


Figure 15.cont. Images zircon and xenotime outgrowths on the margins of zircon.

BSE images shows that zircon outgrowths have a lower BSE signal intensity than their host zircons (irrespective of BSE zoning within the host), similar in brightness to dark BSE zircon. Zircon outgrowths characteristically have a slightly mottled appearance in BSE, also similar to that displayed by dark BSE zircon, and often contain bright BSE inclusions. These high BSE contrast grains are likely to be xenotime (due to brightness of mineral in BSE) but areas of slightly higher BSE intensity than the outgrowth areas are zircon and have a similar brightness to the host zircon (Fig. 15d). These take the form of thin (0.2 μm wide and upto 2 μm long) bright streaks (Fig. 14f), roughly spherical bright spots (0.2-1 μm) (Fig. 15a), 0.2-1 μm distorted cubes (Fig. 14f) some of which show euhedral edges (Fig. 15a), and sub-hexagonal shaped domains (Fig. 15d) can also be identified. The outer tips of zircon outgrowths commonly appear bright in BSE (Fig. 15a,b,e,g,h).

Bright areas within zircon outgrowths are commonly found in conjunction with xenotime outgrowths (Fig. 16, see sections 3.7.2 & 3.7.3). Zircon outgrowths in xenotime-poor slates appear more homogeneous in BSE images than their counterparts in rocks where xenotime is abundant (Fig. 16c). On rare occasions, zircon outgrowths have been found to be homogeneous in BSE images in xenotime-rich slates and are in close proximity (*c.*100 μm) to zircons with patchy outgrowths despite apparently little difference in the adjacent mineral assemblage (Fig. 14j).

Zircon outgrowths are seldom found on zircon in quartzites and psammities (Table 1) but where outgrowths are present, they are often smaller (<3 μm) than those in slates (Fig. 17). Typically the rocks that contain zircon outgrowths have a higher phyllosilicate content than the other quartz-dominated samples, although simply containing more phyllosilicate minerals is not necessarily an indication the rock will contain zircon outgrowths. Furthermore, where zircon outgrowths have been found in quartzites and psammities, these rocks are often from a sequence dominated by slates, most of which contain zircon outgrowths. In slates (BAL1, BAL1B, BAL3, EAS1) containing alternating phyllosilicate-rich and fine-grained quartz layers (upto 1mm in thickness), zircons outgrowths are only ever found on zircons in phyllosilicate-rich bands. However, there is a possible bias in this observation as the number of host zircons in the quartz-rich areas is upto an order of magnitude lower than in phyllosilicate layers.

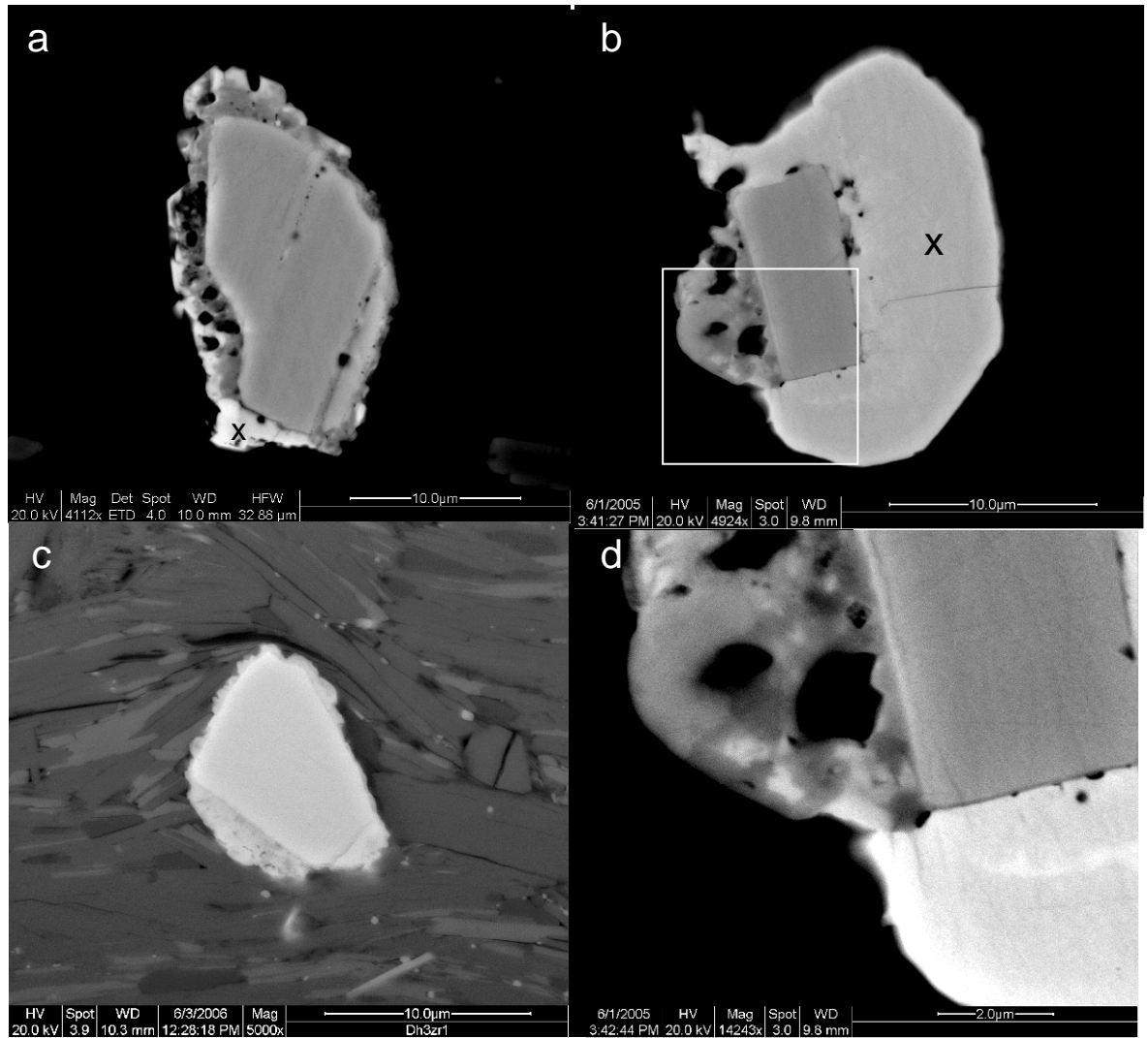


Figure 16. BSE images zircon and xenotime outgrowths on the margins of zircon.

a Zircon with zircon outgrowths. High BSE intensity on the tips of outgrowth is result of xenotime on tips. Xenotime also forms outgrowth at the bottom of the image (BAL1D). **b** Rectangular detrital zircon with inclusion-rich and sub-hexagonal zircon outgrowth and large xenotime overgrowth (BAL1B). **c** Zircon with large homogeneous BSE zircon outgrowth and frilly outgrowth projecting into the surrounding matrix (Dh2). **d** Enlarged area from **b** showing xenotime blocks in zircon outgrowth. Also shows the heterogeneous BSE intensity of the zircon outgrowths.

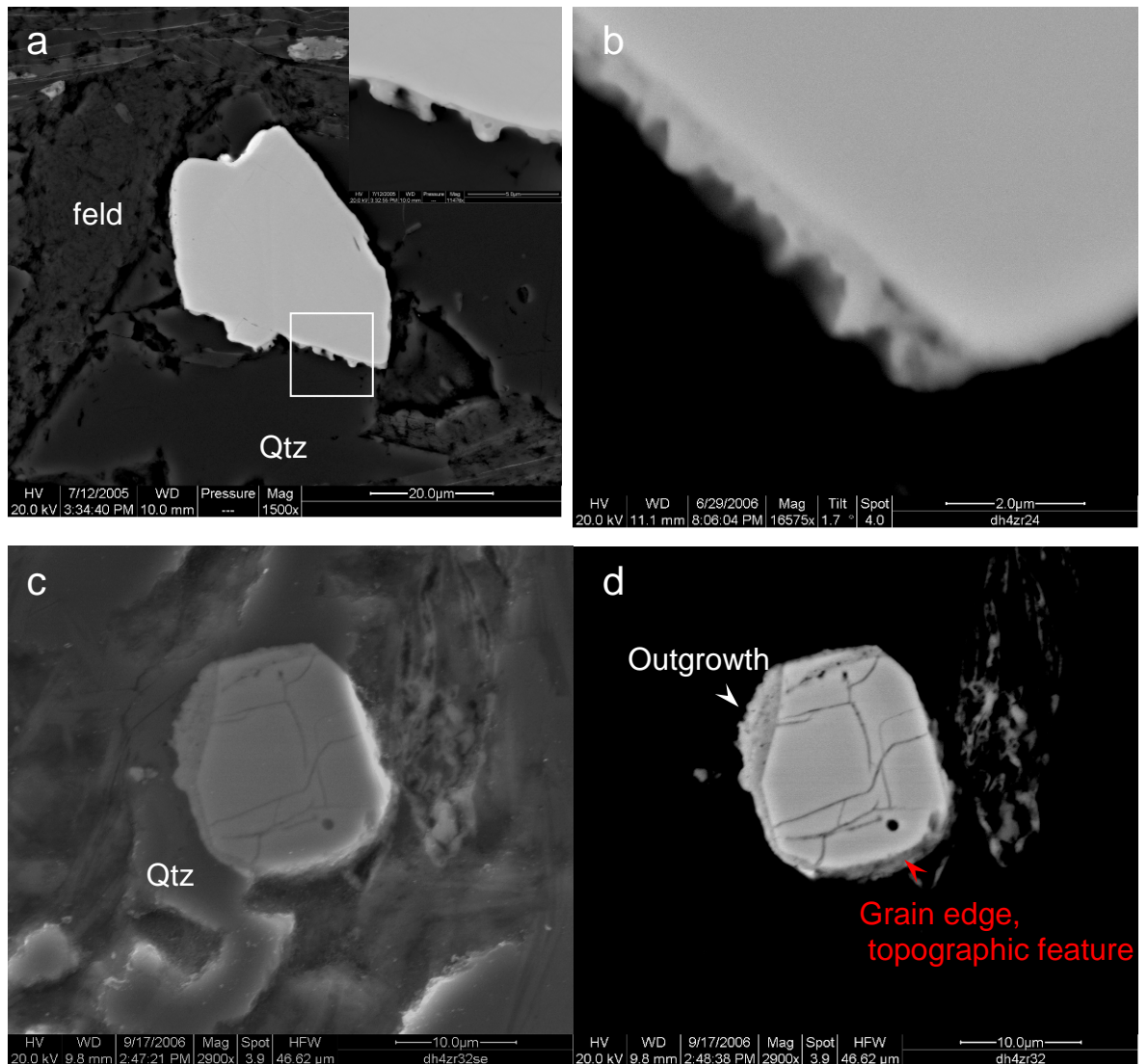


Figure 17. Images of zircon with zircon outgrowths.

a Zircon outgrowth serrations on host zircon against quartz with inset high magnification image of outgrowth (BAL3) and **b** shows pyramidal zircon outgrowth serrations (Dh4). **c** SE & **d** BSE images of zircon showing difference between outgrowth and grain edge. Outgrowth has formed adjacent to quartz (Dh4).

3.7.2 Xenotime outgrowths on zircon

Xenotime has a higher mean atomic number than most other minerals, including zircon, allowing it to be easily identified using high contrast BSE imaging. This property of xenotime also allows it to be distinguished from zircon in areas where there are complex, sub-micron intergrowths between the two minerals (Fig. 16).

In slates and phyllites, xenotime projects $c.5\mu\text{m}$ on average from the host zircon. Xenotime occasionally completely encases the host zircon as an overgrowth (Fig. 18g) but otherwise forms outgrowths of partially surrounding crusts or isolated grains on the margins of the host zircon (Fig. 18a-f). Where the host zircon retains an octagonal to sub-octagonal shape, isolated xenotime outgrowths may be found on opposing corners of the host (Fig. 18h&i). Xenotime outgrowths more commonly form two, three or four separate outgrowths on the different faces of the host zircon as opposed to a single continuous outgrowth. A large xenotime outgrowth can be present on a single host zircon whilst all neighbouring zircons lack outgrowths (Fig. 19h). In such instances, the zircon with the outgrowth is in communication with the phyllosilicate matrix whereas neighbouring zircons are entirely surrounded by quartz.

There is a good correlation between the habit of xenotime outgrowths and host lithology and grain size. Xenotime in quartzites and psammities (coarser grained rocks) is generally smooth and rounded where rounded subhedral blocks are common (Fig. 18f, j & k) as are larger ($>5\mu\text{m}$) pyramidal-shaped outgrowths (Fig. 18e). However, in phyllosilicate-rich lithologies (which are typically finer grained), xenotime is much more irregularly-shaped, forming jagged outgrowths and frills (Fig. 18a-c,i). The exception to this is the occasional euhedral xenotime outgrowth where it forms against the cleavage plane of a mica (Fig. 19b&c). Very thin ($<100\text{nm}$) spines of xenotime may occur between the cleavage planes of micas (Fig. 18b) and xenotime may also partially surround matrix quartz grains (Fig. 19d). Fine-grained ($<2\mu\text{m}$) quartz is the most common inclusion in the xenotime (e.g. Fig. 19f) as determined by Si peak on EDX analysis spectra, coupled with a very low BSE intensity. Xenotime is also larger when adjacent to mica (Fig. 19e) and outgrowths are generally more rounded beside matrix quartz (Fig. 18c).

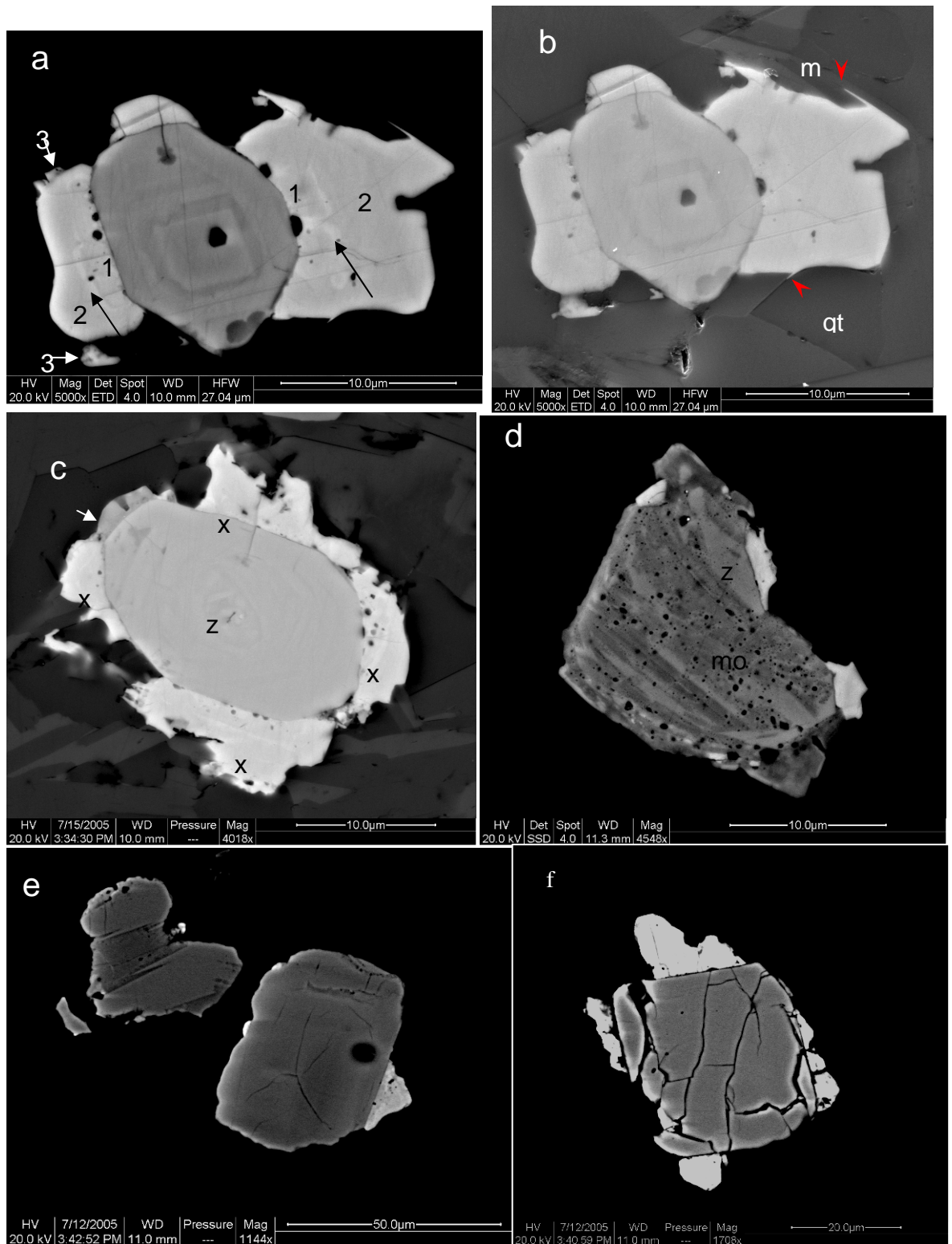


Figure 18. Images of xenotime outgrowths on zircon. Caption is on page 54.

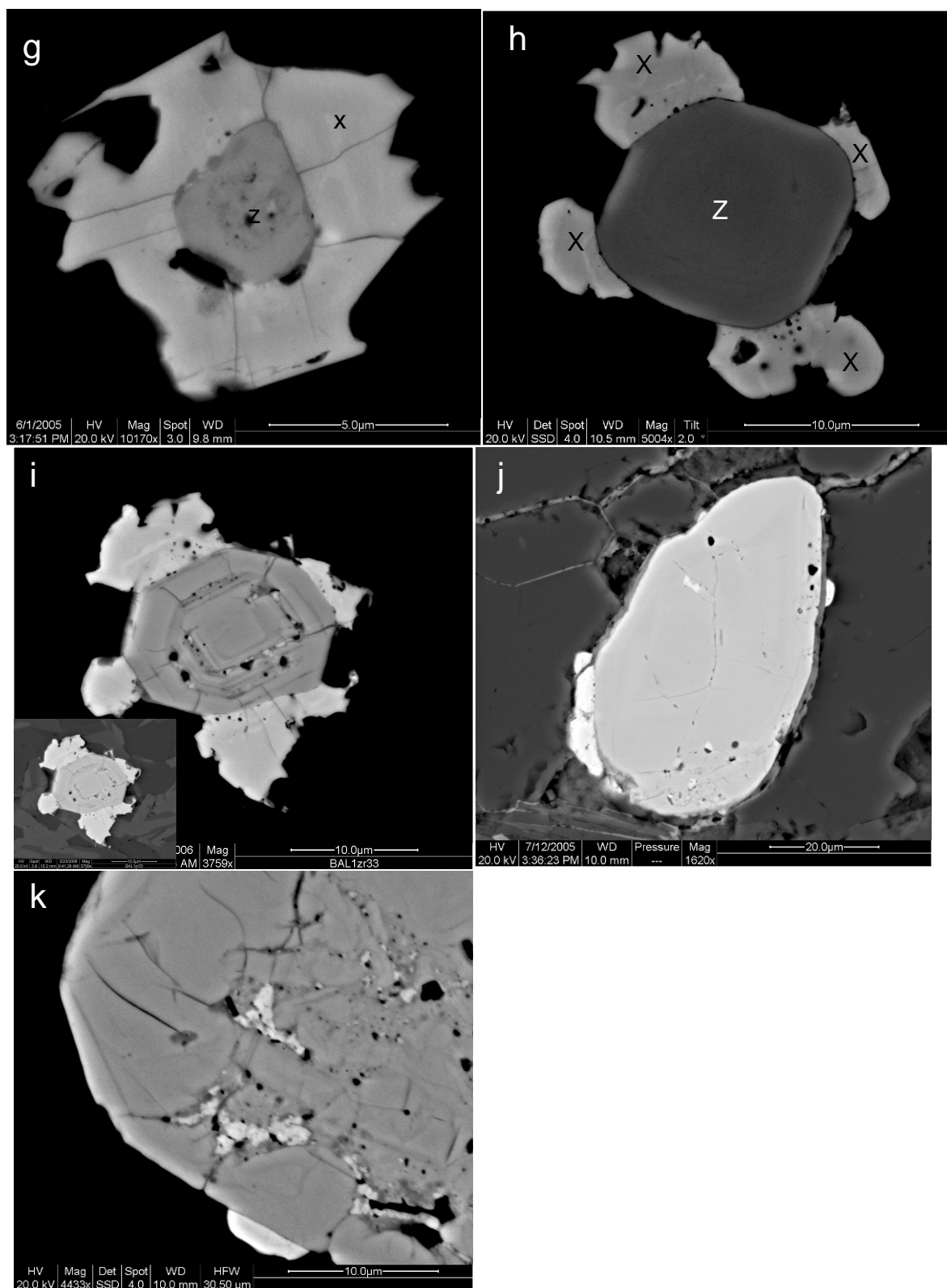


Figure 18. Images of xenotime outgrowths on zircon. Caption is on page 54.

Figure 18. Images of xenotime outgrowths on zircon

All BSE images unless stated otherwise. **a** Subhedral concentrically zoned host zircon with xenotime outgrowths that show three textural phases. Inclusions appear along the margin between zircon and xenotime outgrowth and within zone 1 of the outgrowth. The limits of zone 1 are defined by a high BSE intensity band (black arrow). The second growth zone is more homogeneous with a third phase of growth (white arrow) mantled to zone 2 (BAL1B). **b** SE image of **a** showing outgrowth relationship with matrix. Arrows point to thin spines of xenotime along matrix boundaries (m=mica, qtz=quartz). **c** SE image of zircon with irregular xenotime outgrowth showing association with matrix. Arrow points to zircon outgrowth. Xenotime forms on four faces of the host zircon (BAL1B). **d** Streaky dark BSE/light BSE zircon with high BSE intensity xenotime forming on light BSE and dark BSE zircon. Dark BSE zircon contains abundance of pores. (BAL1C). **e** Large pyramidal shaped xenotime outgrowth forming on zoned zircon (BAL3). **f** Fractured host zircon with four separate xenotime outgrowths on all sides of host. Note absence of fractures in larger xenotime outgrowths (BAL3). **g** Dark BSE zircon with pores surrounded by xenotime overgrowth. Xenotime contains fractures that radiate from the zircon-xenotime boundary. Xenotime margins protrude into matrix (BAL1B). **h** Sub-rounded zircon with xenotime outgrowths on four opposing corners of grain. Some xenotime outgrowth grain boundaries are rounded and note inclusion-rich boundary between zircon and xenotime (BAL1A). **i** Euhedral zircon with concentric zoning and dark BSE interior. Radial fractures in light BSE zircon are associated with dark BSE zones. Xenotime outgrowths are attached to four opposing faces on zircon. Inset shows relation to matrix (BAL1A). **j** Rounded zircon with blocky xenotime outgrowths. Phyllosilicate coating around host zircon and between xenotime outgrowth (BAL3). **k** Zircon with xenotime infilling cavities in dark BSE interior. Also xenotime outgrowth on zircon grain edge (BAL3).

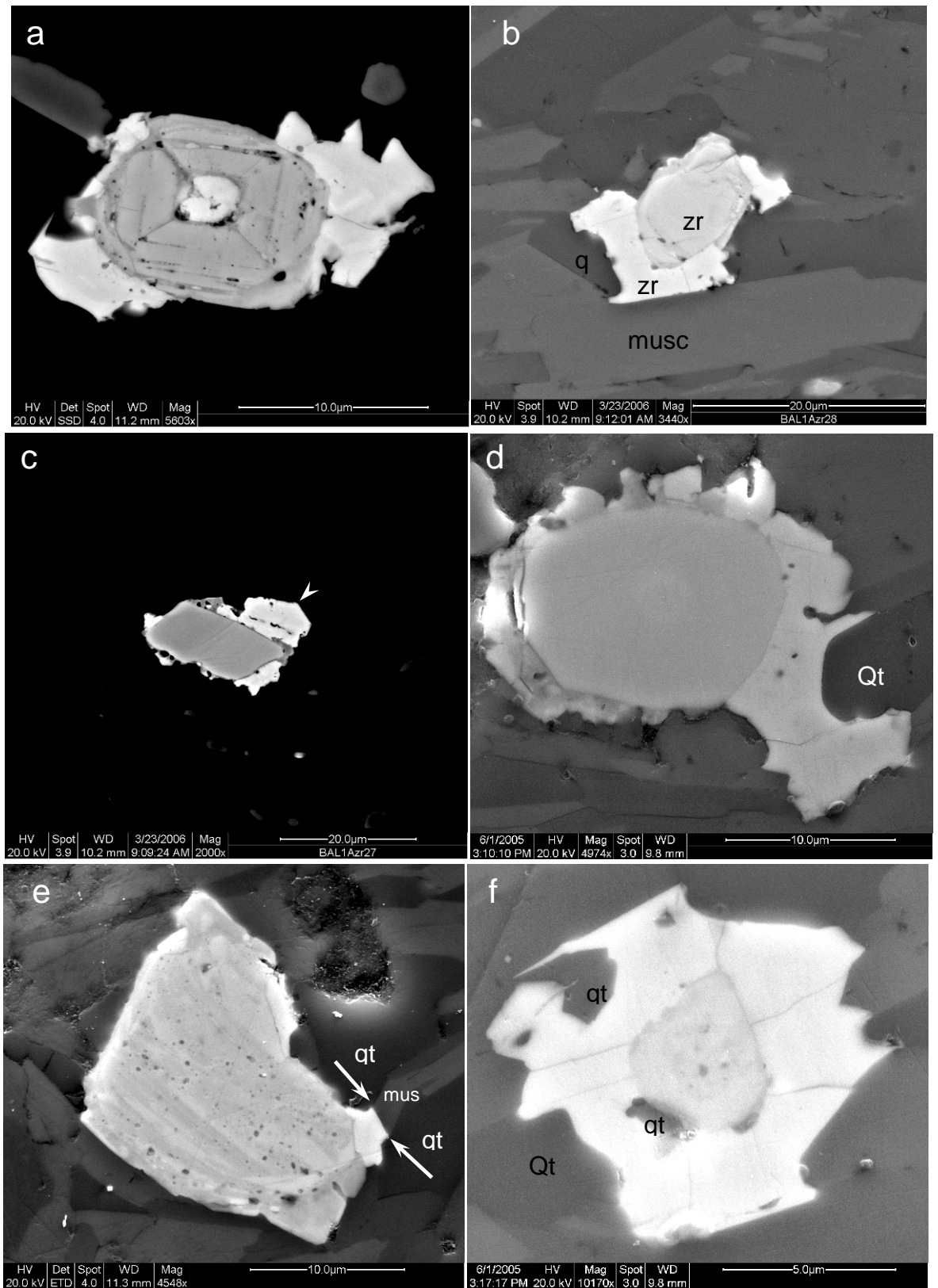


Figure 19. Images showing examples of xenotime outgrowths on zircon. Figure captions are on following page.

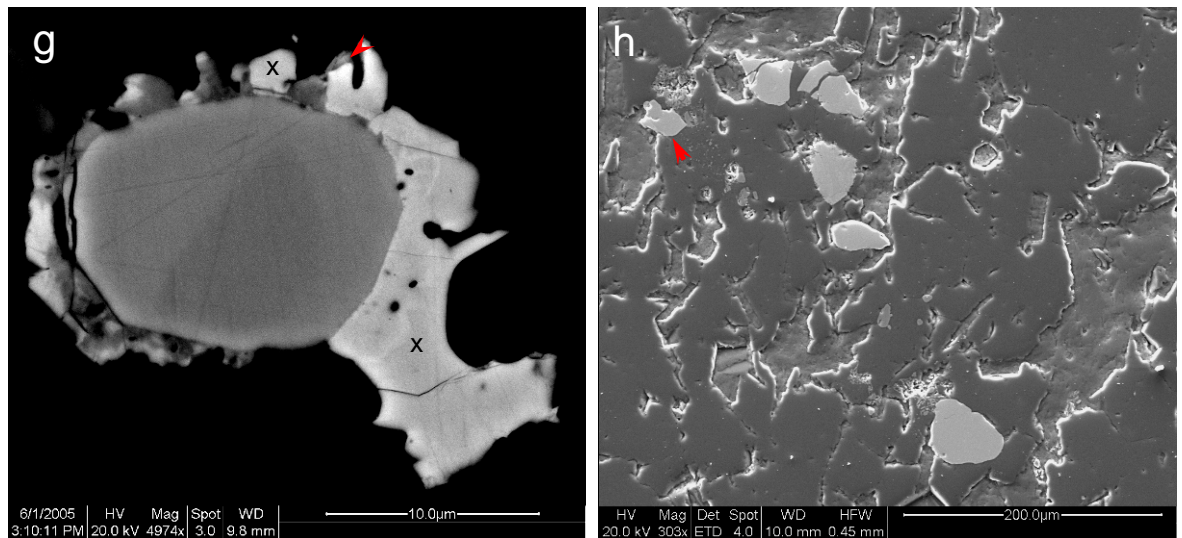


Figure 19. Images showing examples of xenotime outgrowths on zircon

a BSE image of light BSE zircon with radial fractures and thin concentric dark BSE zircon zones. Xenotime forms outgrowths on the margin of the zircon and the xenotime inclusion in the centre of zircon (BAL1A). **b** SE image of zircon with straight-edged xenotime outgrowth adjacent to muscovite (musc) and growing around quartz (q) (BAL1A). **c** BSE image of zircon with zircon and xenotime outgrowths. Arrow points to euhedral shape of xenotime outgrowth (BAL1A). **d** SE image of **g** showing xenotime growing around quartz grain (BAL1A). **e** SE image of Fig. 18d showing xenotime outgrowth with preferential growth adjacent to muscovite (musc) over quartz (qtz). **f** SE image of Fig. 18g showing qtz inclusion in xenotime outgrowth. **g** BSE image of rounded zircon host with zircon and xenotime outgrowth. Arrow points to zircon on xenotime outgrowth (BAL1A). **h** Combined BSE & SE image showing zircon in phyllite BAL3. Arrow points to the only zircon with xenotime outgrowth.

Using BSE images, three distinct domains can be identified within xenotime outgrowths on zircon in slates and phyllites (Fig. 18a,h,i). The innermost domain is frequently inclusion-rich, particularly along the xenotime-host zircon boundary although outgrowths appear to be less inclusion-rich in quartzite and psammite. A bright band can be traced between the first and second domain and is roughly parallel to the edge of the host zircon. This second domain characteristically lacks inclusions and is weakly zoned with a slightly more intense BSE signal towards the edge of the outgrowth (although care must be taken to avoid this being mistaken for charging). The outer margins of this second phase often have fingers of xenotime that protrude out into the matrix. On the fringes of some outgrowths, isolated euhedral μm -sized xenotime represents a third phase of growth and are separated from earlier xenotime by a thin ($<0.2\mu\text{m}$) high intensity BSE band.

Occasionally, where xenotime completely surrounds the host zircon as an overgrowth, fractures radiate from the contact between the xenotime and host zircon to the outer edge of the xenotime (Fig. 18g).

3.7.3 The relationship between of zircon and xenotime outgrowths

Xenotime and zircon outgrowths on the margins of zircon are often contiguous, frequently surrounding one another (Fig. 14a and see section 3.7.1). The shape of contact between zircon and xenotime varies from straight (Fig. 19g, 15d) to slightly irregular and curved to jagged (Fig. 14a). The boundary between zircon and xenotime outgrowths is usually sharply defined but occasionally there can be a gradation in BSE signal intensity from xenotime into zircon (Fig. 14a). Thin ($<0.2\mu\text{m}$) spines of xenotime may also protrude into the zircon outgrowths (Fig. 14a) and isolated crystals of xenotime are partially (Fig. 14a, 15d) or completely (Fig. 16d) surrounded within zircon outgrowths. However, regardless of abundance, xenotime outgrowths generally protrude further into the matrix than zircon outgrowths.

Very thin ($<0.5\mu\text{m}$) strips of dark BSE zircon have been observed between the host zircon and xenotime (Fig. 15d & 19c). Phyllosilicate coatings, $2\mu\text{m}$ thick and partially surrounding the host zircon, have also been noted between the host zircon and the xenotime outgrowth (Fig. 18j and c.f. (Watt et al., 2000) although these are rare. No zircon has been observed within xenotime outgrowths.

3.8 Other occurrences of xenotime

3.8.1 Overgrowths on detrital xenotime

Small ($c.10\mu\text{m}$ in diameter) well-rounded to subhedral xenotime cores are encased by upto $5\mu\text{m}$ thick xenotime overgrowths (Fig. 20). Although uncommon, these features have only been observed in slate samples and are absent from other lithologies. It is likely the well-rounded to subhedral xenotime cores are of detrital origin. The margins of these xenotime overgrowths range from smooth and rounded subhedral blocks to irregular and jagged with spines that project along cleavages of individual micas in the adjacent matrix. Overgrowths of xenotime on detrital xenotime appear almost identical in form to those found on zircon and can also be divided into three distinct domains (c.f. section 3.7.2). However, two subtle differences are observed. Firstly a slightly darker BSE, $2\mu\text{m}$ wide band exists within the xenotime that immediately surrounds the host zircon (Fig. 20b). Secondly, xenotime outgrowths on xenotime are characterised by a more irregular-shaped and discontinuous bright strip which occurs between the first and second domain of the xenotime overgrowth (Fig. 20b).

3.8.2 Discrete xenotime within the matrix

Discrete, flattened oval xenotime ($3\text{-}10\mu\text{m}$ along its length) is found within the matrix of slates (Fig. 21). They are rare and only ten grains were present in thin section of a slate with abundant xenotime outgrowths. Discrete xenotime has smooth edges when adjacent to quartz and irregular, frilly and spikey margins when adjacent to phyllosilicates.

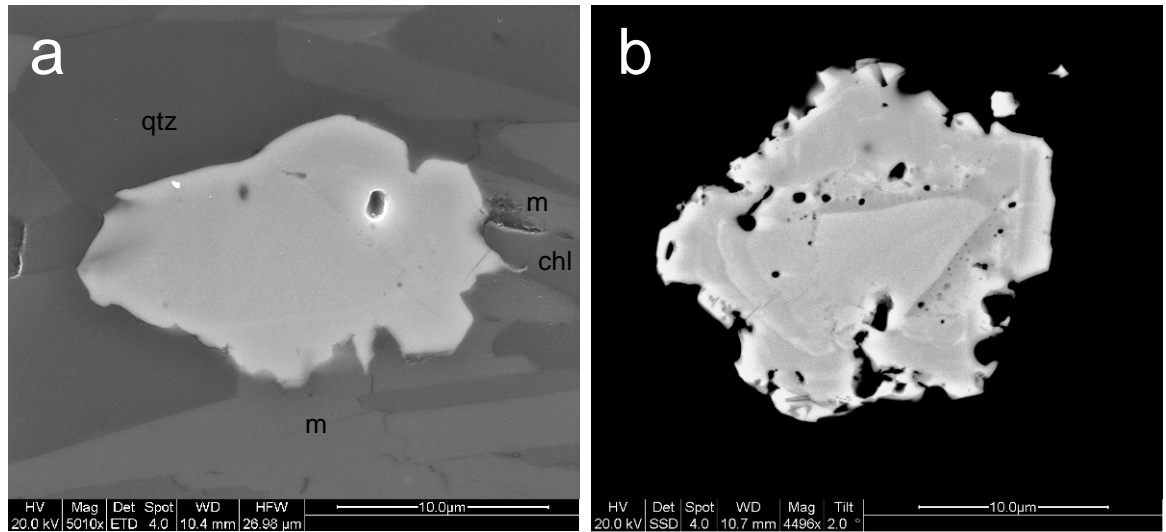


Figure 20. Xenotime overgrowths on xenotime

a SE image of detrital xenotime with xenotime overgrowth showing relationship xenotime outgrowth has with the surrounding matrix. (qtz=quartz, m=muscovite, chl=chlorite) (BAL1A). **b** High contrast BSE image of detrital xenotime with xenotime overgrowth. Reveals inclusion-rich rim around the host xenotime with a thin bright BSE band that surrounds inclusion-rich area (BAL1A).

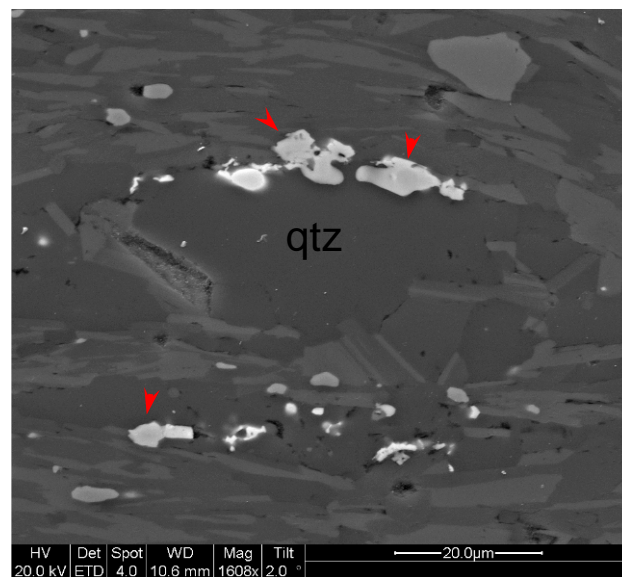


Figure 21. BSE image displaying discrete xenotimes (arrows) adjacent to quartz grain within a slate matrix (BAL1A).

3.9 Chemistry, CL and EBSD of zircon and xenotime

3.9.1 Light BSE zircon

Zircon generally has a composition of *c.*65% ZrO₂, *c.*33% SiO₂ and 1-1.5% HfO₂ with small concentrations of Y, REE's and actinide elements (Hoskin and Schaltegger, 2003) and light BSE zircon typically has a composition similar to this. Light BSE zircon is generally strongly luminescent in cathodoluminescence (CL) but is commonly zoned in CL (Watt et al., 2000) and can display a range of CL intensities within the same crystal (e.g. Fig. 4f, 24c). CL spectral analysis of light BSE zircon (Fig. 22a) gives a high intensity peak at 340-380nm. Between 400 and 750nm is a broad low intensity area that plateaus 550-675nm. At the end of the plateau is a broad hump at 685-735nm. Sharp, single line intensity peaks are a result of cosmic rays hitting the detector and do not represent luminescence from zircon (P.R. Edwards, personal communication). Light BSE CL-intense zircon produces high Image Quality (IQ) Kikuchi patterns when analysed using EBSD that have a high Confidence Index (CI) when indexed by EBSD software (Fig. 23).

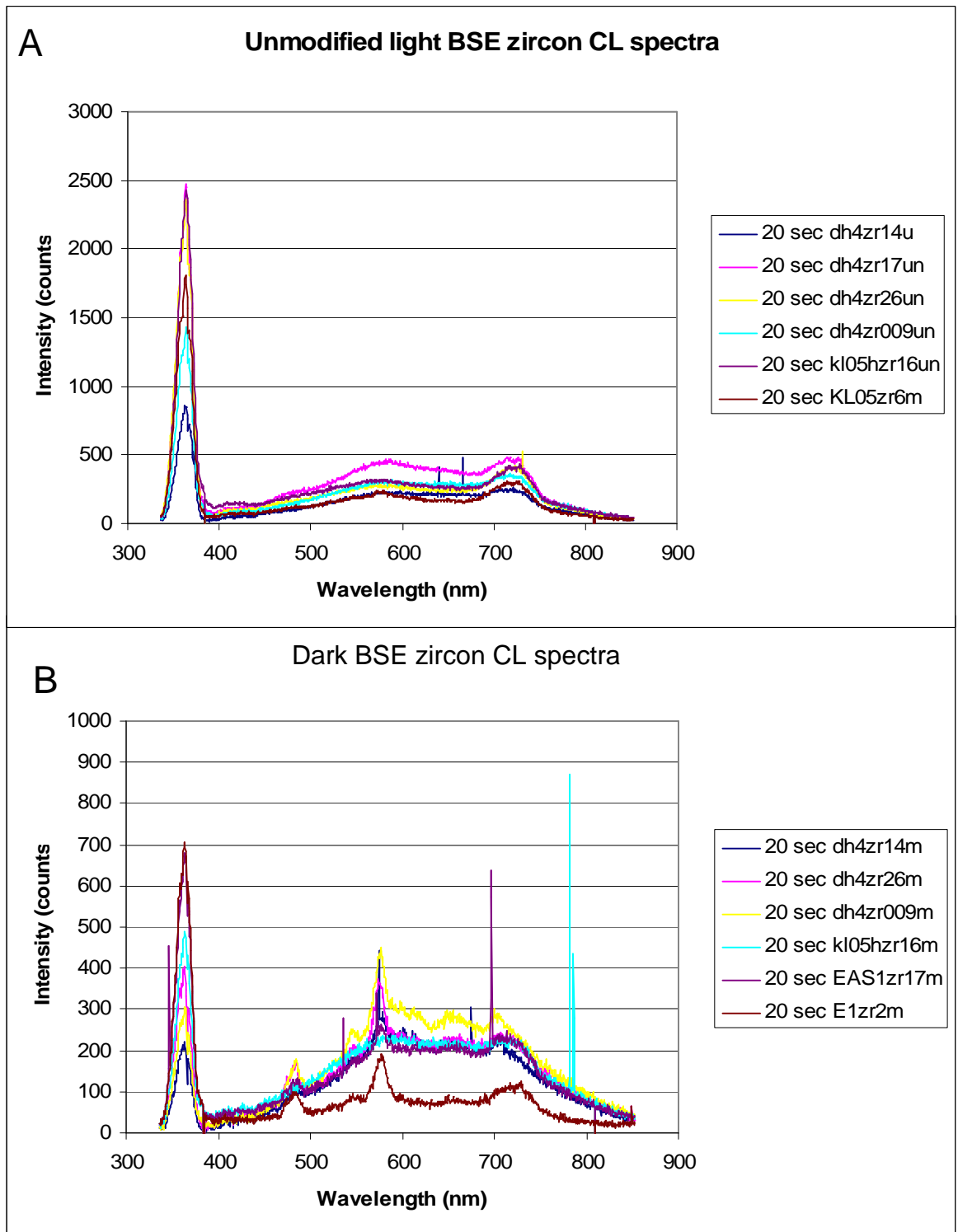


Figure 22. CL emission spectra of from multiple analyses of unmodified light BSE zircon (a) and dark BSE zircon (b). Locations on the grains from where CL analysis was obtained from is shown in Figure 26.

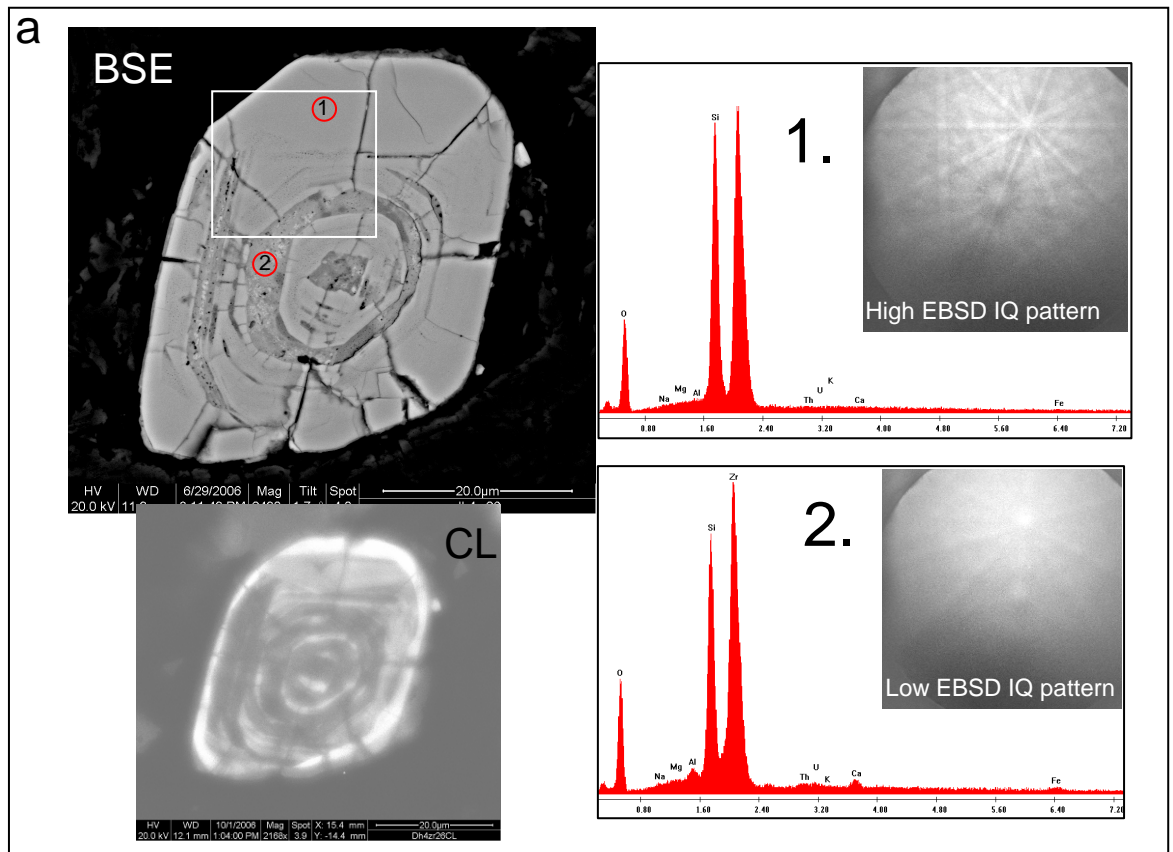
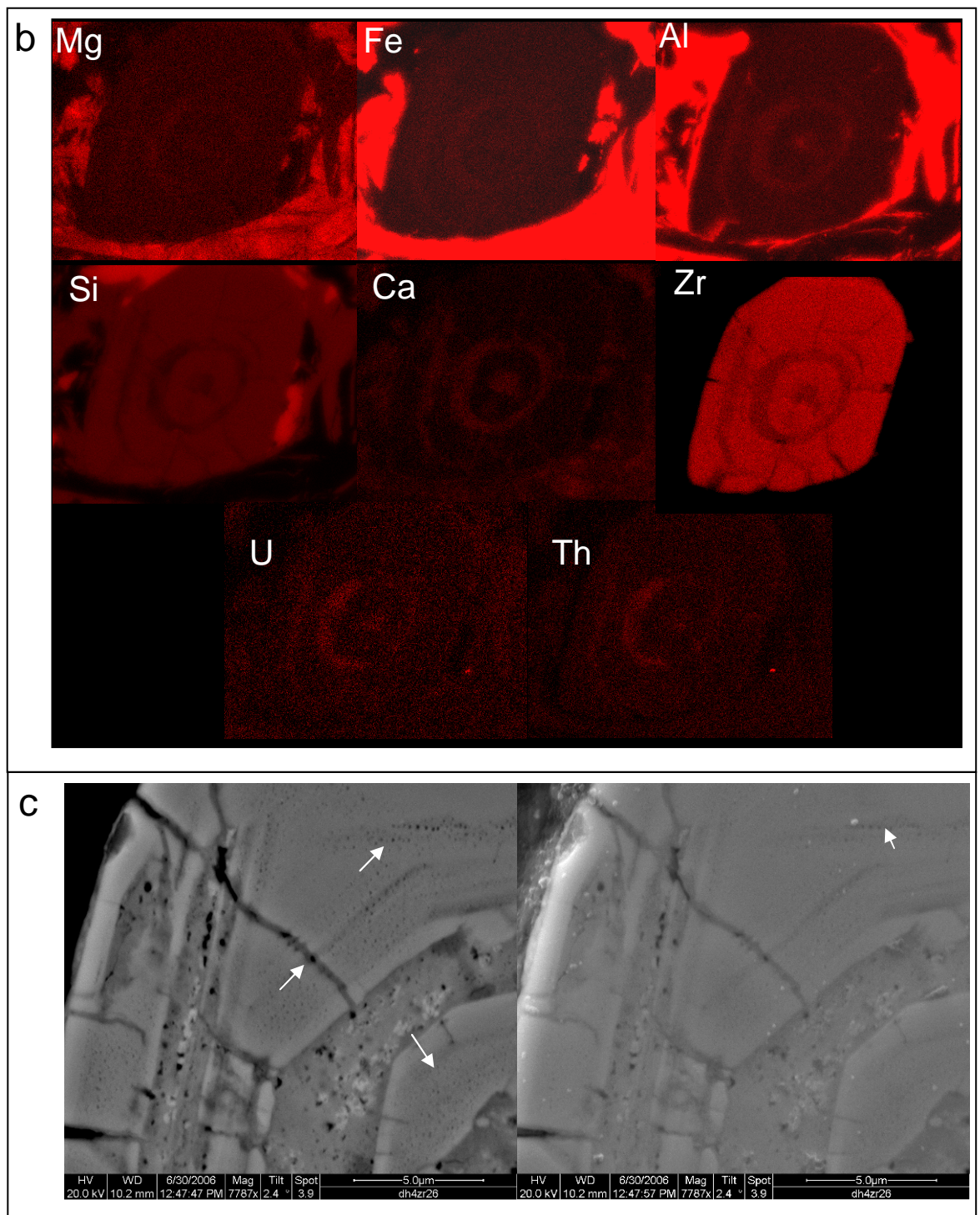


Figure 23. Characterisation of concentric light BSE and dark BSE zoned zircon.

Oscillatory light BSE/dark BSE zoned zircon with radial fractures and porous zircon bands in light BSE zones. Dark BSE zircon contains xenotime inclusions. **a** BSE of zoned light and dark BSE zircon with complementary CL image. CL intensity is always low in corresponding dark BSE zones. EDX and EBSD spot analysis of light and dark BSE zircon show dark BSE zircon is enriched in Ca, Fe and Al on and EDX spectra, noting the difference in Zr to Si peak size compared to light BSE zircon. Dark BSE zircon shows corresponding low IQ EBSD pattern. **b** EDX element maps of **a** show modified growth layers enriched in non-formula elements and U & Th whilst depleted in Si & Zr. **c** High magnification BSE and SE images of area defined in **a**. High BSE intensity, small irregular xenotime grains can be observed within dark BSE zircon and the microstructure also contain an abundance of pores with porous zones in the light BSE domains are also observed (white arrows). (Dh4). Figures 23b-c follow this page.

Figure 23. *cont.*

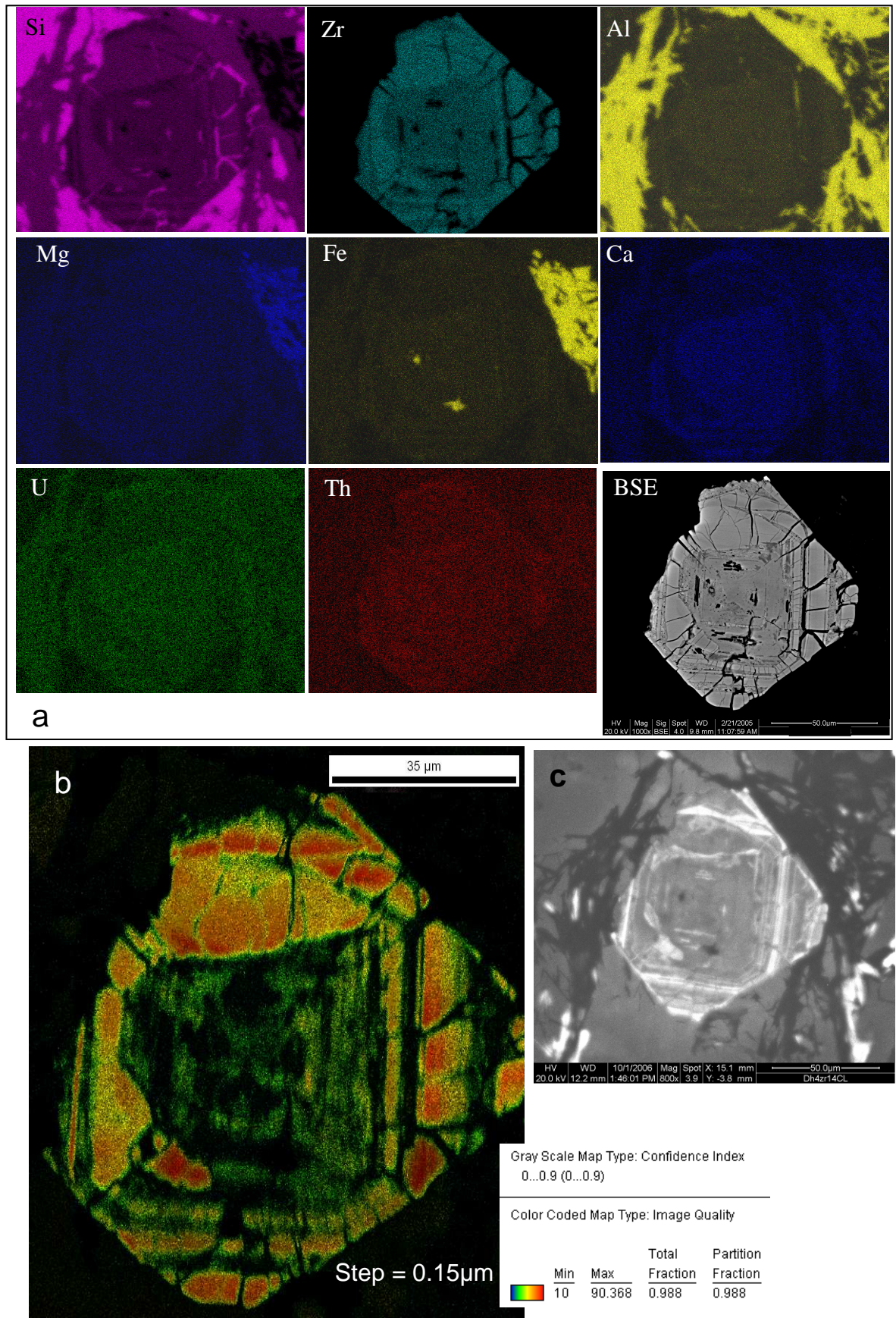


Figure 24. Characterisation of zircon containing dark BSE zircon. Figure caption follows images on next page.

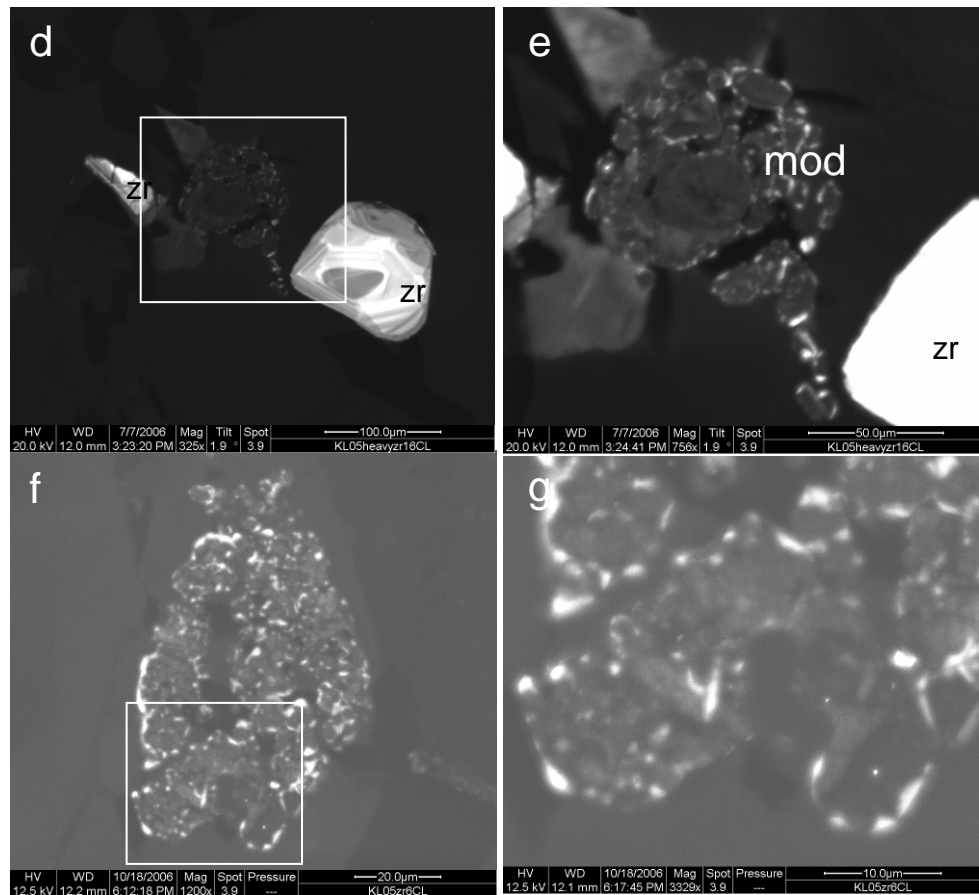


Figure 24. Characterisation of zircon containing dark BSE zircon

a EDX element maps of figure 6d showing dark BSE zircon is enriched in non-formula elements while depleted in Si & Zr. Amounts of Mg, U and Th enriched in dark BSE zircon are close to the detection limits of EDX but maps show very slight enrichment. Quartz (Si-rich parts within zircon grain in Si map) has in filled radial fractures as has occasional phyllosilicates (Al-rich). Fe-rich inclusions in dark BSE zircon represent FeO. **b** Confidence Index (CI) – Image Quality (IQ) EBSD scanned map of figure 6d. CI is the intensity of the colour brightness with bright having a high CI. IQ is shown by colour warmth with red being highest and black lowest. Step size = 0.15 μ m. Light BSE zircon can show a range of crystalline states indicating that some light BSE zircon is partially metamict. Dark BSE core has a low EBSD IQ although some variation exists within that may correlate with slightly higher CL intensity in c which is a CL image of figure 6d showing complex oscillatory zoning within light BSE zircon but also some intensity variations within the equivalent dark BSE area. **d** CL of figure 9b and adjacent unmodified zircons. Zircon containing dark BSE zircon (centre) has a greatly reduced CL intensity signal by comparison to unmodified zircons (zr) that exhibit complex zoning. **e** Higher magnification CL image of area defined in **d** with increased brightness. Note bright CL “blotches” within dark BSE zircon. **f & g** CL of figure 9C showing the same overall low CL emission levels but with bright CL blotches around and throughout the grain.

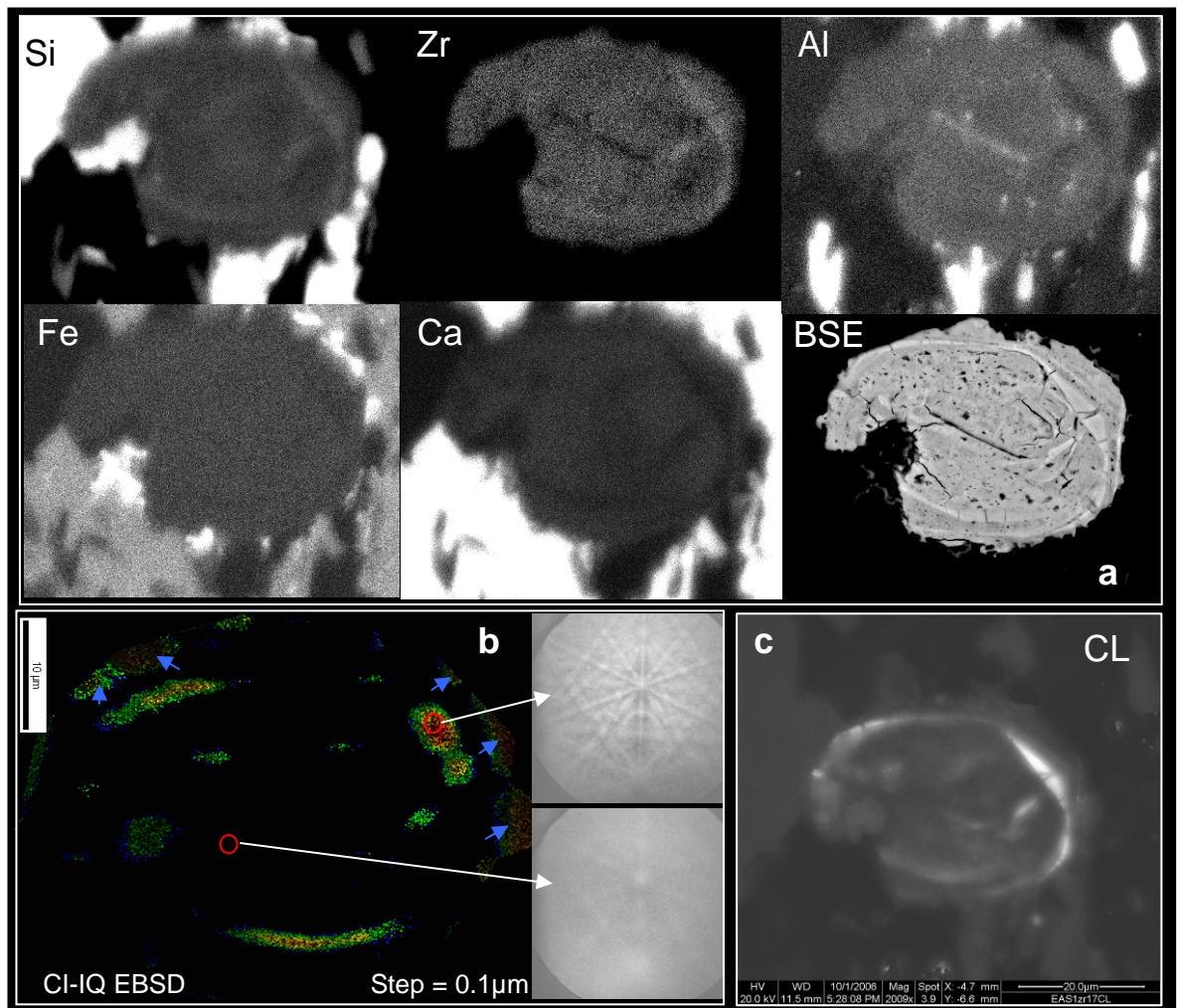


Figure 25. Characterisation of dark BSE zircon in figure 8 containing thin laths of light BSE zircon

a EDX element maps with curved unmodified band showing no enrichment in non-formula elements and higher concentrations of Si & Zr. This unmodified zone correlates with light BSE zircon. **b** Complementary CI-IQ EBSD scanned map of same area with unmodified, light BSE zircon producing higher CI-IQ EBSD patterns compared to very low CI-IQ dark BSE zircon. Kikuchi patterns show EBSD difference in quality between dark BSE and unmodified zircon. Blue arrows on EBSD map point to matrix grains. **c** CL image of same area with unmodified showing high CL emission levels. Dark BSE zircon displays some CL intensity variations that may correlate slightly to differences in non-formula elements.

3.9.2 Dark BSE zircon

Energy Dispersive X-ray Spectroscopy (EDX) SEM spot analysis of dark BSE zircon show that it is enriched in non-formula elements (according to Goldschmidt's rules) Mg, Al, Ca and Fe (Fig. 23,24,25). There is considerable variation in the concentrations of these elements in dark BSE zircon from analyses that contain easily identifiable X-ray peaks, equating to *c.*1-2wt%, to those with no identifiable peaks. This variation is seen from grain to grain and even within the same area of dark BSE zircon. EDX SEM scans reveal that dark BSE zircon is depleted in Zr and Si (Fig. 23b, 24a, 25c). Dark BSE zircon is also characterised by a higher Zr/Si ratio than light BSE zircon and, although this may be subject to large errors, was determined by measuring their relative peak heights on the energy dispersive spectra. EDX scans often show that dark BSE zircon is enriched in U and Th relative to light BSE zircon within the grain (Fig. 23c, 24a). However, BSE images of U and Th rich areas frequently show numerous high BSE intensity <500nm size grains likely to be xenotime inclusions (Fig. 23d). As xenotime can contain several weight percent U and Th, it may be that the enrichment in these elements is representative of xenotime grains rather than the composition of the dark BSE zircon. The xenotime chemistry may also be masked by zircon in EDX analysis because the Y L α and P K α both occur very close the Zr L α peak causing significant overlap. This may also result in a slightly elevated Zr peak and therefore higher Zr/Si ratio.

Ten zircon grains with dark BSE areas, were selected from five thin sections: a phyllosilicate-rich psammite (Dh4); two quartzite samples (KL05& KL05h) and two slates (EAS & EAS1); for analysis by EPMA. Elements analysed were Zr L α , Si K α , Hf L α , Mg K α , Al K α , Ca K α , Fe K α , Y L α and Na K α . Na was analysed because EDX scans showed a possible peak in dark BSE zircon (Fig.23a). However no Na was detected in EPMA analysis and apparent Na enrichment is thought to be the result of peak interference from the Mg K α peak in the energy dispersive spectra. P was not analysed as the ZrL α peak interferes with the PK α peak in EPMA. Mn (Speer, 1982), U and Th were also excluded from the analysis because of the lack of suitable standards. Several dark BSE zircon areas were analysed by line scan with a 2 μ m step size in an attempt to correlate variations in composition with BSE signal intensity, CL intensity and EBSD IQ. The remaining data has come

from single spots analysis of light and dark BSE zircon. Light BSE zircon was analysed as a reference “standard” at the end of each analysis run in order to check any drift in the analysis totals. The zircons analysed and the location of analysis on these zircons is presented in Fig. 26.

3.9.2.1 Anomalous data points

Reasonable trends and clusters of data points can be seen in most element plots of EPMA data but there is also a significant scatter of data within all graphs (Fig.27). The trends observed probably represent variations due to chemical substitutions in dark BSE zircon but some analyses are inevitably contaminated by small inclusions as a result of the dark BSE zircon microstructure. Contaminated analyses can be identified as they show a consistent and predictable deviation from the overall trend in different graphs. It is the aim of this section to justify removal of these contaminated data points from the dark BSE zircon data set.

Inclusions within dark BSE zircon are normally of similar composition to the surrounding matrix, as determined by BSE images and EDX analysis and therefore quartz (Si), feldspar (Si, Al), chlorite (Si, Al, Fe, Mg), muscovite (Si, Al), biotite (Si, Al, Fe, Mg), carbonate (Ca, Mg) and pyrite (Fe) are likely contaminants. Xenotime inclusions (Y) have also been identified in BSE images of dark BSE zircon and consequently are a predicted contaminant. The effective trends that analyses with inclusions will be predicted to follow have been identified in the relevant element plots in Figure 27. For simplification, muscovite, biotite and chlorite will be referred to as phyllosilicates (abbreviated to phyllo) in these plots unless specified otherwise.

Data points encircled in red indicate the influence of phyllosilicate and feldspar minerals (Fig. 27a-c). Figure 27a also shows unusual Zr-rich points encircled in gold. The composition of these Zr-rich contaminants is not entirely clear but may possibly represent some baddeleyite (ZrO_2) inclusions, although this seems unlikely as baddeleyite typically forms in silica-depleted environments. In Figure 27c, a further group of points (encircled in green) can also be identified that have a slight phyllosilicate or feldspar influence. Fig. 27d&e identify points encircled in blue that are contaminated by xenotime. Besides the Al-rich points highlighted in red in Fig. 27d that

have an obvious phyllosilicate influence, some Al enriched points also appear to be contaminated by inclusions of a different composition and are highlighted in grey. These same points are also Ca-rich (in grey, Fig. 27e) and two of these points are the same Zr-rich, Si-poor anomalous points highlighted in gold in Figure 27a. The nature of these inclusions these inclusions is not clear, however these points are clearly not representative of dark BSE zircon. Figure 27f identifies points in purple that are Fe-rich and likely to be contaminated by biotite or chlorite as they also show relative enrichment in Al (Fig. 27c&d). Point 98, is also encircled in purple in Fig. 27f, is particularly Fe-rich but does not show Al-enrichment is likely to be contaminated by FeO or FeS.

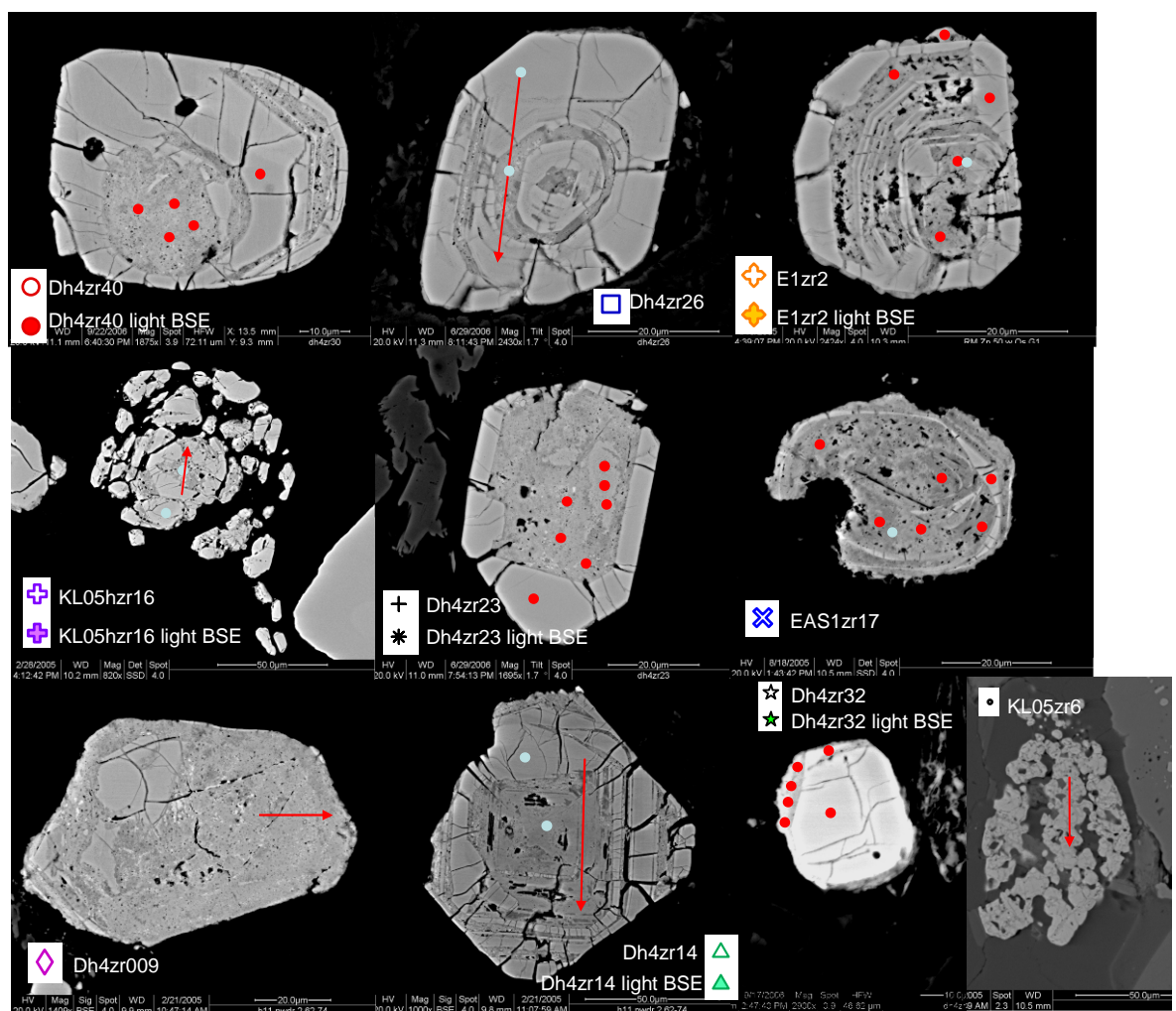


Figure 26. BSE images of zircons analysed by EPMA and the locations on them where analysis was collected via line scan analysis (red arrow), spot analysis (red spots) and CL spectra (blue spots). On each grain shows the symbol that refers to element plots in figures 27-31.

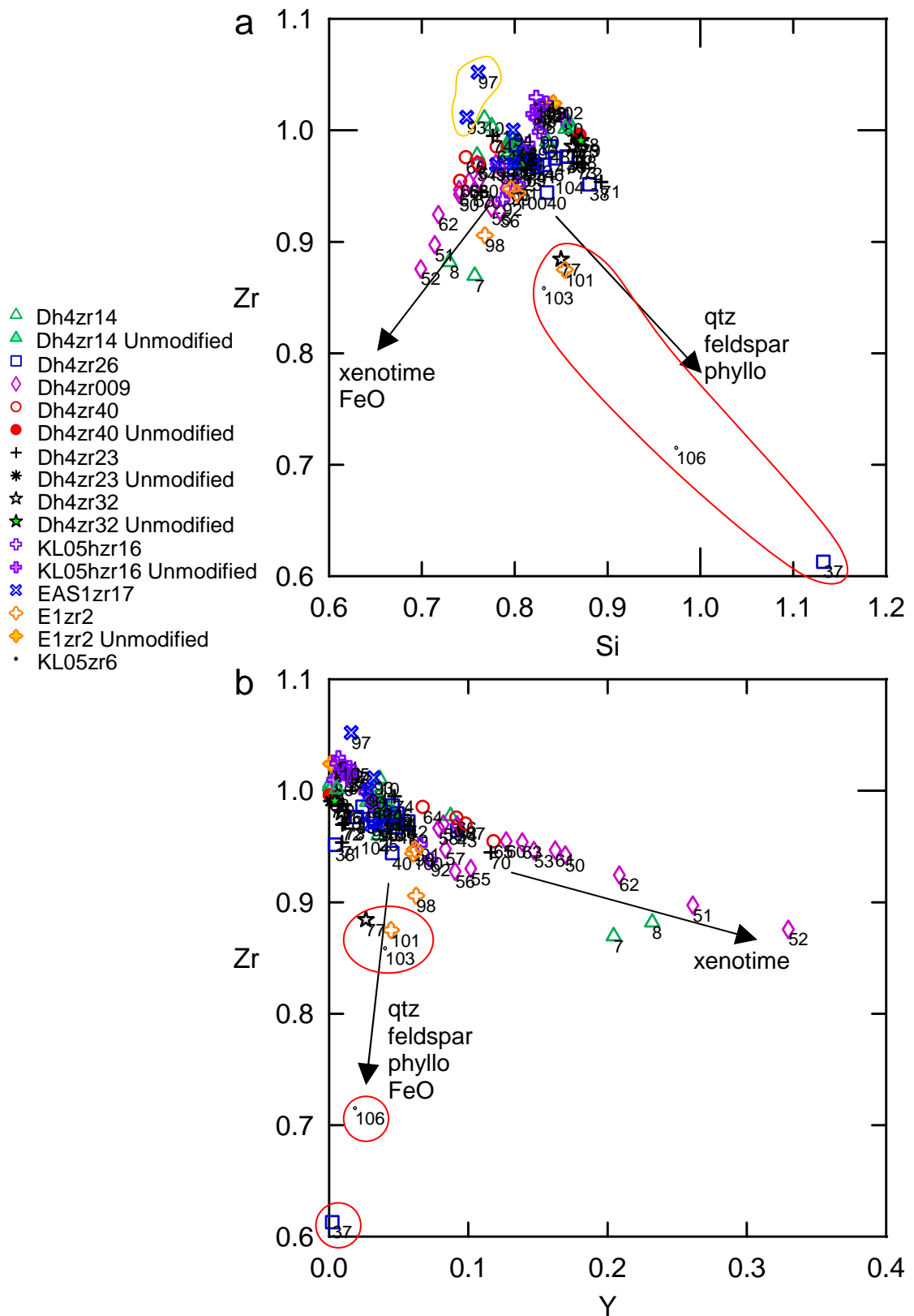


Figure 27. Element plots from dark BSE zircon EPMA analysis and weeding of anomalous data points.

Units are c.p.f.u.

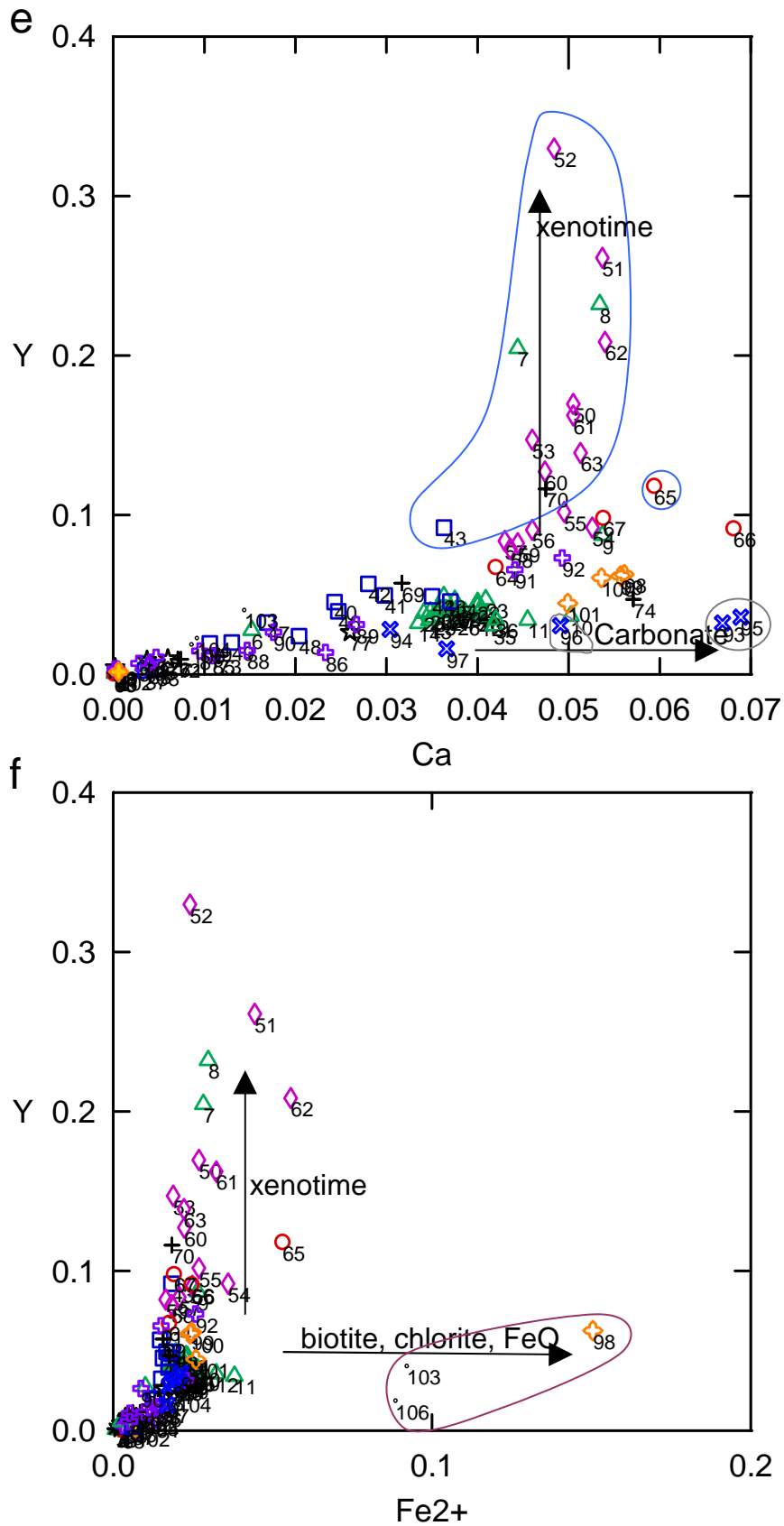


Figure 27. *cont.* Element plots from dark BSE zircon EPMA analysis and weeding of anomalous data points. Units are c.p.f.u.

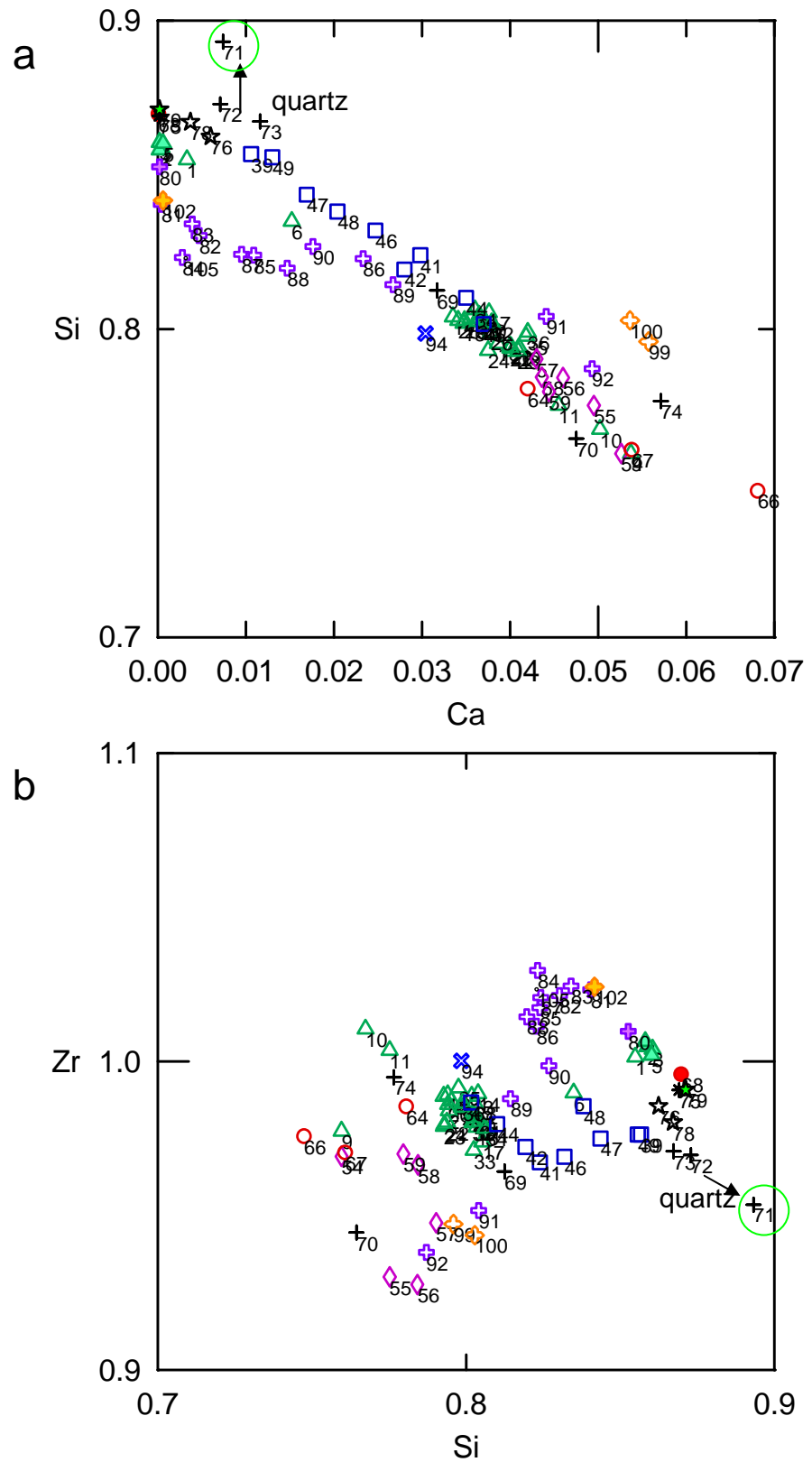


Figure 28. Element plots from dark BSE zircon EPMA analysis and weeding of anomalous data points, round 2. Units are c.p.f.u.

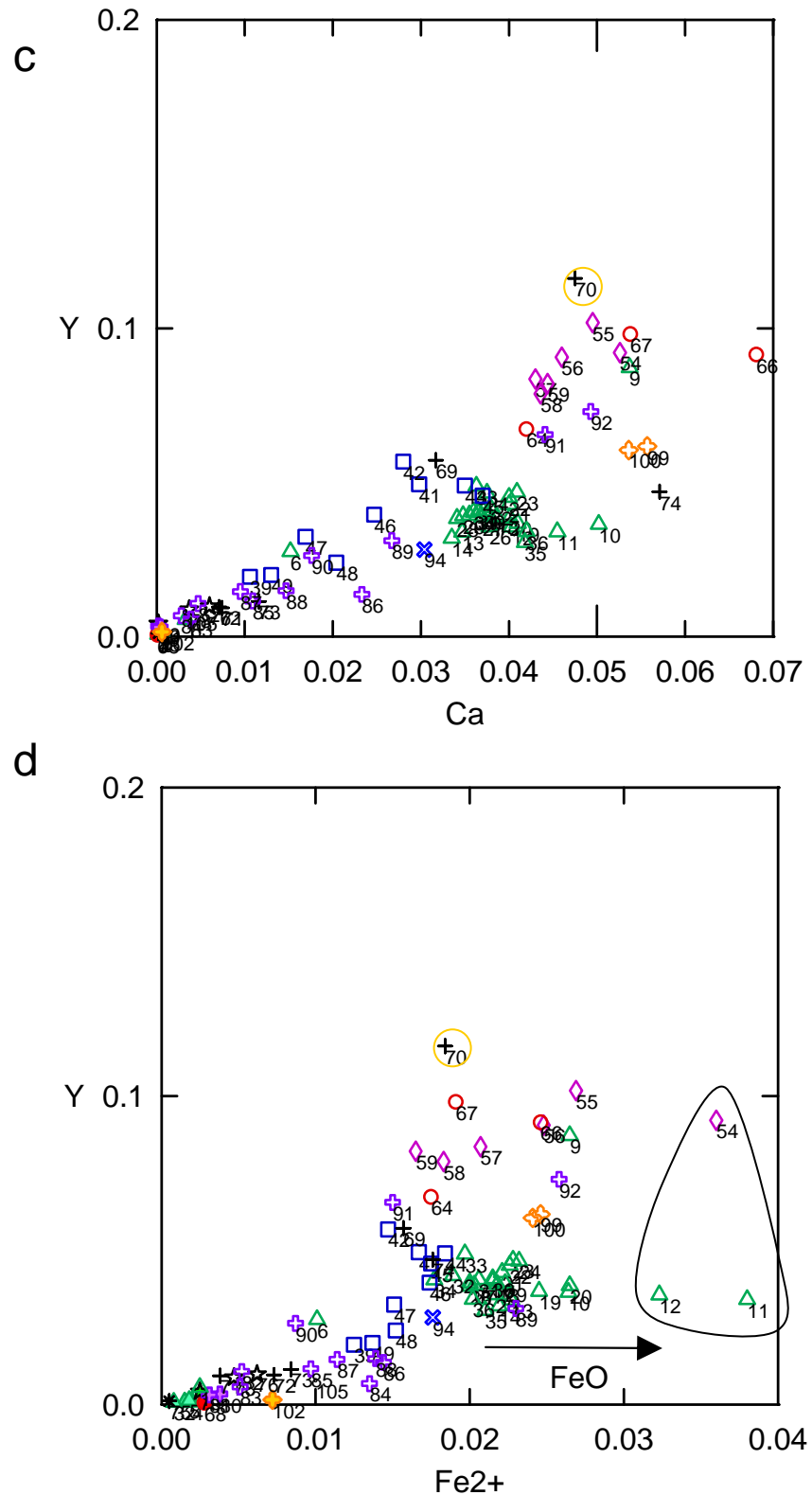


Figure 28 *cont.* Element plots from dark BSE zircon EPMA analysis and weeding of anomalous data points, round 2. Units are c.p.f.u.

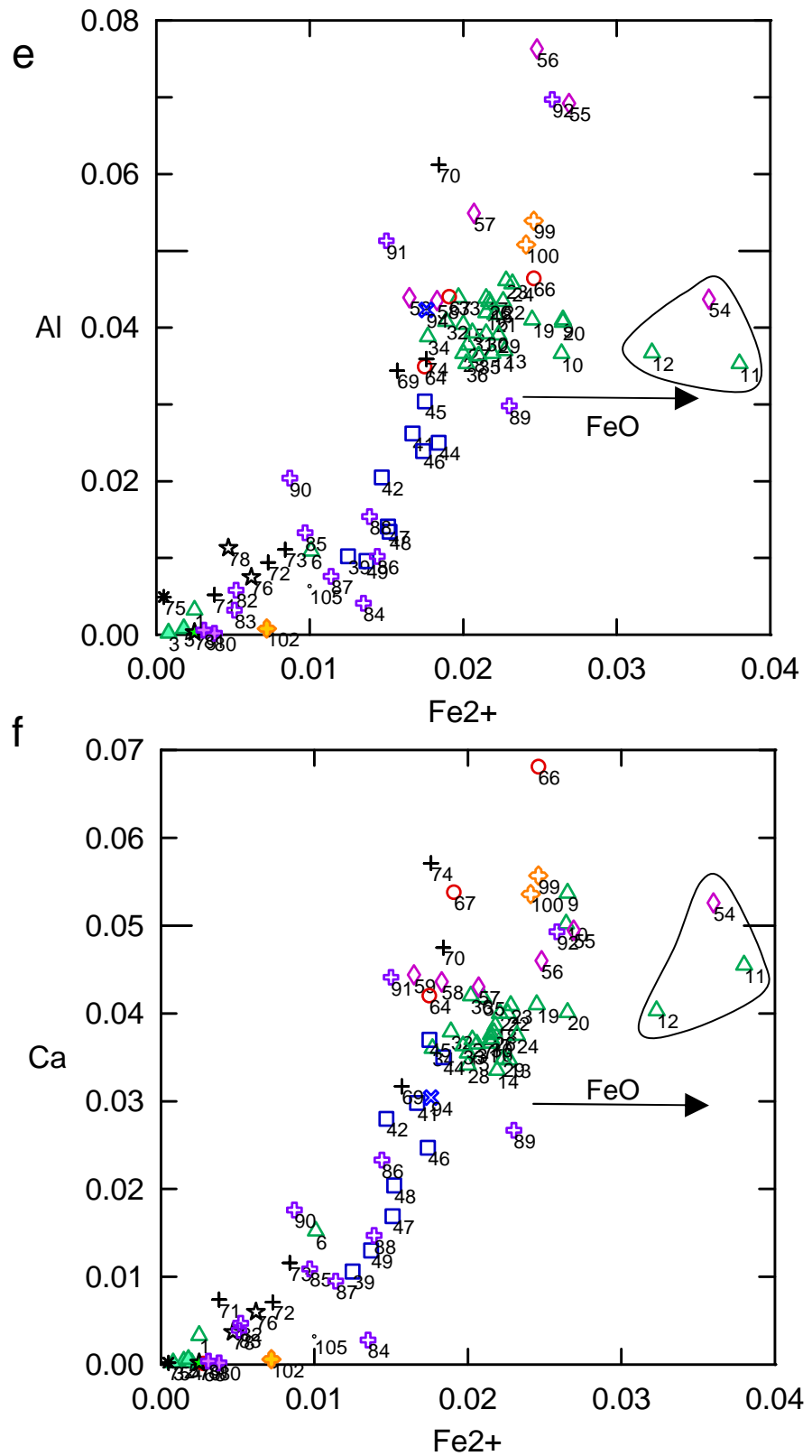


Figure 28 cont. Element plots from dark BSE zircon EPMA analysis and weeding of anomalous data points, round 2. Units are c.p.f.u.

The contaminated data points identified were removed and on plotting the rescaled graphs from the reduced data set (Fig. 28), it was apparent that particular data points still persisted to deviate from the overall trend. These deviations followed the predicted trends identified in Figure 27 but were likely not obvious because of the scale of the plots. Figure 28a&b identifies a point circled in green that is likely the result of a quartz inclusion analysed. The Y-rich point circled in yellow in Fig. 28c&d probably due to a xenotime inclusion and points encircled within the black line (Fig. 28d-f), the result of minute FeO inclusions.

3.9.2.2 Chemical analyses

Chemical compositions of the zircons analysed with all the above anomalous points removed is presented in Table 2 with concentrations given in cations per formula unit. This data has been reproduced as element weight percent (wt%) in Appendix B.

Overall, light BSE zircon that contains dark BSE zircon has a typical zircon composition but has a relatively low Si content for all greenschist facies rocks studied. This results in a high Zr/Si ratio compared to stoichiometric zircon and is most apparent in zircon from KL05 and Eas samples. Hf is concentrated around 1wt% in light BSE zircon but varies from 0.7 to 1.5wt% while Fe and Y can be present in trace amounts. Light BSE zircon has a typical average analysis total close to 100% but dark BSE zircon analysis totals are significantly lower, averaging 89.75% (± 4.3). Dark BSE zircon can be depleted by several wt% in Zr and Si compared to the light BSE zircon. When plotted as c.p.f.u., Zr and Si display a wide spread in data and are relatively poorly correlated (Fig.29a). Dark BSE zircon exhibits an increase in Zr/Si ratio but this shows no correlation with Hf, which appears to be in similar concentrations in light BSE and dark BSE zircon (Fig. 29b).

Non-formula element enrichment would appear to be coupled to Zr and Si depletion in dark BSE zircon (Fig. 29c&d). Trends in both plots exhibit a relationship that closely follows a 1:3 (Zr or Si:Sum of non-formula elements) substitution (Fig. 29c&d). Non-formula elements enriched are Mg (upto 0.015 c.p.f.u. (c.0.08wt%)), Al (upto 0.08 c.p.f.u. (c.0.5wt%)), Ca (upto 0.07 c.p.f.u.

(c.0.8wt%), Fe (upto 0.03 c.p.f.u. (c.0.6wt%)) and Y (upto 0.1 c.p.f.u. (c.3wt%)). Y enrichment exhibits a strong correlation with Zr depletion (Fig. 29e) and Si depletion (Fig. 29f), closely following a 1:1 substitution trend in both instances. This 1:1 substitution trend with Zr is replicated by the other non-formula elements Al (Fig. 29g) and Ca (Fig. 29h). The only truly linear relationship (where $r^2 > 0.8$) in dark BSE zircon is Ca-Al (Fig. 29i, $r^2 = 0.82$). However, Si:Al and Si:Ca ratios are 3:2 and 2:1 respectively (Fig. 29j&k)

All the substitution trends in this study have been estimated visually. Regression lines have not been used because they do not take into account the variation within individual analyses and due to minor contamination by inclusions that cannot be “weeded out”. This is because it is not the primary aim of this study to determine the atomic substitution mechanisms in zircon.

Zr depletion follows a relatively poorly defined trend with Mg (Fig. 29l) but roughly follows a 10:1 Zr:Mg substitution relationship. Mg is concentrated in dark BSE zircon in amounts often below the detection limits of the EPMA and may explain this poor correlation with Zr. However, Mg does exhibit a reasonable correlation with non-formula elements, particularly Ca (Fig. 29m) appearing to follow an exponential curve. Si and Mg display a similar 10:1 relationship as Zr (Fig. 29n). Fe displays a fairly broad spread of data when plotted against Zr but there is an overall rough correlation of 2:1 with Zr depletion and Fe enrichment (Fig. 29o). Similarly, there is reasonable spread in the data as Si depletion and Fe enrichment follow a 4:1 respectively (Fig. 29p).

Sample	Analysis No.	Mg	Al	Si	Ca	Fe2+	Y	Zr	Hf	Total c.p.f.u.	Zr/Si	Zr/Hf	Total wt%
<i>Light BSE zircon</i>													
dh4zr14	2	0.000	0.000	0.859	0.000	0.002	0.001	1.005	0.012	1.879	1.170	81.086	98.44
dh4zr14	3	0.000	0.000	0.861	0.000	0.001	0.001	1.004	0.012	1.878	1.167	87.037	98.13
dh4zr14	4	0.000	0.000	0.858	0.000	0.002	0.001	1.007	0.011	1.879	1.173	88.924	97.99
dh4zr14	5	0.000	0.001	0.860	0.001	0.002	0.001	1.002	0.012	1.879	1.165	81.666	98.16
dh4zr40	68	0.000	0.000	0.870	0.000	0.003	0.001	0.996	0.008	1.878	1.145	119.750	99.67
dh4zr23	75	0.000	0.005	0.869	0.000	0.001	0.001	0.991	0.011	1.878	1.140	88.109	98.18
dh4zr32	79	0.000	0.000	0.871	0.000	0.003	0.004	0.991	0.009	1.878	1.137	109.281	101.05
kl05hzt16core	80	0.000	0.000	0.853	0.000	0.004	0.003	1.010	0.011	1.881	1.184	89.907	99.54
kl05hzt16core	81	0.000	0.001	0.840	0.000	0.003	0.003	1.023	0.012	1.883	1.218	84.890	99.23
E1zr2	102	0.000	0.001	0.842	0.001	0.007	0.002	1.024	0.008	1.885	1.217	125.222	100.80
<i>Dark BSE zircon</i>													
dh4zr14	1	0.001	0.003	0.855	0.003	0.003	0.006	1.001	0.012	1.883	1.171	83.808	97.30
dh4zr14	6	0.005	0.011	0.835	0.015	0.010	0.028	0.990	0.012	1.906	1.186	80.074	93.13
dh4zr14	9	0.010	0.041	0.760	0.054	0.027	0.087	0.977	0.013	1.969	1.287	73.743	84.59
dh4zr14	10	0.012	0.037	0.767	0.050	0.026	0.036	1.011	0.014	1.953	1.317	74.877	89.94
dh4zr14	13	0.003	0.037	0.802	0.035	0.023	0.034	0.989	0.012	1.933	1.233	83.274	88.51
dh4zr14	14	0.003	0.037	0.804	0.034	0.022	0.032	0.990	0.011	1.932	1.231	88.748	89.19
dh4zr14	15	0.003	0.040	0.803	0.036	0.020	0.039	0.981	0.012	1.935	1.222	85.707	87.88
dh4zr14	16	0.003	0.042	0.803	0.037	0.022	0.040	0.979	0.011	1.937	1.218	90.401	87.72
dh4zr14	17	0.003	0.044	0.805	0.038	0.022	0.040	0.974	0.012	1.937	1.209	81.974	88.15
dh4zr14	18	0.004	0.043	0.795	0.039	0.022	0.039	0.987	0.011	1.939	1.241	91.268	87.94
dh4zr14	19	0.004	0.041	0.794	0.041	0.025	0.037	0.989	0.011	1.941	1.246	94.574	87.33
dh4zr14	20	0.004	0.041	0.794	0.040	0.027	0.039	0.986	0.012	1.942	1.242	86.109	88.35
dh4zr14	21	0.004	0.042	0.794	0.040	0.022	0.043	0.984	0.012	1.941	1.239	84.639	88.49
dh4zr14	22	0.005	0.043	0.794	0.040	0.023	0.045	0.980	0.013	1.943	1.235	78.424	88.13
dh4zr14	23	0.005	0.046	0.793	0.041	0.023	0.047	0.979	0.011	1.944	1.235	88.688	87.69
dh4zr14	24	0.005	0.046	0.793	0.038	0.023	0.047	0.980	0.013	1.943	1.235	77.982	87.97
dh4zr14	26	0.005	0.043	0.799	0.038	0.022	0.036	0.985	0.011	1.938	1.233	92.708	89.12
dh4zr14	27	0.004	0.038	0.802	0.037	0.020	0.039	0.983	0.013	1.935	1.225	77.697	89.38
dh4zr14	28	0.003	0.037	0.803	0.034	0.020	0.038	0.987	0.012	1.933	1.229	84.721	89.80
dh4zr14	29	0.004	0.039	0.803	0.035	0.022	0.039	0.982	0.012	1.935	1.224	85.150	89.31

Table 2 EPMA analyses from zircon containing dark BSE zircon. Data is in c.p.f.u. calculated to 4(O)

Sample	Analysis No.	Mg	Al	Si	Ca	Fe2+	Y	Zr	Hf	Total c.p.f.u.	Zr/Si	Zr/Hf	Total wt%
dh4zr14	30	0.003	0.039	0.803	0.037	0.022	0.041	0.980	0.012	1.936	1.221	82.411	88.69
dh4zr14	31	0.003	0.039	0.804	0.037	0.021	0.041	0.981	0.011	1.935	1.219	92.522	88.72
dh4zr14	32	0.004	0.041	0.802	0.038	0.019	0.042	0.980	0.011	1.936	1.222	88.192	88.75
dh4zr14	33	0.004	0.044	0.803	0.036	0.020	0.049	0.971	0.012	1.939	1.210	78.275	87.93
dh4zr14	34	0.004	0.039	0.806	0.036	0.018	0.040	0.978	0.013	1.934	1.214	78.535	89.25
dh4zr14	35	0.007	0.036	0.798	0.042	0.021	0.031	0.991	0.013	1.938	1.243	78.710	90.51
dh4zr14	36	0.007	0.035	0.799	0.042	0.020	0.034	0.987	0.014	1.938	1.235	71.325	90.91
dh4zr26	39	0.003	0.010	0.857	0.011	0.013	0.019	0.976	0.010	1.898	1.140	101.712	94.86
dh4zr26	41	0.005	0.026	0.824	0.030	0.017	0.049	0.967	0.009	1.927	1.174	107.442	88.16
dh4zr26	42	0.005	0.021	0.819	0.028	0.015	0.057	0.972	0.010	1.926	1.187	98.684	88.19
dh4zr26	44	0.005	0.025	0.810	0.035	0.018	0.049	0.980	0.010	1.932	1.209	98.993	87.62
dh4zr26	45	0.006	0.030	0.802	0.037	0.018	0.046	0.987	0.010	1.935	1.231	95.528	87.50
dh4zr26	46	0.004	0.024	0.832	0.025	0.017	0.040	0.969	0.010	1.920	1.165	98.260	91.31
dh4zr26	47	0.002	0.014	0.844	0.017	0.015	0.032	0.975	0.009	1.908	1.156	106.764	92.57
dh4zr26	48	0.003	0.013	0.838	0.020	0.015	0.024	0.986	0.010	1.909	1.176	101.985	93.15
dh4zr26	49	0.002	0.010	0.856	0.013	0.014	0.020	0.976	0.009	1.900	1.141	104.151	96.19
dh4zr009	55	0.009	0.069	0.775	0.050	0.027	0.102	0.930	0.013	1.974	1.200	73.212	82.86
dh4zr009	56	0.007	0.076	0.784	0.046	0.025	0.091	0.928	0.012	1.968	1.183	80.487	83.64
dh4zr009	57	0.005	0.055	0.790	0.043	0.021	0.084	0.948	0.011	1.956	1.199	89.296	84.13
dh4zr009	58	0.004	0.044	0.784	0.044	0.018	0.079	0.967	0.011	1.950	1.232	86.607	84.57
dh4zr009	59	0.004	0.044	0.780	0.044	0.017	0.082	0.970	0.011	1.951	1.244	88.076	83.14
dh4zr40	64	0.005	0.035	0.781	0.042	0.018	0.067	0.985	0.012	1.945	1.262	81.670	85.61
dh4zr40	66	0.009	0.046	0.748	0.068	0.025	0.092	0.976	0.014	1.976	1.305	72.550	80.82
dh4zr40	67	0.006	0.044	0.761	0.054	0.019	0.098	0.971	0.012	1.964	1.276	83.668	82.06
dh4zr23	69	0.003	0.034	0.813	0.032	0.016	0.057	0.964	0.012	1.931	1.187	83.167	86.94
dh4zr23	72	0.000	0.009	0.873	0.007	0.007	0.010	0.970	0.011	1.887	1.111	85.961	96.73
dh4zr23	73	0.001	0.011	0.867	0.012	0.008	0.011	0.971	0.011	1.892	1.119	90.341	96.10
dh4zr23	74	0.012	0.036	0.777	0.057	0.018	0.047	0.995	0.012	1.953	1.281	80.489	88.69
dh4zr32	76	0.001	0.008	0.862	0.006	0.006	0.010	0.986	0.010	1.888	1.143	104.116	97.36
dh4zr32	78	0.001	0.011	0.867	0.004	0.005	0.009	0.980	0.009	1.886	1.131	107.553	102.28
kl05hzt16core	82	0.000	0.006	0.830	0.005	0.005	0.011	1.021	0.012	1.891	1.230	82.423	97.55
kl05hzt16core	83	0.000	0.003	0.834	0.004	0.005	0.006	1.025	0.011	1.888	1.228	90.179	95.66
kl05hzt16core	84	0.001	0.004	0.823	0.003	0.014	0.007	1.030	0.013	1.894	1.251	77.233	95.78
kl05hzt16core	85	0.001	0.013	0.824	0.011	0.010	0.012	1.017	0.012	1.900	1.235	86.008	91.92

Table 2 cont.

Sample	Analysis No.	Mg	Al	Si	Ca	Fe2+	Y	Zr	Hf	Total c.p.f.u.	Zr/Si	Zr/Hf	Total wt%
kl05hzzr16core	86	0.002	0.010	0.823	0.023	0.014	0.014	1.011	0.011	1.909	1.229	94.051	91.86
kl05hzzr16core	87	0.001	0.008	0.824	0.010	0.011	0.015	1.021	0.010	1.899	1.238	101.994	92.92
kl05hzzr16core	88	0.002	0.015	0.820	0.015	0.014	0.015	1.015	0.011	1.906	1.238	94.291	91.54
kl05hzzr16core	89	0.002	0.030	0.814	0.027	0.023	0.031	0.988	0.010	1.925	1.213	96.131	89.63
kl05hzzr16core	90	0.001	0.020	0.827	0.018	0.009	0.026	0.999	0.008	1.907	1.208	123.558	93.93
kl05hzzr16core	91	0.002	0.051	0.804	0.044	0.015	0.066	0.952	0.011	1.945	1.184	84.933	85.99
kl05hzzr16core	92	0.010	0.070	0.787	0.049	0.026	0.073	0.938	0.013	1.966	1.192	73.250	85.29
eastzr17	94	0.004	0.042	0.799	0.030	0.018	0.028	1.000	0.008	1.930	1.253	120.843	93.04
E1zr2	99	0.014	0.054	0.796	0.056	0.025	0.062	0.947	0.010	1.962	1.190	98.860	86.00
E1zr2	100	0.014	0.051	0.803	0.054	0.024	0.061	0.944	0.010	1.959	1.176	97.005	87.03
KL05zr6	105	0.001	0.006	0.823	0.003	0.010	0.008	1.023	0.019	1.893	1.244	55.038	96.49

Table 2 cont.

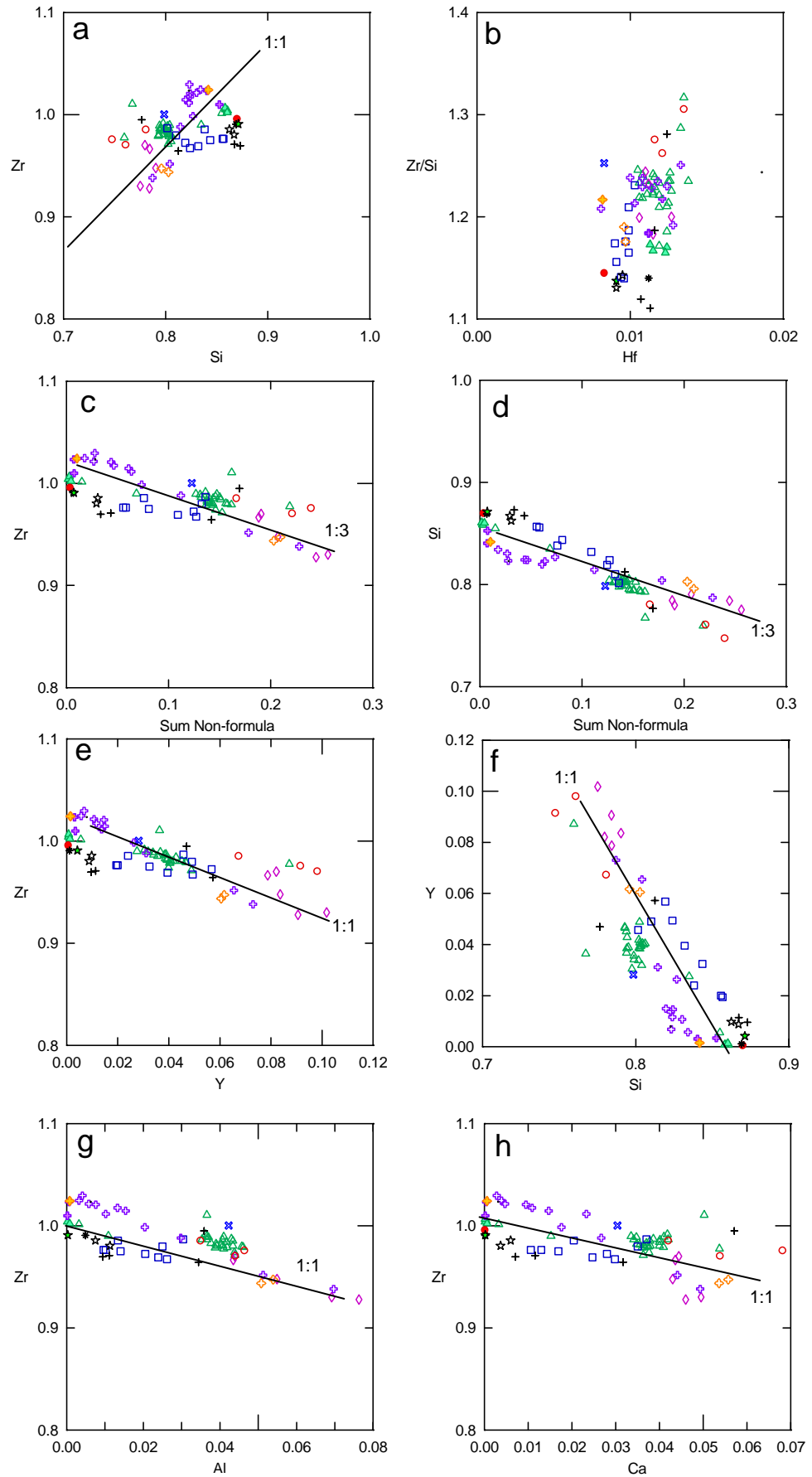


Figure 29. Element plots of data presented in Table 2 from dark BSE zircon EPMA analysis

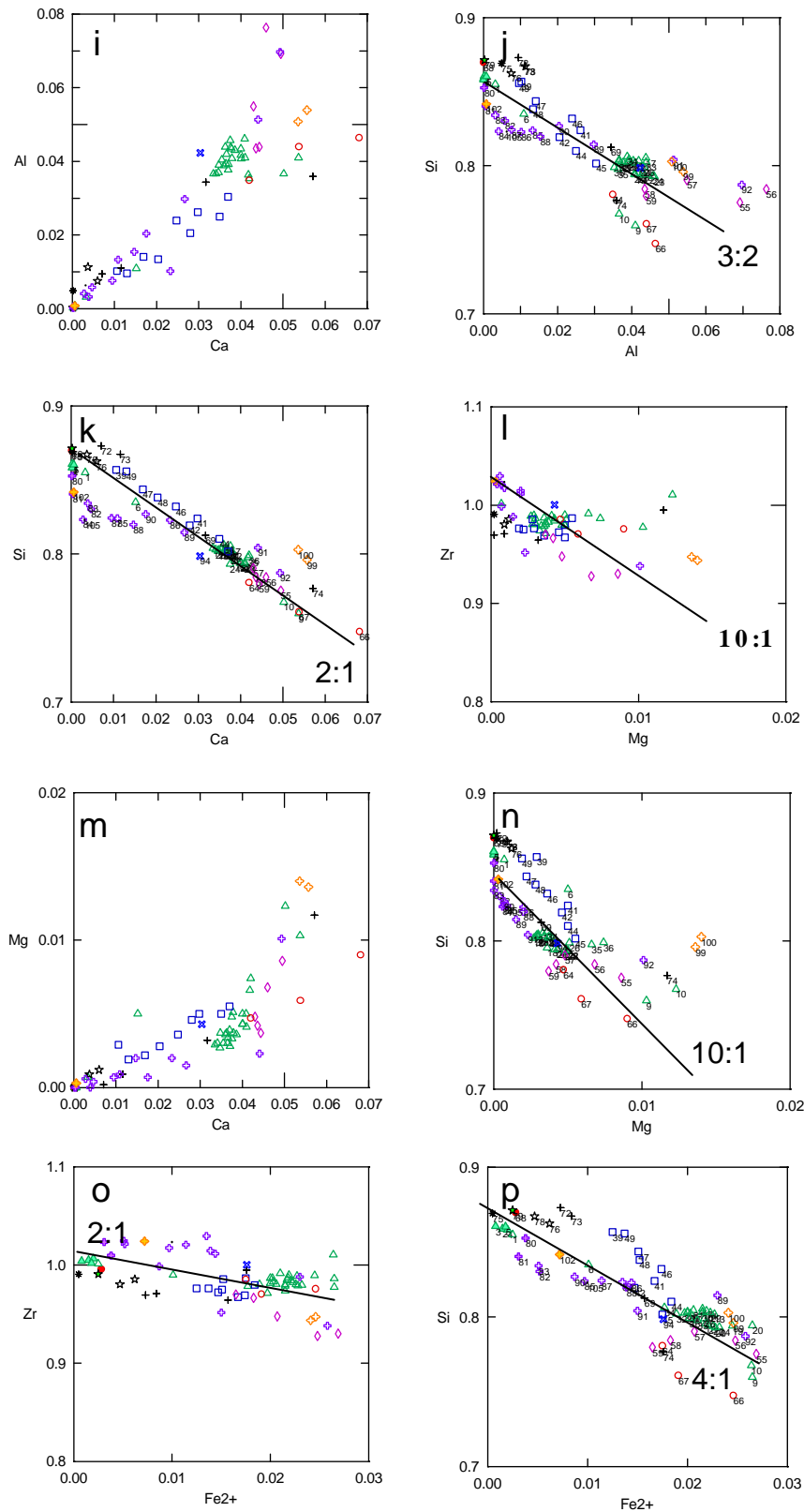


Figure 29.cont. Element plots of data presented in Table 2 from dark BSE zircon EPMA analysis.

Units are c.p.f.u.

When plotted together, non-formula elements display a relatively good correlation with one another in dark BSE zircon zones (Fig. 29q). Y is typically the most enriched of the non-formula elements although Al and Ca closely follow a similar distribution and concentration to Y. Fe is considerably less enriched than these non-formula elements although Mg is least enriched of all non-formula elements. However, it is noticeable that individual grains exhibit unique non-formula element distributions and non-formula element relationships. Element plots also display similar patterns where there is variation within the overall trend. Data from analyses of individual grains appear to define slightly different substitution trends. An example that illustrates this point, is data from Dh4zr14 (green triangle) defines a substitution trend that follows 1:6 Zr:Sum of non-formula elements (Fig. 30) whereas the Zr:Sum of non-formula elements relationship trend in KL05hzc16 is 1:2 (purple plus sign and Fig. 31). In Dh4zr14, Zr-Al, Zr-Ca and Zr-Y all roughly exhibit 1:2 trends (Fig. 30) compared to 1:1 for KL05hzc16 (Fig. 31). Si-Y plots however show that Dh4zr14 follows a 1:2 Si:Y trend while KL05hzc16 that follow a 1:1 substitution trend. Further variation can also be observed in the non-formula element plots where individual grains follow distinctive substitution trends.

The variability between individual grains indicates that the chemistry of dark BSE zircon may be influenced by the local conditions in which it became modified. The variation in conditions may be environmental or caused by differences in the individual properties of the grain itself. The overall CL and EBSD qualities of dark BSE zircon are to now be established so that a relationship between BSE, CL, EBSD and the chemical properties of individual grains can be investigated.

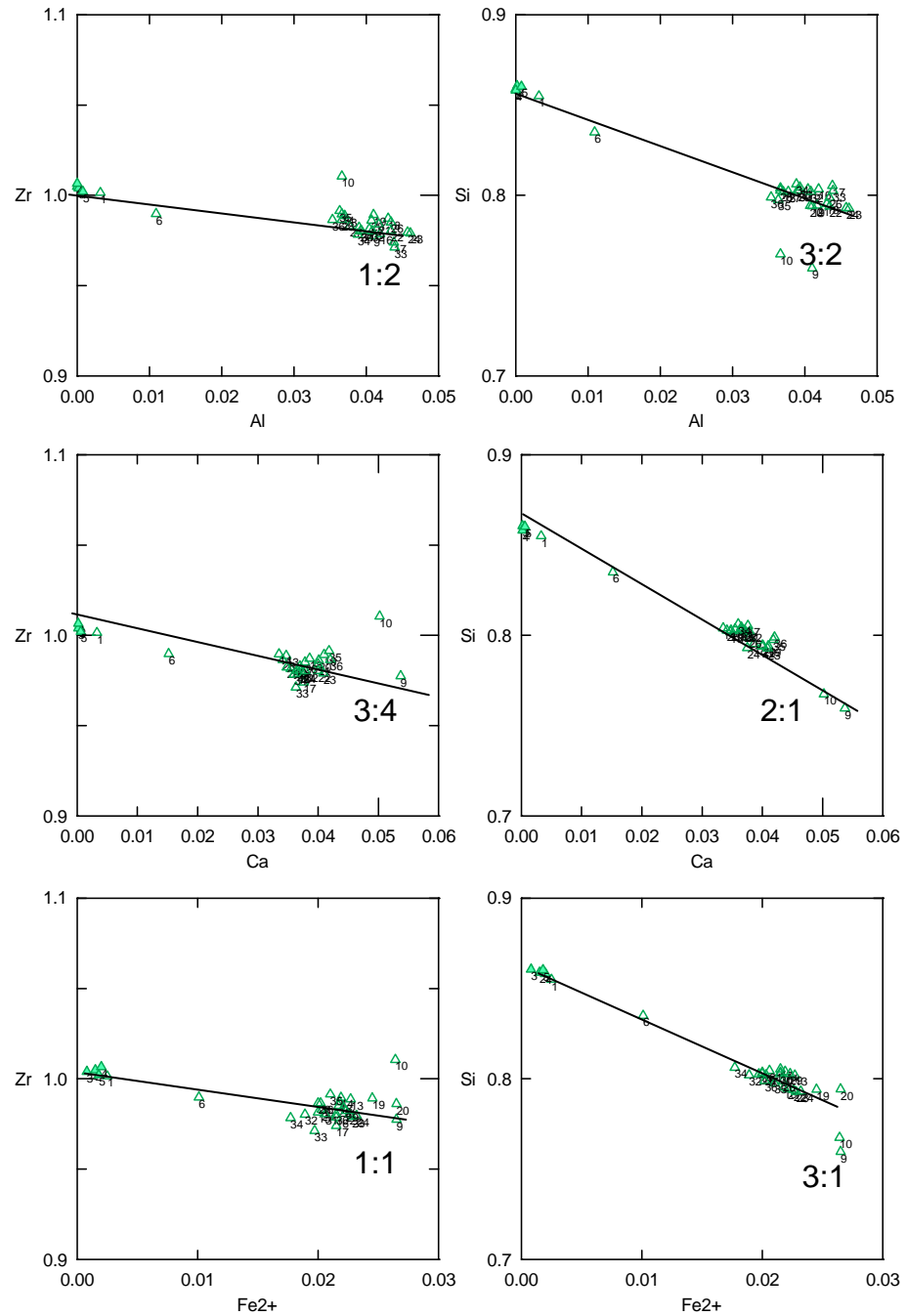


Figure 30. Element plots for zircon Dh4zr14. Units are c.p.f.u.

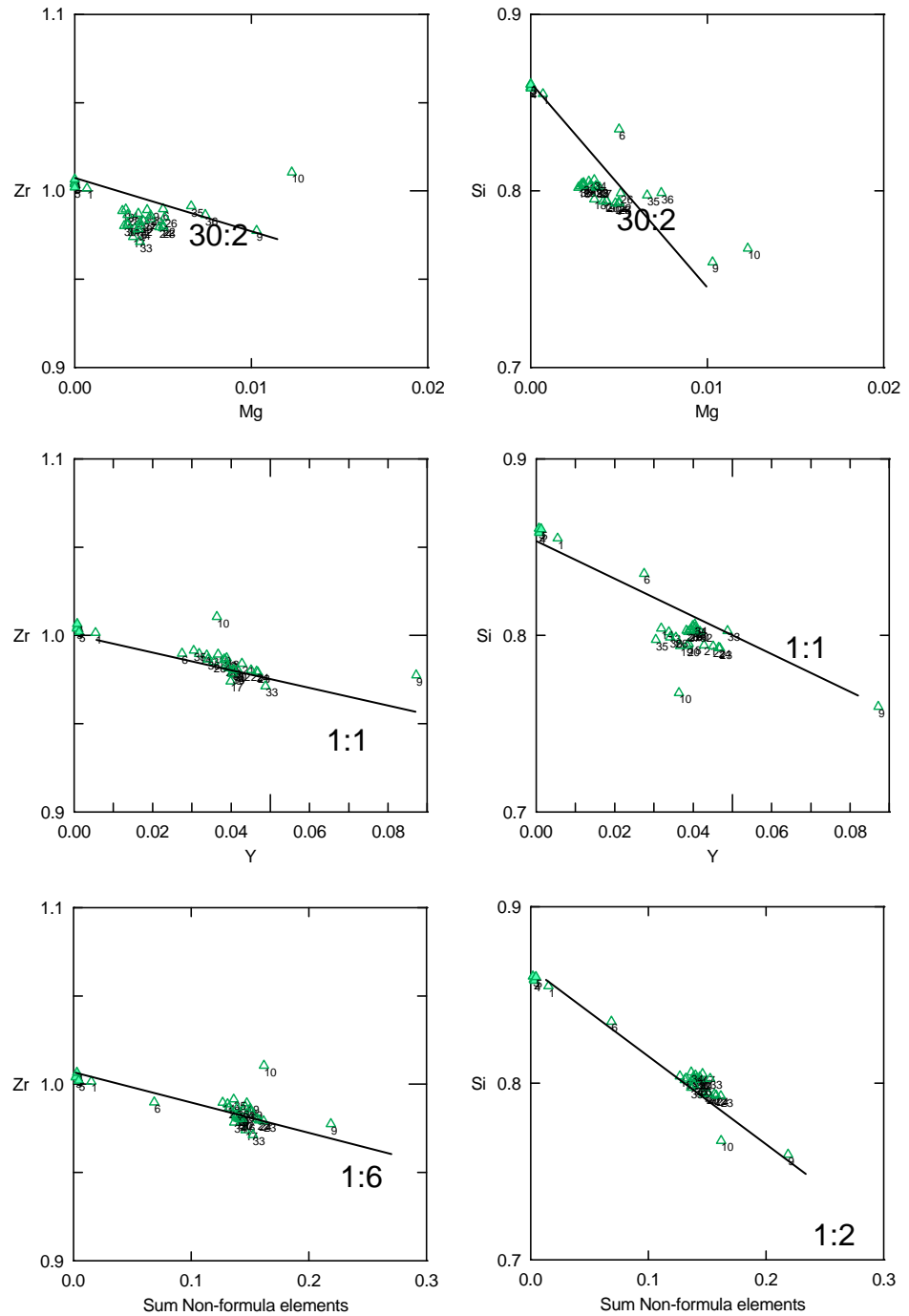


Figure 30 cont.. Element plots for zircon Dh4zr14. Units are c.p.f.u.

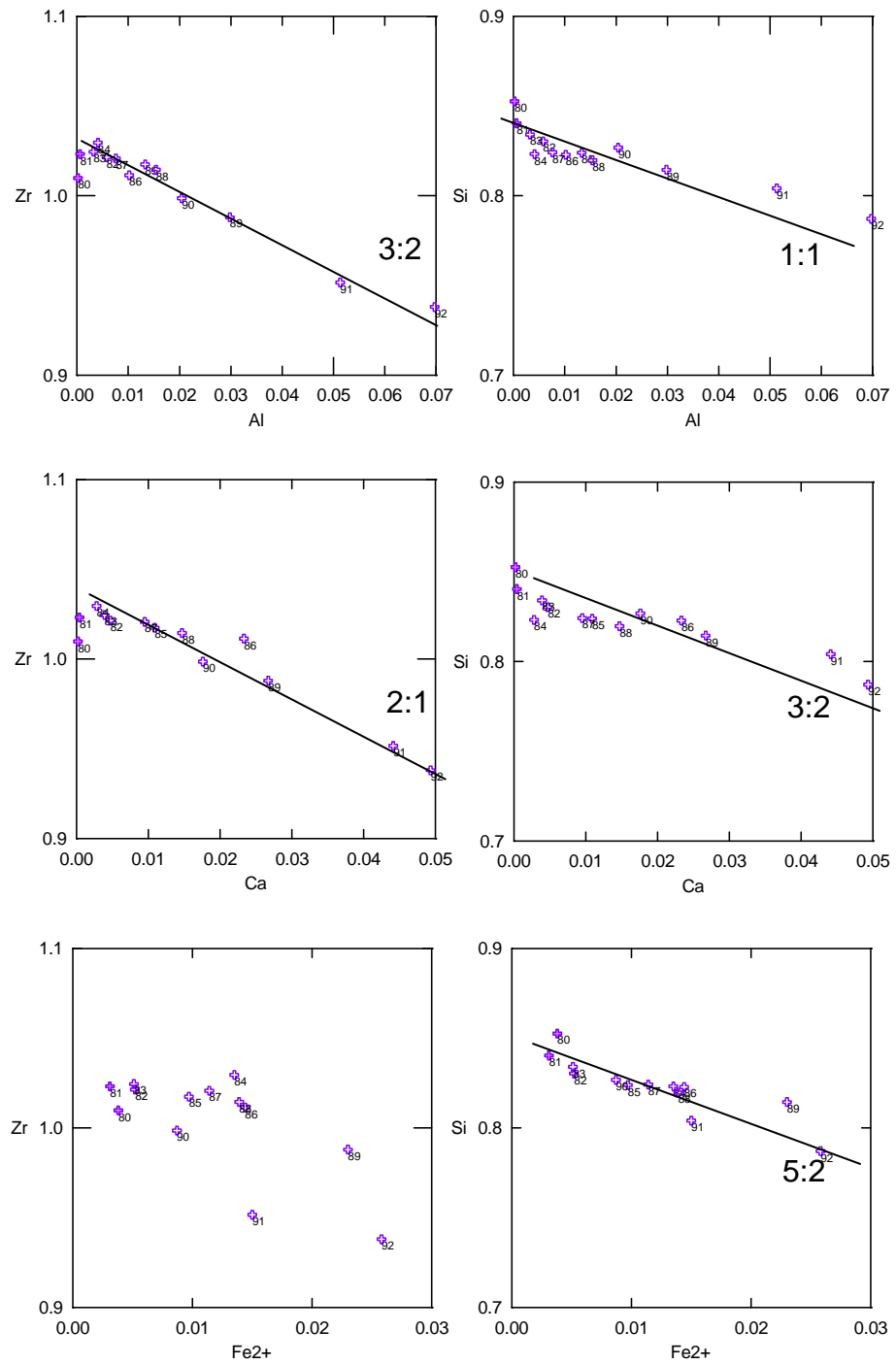


Figure 31. Element plots for zircon KL05hzi16. Units are c.p.f.u.

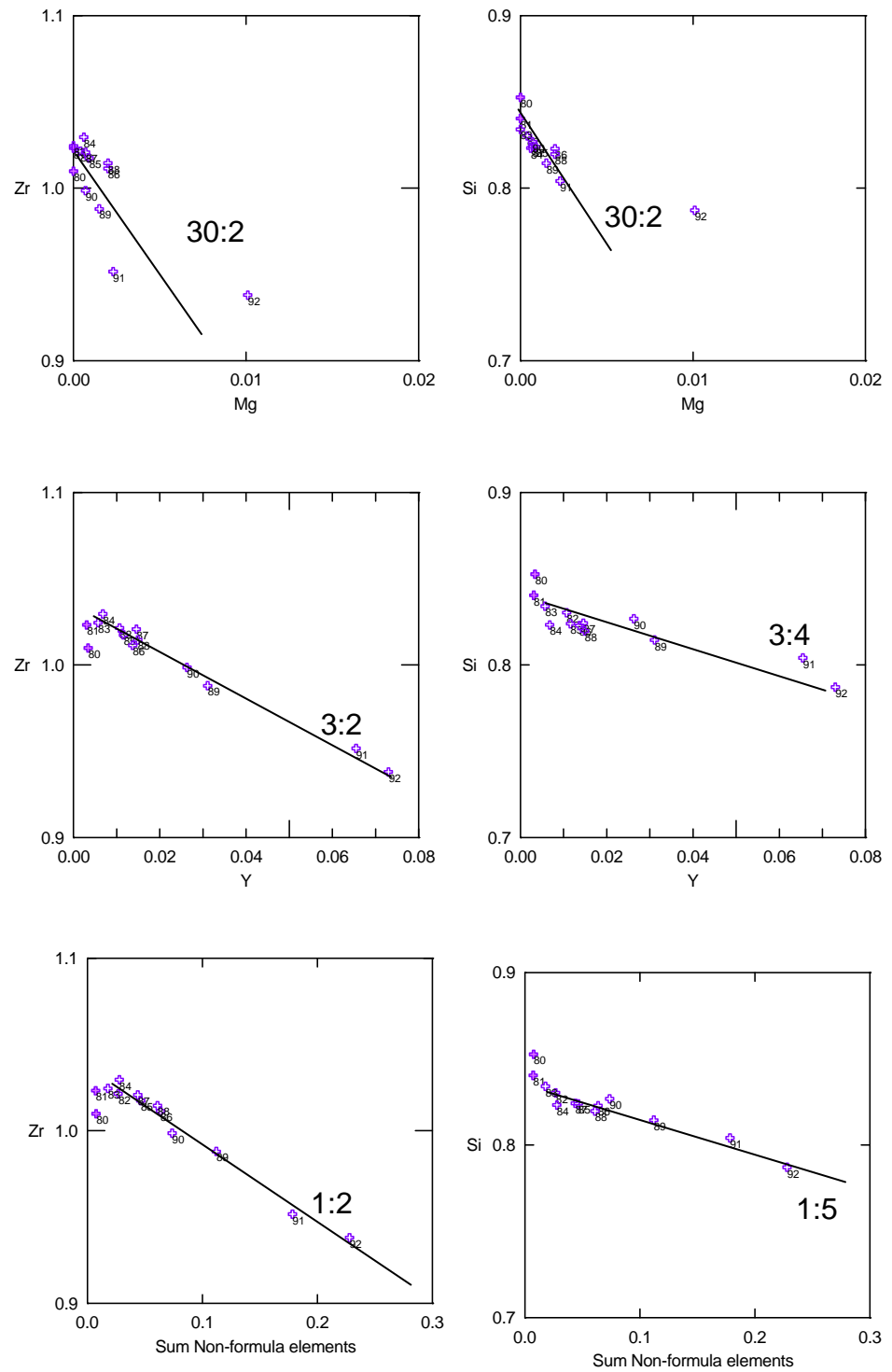


Figure 31. Element plots for zircon KL05hrz16. Units are c.p.f.u.

3.9.2.3 EBSD, CL and BSE

EBSD analysis of dark BSE zircon produces very weak Kikuchi patterns (low IQ) (Fig. 23b, 24a, 25b). Variations in BSE intensity within the dark BSE zircon do appear to have some relation to the quality of EBSD pattern with slightly brighter BSE areas giving slightly higher IQ EBSD patterns (Fig. 24a).

In general, light BSE zircon is easily identified within dark BSE areas by having normal zircon BSE emission levels, strong CL signal, high EBSD IQ patterns and typical zircon composition (Fig. 25).

Typically, dark BSE zircon has a very low intensity in CL when compared to light BSE zircon (Fig. 23a, 24b-f, 25c). Some dark BSE zircons in quartzites have an overall very weak CL signal but with bright specks near and around the grain edges (Fig 24c-f). SE imaging confirms this is not due to charging effects around the grain. Light BSE zircon in Figure 24d is also particularly low in CL but despite this, very weak CL zoning can still be seen. However, the variable CL intensity of light BSE zircon in these grains mean that when CL intensities are low in light BSE zircon, the boundary between light and dark BSE zircon is not always obvious in CL images (Fig. 24b).

CL spectra of dark BSE zircon shows a major reduction in intensity at the peak 340-380nm (Fig.22b). Unlike light BSE zircon, dark BSE zircon has a small peak at 470-485nm with a larger peak at 575-580nm and is due to the emission centre of Dy. The broad plateau area is also slightly depressed compared to light BSE zircon but still maintains the hump at the end of the plateau. However, Dy appears to be the main activator for CL in dark BSE zircon. It should be noted that U also quenches CL in zircon and may be a cause for overall low CL (2005b (Rubatto and Gebaurer, 2000)). The remaining peaks do not correspond with emission bands from other known CL-active REE or other causes of luminescence in zircon. The details of CL emission centres in silicate minerals, such as zircon, is extremely complex (2005b) and outwith the scope of this study.

There is considerable variation both in the CL and EBSD properties of dark BSE zircon. To assess

whether these variations are related to differences in chemistry, and to examine if there is a relationship with BSE signal intensity (which varies in dark BSE zircon), is best determined by examining individual zircons in greater detail.

3.9.2.4 Zircon Dh4zr14

Zircon Dh4zr14 has a dark BSE core with multiple radial fractures in the outer light BSE zircon and concentric fractures along the light-dark BSE zircon boundary (Fig. 24a&b). The dark BSE core displays variations in BSE intensity and contains several large (>5 μ m across) inclusions within the microstructure. EDX scans of the grain reveal that most inclusions are quartz (Si element map, Fig.24a) but also contains two 5-10 μ m sized FeS inclusions (Fe element map, Fig. 24a). Bands of light BSE zircon are present in the dark BSE core and follow parallel to the euhedral zoning pattern of outer light BSE growth layers. As such they are considered to represent bands of the original zircon.

A line scan with a 2 μ m step size intersects the dark BSE core that, along the line of analysis, contains numerous sub-micron sized high BSE intensity inclusions, patches of particularly low BSE intensity and a faint dark BSE band that follows parallel with light BSE zoning at the outer margins of the core (Fig. 32a). The light BSE zircon has a typical, unmodified zircon composition (Fig. 32a). Patches of very dark BSE zircon typically coincide with analyses that are considered to be anomalous and are therefore unlikely to represent dark BSE zircon. An Y-rich point coincides with the domain containing multiple sub-micron sized high BSE intensity inclusions and it is likely this is the result of a small xenotime component within the analysis that was not removed during the weeding process. Otherwise Y, Ca and Al are concentrated in very similar amounts and share a similar relationship. The substitution of Fe and Mg in dark BSE zircon is less but they both follow a similar profile to Y, Ca and Al. Hf varies very little from the light to the dark. There is some small variation in the concentration of non-formula elements in dark BSE zircon but this does not appear to be reflected BSE intensity that is relatively homogeneous along the line of analysis. Where BSE intensity does vary considerably, it would appear to relate areas containing inclusion that are anomalous points (analysis numbers 7&8 in Fig.27d and analysis numbers 11&12 in Fig.28d).

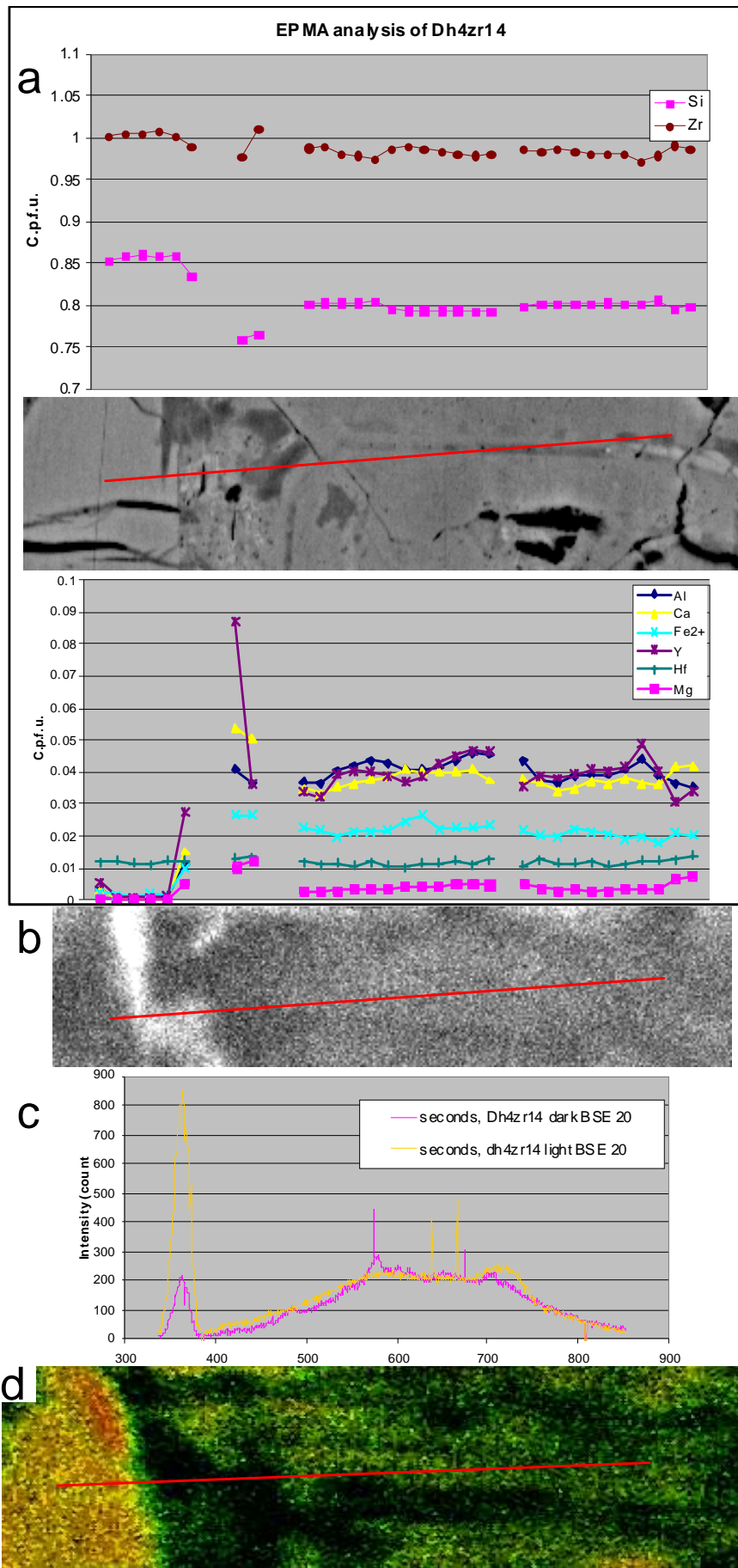


Figure 32. Detailed analysis of EPMA traverse area of zircon Dh4zr14 with figure caption on the following page.

Figure 32. Detailed analysis of EPMA traverse area of zircon Dh4zr14

a High magnification BSE image of Dh4zr14 (Fig. 24) showing EPMA traverse (red line) with EPMA c.p.f.u. data profile from line scan. Blank data points in traverse represent anomalous data removed during weeding process. **b** CL image of area in BSE image in **a**. **c** CL spectra of light and dark BSE zircon in Dh4zr14. CL points defined in figure 26. **e** CI-IQ EBSD map of area of BSE image in **a**.

CL and EBSD with BSE and chemistry

CL images of the core show an overall low CL intensity (Fig. 32b&c). Where BSE intensity is particularly low within the area of analysis, it can be broadly related to areas of low CL intensity. CL intense areas in this core are as a consequence of inclusions and thin bands of light BSE zircon. Slightly more intense CL parts of the dark BSE zircon can also be correlated to a slight increase in EBSD IQ (Fig. 24a, green colour). Unfortunately along the line of EPMA analysis, EBSD IQ is too low to determine any variations with BSE intensity apart from where xenotime inclusions are present (very high Y concentration) which can be correlated to a slight increase in EBSD IQ. As a general comment, non-formula elements incorporated into zircon will alter its crystalline properties and may reduce the CI when indexed against the zircon data files in the EBSD software. However this should not affect the IQ pattern of the zircon.

Large variations in the BSE intensity within dark BSE zircon therefore appear to mostly relate to areas concentrated in inclusions and do not relate to the true chemistry of dark BSE zircon.

3.9.2.5 Zircon KL05hzt16

Zircon KL05hzt16 is a fragmented grain within a quartz matrix (Fig.33a). Individual fragments are typically rounded with few sharp grain edges. The grain is broken up along what would appear to be original growth zones within the zircon. Individual fragments typically have bands of dark BSE zircon and the central part of the grain has a dark BSE zircon core surrounded by light BSE zircon. Dark BSE zircon is again characterised by an enrichment in non-formula elements and a low EBSD IQ pattern (Fig. 33a). The zircon to the bottom right hand of the image in Figure 33a has a high EBSD IQ pattern (Fig. 33c) whereas by comparison, light BSE zircon has a lower EBSD IQ in a high-resolution EBSD scan of KL05hzt16 (Fig. 33b). However, Figure 33b reveals some small slivers of high EBSD IQ domains (yellow-red colour) within light BSE zircon but is not reflected in a change in BSE intensity. Within the central core, light BSE zircon has a moderate EBSD IQ that forms a well-defined boundary with low EBSD IQ dark BSE zircon.

A CL image (Fig. 24a) reveals that the fragmented zircon has a significantly reduced in CL intensity when compared to the strongly luminescent zircon in the bottom right of the image. A higher magnification CL image (Fig. 33d) shows blotches of strongly luminescent zircon round the margins of individual fragments of the broken grain but this has no correlation to either BSE or EBSD IQ (Fig. 33a&b) and is not due to charging. Overall the more weakly luminescent areas display some variation that is slightly darker in some of the dark BSE zircon. Slightly stronger luminescent areas within zircon can be correlated with a slightly higher EBSD IQ (yellow colour).

An EPMA line scan, with 2 μ m step size intersects the dark BSE core and the surrounding light BSE zircon (Fig.34a). Higher magnification images of the core (Fig. 34) reveal dark BSE zircon has several higher BSE intensity blotches (*c.* 2 μ m across). In general, the line scan shows that slightly higher BSE intensity areas in the core have a lower concentration of non-formula elements than the darker BSE areas of the core. Zr and Si are inversely coupled to this and show a small depletion when non-formula element concentration is low but a large depletion in dark BSE zircon where non-formula concentrations are higher. BSE intensity varies considerably across the line of analysis but this is not replicated by a consistent enrichment of non-formula elements and neither do chemical variations appear to be related to any systematic change in EBSD IQ or variation in CL.

In summary, dark BSE zircon is enriched in non-formula elements but individual grains appear to have slightly different substitution relationships that can result in slight variation in the relative amounts of non-formula elements. Within individual grains there is little variation in the relative amounts of non-formula elements in dark BSE zircon. However, areas of particularly low BSE intensity in dark BSE zircon are generally heavily enriched in Y and Fe. However, these areas do not represent the true composition of dark BSE zircon are likely to be other mineral phases that have developed with dark BSE zircon as it formed. However, variations in the relative amounts of non-formula elements do not appear to have any affect on BSE intensity, CL intensity or EBSD IQ.

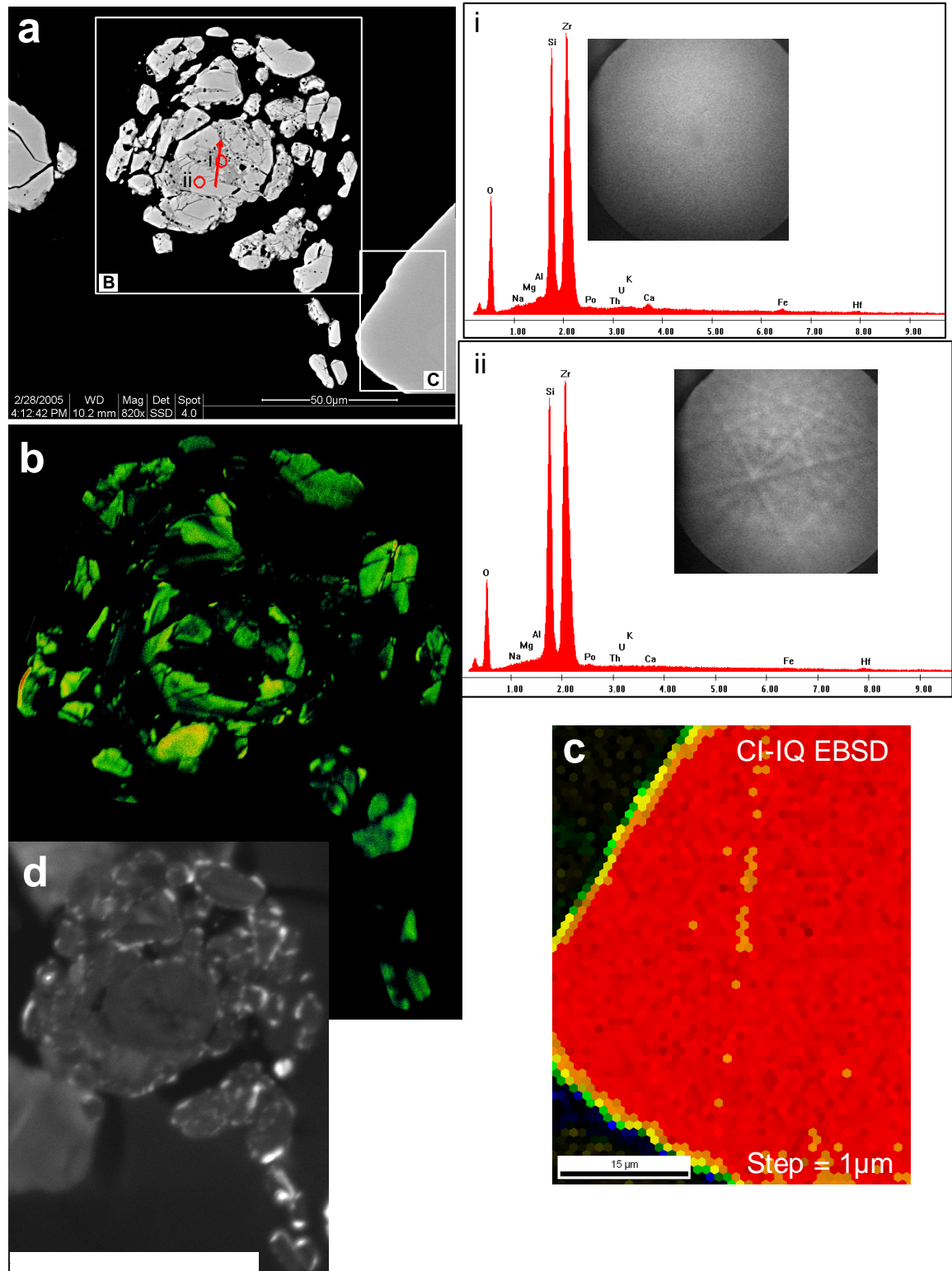


Figure 33. Characterisation of zircon KL05hzc16

a BSE image of figure 9b with EBSD and EDX analysis spots (i) Dark BSE area showing no EBSD pattern and enrichment in non-formula elements compared to light BSE zircon which has a high IQ kink pattern (ii). **b** CI-IQ EBSD scanned map of area defined in **a**. Shows dark BSE zircon with no EBSD IQ but also identifies moderately metamict light BSE zircon (green colour), yellow colour indicates slightly radiation damaged zircon while red colour indicates crystalline zircon. Step size = 0.1 μm. **c** CI-IQ EBSD scanned map of area shown in **a**, displays homogeneous high CI-IQ unmodified light BSE zircon. **d** CL image of **a**.

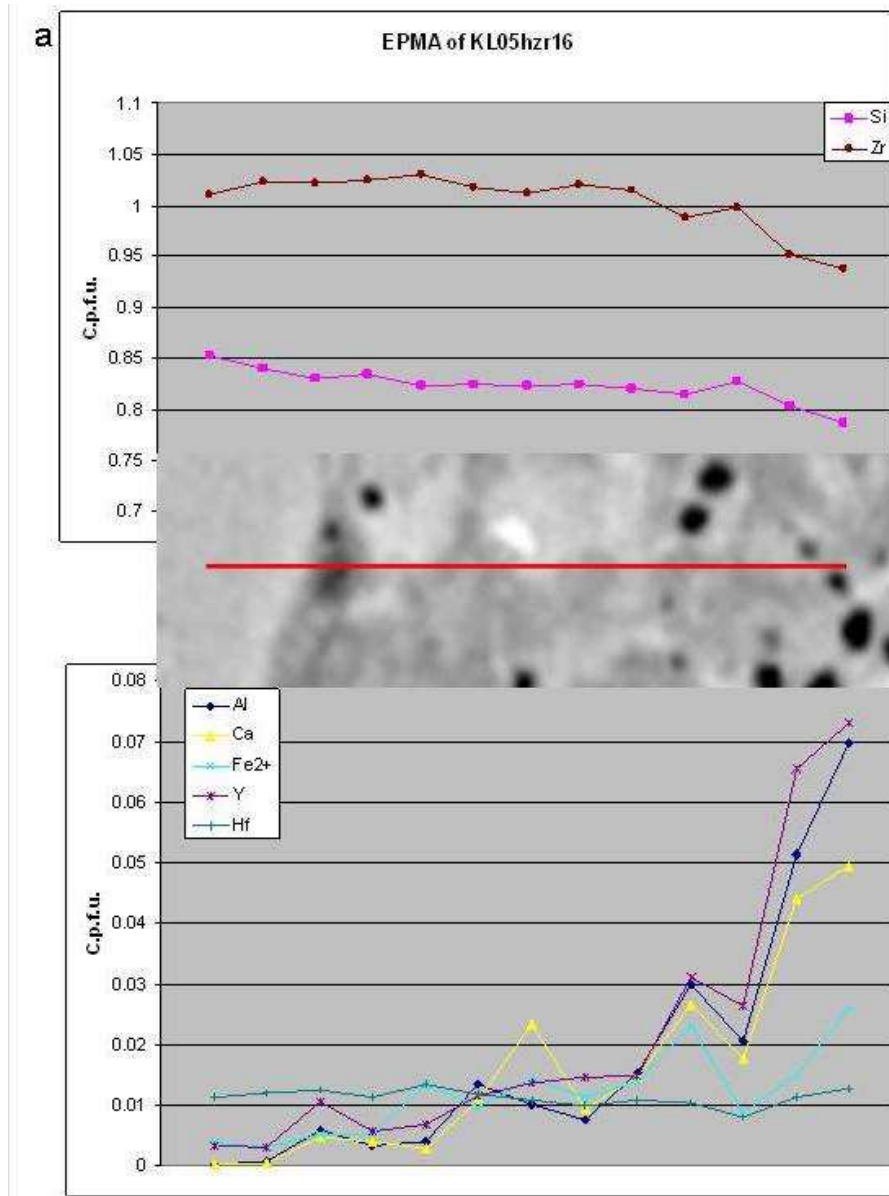


Figure 34. Detailed analysis of EPMA traverse of zircon KL05hzt16

a High magnification BSE image of dark BSE zircon core in KL05hzt16 from figure 34a, showing EPMA traverse (red line) line scan location and data profile plotted in c.p.f.u.. **b** CI-IQ EBSD map showing EPMA line of analysis with **c** a CI EBSD map of **b**. **d** CL image showing location of EPMA analysis. **e** CL spectra of dark and light BSE zircon in KL05hzt16 with locations of CL points defined in figure 26 . **b-d** continues on the following page.

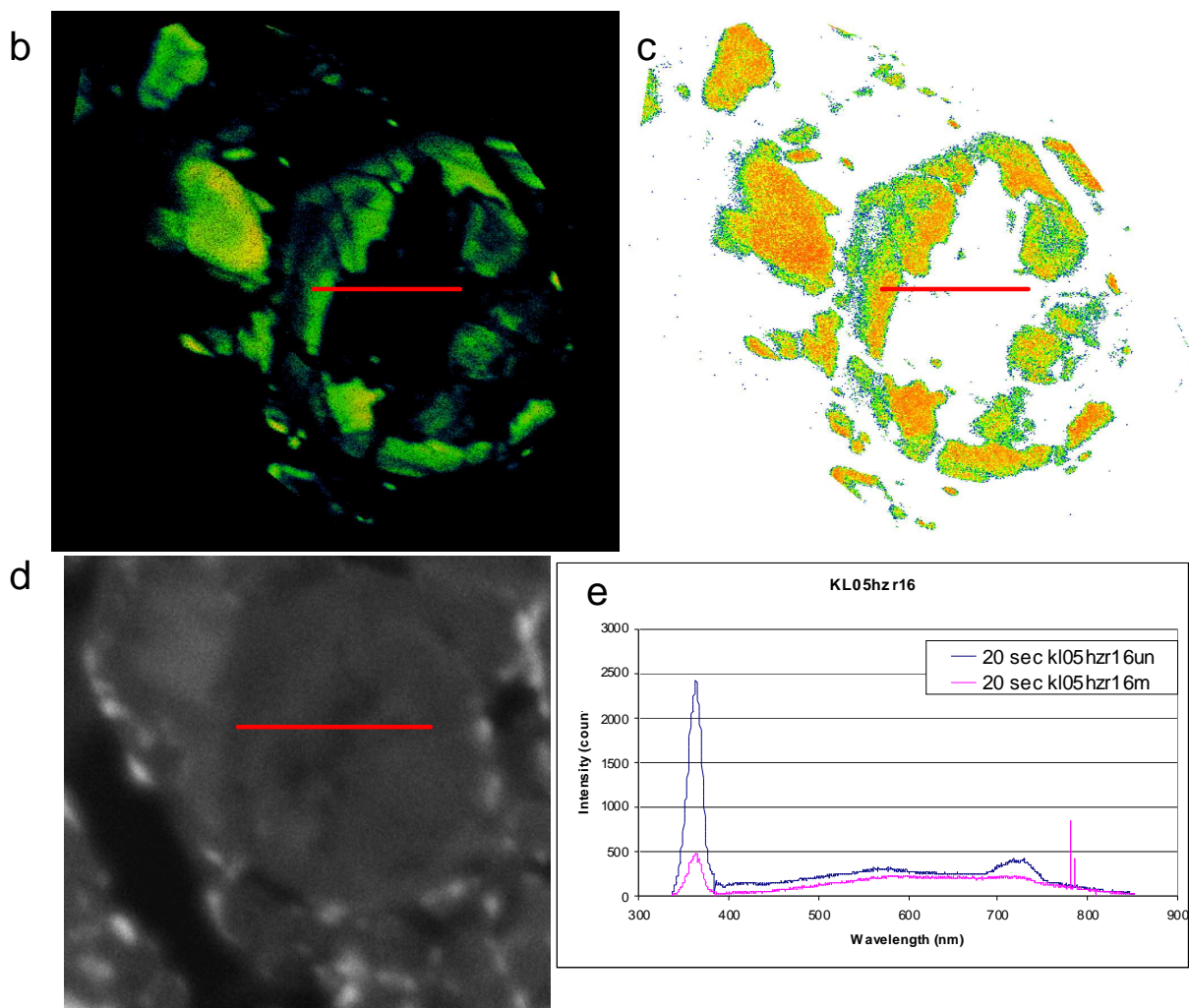


Figure 34. cont.

	Overall	Dh4zr14	KL05hxr16
Zr:Al	1:1	1:2	3:2
Si:Al	3:2	3:2	1:1
Zr:Ca	1:1	3:4	2:1
Si:Ca	2:1	2:1	3:2
Zr:Fe	2:1	1:1	-
Si:Fe	4:1	3:1	5:2
Zr:Mg	10:1	30:2	30:2
Si:Mg	10:1	30:2	30:2
Zr:Y	1:1	1:1	3:2
Si:Y	1:1	1:1	3:4
Zr:NFE	1:3	1:6	1:2
Si:NFE	1:3	1:2	1:6
(Zr+Si):NFE	2:3	2:3	2:3

Table 3 Estimated substitution relationships in dark BSE zircon. NFE = Non-formula elements.

3.9.3 Light BSE, low EBSD IQ zircon

The subhedral to well-rounded grain shown in Figure 35 is concentrically zoned in BSE. The core has a relatively low BSE intensity (although BSE intensity is still considerably higher than dark BSE zircon) and apparently randomly orientated cracks that are almost completely contained within the core. Immediately surrounding the core is a high BSE intensity growth layer and multiple fractures radiate from the outer boundary of this zone to the edges of grain. Fractures are generally rare in this zone apart from a fracture concentric with zoning. Within this high BSE intensity band small cavities (upto 10 μ m long) elongated to the zoning pattern, are present particularly around the tips of fractures (Fig. 35a). Fractures that radiate from this band are in communication with the grain edge around the whole grain with the exception of an area at the bottom right of the grain in Fig. 35. Radial fractures, present in the inner lower BSE contrast growth zones, are absent in the high BSE intensity outer margin. These fractures terminate at the low-high BSE intensity boundary and around these fractures small cavities can also be observed in the high BSE contrast area. A zircon sliver on the margin of the grain projects into the matrix and around a quartz grain (Fig. 35b).

The EBSD map (Fig. 35c) of the grain identifies a band of low EBSD IQ around the high IQ core of the grain. This band correlates to the high BSE intense zone but in particular, relates to the areas where small cavities are observed. The remainder of the high BSE contrast area produces moderate EBSD IQ patterns. The high BSE contrast margin lacking radial fractures also has a low EBSD IQ that again correlates to the band where cavities are observed. EDX scans revealed no compositional variations.

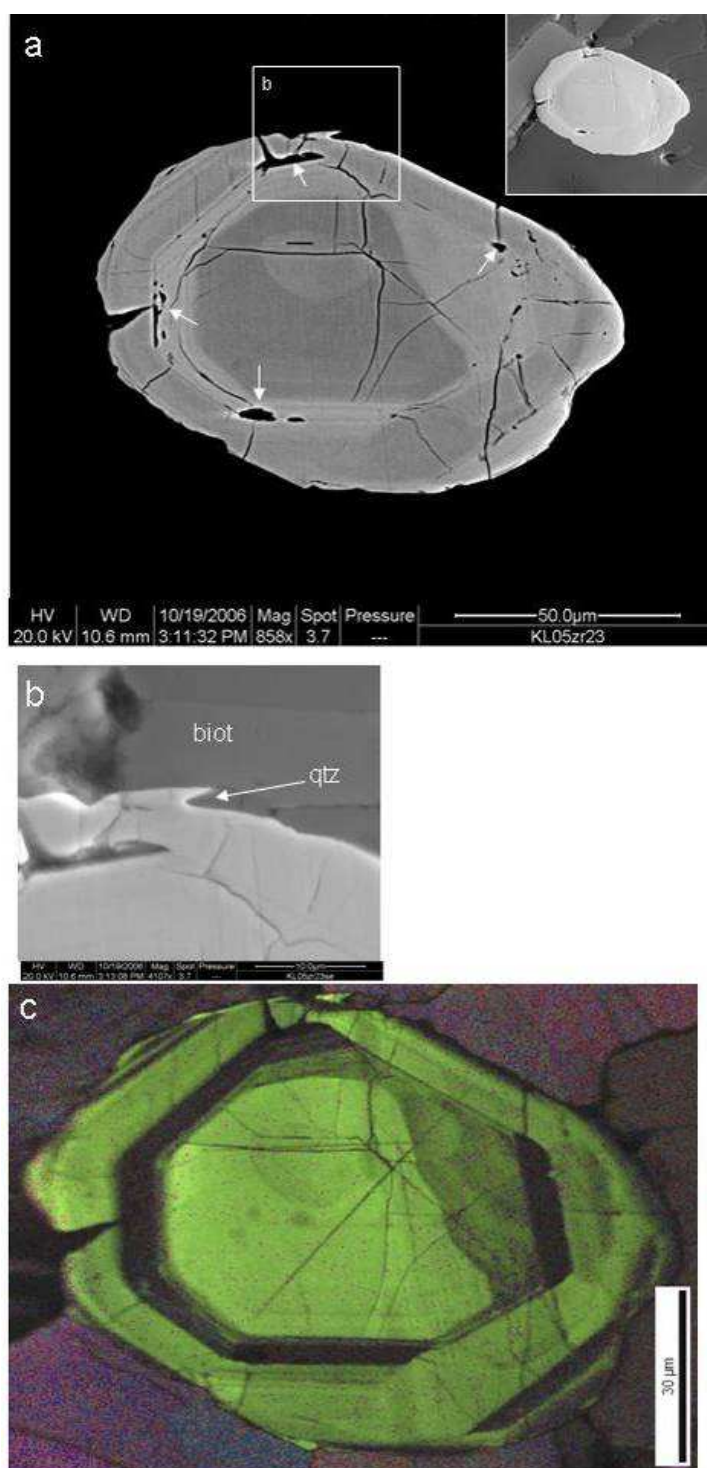


Figure 35. Characterisation of zircon KL05zr22

a BSE image of rounded detrital zircon showing thin elongate cavities (white arrows) aligned parallel to zoning and associated with fractures to the grain edge. Cavities are thought to be the result of dissolution (KL05), SE image is inset. **b** SE image of sliver of zircon protruding from the margin and between quartz and mica. **c** EBSD IQ-inverse pole figure (IPF) map showing a low IQ metamict band that correlates with high BSE intensity growth layer where cavities have developed.

3.9.4 Porous zones in zircon

Zircon Dh4zr17 was analysed using two EPMA line scans, with a 1µm step size (Fig. 36a). The data from this analysis is presented in Table 4. An EDX scan of the area in Figure 36a identifies a 2-3 µm wide band enriched in Fe and slightly depleted in Zr and Si (Fig. 36c). This band is intersected by EPMA line scan a. Line scan a intersects a zone where pores are sparse, a zone where pores are heavily concentrated and a light BSE zone (Fig. 36a&b). Line scan a shows Fe is concentrated within areas where pores are both abundant and sparse. Fe enrichment would appear to correlate roughly with increasing size and concentration of pores. Other non-formula elements do not show enrichment in porous zircon. Light BSE zircon contains trace amounts of Fe and Y, although Fe is lower than in porous zones. Zr and Si are slightly depleted with Fe enrichment in the porous zircon by Zr:Fe 1:4 and Si:Fe 1:4. The Zr/Si ratio in porous zircon is the same as light BSE zircon and they also have similar weight percent totals of close to 100%. EDX analysis of porous zones in other zircon grains in these rocks give repeatedly similar results as to porous zircon analysed in Dh4zr17.

Scan b intersects light BSE and porous zircon but also dark BSE zircon located around the fracture tips in elongate lobes within porous zones (Fig. 36a). The trace of these fractures associated with dark BSE zircon, is usually connected with the margin of zircon. EDX scans show that the areas where dark BSE zircon is present in these porous zones are markedly depleted in Zr and Si and enriched in Fe, Ca and Al (Fig. 36c). EDX scans also reveal that cracks within the grain microstructure are Al-rich where they are not filled by quartz (Si-rich cracks). Porous zircon identified in scan b is relatively enriched in Y as well as Fe in comparison to porous zircon scan a. However, as shown by scan a, light BSE zircon contains trace amounts of Y and therefore Y enrichment in porous zircon may also be in part controlled by the chemistry of the host zircon. Where pores in zircon are particularly abundant, zircon is heavily enriched in similar amounts of Fe and Y (0.017 c.p.f.u.) but is also slightly enriched in Ca and Al. The enrichment of Y and Fe is likely to reflect the composition of the porous zircon but enrichment of Al and Ca could indicate contamination from dark BSE zircon that is associated with the porous zones. This would also

increase apparent Fe and Y concentrations.

Fe enrichment in porous zircon is correlated with a loss in Zr and Si of 1:4 (Zr or Si):Fe (Fig. 36b). The uptake of Fe and Y in dark BSE zircon in scan b is tied to enrichment of the other non-formula elements Al, Ca and Mg and these show a reasonable correlation with Zr and Si depletion (Fig. 36a&b). However, the Zr/Si ratio does not change in either porous or dark BSE zircon. All porous zones give slightly lower weight percent totals (*c.*99wt%) than light BSE zircon but dark BSE zircon analysed in scan 2 gives totals of *c.* 96wt%.

Generally, EBSD IQ increases as the size and concentration of pores decrease (Fig. 36d). Bands with few, sparsely distributed pores have a medium IQ EBSD pattern (Green colour, Fig. 36d). Where pores are larger and in higher concentration, EBSD IQ is low and often has a low to zero EBSD CI. Not all dark BSE zircon associated with this porous zone shows a low IQ EBSD pattern, indeed, some dark BSE areas have a higher IQ than surrounding porous area.

CL intensity in heavily porous zircon is weak but CL intensity increases slightly in less densely porous zones (Fig. 36e). However, CL intensity shows significant zonation differences in light BSE zircon and can be of similar CL intensity as dark BSE zircon. CL spectra of porous zones is very similar to unmodified light BSE zircon but with a significantly lower intensity peak at 340-380nm and a less pronounced hump around 700nm (Fig. 36f). Overall however, porous zones in zircon correlate to a reduced CL intensity and lower IQ EBSD pattern which become more reduced and of lower IQ respectively with the increasing concentration of pores in zircon (Fig. 36 d&e).

Sample	Analysis No.	Mg	Al	Si	Ca	Fe2+	Y	Zr	Hf	Total c.p.f.u.	Zr/Si	Zr/Hf	Total wt%
dh4zr17a	1	0.000	0.000	0.868	0.000	0.004	0.003	0.996	0.008	1.879	1.147	122.219	100.17
dh4zr17a	2	0.000	0.000	0.870	0.000	0.004	0.003	0.992	0.010	1.879	1.139	102.807	100.62
dh4zr17a	3	0.000	0.000	0.870	0.000	0.003	0.003	0.993	0.009	1.878	1.142	110.721	100.53
dh4zr17a	4	0.001	0.001	0.864	0.002	0.005	0.004	0.994	0.010	1.882	1.151	96.457	100.44
dh4zr17a	5	0.000	0.000	0.867	0.001	0.005	0.003	0.993	0.012	1.880	1.145	83.402	100.23
dh4zr17a	6	0.000	0.001	0.868	0.002	0.011	0.001	0.988	0.013	1.883	1.138	78.799	99.75
dh4zr17a	7	0.000	0.000	0.870	0.000	0.006	0.000	0.992	0.010	1.880	1.141	99.261	100.43
dh4zr17a	8	0.000	0.000	0.868	0.000	0.007	0.000	0.994	0.011	1.880	1.145	89.873	100.91
dh4zr17a	9	0.000	0.000	0.868	0.000	0.008	0.000	0.992	0.011	1.880	1.142	89.086	100.33
dh4zr17a	10	0.000	0.000	0.872	0.000	0.008	0.000	0.989	0.010	1.880	1.134	102.460	100.33
dh4zr17a	11	0.000	0.000	0.866	0.000	0.009	0.000	0.995	0.011	1.881	1.149	89.804	101.09
dh4zr17a	12	0.000	0.000	0.867	0.000	0.010	0.001	0.993	0.011	1.881	1.145	91.182	101.24
dh4zr17a	13	0.000	0.000	0.867	0.000	0.011	0.001	0.992	0.011	1.882	1.143	87.232	101.57
dh4zr17b	14	0.000	0.000	0.872	0.000	0.003	0.001	0.992	0.009	1.877	1.138	104.813	99.84
dh4zr17b	15	0.000	0.000	0.870	0.000	0.002	0.001	0.993	0.011	1.877	1.141	90.128	99.97
dh4zr17b	16	0.000	0.000	0.870	0.000	0.002	0.001	0.991	0.013	1.877	1.139	77.946	100.08
dh4zr17b	17	0.000	0.000	0.871	0.000	0.002	0.001	0.991	0.012	1.877	1.138	84.494	99.86
dh4zr17b	18	0.000	0.000	0.874	0.000	0.002	0.001	0.987	0.013	1.877	1.130	78.294	99.83
dh4zr17b	19	0.000	0.000	0.868	0.000	0.002	0.001	0.993	0.012	1.878	1.143	80.690	99.68
dh4zr17b	20	0.000	0.003	0.866	0.001	0.002	0.002	0.993	0.012	1.879	1.146	82.612	99.58
dh4zr17b	21	0.001	0.009	0.866	0.003	0.005	0.005	0.985	0.010	1.885	1.138	94.040	98.72
dh4zr17b	22	0.001	0.011	0.867	0.003	0.010	0.004	0.981	0.010	1.887	1.132	101.658	98.20
dh4zr17b	23	0.000	0.006	0.870	0.002	0.006	0.004	0.984	0.010	1.882	1.131	95.926	98.66
dh4zr17b	24	0.000	0.002	0.869	0.001	0.005	0.003	0.990	0.011	1.880	1.139	93.118	99.00
dh4zr17b	25	0.000	0.002	0.868	0.001	0.004	0.003	0.991	0.011	1.880	1.142	91.609	98.77
dh4zr17b	26	0.000	0.005	0.868	0.002	0.005	0.003	0.988	0.011	1.882	1.138	87.571	98.80
dh4zr17b	27	0.001	0.006	0.870	0.002	0.005	0.003	0.985	0.011	1.882	1.132	92.224	98.17
dh4zr17b	28	0.001	0.005	0.868	0.002	0.003	0.004	0.987	0.012	1.882	1.137	84.346	98.44
dh4zr17b	29	0.001	0.003	0.865	0.002	0.004	0.004	0.990	0.012	1.882	1.144	79.621	98.14
dh4zr17b	30	0.000	0.002	0.868	0.003	0.004	0.003	0.989	0.012	1.881	1.139	80.309	99.15
dh4zr17b	31	0.001	0.003	0.865	0.002	0.004	0.005	0.990	0.013	1.882	1.144	77.814	98.92
dh4zr17b	32	0.000	0.003	0.866	0.002	0.007	0.007	0.986	0.012	1.884	1.139	83.249	97.90
dh4zr17b	33	0.000	0.003	0.864	0.004	0.009	0.012	0.981	0.014	1.887	1.135	72.246	97.53

Table 4 EPMA analyses of porous zircon with values presented in c.p.f.u. calculated to 4(O)

Sample	Analysis No.	Mg	Al	Si	Ca	Fe2+	Y	Zr	Hf	Total c.p.f.u.	Zr/Si	Zr/Hf	Total wt%
dh4zr17b	34	0.000	0.005	0.858	0.005	0.013	0.015	0.983	0.013	1.892	1.146	77.490	96.94
dh4zr17b	35	0.001	0.007	0.861	0.007	0.013	0.016	0.975	0.012	1.894	1.132	78.019	96.05
dh4zr17b	36	0.001	0.007	0.860	0.008	0.014	0.013	0.978	0.013	1.893	1.137	73.610	96.36
dh4zr17b	37	0.001	0.005	0.865	0.007	0.017	0.007	0.977	0.013	1.892	1.130	73.504	97.06
dh4zr17b	38	0.002	0.006	0.858	0.011	0.015	0.006	0.984	0.013	1.894	1.148	75.696	97.11
dh4zr17b	39	0.003	0.007	0.854	0.013	0.013	0.006	0.988	0.013	1.896	1.157	77.747	96.87
dh4zr17b	40	0.001	0.004	0.862	0.006	0.005	0.004	0.992	0.011	1.885	1.152	90.163	98.84
dh4zr17b	41	0.000	0.001	0.866	0.001	0.004	0.002	0.995	0.010	1.880	1.149	98.493	99.67
dh4zr17b	42	0.000	0.001	0.872	0.001	0.005	0.002	0.988	0.011	1.879	1.133	89.383	99.07
dh4zr17b	43	0.001	0.002	0.868	0.002	0.009	0.003	0.988	0.011	1.883	1.138	92.452	98.53
dh4zr17b	44	0.001	0.003	0.872	0.003	0.013	0.003	0.979	0.012	1.885	1.123	81.710	98.06
dh4zr17b	45	0.000	0.004	0.873	0.003	0.013	0.003	0.978	0.011	1.886	1.120	89.804	97.51

Table 4 cont.

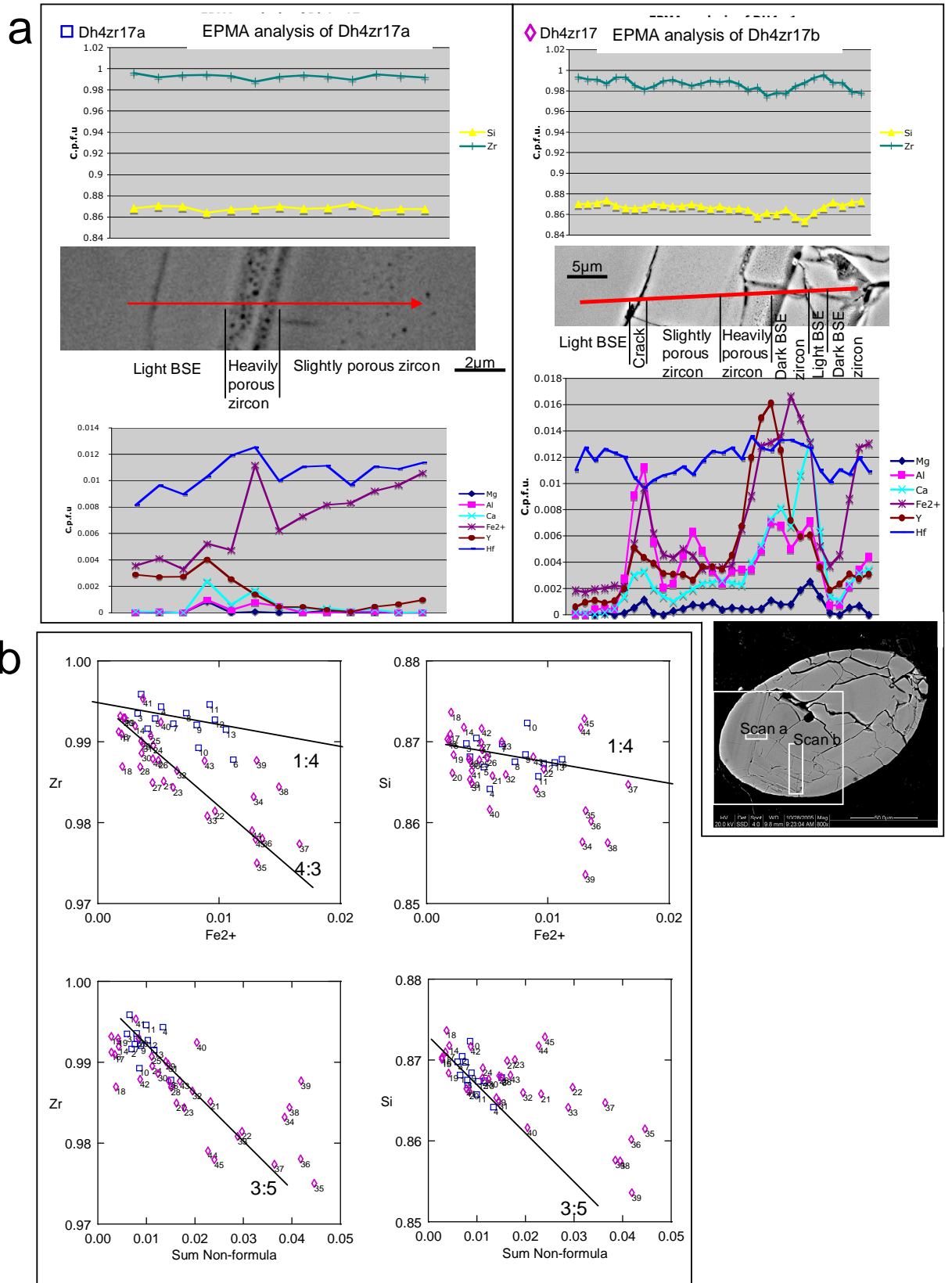


Figure 36. Characterisation of zircon dh4zr17 with caption on page 106.

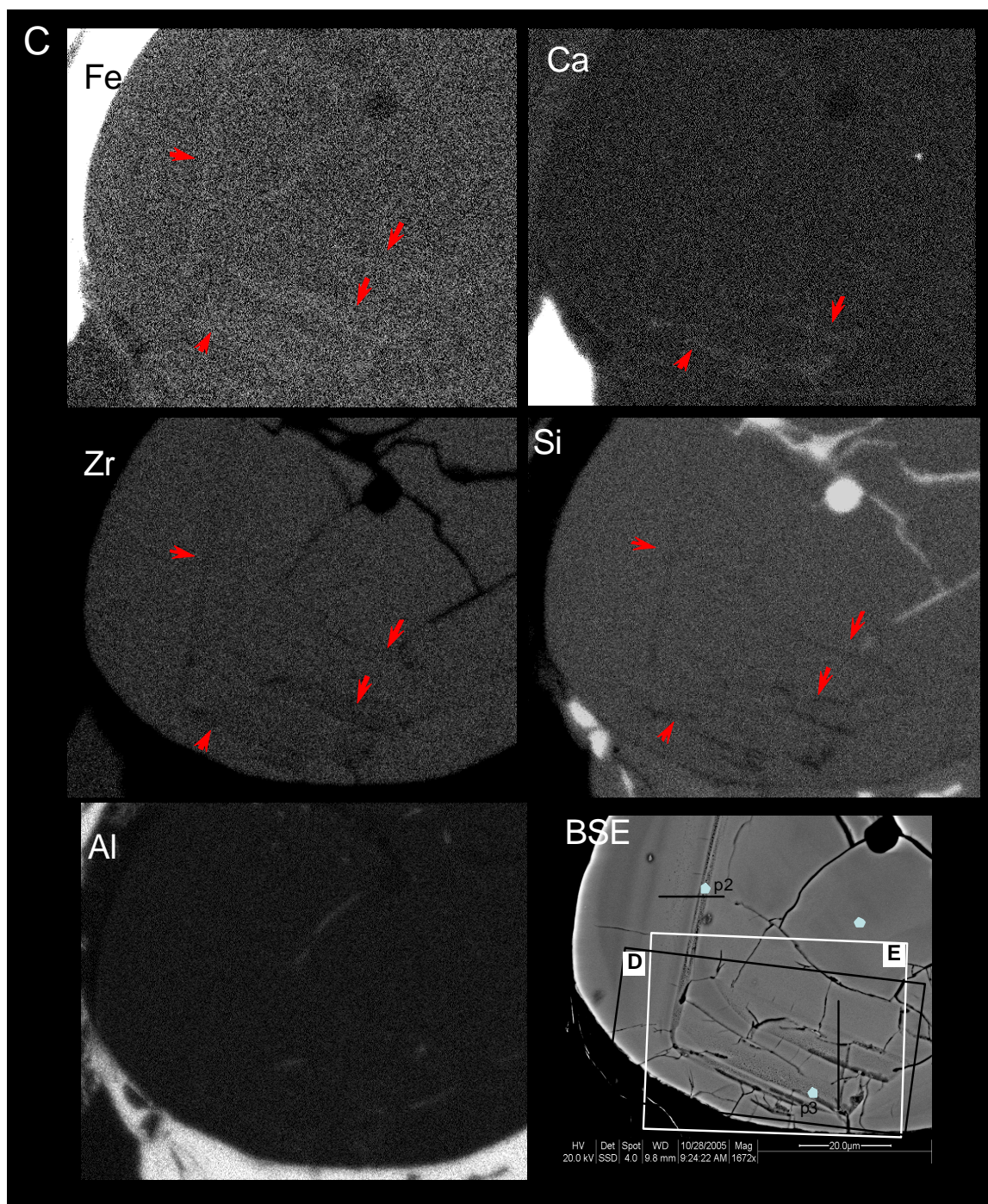


Figure 36. Characterisation of zircon dh4zr17 with caption on page 106.

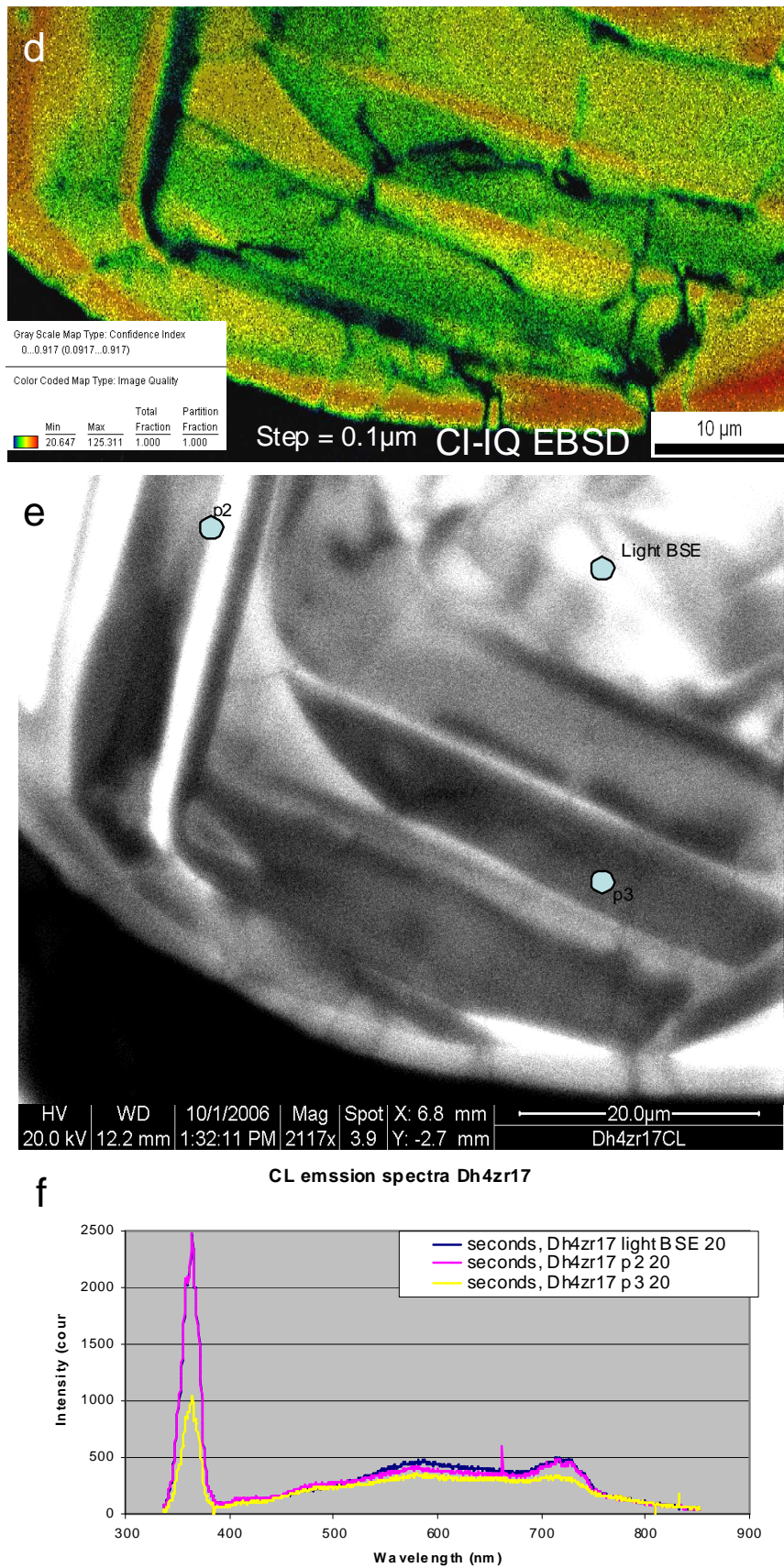


Figure 36. Characterisation of zircon dh4zr17 with caption on following page.

Figure 36. Characterisation of zircon dh4zr17

a BSE images of the EPMA lines of traverse from zircon in figure 13a and EPMA data profiles in c.p.f.u. Areas of line scan analysis are displayed in BSE image of the whole grain. **b** Element plots of porous zircon from data in Table 4. **c** EDX element maps showing porous zones enriched in Fe (red arrows) and depleted in Zr & Si. Dark BSE zircon can also be seen to be enriched in Al and Ca. **d** CI-IQ EBSD scanned map of area defined in BSE image in **c**. Shows high CI-IQ patterns in unmodified light BSE zircon and lower CI-IQ in porous areas. Areas where pores are heavily concentrated show lower CI-IQ than areas where pores are sparsely concentrated. Step size = 0.1 μ m. **e** CL image of area defined in **c** showing lower emission levels in porous areas and very low levels in dark BSE zircon of porous zones. **f** CL spectra of porous, light BSE and dark BSE zircon with locations defined in **e**.

3.9.5 Zircon Outgrowths

Thirty zircons with outgrowths were chosen for analysis by EPMA from thin sections BAL1, BAL1B and E1. These samples were chosen because they contain the largest and most abundant zircon outgrowths. However, the problem with analysing zircon outgrowths using the EPMA is that the effective spot size (*c.*1.5-2 μ m) is around the average size of the outgrowth (*c.*2 μ m). In order to acquire chemical information about the outgrowths without the interference of the matrix or the host zircon, the following strategy was devised. A series of analysis points was taken in 1 μ m increments from the unmodified light BSE host zircon, over the outgrowth and into the matrix. It was hoped that by using this strategy, some information could be obtained about the chemistry of the outgrowths. A problem associated with this strategy was that some of the data collected was contaminated due to the matrix being analysed. As such the following section sets out to systematically identify and remove anomalous or contaminated points in the data set. Multiple iterations of “weeding” the data have been required because of the inclusion-rich nature of zircon outgrowths.

3.9.5.1 Anomalous points

A group of data points encircled in red are significantly depleted in Zr and are so far displaced from what might be considered a reliable zircon analysis that they are believed to contain contaminants (Fig.37a). Contamination by matrix minerals mean data points plots in predictable trends as depicted in Figure 37a&b. The data points highlighted in red in Figure 37a&b are dominated by xenotime and phyllosilicate inclusions. A Zr-rich point circled in gold plots considerably away from the overall cluster of data (Fig. 37a &b). The mineral inclusion that has caused this deviation is uncertain but may possibly be baddeleyite (ZrO₂) although this appears to be unlikely as silica is readily available in these environments. Points highlighted in blue in Figure 37b-d indicate Y enrichment from xenotime inclusions that are not obvious in Figure 37a. Figure 37d also reveals a group of points encircled in Fe (circled in green), some which have been identified as phyllosilicates from plots in Figure 37a&b but those points not identified as contaminated by phyllosilicates are likely to be some Fe-rich phase (e.g. iron oxides, pyrite).

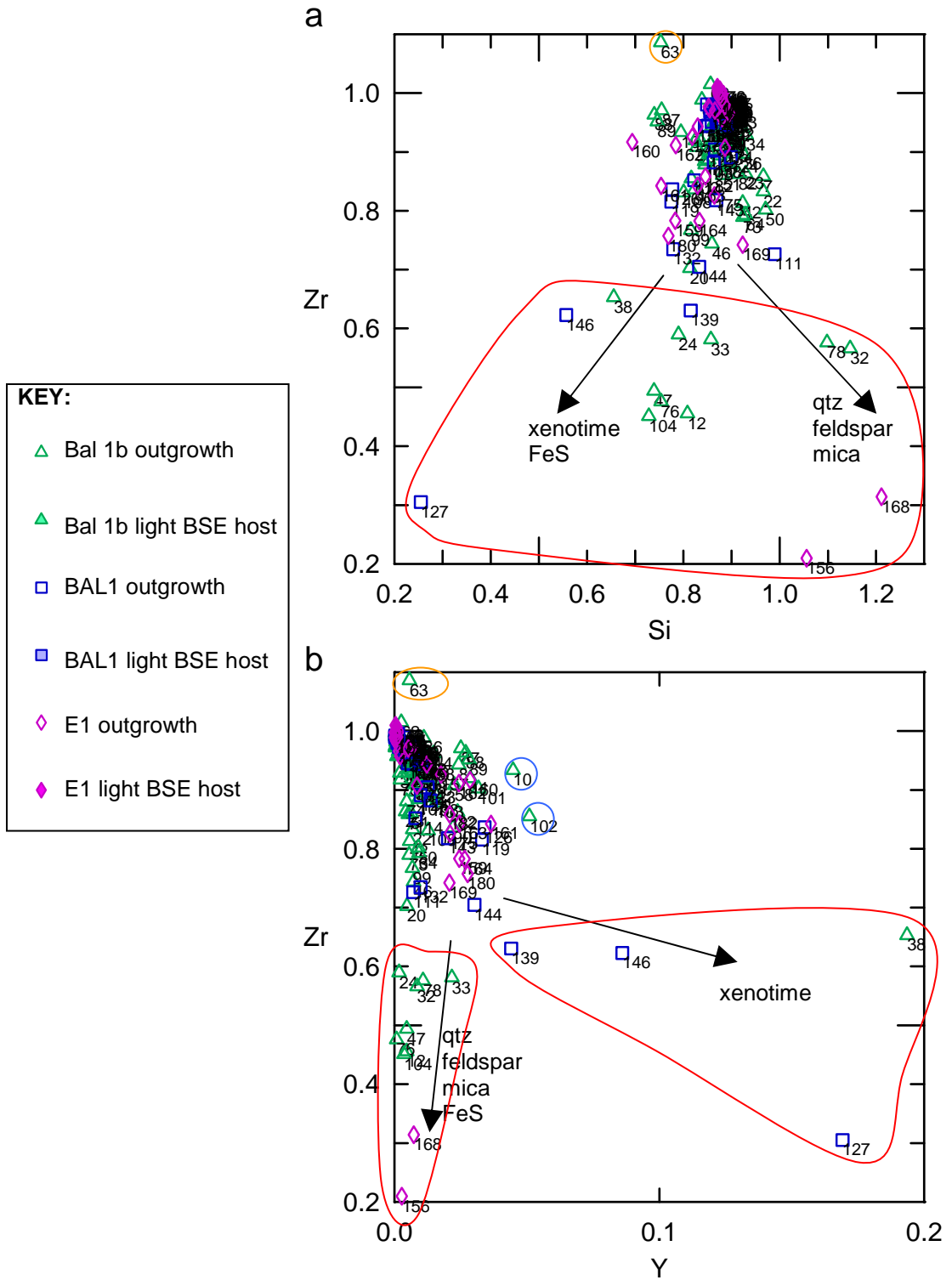


Figure 37. Element plots of EPMA data of zircon outgrowths showing anomalous data points. Units are in c.p.f.u.

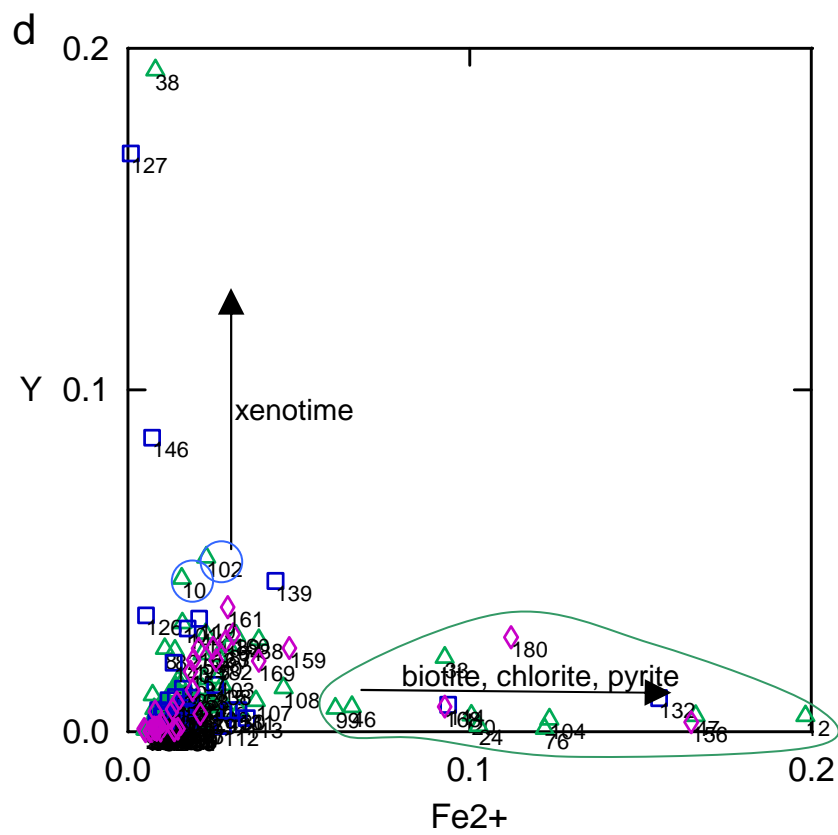
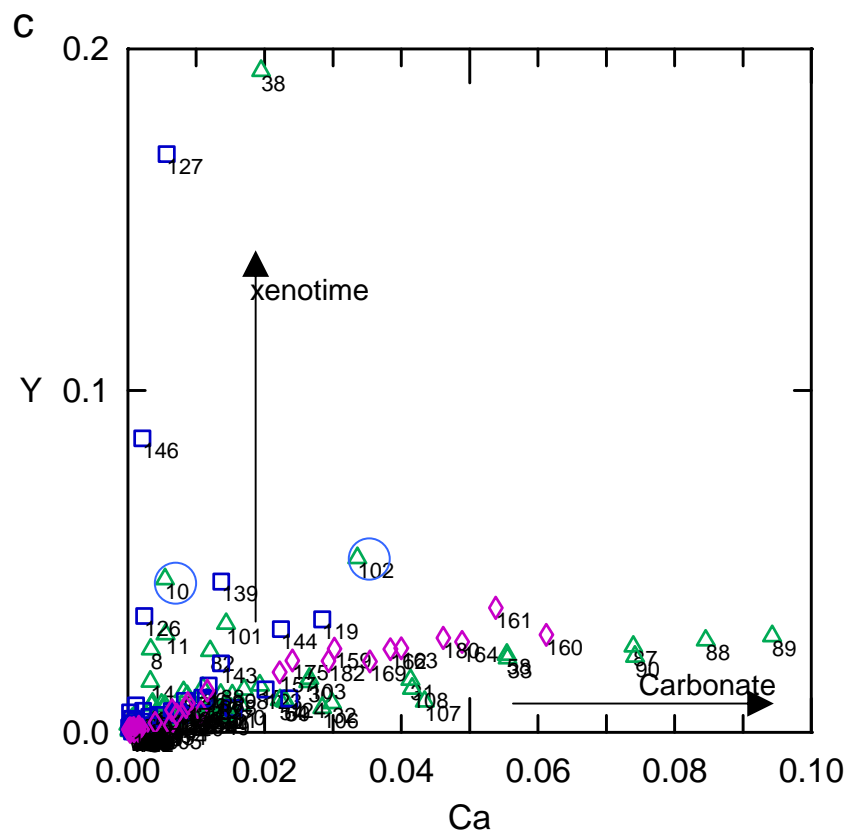


Figure 37. cont.

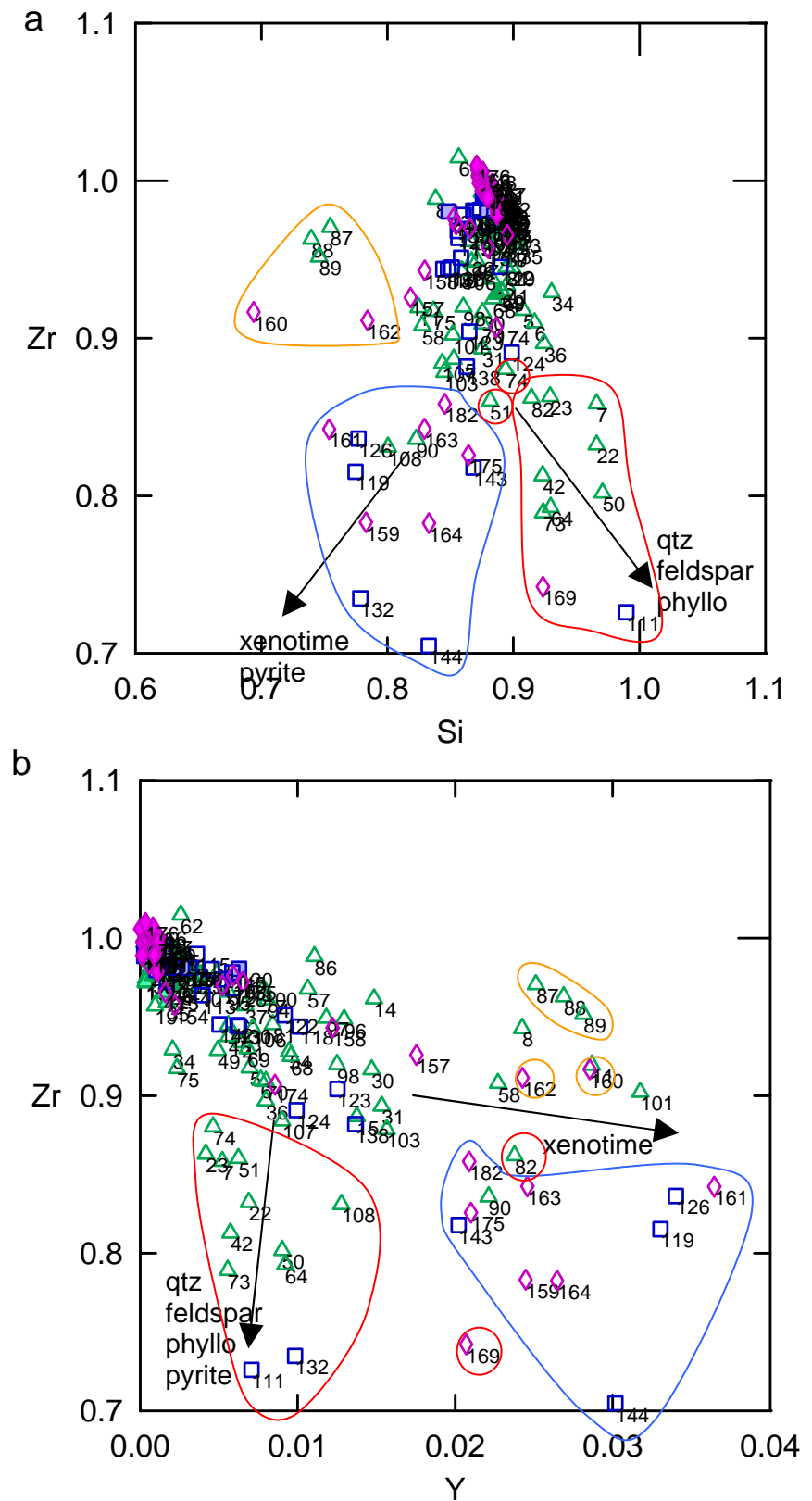


Figure 38. Element plots of EPMA data of zircon outgrowths showing anomalous data points from second stage in the “weeding” process. Units are in c.p.f.u.

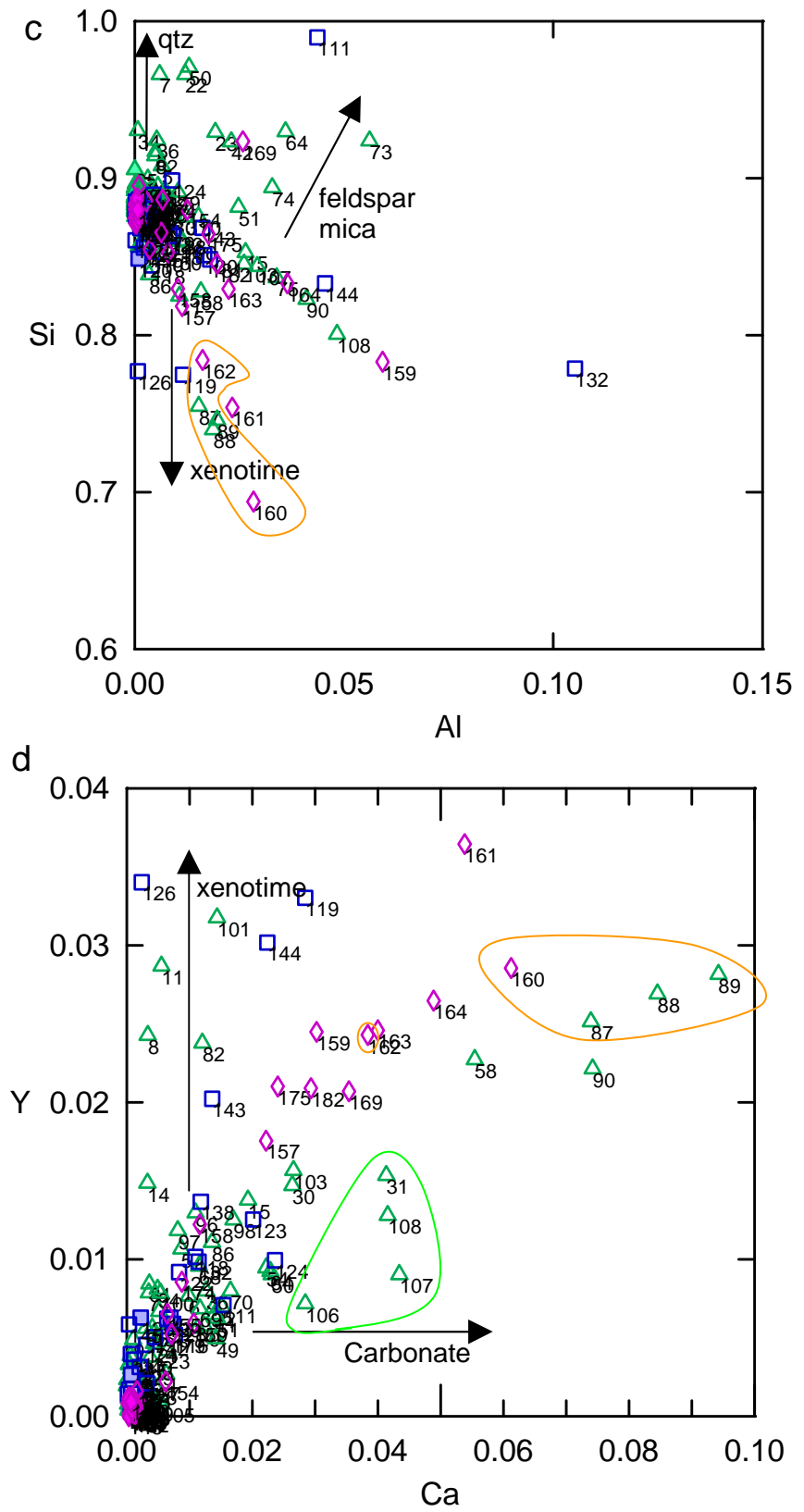


Figure 38. cont.

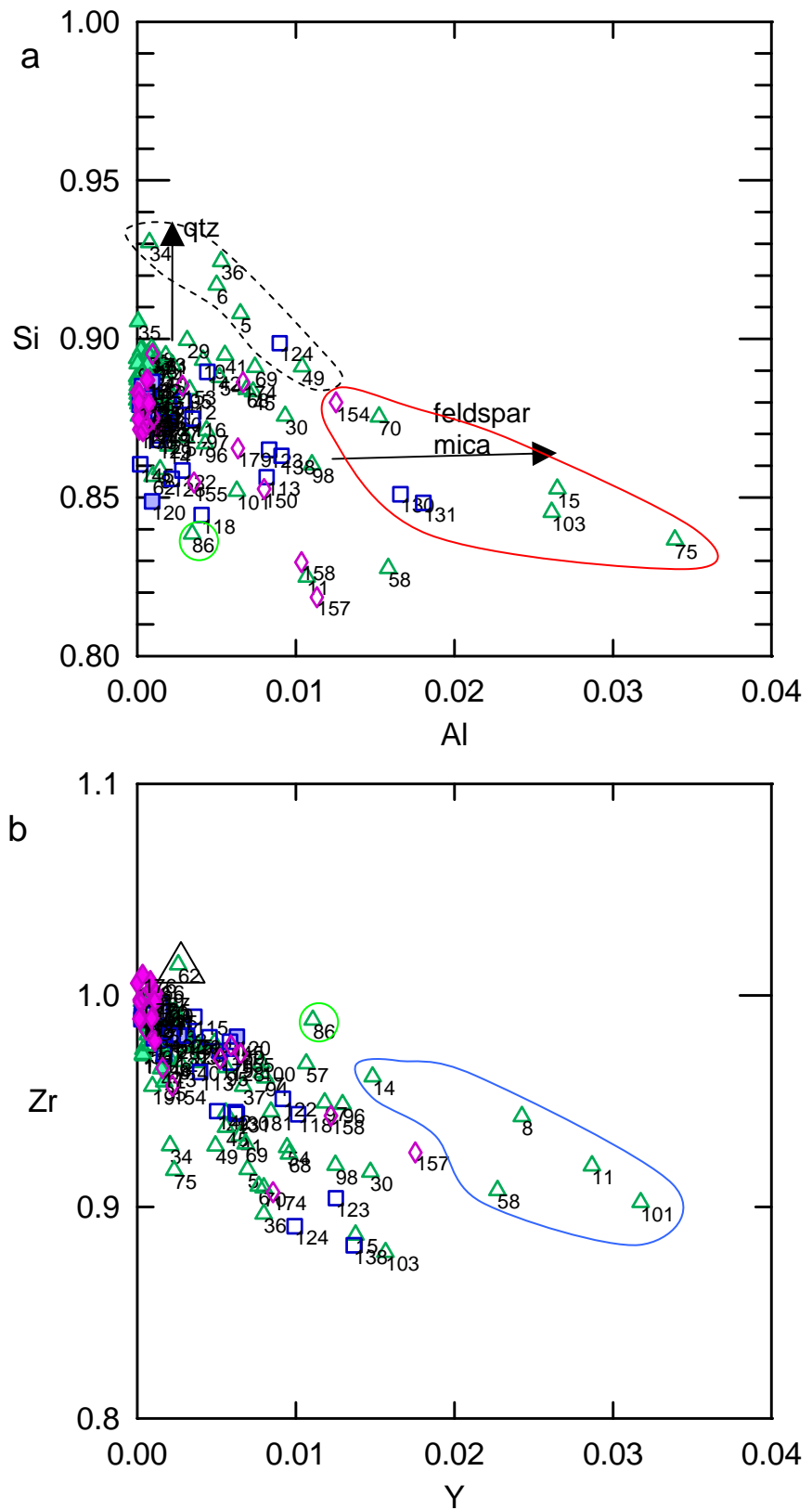
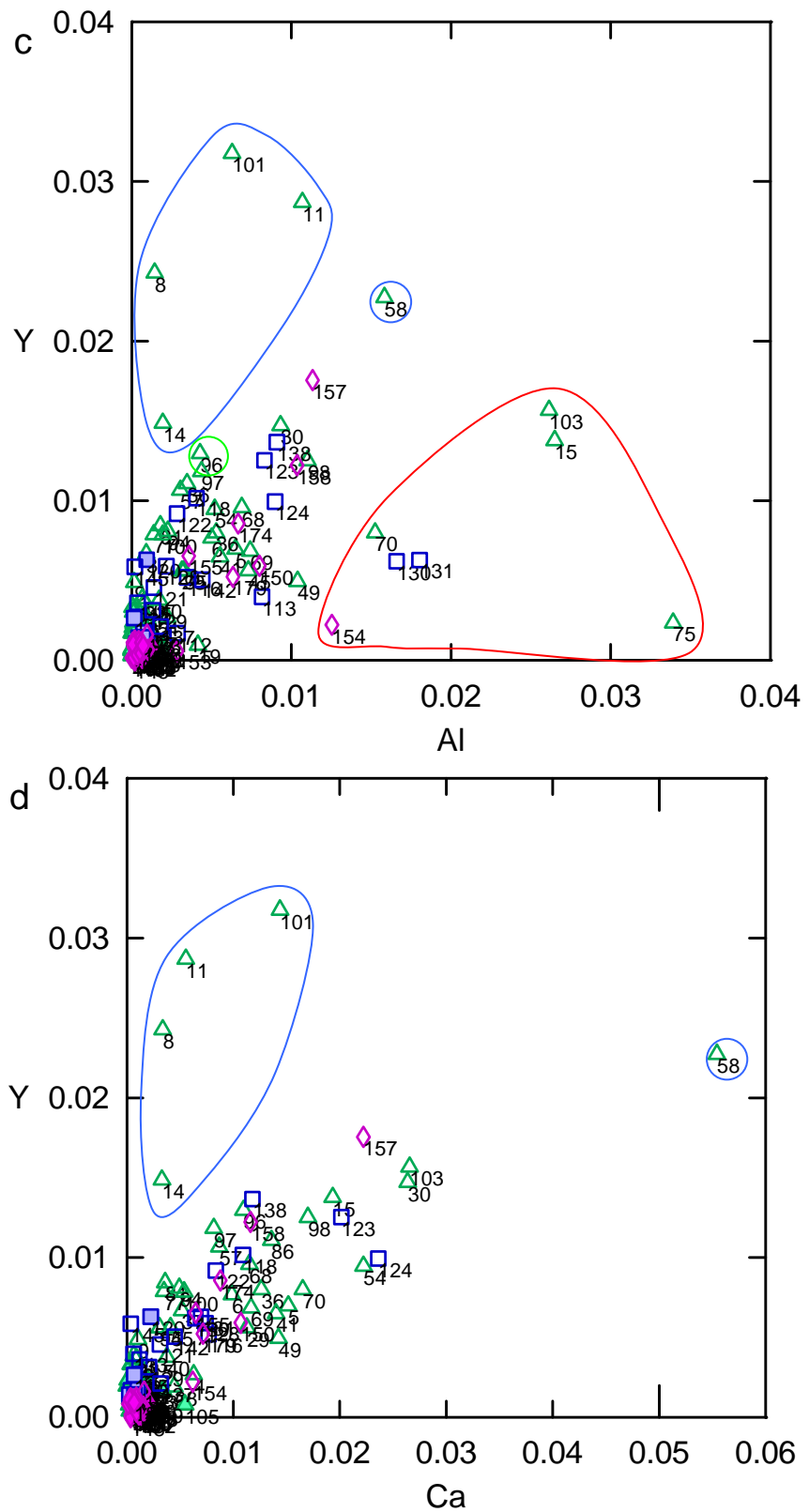


Figure 39. Element plots of EPMA data of zircon outgrowths showing anomalous data points. Third stage of the “weeding” process. Units are in c.p.f.u.

Figure 39. *cont.*

The data points highlighted above have been removed from the data set. With these points removed, the plots have been rescaled and again, analyses plot trends that follow predictable deviations due to contaminants. Figure 38a&b identifies data points that probably contain xenotime or Fe-oxide (encircled in blue) and those that contain quartz, feldspar or phyllosilicates (encircled in red). There may be some overlap between the points in the encircled areas (e.g. data points encircled in blue in Fig. 38a may be encircled in red in Fig. 38b), and this may be caused by some data points containing both xenotime and phyllosilicate inclusions. Points highlighted in gold are Si-poor, Y- and Ca- rich and consistently group away from the overall trend of data (Fig. 38a-d). However, it is unclear as to the identity of these inclusions due to the relatively elevated Zr content (Fig. 38a). Data points highlighted in green in Figure 38d would appear to indicate some carbonate contamination.

Refinement of the data set shows there remain contaminants that are probably due to the influence of mica or feldspar (Fig.39a&b). Figure 39a also displays the influence of quartz grains (dashed line) although some of the more Al-rich points in the dashed line are likely to be both quartz and mica or feldspar phases. A xenotime contaminant probably also remains (highlighted in blue, Fig. 39b-d). The point highlighted in green (Fig. 39b&c) may be some point slightly enriched in xenotime as it is also Si-poor (Fig. 39a). The point in the black triangle (Fig. 39b) appears unusually enriched in Zr and may represent a poor analysis.

The above analyses have all been removed from the data set as they show a consistent and predictable deviation from the data set.

3.9.5.2 Zircon outgrowth chemistry

Weeded zircon outgrowth data is presented in Table 5. Host zircons to outgrowths have a normal zircon composition giving around 100wt% totals. Host zircons are relatively enriched in Fe, ranging from 0.0048 c.p.f.u. (0.14wt%) to 0.0157 c.p.f.u. (0.48wt%). Zr/Si ratios in host zircons average 1.12, slightly above that of ideal zircon. There is a wide spread of Hf contents within the host zircons.

In a similar pattern to dark BSE zircon, zircon outgrowths are depleted in Zr and Si upto 0.1 c.p.f.u. (7wt% and 4wt% respectively). On average, zircon outgrowths have a slightly lower Zr/Si ratio than the host zircon. Zr and Si depletion show a relatively poor correlation when plotted against one another (Fig.40a). There would appear to be two trends here although they are poorly defined. A group of points plot fairly closely to a Zr:Si 1:1 relationship trend where zircon outgrowths are depleted in Zr and Si while another group of points plot a 2:1 (Zr:Si) depletion (Fig. 40a). Despite a variable Hf content in zircon outgrowths (Fig. 40b) there is an indication some zircon outgrowths reflect the Hf concentration of their host (Fig. 40c). Hf exhibits no consistent overall correlation with either Zr or Zr/Si ratio (Fig. 40b&d) or any of the other elements analysed.

Zircon outgrowths are enriched in non-formula elements at the expense of Zr and Si. Zr depletion follows a relatively well-defined 3:2 (Zr:Non-formula elements) substitution trend with non-formula elements (Fig. 40e). Si depletion exhibits a slightly greater spread in the data set with some points following a 1:2 (Si:Non-formula elements) substitution trend and others a 1:1 (Fig. 40f). Non-formula elements Al (upto 0.012c.p.f.u. (0.8wt%)), Ca (upto 0.025c.p.f.u. (1wt%)), Fe (upto 0.035c.p.f.u. (1wt%)) and Y (upto 0.015c.p.f.u. (1.5wt%)) (Mg was not analysed in zircon outgrowths) are enriched in zircon outgrowths. The enrichment of Al in some zircon outgrowths plot along a relatively well-defined 10:1 (Zr:Al) trend with Zr loss (Fig. 40g). However some scatter in this may suggest that some outgrowths points plot along a 5:1 Zr:Al substitution trend. Si-Al plots shows considerable spread but plot along a general 4:1 substitution trend (Fig. 40h). Note that zircon outgrowths that plot along a steep Zr-Al slope mark a trend that follows a shallow slope in the Si-Al graph and vice versa (compare Fig. 40g&h). Ca enrichment for Zr plots along a

6:1 (Zr:Ca) trend (Fig. 40i) however Si:Ca mark a trend indicating a 1:1 substitution relationship (Fig. 40j). Y enrichment in zircon outgrowths roughly defines a 20:3 substitution relationship with Zr (Fig. 40k.) and a 3:1 (Si:Y) substitution relationship (Fig. 40l). Fe in zircon outgrowths shows considerable spread when plotted against both Zr and Si (Fig. 40m&n). Zr:Fe plot a wide range of substitution trends 1:1-10:1, while slightly less spread is observed in Si:Fe plots (1:1-5:1). Zircon outgrowths that appear to plot along a 5:1 Zr:Fe trend, follow a 1:1 trend in the Si plot. Hf and Fe show no discernable trend.

Non-formula elements in zircon outgrowths show an overall correlation with one another when plotted although all show considerable variation (Fig. 41 a). Zircon outgrowths are typically most enriched in Fe, followed by Ca and Y with Al usually the least enriched of the non-formula elements. Ca and Y vary quite considerably where Ca can be significantly more enriched than Y and vice versa. This is not a simple substitution however as Ca and Y show considerable and apparently unrelated variation (Fig 41b). Where Ca is most enriched in zircon outgrowths, Fe is often relatively depleted although this relationship is poorly defined (Fig 41c). Y-Al, Y-Fe, Al-Fe and Al-Ca (Fig. 41) all display a similar relatively poorly defined general trend of coupled enrichment.

The above weeding method is only capable of removing anomalous points displaying an obvious and predictable deviation from the overall trend. However, due to the thickness and inclusion rich nature of zircon outgrowths there are likely to remain points in the data set that are still slightly influenced by minute inclusions or very small quantities of matrix. Although the effect on zircon outgrowth chemistry is very small it may cause slight deviations in the non-formula element distribution of zircon outgrowths. Therefore it is likely that zircon outgrowths have a rather less varied chemistry than described here.

Sample	Analysis no	Al	Si	Ca	Fe2+	Y	Zr	Hf	Cpfu total	Zr/Si	Zr/Hf	Total wt%
<i>Host zircon</i>												
'bal1bz8a	1	0.000	' 0.881	0.001	0.007	0.000	0.997	0.024	1.911	1.132	40.798	99.86
'bal1bz8c	2	0.000	' 0.883	0.001	0.007	0.000	0.995	0.024	1.910	1.127	40.901	99.39
'bal1bz8d	3	0.000	' 0.883	0.001	0.007	0.001	0.994	0.023	1.909	1.126	42.777	99.52
'bal1bzc23a	16	0.000	' 0.894	0.000	0.010	0.000	0.974	0.034	1.913	1.090	28.949	99.46
'bal1bzc23b	17	0.000	' 0.897	0.001	0.010	0.000	0.972	0.034	1.913	1.084	28.919	99.07
'bal1bzc23c	18	0.000	' 0.896	0.001	0.008	0.000	0.972	0.035	1.913	1.084	28.146	98.77
'bal1bz25-4a	21	0.001	' 0.889	0.001	0.010	0.001	0.978	0.027	1.908	1.100	36.306	100.07
'bal1bz26a	25	0.000	' 0.888	0.001	0.006	0.001	0.988	0.023	1.908	1.113	42.703	99.72
'bal1bz26b	26	0.000	' 0.894	0.001	0.005	0.001	0.981	0.024	1.906	1.098	41.094	98.67
'bal1bz26c	27	0.000	' 0.889	0.001	0.007	0.001	0.987	0.023	1.908	1.110	42.318	99.48
'bal1bz28c	35	0.000	' 0.905	0.003	0.008	0.002	0.959	0.026	1.903	1.059	37.446	99.48
'bal1bz30a	39	0.000	' 0.887	0.000	0.009	0.003	0.980	0.022	1.902	1.105	44.191	99.43
'bal1bz32a	44	0.001	' 0.896	0.001	0.014	0.002	0.965	0.030	1.909	1.078	32.066	99.97
'bal1bz34a	52	0.000	' 0.887	0.001	0.007	0.000	0.991	0.021	1.907	1.118	47.852	100.20
'bal1bz34d	55	0.000	' 0.885	0.001	0.007	0.001	0.991	0.025	1.909	1.120	39.019	99.67
'bal1bz34e	56	0.000	' 0.885	0.001	0.007	0.001	0.991	0.023	1.907	1.119	43.785	99.40
'Bal1bz36a	59	0.000	' 0.886	0.001	0.006	0.001	0.990	0.026	1.909	1.118	38.019	99.43
'Bal1bz36a	60	0.000	' 0.880	0.001	0.008	0.002	0.993	0.024	1.907	1.129	40.908	99.57
'bal1bz36a	61	0.000	' 0.880	0.001	0.007	0.002	0.992	0.023	1.906	1.126	42.579	99.52
'bal1bz39a	65	0.000	' 0.883	0.000	0.010	0.001	0.990	0.025	1.910	1.121	39.510	101.39
'bal1bz39a	66	0.000	' 0.884	0.001	0.011	0.001	0.989	0.023	1.909	1.119	42.808	100.43
'bal1bz39b	67	0.001	' 0.892	0.001	0.011	0.002	0.976	0.026	1.907	1.095	37.878	99.74
'bal1bz42a	71	0.000	' 0.885	0.000	0.008	0.001	0.986	0.032	1.912	1.114	31.191	100.09
'bal1bz42b	72	0.002	' 0.875	0.001	0.008	0.001	0.993	0.032	1.912	1.135	30.668	100.93
'bal1bz43a	79	0.000	' 0.878	0.000	0.011	0.002	0.991	0.028	1.910	1.128	35.165	100.49
'bal1bz43b	80	0.000	' 0.882	0.000	0.010	0.002	0.985	0.029	1.909	1.117	34.228	100.03
'bal1bz45a	83	0.000	' 0.884	0.001	0.010	0.002	0.984	0.031	1.911	1.113	31.985	99.93
'bal1bz45b	84	0.000	' 0.879	0.001	0.009	0.002	0.991	0.030	1.911	1.128	33.398	100.40
'bal1bz45c	85	0.000	' 0.876	0.001	0.009	0.002	0.992	0.031	1.911	1.133	32.491	99.71
'bal1bz47a	91	0.000	' 0.892	0.001	0.005	0.001	0.985	0.022	1.905	1.104	45.522	100.09
'bal1bz37a	105	0.001	' 0.882	0.005	0.014	0.001	0.985	0.027	1.915	1.117	36.413	100.07
'zr8-1d	109	0.000	' 0.885	0.001	0.016	0.001	0.984	0.026	1.913	1.112	38.514	99.77

Table 5 EPMA analyses of zircon outgrowths and the zircon hosts to those outgrowths. Presented in c.p.f.u. calculated to 4(O).

Sample	Analysis no	Al	Si	Ca	Fe2+	Y	Zr	Hf	Cpfu total	Zr/Si	Zr/Hf	Total wt%
'zr8-1e	110	0.001	0.886	0.001	0.015	0.001	0.980	0.028	1.913	1.105	35.447	99.53
'zr13-2a	117	0.001	0.881	0.001	0.010	0.002	0.983	0.034	1.912	1.115	29.296	99.40
'zr13-1a	120	0.001	0.849	0.002	0.009	0.006	0.980	0.032	1.880	1.155	30.637	100.80
'zr13-1f	125	0.000	0.879	0.001	0.008	0.003	0.981	0.033	1.905	1.116	29.521	99.42
'zr12-1e	133	0.001	0.877	0.001	0.015	0.000	0.992	0.031	1.917	1.131	32.466	100.24
'zr12-1f	134	0.001	0.879	0.001	0.015	0.000	0.990	0.031	1.917	1.127	31.684	100.09
'zr12-1g	135	0.001	0.880	0.001	0.015	0.000	0.989	0.031	1.917	1.123	31.765	99.80
'zr12-1h	136	0.001	0.877	0.001	0.015	0.000	0.991	0.032	1.917	1.130	31.356	99.95
'zr11-4a	140	0.000	0.876	0.000	0.011	0.001	0.996	0.025	1.910	1.136	40.044	100.44
'zr11-4b	141	0.001	0.879	0.001	0.011	0.001	0.992	0.024	1.909	1.129	41.404	99.76
'eazr1-1a	147	0.000	0.883	0.000	0.005	0.000	0.998	0.021	1.907	1.130	48.122	99.19
'Ezr1-1b	148	0.000	0.876	0.000	0.006	0.000	1.006	0.021	1.909	1.148	47.054	99.80
'Ezr1-1c	149	0.001	0.872	0.002	0.005	0.001	1.003	0.026	1.910	1.150	38.097	98.35
'Ezr1-1e	151	0.000	0.883	0.001	0.007	0.000	0.997	0.020	1.908	1.129	49.989	99.92
'Ezr1-1f	152	0.001	0.887	0.001	0.007	0.000	0.989	0.024	1.909	1.115	41.159	99.20
'Ezr2e	165	0.000	0.878	0.001	0.008	0.001	0.998	0.023	1.909	1.137	42.985	99.07
'Ezr2f	166	0.000	0.871	0.000	0.008	0.001	1.007	0.023	1.910	1.155	43.327	99.17
'Ezr2h	167	0.000	0.874	0.000	0.008	0.001	1.001	0.024	1.910	1.145	41.101	100.18
'Ezr4-3a	170	0.000	0.875	0.001	0.009	0.001	0.997	0.032	1.914	1.140	30.723	99.54
'Ezr4-3b	171	0.000	0.880	0.001	0.008	0.001	0.990	0.035	1.915	1.124	28.477	98.51
'Ezr4-3c	172	0.001	0.887	0.000	0.009	0.001	0.978	0.037	1.914	1.103	26.301	99.26
Ezr5	176	0.000	0.871	0.001	0.010	0.000	1.010	0.018	1.910	1.159	56.593	100.07
'Ezr1-5a	181	0.001	0.880	0.001	0.015	0.001	0.989	0.028	1.914	1.124	35.351	99.14
<i>Zircon Outgrowths</i>												
'bal1bz8e	4	0.002	0.892	0.006	0.008	0.003	0.969	0.022	1.902	1.086	43.866	97.93
'bal1bz10b	9	0.000	0.885	0.001	0.009	0.005	0.977	0.024	1.901	1.105	40.545	99.35
'bal1bzr16a	13	0.001	0.887	0.001	0.014	0.004	0.977	0.020	1.902	1.101	48.360	98.86
'bal1bzr23d	19	0.004	0.893	0.002	0.013	0.001	0.957	0.034	1.903	1.071	28.367	98.89
'bal1bz26d	28	0.001	0.897	0.004	0.007	0.002	0.969	0.022	1.903	1.080	43.077	99.24
'bal1bz26e	29	0.003	0.900	0.011	0.010	0.006	0.944	0.023	1.897	1.050	41.256	97.63
'bal1bz26f	30	0.009	0.876	0.026	0.016	0.015	0.916	0.025	1.884	1.047	36.533	92.96
'bal1bz28e	37	0.001	0.894	0.005	0.008	0.007	0.957	0.023	1.895	1.070	40.877	98.51
'bal1bz30b	40	0.002	0.889	0.004	0.011	0.004	0.968	0.025	1.903	1.089	38.844	97.48

Table 5 cont.

Sample	Analysis no	Al	Si	Ca	Fe2+	Y	Zr	Hf	Cpfu total	Zr/Si	Zr/Hf	Total wt%
'ballbz30c	41	0.006	0.895	0.014	0.016	0.006	0.934	0.029	1.900	1.043	32.314	94.94
'ballbz30e	43	0.000	0.885	0.001	0.010	0.003	0.984	0.022	1.904	1.112	44.117	99.80
'ballbz32b	45	0.007	0.883	0.004	0.019	0.006	0.938	0.027	1.884	1.062	34.630	98.22
'ballbz33a	48	0.001	0.893	0.001	0.013	0.002	0.970	0.026	1.906	1.086	37.044	98.44
'ballbz34b	53	0.001	0.895	0.002	0.008	0.001	0.976	0.023	1.906	1.090	41.827	98.97
'ballbz34c	54	0.005	0.888	0.022	0.017	0.009	0.928	0.028	1.898	1.045	33.225	91.15
'ballbz34f	57	0.003	0.869	0.009	0.007	0.011	0.968	0.024	1.890	1.114	40.872	94.94
'ballbz39c	68	0.007	0.884	0.012	0.020	0.010	0.925	0.026	1.884	1.046	35.169	92.09
'ballbz39d	69	0.007	0.891	0.012	0.016	0.007	0.930	0.025	1.888	1.044	36.865	96.41
'ballbz42g	77	0.001	0.881	0.003	0.011	0.008	0.963	0.031	1.899	1.094	30.861	97.42
'ballbz43c	81	0.002	0.895	0.004	0.011	0.008	0.945	0.029	1.893	1.056	33.010	98.42
'ballbz43d	92	0.000	0.889	0.000	0.007	0.003	0.976	0.026	1.903	1.098	37.543	99.33
'ballbz47c	93	0.001	0.888	0.001	0.008	0.004	0.976	0.025	1.902	1.099	38.556	99.50
'ballbz47d	94	0.002	0.882	0.005	0.010	0.008	0.961	0.026	1.893	1.090	37.430	98.07
'ballbz47e	95	0.003	0.884	0.003	0.008	0.006	0.966	0.025	1.895	1.093	38.297	97.15
'ballbz47f	96	0.004	0.867	0.011	0.014	0.013	0.948	0.028	1.886	1.094	33.995	93.91
'ballbz47g	97	0.004	0.871	0.008	0.014	0.012	0.949	0.029	1.887	1.090	33.280	94.53
'ballbz47h	98	0.011	0.860	0.017	0.022	0.013	0.920	0.029	1.871	1.069	32.025	93.17
'ballbz46a	100	0.002	0.877	0.005	0.012	0.008	0.968	0.024	1.896	1.104	39.591	98.48
'zr9-3a	112	0.003	0.880	0.000	0.028	0.002	0.972	0.032	1.917	1.104	30.648	100.17
'zr9-3b	113	0.008	0.856	0.001	0.035	0.004	0.964	0.033	1.900	1.125	29.584	99.56
'zr11-1c	115	0.000	0.876	0.001	0.014	0.004	0.990	0.021	1.906	1.130	47.747	99.77
'zr11-1d	116	0.003	0.875	0.008	0.017	0.005	0.974	0.021	1.903	1.113	45.856	97.00
'zr13-2b	118	0.004	0.844	0.011	0.014	0.010	0.944	0.037	1.864	1.118	25.802	97.25
'zr13-1b	121	0.001	0.869	0.003	0.010	0.005	0.980	0.033	1.901	1.127	30.106	99.37
'zr13-1c	122	0.003	0.858	0.008	0.012	0.009	0.951	0.031	1.873	1.108	30.837	97.50
'zr13-1d	123	0.008	0.865	0.020	0.016	0.013	0.904	0.031	1.857	1.045	29.579	91.53
'zr12-1a	128	0.002	0.856	0.007	0.016	0.006	0.968	0.031	1.886	1.131	31.624	99.48
'zr12-1b	129	0.001	0.868	0.002	0.015	0.003	0.981	0.031	1.902	1.130	31.229	99.67
'zr12-1i	137	0.002	0.874	0.003	0.018	0.002	0.981	0.032	1.912	1.123	30.278	99.11
'zr12-1j	138	0.009	0.863	0.012	0.026	0.014	0.882	0.029	1.834	1.022	30.144	94.37
'zr11-4c	142	0.004	0.890	0.005	0.012	0.005	0.945	0.023	1.884	1.063	40.560	99.61
'zr11-4f	145	0.000	0.860	0.000	0.010	0.006	0.978	0.027	1.883	1.137	35.611	99.96

Table 5 cont.

Sample	Analysis no	Al	Si	Ca	Fe2+	Y	Zr	Hf	Cpfu total	Zr/Si	Zr/Hf	Total wt%
'Ezr1-1d	150	0.008	0.853	0.011	0.008	0.006	0.976	0.029	1.891	1.145	33.229	94.69
'Ezr1-1g	153	0.003	0.885	0.002	0.009	0.001	0.984	0.023	1.906	1.111	41.954	97.34
'Ezr3a	155	0.004	0.855	0.006	0.013	0.007	0.972	0.022	1.879	1.138	44.334	97.74
'Ezr3c	157	0.011	0.818	0.022	0.018	0.018	0.926	0.022	1.835	1.131	42.656	93.98
'Ezr3d	158	0.010	0.830	0.012	0.019	0.012	0.943	0.021	1.847	1.137	44.933	97.50
'Ezr4-3d	173	0.001	0.895	0.002	0.009	0.002	0.966	0.038	1.912	1.079	25.478	98.53
'Ezr4-3e	174	0.007	0.886	0.009	0.014	0.009	0.907	0.038	1.870	1.023	23.558	94.67
'Ezr5b	177	0.001	0.873	0.002	0.014	0.000	0.998	0.029	1.917	1.144	34.177	100.39
'Ezr5c	178	0.001	0.875	0.002	0.014	0.001	0.994	0.030	1.916	1.136	33.281	100.03
'Ezr5d	179	0.006	0.865	0.007	0.021	0.005	0.970	0.026	1.901	1.121	37.725	99.12

Table 5 cont.

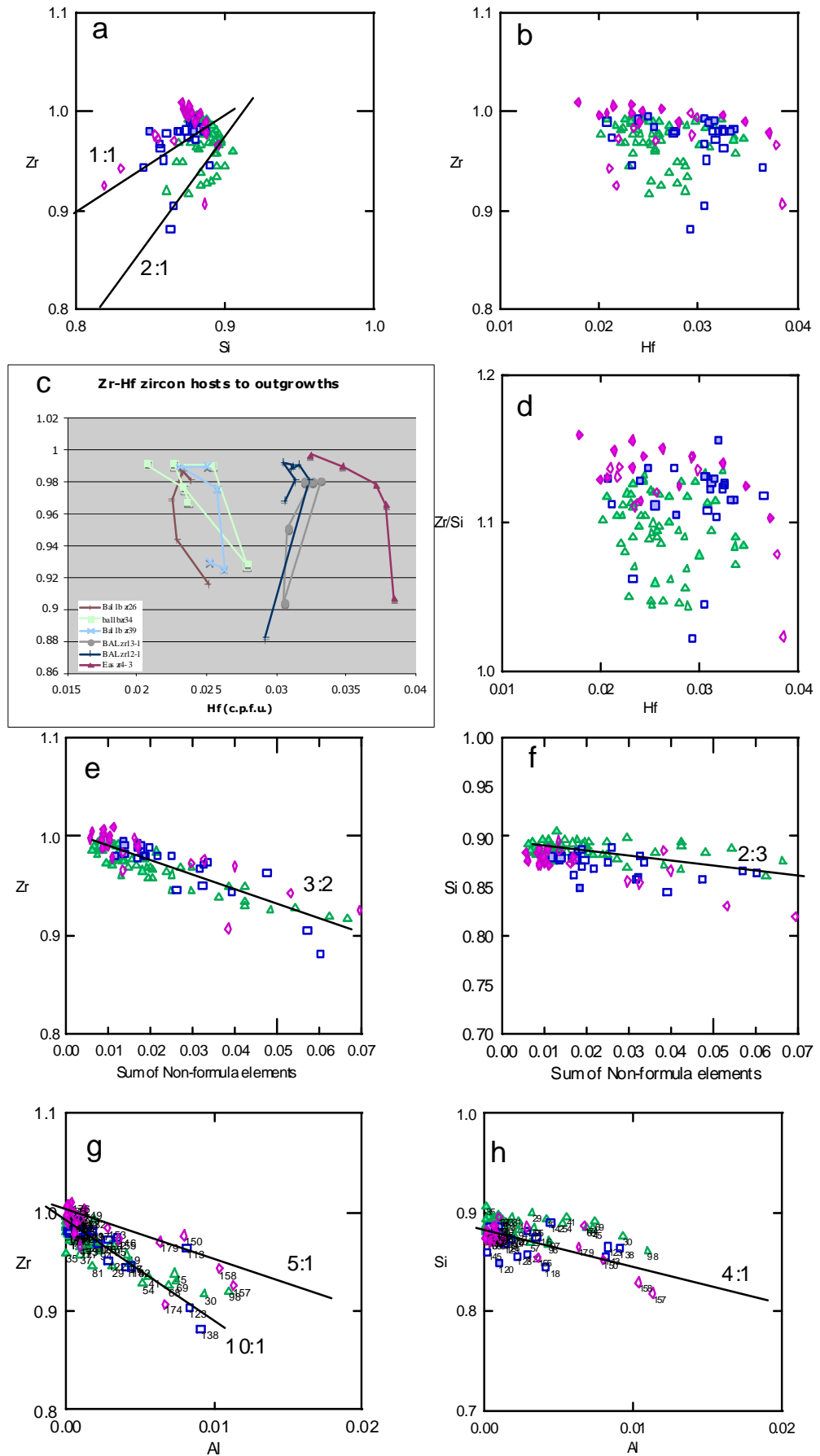


Figure 40. Element plots of EPMA analyses of zircon outgrowth data from Table 5.

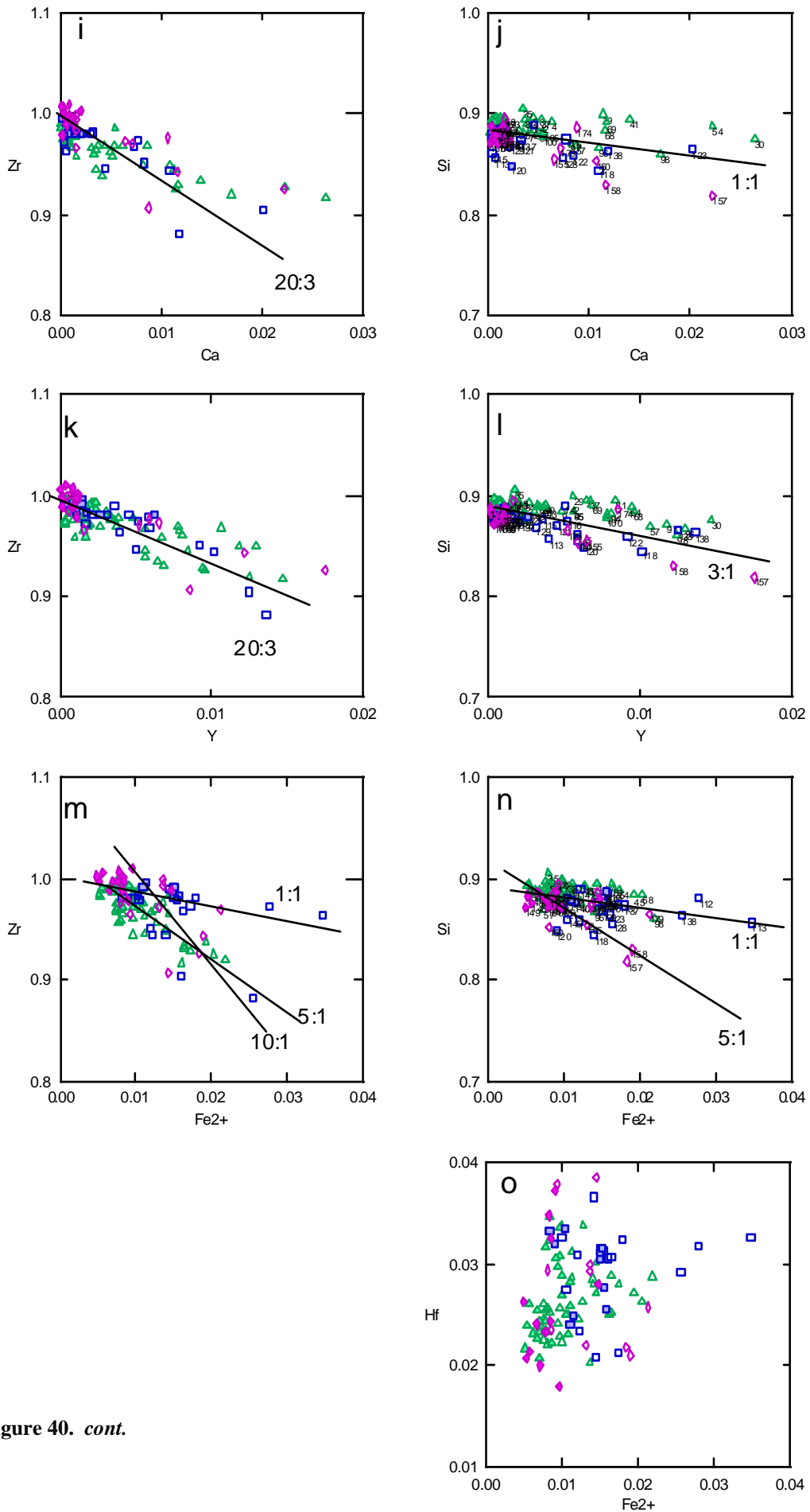


Figure 40. *cont.*

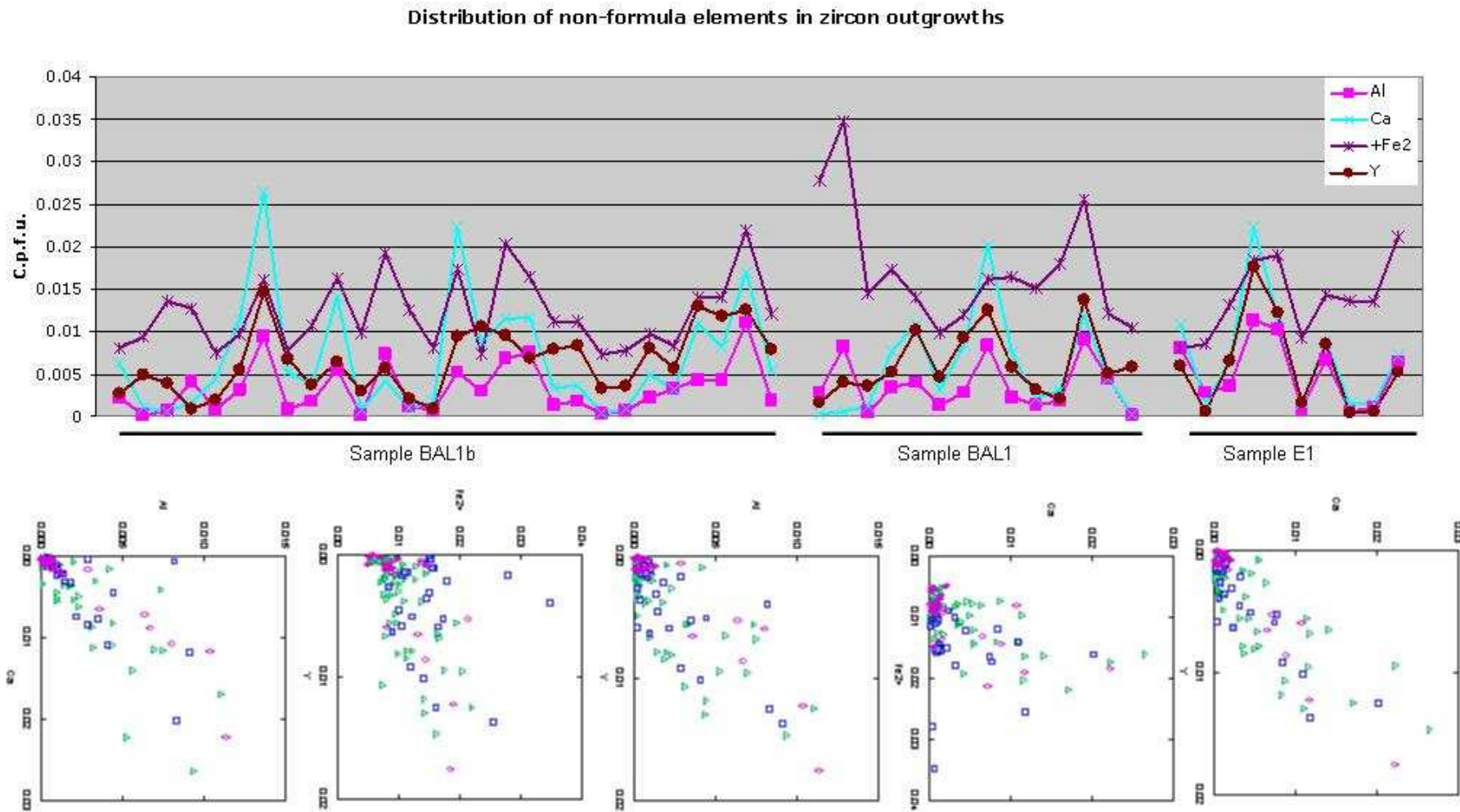


Figure 41. Non-formula element distribution profile and element plots of zircon outgrowths. All units are c.p.f.u.

3.9.5.3 CL and EBSD

Determining the CL intensity of zircon outgrowths is difficult due to the small size. Images taken using CL show that zircon outgrowths are weakly luminescent compared to the host zircon (Fig. 42a&b).

Zircon outgrowths produce very low IQ patterns when analysed using EBSD (Fig. 42c). However, xenotime inclusions in outgrowths produce high IQ EBSD patterns and therefore xenotime domains in zircon outgrowths can be readily identified using EBSD techniques (Fig. 42d, see section 3.9.7 and Chapter 5).

3.9.6 Chemical comparison of zircon microstructures

Dark BSE zircon and porous zircon display a similar composition in most plots. This is expected as some dark BSE zircon is often associated with porous zircon. The comparison will therefore focus on the composition of dark BSE zircon and zircon outgrowths, drawing attention to variations in porous zircon chemistry where applicable.

Zr-Si plots (Fig.43a) reveal that zircon outgrowths are more depleted in Zr than dark BSE zircon but zircon outgrowths are more Si-rich. Zircon outgrowths data clusters roughly along a 2:1 Zr:Si trend whereas dark BSE zircon data generally clusters along a 1:1 relationship. Zr/Si is lower in zircon outgrowths compared to its hosts but dark BSE zircon has a higher Zr/Si in comparison to the parent composition. Hf concentration in zircon outgrowths and dark BSE zircon are distinct (Fig. 43b). Hf concentration varies considerable more in zircon outgrowths in comparison to dark BSE zircon where Hf contents vary much less. Zircon outgrowths contain appreciably more Hf compared to dark BSE zircon, as do their hosts. This seems unusual as Hf does not seem to be involved with any particular substitutions in either zircon outgrowths or dark BSE zircon. The grain E1zr2 was analysed both as a light BSE host and as a light BSE zircon containing dark BSE zircon. The two points are highlighted in Figure 43c. Despite analysing light BSE zircon at

different locations on the grain, the two data points are from the same growth layer indicating there is significant deviation in the Hf concentration between the analysis sets. It would therefore appear

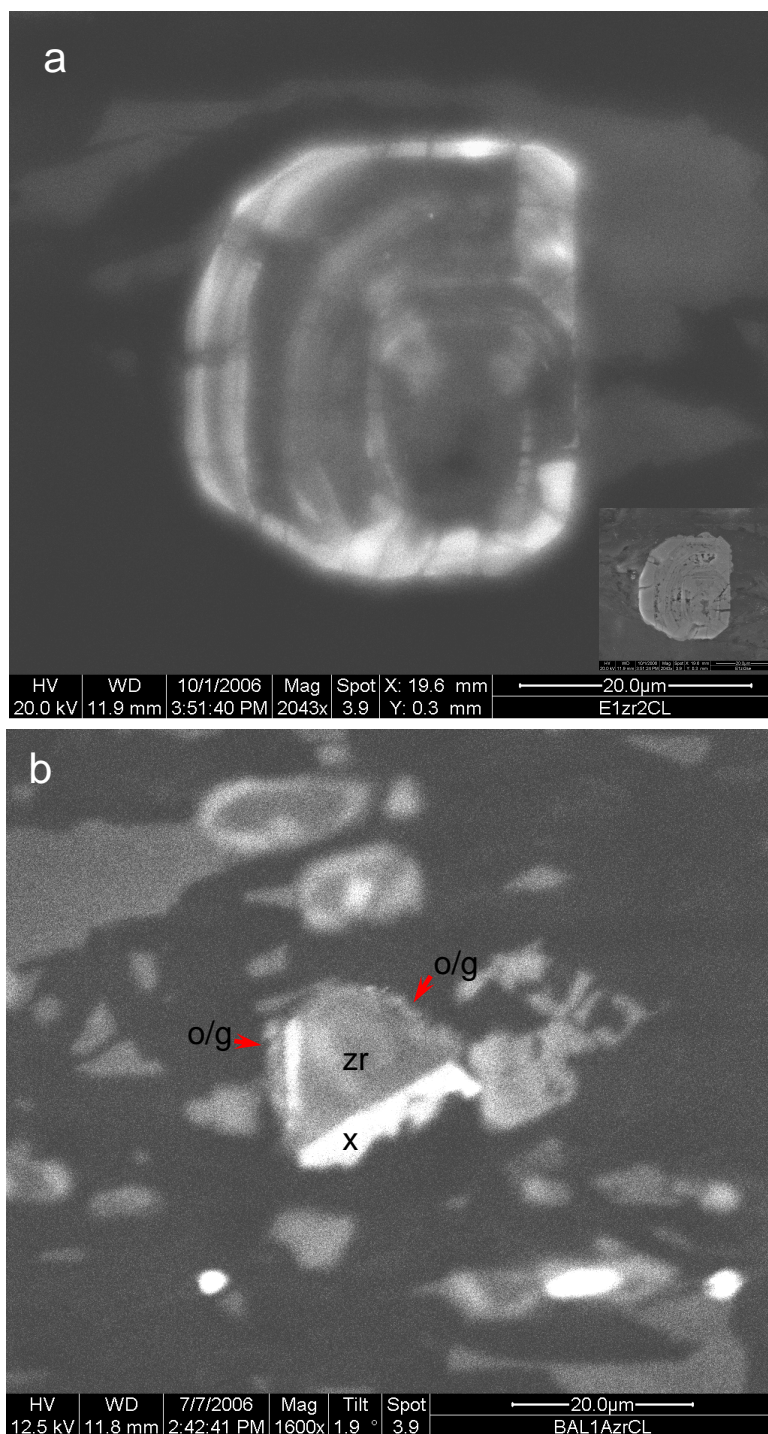


Figure 42. Character of zircon outgrowths. Figure caption is on 127.

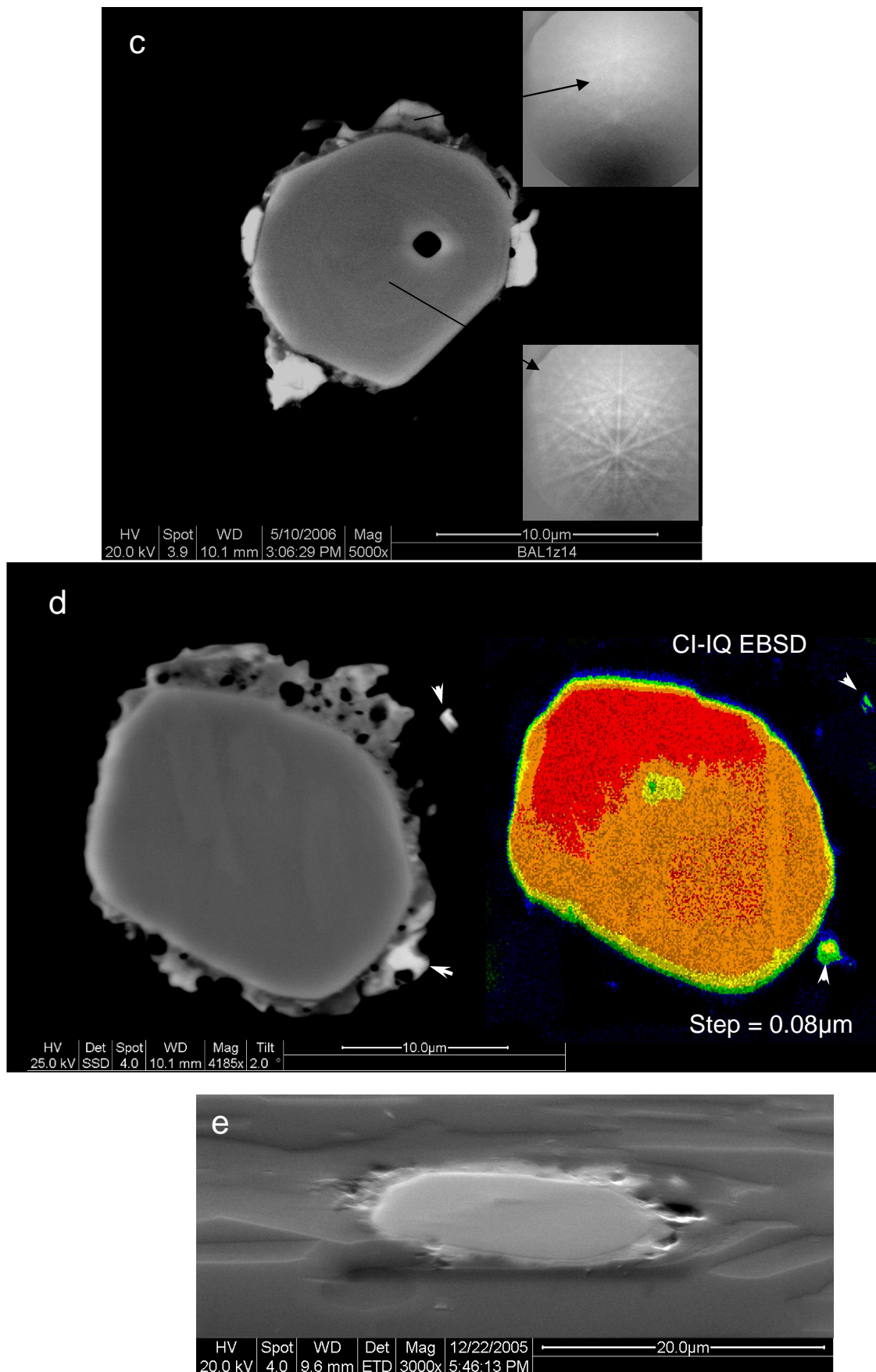


Figure 42. Character of zircon outgrowths. Figure caption is on following page

Figure 42. Character of zircon outgrowths

a CL image of zoned dark and light BSE zircon (fig. 6k). Equivalent light BSE zircon shows predominantly high CL intensity while equivalent dark BSE zircon has very low CL intensity. Inset shows complementary SE image with zircon outgrowth along the top margin of the grain. Note outgrowth cannot be observed in the CL image. **b** CL image of figure 14d with host zircon with zircon (o/g) and xenotime (x) outgrowths. Shows xenotime is considerably more luminescent than zircon. Zircon outgrowths have low CL intensity **c** BSE image of zircon with zircon and xenotime outgrowths. Zircon outgrowths have low IQ EBSD kikuchi patterns compared to its host zircon. **d** Left hand image is BSE showing zircon with a zircon outgrowth that contains xenotime (arrows). Right hand image is complementary CI-IQ EBSD map, step size = 0.08 μ m. White arrows point to xenotime grains that index well in comparison to zircon outgrowths. **e** SE image of host zircon and polished down outgrowth with SEM stage tilted (70°) (BAL).

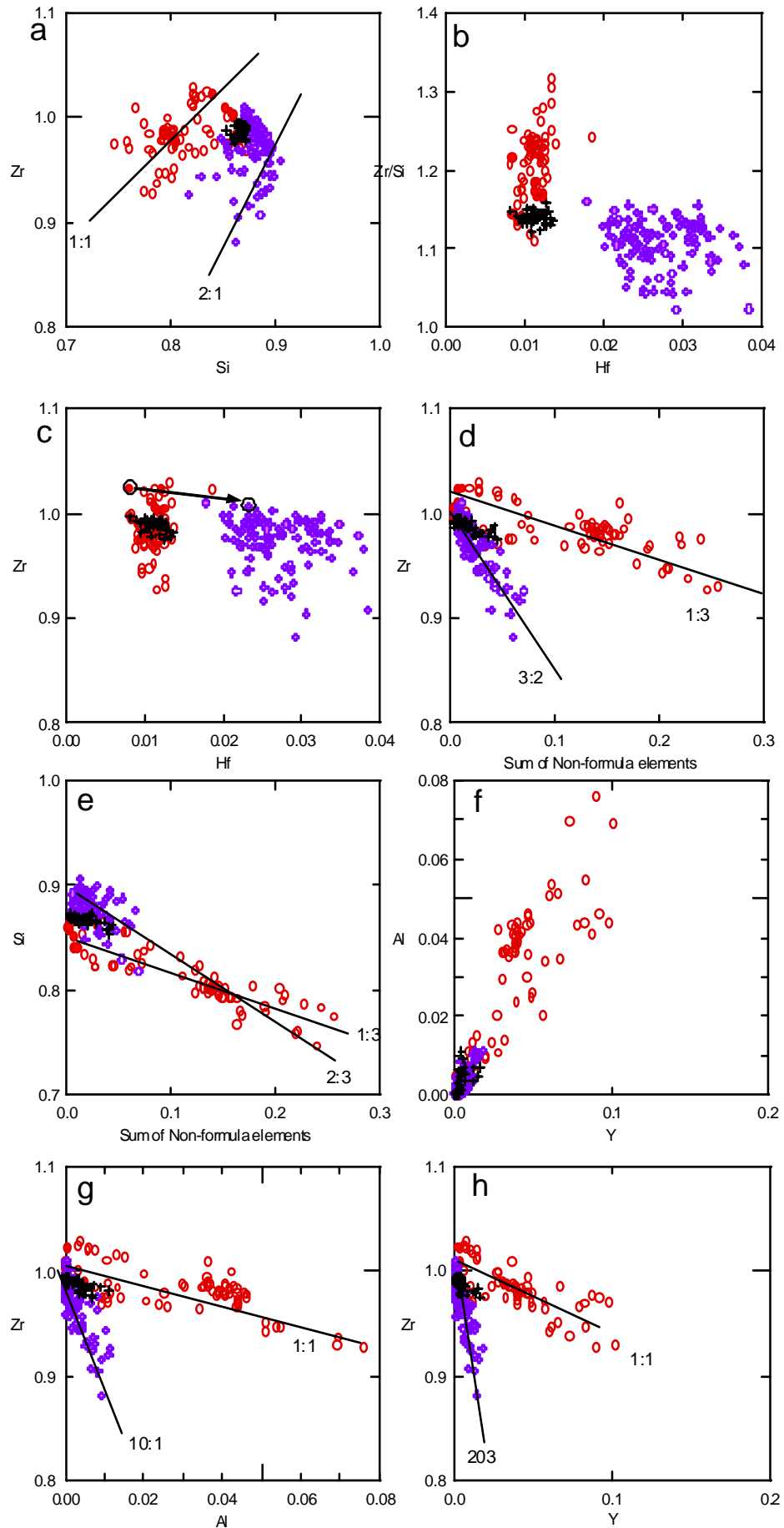


Figure 43. Chemical comparison of zircon textures in greenschist facies rocks. Units in c.p.f.u.

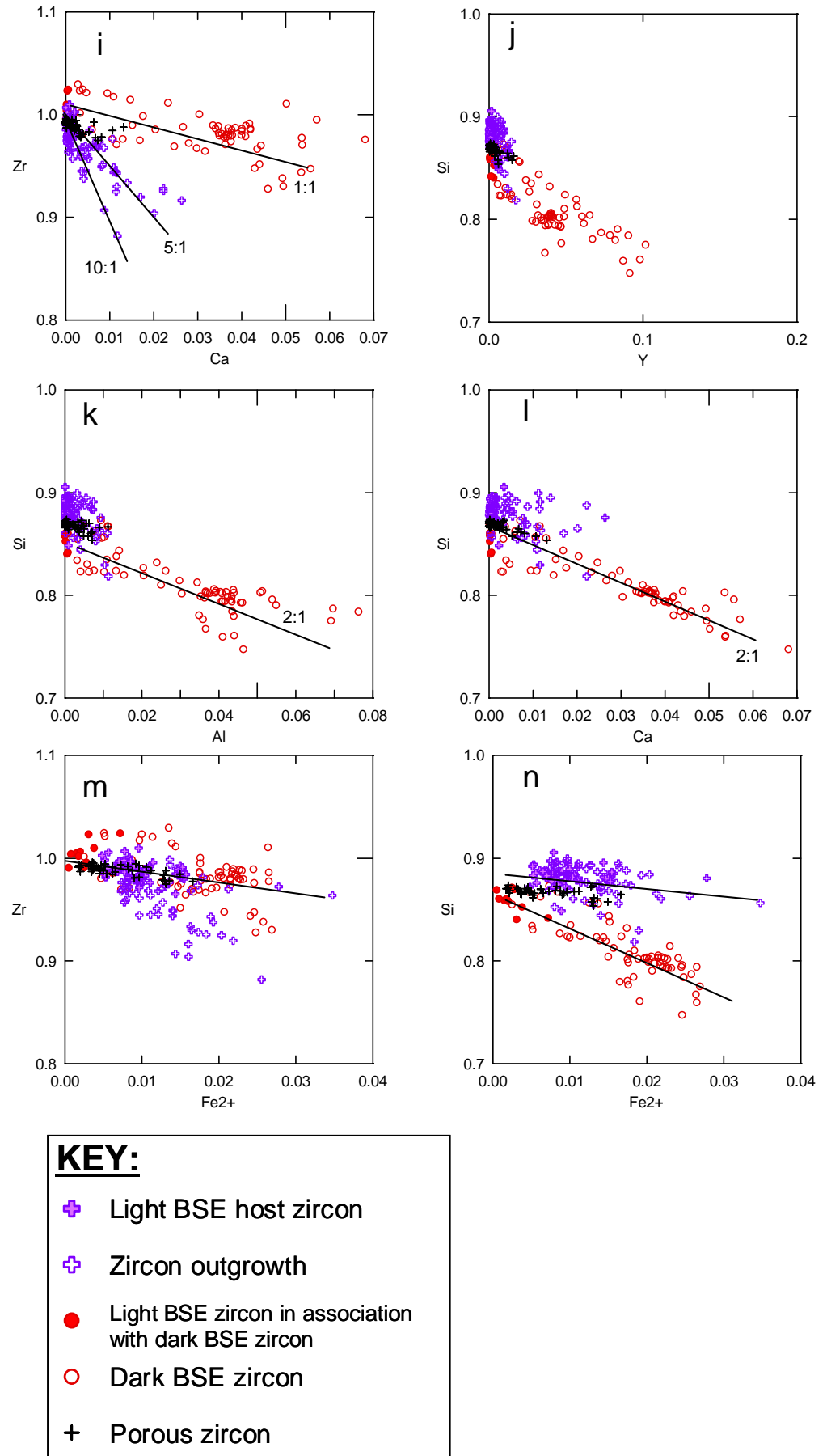


Figure 43. cont.

that Hf concentrations are not distinct and that Zr outgrowths have Hf concentrations similar to dark BSE zircon. This is likely due to problems with the Hf standard as outlined in Chapter 2.

Overall Zr and Si depletion in dark BSE zircon mark reasonably well-defined 1:3 substitution relationships when plotted against the sum of the non-formula elements (Fig. 43d&e). Zircon outgrowths plot along a 3:2 (Zr:Sum of non-formula elements) trend however and Si loss marks a general 2:3 substitution relationship (Si:Sum of non-formula elements) with enrichment of non-formula elements in zircon outgrowths. Dark BSE zircon is enriched in non-formula elements by as much as three times that of zircon outgrowths, the majority of which is accounted for by the high Al and Y contents in dark BSE zircon and to a lesser extent Ca. The strong correlation of Y and Al enrichment in dark BSE zircon (fig 43f & h) suggests that available Y promotes the uptake of Al. This is not observed in zircon outgrowths and is possibly due to the majority of available Y being readily incorporated into xenotime which also form as outgrowths in these rocks. Al, Ca and Y all display a 1:1 substitution relationship with Zr loss in dark BSE zircon as does Si:Y (fig. 43g-j). This contrasts with zircon outgrowths where there is significant variability in element substitutions (Zr:Ca = 5:1, Zr:Y = 20:3, Zr:Al = 10:1). Si:Ca and Si:Al in dark BSE zircon display a 2:1 relationship while Si:Ca is 1:1 and Si:Al is 20:3 in zircon outgrowths (fig. 43k & l). Zircon outgrowths and dark BSE zircon do however contain very similar concentrations of Fe. Although there is considerable variation in the Fe with Zr and Si in both zircon outgrowths and dark BSE zircon, broadly speaking Zr:Fe data spreads between 1:1-2:1 trend lines in dark BSE zircon and 1:1-10:1 in zircon outgrowths while Si:Fe in dark BSE zircon broadly display a 3:1 substitution trend compared to a 1:1 Si:Fe substitution trend in zircon outgrowths.

EPMA totals of zircon outgrowths produce totals below 97%. Dark BSE zircon EPMA totals average 89.8%(±4.3). Other than those elements analysed in EPMA, no further elements were identified in EDX spectra of dark BSE zircon or zircon outgrowths. This strongly suggests the presence of some hydrous component. However, Y substitution into the zircon structure is strongly coupled to the uptake of P. The P K α peak is at the same position as Zr L α on the EDX spectra and therefore P would be masked by the presence of Zr. P was omitted from EPMA due to the

strong interference of the Zr $L\alpha$ peak with the P $K\alpha$. As Y is considerably enriched in dark BSE zircon compared to zircon outgrowths, this would likely be coupled with a significant increase in P which may account for the considerable difference both in wt% totals and total molar volume. It is also possible that some of the low totals may be caused by the non-uniform surface of zircon outgrowths. Zircon outgrowths and dark BSE zircon polish down relative to the host grain which stands proud (Fig. 42e) and give close to perfect analytical totals. To minimise this effect, all the thin sections analysed have been polished with colloidal silica for 5-10 minutes. Despite polishing, achieving a finished polish where the outgrowth or dark BSE area is level with the host grain is not always possible. The absence of P from EPMA analysis is only likely to have a slight effect totals and still suggests a hydrous component is responsible for the low wt% totals.

The higher average of total c.p.f.u. in dark BSE zircon $1.93 (\pm 0.02)$ compared to light BSE $1.88 (\pm 0.002)$ indicates that the substitution of some non-formula elements occurs at interstitial sites in the lattice. Zircon outgrowths have similar c.p.f.u. totals ($1.89 (\pm 0.02)$) to light BSE hosts ($1.91 (\pm 0.005)$).

In summary dark BSE zircon is the most non-formula element rich zircon, owed mainly to the relatively high concentrations of Y and Al. Zircon outgrowths are distinct by having relatively little Si lost and containing high levels of Fe relative to the other non-formula elements. Porous zircon has a similar chemistry to light BSE zircon but enriched in Fe. The chemical properties of all these features are summarised in Table 6, along with other crystallographic and luminescent properties.

	BSE intensity	EBSD IQ	CL intensity	Composition
Light BSE	high	high	high	Unmodified
Dark BSE	low	low	low	NFE rich, esp. Y & Al
Porous	high	mod	low	Fe rich
Outgrowths	low	low	low	NFE rich, esp. Fe

Table 6 Summary of greenschist zircon textures

3.9.7 Xenotime

Preliminary EPMA analysis of xenotime outgrowths was carried out. The results are not presented as it is not the purpose of this study to analyse the detailed chemistry of xenotime and its complex substitution mechanisms. However the concentration of U and Th in xenotime outgrowths gives an important indication of their availability during xenotime growth. Large errors are expected on both U and Th because of a lack of a good standard and the values quoted here are to act only as guide. Despite this, rough values have been obtained revealing that xenotime contains upto 0.5wt% U with an average of 0.05wt%. These concentrations of U are unusually low when compared to other diagenetic and metamorphic xenotime which is 0.42wt% U (this value is the average of data from Table 1 in Rasmussen (2005a)). Th is concentrated upto 2wt% in xenotime with an average of 0.2wt% and is comparable with the average Th of diagenetic and metamorphic xenotime in Rasmussen (2005a) which is 0.23wt% Th. However, from the xenotime EPMA data, U/Th ratios for xenotime outgrowths in greenschist rocks from this study is below 1 which is unusual for xenotime (typically $U/Th > 1$, (Rasmussen, 2005a)).

Xenotime is strongly luminescent in CL, and is slightly more luminescent than unmodified zircon (Fig. 42c). Xenotime has a high IQ EBSD patterns and EBSD inverse pole figure maps show that xenotime forms epitaxial overgrowths (Fig.44). By a combination of BSE intensity, CL intensity and EBSD IQ, it is therefore possible to identify sub-micron xenotime domains within zircon (Fig. 42e) which is not always possible through chemical analysis (see Chapter 5).

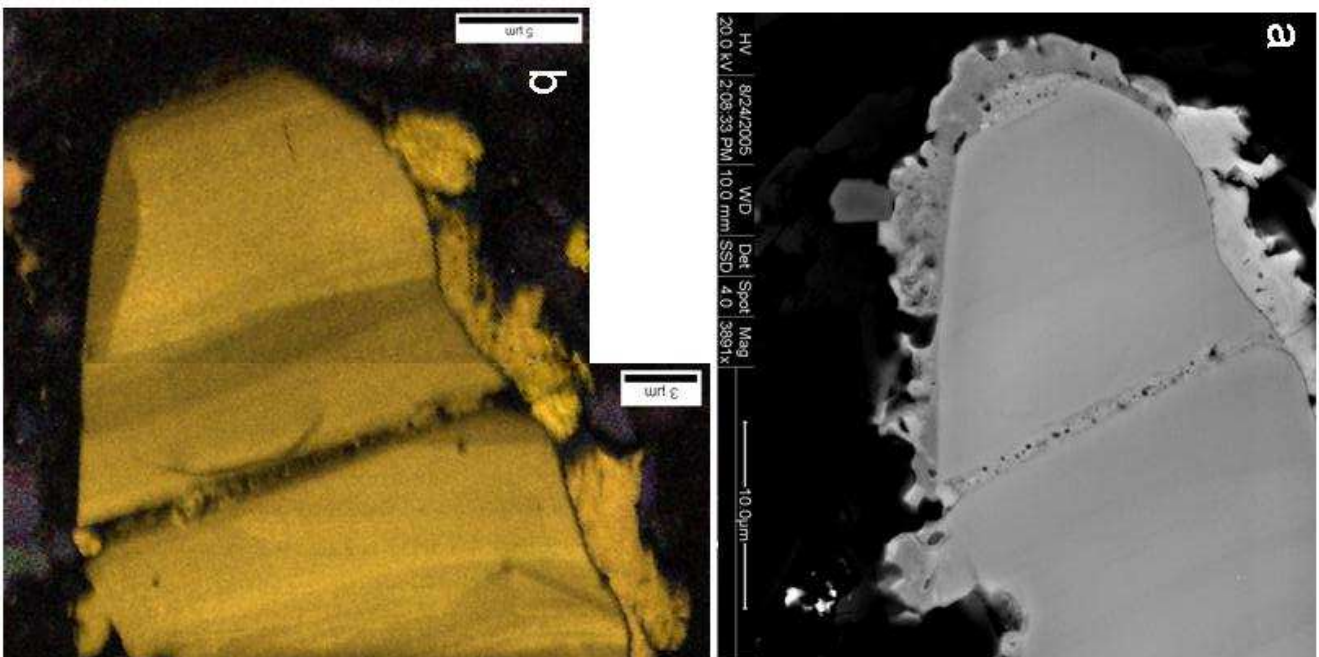


Figure 44. Image with zircon and xenotime outgrowth on detrital zircon

a BSE image of host zircon with crack through the grain that is sealed by dark BSE zircon and leads into a zircon outgrowth.

Higher BSE intensity outgrowth is xenotime that is also present as minute inclusion in dark BSE zircon. **b** IQ-Inverse pole

figures (IPF) EBSD map of same grain showing epitaxial xenotime outgrowths. Zircon outgrowths give no EBSD pattern. Step

size = 0.1 μm.

3.10 Interpretation

3.10.1 General zircon character

Overall, larger zircons $>30\mu\text{m}$ are subhedral to well-rounded and indicate they have undergone a degree of processing by transportation as a sediment. A small proportion of zircon grains (c.1-2% of zircon population) preserve an original euhedral habit and could represent input from proximal volcanic horizons that are found within the Southern Highland, Appin and Argyll Groups (Harris et al., 1994) while other euhedral grains may have been protected as inclusions in large ($>100\mu\text{m}$) detrital quartz grains (Fig.4c&d). Of the smaller zircons $<30\mu\text{m}$, some are well-rounded, oval-shaped grains reflecting significant sedimentary reworking. However, although most grains have some rounded features many also have sharp, angular margins. The rounded edges of these grains indicate some sedimentary reworking but the angular edges are likely to represent the broken fragments of larger grains. Slates and phyllites contain a large proportion of such zircons with large ($>30\mu\text{m}$) complete, rounded zircon rare in these rocks (Table 1). Psammites tend to have a more varied zircon population containing many large well-rounded grains but also some smaller rounded and fractured zircons but quartzites typically have a fairly limited size range of larger (30-60 μm) rounded zircons. As a result the great majority of zircon in these rocks is originally detrital.

In general, light BSE zircon with a strong CL signal is fully crystalline, as determined by high EBSD IQ, and has a typical zircon composition (e.g. compare with Hoskin and Schaltegger (2003) is considered to be unmodified from when deposited as a sediment in the rock.

3.10.2 Dark BSE zircon

Dark BSE zircon is observed in all the samples studied and commonly found in association with light BSE zircon that defines the original growth zones of the grain (e.g. Fig.6). However in contrast to light BSE zircon, dark BSE zircon exhibits a modified composition, enriched in the non-formula elements Y, Ca, Al, Fe and Mg which is linked to a depletion in Zr and Si. Dark BSE

zircon also consistently produces low EBSD IQ patterns and a low CL signal intensity.

3.10.2.1 Metamictization

The presence of zircon in high-grade rocks is testament to its durability when crystalline. Therefore it is highly unlikely that zircon in its crystalline state has become chemically modified to dark BSE zircon in typical low-grade metasediments. Furthermore, zircon in close proximity to zircon with dark BSE domains has remained completely unmodified and the process that produces dark BSE zircon generally affects particular growth zones or domains in the grain while other growth layers remain unmodified. The process generating dark BSE zircon must therefore be related to the original chemistry of these growth zones but also to structural defects within these zones. In its metamict state, zircon is 2-3 more times more susceptible to dissolution in the presence of hydrothermal fluids than when fully crystalline (Ewing et al., 2003). Metamict zircon forms from the recoil of radioactive isotopes from alpha particle decay. This generates localised amorphous areas in zircon lattice (c.3nm in diameter, (Geisler et al., 2007)) around the decaying actinide elements. The accumulation and overlap of amorphous clusters in the lattice results in metamict zircon. Therefore, below the annealing temperature of zircon, *c.*<250°C (Geisler et al., 2003a; Garver et al., 2005; Nasdala et al., 2005; Siyanbola et al., 2005), zircon accumulates radiation damage (Murakami et al., 1991). The amount of damage that is accumulated is both a function of time and the concentration of U and Th. The heterogeneous distribution of actinide elements within zircon, and the possible different ages of zircon zones, can lead to range of crystalline states within a single crystal. The result is that some growth zones can be particularly susceptible to dissolution (completely metamict), other growth zones are slightly more resistant to dissolution (partially metamict) and other parts of the zircon remain insoluble (crystalline zircon).

3.10.2.2 Process of dark BSE zircon formation

Minute irregularities along the margins of dark BSE zircon exposed to the matrix in slates are observed to have intergrown with matrix minerals of metamorphic origin (e.g. chlorite and muscovite, Fig.6c, 7 & 8). In some instances, dark BSE zircon appears to have grown out of original zoning layers defined by light BSE zircon, engulfing the light BSE zircon fragment as it

formed (Fig. 7c). The fragile nature and minute size of the dark BSE zircon intergrown with the rock matrix strongly suggest that they have a metamorphic origin, having formed at or below peak metamorphism conditions (<350°C). This can be constrained further by the likelihood that soon above the annealing temperature for zircon (c.250°C), radiation damage accumulation diminishes and metamict zircon may at least be partly repaired. Therefore, it is most likely that dark BSE zircon developed around temperatures or below the annealing temperature of zircon. It should be emphasised that there is some debate as to the precise annealing temperature for zircon and the temperature at which zircon anneals is thought to be partly controlled by the amount of radiation damage in the zircon. Zircon with little radiation damage apparently anneals at lower temperature to zircon that is heavily radiation damaged (Geisler et al., 2003a). Therefore the general annealing temperature of c.250°C is assumed (Nasdala et al. 2005b).

The abundance of holes and inclusions in many dark BSE zircon suggest a significant volume change that may occur during the alteration of light BSE zircon (e.g. Putnis, 2002; Tomaschek et al., 2003) and the preservation of the overall grain shape (e.g. Fig. 8) would suggest that dark BSE zircon has recrystallised from previously metamict zircon. The amorphous areas in radiation damaged zircon are likely to be out of equilibrium with fluid phases and therefore susceptible to dissolution (e.g. Geisler et al., 2003a). The amorphous areas of the zircon exposed to the fluid will dissolve provided the fluid phase is under-saturated with respect to Zr or Si (the main components of zircon). If enough zircon is dissolved to saturate the fluid in Zr then the fluid may also become supersaturated causing dark BSE zircon to precipitate (the issue of supersaturation will be discussed in greater detail in Chapter 6). This is therefore a dissolution-reprecipitation process that, in effect, “recrystallises” the metamict regions of the zircon. The micro-porosity generated during this dissolution-reprecipitation process indicates that the fluid is on the cusp undersaturation and supersaturation throughout. Where porosity size is large, it may be that there is lag time between when the zircon was dissolved and when precipitation took place. In dark BSE zircon with virtually no pores, it would suggest that precipitation is almost simultaneous with dissolution. The very low total weight percent totals of dark BSE zircon suggests hydrous species are also gained in the precipitating phase. Instances where the volume of zircon dissolved would appear significantly

more than the volume of dark BSE zircon precipitated (e.g. Fig. 9c) indicates that a net loss of zircon may occur during this dissolution-reprecipitation process.

It is important that some crystalline component of the original zircon remains onto which dark BSE zircon can nucleate as it is improbable that dark BSE zircon will crystallise onto an amorphous medium. Either the metamict area undergoing alteration is not heavily damaged (i.e. beyond the 1st percolation point but not the 2nd) in which case the crystalline remnant structure within the metamict area may provide a focus for nucleation or, and more likely in most cases, crystalline growth domains in the zircon provide points for dark BSE zircon nucleation. Without suitable sites for nucleation, zircon may be completely dissolved without reprecipitation and Zr mobilised from the site of dissolution. There are very rare occasions where there is no light BSE zircon in grains that have altered to dark BSE zircon. This may be explained by the crystalline skeleton in moderately damaged zircon providing a medium for dark BSE zircon to precipitate on. It should also be considered that imaging of grains in thin-section only provides a 2-D view. In 3-D, apparently entirely dark BSE zircon may contain small crystalline areas on which dark BSE zircon nucleated.

3.10.2.3 Variation in microstructure

Since there are often several different populations of detrital zircons in sediments and sedimentary rocks, the U and Th contents and ages of zircon will vary considerably. As a function of the time the zircon has spent below its annealing temperature, this leads to significant variability in the behaviour of the zircon population coupled to a range of crystalline states (crystalline to fully metamict zircon).

The wide range in dark BSE zircon chemistry may suggest that the crystalline skeletal framework within metamict areas remains with only the amorphous volume going into solution. In zircon where radiation damage has just reached the 1st percolation point, the amorphous volume will be less in comparison to a heavily damaged zircon (i.e. beyond the 2nd percolation point). Zircon with a higher amorphous volume has a greater volume into which non-formula elements can be

concentrated than less damaged areas. However, while the degree of metamictization is likely to be the main control on the overall amounts of non-formula elements concentrated in dark BSE zircon, it is unlikely that metamictization dictates what non-formula elements are substituted into the zircon structure, i.e. different substitution trends between the chemistry individual zircons is more likely controlled by conditions in the local environment rather than the grain itself. It is also conceivable that the degree of metamictization will affect the microstructure of the recrystallised areas. Heavily damaged zircon may experience more rapid dissolution which may cause the fluid to become supersaturated in Zr faster. In such instances, the time between dissolution and precipitation is reduced, producing a microstructure that is less porous. However, as the U and Th contents of the zircons studied remains unknown, the decay dose cannot be determined and therefore these features cannot presently be correlated to the radiation damage. These features may also be dependent on other factors that are explored in Chapter 6.

3.10.2.4 Crystallinity

The textural evidence presented above suggests that dark BSE zircon formed as a result of dissolution-reprecipitation and this would appear to be well founded. However, low IQ EBSD patterns suggest that dark BSE zircon has a poor crystallinity and this contradicts the textural evidence. This is also the case for zircon outgrowths. The formation of new zircon crystals by precipitation should result in a high EBSD IQ and may also be expected to show an increase in CL intensity (e.g. Geisler et al., 2003a). Neither property is observed in dark BSE zircon.

Images show variable BSE intensity within dark BSE zircon whilst containing bright BSE (likely to be xenotime) and dark BSE (possibly quartz) inclusions only a few nm to tens of nm across. This indicates significant heterogeneity at the mesoscopic scale. Zircon outgrowths also display significant heterogeneity at the mesoscopic scale and have similar properties to dark BSE zircon. Zircon outgrowths can be spatially linked to dark BSE zircon in some grains and therefore their structure must be similar. TEM analysis of zircon outgrowths (Chapter 5) reveals that outgrowths are composed of multiple mis-orientated nanocrystalline zircon. It is therefore likely that dark BSE zircon shares a similar nanocrystalline structure. However the mis-orientation of nanocrystals is

key in this interpretation because this would act to significantly degrade the EBSD signal. Extremely finely nanocrystalline zircon may also be too small to give a reliable EBSD analysis using the SEM due to the diameter size of the electron beam (electron beam interaction area for EBSD is *c.*50nm (Humphreys, 2001)). Grain boundaries and the mis-orientation of these grains over the analysed area are also likely to suppress CL. Without the nanocrystalline structure, the formation of dark BSE zircon would act as an impermeable and insoluble barrier that prevents fluids from communicating with the alteration front. A nano-crystalline dark BSE zircon structure not only offers a possible explanation to both these analytical discrepancies but also provides a mechanism by which fluid can communicate with the alteration front. Furthermore, the grain boundaries within nanocrystalline dark BSE zircon may act as a sponge for fluids.

The retention of U and Th within dark BSE zircon (Fig.23c,24a) suggests that dark BSE zircon is likely to become metamict again. Therefore to attribute the low EBSD IQ pattern of all dark BSE zircon domains to nanocrystallinity would be wrong. It is therefore necessary to assess whether dark BSE zircon may become metamict again (i.e. amorphous volume reaches 1st percolation point) making it susceptible to subsequent alteration. To determine this the U and Th contents from zircon in Dalradian metasedimentary rocks used in provenances studies has been used (Nemchin and Cawood, 2005). These analyses came from ion probe points that are likely to give a rough approximation as to the actinide concentration in the zircons examined in this investigation. It should be noted that although a wide range of actinide concentrations were measured, they are probably not representative of the entire zircon population in the rocks analysed by Nemchin and Cawood (2005). This data came from analyses of zircon separates from a semipelite in the Ben Lawers Schist from the Argyll Group. However, it should be strongly emphasised that U and Th contents obtained by these authors may only represent the actinide concentration comparable to unmodified light BSE zircon and unlikely to be typical of dark BSE zircon. This is because dark BSE zircon represents domains that have become metamict and experienced alteration. Therefore they are likely to have higher U and Th concentrations than unmodified zircon. Consequently, U and Th contents from a group of Sri Lanken zircons have also been included (Nasdala et al., 2004). These zircons have been selected as they contain a range of radiation damage doses with a genesis

age comparable to the deposition age of the Dalradian rocks (570Ma compared to 800-470Ma respectively).

Table 7 displays the age at which a zircon of a given U and Th concentration will reach 1st percolation point (i.e. $D_{\alpha} = 3.5 \times 10^{18}$ from Salje et al. (1999)). This illustrates that particularly U- and Th- rich zircon may become metamict several times during the history of the rock and may be susceptible to multiple phases of alteration.

Zircon age (Ma)	U (ppm)	Th (ppm)	Notes
1063	869	197	Zircon 474-1A, Nemchin and Cawood, 2005
1570	541	191	Zircon 474-1B, Nemchin and Cawood, 2005
610	1558	471	Zircon 474-21A, Nemchin and Cawood, 2005
3210	204	97	Zircon 474-25B, Nemchin and Cawood, 2005
3785	158	42	Zircon 474-18, Nemchin and Cawood, 2005
493	1945	625	Sri Lanken zircon C27, Nasdala et al., 2004
319	3087	810	Sri Lanken zircon K6, Nasdala et al., 2004
188	5568	344	Sri Lanken zircon N17, Nasdala et al., 2004
940	1000	200	Theoretical
800	1200	200	Theoretical

Table 7 The age at which a zircon with a given actinide content will reach the 1st percolation point ($D_{\alpha} = 3.5 \times 10^{18}$ from Salje et al. (1999)).

3.10.2.5 Protection

Metamict zircon encased by unmodified light BSE zircon will remain protected from fluids during metamorphism. However, metamictization in zircon causes a volume swelling of amorphous areas upto 18% (e.g. Lee and Tromp, 1995; Ewing et al., 2003). If the stress from the swelling metamict growth layers is sufficient to break the surrounding light BSE zircon, a series of radial and concentric fractures are generated. These fractures provide pathways for fluids to communicate with metamict areas in the grain enabling them to become modified into dark BSE zircon. The growth of quartz, muscovite and chlorite along these fractures is common and evidence of fluid infiltration. The growth of these minerals can also result in the zircon becoming dispersed locally within the matrix (e.g. Fig. 9b).

Metamict zircon that is exposed to the fluid early in the rocks history will readily alter to dark BSE zircon during prograde metamorphism. However metamict zircon may be initially protected from fluids either as an inclusion in a larger grain (e.g. quartz) or encased by light BSE zircon. The metamict zircon will be exposed to the fluid if liberated from enclosing grain (i.e. the quartz grain recrystallises) or metamictization is sufficient to induce fracturing of the protecting light BSE zircon shell. Young (relative to the age of sediment deposition) U-rich zircon may also become metamict during prograde metamorphism. Metamict zircon in the above instances will probably alter to dark BSE zircon provided metamict areas have not annealed (i.e. the temperature of the rock is below 250°C). Alteration to dark BSE zircon may be enhanced due to the increased temperature at these which metamict zircon is exposed to the fluid.

Above 250°C (the annealing temperature for zircon), radiation-damage in zircon may begin to be repaired and any further alteration will decrease with the rate at which damaged zircon is annealed. Consequently, zircon either not metamict enough to alter (i.e. interconnection of amorphous clusters has not reached the 1st percolation point) or metamict zircon that is protected may become repaired whilst above the annealing temperature. During uplift and exhumation after peak metamorphism, radiation-damage will accumulate again in zircon once below 250°C once the rock is below the annealing temperature. However, the period of uplift and exhumation is unlikely to provide time for zircon to accumulate enough radiation damage to alter. Alteration during uplift and exhumation is therefore difficult in comparison to prograde metamorphism as radiation damage would be required to accumulate rapidly and would only be possible in a U-rich zircon. This is made more unlikely as most U-rich zircon would have altered to dark BSE zircon during prograde metamorphism, unless protected fluid phases. Penetrative deformation at higher grades may cause grains to be exposed to fluids that were previously protected and such instances may allow metamict zircon to alter in the retrograde cycle of the rock. Once the rock is exhumed, the temperature will be too low to alter metamict areas but damage will continue to accumulate. This indicates that a considerable amount of low temperature zircon in greenschist facies rocks probably formed during prograde metamorphism. The presence of hydrous species in dark BSE zircon formed during prograde metamorphism is an intriguing observation that is in contrast to most

reactions during prograde metamorphism.

If a rock experiences temperatures in excess of the annealing temperature of zircon, the majority of dark BSE zircon is likely to form during prograde metamorphism. If metamict zircon does not alter during this period, it is unlikely to develop dark BSE zircon during that metamorphic cycle. The various times at which dark BSE zircon may preferentially alter during metamorphism may provide an explanation as to the considerable variety in the microstructures that exists in dark BSE zircon. Furthermore, variations in chemical substitutions in dark BSE zircon may also reflect the multistage formation of dark BSE zircon during metamorphism.

3.10.2.6 Crushed and fragmented zircon

The mechanical strength of zircon is reduced by as much as 40% in its metamict state and is coupled to a 29% decrease in its elastic modulus (Chakoumakos et al., 1991). Therefore zircon grains with a metamict component are susceptible to breaking under tectonic stress (Fig.10). Crushed or fragmented zircons such as these are virtually absent from slates (Table 1) and found only in coarser-grained rocks. This is probably due to the larger grain size of matrix in quartzites and psammites which are likely to exert greater strain on individual zircons. It may also be a lithological constraint whereby a more homogeneous quartz matrix would cause more stress on zircons at grain boundaries than a rock with a more heterogeneous mineral assemblage. Typically the metamict component of the crushed zircon will alter to dark BSE zircon during this process, recrystallising around the light BSE zircon fragments (Fig.10b).

3.10.2.7 Shape of dark BSE zircon margins

In quartzites, dark BSE zircon is usually associated with anhedral bays that cross-cut internal zoning features of the zircon grain (e.g. Fig.9c). Light BSE zircon particles that have been broken off from zircons during metamorphism are often associated with dark BSE zircon and commonly have rounded grain edges. Embayments, now filled by matrix minerals, are likely to be the result of dissolution as are the rounded margins of the zircons in these rocks. Rounded margins to broken fragments of light BSE zircon are not observed in the other lithologies studied. Quartzites have

experienced slightly higher grade metamorphic conditions (upto 450°C) and the zircons in these rocks would appear to have undergone slight dissolution as a result. In contrast, the margins of dark BSE zircon in lower temperature slates, phyllites and psammities (c.300-350°C) are very irregular and have formed delicate intergrowths with the matrix.

3.10.3 Metamict zircon

Metamict zircon is thought to alter to dark BSE zircon during metamorphism upto the annealing temperature of zircon 250°C. However after the metamorphic event zircon will continue to accumulate radiation damage. Metamict light BSE zircon is produced and can be observed in EBSD scans (Fig. 33, 35). The dominant light BSE zircon exhibits moderate EBSD IQ patterns (green colour, Fig. 33), indicating it is partially metamict. The grain contains dark BSE zircon that probably developed as a result of being more metamict than the surrounding zircon during prograde metamorphism. Although the partially metamict light BSE zircon may have accumulated some damage during prograde metamorphism, it was insufficient for the zircon to alter. Therefore once the rock experienced temperatures above the zircon annealing temperature any damage in unaltered areas were repaired. However, once the rock reached temperatures below the zircon annealing temperature, damage could begin to accumulate again. This damage has continued to accumulate long after the rock has been tectonically active resulting in partially metamict zircon with only thin bands of crystalline zircon preserved.

Fully metamict zircon has been identified (Fig. 35). In this instance, small elongate cavities around the tips of fractures generated by the radiation damaged growth layer represent dissolution of the metamict zone. However, the metamict zircon layer remains chemically unmodified. This may indicate that metamict zircon can still be dissolved, perhaps even at ambient temperatures but without the production of dark BSE zircon.

As a general point, there would appear to be very little fully metamict zircon found around the margins of dark BSE zircon. This indicates that the dissolution-reprecipitation process is relatively efficient and is perhaps a relatively rapid process once initiated.

3.10.4 Porous zones in zircon

As pores in zircon are confined to particular growth zones in the grain, this feature must relate to the original composition of that zone. Radial fractures in the surrounding light BSE zircon are commonly associated with porous zones and most likely caused by the swelling of these porous zones. Dark BSE zircon is also found within porous growth zones where fractures are in communication with the edge of the grain (Fig. 13, 23c).

Porous zircon zones have a reduced CL intensity and lower EBSD IQ patterns than light BSE zircon. Furthermore they are also enriched in Fe and possibly Y but show no other chemical modification. Zircon with a high concentration of pores strongly correlates to low EBSD IQ patterns. However, care must be taken in attributing a reduced EBSD IQ pattern to a loss of crystallinity because EBSD analysis on a pitted surface (caused by pores) is likely to degrade the EBSD pattern. As a consequence, it is difficult to assess whether porous zircon zones with low EBSD IQ patterns actually represent a loss in crystallinity (i.e. partially metamict) or due to an increase in the size and concentration of the pores themselves. However, radial fractures spatially linked with porous zircon that is also in association with dark BSE zircon, make it likely that low EBSD IQ patterns are in part a result of radiation damage. This may suggest that the formation of porous zircon is another response to metamictization. The degradation of EBSD IQ is still likely to be exaggerated by the pitting on the polished surface of the zircon.

What the actual pores themselves represent is difficult to assess. The consistent enrichment of Fe in porous zircon and the association of features that strongly relate to metamictization possibly suggest some solid-state recrystallisation mechanism. However, the size of the microstructure of porous zircon is at the resolution limits of the SEM using conventional methods and analysis of these zones using higher resolution techniques is required to gain a better understanding of the composition and microstructure of porous zircon before any definitive conclusions can be reached.

3.10.5 Zircon and xenotime outgrowths

Zircon and xenotime outgrowths can be observed on the rounded margins of the host zircon and outgrowths cross-cut the internal zoning patterns of the host (Fig.14a). The delicate structure and minute size of zircon outgrowths indicate that they would be unable to survive sedimentary reworking. Similarly, the thin spines of xenotime that protrude between micas in the matrix would disintegrate during sedimentary processing. Zircon outgrowths are also observed on the edge of a broken zircon (Fig. 14c) indicating that zircon growth has post-dated the fracturing of the grain within the rock. Consequently zircon and xenotime outgrowths are thought to have a post-depositional origin. Since outgrowths contain inclusions of matrix minerals and project into and finger between muscovite and chlorite suggesting that zircon and xenotime growth, is contemporaneous with the growth of metamorphic minerals or more likely post-dates it.

3.10.5.1 Zircon outgrowths

The adjacent mineralogy has little obvious control on where zircon outgrowths nucleate and grow on the host grain based on textural observations. Phyllosilicates adjacent to the zircon may promote more new zircon growth than quartz (Fig. 15c) but many zircon outgrowths still form adjacent to quartz grains apparently in preference to other matrix minerals (Fig. 17). Similarly, the surrounding mineralogy has little influence on the shape of the zircon outgrowth. Euhedral zircon outgrowths are rare but have been observed adjacent to quartz as well as phyllosilicates. Zircon outgrowths also do not appear to have any preferred orientation or show any relationship to the cleavage in slates (either parallel or perpendicular to cleavage or in pressure shadows linked to the host zircon) (Fig. 16c) and neither do they form at any particular location on the host zircon.

Zircon outgrowths on the margins of some host zircons can be related to internally modified areas that display evidence of dissolution. However this is only observed in larger zircons where the protolith zircon can still be recognised (Fig. 6k, 13a, 14i). In these instances, modified areas are linked to zircon outgrowths through a series of metamict generated fractures in the light BSE part of the grain. These fractures provide pathways for fluids to mobilise Zr from the modified interior

to the outer edge of the grain with dark BSE zircon often observed in these fractures apparently sealing them. However, most zircon outgrowths are found on the margins of completely unmodified zircon and implies Zr is transported by fluids from zircon that has experienced dissolution elsewhere in the rock. No proximal link between these features has been identified i.e. unmodified zircon close proximity to a zircon experiencing dissolution often does not have zircon outgrowths, even if outgrowths are relatively abundant in the rock. Although the source of Zr is due to the dissolution of zircon elsewhere, the exact source is not entirely clear. However, the link between similar Hf contents of the host zircon to the zircon outgrowth may suggest a local source.

The preservation of very fragile zircon outgrowths that finger between matrix grains does suggest that they formed relatively late in the rock history as it is unlikely they will survive deformation at higher grades. This may indicate precipitation from fluids present in the rock that may become supersaturated with Zr as temperatures fall during the retrograde part of the metamorphic cycle. However it also possible that a very low temperature event, perhaps by shallow burial some time after metamorphism, allowed a small amount of Zr to be mobilised in the rock and zircon to crystallise. The most likely source of Zr in this instance is from dark BSE zircon which is shown to be the most U and Th of the zircon studied and hence, the most likely to become metamict again.

Care must be taken when analysing differences in the BSE intensity of zircon outgrowths as high BSE signal intensity on some of the outermost tips of zircon outgrowths may be due electron charging where the outgrowth does not have a smooth contact with the matrix (Fig. 15a&b,e). Therefore SE images should be taken of all grains studied to accompany BSE images. This means that these features can be quickly resolved assigning them to either the physical attributes of the zircon or due to electron charging from topographic variations in the thin section. In order to minimise any such charging effects it is recommended that all thin sections be given a final polish using colloidal silica.

3.10.5.2 Xenotime outgrowths

In the Ballachulish slates (samples BAL1a-d), where xenotime appears to be especially abundant as

outgrowths on zircon, upto three separate generations of xenotime can be identified within outgrowths. Xenotime outgrowths from samples other than Ballachulish typically display a homogeneous xenotime outgrowth when analysed in BSE imaging indicating only a single phase of growth.

In xenotime outgrowths from Ballachulish slate, numerous $<0.5\mu\text{m}$ spherical silicate inclusions (probably quartz based on its mean atomic number in BSE images) are concentrated throughout the first stage of xenotime growth and implies growth was relatively rapid. Despite xenotime being absent from quartzite rocks, medium to coarse-grained samples Dh4 and BAL3 contain xenotime outgrowths where inclusions are less common implying that the size of inclusions is controlled by the grain size of the matrix.

Inclusions in xenotime outgrowths are confined within an area marked by a very thin bright band implying a change in xenotime composition, presumably dictated by a change in fluid chemistry. The second part of the xenotime outgrowth is mostly inclusion free but the outer margins can be seen surrounding larger matrix grains. This suggests a change in the rate at which xenotime has grown or perhaps marks a point where matrix minerals have grown larger as a result of increased metamorphic grade or recrystallisation after deformation. The final phase of xenotime growth is defined by small ($<2\mu\text{m}$) xenotimes that grow on the outer margins of the second xenotime phase.

Phyllosilicates, and in particular muscovite, appear to promote xenotime growth more than quartz (Fig. 19e) with larger xenotime outgrowths more often found growing around and engulfing small ($<10\mu\text{m}$) quartz grains (Fig. 19d). Xenotime has been observed forming on the 4 opposing faces of a host zircon crystal instead of forming one smaller complete overgrowth and so the surrounding matrix plays no obvious role in controlling the location of outgrowths (e.g. Fig. 18i). In rocks where xenotime outgrowths are not as abundant (e.g. psammites), xenotime outgrowths are typically much larger where present and apparently crystallise on one particular host zircon in preference to numerous other potential zircons (Fig. 19h). This is possibly due to the relative mobility of Y and P in the fluid phase.

The xenotime outgrowths described here are analogous to those described by Rasmussen (2005a) where xenotime outgrowths were studied in rocks of a similar type and grade.

3.10.5.3 Interactions of zircon and xenotime outgrowths

Zircon outgrowths that form in xenotime deficient rocks (Easdale Slates and Dunoon Phyllites) are generally more homogeneous in BSE and do not exhibit the mottled BSE contrast of zircon outgrowths that have formed in rocks where xenotime is an abundant phase (compare Fig. 14j and Fig. 15a). The mottled BSE contrast in zircon outgrowths is produced because of a difference in mean atomic number and BSE intense areas in the zircon outgrowth have a similar BSE intensity to xenotime outgrowths. Furthermore, homogeneous zircon outgrowths produce low IQ EBSD patterns whereas xenotime outgrowths have high IQ EBSD patterns. Areas in zircon outgrowths with a mottled appearance in BSE produce intermediate IQ EBSD patterns indicating that there is probably a xenotime component within these parts of the outgrowth. This feature is analysed in greater detail in chapter 5.

Dark BSE zircon is occasionally observed between the boundary of the unmodified host zircon and the outgrowing xenotime (Fig. 15d) indicating that Zr was mobile before at least the final phase of xenotime growth.

3.10.6 Xenotime and dark BSE zircon

Xenotime is found as spherical to irregular elongate shaped inclusions within the cavities and holes of dark BSE zircon and also observed sealing fractures in zircon. Unmodified light BSE zircon is completely free of xenotime implying that some xenotime precipitates from fluids that are also responsible for the alteration of the dark BSE areas. However, the production of porosity in dark BSE zircon may imply that in some xenotime is present as a later pore filling phase that is not synchronous with the formation of dark BSE zircon.

Xenotime outgrowths mostly form on the edge of light BSE zircon grains but on rare occasions are

also found on margins of dark BSE zircon. Even when xenotime is found on dark BSE margins, it typically grows on the most BSE intense part of the zircon (Fig. 18d). This is probably due to xenotime requiring a relatively similar crystalline host. A zircon structure containing non-formula elements may not be as favourable for xenotime growth as unmodified crystalline light BSE zircon.

3.10.7 Linking zircon features and behaviour

Dark BSE zircon occasionally lacks cavities and this suggests that fluids can cause metamict areas to recrystallise in-situ with little or no Zr lost from the grain (e.g. Fig. 6m). However, cavities present in dark BSE zircon can usually be associated with zircon outgrowths on the unmodified light BSE margins of the grain. In some cases this would appear to be a relatively balanced process i.e. volume of zircon outgrowths equals the volume lost in cavities (Fig. 6k&14i). Metamict generated fractures that provides communication between these features in the zircon are apparently sealed by dark BSE zircon (Fig. 13a&14i). This is further evidence that Zr can be mobilised in localised environment from the modified interior to the outer margin of the grain through a series of metamict generated fractures. Where cavities are abundant in dark BSE zircon but have no outgrowths on the margins (Fig.9), it implies that Zr taken into solution has been mobilised from the grain. Porous bands in zircon also appear to have an intimate relationship to dark BSE zircon.

3.10.8 U, Th and Pb concentration in low temperature zircon

Despite not analysing U, Th and Pb due to a lack of suitable standards, some general comments can still be made about the likely concentration of these elements in dark BSE zircon and zircon outgrowths. The benefit of this is that one can attempt to assess the usefulness of low-temperature zircon with respect to future analytical work. Experiments on the hydrothermal alteration of metamict zircon consistently reveal altered areas have undergone substantial Pb loss (Geisler et al., 2003a) and it likely that dark BSE zircon has experienced similar Pb loss. However, while some studies have been found altered areas to be depleted in U and Th with respect to unaltered zircon (Geisler et al., 2003b), other studies have witnessed no such change in U and Th, and in some

instances, altered areas are even slightly enriched from the starting material (Utsunomiya et al., 2007). EDX scans of dark BSE zircon in the rocks studied here consistently show a higher U content in comparison to the rest of the unmodified grain. Although dark BSE zircon formed from metamict zircon, its retention of U within the structure means that dark BSE zircon is the most likely to become metamict again.

Actinide concentration in zircon outgrowths is likely to be very low as xenotime outgrowths will act as a sink for U and Th. A low U and Th content in zircon outgrowths is made all the more probable by the fact that little U and Th is liberated during the alteration of metamict zircon to dark BSE zircon. Xenotime outgrowths may potentially cause localised radiation damage within the host zircon or zircon outgrowths due to He particle trajectory from α -decay events in the xenotime (Nasdala et al., 2005). If the decay dose in xenotime is sufficiently high to cause extensive alpha particle damage in the zircon (host or outgrowth), the damaged zircon may alter or Zr may be mobilised in a fluid phase.

3.11 Summary

Zircon has a wide and varied response to low temperature greenschist facies metamorphic events as a consequence of radiation damage that accumulates in actinide-bearing zircon. The key findings from this chapter are:

- The formation of dark BSE zircon via a dissolution-reprecipitation process
- Zr is mobilised from zircon that has experienced dissolution and precipitated as outgrowths on the margins of unmodified zircons
- Metamict zircon has a self-inducing fracture mechanism which allows fluids to access these domains which catalyses the above processes.
- Porous zircon appears to be intimately linked to dark BSE zircon as they are both found in the same growth zones in zircon and porous zircon may therefore be another response to metamictization.

- Xenotime has an intimate relationship with low-temperature zircon.
- The chemistry of dark BSE zircon varies between individual grains possibly as a result of the local environment in which they formed.
- Dark BSE zircon and zircon outgrowths have different substitution relationships, particularly with respect to Si.

However, outstanding questions remain. When during the metamorphic cycle do the processes of dissolution, reprecipitation and new growth initiate? Chapter 4 sets out to determine this, investigating the behaviour of zircon in diagenetically altered sedimentary rocks. Other important questions are what is the microstructure of zircon outgrowths and dark BSE zircon and is the low IQ EBSD pattern from these textures a function of their microstructure? Chapter 5 seeks to address these issues by studying the microstructure of zircon outgrowths at the sub-micron level using high-resolution techniques.

The unstable nature of radiation damaged zircon in low temperature rocks and the abundance low temperature zircon features have consequences for reliable age dating of whole grains. Misinterpretation of dissolution-reprecipitation features may lead to false ages of events. Understanding the processes that produce these features is essential for the reliable and correct interpretation of U-Pb ages in zircon. However, dating zircon outgrowths and dark BSE zircon ages may provide information on timing of fluid flow events during metamorphism. The dissolution of radiation damaged zircon by low temperature fluids is also a concern for the safe storage of nuclear waste.

4

Zircon and xenotime behaviour during diagenesis

4.1 Introduction

Investigations of zircon in greenschist facies metasediments reveal an abundance of in-situ low temperature secondary features with detrital zircon in slates preserving zircon outgrowths on their margins (Chapter 3). However it remains unclear when the processes that form these features initiate. The principle aim of this chapter is to therefore resolve this question by studying the behaviour of zircon in sedimentary rocks.

This chapter identifies abundant dark BSE zircon within zircon in these rocks. The majority of such textures are identified to form via dissolution-reprecipitation reactions (Group 1 dark BSE zircon). However evidence for a diffusion-driven structural recovery cation exchange process is also observed (Group 2 dark BSE zircon). Sub-micron sized zircon outgrowths are observed on the margins of detrital zircon as are larger xenotime outgrowths. Occurrences of zircon outgrowth are rare however, indicating Zr is not mobilised on the same scale as it is in greenschist facies metasediments. Still, these findings provide compelling evidence that, as a consequence of radiation damage, processes of zircon alteration, dissolution and precipitation are well established at temperatures $<100^{\circ}\text{C}$ and Zr may also be mobilised.

4.2 Methods, regional setting and samples

The characterisation of the textures and microstructures found in zircon and xenotime from diagenetically altered sedimentary rocks has been achieved using BSE, SE and CL imaging techniques. Zircon has also been chemically analysed using EPMA and SEM EDX. Crystallographic properties of zircon have been determined using EBSD. These techniques have been applied to establish the textural, microstructural, chemical and crystallographic properties of zircon and xenotime in sedimentary rocks so that a comparison can be made between with those in greenschist facies metasediments described in Chapter 3. Many of the textures and microstructures described in this chapter are similar to those in Chapter 3.

Rock samples were collected from the South East of Fife in Scotland, along a coastal section located between Kirkcaldy and Leven (Lower Largo) (Fig.45). Here, an almost continuous sequence of upper Carboniferous sedimentary rocks are interbedded with occasional tuffaceous horizons and basaltic lavas (Read et al., 2002). Volcanic vents, which are interspersed throughout the region, are further evidence of late Carboniferous igneous activity. These rocks provide an ideal natural laboratory for studying zircon behaviour as they have been extensively characterised due to coal and oil-bearing units found throughout this area. This includes vitrinite reflectance work that allows the maximum temperature these rocks experienced to be determined. The outcrop of strata along the Fife coastline also represent a wide variety of lithologies which are exposed as an almost continuous sequence allowing easy sampling and a broad selection of rock types to be collected the stratigraphy to be easily determined. Perhaps most importantly, this area was chosen for sampling as rocks from the Millstone Grit series outcrops here. The equivalent unit in Yorkshire, England has been shown to contain zircons with large and abundant xenotime outgrowths, projecting out upto 100 μ m, (Butterfield, 1936; Rasmussen, 2005b) and Zr mobilisation has also been postulated.

Vitrinite reflectance work has been carried out on borehole samples of Carboniferous age from many points around the Fife and Lothian area (Raymond and Murchison, 1991). The purpose of this work was to observe the effects exinitic macerals have on vitritine reflectance and, among other boreholes studied, this was conducted on samples from two boreholes located in the Firth of

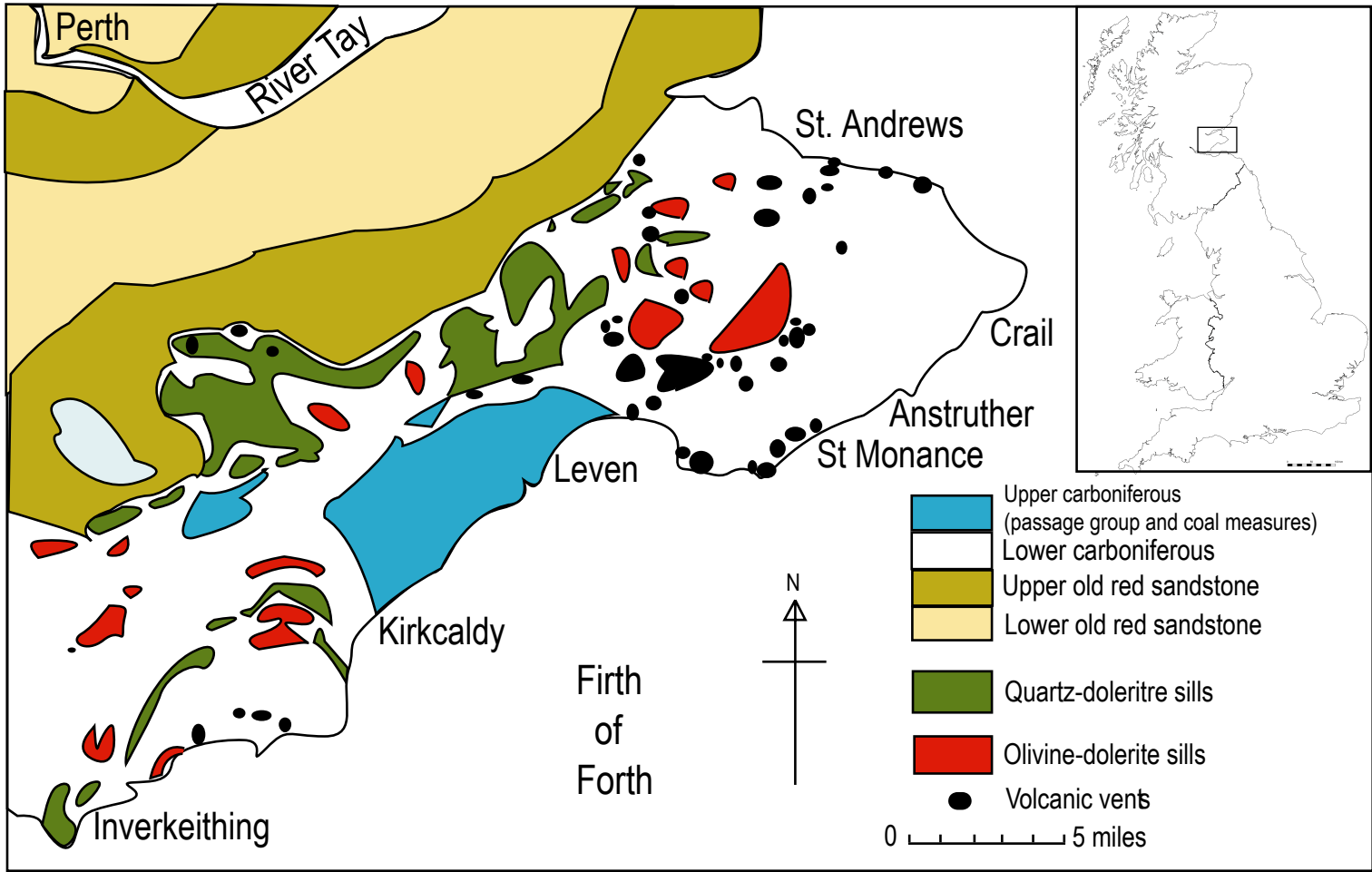


Figure 45 Geological map of the Fife area.

Forth (grid reference of boreholes is not stated), approximately 5km south from where the samples were collected for this study. The boreholes (Firth of Forth Tower Borehole No.1 and No.2) pass through several units including the Upper Limestone Group. Vitrinite reflectance data from this unit indicate a value 0.70 – 0.80 %R_v which Raymond and Murchison (1991) interpret to represent a maximum temperature around 95°C based on work by Murchison et al. (1985). These vitrinite reflectance values for the Upper Limestone Group are also replicated from other boreholes the around the Fife and Lothian area (Raymond and Murchison, 1991). This indicates that the maximum temperature for diagenesis is also around 95°C which significantly below the annealing temperature for zircon (250°C) (Nasdala et al., 2004). This means that no metamict zircon in the rocks studied in this chapter can have undergone annealing by temperature alone.

Two sets of samples were collected and made into thin sections. The first sample set, prefix KULM, was collected from a sedimentary sequence in the Upper Limestone Group that outcrop along the Kirkcaldy beach beside the castle in Ravenscraig Park (Grid Ref. NT 291 923 to NT 301 926). A siltstone (KULM2) and four quartz arenites (KULM1, KULM3, KULM4 and KULM5), varying from very fine (30µm, KULM1) to coarse grained (200µm, KULM5) were sampled. All have been cemented by micrite and occasionally thin discontinuous bands (*c.*1mm long) of organic-rich matter are also preserved. Most samples contain banding defined by muddier layers with 100-200µm illite and chlorite grains present. Quartz is typically recrystallised and found as both monocrystalline and polycrystalline. Only occasional feldspar grains are also present. For detailed thin section descriptions see Appendix C. The second sample set, prefix LmillG, was collected on the coastal section at Lower Largo, Leven (Grid Ref. NO 437 021) and are also rocks from the Upper Limestone Group. The rocks range from fine (50 µm) to very coarse grained (1mm) quartz arenites with a micritic cement. An organic-rich micritic limestone (LmillG2) was also sampled but zircon was absent from this rock. No original porosity is present in any of the rocks. A brief summary of thin section characteristics is given in Table 8.

Sample	Rock type and grain size	Total no. of zircons per section*	Zircon size distribution	Completely unmodified zircon	Fragmented zircon	Dark BSE zircon	%age of zircon with zircon outgrowths	%age of zircon with xenotime outgrowths
K-ULM-1	Quartz arenite, <i>c.</i> 100 μ m	1040	10-50 μ m, $A_v = 20\mu$ m	38%	4%	58%	15%	0%
K-ULM-2	Siltstone <30 μ m	533	<5-30 μ m, $A_v = 20\mu$ m	31%	8%	61%	0%	7%
K-ULM-3	Quartz arenite, <i>c.</i> 50- 100 μ m	297	5-50 μ m, $A_v = 20\mu$ m	36%	0%	64%	9%	0%
K-ULM-4	Quartz arenite, <i>c.</i> 50-100 μ m	442	5-100 μ m, $A_v = 25\mu$ m	46%	8%	46%	0%	15%
K-ULM-5	Quartz arenite, <i>c.</i> 500 μ m	102	20-200 μ m, $A_v = 20\mu$ m	67%	33%	0%	0%	0%
L-MILLG-1	Quartz arenite, <i>c.</i> 0.5-1mm	192	10-200 μ m, $A_v = 30\mu$ m	67%	33%	0%	0%	0%
L-MILLG-2	Marl, <5 μ m	Absent	-	-	-	-	-	-
L-MILLG-3	Quartz arenite, <i>c.</i> 100-200 μ m	504	20-100 μ m, $A_v = 50\mu$ m	79%	14%	7%	0%	0%
L-MILLG-4	Quartz arenite, <i>c.</i> 0.1-1mm	540	10-100 μ m, $A_v=40\mu$ m	60%	0%	40%	0%	0%
Average:				53.0%	12.5%	34.5%	3%	3%

Table 8 Rock types and associated zircon textures in sedimentary rocks. *number has been calculated (see 2.5)

4.3 General zircon distribution and character

Thin section examination shows that zircon is generally distributed evenly throughout finer grained layers but is concentrated in heavy mineral bands within coarser grained quartz arenites. A typical thin section contains *c.*400 zircons although this varies from as little as *c.*100 grains per thin section to as many as *c.*1000. Finer grained rocks contain more but smaller (5-30 μ m) zircon than coarser grained samples. A large proportion of zircons in the finer grained quartz arenites are fragments of previously larger grains as indicated by their sharp, angular grain edges (Fig. 46). A significant proportion of well-rounded zircon is also observed. In coarser grained rocks, zircons are less numerous but are larger (20 – 60 μ m). They vary in shape from subhedral to well-rounded and many of these zircons are fractured. Whilst a few zircons are homogeneous in BSE, most show some weak simple or sector zoning or more complex oscillatory or concentric zoning (Fig. 46). Virtually all zircon in these rocks is considered to have undergone a degree of sedimentary reworking before incorporation into the rock.

The relative proportions of zircon textures and microstructures found in individual samples are presented in Table 8, with values displayed as percentage by number of grains. Fine-grained rocks contain a significantly larger percentage of zircons with a low BSE intensity areas or zones, termed dark BSE zircon. As such, these rocks have a much smaller percentage of completely unmodified zircon. Rocks with a large percentage of dark BSE zircon generally contain some zircons (unmodified or dark BSE zircon) with zircon or xenotime outgrowths on their margin. However, zircon and xenotime outgrowths on zircon are mutually exclusive. Coarse-grained rocks contain the highest percentage of unmodified zircon but also a greater proportion of fractured or fragmented zircons. However, dark BSE zircon was absent from the zircon population in 2 of the 11 rocks. These samples showed no discernable difference in lithology, grain size of the rock or zircon grain size to those containing dark BSE zircon.

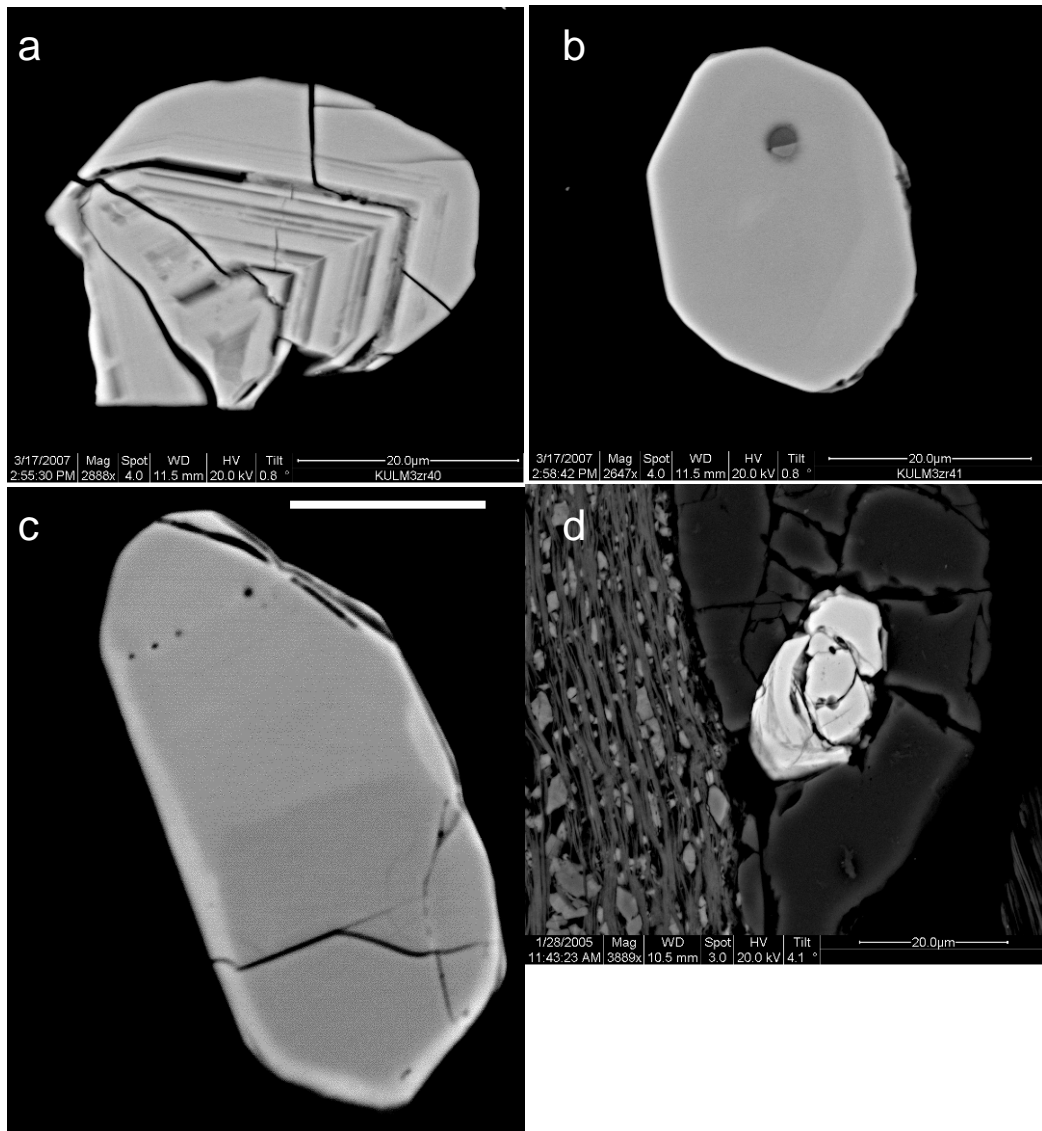


Figure 46 BSE images of zircon in sandstone

- a** Zircon fragment with some rounded margins. Internal concentric euhedral zoning (KULM3). **b** Sub-euhedral zircon with weak BSE zoning and round apatite inclusion(KULM3). **c** Simply zoned zircon with sub-euhedral margins and slight cracking. Scale bar = 20µm, BSE image from Cambridge SEM (KULM3). **d** Cracked zircon as an inclusion in cracked quartz grain (KULM4).

4.4 Dark BSE zircon

Dark BSE zircon is found in the majority of the polished rock sections studied, averaging *c.*35% of the zircons in the rock, and above 60% in some samples (Table 8). However, dark BSE zircon in chapter 3 has been broadly generalised as a single population. On the studying the dark BSE zircon in sedimentary rocks it is apparent that the microstructure of dark BSE zircon can be divided into two groups. Group 1 dark BSE zircon is characterised internally by holes, cavities and inclusions, sometimes in great abundance and by irregular-shaped margins where in contact with the matrix (Fig. 47 & 48). It is Group 1 dark BSE zircon that almost completely dominates the dark BSE zircon in the greenschist facie metasedimentary rocks. By contrast, Group 2 dark BSE zircon shows almost perfect preservation of the shape of the parent detrital grain, regardless of whether Group 2 dark BSE zircon is in contact with the matrix. Group 2 dark BSE zircon is defined by an absence of holes, cavities and inclusions (Fig. 52). In the sedimentary rocks studied, Group 1 dark BSE zircon is the more abundant than Group 2 dark BSE zircon in a ratio of about 4:1. Although uncommon, Group 1 and Group 2 dark BSE zircon can both be found in the same grain (Fig. 47j&k). In these instances, Group 2 dark BSE zircon forms a boundary with Group 1 dark BSE zircon parallel to light BSE zircon zoning.

4.4.1 Group 1 dark BSE zircon

Group 1 dark BSE zircon is often observed in concentric rings within zircon that is parallel to light BSE zircon zoning but is also found in larger irregular domains or within the core of the zircon (Fig. 47). Group 1 dark BSE zircon usually forms an abrupt and well-defined boundary with light BSE zircon (Fig. 47a-h) although the boundary is not always parallel to the zoning of light BSE zircon within the grain (Fig. 47i, 47k, 48a).

Light BSE zircon is frequently preserved in Group 1 dark BSE zircon in variety of microstructures. Thin shards, laths or bands of light BSE zircon are found in Group 1 dark BSE zircon that replicate the zoning structure in the adjacent light BSE zircon (Fig. 47c, 47d, 47h). Where light BSE zircon fails to match the zoning structure of the surrounding light BSE zircon, it is usually present as lobes

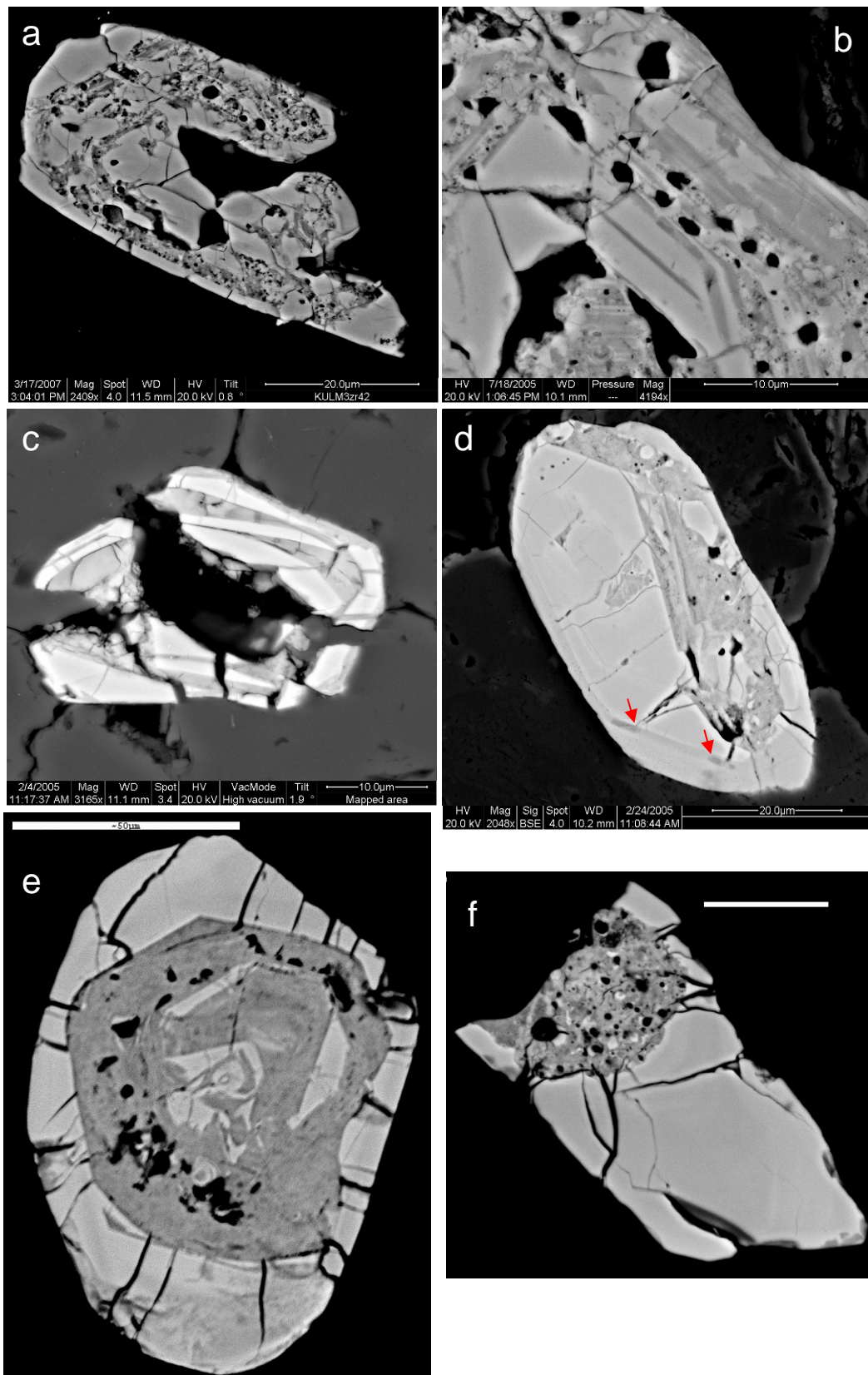
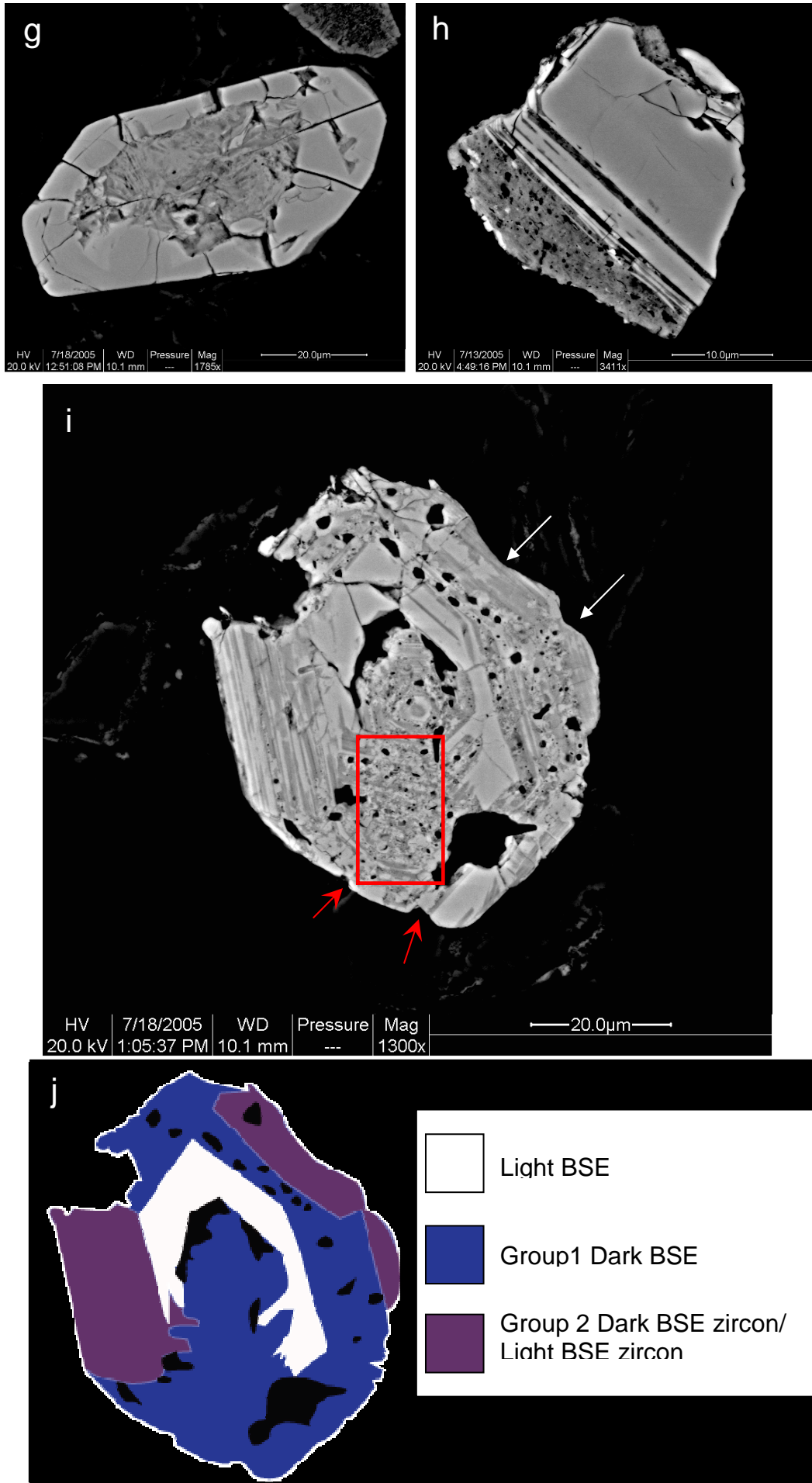


Figure 47 Images of the varying microstructure of dark BSE zircon. Caption on page 162.



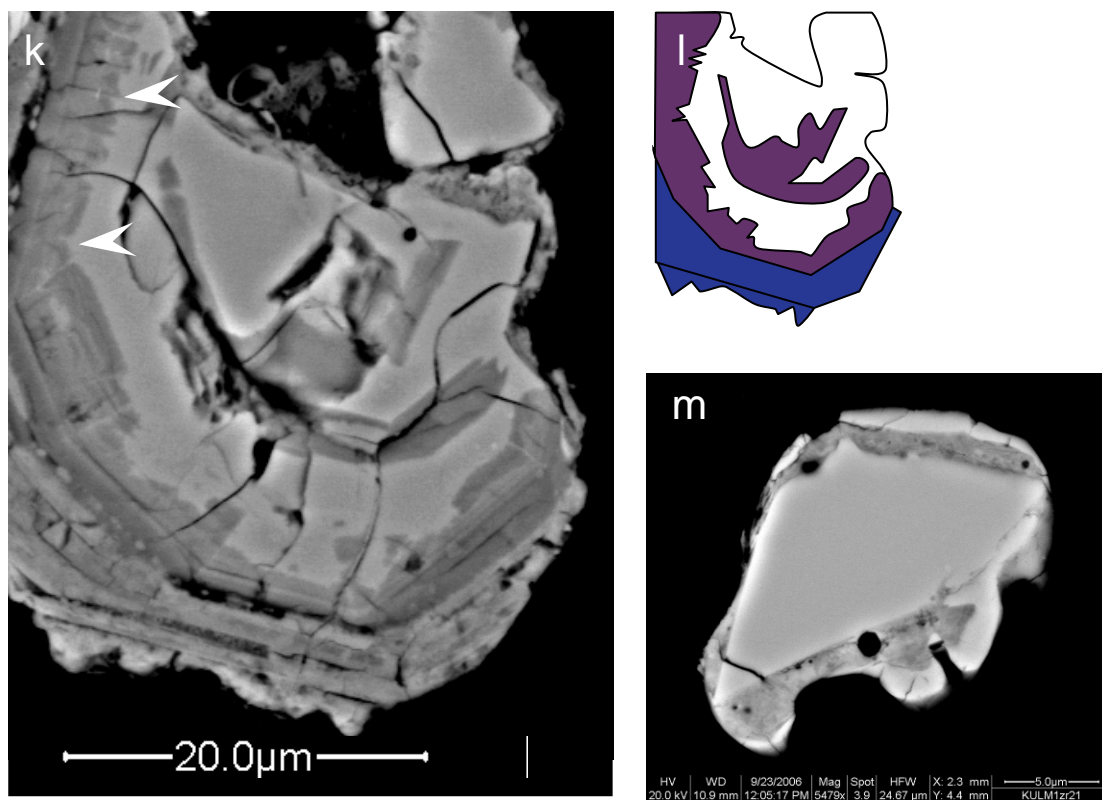


Figure 47cont. Caption on following page.

Figure 47 Images of the varying microstructure of dark BSE zircon

All images are BSE unless stated otherwise **a** Zircon with group 1 dark BSE zircon confined mainly to euhedral zoning. Margins have large embayments (KULM3). **b** Group 1 and 2 dark BSE zircon within euhedral zones (KULM3), higher magnification area in image of **i**. **c** Fragmented zircon with laths of light BSE zircon in dark BSE zircon domains (KULM4). **d** Well-defined light BSE zircon zones with group 1 dark BSE zircon domain. Red arrows point to group 1 dark BSE zircon at the fracture tip within a porous zone. (KULM3). **e** Sub-euhedral shaped zircon with outer light BSE zircon layer displaying radial fractures. Group 1 dark BSE zircon core with irregular cavities and contorted light BSE zircon in the centre. Light BSE zircon in dark BSE zircon further from the centre, repeats zoning with outer light BSE zircon (L-millG3). **f** Zircon fragment with radial fractured outer light BSE zircon layer and group 1 dark BSE zircon core (KULM4). Scale bar = 20µm. **g** Sub-euhedral shaped zircon with dark BSE core and outer radially fractured light BSE zircon. Dark BSE core preserves small light BSE domains (KULM3). **h** Zircon fragment with dark BSE zircon outer domain. Small xenotime inclusions are within and form on the margin of dark BSE zircon (KULM1). **i** Sub-rounded zircon contain group 1 and 2 dark BSE zircon. Area defined in white box is shown in **b**. Red box shows light-dark BSE zircon complex. Red arrows point to notches in the margin and white arrows point to smoothed undulations (KULM3). **j** Schematic drawing of textures present in **i**. **k** Sub-euhedral zircon with inward penetrating alteration front. Light and dark BSE zircon display a boundary roughly parallel to euhedral zoning punctuated by v-shaped clefts (white arrow). Group 1 Dark BSE zircon at the bottom of the image has formed outgrowth features (KULM1). **l** Schematic drawing of textures present in **k**. **m** Dark BSE zircon outer layer surrounding light BSE zircon core. Segment light BSE zircon rim surrounds dark BSE zircon (KULM1).

or contorted bands in Group 1 dark BSE zircon domains (Fig. 47d, 47e, 47g) and in some instances light BSE zircon is displaced by Group 1 dark BSE zircon (Fig. 47e). More occasionally, light and dark BSE zircon form a mosaic-like microstructure of sub-angular to rounded light BSE zircon domains set in a matrix of dark BSE zircon or cross-cut by thin ($<0.1\mu\text{m}$) dark BSE veins (Fig. 48a). In such grains, light and dark BSE zircon has a poorly structured relationship that does not follow any obvious zoning patterns. Furthermore, complexes of dark-light BSE zircon, where concentric euhedral zoning in light BSE zircon has been disrupted, give rise to a mottled BSE contrast (Fig. 47i, red box). This occurs particularly when Group 1 and Group 2 dark BSE zircon are present in the same grain.

Group 1 dark BSE zircon confined within light BSE zircon is usually associated with radial fractures in the outer light BSE zircon (Fig. 47e-g). These fractures are orientated roughly perpendicular to and extend from the dark-light BSE zircon interface through light BSE zircon to grain margin. Occasional concentric fractures are also noted along this interface. Where the fracture is in communication with the grain edge, small cavities have been observed at the fracture tip in dark BSE zircon (Fig. 47e).

Some zircon grains are composed predominantly of Group 1 dark BSE zircon with little or no light BSE zircon (Fig. 48). Zircon dominated by dark BSE often has small thin ($<2\mu\text{m}$) blocks or segmented crusts of homogeneous, light BSE zircon around the margin of the grain (Fig. 48, blue arrows). Segmented crusts have been examined in SE and this confirms that the effect is not due to charging (Fig. 48d). Although most commonly found on zircon composed predominantly of dark BSE zircon, segmented crusts may also appear on thin bands of Group 1 dark BSE zircon where it surrounds light BSE zircon (Fig. 47m).

The margins of Group 1 dark BSE zircon vary considerably in shape where they border the matrix (Fig. 47, 48, 49). Overall most margins are smooth but at higher magnification are very irregular and punctuated by rounded shallow (upto $3\mu\text{m}$ deep) notches (Fig. 47f, 47i, 47m, 48a, 48d) or deeper ($>3\mu\text{m}$) inward penetrating channels. These features are associated with irregular shaped

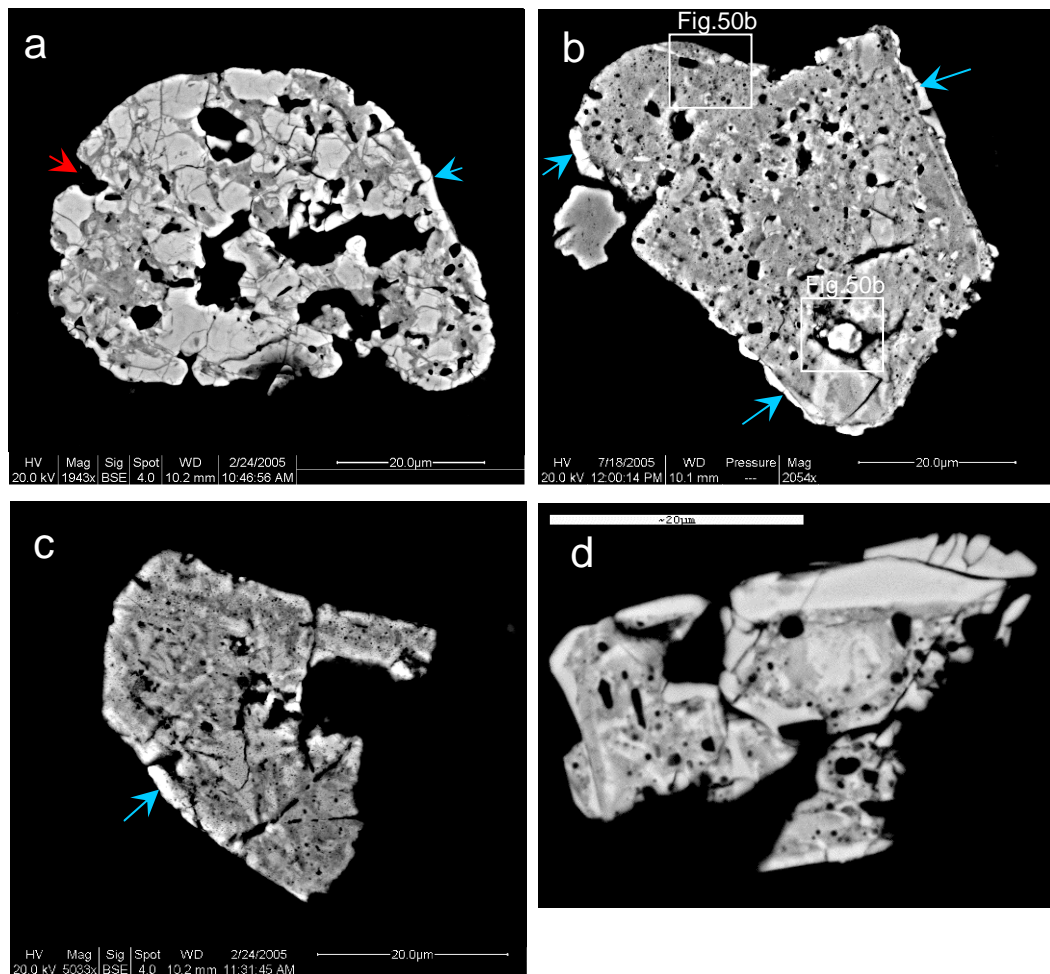


Figure 48 Grains containing predominantly dark BSE zircon

a Mosaic zircon containing light BSE zircon blocks within a dark BSE zircon matrix. Margins have notches (red arrow) and large embayments with large internal cavities and inclusions. Blue arrow points to light BSE zircon rim (KULM3). **b** Almost entirely group 1 dark BSE zircon with significant internal heterogeneity. Blue arrow points to segmented light BSE zircon crust. Areas defined in boxes correspond to areas enlarged in the stated figures (KULM3). **c** Almost entirely group 1 dark BSE zircon internal discontinuities. Blue arrow points to light BSE zircon crust (KULM3). **d** Group 1 dark BSE zircon with heavily embayed margins and light BSE zircon crust. Scale bar = 20 μ m, (KULM3).

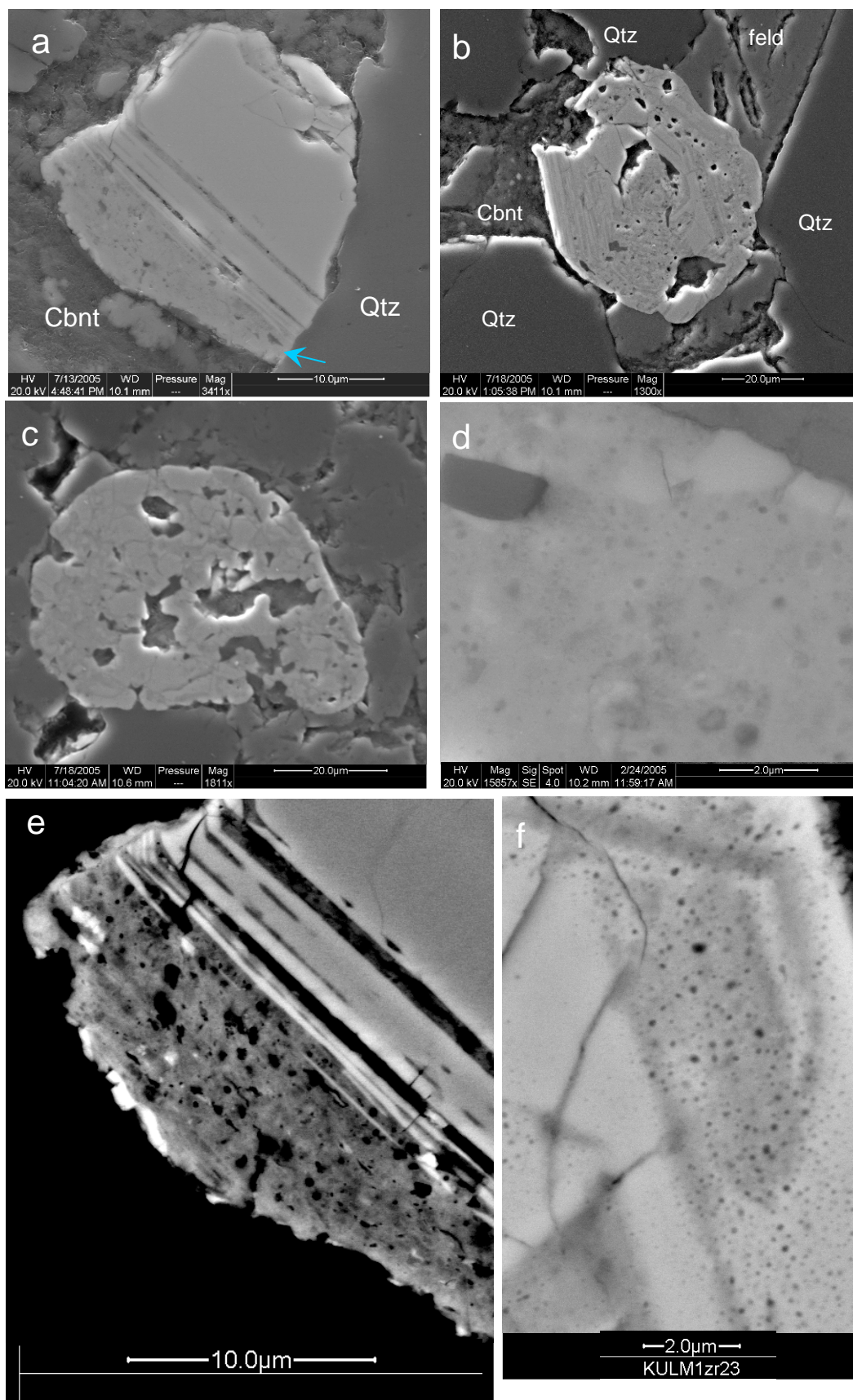


Figure 49. Caption on the following page.

Figure 49 Images of zircon containing dark BSE zircon with porous, cavities and inclusions in their microstructure.

a SE image of Fig.47h. Dark BSE zircon forms irregular margins with carbonate cement (cbnt) but smoothed margins with quartz (qtz, arrow) (KULM3). **b** SE image of Fig. 47i. Grain exhibits internal cavities and inclusions (KULM3). Cavities may represent grains that have been plucked during polishing. **c** SE image of Fig.48a which displays large matrix-filled inclusions with the grain (KULM3). **d** SE image of blebed microstructure in area defined in Fig. 48b. Inclusion is of quartz. Also note homogeneous blocks of zircon on the rim. **e** Enlarged BSE image of Fig. 47h showing complex microstructure of group 1 dark BSE zircon. Irregular and spherical shaped holes and inclusions dominate the microstructure as do vein-like features. Small inclusions of high BSE intensity xenotime can also be seen (KULM3). **f** BSE image of pores within well-defined zone in zircon (KULM1).

holes and channels that extend into the interior from the margins of the grain (Fig. 47a, 47i, 48). The margins of these channels inside the zircon are also highly irregular with $<1\mu\text{m}$ deep notches and clefts yet have an overall rounded and smoothed appearance (Fig. 48a, 48d). Channels have been filled by matrix minerals, mostly carbonate and clay (Fig. 49). Despite these disruptions to the grain microstructure the original outline of the parent zircon is still recognisable in all cases, even grains dominated by Group 1 dark BSE zircon. Group 1 dark BSE zircon is also occasionally found as sub-euhedral outgrowth-like features where in contact with the matrix (Fig. 47k).

4.4.1.1 Internal features and macrostructure of Group 1 dark BSE zircon.

On a macroscopic scale, Group 1 dark BSE zircon can contain an abundance of $0.3\text{-}3\mu\text{m}$ holes and inclusions (Fig. 47,48,49). These occur as well- to poorly- shaped spheres (Fig. 47a-f, 48b-d, 49a-e) but may also form highly irregular shaped inclusions (Fig. 47a, 47e, 47f, 48b, 49b, 49c, 49e). The latter include very thin and elongate vein-like features that are aligned parallel to light BSE zircon zoning (Fig. 49e). Only the composition of larger inclusions ($>2\mu\text{m}$) can be determined and show they are often comprised of material similar to the surrounding matrix. High BSE intensity xenotime inclusions are observed in Group 1 dark BSE zircon (Fig. 49e) and range from minute specs ($<30\text{nm}$) to $c.1\mu\text{m}$ long. Matrix-filled cavities within the zircon macrostructure can be large ($3\text{-}12\mu\text{m}$ long), uneven in shape and slightly rounded margins (Fig. 48, 49).

High magnification BSE and SE images reveal the mesostructure of Group 1 dark BSE zircon to be exceedingly intricate (Fig. 49d-f & 50). Group 1 dark BSE zircon often has a mottled appearance in BSE caused by irregular patches of slightly varying BSE contrast. Dark spherical blebs ($<50\text{-}300\text{nm}$) are often prevalent in Group 1 dark BSE zircon and some display a slightly brighter BSE ring around them (Fig.50a). These brighter rings are not observed in SE imaging and are therefore not caused by charging although it remains inconclusive as to whether the dark areas represent mineral inclusions, nano-sized voids or zircon of a different composition. High magnification ($c. \times 12000$) BSE images of the edges of topographically depressed areas in Group 1 dark BSE zircon exposes an intricate and elaborate cross cutting network of slightly darker BSE nanometre-thin veinlets (Fig. 50b).

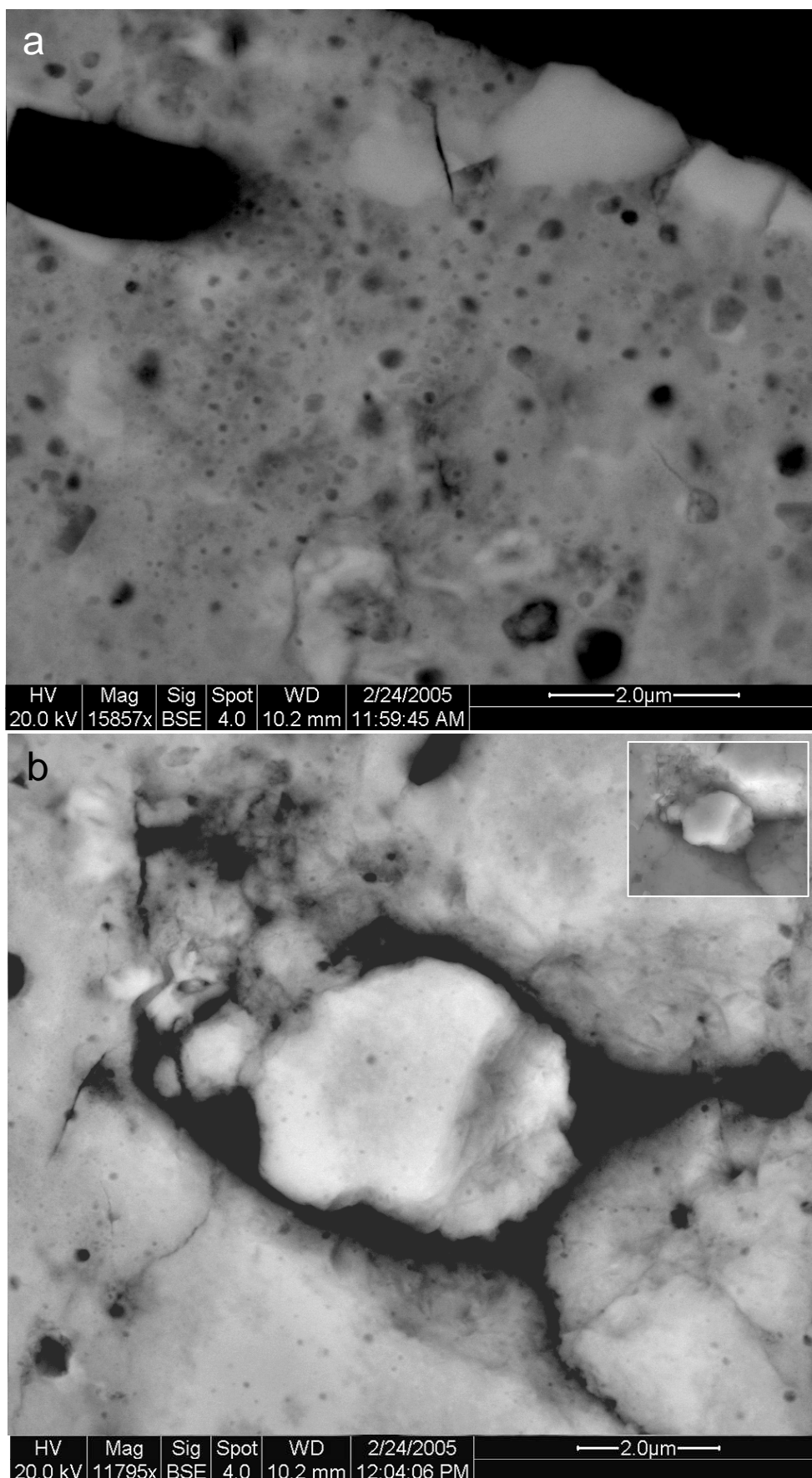


Figure 50 Caption on next page.

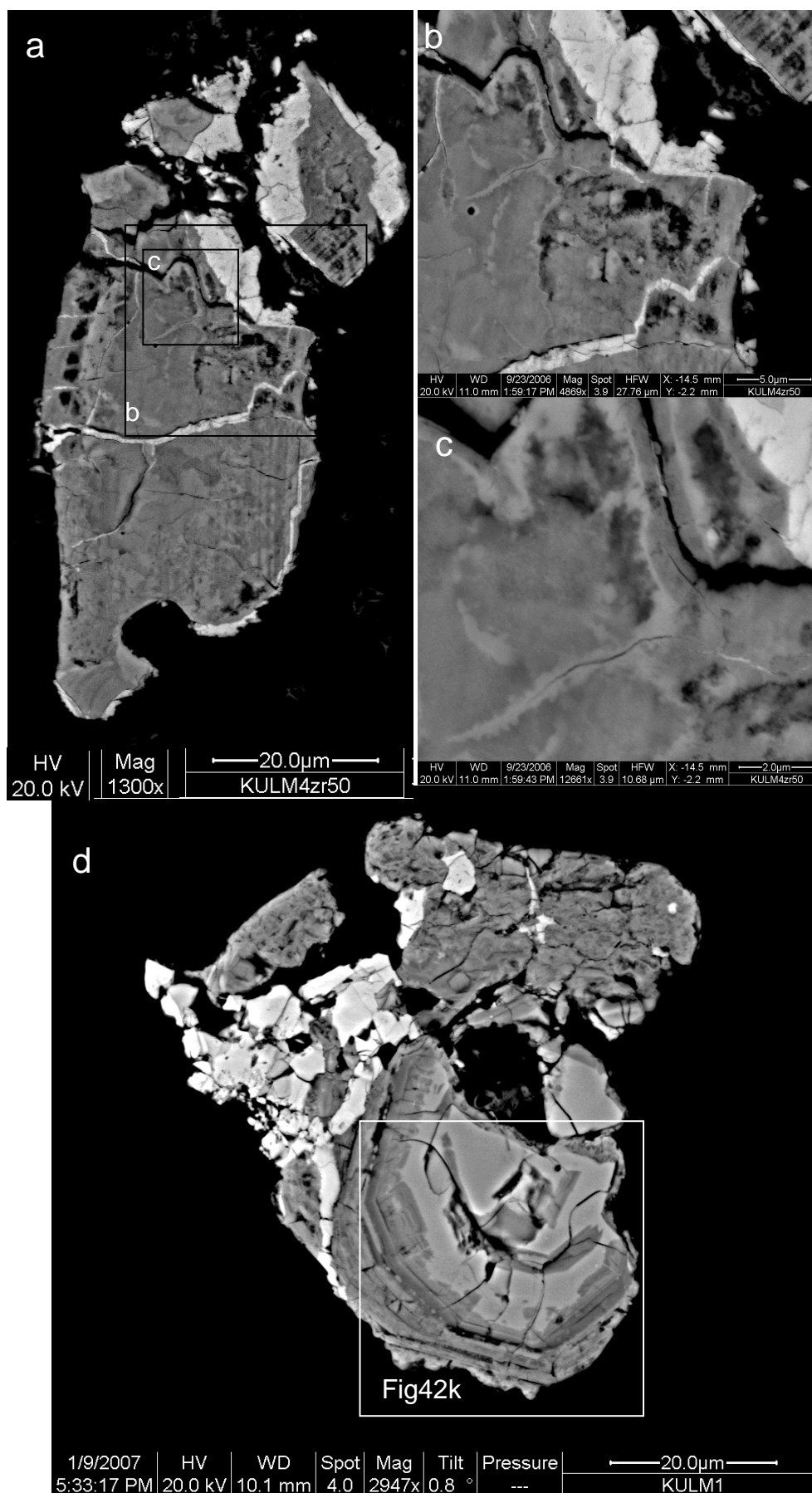


Figure 51 BSE images of dark BSE zircon cemented by xenotime. Caption on following page.

Figure 50 High magnification images of porous microstructure in dark BSE zircon for images on page 167

Areas of images are defined in Fig.48b. **a** SE image showing complex microstructure of group 1 dark BSE zircon. **b** BSE image showing intricate microstructure. SE image is inset.

Figure 51 BSE images of dark BSE zircon cemented by xenotime for images on page 168

a Fragmented dark BSE zircon with thick xenotime rims around fragments. Xenotime has also filled along cracks (KULM4). **b** Enlarged image of area defined in **a** displaying the blocky nature of xenotime rims. **c** Enlarged image of area defined in **a**. Shows thin light BSE veins with irregular margins in group 2 dark BSE zircon. **d** Fragments of dark BSE zircon cemented by blocky xenotime. Xenotime is also present as inclusions and thin veins in dark BSE zircon (KULM1).

Group 1 dark BSE zircon that contains abundant inclusions and holes, display minute irregularities on their margins with the matrix (Fig.48 & 49e). This is more pronounced when adjacent to a fine-grained carbonate or clay matrix than when adjacent to the relatively coarse quartz (Fig. 49a). Blocky and pyramidal xenotime, of similar size to the inclusions, is also found on these margins where they are contact with the matrix (Fig. 49e). Furthermore, fragments of Group 1 dark BSE zircon can be cemented by large amounts of xenotime that also seals fractures or cracks within the zircon (Fig.51 and see section 4.6.2).

4.4.2 Group 2 dark BSE zircon

Grains containing Group 2 dark BSE zircon retain an almost perfect shape of the parent zircon (Fig.52), however, some margins also appear slightly concave adjacent to feldspar and quartz (Fig. 47i, 52b, 52e). The boundary between light and dark BSE zircon is observed as an irregularly shaped, inward penetrating front usually roughly parallel to zoning and punctuated by *c.*1 μ m deep v-shaped clefts (Fig. 52 & 47k). Group 2 dark BSE zircon preserves thin laths, fingers and lobes of light BSE zircon with irregular boundaries and are often isolated. The boundary can however form straight euhedral margins (Fig. 52c-e) and where so, Group 2 dark BSE zircon commonly display thin streaks of light BSE zircon, aligned roughly parallel to the light-dark BSE boundary giving a stripped appearance (Fig. 52c-g).

Fractures and cracks are common in light BSE zircon that contain Group 2 dark BSE zircon but are fewer and in a more random orientation compared to radial fractures associated with Group 1 dark BSE zircon. Radial fractures are completely absent from zircon with Group 2 dark BSE zircon. However within Group 2 dark BSE zircon, thin (<50nm) cracks form roughly parallel to euhedral light BSE zircon zoning (Fig. 52a & 52c) and can cause a rib-like microstructure. These cracks are not observed in Group 1 dark BSE zircon.

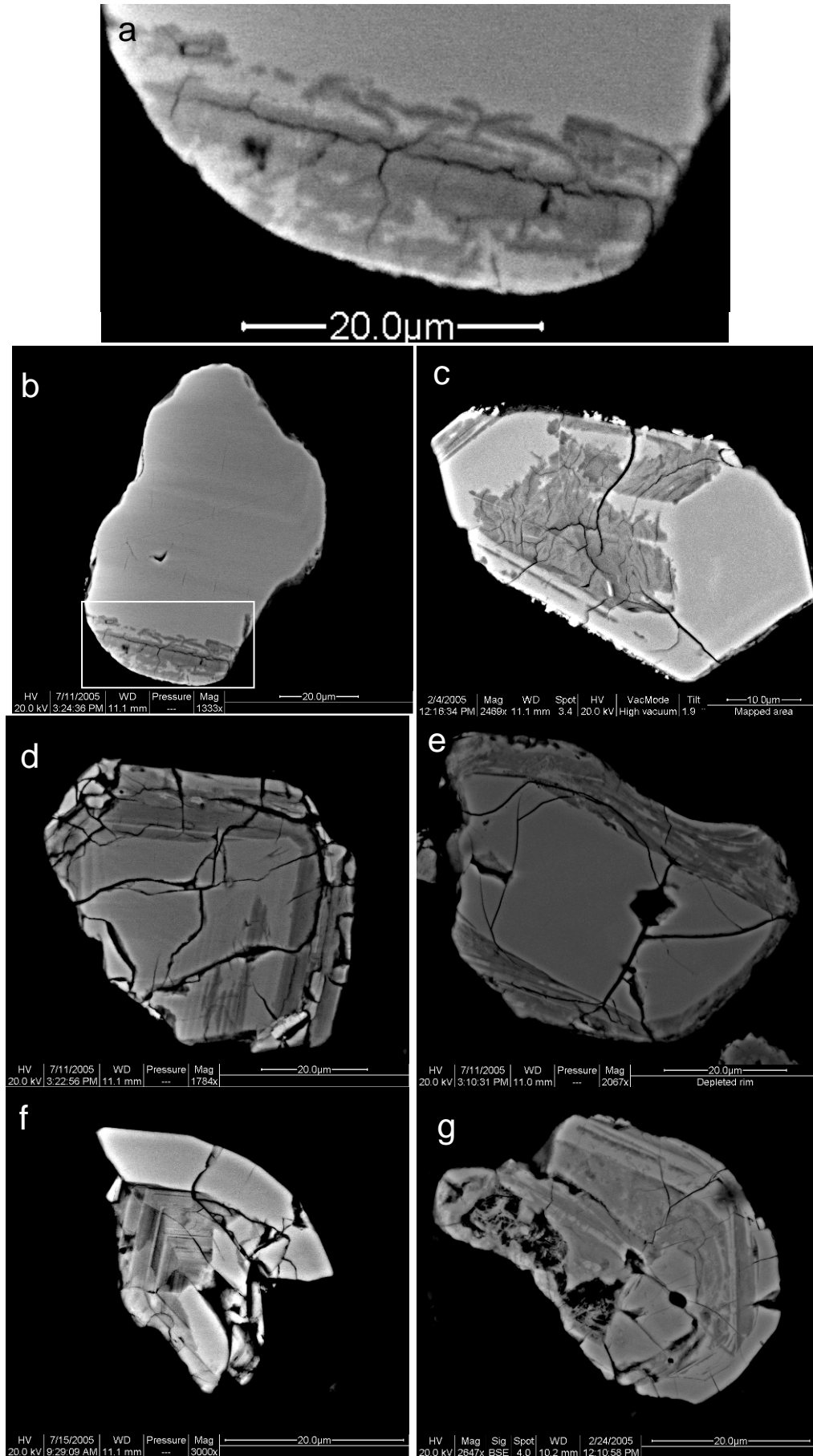


Figure 52 BSE images of Group 2 dark BSE zircon Caption on following page.

Figure 52 BSE images of Group 2 dark BSE zircon

a&b Rounded zircon displaying weak oscillatory zoning with a group 2 dark BSE zircon domain at the bottom of the image. Group 2 dark BSE zircon domain exhibits thin veins that run parallel and perpendicular to oscillatory zoning. Irregular patches and lobes of light BSE zircon are present in group 2 dark BSE zircon (KULM1). **c** Zircon with euhedral grain edges and large group 2 dark BSE zircon with irregular domains of light BSE zircon preserved within. Grain displays slight cracking in both light and dark BSE zircon but group 2 dark BSE zircon exhibits rib-like veins that run roughly parallel with light-dark boundary. Minute xenotime outgrowths are observed along the grain edge (KULM4). **d** Zircon fragment with multiple cracks both in light and dark BSE zircon. Group 2 dark BSE zircon forms along euhedral boundaries and has stripped appearance (KULM1). **e** Zircon grain with smoothed margins and light BSE zircon interior. Group 2 dark BSE zircon forms a partly surrounding outer rim and displays stripes that run parallel with light-dark BSE zircon boundary. There is slight cracking within the grain (L-millG3). **f** Zircon fragment with euhedral, oscillatory zoning group 2 dark BSE zircon and light BSE zircon rim (KULM-T). **g** Rounded zircon fragment with group 2 dark BSE zircon zones. Group 2 dark BSE zircon has a mottled appearance (KULM3).

4.5 Porous zones in light BSE zircon

Spherical to elongate dark BSE pores, <50nm to 300nm in diameter, have been observed in particular growth zones or domains of light BSE zircon (Fig.53 & 49f). Within these areas, pores have a relatively even distribution. In darker BSE areas of porous zones, thin bright BSE rims surround some pores. Group 1 dark BSE zircon is occasionally found around the tips of fractures in porous light BSE zones (Fig. 47d). These pores are similar to those described in Group 1 dark BSE zircon, section 4.4.1.1.

4.6 Outgrowths on the margins zircon

4.6.1 Zircon outgrowths

Occasional jagged, saw-tooth shaped zircons project 200nm-1µm from the margins of light BSE zircon (Fig.54). They have a lower BSE intensity than the host zircon, similar to dark BSE zircon, and are present either as a series of serrations or isolated euhedral prisms. They have been identified as zircon by their BSE contrast as they are too small for chemical determination. Occurrences of zircon outgrowths are generally rare (Table 8) however zircon outgrowths are concentrated in two of the rocks studied (KULM1 & KULM3). Both are fine-grained (50-100µm) quartz arenites with a micritic cement and zircon outgrowths can be present on upto 15% of the zircon grains examined in these rocks (Table 8).

Zircon outgrowths have been found adjacent to a variety of matrix minerals including detrital K-feldspar (>200µm wide), carbonate cements and smectite grains. Outgrowths form on the outermost face of the host grain and also protrude from the point where internal fractures terminate at the edge of host zircon (Fig. 54b). Zircon outgrowths can often be spatially linked to dark BSE zircon within the host grain by cracks or fractures in the light BSE zircon (Fig. 54b, 54c,55a). In addition, zircon outgrowths are observed on unmodified zircon (Fig. 54d & 54h).

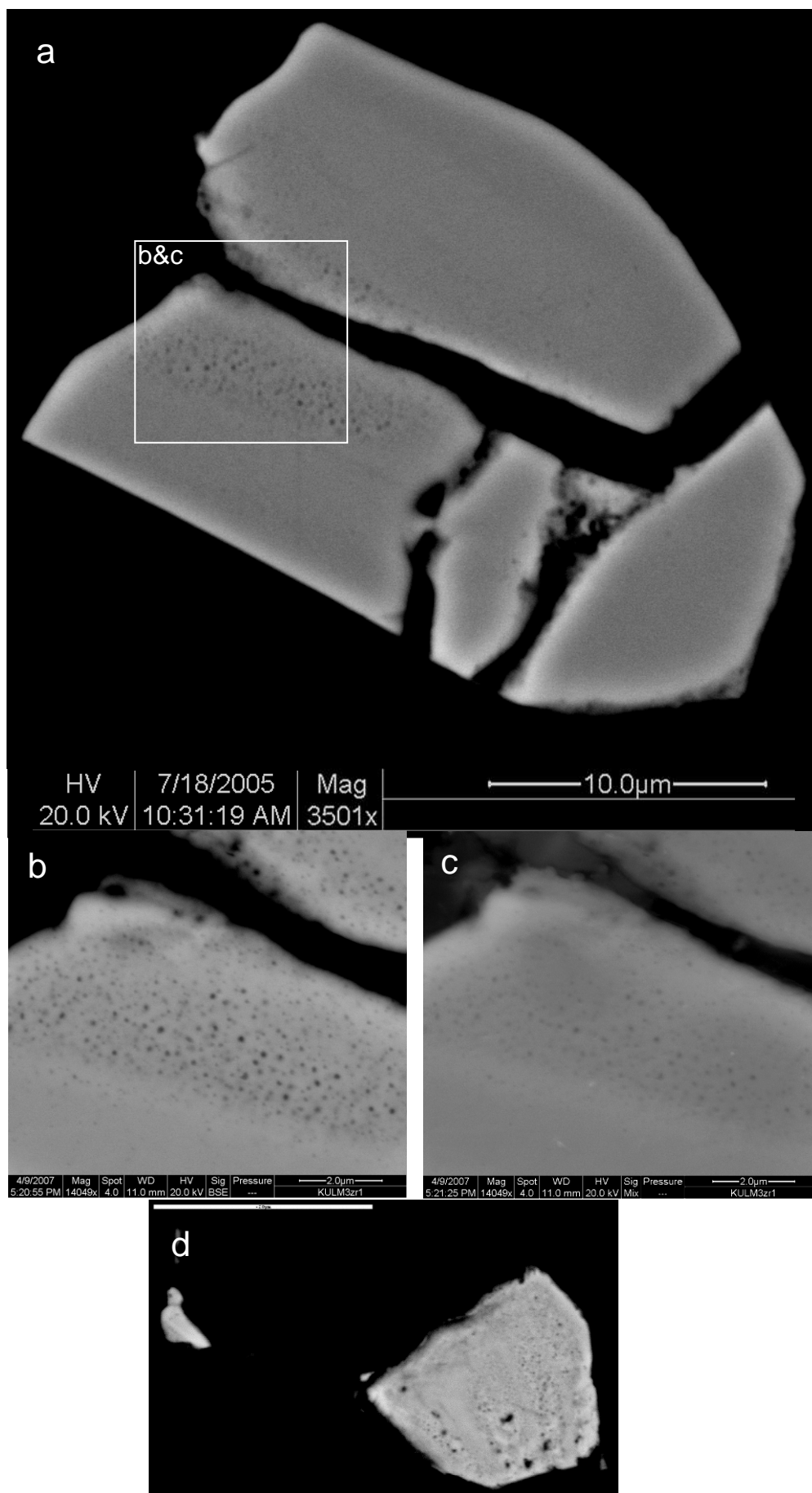


Figure 53 Images of porous zones in zircon. Figure caption on page 178.

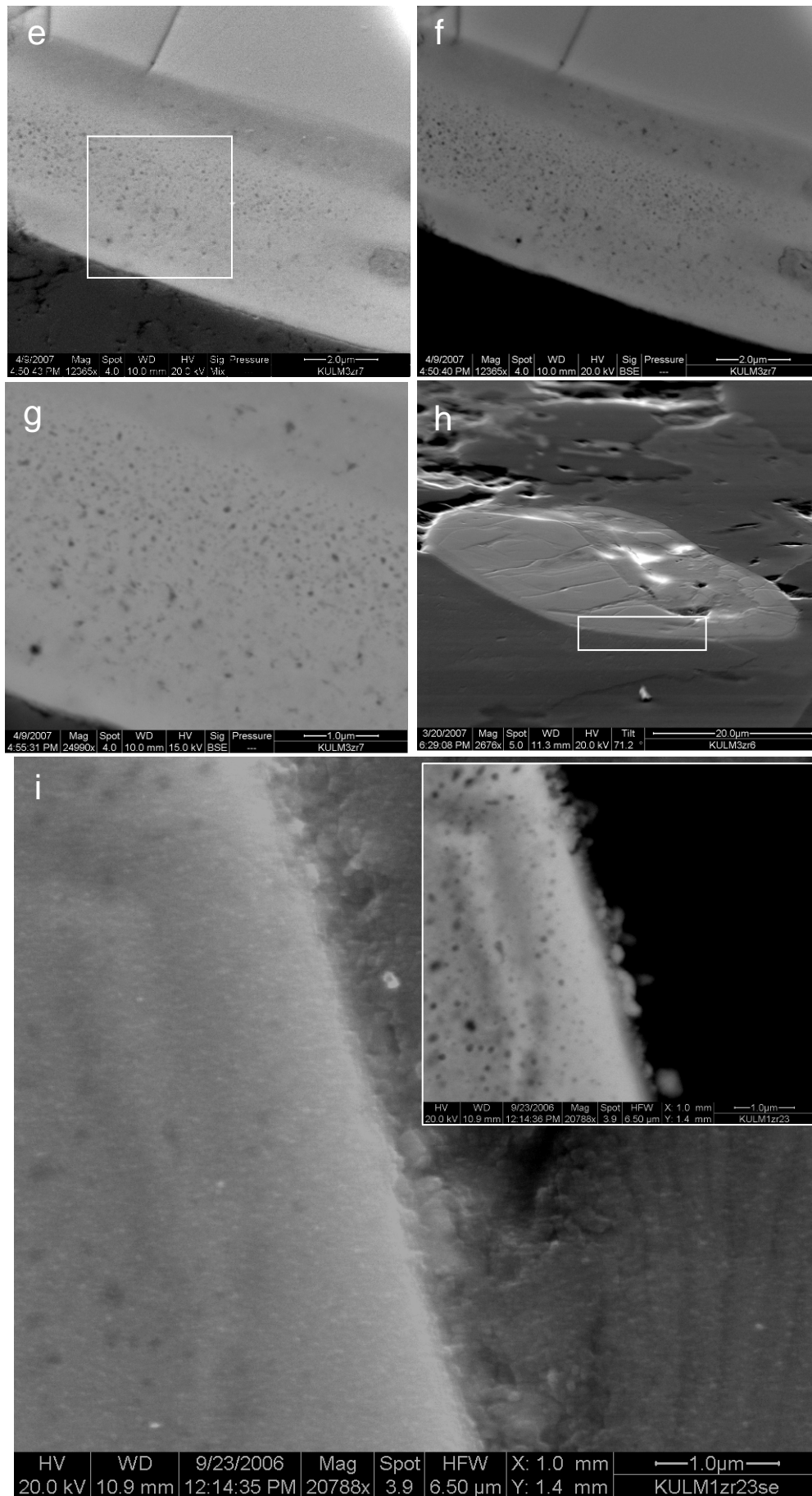


Figure 53 Images of porous zones in zircon. Caption is on following page.

Figure 53 Images of porous zones in zircon

a-c Fragmented zircon with dark BSE porous core. The boundaries of porous zones are parallel with weak zoning in light BSE zircon. **a&b** are BSE images, **c** is SE image. Observe that no charging occurs round the dark BSE pores. (KULM3). **d** Stripped porous zones in zircon. **e-h** Porous zone in zircon from Fig.47d (KULM3). **e&f** are complementary SE and BSE images respectively and show the close association porous zones have with dark BSE zircon. **g** is a high magnification BSE image illustrating the varied shape of dark pores. **h** is an SE image of Fig.47d with stage tilted to 70° and shows charging effects. Area defined in **h** is enlarged in **e-g**. **i** SE image of porous zircon with xenotime outgrowths on the margin. Again, note absence of charging. Inset is complementary BSE image. (KULM1).

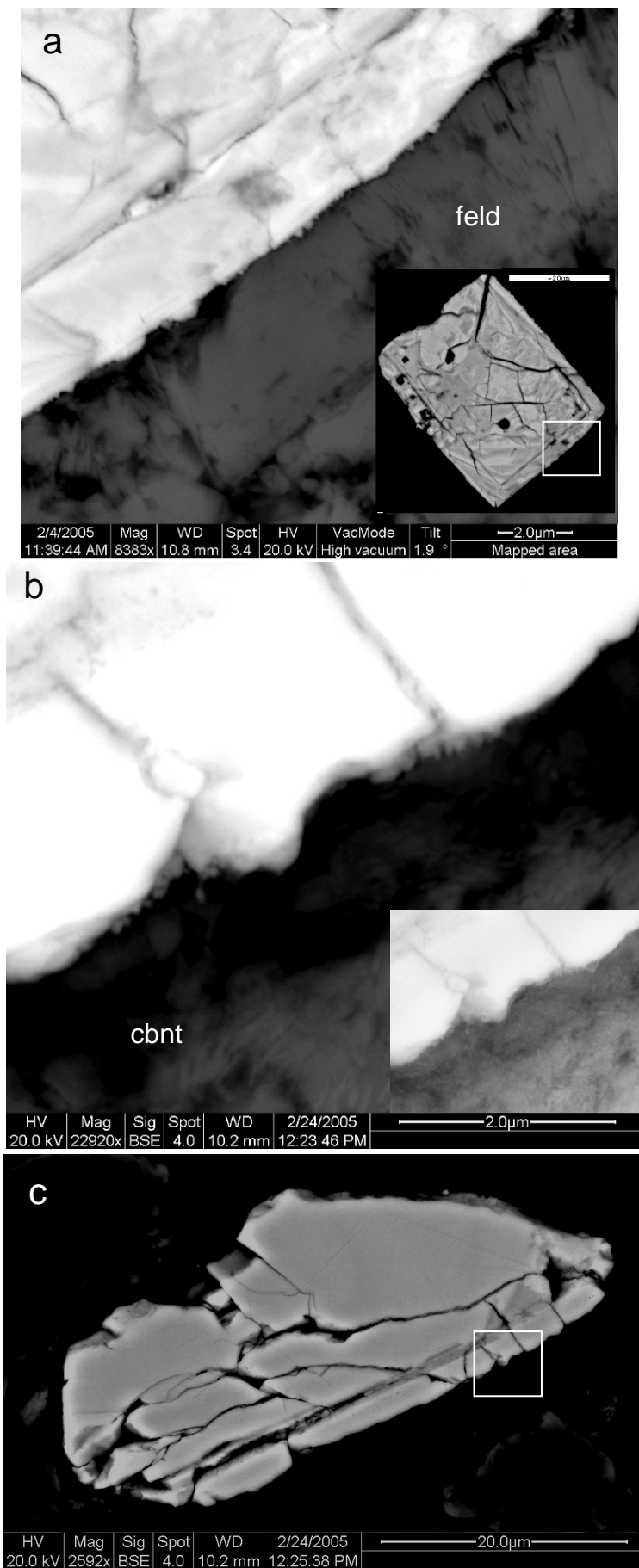


Figure 54 Zircon outgrowths on zircon. Caption on page 181.

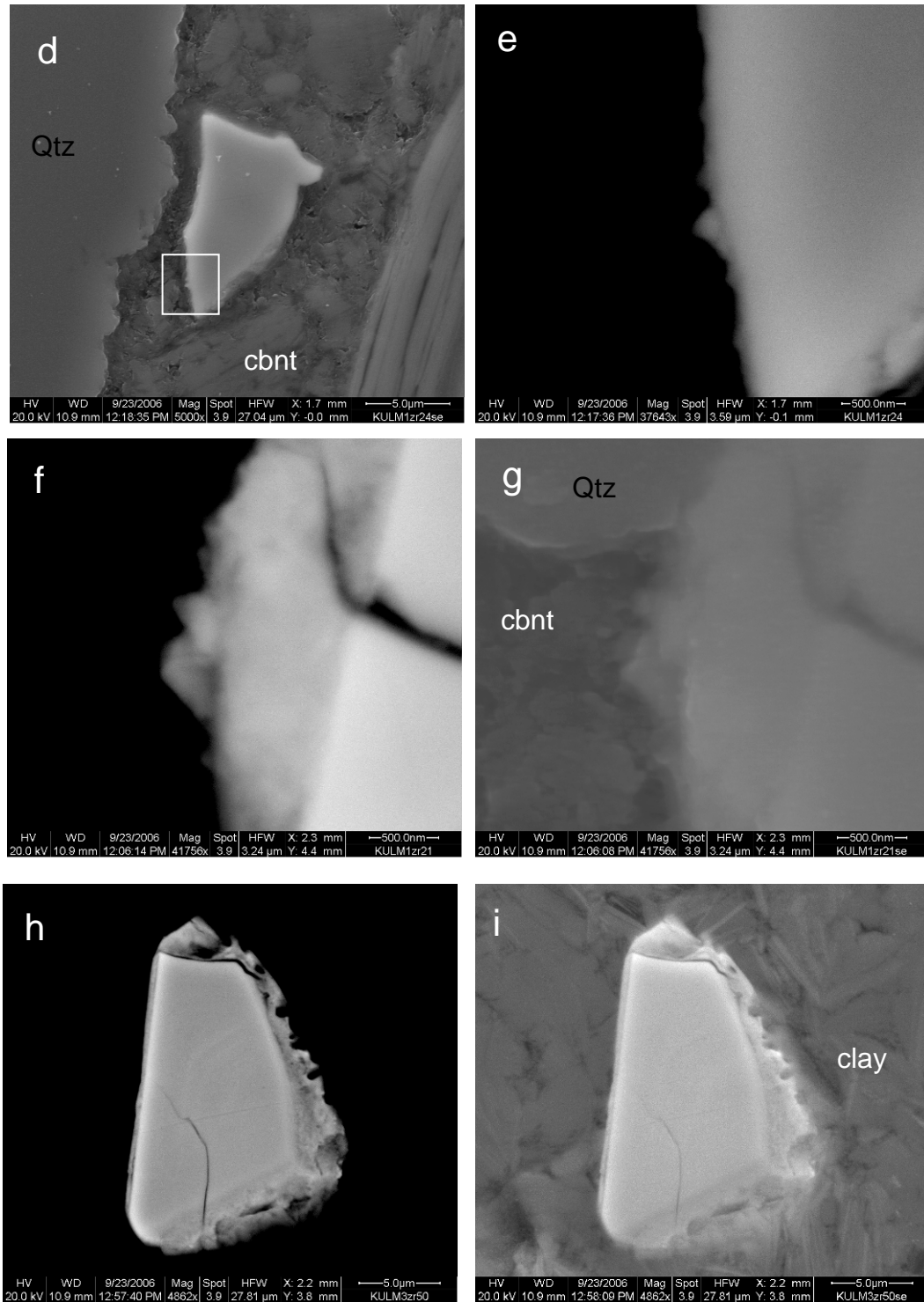


Figure 54 Zircon outgrowths on zircon. Caption on following page.

Figure 54 Zircon outgrowths on zircon

a Minute serrations and blocks of zircon outgrowths on the margin of alter zircon adjacent to a feldspar . Inset shows area enlarged on the grain. Both BSE images. (KULM4). **b** BSE image of serrations of zircon outgrowths that protrude from dark BSE zircon filled fractures. Inset in **b** is SE image displaying adjacent micrite cement (cbnt) with **c** showing location on grain where outgrowths occur. In this, outgrowths can be spatially linked to dark BSE zircon zone (KULM3). **d&e** Zircon with minute zircon pyramidal outgrowth on its margin. Outgrowth is adjacent to carbonate cement (cbnt). **d** is SE image and **e** is BSE image. (KULM1). **f&g** Complementary BSE and SE images respectively showing minute euhedral zircon outgrowths against a micrite cement (cbnt) and not against adjacent quartz (qtz). (KULM1). **h&i** Complementary BSE and SE images respectively that illustrate the irregular margins of zircon outgrowth structure when adjacent to clays. Feature at the bottom of the grain is not an outgrowth but a topographic feature (KULM3).

4.6.2 Xenotime outgrowths

Xenotime outgrowths are rare, present in only two of the sectioned rocks studied; a marl (KULM2) and a fine-grained (50-100 μ m) quartz arenite cemented by calcite (KULM4). Xenotime can be found on 7% and 15% of the zircons respectively but is absent from all other samples (Table 8). Zircon and xenotime outgrowths do not generally appear in the same polished section and xenotime inclusions within Group 1 dark BSE zircon are typically only found where xenotime outgrowths are present in the rock.

Xenotime outgrowths form on the margins of zircon as individual pyramids (Fig. 55), serrated xenotime (Fig. 55a,56d-i), rounded pyramids (Fig. 55d,11c), sub-hexagonal and sub-euhedral blocks (Fig. 56a), circular-shaped grains (Fig. 56c) and irregular fingers that protrude 0.5-4 μ m into the matrix (Fig. 56a). Occasionally, xenotime forms rims upto 20 μ m thick on the fragmented margins of Group 1 dark BSE zircon and this can also be in the form of a blocky cement around zircon fragments (Fig.51). The cement exhibits slight BSE contrast variations unrelated to any obvious structure. Zircon with large xenotime rims also has cracks across the grain sealed by xenotime and contain xenotime in irregular-shaped discontinuities within Group 1 dark BSE zircon. No xenotime outgrowths have been observed completely surrounding the host zircon.

Larger xenotime outgrowths are present on small (<2 μ m) matrix zircon (Fig. 56a&b) and often contain small (<1 μ m) irregularly-shaped inclusions along the boundary with the host. Inclusions have a low BSE intensity but cannot be identified due to their small size. Smectite grains are also seen to terminate perfectly where xenotime outgrowths form (Fig. 55b&c). Dark BSE zircon is occasionally found between the host zircon and xenotime outgrowth and can be spatially linked Group 1 dark BSE zircon within the host zircon (Fig. 55a). The zircon between the xenotime outgrowth and host is also slightly porous (<100nm wide) and forms a poorly defined, transitional boundary with the xenotime. No detrital xenotime has been observed in any of these samples.

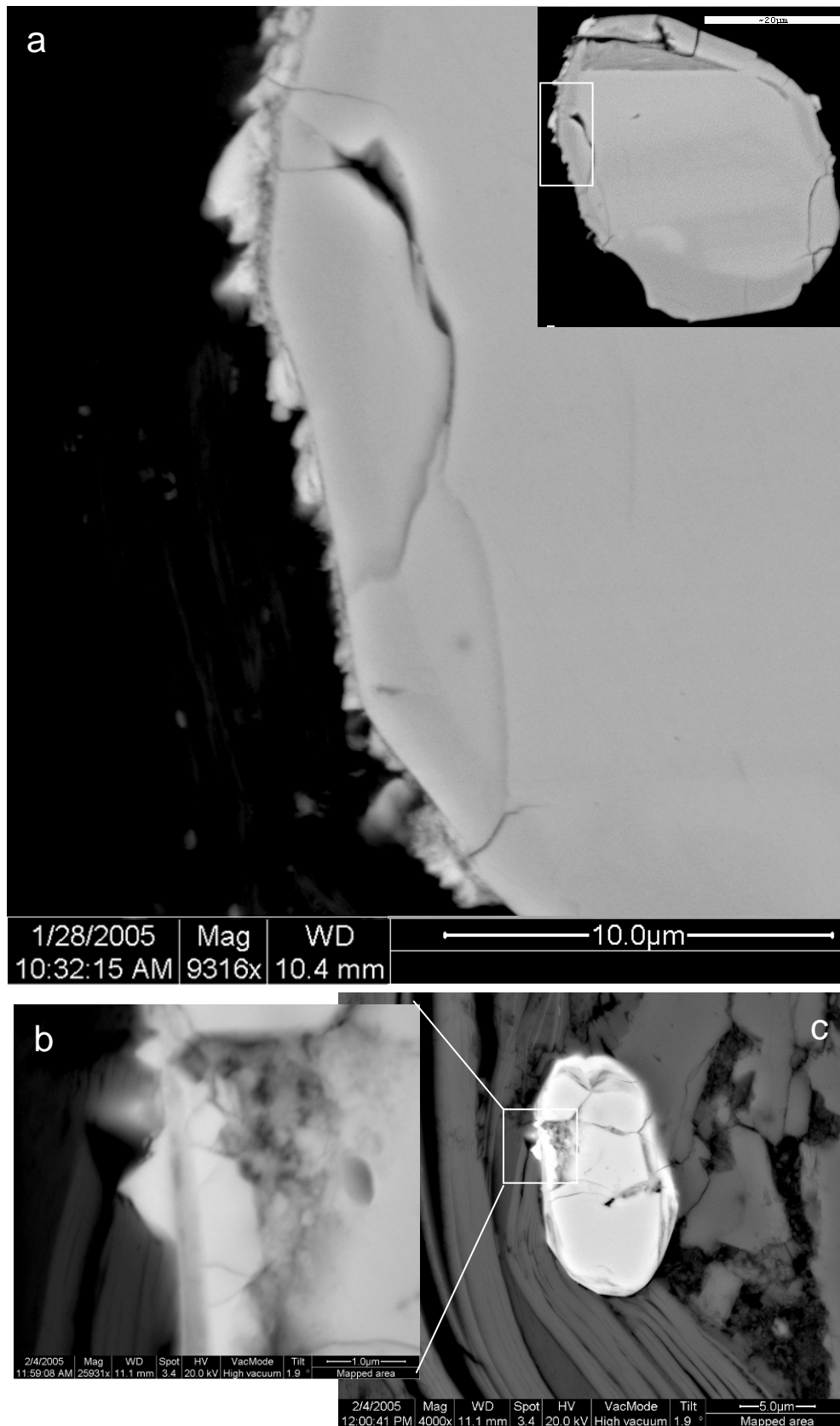


Figure 55 Pyramidal xenotime outgrowths on zircon Caption on page 186.

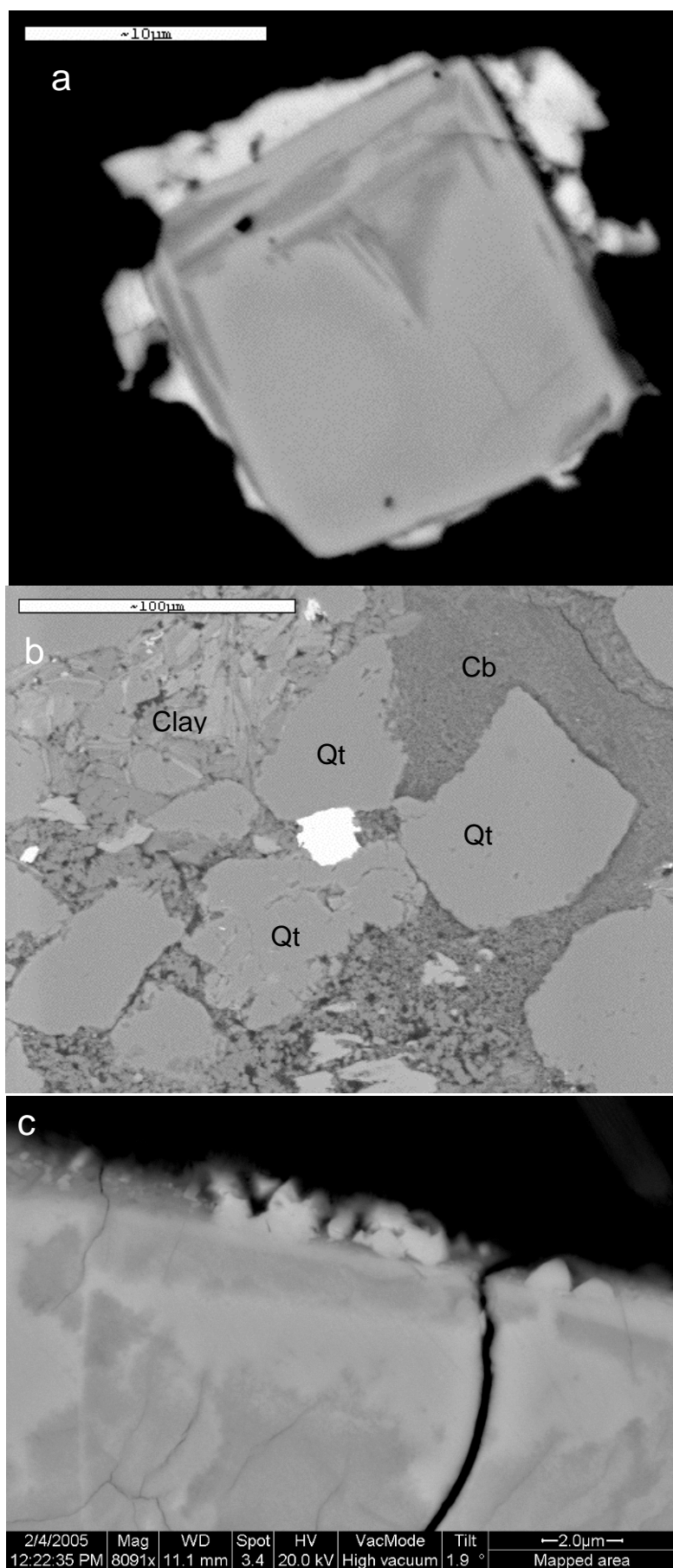


Figure 56 Xenotime outgrowths on zircons. Caption on page 186

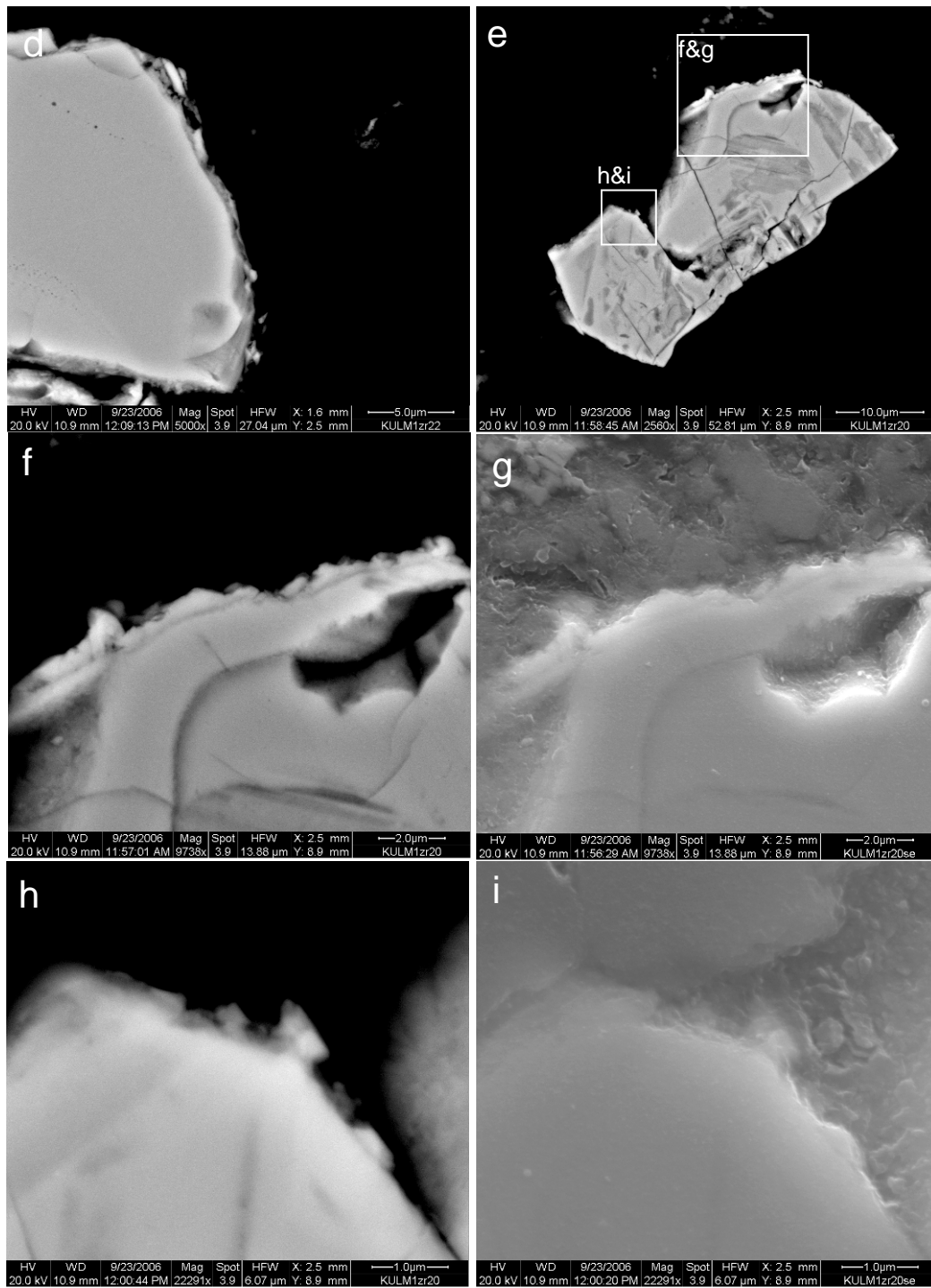


Figure 56 Xenotime outgrowths on zircons. Caption on following page.

Figure 55 Pyramidal xenotime outgrowths on zircon on page181

a BSE image of blocky and pyramidal xenotime and serrated zircon outgrowths that can be spatially linked to dark BSE zircon domain within the host grain (inset). (KULM3). **b&c** BSE images of pyramidal xenotime outgrowth that is coincident with smectite lath. Host grain has internal dark BSE zircon domains. (KULM4).

Figure 56 Xenotime outgrowths on zircons on pages186 and 188

a&b BSE images of euhedral zircon with blocky, sub-euhedral xenotime outgrowths around its margin. Xenotime can be seen partly encompassing matrix grains with which it forms euhedral margins. Irregular fingers of xenotime extend out into a micrite matrix (cbnt). (KULM4). **c** BSE image of rounded blocks, circular and minute euhedral xenotime of the margin of zircon. (KULM4). **d** BSE image of flattened and elongate xenotime blocks on the margin of zircon. **e-i** display the various forms of xenotime outgrowths on zircon. **f&g** are complementary BSE and SE images respectively as are **h&i**. (KULM1)

4.7 Chemistry and EBSD and their correlation with CL & BSE intensity in zircon

This section investigates the chemistry and crystallographic properties of zircon in sedimentary rocks. Initially, chemical data has been analysed from the whole population to give a general overview of the trends within data sets and zircon textures. However to obtain a more detailed understanding regarding the behaviour of some zircons, individual grains have been selected to identify and highlight particular features or trends.

4.7.1 Light BSE zircon

Light BSE zircon generally emits a moderate to high intensity CL signal, although there can be significant variations from zone to zone (e.g. Fig. 63b). Light BSE zircon has a composition of typical zircon (e.g. Fig. 63f) and EBSD analysis of light BSE, moderate to high intensity CL zircon results in high IQ patterns (orange to red in colour, e.g. Fig. 63b) indicating it is fully crystalline.

4.7.2 EPMA analysis and results

4.7.2.1 EPMA strategy

Thin sections KULM3 and KULM4 were selected for EPMA analysis because of the relative abundance and diversity of dark BSE zircon textures. Data was collected by line scan analysis across seven dark BSE areas selected from six zircons in KULM3 and multiple spot analyses from three zircons in KULM4. Line scan analysis was carried out so that relationships between chemistry, BSE & CL intensity and EBSD IQ could be examined and, where possible, identify trends. This will be investigated in sections 4.7.3 through to 4.7.6. Light BSE zircon was analysed as reference “standard” at the end of each analysis run to check any drift in the results. Figure 57 shows analytical spots for each grain.

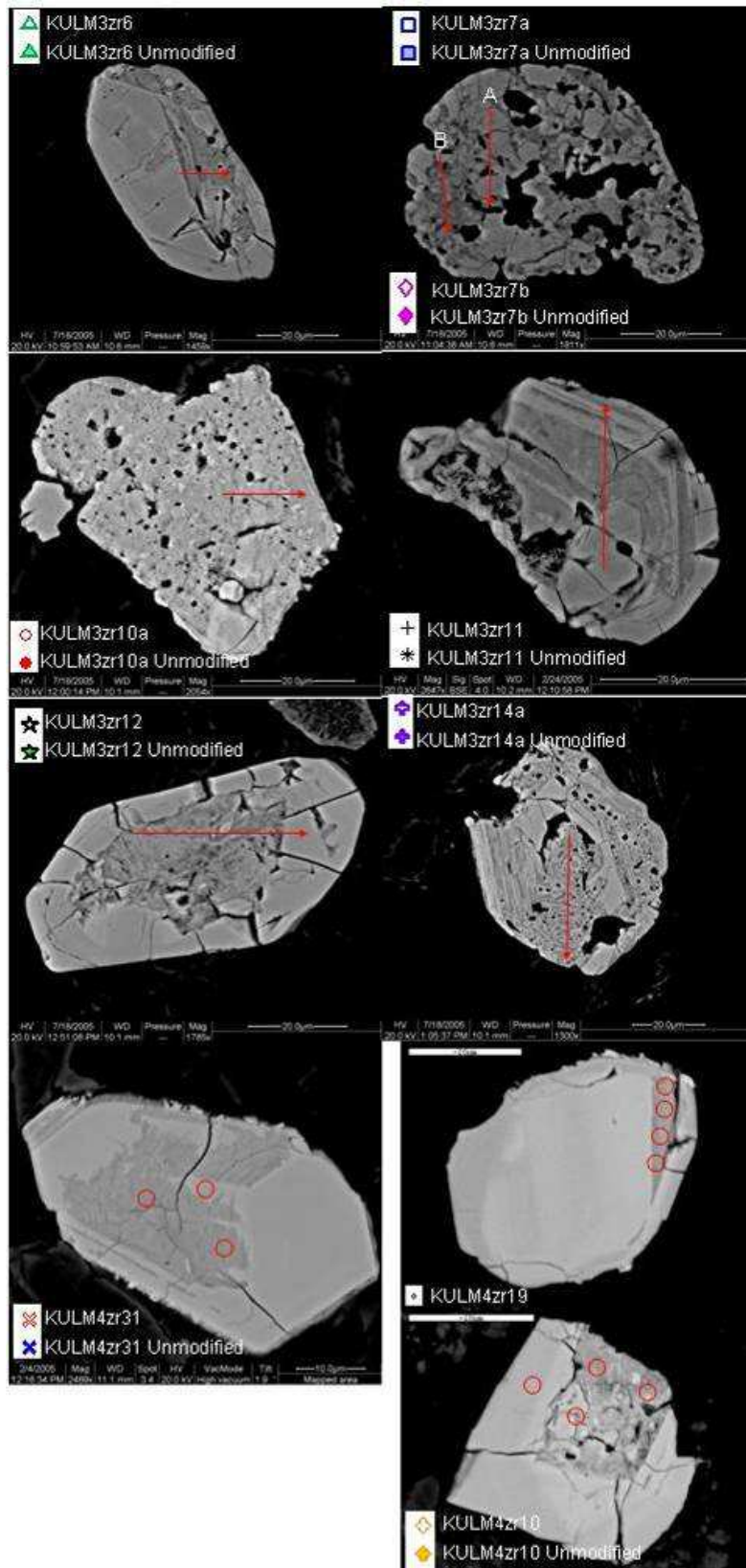


Figure 57 BSE images of zircons analysed by EPMA and the locations on them where analysis was collected via line scan analysis (red arrow), spot analysis (red spots). Beside each grain shows the symbol that refers to element plots in figures 58-60.

Although every attempt was made to avoid inclusions in the zircon, the inclusion-rich nature of Group 1 dark BSE zircon means that some were inevitably probed during line scan analysis. Most inclusions obvious in BSE imaging were avoided and therefore the majority of analysed inclusions are small in size. As such, their influence on the overall chemistry may be relatively subtle. Even so, inclusions within the analysed volume give rise to significant scatter within data set when plotted. The following section sets out to identify, justify and remove these points from the data set as they do not represent the chemistry of the zircon. Additionally, abnormal data points identified are removed from the data set progressively so each subsequent group of data plots has been weeded of these inclusions. Each symbol in the data plots relates to a different set of analysis. Light BSE zircon from each analysis set is represented by the same symbol as dark BSE zircon but with the colour filled. This is so a comparison between the composition of unmodified zircon (light BSE zircon) and modified zircon (dark BSE zircon) can be made. Furthermore, individual data points have been sequentially numbered to allow for easy identification and correlation on different element plots.

4.7.2.2 Anomalous points in EPMA data

Inclusions in dark BSE zircon are typically of similar composition to the surrounding matrix as determined from BSE images and EDX analysis. Therefore quartz, carbonate, feldspar and clays are likely candidates. Xenotime inclusions in dark BSE zircon have also been identified in BSE images and so are expected in the analysis.

Zr-poor (Fig.58a), Si- and Al-rich (Fig. 58b) points are highlighted in red and likely to be the result of clays or feldspar contamination. On this plot (Fig. 58a&b) the point encircled in green probably represents the influence of quartz. Data points heavily enriched in Y are highlighted in blue in Figures 58a, 58c-f and likely to be result of xenotime contamination. There are some analyses that plot between the groups encircled in the blue and red line (Point 7 in red and Point 59 in blue, Fig. 58a-c) and probably represent contamination from a combination of xenotime and clays or feldspar. Analyses encircled by the dashed line in Figure 58a are unusually Si-poor but do not show any particular deviation from the overall cluster in data in other element plots. It is not clear what

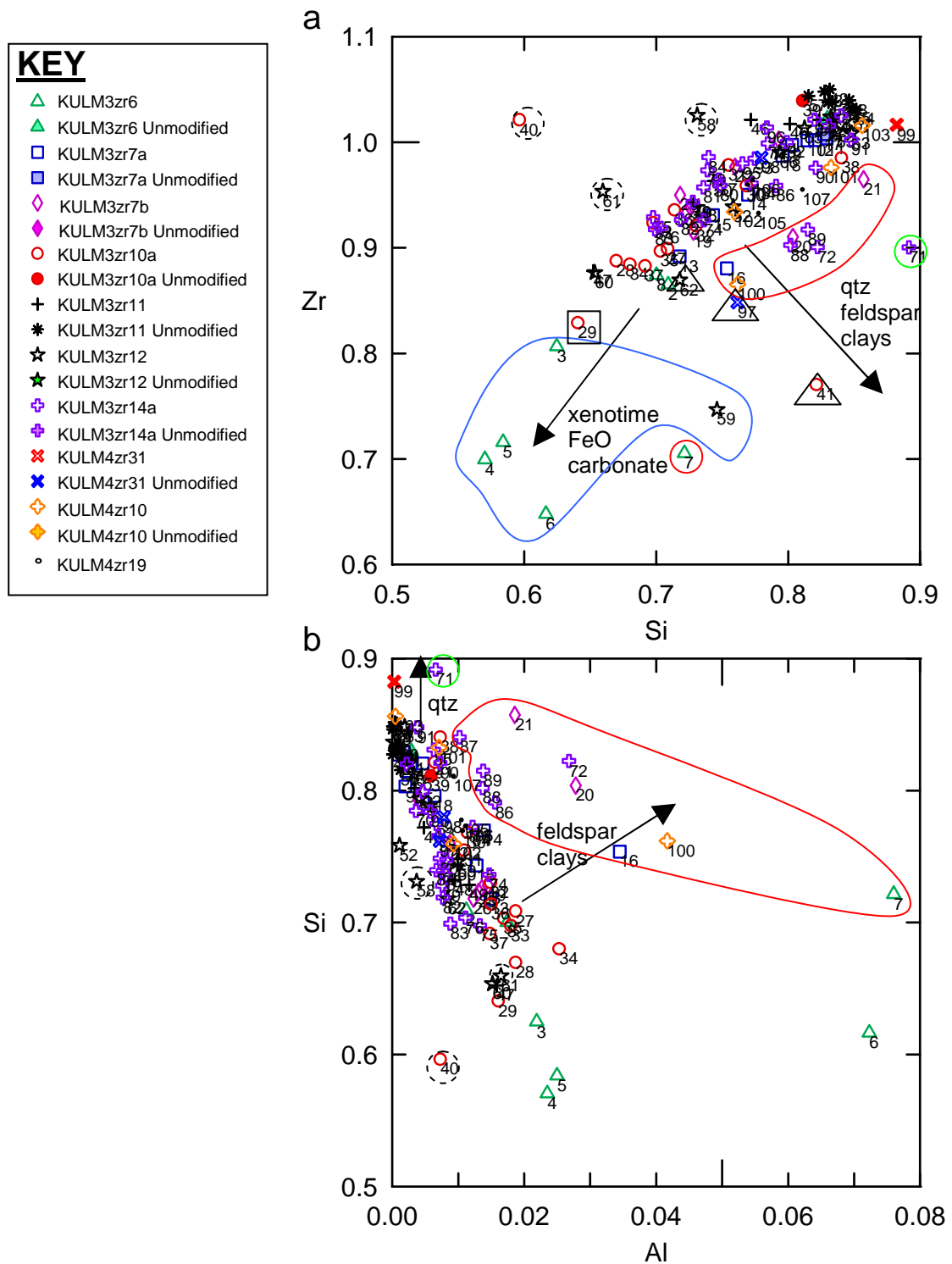


Figure 58 C.p.f.u. element plots from EPMA analysis of sedimentary zircons. Points highlighted are considered to be contaminated or anomalous analyses.

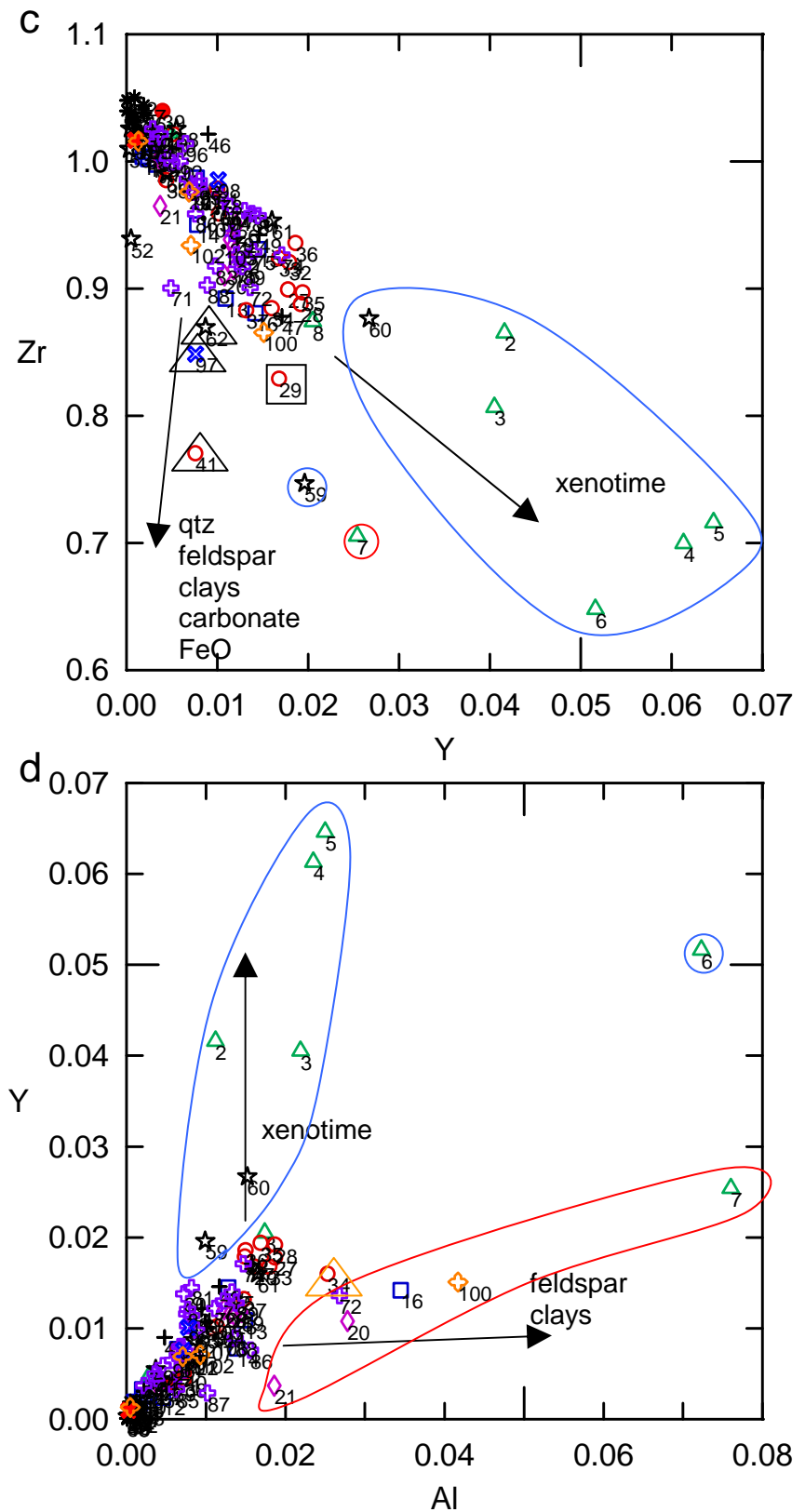


Figure 58 cont.

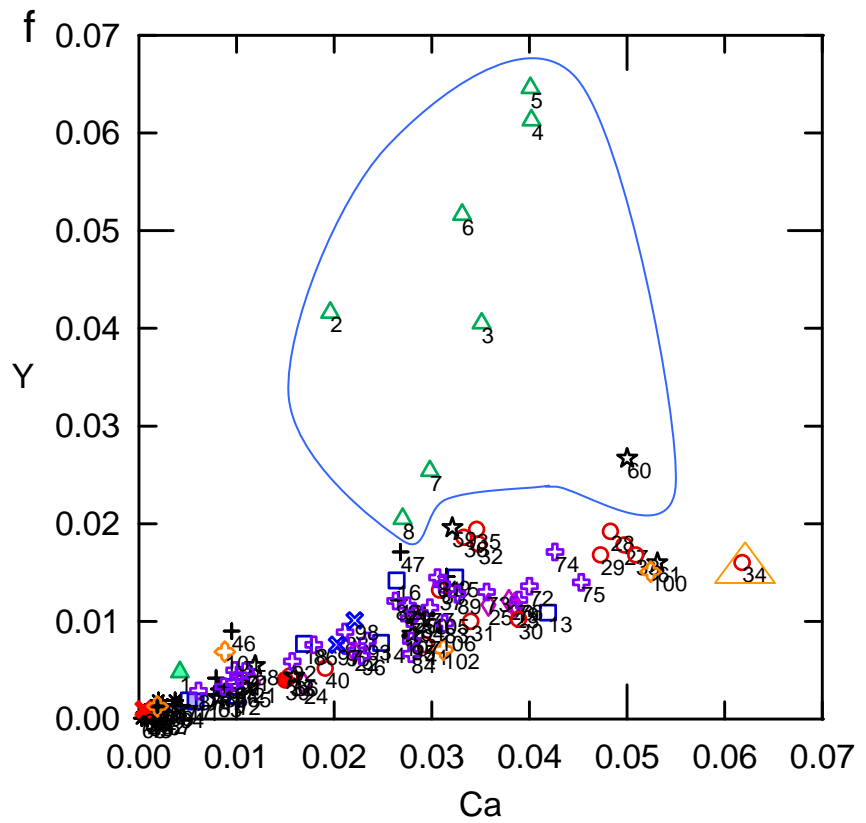
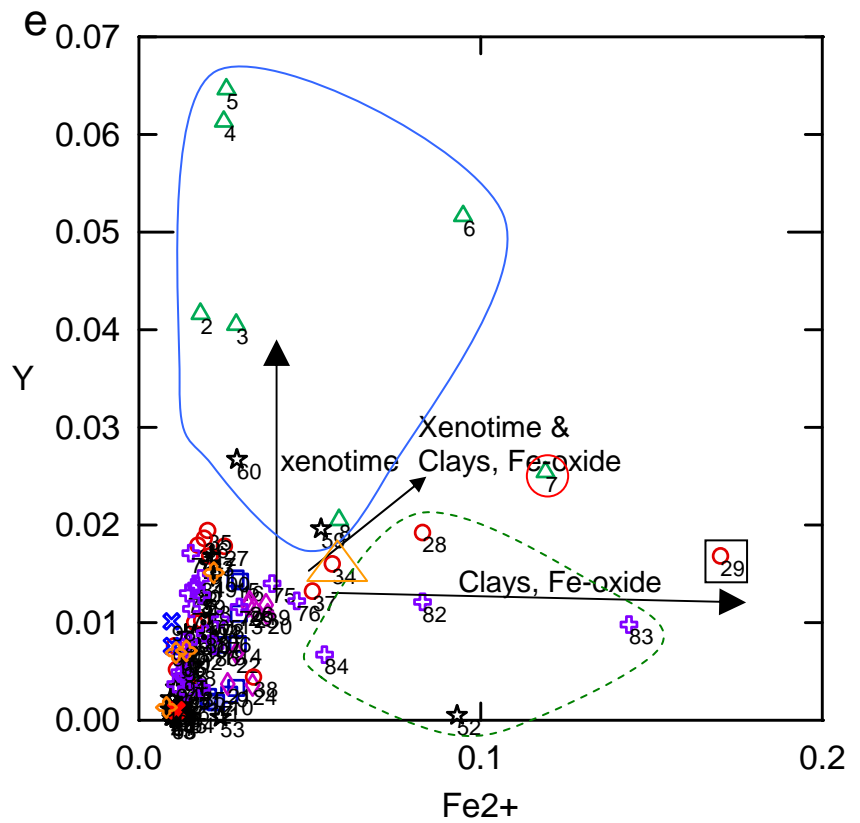


Figure 58 cont.

mineral phase may have caused this however these analyses are unlikely to represent dark BSE zircon and possibly represent bad analyses. Analyses highlighted in the green dashed line in Figure 58e are likely to be caused by FeO contamination rather than clays as they do not show a deviation in Al-plots. The analyses marked by the golden triangle in Figures 58d&e is likely to be the influence of contamination by clay while the analysis shown in the black box (Fig. 58a &e) is significantly contaminated by FeO. Analyses highlighted in black triangles (Fig. 58a&c) plot along the predicted trend lines for clays, feldspar and FeO but these same analyses show no Al (Fig. 58b) or Fe (Fig. 58e) enrichment. It is probable these analyses are the influence of contamination from some mineral phase whose main components were not analysed during EPMA.

With the above analyses removed, the data set has been replotted. Figure 59a-c reveal two analyses highlighted in red that deviate significantly from the overall cluster of data. It is not clear what mineral phase has caused this but possibly indicates contamination from carbonate or apatite inclusions. An isolated analysis plots considerably away from the overall cluster of data in Figures 59b&c (highlighted in yellow) and while it is not clear what the composition of the contaminant mineral phase is, this analysis is unlikely to be representative of dark BSE zircon.

All plots and tables referring to the composition of zircon from hereon have been constructed with all the anomalous and contaminated data points removed.

4.7.2.3 Overall chemistry and trends

The data from sedimentary zircon analysis is presented in Table 9 with all anomalous and contaminated data points removed. This data has been reproduced as weight percent in Appendix D. Light BSE zircon from both samples reveals an average Zr/Si ratio 1.23 (± 0.04) (calculated from c.p.f.u.), significantly higher than stoichiometric zircon. This seems unusual and is potentially a problem with the Si standard, although this does seem highly unlikely. However if this is an analytical issue, unlikely though it may be, this will only affect the absolute values for Si but does not change the relative relationship between light and dark BSE zircon. Typically zircon only contains trace amounts of Fe, yet light BSE zircon Fe also varies significantly (0.2-0.6wt%) but

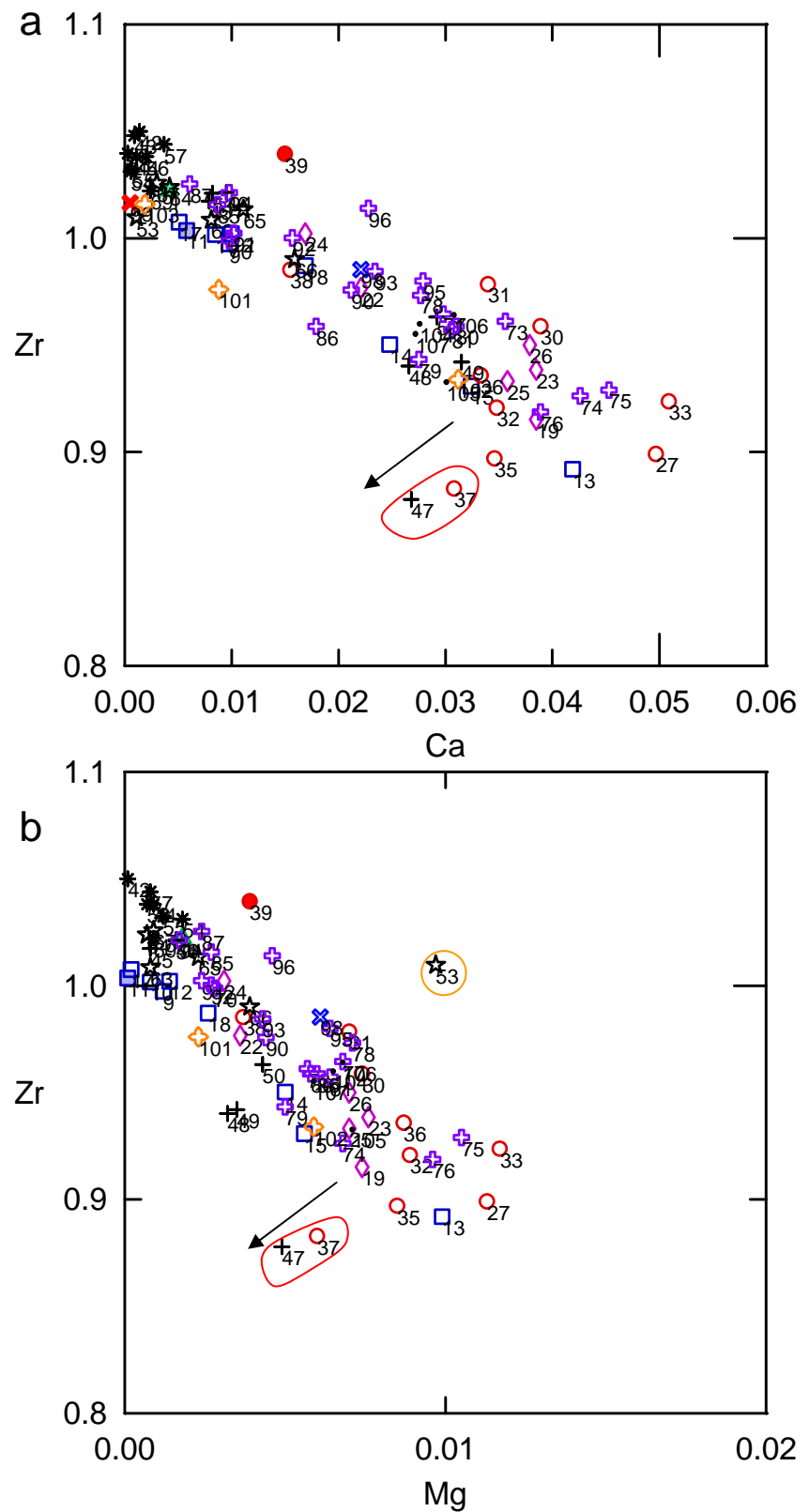


Figure 59 C.p.f.u. element plots from EPMA analysis identifying anomalous analyses after first round of “weeding”.

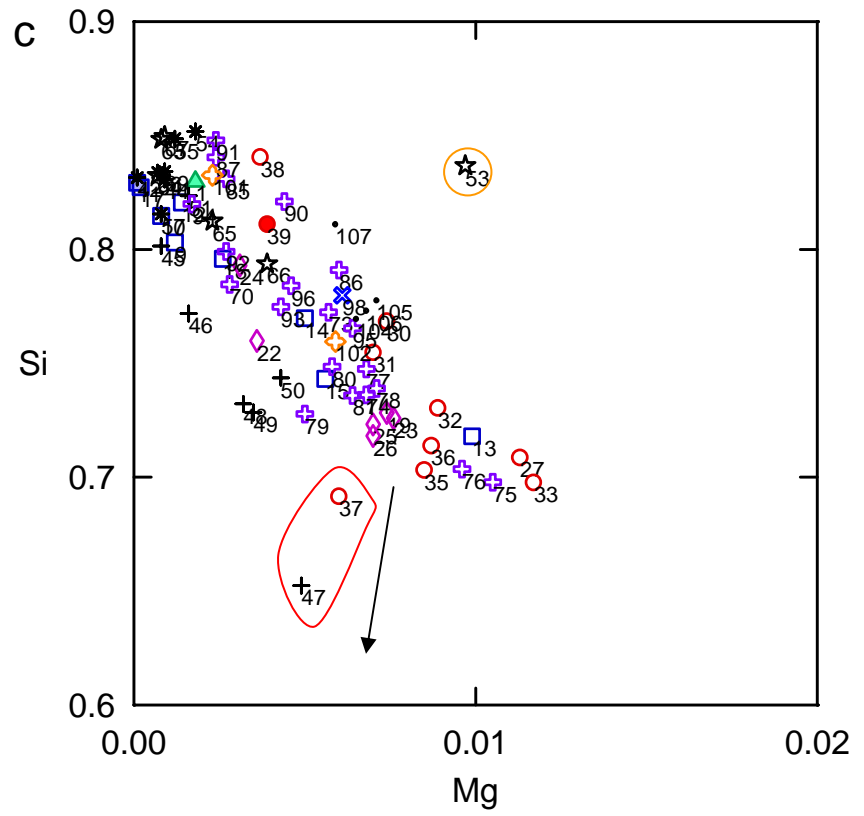


Figure 59 cont.

Sample	Analysis No.	Mg	Al	Si	Ca	Fe2+	Y	Zr	Hf	Total c.p.f.u.	Zr/Si	Zr/Hf
<i>Light BSE zircon</i>												
KULM3zr6	1	0.002	0.003	0.830	0.004	0.015	0.005	1.022	0.008	1.888	1.232	126.185
KULM3zr7a	11	0.000	0.002	0.829	0.006	0.023	0.002	1.004	0.019	1.883	1.210	53.663
KULM3zr10a	39	0.004	0.006	0.811	0.015	0.014	0.004	1.039	0.015	1.909	1.281	69.293
KULM3zr11	42	0.000	0.001	0.832	0.001	0.009	0.001	1.050	0.012	1.906	1.263	89.735
KULM3zr11	43	0.000	0.000	0.827	0.001	0.009	0.000	1.048	0.011	1.897	1.266	94.405
KULM3zr11	44	0.001	0.001	0.831	0.001	0.009	0.001	1.038	0.012	1.893	1.250	90.261
KULM3zr12	54	0.002	0.000	0.852	0.001	0.015	0.001	1.031	0.012	1.913	1.211	87.381
KULM3zr12	55	0.001	0.000	0.849	0.001	0.013	0.001	1.032	0.011	1.908	1.217	90.553
KULM3zr12	56	0.001	0.001	0.834	0.002	0.014	0.002	1.038	0.011	1.902	1.245	91.061
KULM3zr12	57	0.001	0.001	0.816	0.004	0.012	0.002	1.044	0.016	1.895	1.280	66.490
KULM3zr12	68	0.000	0.000	0.846	0.000	0.010	0.000	1.040	0.012	1.908	1.228	85.213
KULM3zr12	69	0.001	0.001	0.834	0.002	0.009	0.002	1.022	0.012	1.883	1.225	85.175
KULM4zr31	99	0.000	0.000	0.882	0.001	0.011	0.001	1.017	0.011	1.922	1.152	95.000
KULM4zr19	104	0.007	0.011	0.770	0.028	0.019	0.010	0.960	0.012	1.815	1.247	80.664
KULM4zr19	105	0.007	0.011	0.778	0.030	0.019	0.011	0.933	0.011	1.799	1.199	84.791
KULM4zr19	106	0.007	0.011	0.773	0.031	0.022	0.009	0.964	0.012	1.829	1.247	81.703
KULM4zr19	107	0.006	0.009	0.811	0.027	0.019	0.009	0.955	0.012	1.848	1.178	81.641
<i>Dark BSE zircon</i>												
KULM3zr7a	9	0.001	0.002	0.803	0.010	0.029	0.003	0.997	0.018	1.863	1.242	56.989
KULM3zr7a	10	0.001	0.002	0.815	0.009	0.026	0.003	1.002	0.019	1.875	1.229	54.141
KULM3zr7a	12	0.001	0.005	0.821	0.010	0.020	0.002	1.002	0.020	1.881	1.221	51.385
KULM3zr7a	13	0.010	0.015	0.718	0.042	0.029	0.011	0.892	0.016	1.733	1.242	54.384
KULM3zr7a	14	0.005	0.014	0.770	0.025	0.029	0.008	0.950	0.016	1.817	1.234	57.939
KULM3zr7a	15	0.006	0.013	0.743	0.032	0.028	0.015	0.931	0.016	1.784	1.253	57.104
KULM3zr7a	17	0.000	0.001	0.827	0.005	0.021	0.002	1.008	0.021	1.884	1.218	48.438
KULM3zr7a	18	0.003	0.006	0.796	0.017	0.024	0.008	0.987	0.013	1.854	1.240	75.351
KULM3zr7b	19	0.007	0.015	0.728	0.039	0.037	0.012	0.915	0.022	1.775	1.257	41.600
KULM3zr7b	22	0.004	0.009	0.760	0.022	0.029	0.007	0.977	0.021	1.828	1.285	45.850
KULM3zr7b	23	0.008	0.014	0.726	0.039	0.034	0.011	0.938	0.016	1.785	1.293	58.286

Table 9 EPMA analyses of sedimentary zircon containing dark BSE zircon. Presented in c.p.f.u. calculated to 4(O).

Sample	Analysis No.	Mg	Al	Si	Ca	Fe2+	Y	Zr	Hf	Total c.p.f.u.	Zr/Si	Zr/Hf
KULM3zr7b	24	0.003	0.004	0.793	0.017	0.033	0.004	1.002	0.019	1.875	1.264	53.594
KULM3zr7b	25	0.007	0.013	0.723	0.036	0.032	0.012	0.933	0.016	1.772	1.291	57.605
KULM3zr7b	26	0.007	0.012	0.718	0.038	0.032	0.012	0.950	0.015	1.785	1.323	64.189
KULM3zr10a	27	0.011	0.019	0.709	0.050	0.025	0.018	0.899	0.017	1.747	1.269	53.838
KULM3zr10a	31	0.007	0.011	0.755	0.034	0.016	0.010	0.979	0.015	1.826	1.296	67.483
KULM3zr10a	33	0.012	0.018	0.698	0.051	0.021	0.017	0.924	0.016	1.755	1.324	58.462
KULM3zr10a	36	0.009	0.015	0.714	0.033	0.019	0.019	0.936	0.013	1.758	1.311	70.368
KULM3zr10a	37	0.006	0.015	0.692	0.031	0.051	0.013	0.883	0.013	1.703	1.277	68.442
KULM3zr10a	38	0.004	0.007	0.841	0.016	0.034	0.004	0.985	0.014	1.904	1.172	70.878
KULM3zr11	45	0.001	0.003	0.801	0.008	0.014	0.004	1.017	0.011	1.860	1.269	93.330
KULM3zr11	46	0.002	0.005	0.772	0.010	0.014	0.009	1.021	0.011	1.843	1.323	93.706
KULM3zr11	48	0.003	0.010	0.732	0.027	0.020	0.012	0.940	0.012	1.756	1.284	79.678
KULM3zr11	49	0.004	0.012	0.728	0.032	0.022	0.015	0.942	0.012	1.766	1.293	77.221
KULM3zr11	50	0.004	0.010	0.744	0.029	0.021	0.011	0.963	0.011	1.793	1.295	86.000
KULM3zr11	51	0.002	0.002	0.824	0.008	0.017	0.003	1.021	0.014	1.890	1.240	75.622
KULM3zr12	53	0.010	0.000	0.837	0.001	0.024	0.000	1.010	0.012	1.894	1.207	84.133
KULM3zr12	63	0.001	0.002	0.848	0.008	0.009	0.002	1.009	0.015	1.895	1.189	65.915
KULM3zr12	64	0.001	0.001	0.832	0.004	0.009	0.001	1.024	0.017	1.890	1.230	60.224
KULM3zr12	65	0.002	0.003	0.812	0.011	0.011	0.003	1.013	0.016	1.873	1.247	62.556
KULM3zr12	66	0.004	0.004	0.794	0.016	0.013	0.004	0.990	0.013	1.839	1.248	73.896
KULM3zr12	67	0.001	0.001	0.850	0.003	0.010	0.000	1.026	0.012	1.902	1.207	84.074
KULM3zr14a	70	0.003	0.004	0.785	0.010	0.013	0.005	0.999	0.010	1.828	1.273	100.889
KULM3zr14a	73	0.006	0.012	0.772	0.036	0.014	0.013	0.961	0.010	1.824	1.244	98.071
KULM3zr14a	74	0.007	0.015	0.736	0.043	0.015	0.017	0.926	0.011	1.770	1.258	86.561
KULM3zr14a	75	0.011	0.013	0.698	0.045	0.039	0.014	0.929	0.011	1.759	1.331	88.476
KULM3zr14a	76	0.010	0.011	0.704	0.039	0.046	0.012	0.919	0.011	1.751	1.306	85.074
KULM3zr14a	77	0.007	0.008	0.748	0.030	0.015	0.011	0.965	0.011	1.794	1.290	90.991
KULM3zr14a	78	0.007	0.008	0.739	0.028	0.024	0.010	0.973	0.011	1.799	1.317	91.821
KULM3zr14a	79	0.005	0.008	0.728	0.028	0.029	0.012	0.943	0.010	1.763	1.296	90.702
KULM3zr14a	80	0.006	0.007	0.749	0.031	0.017	0.014	0.959	0.010	1.792	1.281	93.087

Table 9 cont.

Sample	Analysis No.	Mg	Al	Si	Ca	Fe2+	Y	Zr	Hf	Total c.p.f.u.	Zr/Si	Zr/Hf
KULM3zr14a	81	0.006	0.008	0.736	0.031	0.018	0.015	0.957	0.010	1.781	1.301	92.038
KULM3zr14a	85	0.003	0.006	0.831	0.009	0.018	0.003	1.016	0.011	1.897	1.222	93.174
KULM3zr14a	90	0.004	0.007	0.821	0.021	0.013	0.008	0.976	0.010	1.860	1.189	96.614
KULM3zr14a	91	0.002	0.004	0.848	0.010	0.013	0.005	1.002	0.010	1.894	1.182	100.230
KULM3zr14a	92	0.003	0.005	0.799	0.016	0.013	0.006	1.000	0.010	1.851	1.252	102.051
KULM3zr14a	93	0.004	0.007	0.775	0.023	0.015	0.008	0.985	0.010	1.826	1.271	102.552
KULM3zr14a	94	0.002	0.002	0.820	0.010	0.011	0.004	1.021	0.010	1.880	1.246	101.119
KULM3zr14a	95	0.006	0.007	0.765	0.028	0.013	0.008	0.980	0.010	1.818	1.280	94.231
KULM3zr14a	96	0.005	0.006	0.784	0.023	0.012	0.007	1.014	0.009	1.859	1.293	112.656
KULM4zr31	98	0.006	0.008	0.780	0.022	0.010	0.010	0.985	0.010	1.831	1.264	99.525
KULM4zr10	101	0.002	0.007	0.833	0.009	0.011	0.007	0.976	0.013	1.857	1.172	77.460
KULM4zr10	102	0.006	0.009	0.760	0.031	0.014	0.007	0.934	0.018	1.779	1.230	52.173
KULM4zr10	103	0.000	0.001	0.856	0.002	0.008	0.001	1.016	0.014	1.898	1.186	74.146

Table 9 cont.

never drops below 0.2wt%. Such high elevated Fe concentrations were not observed in light BSE zircon from greenschist facies rocks (see section 3.8) which were analysed earlier but during the same batch of EPMA. The data between the light BSE zircon in greenschist facies rocks and sedimentary rocks shows a jump in Fe content in light BSE zircon from sedimentary rocks suggesting that elevated Fe levels are not an artefact of EPMA. Light BSE zircon also contains trace amounts of Ca (c.0.1wt%) but has an otherwise typical composition with Hf concentrated in variable amounts between individual zircons but Hf also varies slightly between individual growth zones in the same grain (0.75-1.5wt%). EPMA of light BSE zircon in both rocks gives almost 100wt% totals and an average total c.p.f.u. of 1.88 (± 0.04). This is in contrast to sedimentary dark BSE zircon that shows consistently low wt% totals averaging 95.8% (± 2.4) and average total c.p.f.u. of 1.82 (± 0.05). For the purposes of this section, Group 1 and Group 2 dark BSE zircon are to be considered as one group but comparison between these groups will be addressed in the following sections.

Sedimentary dark BSE zircon is depleted in both Zr and Si and the depletion follows a close 1:1 relationship (Fig. 60a) although dark BSE zircon has a Zr/Si ratio of 1.26(± 0.04) that is slightly higher than light BSE zircon, within error. There is a relatively wide variation in Hf contents in dark BSE zircon but individual grains have distinctive Hf concentrations that vary very little from the unmodified composition, even despite small variations within the parent grain (Fig. 60b). This suggests that Hf in dark BSE zircon is inherited from the parent composition.

Loss of Zr and Si in dark BSE zircon is coupled to a gain in non-formula elements, Ca (upto 0.05 c.p.f.u. (1.1wt%)), Al (upto 0.02 c.p.f.u. (0.25wt%)), Fe (upto 0.05 c.p.f.u. (1.3wt%)), Mg (upto 0.01 c.p.f.u. (0.15wt%)) and Y (upto 0.02 c.p.f.u. (0.9wt%)). The paths that analyses depleted in Zr and Si follow is a relatively well-defined 3:2 substitution trend when plotted against the sum of the non-formula elements (Fig. 60c & d). Al, Ca, Mg and Y follow general substitution trends with both Zr (Fig. 60e) and Si (Fig. 60f). These substitution relationships are summarised in Table 10. Despite mostly following these substitution trends, there is some spread in the data but this is particularly apparent in Si-Al plot. The Zr-Al plot shows a much better defined trend (Fig. 60e)

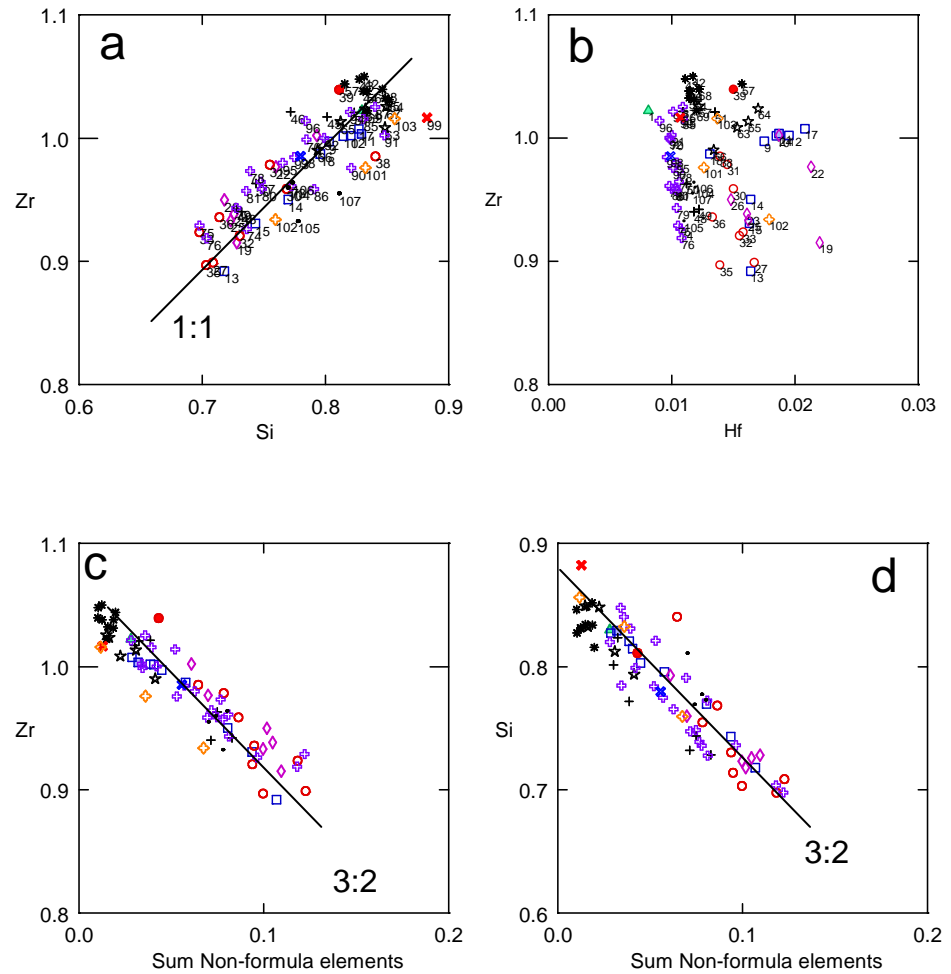


Figure 60 Element plots of dark BSE zircon EPMA analyses with all anomalous points removed. Units are c.p.f.u.

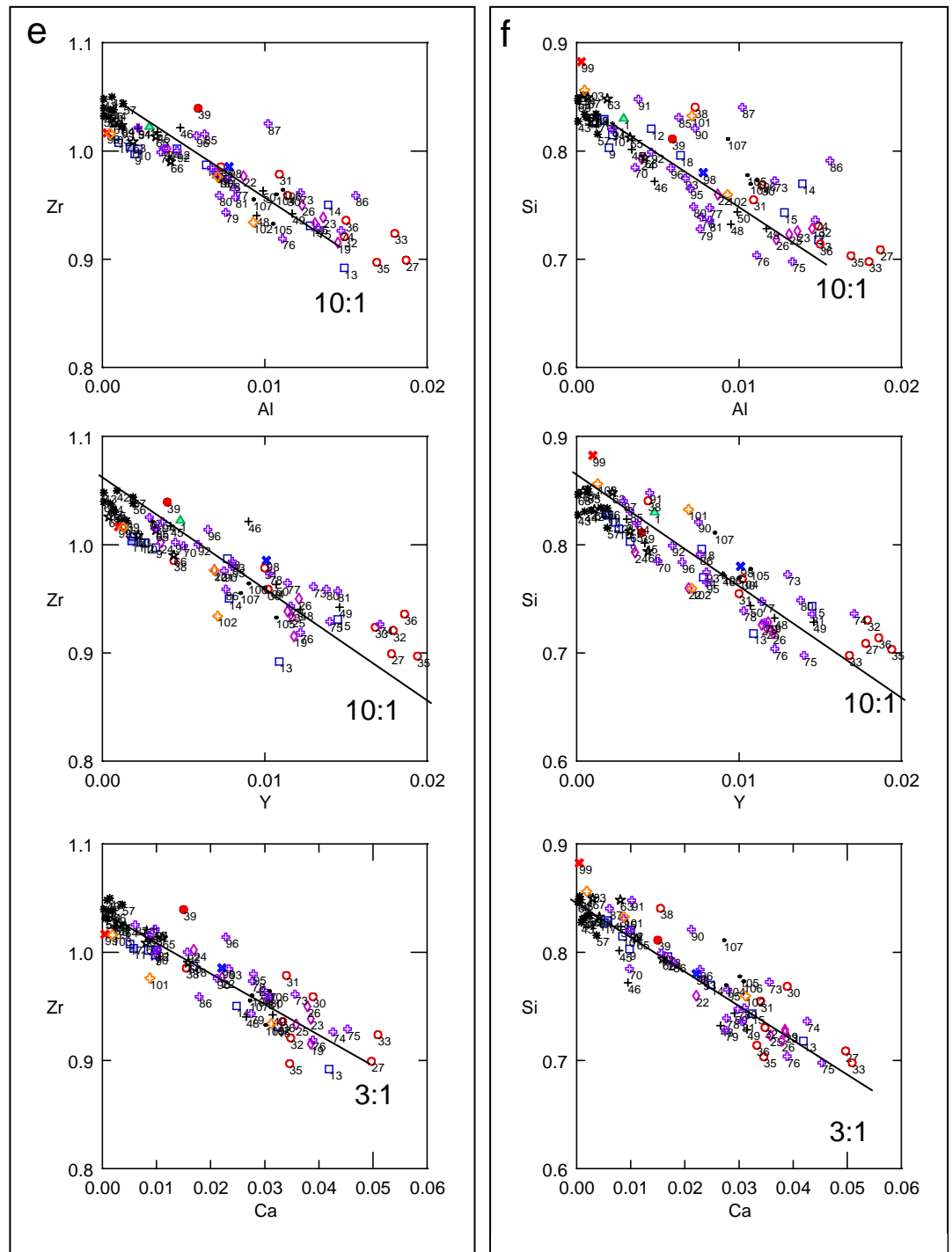


Figure 60 cont.

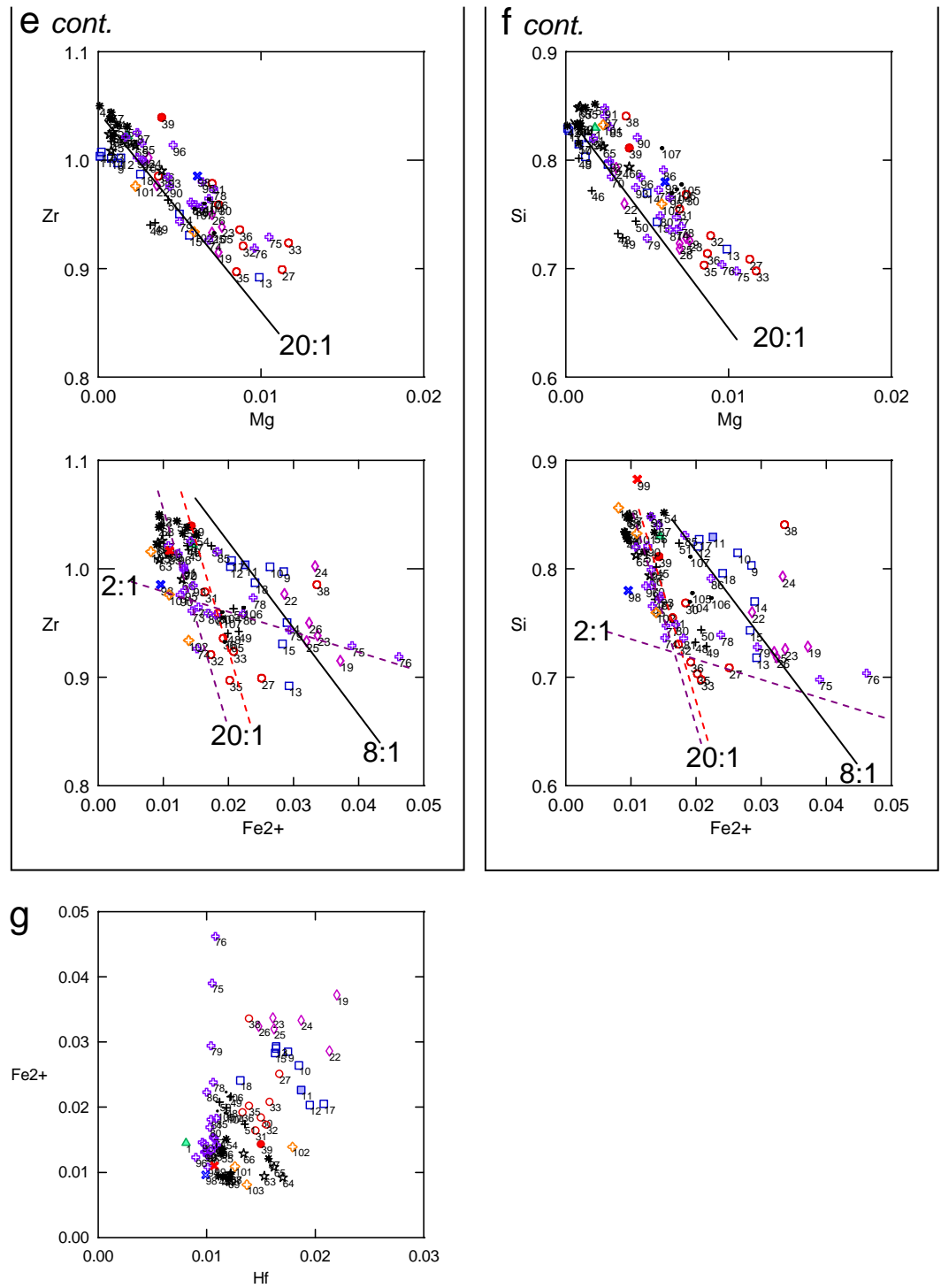


Figure 60 cont.

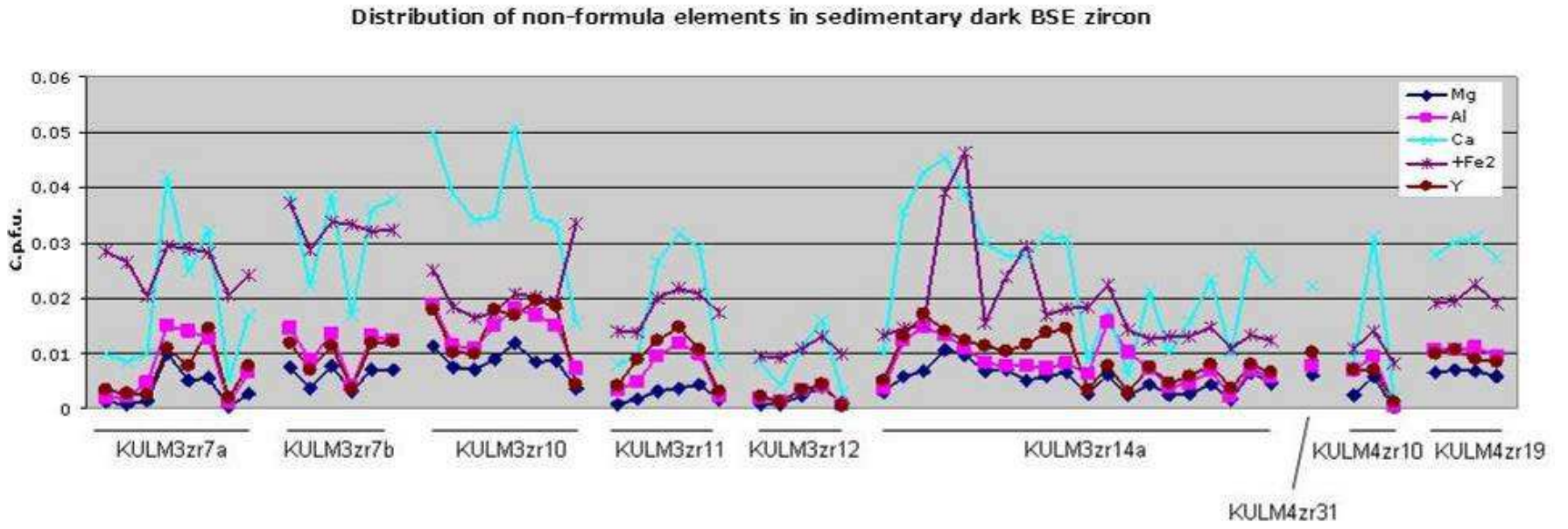


Figure 61 Distribution of non-formula elements (c.p.f.u.) in sedimentary dark BSE zircon

suggesting that a considerable number of points still have a very small contamination from clays. However the variation caused by clay contamination is very small, as is their effect on the overall chemistry, and therefore these data points have not been removed from the data set.

Despite most non-formula elements having relatively well-defined trends with Zr and Si depletion, overall Fe shows considerable spread when plotted against either Zr (Fig. 60e) or Si (Fig. 60f) and this spread cannot be linked to variations in Hf (Fig. 60g). Individual grains appear to show distinctive trends on Zr-Fe and Si-Fe plots but also on a number of different chemical plots involving non-formula elements (Fig. 60e & f). This suggests is that individual grains have slightly different chemistry and may indicate that changes in the local environment affect the chemical equilibrium in the dark BSE zircon.

The concentration and distribution of non-formula elements throughout dark BSE zircon (Fig. 61) reveal considerable variation between Ca and Fe, the most enriched non-formula element. Al and Y show relatively similar behaviour and are often present in similar quantities. Mg typically mimics the Al and Y profile but is usually slightly lower in concentration. Ca displays a similar pattern to Al and Y although the Ca enrichment is often greatly exaggerated by comparison, particularly when Al and Y are concentrated above 0.01 c.p.f.u.. Fe has the most distinctive profile, replicating the pattern of the other non-formula elements in some cases (zircon KULM3zr7a, KULM3zr11, KULM4zr19) while in other instances Fe appears totally independent of the other non-formula elements.

In summary, dark BSE zircon in sedimentary rocks is depleted in Zr and Si with a Zr/Si ratio that is slightly higher than unmodified zircon. Dark BSE zircon has a lower total c.p.f.u. than light BSE zircon and lower total wt%. The gain of non-formula elements displays a relatively well-defined substitution relationship with Zr and Si loss with the exception of Fe that shows considerable variability. Hf appears to remain relatively constant in light and dark BSE zircon.

In order to establish how chemical variations in dark BSE zircon vary, the following sections will examine the chemistry of individual zircon and how this relates to the individual properties of these

grains.

4.7.3 Group 1 dark BSE zircon individual grain study

4.7.3.1 Zircon KULM3zr7

Mosaic-like zircons have an overall low CL intensity but do exhibit intensity variations which mimic the BSE pattern i.e. light BSE = brighter CL (Fig.62a&b). This is generally considered unusual for zircon as CL normally shows an opposite zoning pattern to BSE (Lee and Tromp, 1995).

In the mosaic texture of KULM3zr7, Group 1 dark BSE zircon generally has a low EBSD IQ (blue-green colour), with light BSE zircon giving a moderate IQ EBSD pattern (predominantly green - yellow colour, Fig.62c). Small blotches of higher crystallinity appear within light BSE zircon domains but this is not coupled to a change in BSE contrast or CL intensity. The high IQ EBSD patterns (orange to red colour) domains correlate with segmented and strongly luminescent rims. Fig.62d shows the whole grain is in crystallographic continuity.

Zr and Si display very similar substitution relationships when plotted against a variety non-formula elements (Fig.62e). However, the substitutions involving Y are poorly defined and there is considerable scatter in the Fe data where no well defined relationship is observed. The poor correlation between Zr and Si depletion and Fe is probably due to the light BSE blocks also enriched in Fe (Fig.57f).

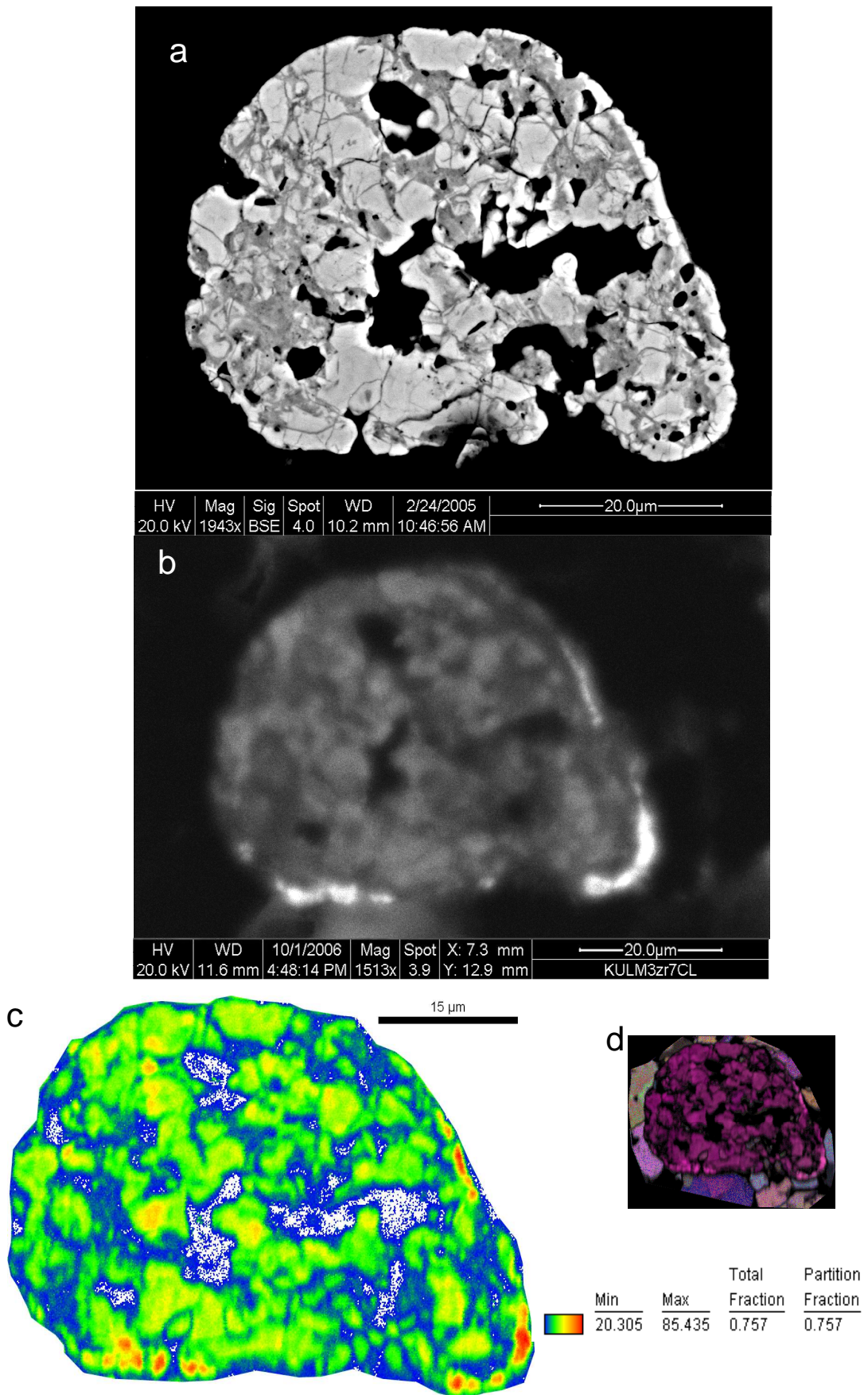


Figure 62 Detailed analysis of zircon KULM3zr7. Caption on page 208.

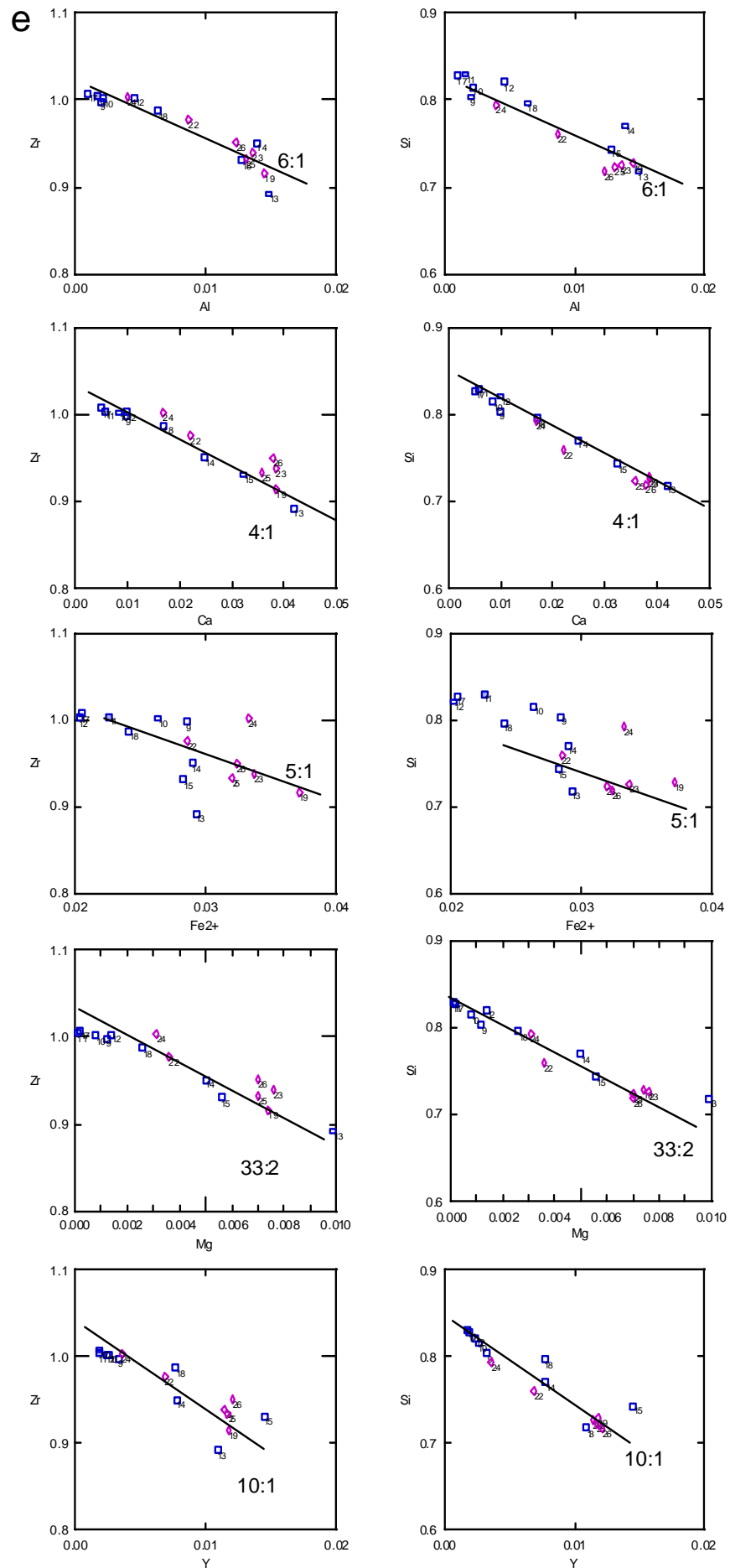


Figure 62 cont. Caption on page 208.

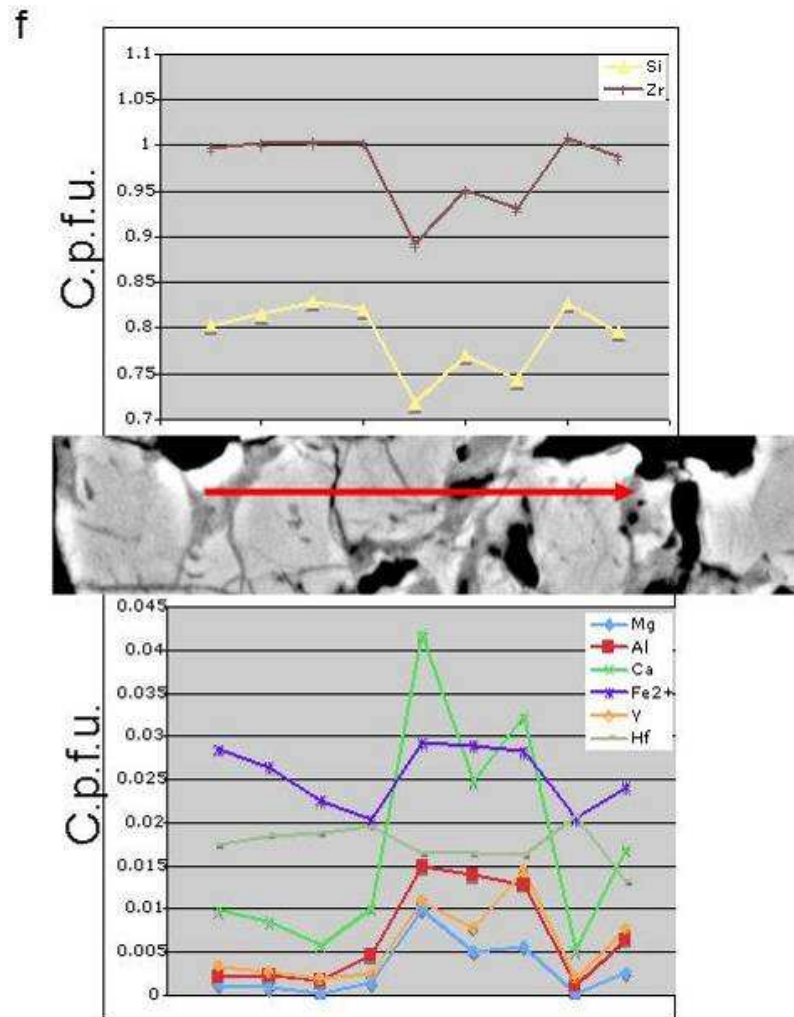


Figure 62 Detailed analysis of zircon KULM3zr7

a BSE image of Fig.48a showing light BSE zircon blocks within a dark BSE zircon matrix but with high BSE intensity segmented rim on right hand side of grain. **b** Complimentary CL image of **a** showing very CL intense rims that correlate to BSE intense segments. Dark BSE zircon has low CL intensity but light BSE blocks within dark BSE zircon vary from very low to moderate CL intensity. **c** EBSD IQ map of **a** with key. Shows strongly luminescent areas correlate to high EBSD IQ. The central areas to some high IQ domains that relate to the centres of light BSE zircon blocks. **d** is an IQ-inverse pole figure map from same scan, step size = $0.1\mu\text{m}$ and shows that the grain has remained in crystallographic continuity. **e** Element plots of EPMA analyses of zircon in **a**. **f** element profile from line scan analysis of through zircon in **a**. For line scan location on grain, see figure 57.

4.7.3.2 Zircon KULM3zr6

Zircon KULM3zr6 has a Group 1 dark BSE zircon domain that contains small areas of light BSE zircon (Fig.63a). A porous zone continues from the bottom end of the grain and round its left hand side, with the remainder of the grain predominantly composed of light BSE zircon. The porous zone will be considered in section 4.7.6. The zoning in the light BSE zircon is more striking in CL images which reveals a high intensity rounded core surrounded by low intensity euhedral shaped zones (Fig.63b). The presence of light BSE zircon in dark BSE zircon areas is also reflected in the CL signal as bright domains.

EBSD mapping reveals a strong correlation between the quality of the EBSD pattern and the CL intensity (i.e. high IQ zircon = bright CL zircon). The CL image almost exactly matches the black and white EBSD IQ map (Fig.63b&c). Group 1 dark BSE zircon has a typically low EBSD IQ. Around the central core in the main light BSE zircon domain, lower EBSD IQ zircon (green colour), which is dark in CL, relates to the lightest BSE zircon zone (Fig.63d). Where light BSE zircon is crystalline (orange to red IQ colour, Fig.63d&e), its margins with Group 1 dark BSE zircon form sharp and well-defined euhedral boundaries. However, where partially metamict light BSE zircon is in contact with Group 1 dark BSE zircon, the margins is more irregular (63d). An inverse pole figure EBSD map (inset, Fig.63d) shows the grain to be in crystallographic continuity.

EDX element mapping shows Group 1 dark BSE zircon is enriched in Al and Ca but also slightly enriched in Fe, Mg and U while depleted in Zr and Si (Fig.63f). Very small Al- and Fe- rich domains can also be observed.

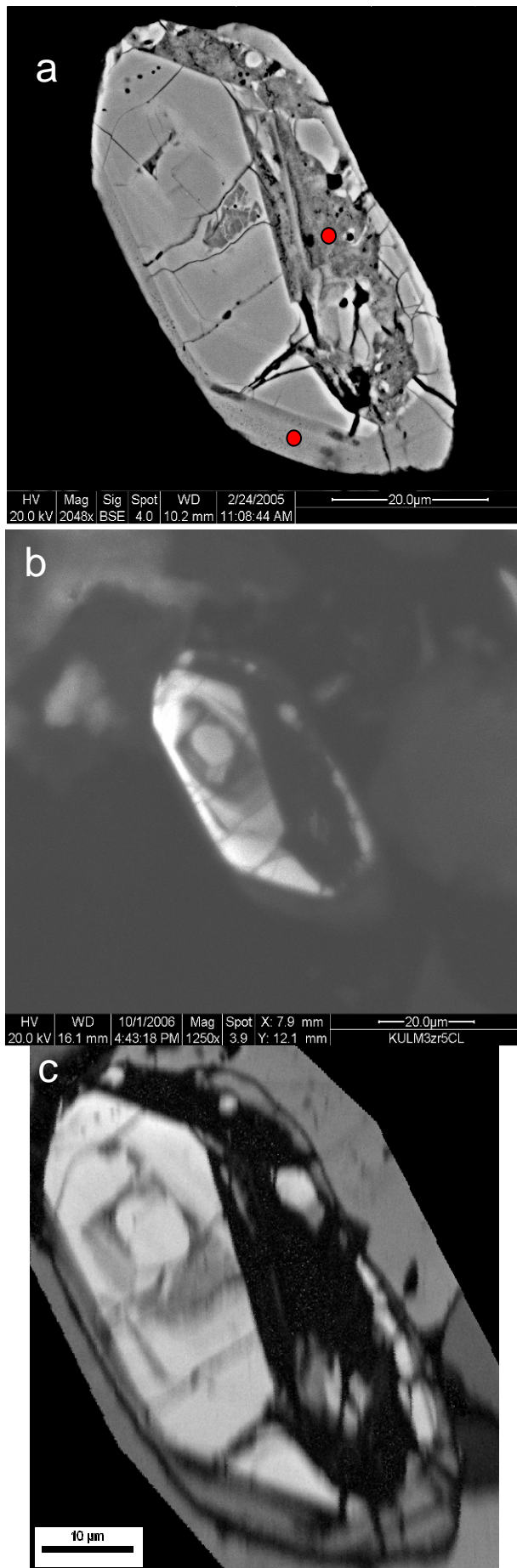


Figure 63 Detailed analysis of zircon KULM3zr6. Caption on page 213.

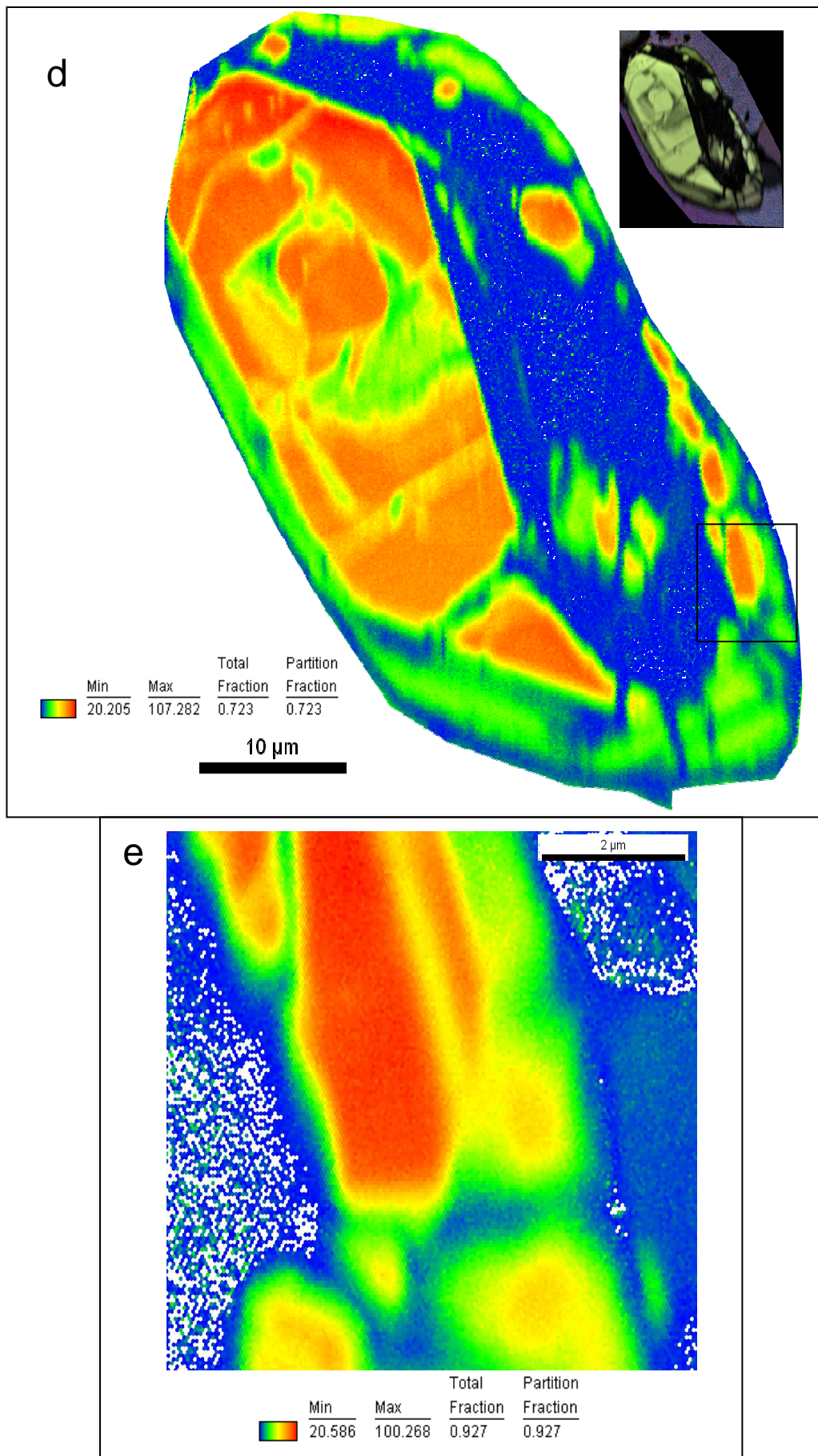


Figure 63 Detailed analysis of zircon KULM3zr6. Caption on page 213.

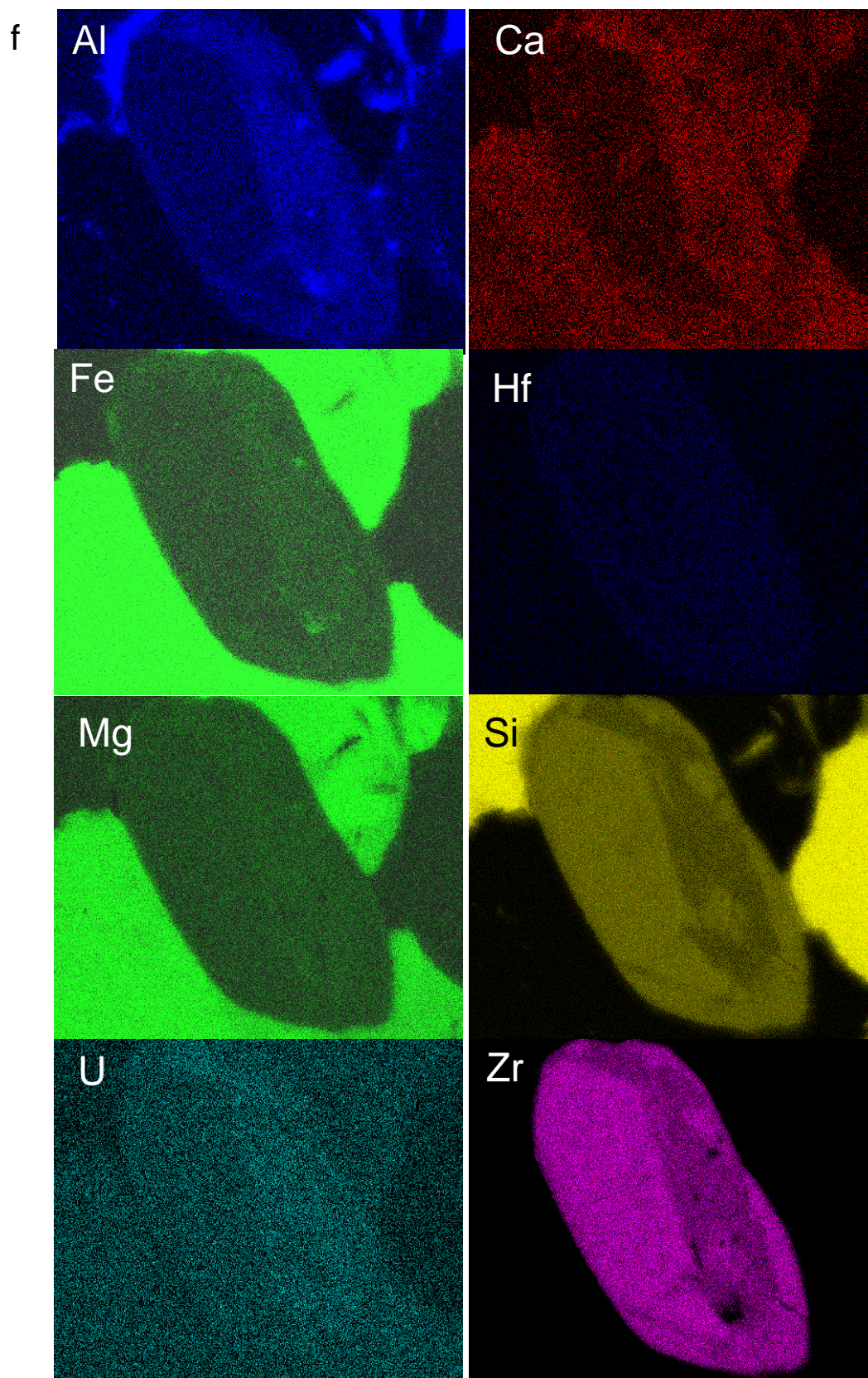


Figure 63 Detailed analysis of zircon KULM3zr6. Caption on following page.

Figure 63 Detailed analysis of zircon KULM3zr6

a BSE image of Fig.47d, red dots mark EDS analysis points. Group 1 dark BSE zircon dominates the right hand side of the grain with small domains of unmodified crystalline zircon. Bottom of grain is porous zircon zone. **b** Panchromatic CL image of **a**. **c** Black and white EBSD scanned IQ map of **a**. **d** Colour coded EBSD IQ map of **c**. Step size = 0.15 μ m. Box defines high resolution (0.05 μ m) EBSD IQ map in **e**. Inset to **d** is an IQ-IPF EBSD map plotted from same scan. **e** shows well-defined boundary between crystalline zircon and dark BSE zircon. Step size = 0.07 μ m. **f** EDX element maps of **a**. Contrast in element maps has been altered to emphasise various features and therefore concentrations are only relative within each individual map.

4.7.3.3 Group 2 dark BSE zircon individual grain study

In zircon grain KULM4zr31, lobes and elongate fingers of light BSE zircon form irregular margins with the inwardly penetrating Group 2 dark BSE zircon (Fig.64a). CL images identify a high CL intensity area with zoned euhedral margins, corresponding to light BSE zircon (Fig. 64b). Group 2 dark BSE zircon has a weak CL intensity but does exhibit slight variations in intensity. Light BSE zircon that forms irregular margins with Group 2 dark BSE zircon has a particularly low CL intensity, darker than the surrounding dark BSE zircon. EDX mapping of the area defined in Figure 64a, identifies variations in Zr, Si and Ca that correlate with BSE intensity (Fig. 64c). The dark BSE zircon, enriched in Ca and poor in Zr and Si, is chemically distinct from light BSE zircon with the elongate fingers of low CL – light BSE zircon being of similar composition to high CL – light BSE zircon. Zircon KULM4zr31 was analysed by EPMA spot analysis however despite the lack of visible inclusions in the microstructure, only two data points remain in the data set, one of which is light BSE zircon. Therefore to determine the composition of Group 2 dark BSE zircon, so that a comparison can be made with Group 1 dark BSE zircon in section 4.7.5, several grains containing the former have had to be considered. Zr and Si in Group 2 dark BSE zircon display identical well-defined substitution trends when they are each plotted against non-formula elements (Fig. 64g). These substitution trends have been summarised in Table 10.

High magnification (x8000), high resolution (75nm step size) EBSD mapping of the red defined area in Fig. 64a shows that fingers of low CL intensity-light BSE zircon have a significantly reduced EBSD IQ in comparison to both the high CL intensity-light BSE zircon domain and the low CL intensity-dark BSE zircon (Fig. 64d). As a general comment, the IQ of EBSD patterns from Group 2 dark BSE zircon increased considerably when a step size of <0.1 μ m was used for EBSD analysis. However, no appreciable increase in EBSD IQ was observed in maps collected using a step <0.075 μ m.

Inverse pole figure data from EBSD analysis shows that Group 2 dark BSE zircon shares the same crystal orientation as the host zircon (Fig. 64e). EBSD maps of zircon KULM4zr31 show a gradual

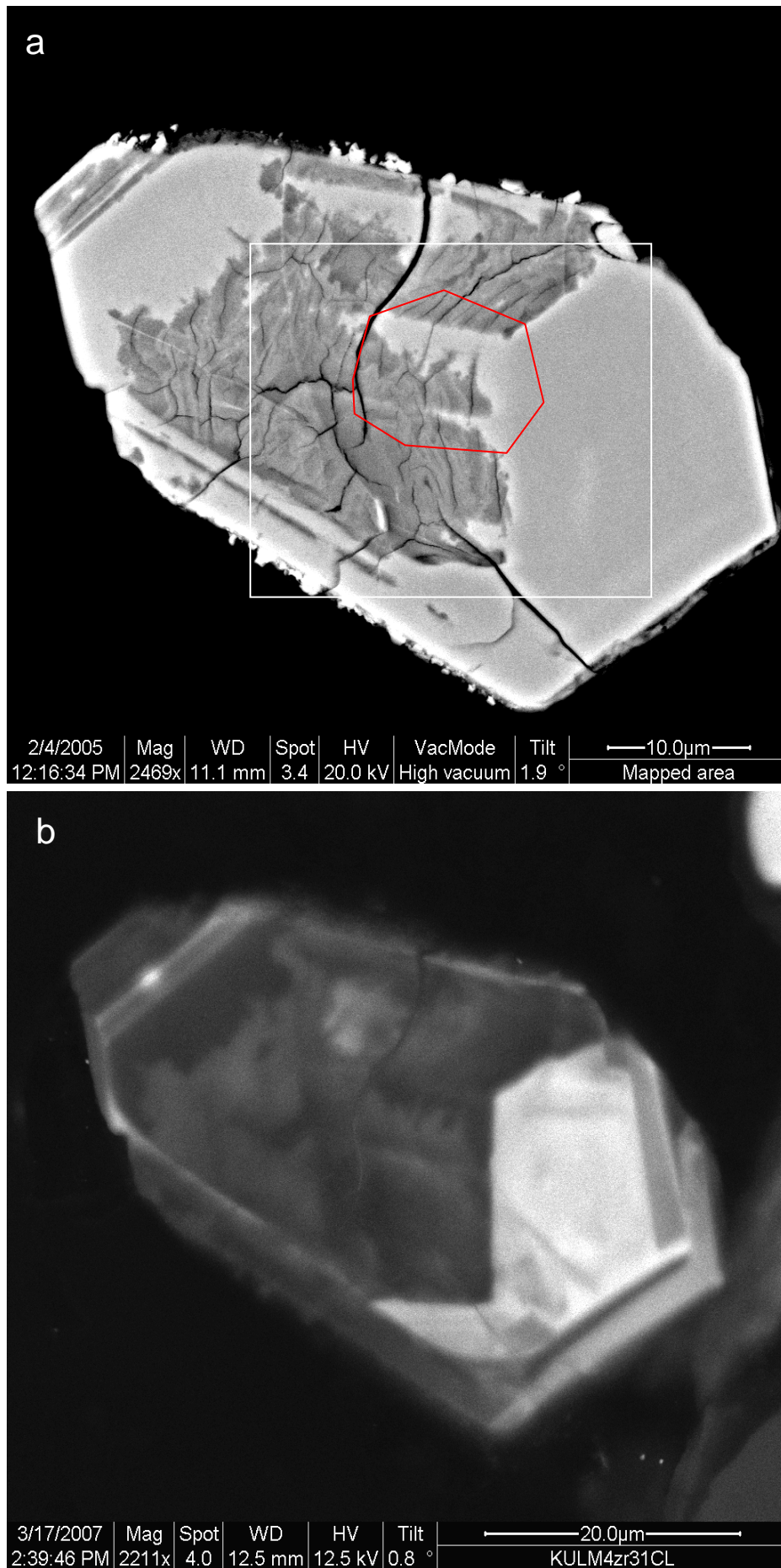


Figure 64 Detailed analysis of Group 2 dark BSE zircon. Caption on page 218

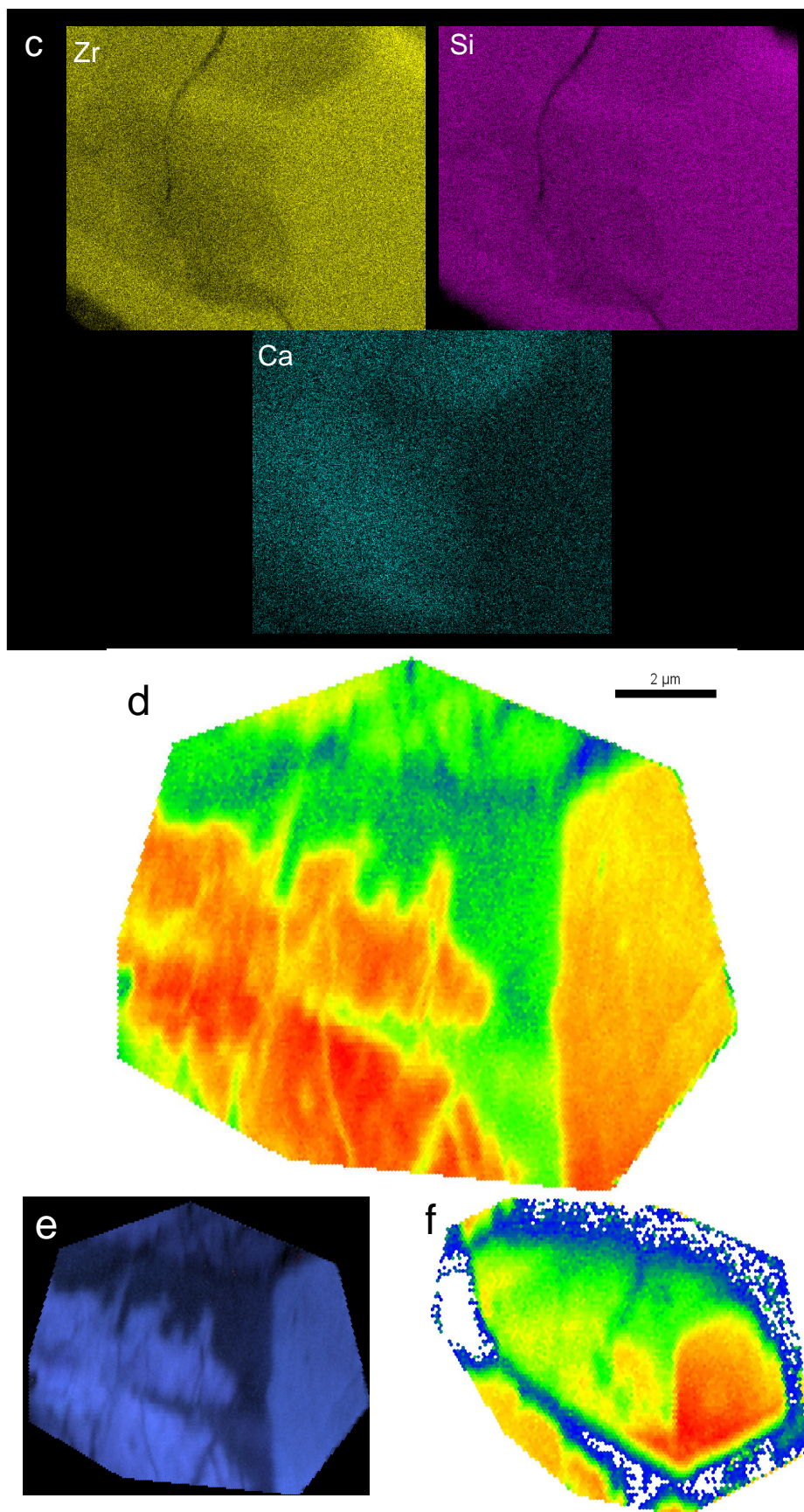


Figure 64 Detailed analysis of Group 2 dark BSE zircon. Caption on page 218.

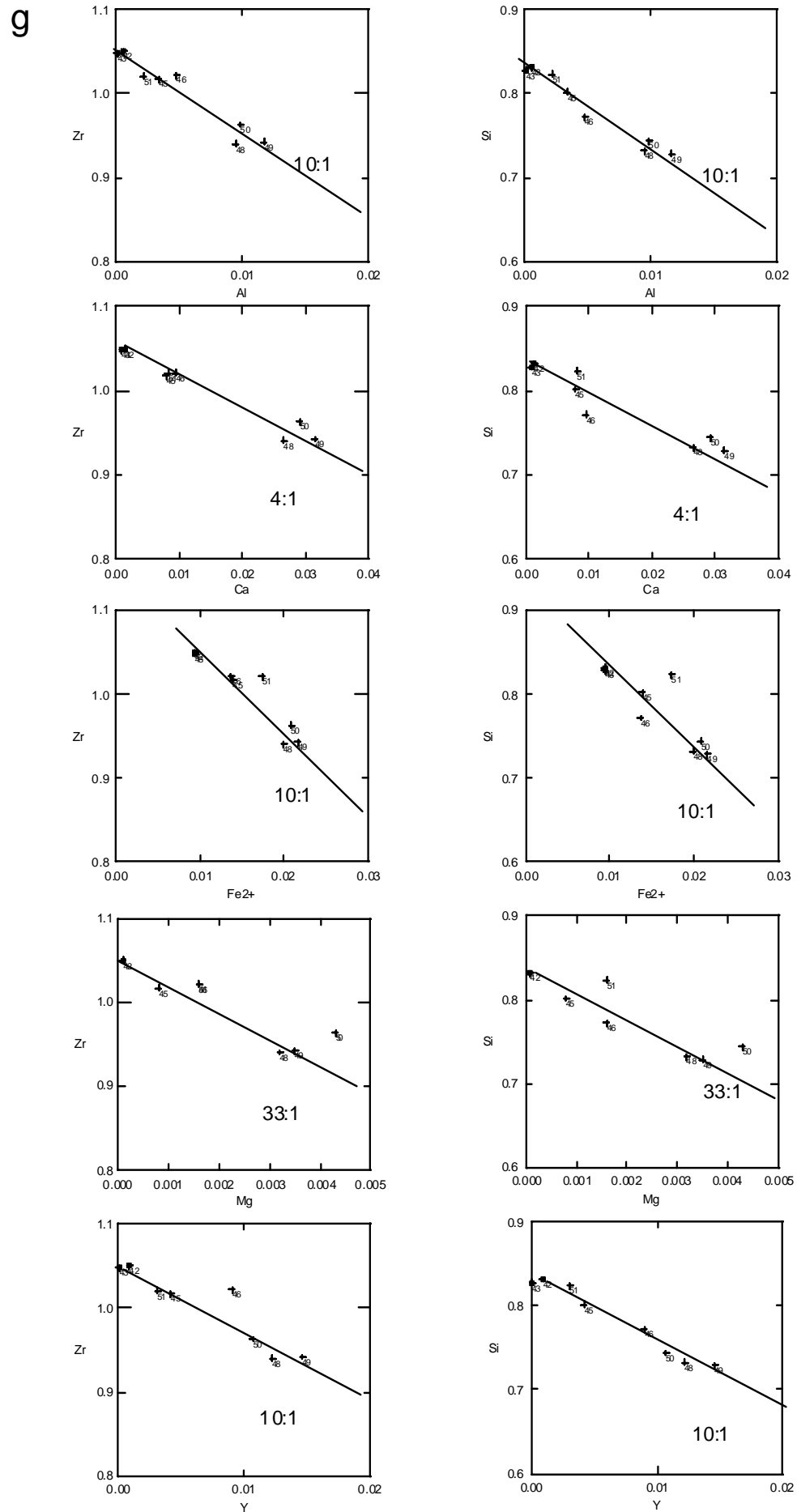


Figure 64 Detailed analysis of Group 2 dark BSE zircon. Caption on following page.

Figure 64 Detailed analysis of Group 2 dark BSE zircon

a BSE image of Fig.52c. Shows inward penetrating alteration front forming irregular margins with thin unmodified laths of zircon. Ribbed fractures present in the recovered Group 2 dark BSE zircon. Area defined in white box is EDX scanned area in **c** and area defined in red is EBSD scanned area in **d&e**. **b** CL image of **a** showing unmodified light BSE zircon laths adjacent to Group 2 dark BSE zircon have a very low CL intensity, even by comparison to dark BSE zircon. **c** EDX element scanned maps. **d** High resolution (0.075 μm step size) EBSD IQ map showing Group 2 dark BSE zircon is structurally recovered while unmodified low CL, light BSE zircon is metamict. Bright CL, light BSE zircon has high EBSD IQ patterns. **e** High resolution (0.075 μm step size) EBSD inverse pole figure (IPF) map of same area showing Group 2 dark BSE zircon recovery is epitaxial to the parent zircon. **f** Low resolution (0.3 μm step size) EBSD IQ map of whole grain in **a**. There is a strong reduction in EBSD IQ from bottom of the image to the top and this is due to charging along the top margin of the grain. **g** Element maps of Group 2 dark BSE zircon.

reduction in image quality towards the top of the images (Fig. 64f) and caused by charging along the top margin where the zircon meets the matrix. The euhedral boundary observed in CL imaging between the high CL intensity-light BSE zircon domain and the low CL intensity-light BSE zircon fingers within the dark BSE zircon, is mimicked by the EBSD IQ pattern.

In contrast to the findings from EBSD analysis of Group 1 dark BSE zircon, Group 2 dark BSE zircon produces a high to very high IQ EBSD pattern (orange to red colour). This is an important distinction between Group 1 and Group 2 dark BSE zircon.

4.7.4 Group 1 and 2 dark BSE zircon

Grain KULM3zr14 has an overall subhedral, slightly rounded shape (Fig.65a). The grain contains a light BSE zircon growth zone that mostly forms a euhedral margin with dark BSE zircon. However, in places, Group 1 dark BSE zircon forms fingers or domains that penetrate inwardly into light BSE zircon, disrupting euhedral zoning. The dark BSE zircon microstructure varies considerably and contains both Group 1 and Group 2 dark BSE zircon forms. Some outer dark BSE zircon domains are inclusion-free and contain thin, discontinuous spines of light BSE zircon. As such this is Group 2 dark BSE zircon. The core contains large holes and irregular shaped inclusions whilst exhibiting a highly disordered complex of dark BSE zircon, small and rounded low BSE intensity inclusions and very small rounded or irregularly shaped domains of light BSE zircon. This is Group 1 dark BSE zircon. Occasionally thin remnants of original euhedral zoning are preserved within the Group 1 dark BSE zircon. Fig.47J is a schematic diagram of the grain microstructure. CL imaging reveals a highly heterogeneous pattern where moderate intensity areas generally correlate to light BSE zircon (Fig. 65b). However, the margins of the zircon display very CL intense blotches around its margin.

IQ EBSD maps reveal that high IQ (red colour) areas relate to BSE intense areas i.e. light BSE zircon (Fig. 65c-i). However, not all light BSE zircon in this grain produces high IQ EBSD patterns and this is particularly true of light BSE zircon in light BSE-Group 2 dark BSE zircon domains (Fig. 65d-g). In these areas, light BSE zircon produces low EBSD IQ (green) whereas the adjacent

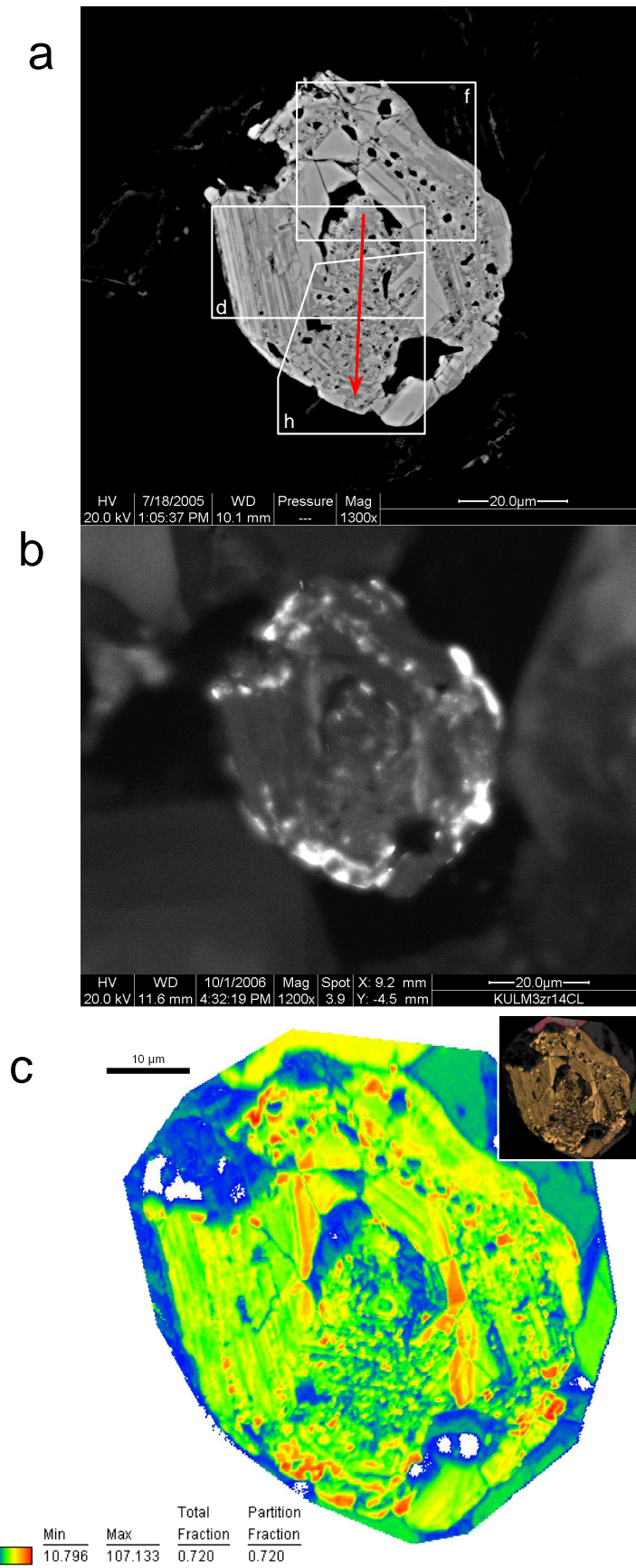


Figure 65 Detailed analysis of zircon containing both Group 1 and Group 2 dark BSE zircon. Caption is on page 226

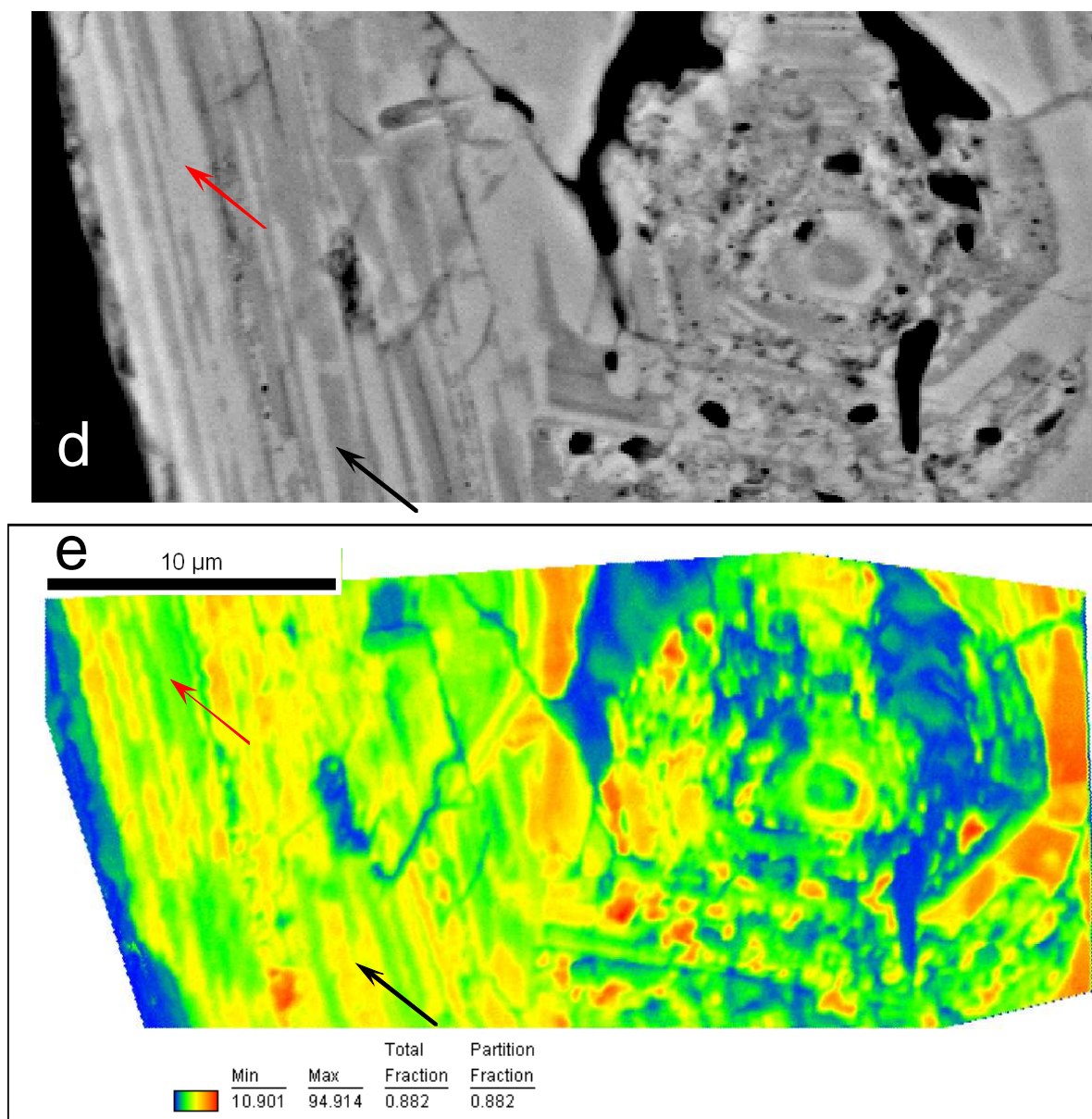


Figure 65 *cont.* Caption is on page 226

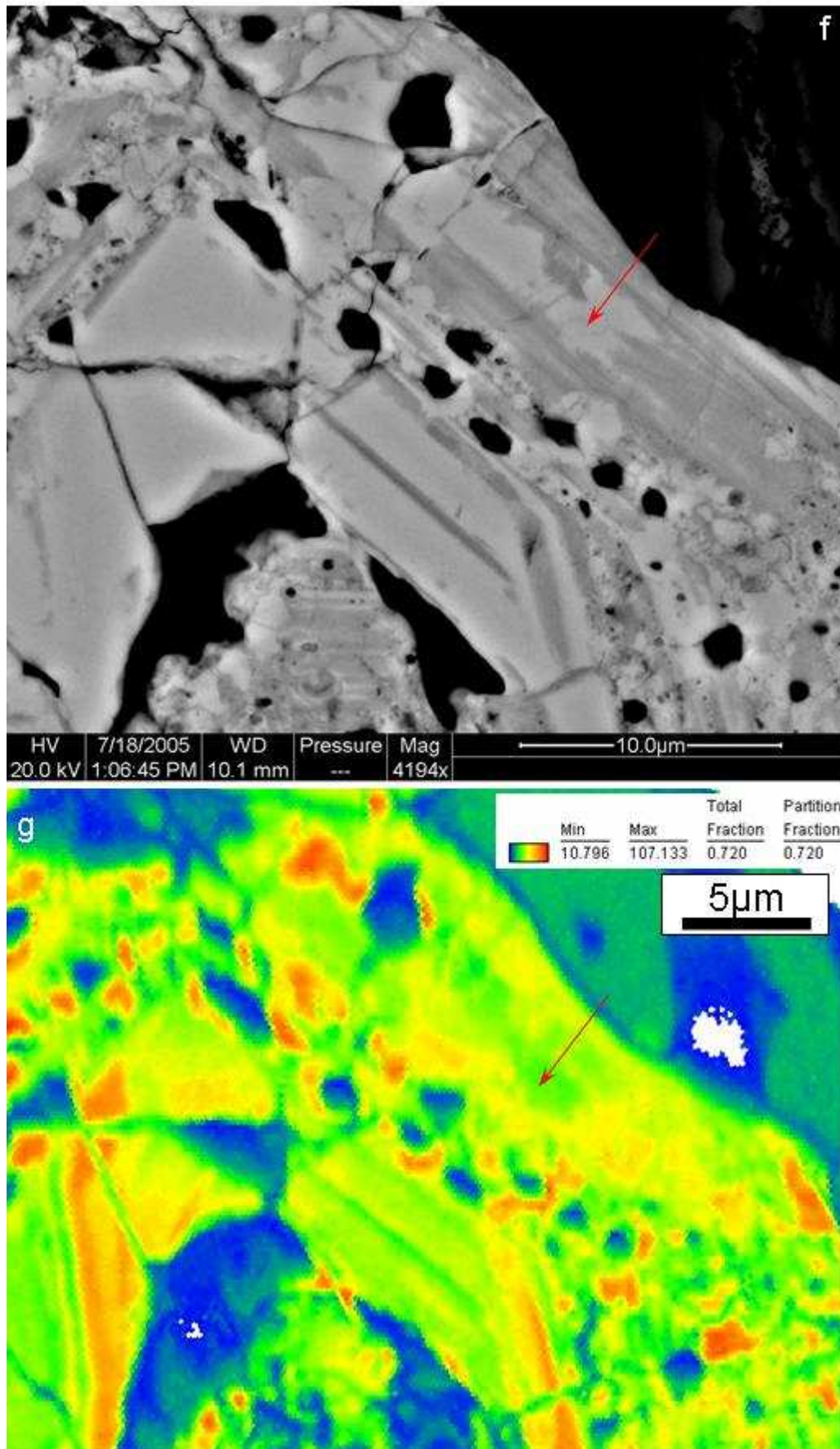


Figure 65 cont. Caption is on page 226

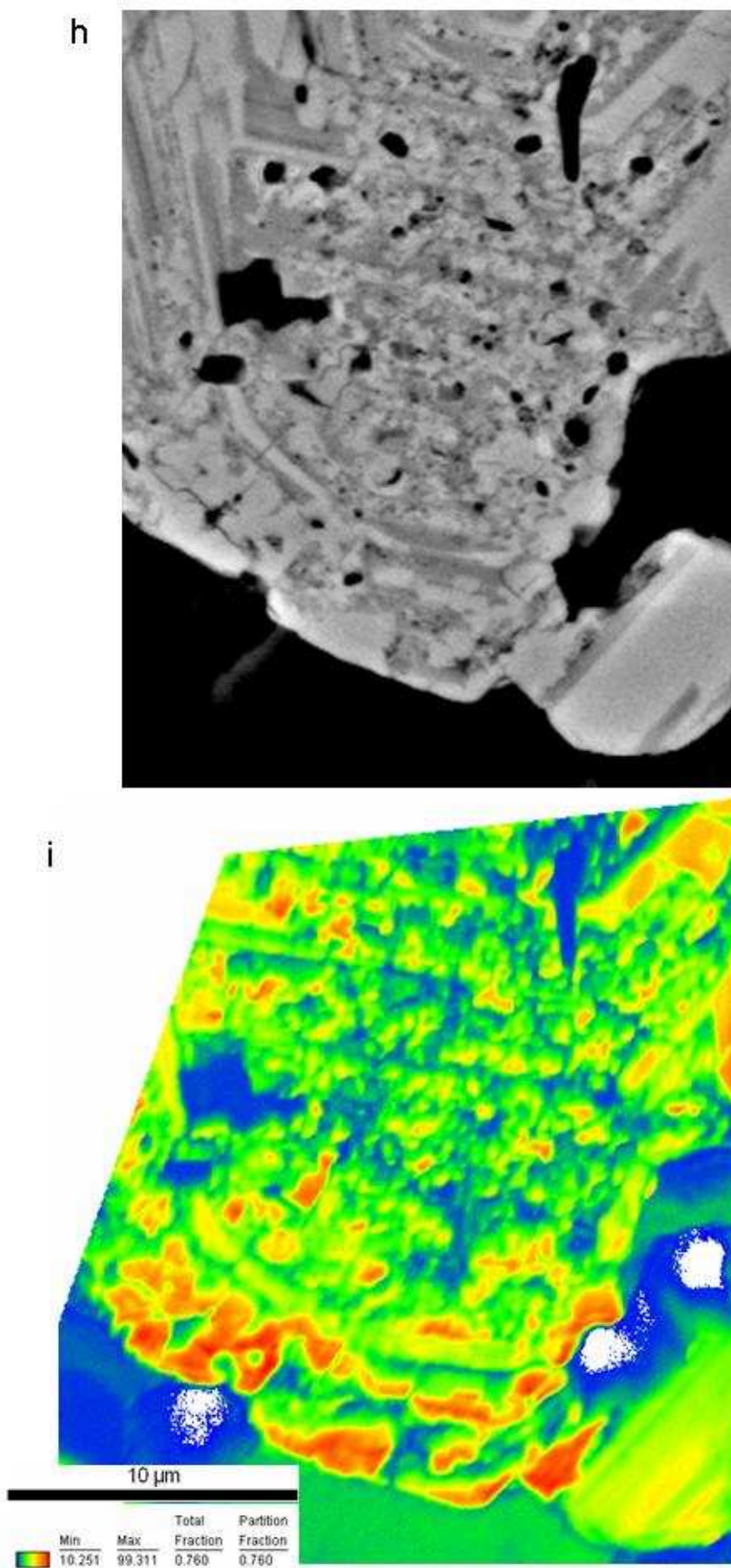


Figure 65 *cont.* Caption is on page 226

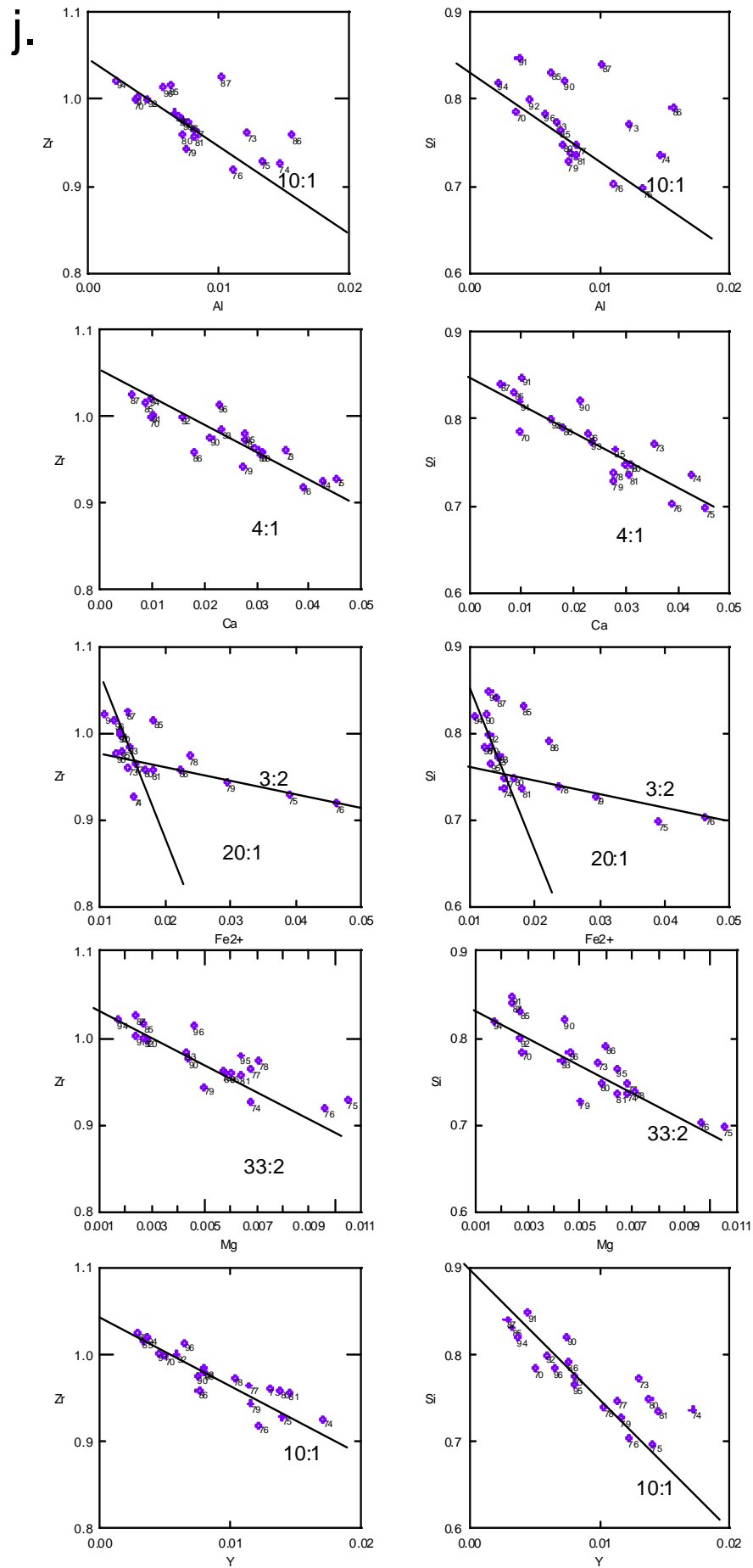


Figure 65 cont. Caption is on page 226

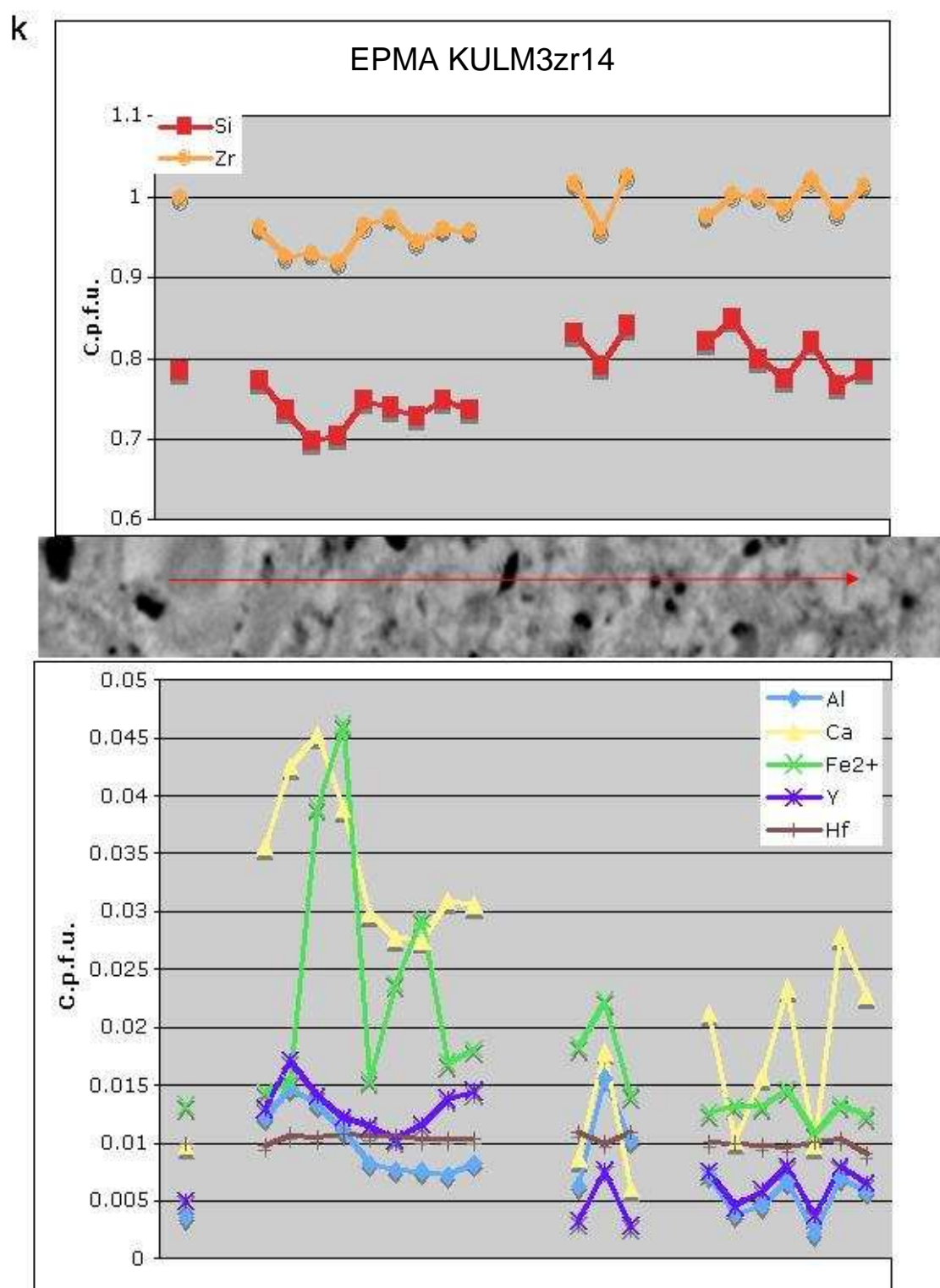


Figure 65 *cont.* Caption is on page 226

Figure 65 Detailed analysis of zircon containing both Group 1 and Group 2 dark BSE zircon

a BSE image of zircon KULM3zr14. Red line indicates location of EPMA line scan analysis at 2 μ m increments. Fig 47j shows schematic of features in **a**. **b** CL image of zircon in **a** showing generally low CL intensity but with some modest CL intensity in both light BSE zircon areas and Group 1 dark BSE zircon. However blotches in and around the grain have no apparent relation to BSE intensity. **c** IQ EBSD map of zircon in **a** with an IQ-inverse pole figure EBSD map is inset. Step size = 0.2 μ m. **c** shows that CL intense blotches relate to areas of high EBSD IQ while **e** demonstrates that the grains holds one crystal orientation. **d**, **f**, **h** are enlarged BSE images of areas defined in Fig.65a with **e**, **g**, **i** IQ EBSD maps of these areas respectively. **e** and **i** have a step size = 0.07 μ m and step size in **g** = 0.2 μ m. Red arrows in **d-g** point to metamict zircon. Black arrows in **d&e** indicate crystalline dark BSE zircon. **j** element plots from EPMA analysis of line defined in **a**. **k** Element profile of data along line of analysis defined in **a**.

Group 2 dark BSE zircon produce moderate to high IQ patterns (yellow and orange), evidence of structural recovery. This indicates that light BSE zircon in Group 2 dark BSE zircon is partially metamict whereas Group 2 dark BSE zircon itself represents metamict zircon that has undergone some form of structural recovery. EBSD analysis of Group 1 dark BSE zircon domain replicates the highly disordered structure observed in BSE imaging (Fig. 65h&i) with the Group 1 dark BSE zircon “matrix” generates low EBSD IQ patterns (blue to green) but all light BSE zircon within Group 1 dark BSE zircon areas produce moderate to high IQ patterns (yellow to red). The crystalline light BSE zircon in Group 1 dark BSE zircon is in contrast to the light BSE zircon in Group 2 dark BSE zircon which is partially metamict. Inverse pole figure data from EBSD analysis shows that the rounded crystalline domains within Group 1 dark BSE zircon share the same crystal orientation as the host grain (inset, Fig. 65c). This implies that the crystalline light BSE zircon represent parts of the original grain.

In CL imaging, strongly luminescence areas correlate to high EBSD IQ areas (Fig. 65b). The rest of the grain is weakly luminescent but light BSE – moderate to high IQ (yellow-orange) areas have a moderately intense luminescence.

EPMA analysis through the Group 1 dark BSE zircon domain in zircon KULM3zr14 reveals all non-formula elements, with the exception of Fe, show a reasonable correlation with Zr and Si depletion (Fig. 65j). The substitution trends observed in KULM3zr14 are the same as those in other sedimentary dark BSE zircon. However Fe-rich analyses that reveal a 3:2 substitution trend with Zr and Si in KULM3zr14 (Fig. 65j), are the same analyses that are enriched in all of the other non-formula elements. Analysis number 74 in Fig. 65j is the most Fe-rich analysis that lies close to a 10:1 substitution trend. However analysis numbers 75 & 76 that plot close to a 3:2 Zr:Fe trend, are found to cluster with analysis number 74 on other non-formula elements plots. This suggests that the enrichment of Fe in analysis numbers 75 and 76 is not at the expense of other non-formula elements. However, by studying the anomalous analyses removed from zircon KULM3zr14 (Fig. 58e), it shows analysis numbers 82-84 contained a Fe-rich component. and this is likely caused by inclusions of FeO that is also responsible for the unusual 3:2 Zr:Fe trend. The EPMA data profile

(Fig.65k) shows that where anomalous analyses in zircon KULM3zr14 have been removed coincides with very low BSE intense inclusions in the Group 1 dark BSE zircon microstructure and these inclusions probably represent minute FeO inclusions. It would also suggest that enrichment of those analyses that lie along a 3:2 Zr:Fe or Si:Fe trend probably reflect the influence of very small FeO inclusions. The effect these relatively small inclusions have on analyses is too small to be easily identified during the “weeding” process and was therefore not removed from the data set.

4.7.5 Chemical comparison of Group 1 & 2 dark BSE zircon

	All sedimentary dark BSE zircon	Group 1 dark BSE zircon KULM3zr14	Group 1 dark BSE zircon KULM3zr7	All Group 2 dark BSE zircon
Zr:Al	10:1	10:1	6:1	10:1
Si:Al	10:1	10:1	6:1	10:1
Zr:Ca	4:1	4:1	4:1	4:1
Si:Ca	4:1	4:1	4:1	4:1
Zr:Fe	20:1	20:1	5:1	10:1
Si:Fe	20:1	20:1	5:1	10:1
Zr:Mg	20:1	33:2	33:2	33:1
Si:Mg	20:1	33:2	33:2	33:1
Zr:Y	10:1	10:1	10:1	10:1
Si:Y	10:1	10:1	10:1	10:1

Table 10 Chemical substitutions in Group 1 and Group 2 dark BSE zircons

The substitution relationships between Zr and Si and the non-formula elements in sedimentary zircon are presented in Table 10. Group 2 dark BSE zircon has very similar Al, Ca and Y substitution trends to Group 1 dark BSE zircon. The most striking difference is the well-defined Fe trend in Group 2 dark BSE zircon. Group 1 dark BSE zircon shows significant scatter in Fe element plots and may be a consequence of the inclusion-rich nature of Group 1 dark BSE zircon. Mosaic zircon containing Group 1 dark BSE zircon appears to follow an enhanced Al substitution trend although the reasons for this are unclear. Group 1 dark BSE zircon typically displays more scatter in element plots whereas Group 2 dark BSE zircon follow much better defined substitution trends that is most likely due to the lack of inclusions. The average total c.p.f.u. of Group 2 dark BSE

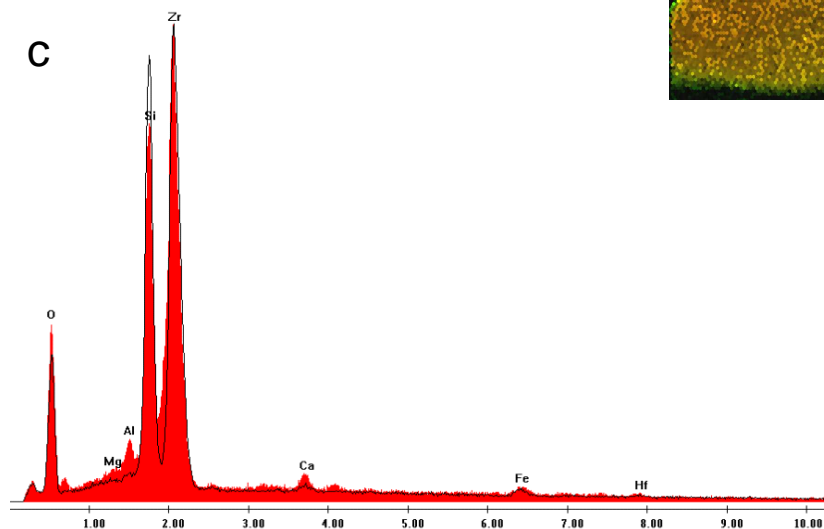
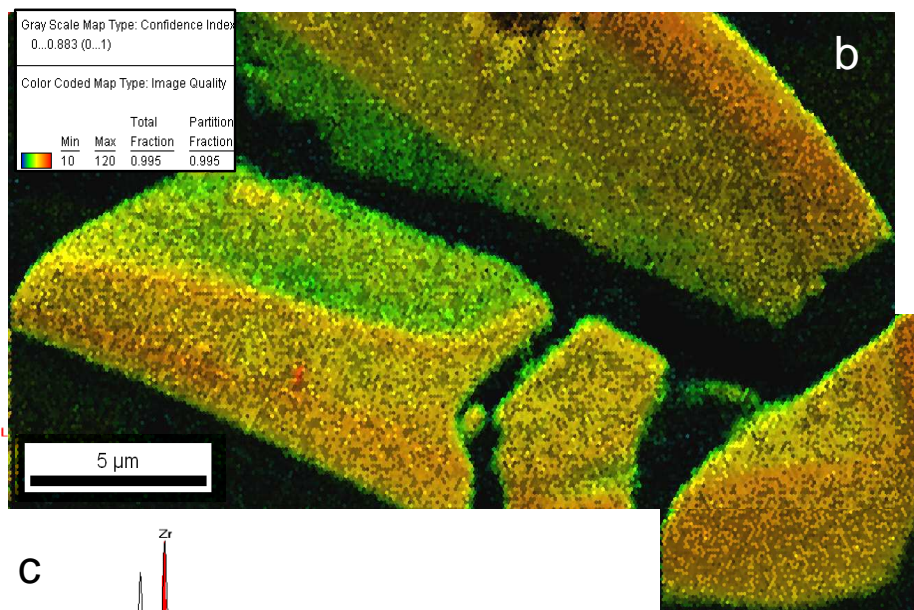
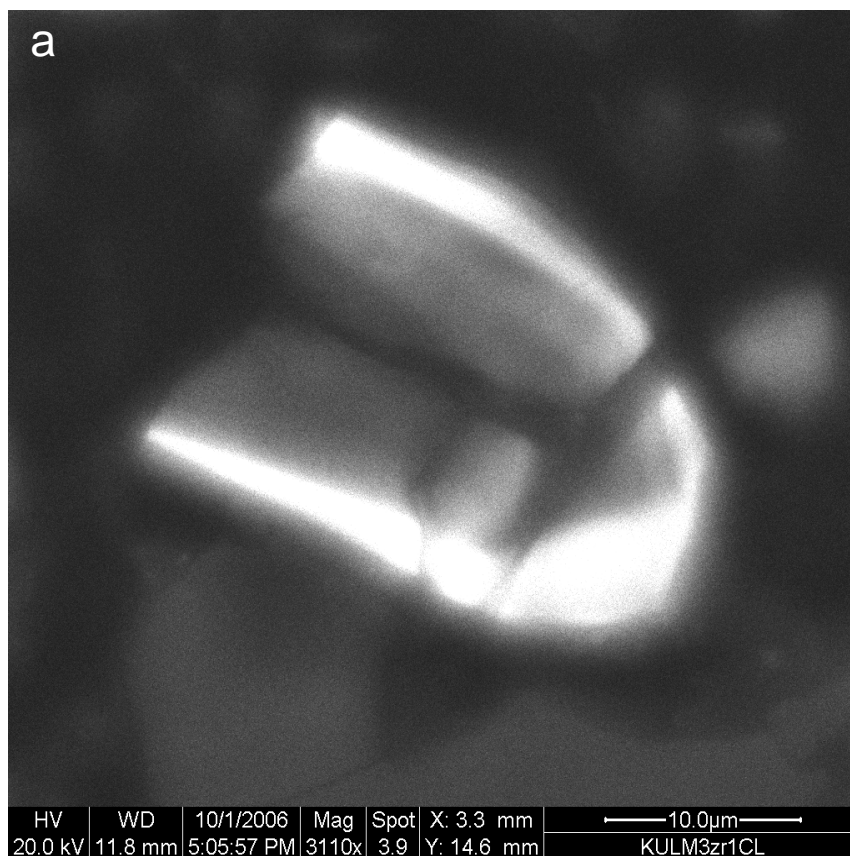
zircon is identical to Group 1 dark BSE zircon indicating that overall chemistry is very similar.

4.7.6 Pores in zircon

Porous growth zones have a low CL intensity although usually slightly higher than dark BSE zircon (Fig. 66a,63b). Zones with porous zircon have a low to moderate EBSD IQ (green - blue) (Fig. 66b and 58d) although Group 1 dark BSE zircon areas found within these zones have an even lower EBSD IQ (Fig. 58d). Chemically, zones with porous zircon are enriched in non-formula elements as determined by EDX analysis but this enrichment is usually not as pronounced in Al and Ca (Y cannot be determined in EDX analysis because it shares the same X-ray peak as Zr) compared to dark BSE zircon and Mg was not found to be present although may be Mg is concentrated in levels below the detection limits of the EDX. However, Fe does appear to be in equal concentrations in both porous zircon and dark BSE zircon (Fig. 66c). The main chemical distinction between porous and dark BSE zircon is the concentration of Zr and Si. EDX elemental maps show the porous zircon zone has similar Zr or Si concentrations as surrounding unmodified zircon and this contrasts with significant loss of Zr and Si in dark BSE zircon (Fig. 58d). Also, a spot analysis comparison between the porous and dark BSE zircon (normalised to Zr levels) reveals that porous zircon has a significantly lower Zr/Si ratio than dark BSE zircon (Fig. 66c).

Figure 66 Detailed analysis of porous zone in zircon. Figure on following page.

a CL image of Fig. 53a with complimentary, high resolution (0.075 μ m step size) EBSD CI-IQ map in **b**. **a** shows porous zone has a low CL intensity that correlates to low EBSD IQ in **b**. Strongly luminescent domains produce high EBSD IQ patterns. **c** Comparison of points from EDX spot analysis on zircon grain in Fig. 63a. Black unfilled line is spectra from porous zone analysis and red filled area is from dark BSE zircon analysis. The spectra has been normalised to the Zr peak.



4.8 Interpretation

4.8.1 Group 1 Dark BSE zircon

Textural evidence suggests the margins of Group 1 dark BSE zircon have formed sub-euhedral “outgrowths” (Fig.47k). It is unlikely these outgrowth-like features could survive sedimentary reworking and, as such, must form after the zircon is incorporated into the sediment. The production of holes and cavities in Group 1 dark BSE zircon is a demonstration of volume change and are also linked with the presence of inclusions in Group 1 dark BSE zircon. These features are related to dissolution-precipitation processes that have also been described in Chapter 3. What has now been identified as Group 1 dark BSE zircon is simply referred to as dark BSE zircon in Chapter 3 but they are considered to be effectively the same as both have identical properties and thought to form by the same process.

4.8.1.1 Discontinuities in the grain microstructure

Light BSE zircon that encases Group 1 dark BSE zircon often display radial fractures caused by the swelling of internal metamict growth zones (upto 18%). Zircon grains preserving evidence of metamict-induced fractures within the rock matrix indicate that fracture development occurred in-situ and post-dates the incorporation of the zircon into the sediment. Metamict generated features are likely to form in young, U-rich grains where damage has accumulated rapidly. Once the protecting light BSE zircon has failed, the metamict generated fractures provide a pathway for fluids to penetrate the metamict layer (Lee and Tromp, 1995) and contact with the fluid phase enables the damaged zircon to alter.

The timing of metamict-generated fractures may be important in the developing microstructure of the dark BSE zircon. There are many variables that control metamict-induced fractures in zircon which have been studied comprehensively by Lee and Tromp (1995). If a simple example of a two shelled zircon, with a metamict inner core, is considered, there are three factors believed to be of greatest importance: the thickness of the confining crystalline zircon (z_c), the thickness of the

metamict zircon (z_m) and the degree of metamictization in the damaged volume. The point at which metamict related fractures propagate through the zircon is related to these factors. If the z_c/z_m ratio is large, the degree of metamictization required to fracture the confining zircon will be greater than in a low z_c/z_m zircon. Therefore if metamictization can generate fracturing in a high z_c/z_m zircon, the metamict domain will alter much more readily on exposure to the fluid phase because the degree of metamictization required to fracture z_c will be greater than a low z_c/z_m zircon. However, fracture development is inhibited as confining pressure increases. Fracture generation from metamict domains at higher confining pressures (e.g. at peak diagenesis *c.*100°C), will require a higher degree of radiation damage and hence the rate at which metamict zircon alters may increase. The rate of alteration is possibly further enhanced by the higher temperatures at which this happens.

4.8.1.2 Volume loss in Group 1 dark BSE zircon and Zr mobility

The shrinkage in volume (upto 18%) of Group 1 dark BSE zircon from metamict zircon can account for the creation of some of the pores and cavities in Group 1 dark BSE zircon domains. However in some cases the cavities and pores constitute far more than an 18% volume change (e.g. Fig. 48a). Minute zircon outgrowths on the margins of zircon can be spatially linked, by metamict generated fractures, to Group 1 dark BSE zircon domains (Fig.54b&c). Furthermore, the fractures that link these features have been sealed by dark BSE zircon, evidence that Zr is mobilised on a microscopic scale from the Group 1 dark BSE zircon zone to the margin of the grain. Zircon outgrowths are also observed on the margins of completely unmodified zircon grains. These grains are apparently distal to zircons that display evidence of dissolution implying Zr may also be mobilised over macroscopic scales within the thin section. However, as thin sections only allow a 2-D view of the rock, it may be in some cases that zircons that display dissolution lie proximal to unmodified zircons preserving outgrowths but are not intersected by the thin section.

Zr transported by the fluid phase from the site of dissolution can account for the relative overabundance in the volume of pores and cavities generated in dark BSE zircon. However there is still a striking mismatch between the volume of cavities and pores created in Group 1 dark BSE

zircon compared with the low volume of zircon outgrowths in sedimentary rocks.

4.8.2 Group 2 Dark BSE zircon

4.8.2.1 Character

Irregularly shaped domains of dull CL-light BSE zircon within Group 2 dark BSE zircon produce low EBSD IQ patterns indicating metamict zircon. EBSD analysis of Group 2 dark BSE zircon however gives a high EBSD IQ which is coupled to a modest increase in CL. Metamict zircon has the same chemical signature as surrounding bright CL, fully crystalline light BSE zircon yet Group 2 dark BSE zircon is enriched in non-formula elements and depleted in Zr and Si. The irregular boundary between the chemically modified but structurally recovered Group 2 dark BSE zircon and the chemically unmodified, but metamict, light BSE zircon represents the limits of an inward penetrating alteration front.

Group 1 and Group 2 dark BSE zircon are chemically very similar. However, Group 1 dark BSE zircon can vary considerably in microstructure as there are instances where Group 1 dark BSE zircon lacks porosity resulting in a microstructure very similar to Group 2 dark BSE zircon. Therefore a key observation in distinguishing between Group 1 and Group 2 dark BSE zircon is the difference in the EBSD IQ. The different crystallographic properties of Group 1 and Group 2 dark BSE zircon suggest they have contrasting mechanisms of formation. A further observation is Group 2 dark BSE zircon is only found in domains that are in contact with the matrix, often beside carbonate cement. As a consequence, Group 2 dark BSE zircon may be exposed to fluids for most its history in the rock.

4.8.2.2 Process of Group 2 dark BSE zircon formation

The perfect preservation of the parent grain shape in the product phase and the complete absence of inclusions or porosity would suggest Group 2 dark BSE zircon has not formed from zircon that has been taken into solution. Therefore it is likely Group 2 dark BSE zircon formed from a solid-state

reaction. As Group 2 dark BSE zircon forms from the alteration of metamict zircon, it indicates that the formation of Group 2 dark BSE zircon occurs in an environment where metamict zircon does not readily go into solution. The most likely scenario where this could happen is if the surrounding fluid phase is saturated with respect to Zr. Group 2 dark BSE zircon has exactly the same total c.p.f.u. as Group 1 dark BSE zircon implying that hydrous species are again important.

The microstructure, chemistry and crystallographic properties of Group 2 dark BSE zircon are very similar to the structurally recovered, non-formula element-rich reaction rims in metamict zircon observed by Geisler et al. (2003a) after experimental hydrothermal alteration. Geisler et al. account for these reactions by the diffusion of water through the amorphous volume which acts as the catalyst for the structural recovery process. A recrystallisation front follows at some unspecified distance behind whereby the nanocrystalline product phase incorporates non-formula elements into unreacted amorphous remnants. This interpretation is for metamict zircon in hydrothermal fluid above 200°C. Below 200°C only minor structural recovery is observed and simply described as “a structural recovery front” (Geisler et al., 2003a) instead of recrystallisation. Zircon was exposed to hydrothermal fluids for 72 hours in this experiment. A similar diffusion driven solid-state recrystallisation mechanism is likely to generate Group 2 dark BSE zircon. Although structural recovery in metamict zircon was very limited in these laboratory experiments by Geisler et al. below 200°C, these effects took place over a period of hours. The presence of similar features in Group 2 dark BSE zircon from sedimentary rocks would suggest that, over geological timescales, extensive structural recovery can occur <100°C.

There would appear to be subtle differences between the observations made by Geisler and co workers in the reaction rims of metamict zircon and Group 2 dark BSE zircon. Although diffusion of hydrous species through the amorphous volume is likely, evidence from EBSD analysis of Group 2 dark BSE zircon and adjacent metamict zircon would suggest that the recovery front follows closely behind where hydrous species have diffused. Epitaxial recovery of the crystalline structure in Group 2 dark BSE zircon dictates that crystallographic information must be transferred from the crystalline remnants within the metamict phase. Observation made from moderately

metamict zircon revealed that crystalline islands present in the amorphous matrix remain in crystallographic continuity with the parent (e.g. Meldrum et al., 1998; Salje et al., 1999), however these papers also state that in more heavily radiation damaged zircon (i.e. where overlap of amorphous clusters beyond the 2nd percolation point) crystalline remnants may not be in crystallographic continuity. This implies that there must remain a sufficient volume of crystalline structure within the metamict zircon for Group 2 dark BSE zircon to develop. These crystalline remnants will act as nucleation points for recovery.

It is likely Group 2 dark BSE zircon is nanocrystalline and this allows the efficient transfer of fluid along crystal boundaries to the recovery front (Geisler et al., 2003a). However, it seems improbable that non-formula elements in Group 2 dark BSE zircon are concentrated into amorphous remnants within the recovered phase (Geisler et al., 2007). The presence of non-formula elements in amorphous remnants within the recrystallised body indicates that amorphous domains would be in communication with the fluid phase. If this is the case then it is likely that the non-formula element-rich amorphous domain will recrystallise. Therefore it would appear more likely that the hydrous species diffusing into metamict areas drive a cation-exchange process whereby non-formula elements may be substituted into the crystal structure of Group 2 dark BSE zircon.

Once diffusion of hydrous species begins, the crystal structure that has recovered provides protection to the metamict area from dissolution. Therefore once the formation of Group 2 dark BSE zircon begins in a metamict domain it cannot switch to Group 1 dark BSE zircon. This may explain that while zircon grains may contain separate domains of Group 1 and Group 2 dark BSE zircon, Group 1 dark BSE zircon is not found within Group 2 dark BSE zircon. However, if conditions permit, it seems that it may be possible for Group 2 dark BSE zircon to form in Group 1 dark BSE zircon domains.

It is not clear how the diffusion-driven structural recovery cation-exchange mechanism that forms Group 2 dark BSE zircon operates at an atomic scale. This illustrates the need to analyse the

reaction fronts between metamict zircon and Group 2 dark BSE zircon using high-resolution techniques (e.g. HR-TEM) to better understand this process.

4.8.2.3 Metamict zircon in Group 2 dark BSE zircon

Remnants of irregularly shaped metamict light BSE domains in Group 2 dark BSE zircon are evidence of a reaction front and that the alteration to Group 2 dark BSE zircon has not reached completion (Fig. 64, 65). Although, some light BSE stripes in Group 2 dark BSE zircon domains appear to have remained unmodified (Fig. 65), EBSD analysis reveals these stripes have a low IQ and, as such, are metamict. Zircon will remain unmodified if the amorphous volume has not reached the 1st percolation point as the amorphous clusters are not interconnected. The interconnection between amorphous areas is considered crucial to allow the diffusion of the hydrous species through the metamict area. Perhaps when structural recovery happened, the amorphous volume in the light BSE stripes had not yet reached the 1st percolation point whereas the surrounding body was more radiation-damaged. This is probably related to the distribution of U within the original grain: zircon that has formed Group 2 dark BSE zircon was more U-rich than the now metamict light BSE zircon. Unfortunately EDX scans or spot analysis does not reveal any variation in U-content between these areas but this is probably due to the thin width of (<1µm thick) stripes and low detection limits of EDX. After structural recovery of Group 2 dark BSE zircon, damage has continued to accumulate resulting in the metamictization of light BSE zircon stripes. It has remained subsequently unmodified because either the fluids that catalyse these reactions are not available or the rock has reached a temperature too low for diffusion to be efficient.

4.8.2.4 Discontinuities in the grain microstructure

The presence of apparently randomly orientated cracks and fractures within Group 2 dark BSE zircon indicates the recovered volume is strained. This can be explained by the shrinking of the amorphous volume upon structural recovery as in its amorphous state, zircon can be upto 18% less dense than crystalline zircon. As the zircon structure is recovered, the density increases and the

resulting strain creates irregular vein-like discontinuities within the recovered microstructure. Strain related discontinuities will probably allow more efficient transport of the fluid phase to the recovery front. As fluids infiltrate along these cracks in the grain, the recovery front spreads outward from these cracks and through the damaged zone (Fig.52a).

4.8.3 Dark BSE zircon – summary and general comments

The features of Group 1 and Group 2 dark BSE zircon are summarised in Table 11.

	Group 1 dark BSE zircon	Group 2 dark BSE zircon
<u>Microstructure</u>	Inclusions, cavities and holes, domains of light BSE zircon	Cracks and light BSE stripes
<u>Light BSE zircon in dark BSE zircon</u>	Mainly fully crystalline	Mostly metamict
<u>Fractures</u>	Associated with radial fractures in outer light BSE zircon	Cracks generated from internal strain
<u>Inclusions</u>	Xenotime and matrix minerals composition	None
<u>EBSD</u>	None to low IQ	Moderate to high IQ
<u>Crystallography</u>	Randomly orientated nanocrystalline zircon	Epitaxial nanocrystalline zircon
<u>Composition</u>	Non-formula element rich	Non-formula element rich
<u>Fluid Composition</u>	Initially undersaturated in Zr	Saturated in Zr

Table 11 Summary of dark BSE zircon properties

Group 1 and Group 2 dark BSE zircon form by different mechanisms but both appear to be “catalysed” by fluids. The key difference would appear to be the concentration of Zr in the fluid phase rather than controls relating the properties of the individual grain (i.e. metamict state). Solutions undersaturated in Zr will probably favour alteration of metamict zircon via a dissolution-precipitation mechanism whereas solutions saturated in Zr will more likely allow a diffusion-driven structural recovery cation exchange mechanism. The relative absence of Group 2 dark BSE zircon in greenschist facies metasedimentary rocks is further evidence that argues local environmental controls are crucial in dictating by which process metamict zircon alters. These environmental controls will be considered in Chapter 6. It is also possible that the polyphase nature of the original zircon could possibly be a controlling factor in the production of either Group

1 or Group 2 dark BSE zircon.

The average weight percent total of Group 2 dark BSE zircon is 95.9wt% (± 2.1) and is very similar to wt% totals in Group 1 dark BSE zircon 96.0wt% (± 2.6). This may indicate that the volume of microporosity in Group 1 dark BSE zircon is similar to the volume of nanoporosity in Group 2 dark BSE zircon that allows communication of the fluid phase with the structural recovery front. However, the generally low weight percent totals are likely to be due to hydrous species and until their concentration can be accurately quantified, the volume of micro- and nano-porosity in dark BSE zircon cannot be determined. Due to the heterogeneous crystal structure of radiation damaged zircon at mesoscopic scales, crystalline remnants within the amorphous fraction will be more resistant to alteration by the fluid phase. Therefore, it is likely these remnants of original crystalline zircon will be preserved within the recrystallised body of both Group 1 and Group 2 dark BSE zircon. This is analogous to unreacted fully crystalline domains found in Group 1 dark BSE zircon at the microscopic scale (e.g. Fig. 63a). Isolated amorphous clusters in crystalline zircon will also be preserved as they are protected from the fluid phase.

The rate at which forms is worth attention. Although there is no way to constrain the absolute rate at which Group 1 and Group 2 dark BSE zircon develop in the natural environment, the absence of metamict zircon associated with Group 1 dark BSE zircon suggests that the dissolution-reprecipitation process is more efficient than the diffusion-driven structural recovery where metamict domains persist in and around the margins of Group 2 dark BSE zircon. This may suggest that if conditions permit, diffusion-driven structural recovery is a background process to Group 1 dark BSE zircon. The fact that diffusion-driven recovery is slower than dissolution-reprecipitation is not a surprising conclusion, particularly as diffusion is likely to be sluggish at low temperatures in metamict zircon.

4.8.4 Segmented rims on Group 1 dark BSE zircon

Light BSE zircon segmented rims have a high CL signal intensity and are fully crystalline as determined by EBSD. Light BSE zircon segmented rims are occasionally found partially

surrounding the edge of Group 1 dark BSE zircon where it is connected to the matrix and especially when the grain is almost completely composed of Group 1 dark BSE zircon. These rims are chemically unmodified, have a high CL signal intensity and are fully crystalline as determined by EBSD. These characteristics suggest it is an original feature of the parent grain. Segmentation would have occurred during the swelling of the metamict volume interior. Strongly luminescent zircon rims are a feature also observed in other studies (Corfu et al., 2003).

4.8.5 Porous zones in zircon

Pores in zircon are concentrated within individual growth zones or domains and therefore their formation must be linked to the original chemistry of that zone. Radial fractures in the outer light BSE zircon that surrounds pore-rich zones are usually fractured perpendicular to their boundary. When analysed, porous zones give a low intensity CL signal and low to moderate IQ EBSD patterns. These features all suggest that porous zones are now metamict. SE images may suggest that some pores may in fact be inclusions. Due to the resolution limitations of the SEM it is not clear whether these are pores, mineral inclusions or possibly fluid inclusions. EDX analysis shows that porous zones in zircon are composed of zircon with a very slight enrichment of non-formula elements and, in particular, Fe (Fig.66c). A feature of its chemistry is that porous zircon has a very similar Zr/Si ratio to unmodified zircon and is lower than dark BSE zircon Zr/Si ratio. The BSE intensity of the zircon between the pores suggests it has a typical composition of unmodified light BSE zircon. This implies that the pores may be enriched in Fe and other non-formula elements and possibly represent inclusions.

Fe enrichment suggests the whole zone became altered in the presence of a fluid and for this to happen it suggests the porous zone was metamict as indicated by the radial fractures present in surrounding light BSE zircon and a slight drop in EBSD IQ within the porous zone. However, it is not understood why dark BSE zircon did not form if porous zircon formed in low temperature environment.

How or why porous zircon forms is not clear but it seems porous zircon is yet another response to

radiation damage. This seems surprising that zircon has so many different responses to metamictization. Perhaps porous zircon represents recovery at higher temperatures from previous metamictization events and the radiation damage related features may suggest it has subsequently become metamict again. It is clear that the resolution limitations of the SEM cannot conclusively determine what porous zircon represents. Further analysis using higher resolution techniques is required to identify the composition of pores and potential inclusions and their mode of formation.

4.8.6 The effect of chemical zoning on zircon behaviour

In concentric, sector or simply zoned zircon, dark BSE zircon usually forms within particular, well-defined growth zones or domains. This is due to different concentrations of actinide elements in individual zones. Actinide-rich zones are likely to become metamict over time whilst zones with low actinide concentrations remain fully crystalline. The abrupt boundary between high EBSD IQ-light BSE zircon and dark BSE zircon represents the interface between fully crystalline (light BSE) zircon and what was previously metamict zircon (now dark BSE zircon). The patterns by which alteration occurs in zircon are thereby a consequence of the original chemical zoning in the grain and light BSE zircon preserved within or around dark BSE zircon shares the same crystal orientation as the host grain (Fig. 65). Therefore crystalline light BSE zircon within dark BSE zircon represents the original zoning of the parent grain.

It is not unusual for cores in zircon to alter to dark BSE zircon and they often preserve islands or contorted laths of unmodified, crystalline light BSE zircon which do not replicate the zonation patterns of outer unmodified growth layers. As such, cores have a separate growth history to the encasing zircon implying they are probably inherited with respect to the mantling zircon. Inherited cores often alter to dark BSE zircon because they are older and can have a different actinide content to the encasing zircon. The complex and contorted zonation patterns they commonly display, is often used as evidence that they formed in a high temperature regime (Corfu et al., 2003). The preservation of islands and contorted laths of light BSE zircon in dark BSE zircon cores is a consequence of the original convoluted zoning patterns.

While most zircon containing dark BSE zircon shows well-defined zoning patterns, some zircons display no evidence of any well-ordered internal structure. In mosaic-like zircon, EBSD analysis shows small pockets of fully crystalline zircon within domains of partially metamict light BSE zircon or fully crystalline zircon surrounded by dark BSE zircon (Fig. 62). The highly variable crystalline condition of light BSE zircon indicates a significant heterogeneity in the distribution of U. Crystallinity loss in light BSE zircon does not follow any apparent internal structure and this is coupled with an equally variable alteration pattern. The boundary between partially metamict light BSE zircon and immediately adjacent dark BSE zircon domains may represent the limits of a reaction front. Alternatively the partially metamict light BSE zircon may not have been sufficiently damaged to react when the fluid phase was present (i.e. amorphous clustering had not become interconnected) and therefore the more heavily radiation damaged zircon was more susceptible to alteration (now dark BSE zircon). Mosaic-like zircons that display these features are likely to have formed as a consequence of extremely complex zoning patterns in the parent zircon. The texture observed in mosaic-like zircon has remarkable resemblance to a resorbed composite zircon or “cauliflower” zircon described by Corfu et al. (2003, Fig. 2.26) from a mafic gneiss. Zircon grains that have almost entirely altered to dark BSE zircon represent whole grains that were almost completely metamict (Fig.48b & c).

Zoning patterns in zircon therefore have an important role in controlling where metamict zircon develops and what sort of microstructure forms during the production of dark BSE zircon. As a result, the provenance of a zircon can have a considerable effect on the microstructure that develops (e.g. the behaviour of an oscillatory zoned zircon from a granite will contrast with a contorted zoning structure in a zircon from a gneiss).

4.8.7 Outgrowths on zircon

The minute size and fragility of xenotime outgrowths and, in particular zircon outgrowths, on the margins of zircon grains, precludes them from surviving sedimentary reworking and hence must be authigenic. Xenotime is also found forming thick cementing rims around fragmented zircons, sealing cracks (Fig.51) within the grain while xenotime outgrowths on zircon partially enclose

matrix minerals (Fig.55b,56a). This further supports an authigenic origin. The surrounding matrix has little influence on where xenotime grows on the zircon grain (Fig.56b) but does appear to affect the shape in larger xenotime outgrowths: quartz grains generate flatter, more cohesive, sub-hexagonal outgrowths compared to thinner, more irregularly shaped forms when adjacent to a fine grained matrix (i.e. clays or fine grained carbonate cement). Dark BSE zircon, observed between the host zircon and xenotime outgrowth, implies that Zr was mobile before xenotime growth started. Zircon and xenotime outgrowths have formed from separate events as there are no intergrowths of these two minerals.

The source of Y and P for xenotime growth is not known but it has been postulated that it is part derived from seawater, the decomposition of organic complexes, clay particles or reduced Fe-oxhydroxies in the matrix and interbedded with shale laminae (Rasmussen, 2005a). However the complete lack of detrital xenotime within these rocks may suggest that dissolution of these grains has provided a source for diagenetic xenotime outgrowths. It is also possible that small amounts of Y and P may be liberated from dissolution of apatite grains that may contain trace amounts of Y.

4.9 Minimum reaction temperature of metamict zircon

The minimum temperature at which metamict zircon may alter or experience dissolution has not yet been constrained. Experiments on the alteration of metamict zircon in acidic solutions indicate that structural recovery of zircon may initiate around 75°C after exposure to the solution for 195 hours (Geisler et al., 2003d). As laboratory experiments cannot replicate the timescales of geological processes it therefore seems likely that metamict zircon in sedimentary rocks experience alteration at temperatures lower than 75°C. There is also evidence for dissolution of metamict zircon on the Earth's surface (Balan et al., 2001). While the temperature at which metamict zircon begins to react to fluids remains unclear, at 100°C the mechanism of alteration and dissolution-precipitation of metamict zircon are well-established as the abundance of dark BSE zircon suggests most metamict zircon has altered to dark BSE zircon. A temperature window between 75°C (from Geisler et al., 2003d) and 100°C (peak temperature of diagenesis) seems insufficient to account for all the low temperature features in zircon and therefore metamict zircon may possibly alter and Zr

be mobile below 75°C.

4.10 Summary

Zircon in sedimentary rocks produces very similar textures to those observed in greenschist facies metasediments (Chapter 3). Dark BSE zircon is seen to form in zircon in sedimentary rocks, however, two groups of textures are noted that form via separate mechanisms. Group 1 dark BSE zircon is the dominant form and is also seen in abundance in greenschist facies metasediments. This forms from the dissolution of metamict zircon coupled with reprecipitation and is thought to form in localised conditions where fluids are undersaturated with respect to Zr. Group 2 dark BSE zircon is not as common and forms by a diffusion-driven structural recovery cation exchange process. It may be this process occurs as a result of localised fluids surrounding the grain being saturated in Zr. Both Group 1 and Group 2 dark BSE zircon can be observed forming on different parts of the same grain. The preservation of the reaction between metamict zircon and Group 2 dark BSE zircon may indicate that the rates at which both forms of dark BSE zircon form are considerably different. Despite the different modes of formation, both groups of dark BSE zircon have very similar compositions.

The original zoning in the parent zircon considerably influences the microstructure of the altered grain. Therefore zircon provenance plays a key role in zircon behaviour. This chapter presents evidence that may suggest extensive xenotime dissolution and mobilisation of Y and P. Evidence for Zr mobilisation is also observed and thought this may initiate below 75°C. The very low temperature that this appears to occur at is a concern for the long-term safe storage of nuclear waste by encapsulation in zircon ceramics.

5

Anatomy of zircon outgrowths

5.1 Introduction

EBSD analysis of zircon outgrowths in low-grade greenschist facies slates produces low image quality (IQ) Kikuchi patterns. This contrasts with adjacent xenotime outgrowths and xenotime inclusions within zircon outgrowths that produce high IQ EBSD patterns (Chapter 3) implying that zircon outgrowths are amorphous whereas adjacent xenotime is fully crystalline. This is unexpected as zircon outgrowths crystallise within the slates and the most common mechanism for causing amorphous zircon is through metamictization. However, this seems unlikely as chemical analysis of xenotime outgrowths, which would act as a sink for actinide elements, revealed that they were relatively poor in U and Th. Therefore zircon outgrowths that grew with xenotime seem unlikely to have U concentrations sufficient to cause metamictization. An alternative cause for low IQ EBSD patterns from zircon outgrowths was the possibility they were nano-crystalline and therefore below the resolution of EBSD analysis. This chapter addresses the question: are zircon outgrowths amorphous? And, if not, what is the structure and character of zircon outgrowths, and what are the orientation relationships of zircon and xenotime outgrowths with respect to the host grain? These questions are addressed by detailed characterisation of a selected outgrowth using a

variety of high-resolution electron microscope techniques. Results show that zircon outgrowths are in fact crystalline but have formed through multiple phases of growth. Analysis also reveals that zircon outgrowths have a complex microstructure with xenotime inclusions and zircon-xenotime complexes.

5.2 Method technique and sample characterisation

Zircon outgrowths have been imaged using transmission electron microscopy (TEM) and low voltage scanning transmission electron microscopy (LV-STEM). These techniques allow high-resolution analysis of the microstructures within zircon outgrowths. Furthermore, using the focused ion beam (FIB) microscope, site specific, electron-transparent cross sections can be prepared of composite grains for characterisation by TEM & LV-STEM (Wirth, 2004, , 2005; Lee and Smith, In press).

Thin section BAL1B is from a greenschist facies slate (Appendix **Error! Reference source not found.**) containing detrital zircons with abundant zircon and xenotime outgrowths. For further descriptions on the rock and the variety of textures found in zircon, see Table 1. A zircon grain was selected from within the thin section that was considered suitable for preparation using the FIB microscope and subsequent TEM and LV-STEM analysis (Fig. 67). This zircon was chosen with the following considerations: the area to be prepared using the FIB microscope had a simplest composition and microstructure; the outgrowth on the host zircon was large enough to be sampled and manipulated using the FIB microscope; the host zircon and outgrowth were representative of those found in the greenschist facies slates. These measures were taken to make the sample preparation as simple as possible as, to the authors knowledge, preparing electron-transparent foils have not been previously attempted on zircon using the FIB microscope. A detailed characterisation of the selected area was made from SEM BSE and SE images taken on the polished surface of the thin section before the preparation of electron-transparent cross section was carried out.

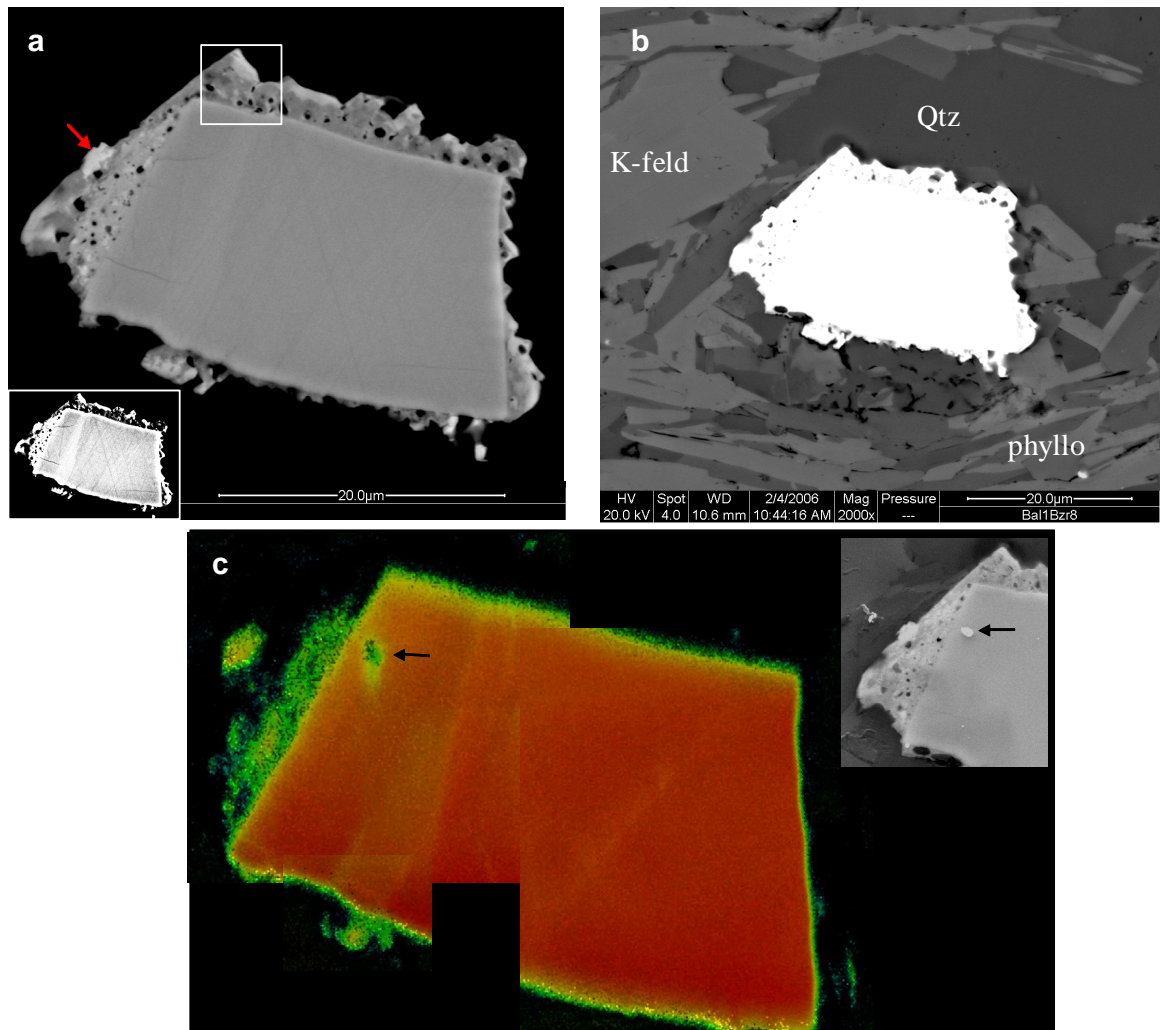


Figure 67 Characterisation of zircon BAL1bzt8.

a and b are BSE images of zircon BAL1bzt8. a displays the complex and heterogeneous nature of zircon and xenotime outgrowths. Red arrow points to high BSE intensity xenotime grain within the outgrowth. Inset into a is a high contrast, low brightness BSE image and shows the tips of outgrowths are BSE intense as is the mottled BSE intensity area of the outgrowth adjacent to the host on the leftmost of the grain. b shows zircon relationship with the surrounding matrix. c is a composite EBSD CI-IQ map of zircon in a. The high IQ domain towards the outgrowth tip can be seen to correlate with the high BSE intense grain in a (red arrow). The higher IQ area of the outgrowth is the zircon-xenotime complex. Black arrow points to spec of dust which is identified in the inset SE image.

The host zircon has four well-defined, although very slightly curved, margins with a slight irregularity on the leftmost bottom part of the margin in Fig. 67a. A high contrast BSE image identifies a 3µm wide band of higher intensity within the host and follows parallel to the right and left margins of the host (inset, Fig. 67a). Two small fractures trace perpendicular from the edge of the host grain for a distance of *c.*5µm towards the centre of the zircon (Fig. 67a). The host zircon is likely to be fragment of larger grain based on grain size and the sharply defined grain edges, which indicate little sedimentary reworking. Such fragments dominate the zircon population in this rock.

Outgrowths surround the host zircon on all four margins but are largest around the top and left margins in the BSE image of the grain (Fig. 67a). Outgrowths are adjacent to muscovite and chlorite (abbreviated to phyllo in Fig. 67b) on three sides, while the outgrowth forming on the remaining side is adjacent to quartz. The outgrowth projects upto 5µm from the host grain at its largest but averages around 3µm. There is significant variation in the BSE intensity within the outgrowth particularly around the tips of the outgrowth and may be caused by charging. The outgrowth contains an abundance of very low BSE intensity inclusions that are generally rounded and range in size <0.1-0.6µm. The more BSE intense areas of the outgrowth can be seen to form individual grains (red arrow, Fig. 67a). Beside this grain, the outgrowth has a band of slightly higher BSE intensity and many small inclusions of variable BSE intensity. The zircon outgrowth preferentially polishes down with respect to the host zircon (*c.*<50nm) but the high BSE signal intensity areas of the outgrowth are flush on the polished surface with the host zircon.

EBSI analysis of the zircon shows that many of the BSE intense areas of the outgrowth have a relatively high EBSI IQ whereas the remainder of the outgrowth has no EBSI pattern (Fig. 67c). As xenotime kikuchi patterns index well in comparison to zircon outgrowths, isolated high IQ areas within the outgrowth are likely to be small xenotime grains which also fits with their high BSE signal intensity. The moderate to high EBSI IQ area correlates with the band of the outgrowth with a slightly higher BSE intensity which is thought likely to be a complex of zircon and xenotime. Orientation relationships in the EBSI maps show that xenotime outgrowths are epitaxial with the host zircon (Chapter 3).

The area of the outgrowth selected for preparation in the FIB microscope is identified in Fig. 67a. High magnification SE SEM images of this area reveal the intricate structure of outgrowth (Fig. 68). It has an overall pyramidal shape with shallow indentations along the contact with the adjacent quartz. The interior of the outgrowth has a domain that is relatively homogeneous but it is otherwise dominated by an area with a distinctive inclusion-rich and heavily dimpled microstructure. The homogeneous part of the outgrowth has a smooth surface and forms a 1 μ m thick anchor shape that defines an area from the outgrowth tip, along the outgrowth edge while extending into the centre of the outgrowth. The heavily dimpled area is preferentially polished down relative to the homogeneous zircon and is slightly fibrous in places (Fig. 68b). The inclusions are circular to elongate and rounded in shape ranging in size 200-700nm each with a thin higher BSE signal intensity rim. Some dimples are irregularly shaped (*c.*<300nm) and some low BSE signal intensity ripple shaped veinlets upto 1 μ m long are also observed.

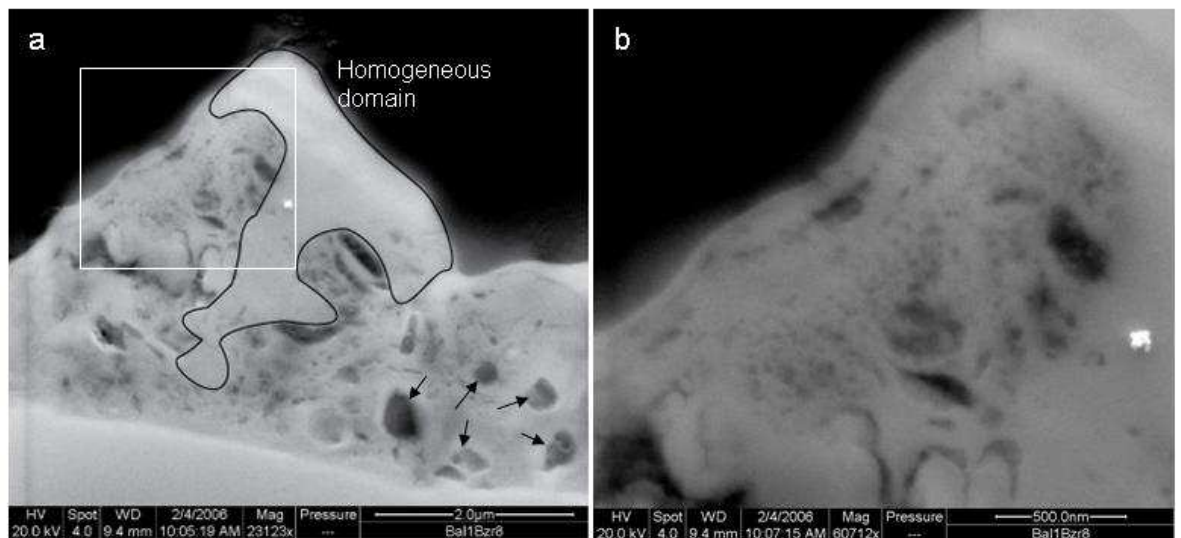


Figure 68 High magnification images of zircon outgrowth microstructure

a&b are high magnification SE images. **a** is the outgrowth region defined in fig. 67a. It reveals an intricate but varied microstructure with pores or inclusion rich areas (arrows) and more homogeneous anchor shaped area that has drawn on to aid the eye. Box in **a** defines area of image in **b** which reveals the almost dimpled microstructure and thin low SE intensity veins. Bright spec on **a** and **b** is a dust particle.

5.3 FIB-prepared foil

5.3.1 Method

Two pairs of FIB-produced trenches were cut into the selected zircon grain (Fig. 69a). The foil extracted from trench 1 fractured during removal however the outgrowth has remained intact and fracturing has not affected the properties of the electron transparent window in the foil (Fig. 69b-d). As the foil extracted from trench 1 was broken, a second trench was milled (trench 2, Fig. 69a). Analysis of the foil from trench 2 revealed that the target outgrowth had been missed and consequently all further reference to a FIB-prepared foil will be to that extracted from trench 1. Although preparing TEM foils by this method enables the detailed analysis of structures in minerals at the microscopic and mesoscopic scale, the fragility of foils does demonstrate the high level of operator skill required to prepare and extract the foils in the FIB microscope.

Placement of the foil in the centre of the TEM grid gives a distinct advantage when it is analysed using LV-STEM. The grid can be placed in one of the eight equally spaced grid holders in the STEM detector. However, in two of the eight positions, the grid is supported over the join between the two detectors. In this instance one of the two detectors will form a bright-field image, the other a dark-field image in which only scattered electrons contribute to the image, which is very useful in LV-STEM work (Lee and Smith, In press). The majority of LV-STEM imaging was carried out using this setup.

Contrast in LV-STEM images is mainly generated by variations in electron scattering due to differences in atomic mass (Z), where the thickness of the foil (t) is constant. Contrast in BSE SEM images of the foil is also created from atomic mass (Z) and will also be influenced by t . Therefore LV-STEM and BSE images should be complementary. It should be emphasised that LV-STEM images are produced from a detector underneath the sample and that BSE images are collected from the backscattering of electrons at a detector situated above the sample. Dark-field & bright-field TEM diffraction contrast images are generated by variations in electron scattering

mainly due to Bragg diffraction. Holes in the carbon film can occasionally be seen through the foil in TEM and LV-STEM images (e.g. Fig. 69a&c) but can easily be identified on SEM SE (Fig. 69d).

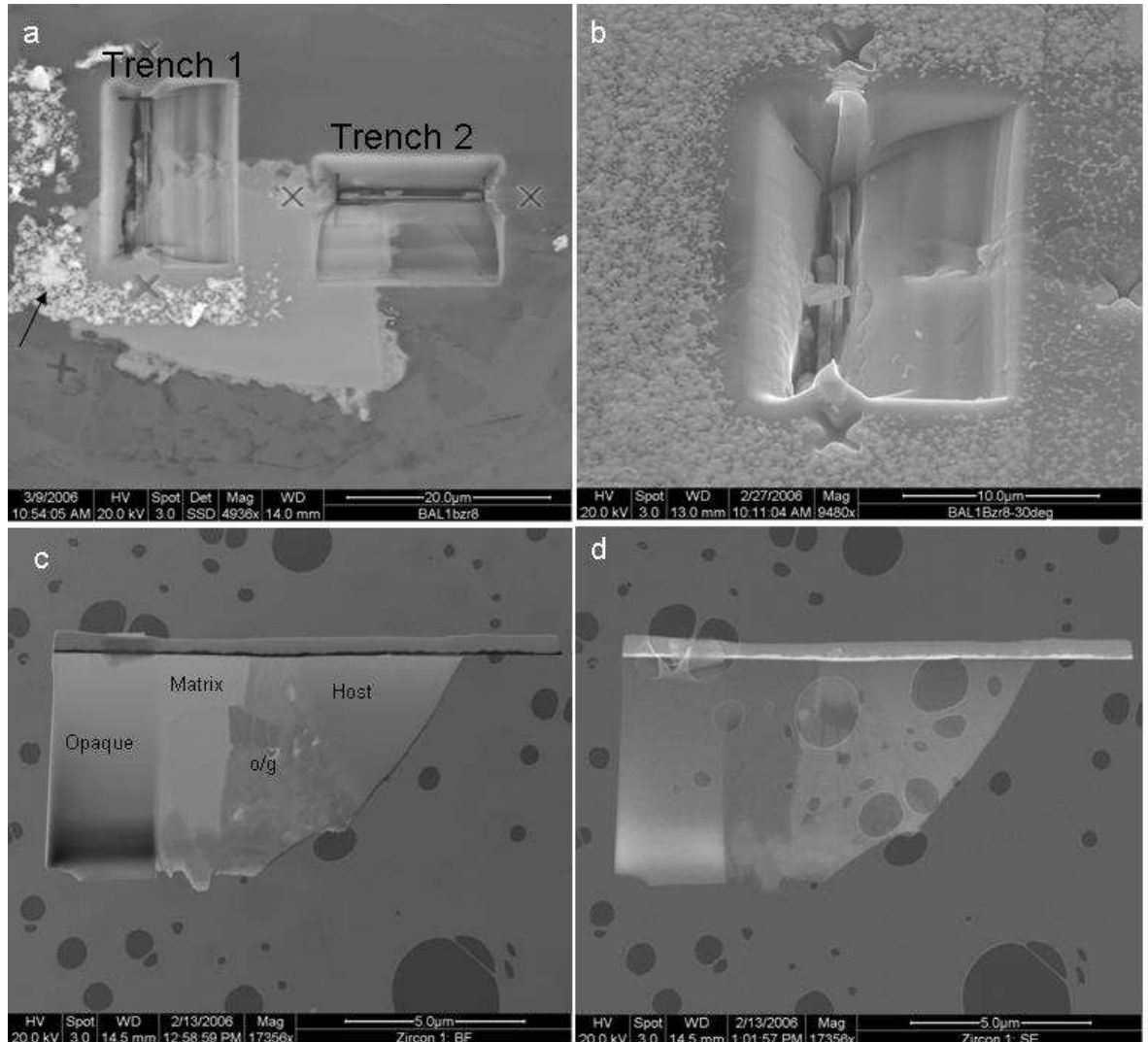


Figure 69 Foils prepared using the FIB microscope

a BSE SEM image showing FIB trench sites on grain BAL1Bzr8. Arrow points to remnants of gold coating that remained after polishing. **b** BSE SEM image of trench 1 with SEM stage tilted at 30°. **c** Bright-field LV-STEM image of broken foil from trench 1 on carbon film. **d** SE SEM image of foil.

5.3.2 Foil morphology

The foil is composed of opaque areas and an electron transparent “window” (Fig. 69c). The leftmost part of the foil is electron opaque and represents one of the two thicker posts which are required to keep the integrity of the foil when extracted. The right hand post broke off during extraction. The base of the foil is darker in bright-field LV-STEM imaging indicating an increase in t where electrons have been scattered away from the bright field detector (Fig. 69c). Associated with this is an increased SE and BSE intensity confirming that the scattering in the bright-field LV-STEM image is due to an increase in t (Fig. 69d & 70b). The Pt strap at the top of the foil is visible in dark-field LV-STEM imaging with the Au coating underneath the Pt strap (Fig. 70a). The irregular margin that extends from the base of the foil to the Pt strap is the broken edge generated when the foil was extracted from the FIB trench.

Image analysis of the foil shows it to be composed of 3 main parts: the host zircon, the outgrowth region, and the matrix (Fig. 70a).

5.3.3 Host zircon

The host zircon is generally homogeneous but dark-field LV-STEM images show a gradual darkening in the host zircon towards the broken edge of the foil (Fig. 70a). This correlates with an increasing BSE intensity indicating either an increase in t or a variation in Z (Fig. 70b). Chemical zoning in zircon is usually abrupt and well-defined therefore it is more likely that this represent a slight thickening of the foil. The boundary between the host zircon and zircon outgrowth is poorly defined using most of the imaging techniques with the exception of dark-field TEM images (Fig. 71b, 71d). The Selected Area Electron Diffraction (SAED) pattern of the host zircon (Fig. 74, with SAED spot defined in Fig. 70a) shows a strong, well-defined diffraction pattern.

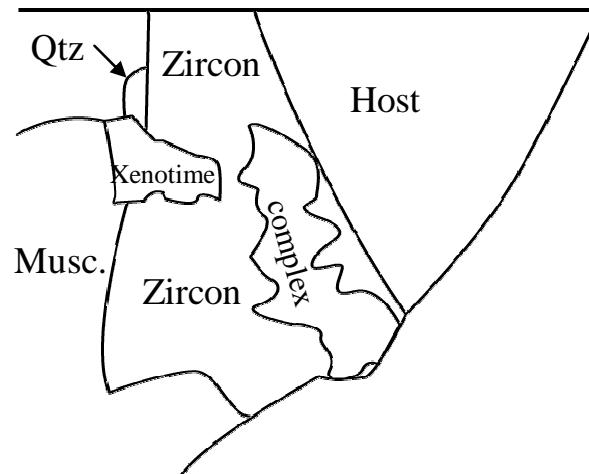
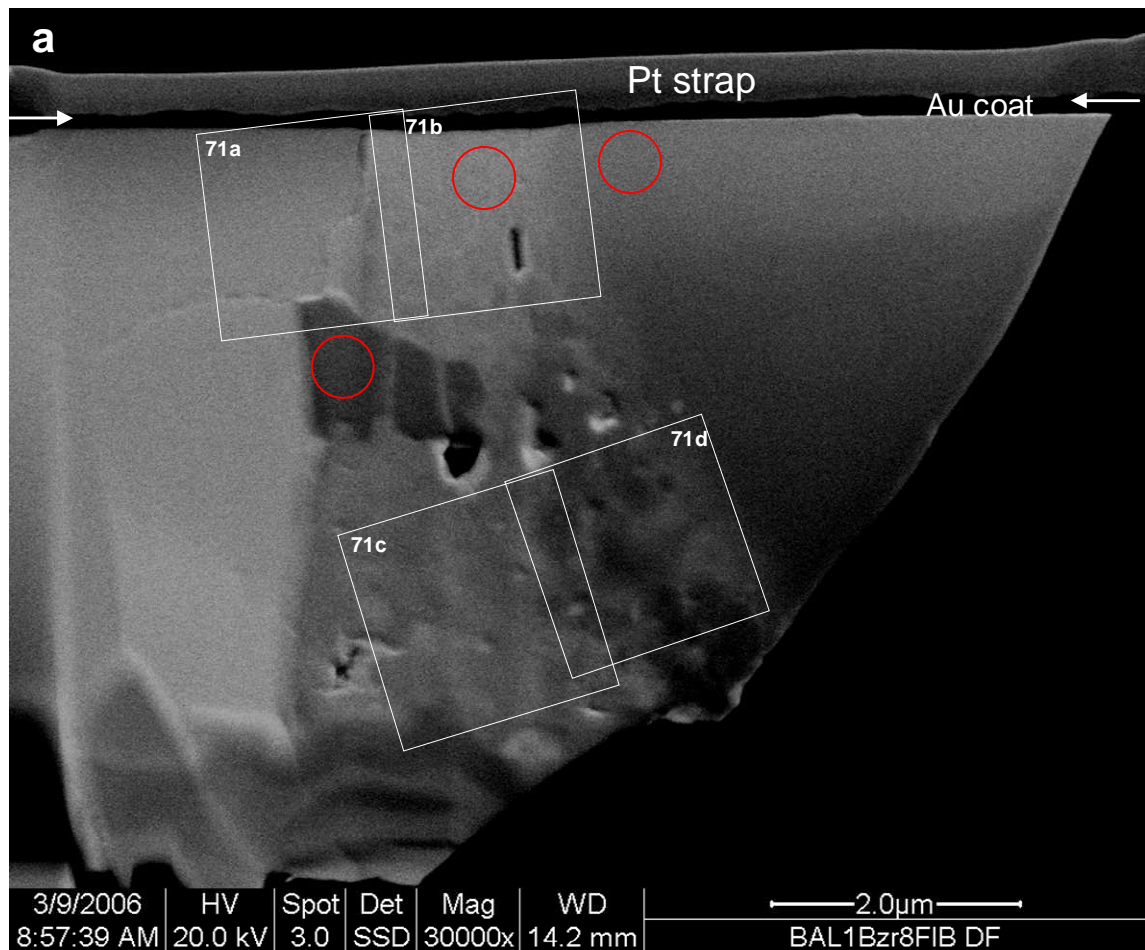


Figure 70 Characterisation of the FIB-prepared foil. Caption on following page.

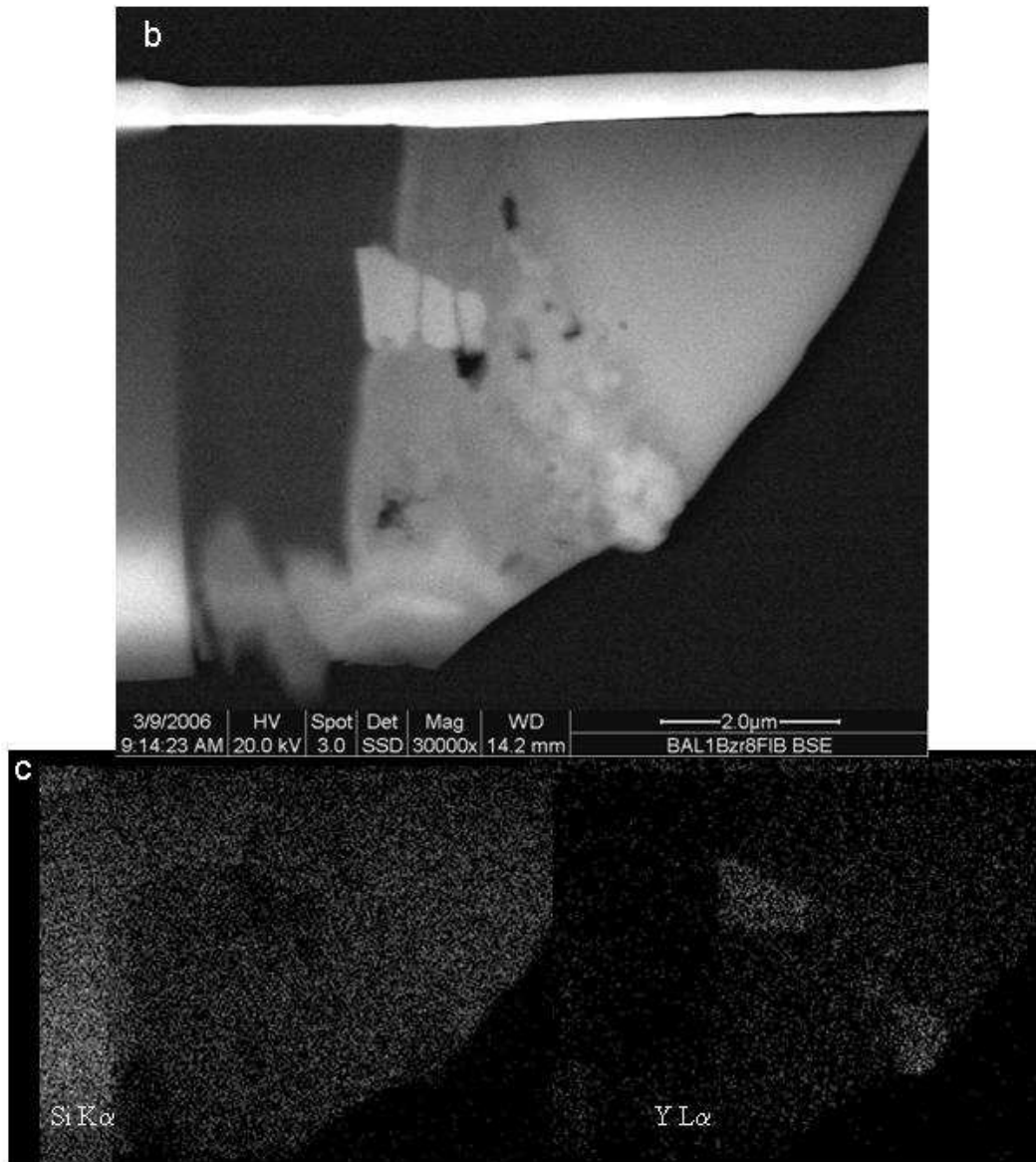


Figure 70 Characterisation of the FIB-prepared foil

a Dark-field LV-STEM image of foil. White boxes define areas of high magnification images in Fig. 71. Red circles show areas of SAED patterns taken using the TEM. White arrows at the top of the foil points to Au coat. The Pt strap is above the Au coat. A schematic diagram of the foil structure helps identify the structures in the foil. **b** BSE SEM image of foil and shows high BSE intense areas within the outgrowth area and these domains relate to Y-rich and Si-poor domains in EDX SEM elemental map scans of foil in **c**. BSE intense areas of the outgrowth are xenotime.

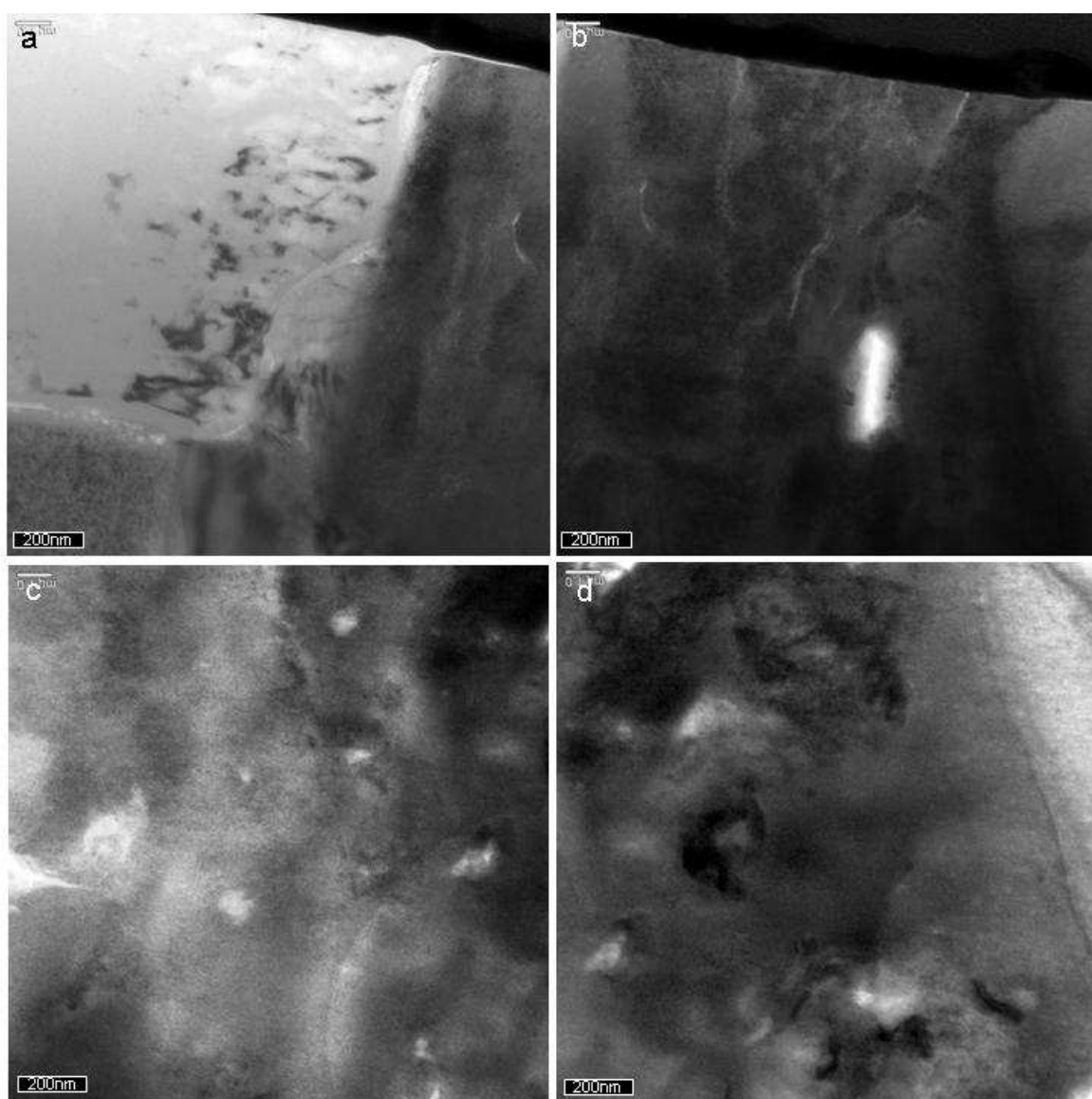


Figure 71 Dark-field TEM diffraction contrast images of areas defined in figure 70a.

a image of the zircon outgrowth and xenotime grain boundary with quartz. Reveals flame-like structure within the quartz adjacent to the outgrowth. **b** image revealing the tiled structure of the zircon outgrowth and shows hole in outgrowth area. **c** shows intricate structure within zircon outgrowth. **d** Some crystalline component can be determined within image of zircon-xenotime complex.

5.3.4 Outgrowth

The outgrowth is upto *c.*1.5 μm wide between the matrix quartz and the host zircon but is *c.*3.5 μm at its widest between host zircon and muscovite. Along the top of the foil (representing the surface of the thin section) and directly beneath the gold coat, the outgrowth is slightly depressed (*c.*50nm at its maximum) with respect to both the host zircon and adjacent quartz (Fig. 69c & 70a).

Dark-field LV-STEM imaging best reveals the features within the outgrowth (Fig. 70a). The outgrowth is relatively homogeneous in contrast but three separate low signal intensity laths over an area *c.*1x1.2 μm and a low signal intensity mottled complex can be recognised within the area adjacent to the host zircon. SEM EDX analysis identifies the more homogeneous area is composed of zircon while the low signal intensity areas in the dark-field LV-STEM image of the outgrowth correspond to either xenotime or zircon enriched in Y (Fig. 70c). The three lath shaped low signal intensity grains in dark-field LV-STEM are revealed to be xenotime by SEM EDX.

5.3.4.1 Zircon outgrowth

The outgrowth is dominated by zircon, the more homogenous domain in Fig. 70a. The zircon outgrowth contains thin and elongate holes, no bigger than 300nm in length that have a high intensity in bright-field TEM images (Fig. 71b). Smaller (<100nm), more irregularly shaped holes and are also visible throughout the outgrowth in bright-field TEM images (Fig. 71c). Bright-field TEM and bright-field LV-STEM images reveal the zircon outgrowth has a tiled microstructure divided by thin, non-diffracting veins (Fig. 71b, 72a&b). Elongate and slightly rounded zircon tiles can be upto *c.*700nm long but also form 200 x 200nm blocky plates or tiles varying from angular to irregularly shaped domains 200-500nm wide (Fig. 72).

A SAED pattern of the tiled zircon shows slightly diffuse diffraction spots indicating that there is some variation in orientation within the selected volume (Fig. 74).

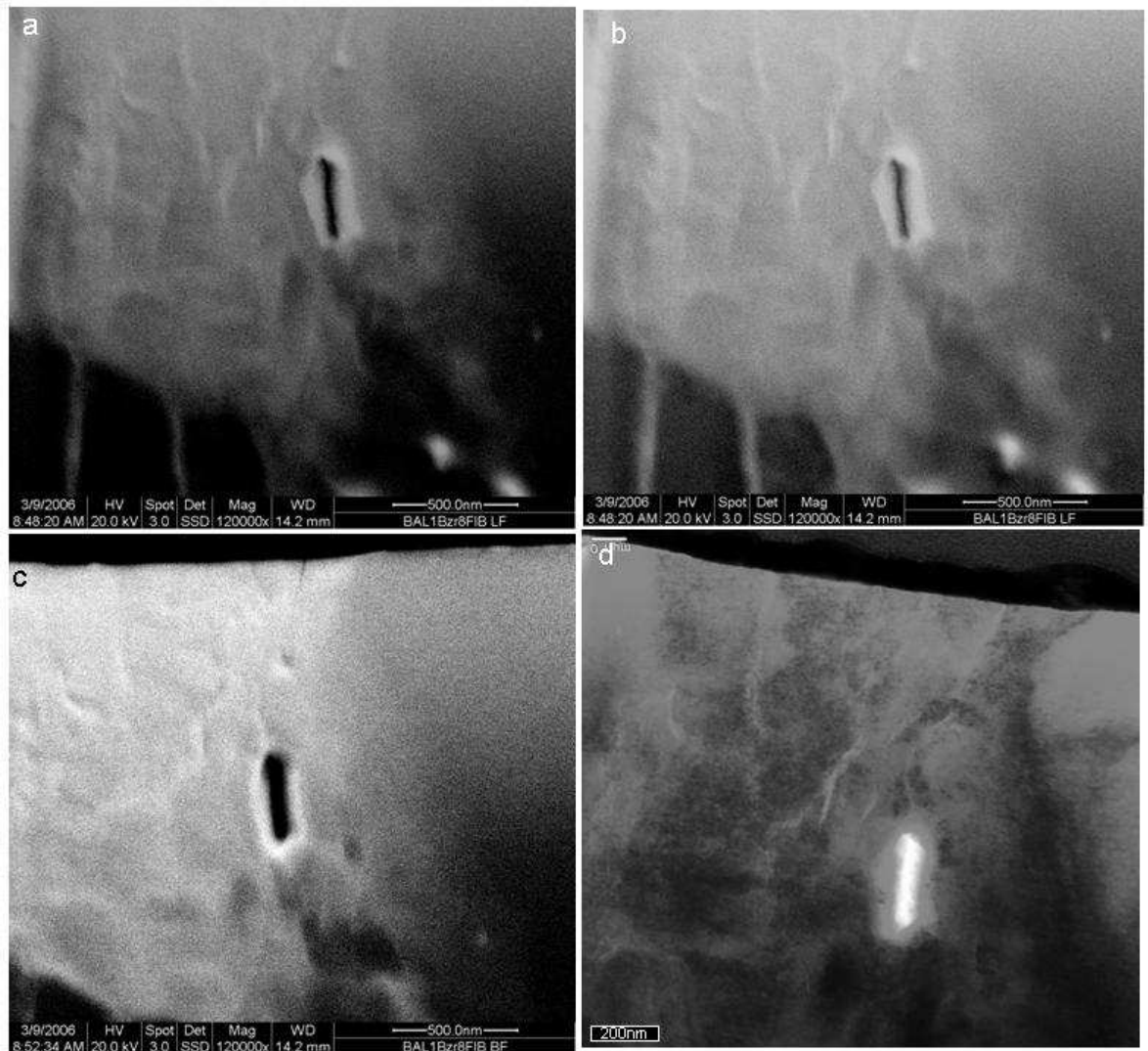


Figure 72. Images revealing the tiled microstructure of zircon outgrowths.

a&b. Bright-field LV-STEM images of host, outgrowth and xenotime platelets. Thin veins of zircon can be seen between xenotime grains. **a** is a high contrast image of **b**. **c&d** are dark-field LV-STEM and dark-field TEM diffraction contrast images respectively of similar area.

5.3.4.2 Xenotime outgrowth

Thin (50nm) bands of fibrous zircon (Fig. 73c) divide the three xenotime laths that have an overall euhedral shape. The outermost of the three xenotimes (with respect to the host zircon) projects into

the adjacent matrix grains from the zircon outgrowth, terminating at the boundary with quartz and muscovite (Fig. 73a). Fig. 73c is a dark-field TEM image with the sample tilted slightly off the Bragg angle of the xenotimes and shows that each xenotime is a single crystal although they share a common orientation. These individual crystals can be seen in BSE SEM images of the foil (Fig. 73d). A SAED pattern of the xenotime laths produces a strong, well-defined diffraction patterns (Fig. 74).

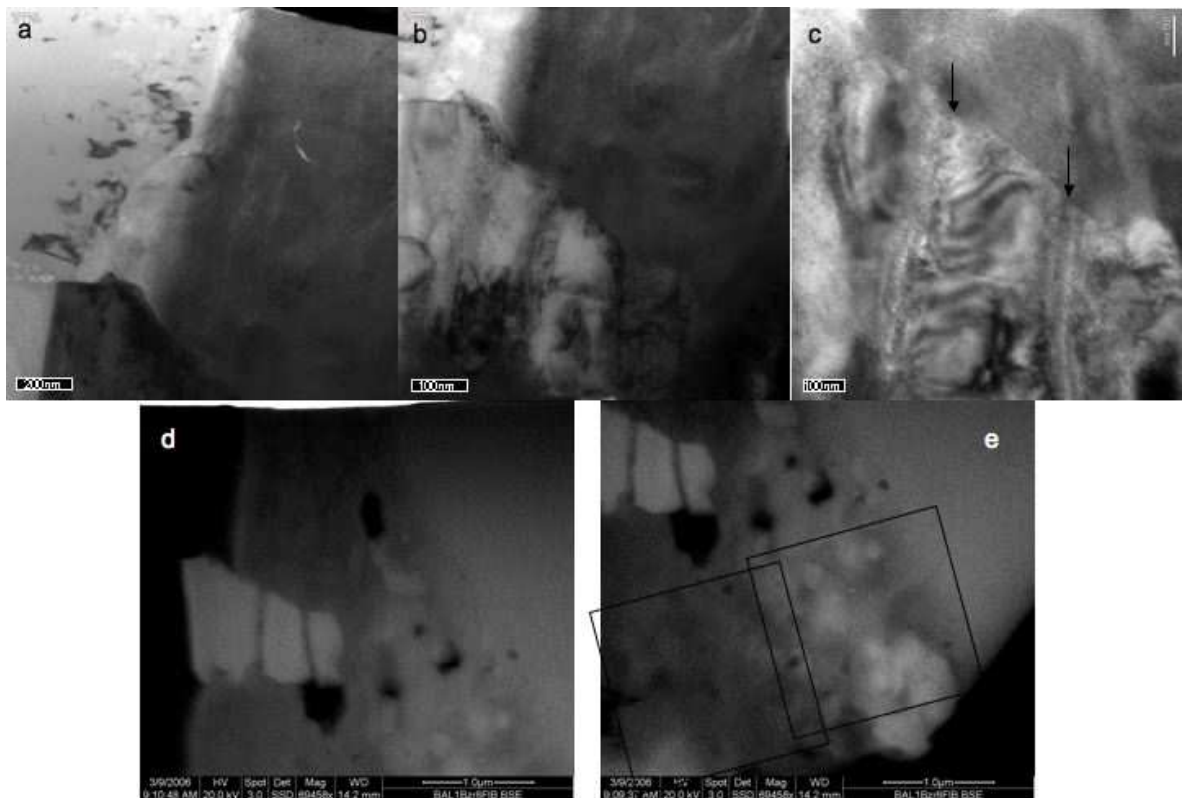


Figure 73. Images identifying microstructural in the outgrowth

a-c. Dark-field TEM diffraction contrast images of outgrowth area with xenotime platelets and quartz grain. Faint large circles on images are due to the underlying holey carbon film. **c** arrows point to zircon veins with fibrous appearance. **d&e** BSE image of outgrowth with xenotime platelets and zircon-xenotime complex. **e** shows areas represented in Fig. 71c & d.

5.3.4.3 Zircon-xenotime complex

Dark-field LV-STEM imaging of the outgrowth identifies a 700 x 1000nm mottled low signal intensity domain between the host zircon and tiled zircon outgrowth (Fig. 70a). BSE SEM imaging

reveals a similar structure with a high signal intensity, similar to that of the xenotime laths (Fig. 70b). This correlation in structures between dark-field LV-STEM and BSE SEM images shows that, in this instance, the scattering of electrons, which controls the contrast variations in dark-field LV-STEM images, is dominated by changes in Z , as the t of foil is constant. This means that Bragg diffraction has little influence on the contrast of the dark-field LV-STEM image.

An element YLa EDX SEM map of the foil shows a high signal intensity that correlates with an area of low signal intensity in a $SiK\alpha$ EDX SEM map (Fig. 70c). Three smaller (200 by 200nm) Y-rich can be identified on the YLa map which correlate to a slightly more intense signal in BSE SEM images than the rest of the complex (Fig. 70b) and a slightly lower contrast in dark-field LV-STEM image (Fig. 70a). Furthermore, these same areas exhibit thickness extinction contours in dark-field TEM contrast images where the sample has been tilted just off the Bragg angle of these grains (Fig. 71c&d). These individual grains would appear to represent small xenotime crystals within a zircon complex that is also enriched in Y.

5.3.5 Matrix grains

Analysis of dark-field LV-STEM images of the matrix shows it is a composite of four separate grains (Fig. 70a): two quartz; muscovite; a Na-Ti-silicate. These were identified using SEM EDX.

The matrix grain at the bottom of the foil shows peaks at Na, Ti and Si. SE SEM imaging of the foil shows that the very base is significantly thicker than the rest of the foil (Fig. 69c). Na and Ti are not readily found together in minerals and it is possible that the base of the foil has had foreign material deposited onto its surface during the milling process. As such, it is ignored for the purposes of this investigation.

The outgrowth shares a boundary with two quartz grains. The grain boundary separating the large matrix quartz grain (Q1) and the small lath shaped quartz (Q2) is only visible in dark field-LV STEM imaging (Fig. 70a). It should be noted that this area of the quartz-outgrowth boundary lies partly over a hole in the carbon film (Fig. 69d). The edge of the hole in the underlying carbon film

is also partly coincident with the boundary between Q1 and Q2 and, as a result, slightly obscures some detail (Fig. 71a).

The zircon outgrowth has a slightly higher BSE intensity rim adjacent to matrix grains (Fig. 70b, 73d) but this is also replicated in SE imaging and therefore most likely caused by charging along the outgrowth-matrix boundary (Fig. 69d). Q1 forms a fairly well-defined, straight boundary with the zircon outgrowth whereas Q2 has a more transitional boundary with the zircon outgrowth. This transitional boundary is only apparent in dark-field TEM diffraction contrast imaging, taken when the sample is tilted to the diffracting angle of xenotime laths (Fig. 71a). With the sample tilted in this orientation, the outermost xenotime lath forms a sharply defined euhedral boundary with Q1. However the boundary between the xenotime and Q2 is blurred as the xenotime half of Q2 shares thickness extinction contours with the xenotime (Fig. 71a). When the sample is tilted slightly away from the diffracting angle of the xenotime laths, a sharply defined boundary can be identified between the xenotime and both quartz grains (Fig. 73a). Furthermore this reveals a small (*c.*50nm) pyramid of xenotime juts out into the boundary between Q1 and Q2.

In dark-field TEM diffraction contrast images Q1 exhibits highly irregular, flame-shaped areas of dark diffraction contrast (Fig. 71a & 73a). These are elongated away from, and roughly perpendicular to the boundary between the quartz grains and zircon outgrowth and dissipate away from the zircon outgrowth-Q1 boundary. Dark diffraction areas range in size from <10-200nm with larger domains of dark diffraction contrast concentrated towards the xenotime lath. Areas of diffraction contrast appear wispy where Q1 is adjacent to the zircon outgrowth and Q1 has a band of homogeneous contrast within it at the boundary with the zircon outgrowth. This band of homogeneous diffraction contrast runs into the flame-like diffraction contrast areas. Coupled with these dark diffraction contrast areas, dark-field TEM diffraction contrast images also identify blotches of lighter diffraction contrast within Q1 (Fig. 71a & 73a). Lighter diffraction contrast domains are more subtly observed but are larger and more extensive towards the pt-strap end of the FIB-prepared slice. The variations between light and dark diffraction contrast within Q1 give a marbled appearance, reminiscent of textures found in high grade metamorphic rock.

Variations in the diffraction contrast within the quartz grain are only observed in dark-field TEM diffraction contrast images where the sample is tilted close to the diffracting angle of the xenotime laths. This feature is absent in all other images.

5.3.6 SAED

Selected area electron diffraction (SAED) patterns (Fig. 74, with SAED areas defined in Fig. 70a) of the tiled zircon have slightly diffuse diffraction spots that show a partial transition into rings. SAED patterns of the individual xenotime laths and of the host zircon, show strong, well-defined diffraction patterns. Analysis of the SAED patterns show that the 101 crystal planes of all areas are parallel or close to parallel.

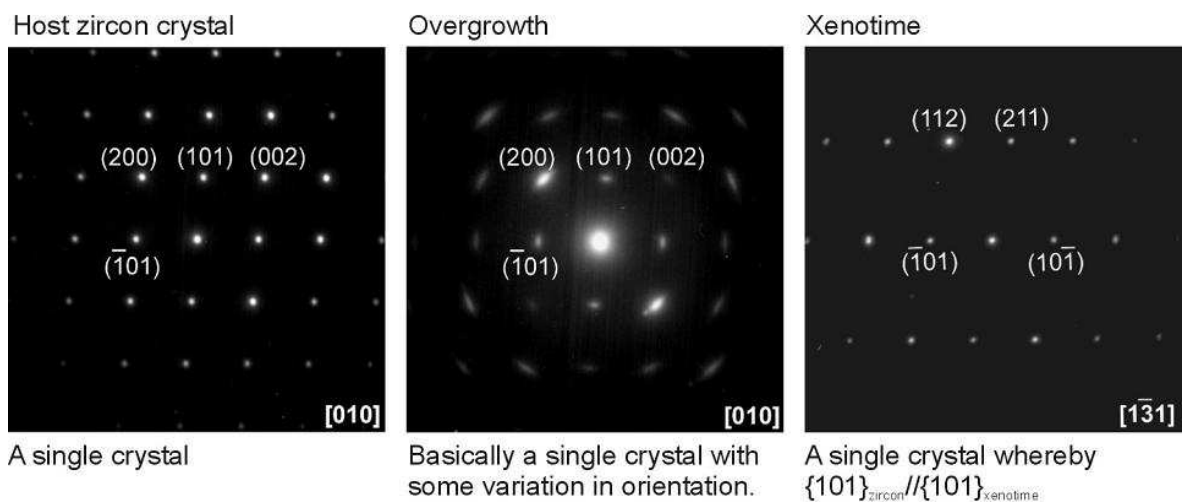


Figure 74 TEM SAED patterns from an area 600nm in diameter on the host zircon, zircon outgrowth and xenotime crystals. SAED locations are defined in Fig. 70a.

5.4 Interpretation

5.4.1 Zircon outgrowth

Zircon forms epitaxial outgrowths with its host but there are minor orientation variations within the

zircon outgrowth as determined by the slightly diffuse diffraction spots in the SAED pattern. As the SAED spot lies over several of the outgrowth tiles, this mis-orientation may be caused by the cracks or dislocations between individual tiles. The diffuse spots in the SAED pattern are likely to demonstrate small variations in crystal orientation within the individual tiles of the selected volume. This may further suggest that individual tiles of the zircon outgrowth have a mesostructure of slightly mis-orientated nano-crystalline grains. The zircon outgrowth is polished-down relative to the host zircon and would suggest it has a different crystalline structure. Both the mis-orientation of nano-crystallites and the polished down nature of zircon outgrowths make it unsuitable for EBSD analysis and is why it produces low to no IQ EBSD patterns.

The host zircon displays no evidence of internal modification indicating that Zr required for zircon growth is supplied from elsewhere. Other zircon grains throughout the rock display evidence of dissolution and as zircon is the largest sink for Zr, it is likely that Zr is sourced and transported from such grains. Zr mobilisation is thought to be related to the episodic release of Zr from metamict zircon that is exposed fluids. Once Zr-saturated fluids reach the host zircon, zircon nucleates and precipitates on the margin. The nano-crystalline structure of the zircon in outgrowths implies that the rate of growth may be relatively rapid.

The size of the outgrowth is appreciably larger at the bottom of the foil where it is in contact with muscovite than at the top of the foil, adjacent to quartz. This may possibly be likely related to the ability for fluids to permeate through the cleavage planes of the muscovite to the host zircon in comparison to the relatively impermeable quartz. However, in general, zircon outgrowths are not consistently thicker adjacent to muscovite based on textural observations (Chapter 3).

The inclusion rich nature of zircon outgrowths is caused by inclusions becoming enveloped through absorption by the outgrowing zircon. This is analogous to the inclusion of quartz during the formation of garnet porphyroblasts. Although there are many holes in the FIB-prepared foil of the outgrowth, it is possible that some represent inclusions that have fallen out of the outgrowth during preparation of the foil. Several minute bits of detritus within the milled pit may represent the

fallen inclusions although it is more likely they are shards from when the foil fractured during removal (Fig. 69b).

5.4.2 Xenotime phases in outgrowth

Based on the similar euhedral morphology of the xenotime laths, it would appear that they were originally a single crystal. This implies that the xenotime grain formed from a single phase of growth, nucleating on some pre-existing zircon outgrowth. Subsequent fracturing of the xenotime has separated it into three individual grains and has allowed fibrous zircon to grow within these fractures indicating zircon was the last phase to precipitate in the outgrowth.

The development of a relatively large independent xenotime crystal indicates that growth either occurs at a time of no zircon precipitation or competes with and outstrips zircon growth. Zircon-xenotime complexes suggest that zircon and xenotime growth was synchronous where neither phase is able to fully develop, forming poorly-defined crystals. As such, the growth of a single xenotime grain requires a period where no zircon is precipitated. Zircon growth is dependant on the episodic release of Zr from other Zr-rich sources (i.e. metamict zircon) elsewhere in the rock. Periods where the fluid phase is undersaturated in Zr provide opportunities for xenotime grains to develop uninhibited. Yet it seems unlikely that such a relatively large xenotime grain could form over a prolonged period of crystallisation during which no zircon precipitates. Thus, for xenotime grains to develop, crystallisation must be rapid and independent of zircon growth whilst zircon-xenotime complexes form as a result of simultaneous crystallisation of both phases. This indicates that the outgrowth formed from multiple phases of growth rather than a single and continuous event.

5.4.3 Sub-domains in quartz and mechanisms accommodating zircon and xenotime growth

Pore space in these metamorphic rocks is negligible and zircon and xenotime are likely to grow at the expense of the surrounding grains in the matrix. Therefore as outgrowths grow, they strain the

surrounding matrix grains. Most grains, such as quartz, are likely to compensate for this strain by pressure solution where fluids are abundant. However, the quartz adjacent to the outgrowth in the FIB-prepared foil reveals some interesting microstructures that indicate an alternative mechanism for strain relief from the outgrowth. Evidence for this comes from the flame-like dark diffraction contrast areas in the adjacent quartz grains. These features are only observed in dark-field TEM diffraction contrast images of the quartz grain, where the sample is tilted to diffracting angle of the xenotime. This indicates this is a crystallographic feature because inclusions of a different composition would be easily identified in BSE SEM and LV-STEM imaging. The flame-like dark diffraction contrast areas also share a diffracting angle with the xenotime laths. Consequently, these areas are likely to represent sub-domains in the quartz that have recrystallised in a similar orientation to the impinging zircon and xenotime. Many of the structures and textures identified here have a similarity to the microstructures observed in quartz caused by intracrystalline deformation at low-temperature, high-strain regimes. Many of the microstructural features and nomenclature are summarised in (Passcheir and Trouw, 2005).

In Figure 71a, half of Q2 shows recrystallisation with the same orientation as the adjacent xenotime. The pyramid of xenotime protruding into Q2 could be an example of low-temperature grain boundary migration or bulging recrystallisation. This occurs when two neighbouring grains have different dislocation densities and the grain boundary may begin to bulge into the grain with the highest defect density (Hirth and Tullis, 1992; Passcheir and Trouw, 2005), in this case Q2.

The recrystallisation microstructure of Q1 is quite different in shape from the recrystallised area in Q2. In Q1, recrystallised areas are elongated perpendicular to the zircon outgrowth boundary. This would suggest that the strain imposed on Q1 by the outgrowing zircon is sufficient to cause dislocation creep within the grain. By moving dislocations and defects within quartz to a free surface, this can act as mechanism that reduces the size and shape of the quartz grain. The direction of dislocation creep would therefore be towards the quartz-zircon boundary. This process is most dominant at the temperature range of 300-400°C (Passcheir and Trouw, 2005) but the presence of a fluid (i.e. H₂O) can dramatically reduce the temperature at which this occurs by upto

100°C (Hirth and Tullis, 1992). The small elongate subgrains and very small solid inclusions only visible using TEM described by Passcheir and Trouw (2005) are analogous to the features in Q1. Passcheir and Trouw (2005) state that deformation lamellae are particularly common in quartz where the lamellae have a sub-basal orientation. It is therefore possible that flame-like dark contrast areas in Q1 represent sub-grain recrystallisation with quartz taking on a preferred orientation of the adjacent grains, imposed on them through strain. Yet Passchier and Trouw (2005) also point out that how lamellae develop and how they should be interpreted is only partly understood. It is also of note that these mechanisms for intracrystalline deformation and recrystallisation in quartz are specific to structural geology and modelled for high-strain tectonic regimes. The strain imposed on quartz during zircon and xenotime growth will be greatly reduced in comparison to high-strain examples. However, these comparisons do appear to provide a model that describes the development of recrystallised areas in quartz adjacent to zircon and xenotime outgrowths.

5.5 Model for outgrowth formation

The absolute timing of events and conditions that lead to the formation of the outgrowth in the FIB prepared foil cannot be constrained at present. Therefore, information regarding the general conditions and timings, for instance when Zr is mobile, has been based on that established in Chapters 3 and 4. The conditions and sequence of events detailed here does not necessarily apply to the specific history of the outgrowth in the FIB prepared foil. The model that has been constructed is therefore a characterisation of the relative events based on the microstructure and features within the FIB prepared foil (Fig. 75). This has been done so that overall impression of how zircon outgrowths form may be had. For simplicity, the muscovite grain is referred to phyllosilicate in the model.

Stage 1: Zr supersaturated fluids migrate to the margin of the host grain. Surrounding phyllosilicates may enhance fluid migration. The alteration of metamict zircon may initiate *c.*75°C (e.g. Hoskin and Schaltegger, 2003) or even below (Chapter 4), and so Zr may be mobile at this

temperature and outgrowths may begin to form very early in the “prograde” history.

Stage 2: Rapid precipitation results in nano-crystalline zircon nucleating on the host zircon. Inclusions are incorporated as zircon grows.

Stage 3: Crystallisation of both zircon and xenotime from the fluid phase result in a zircon-xenotime complex. Within this complex small xenotimes develop. Crystallisation of zircon continues when xenotime growth becomes unfavourable, probably related to the availability of Y or P.

Stage 4: Xenotime crystal grows relatively rapidly between episodes of zircon growth. Zircon growth is then initiated again, continuing to crystallise until formation of outgrowth stops due to reduced availability of Zr during the prograde part of the cycle. This is likely to be linked to when radiation damaged areas become annealed, in the case of zircon this occurs at *c.*250°C (Geisler et al., 2003a).

Stage 5: Late fracturing causes the xenotime crystal to break it into three components. Associated with this zircon outgrowth breaks up forming tiles. The fracturing of zircon into these tiles may occur along the boundaries of different growth phases which would act as lines of weakness.

Stage 6: Very late zircon precipitation, growing along discontinuities in the xenotime. The stress from final growth phase causes sub-grain recrystallisation in adjacent quartz.

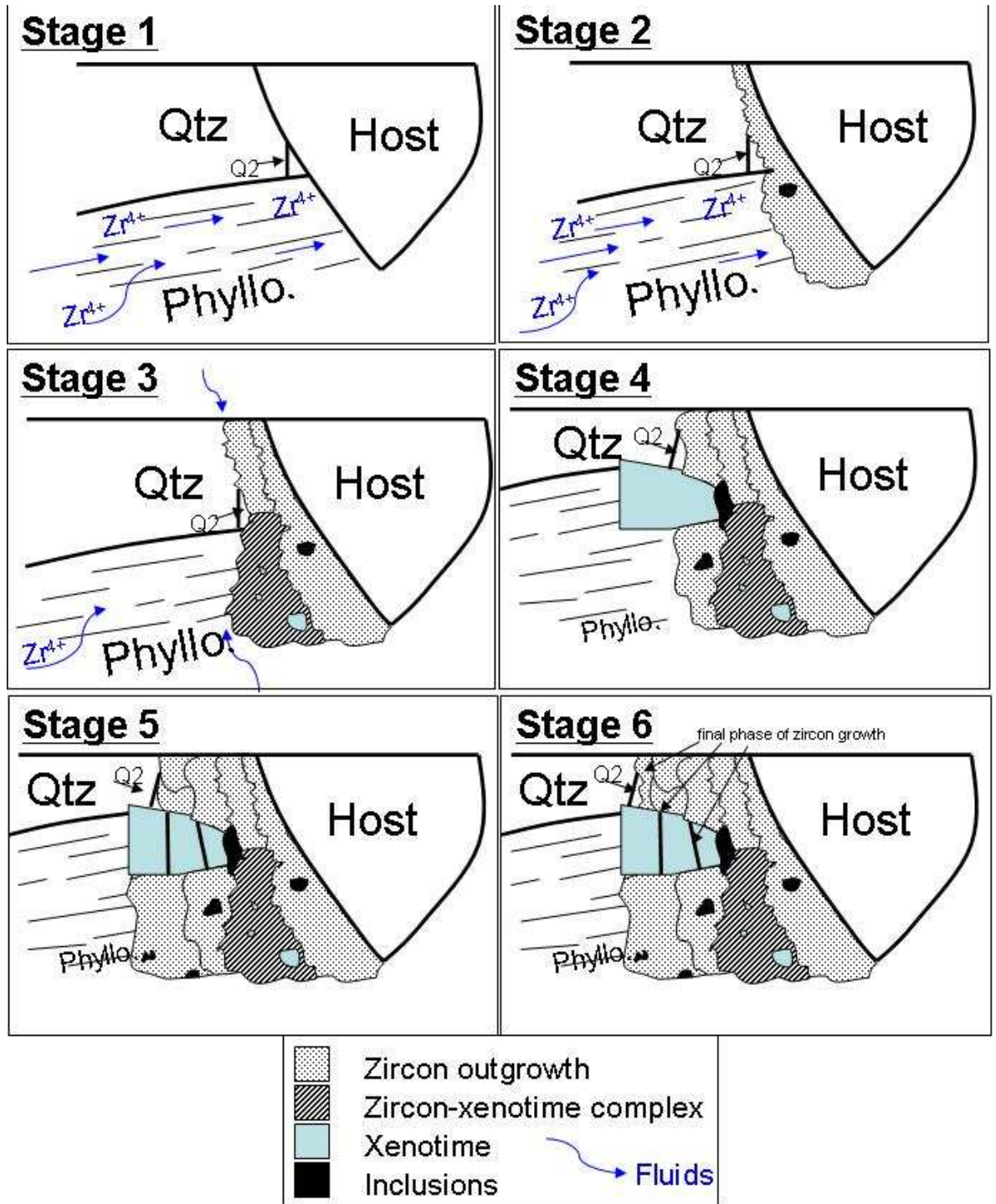


Figure 75 Model of zircon outgrowth formation

As the model in Figure 75 is a generalised view of how zircon outgrowths are formed, the microstructure of outgrowths will vary greatly between individual zircons and from rock to rock as it will be strongly dependent on local conditions. The most important of these factors is the availability of Zr and this is related to the metamict state of individual zircons and temperature, which is controlled by metamorphic grade. Other factors that will dictate zircon outgrowth morphology are the local mineralogy surrounding the zircon, fluid composition and fluid availability. These concepts will be explored in the next chapter.

The significant variation in the microstructure of outgrowths indicates that individual outgrowths form from a number of different stages of growth. For example an outgrowth may form from a single growth event that is possibly from Zr transported from the interior to the exterior of a zircon. Xenotime availability also has a significant role in the development of the outgrowth: when growth favours both zircon and xenotime, it results in zircon-xenotime complexes, or when xenotime forms between episodes of zircon growth, xenotime crystals may form. Where xenotimes form large outgrowths on zircon, at least three phases of growth have been identified (Chapter 3).

5.6 Summary

Zircon outgrowth development occurs in multiple stages because the mobilisation of Zr is episodic. As a result, zircon growth is intimately linked to the metamict state of zircon and how readily Zr is liberated from it. When zircon growth is favourable, rapid crystallisation results in a nanocrystalline tile. In circumstances where both zircon and xenotime growth is favourable, synchronous growth results in complexes of zircon and xenotime. Between periods of zircon growth, xenotime can form individual, well-defined crystals that then become partly surrounded when zircon growth recommences. Fracturing of these xenotimes is evidence of intense, very localised strain that is created during outgrowth formation. These fractures are subsequently sealed by late zircon growth. Such zircon growth may occur from fluids that have become supersaturated with respect to Zr that is most likely to occur in the retrograde part of the metamorphic cycle. The result is that development of outgrowths on zircon is extremely complex, generating a unique microstructure on each host zircon.

6

Zircon behaviour in shallow crustal environments

Crystalline zircon is stable in virtually all low temperature environments and therefore the zircons response to low temperature conditions can be broadly explained by the effects that radiation damage has on crystal structure. However some of the low temperature responses of zircon relate to particular lithologies (e.g. zircon outgrowths in slates) and, coupled to the wide range of zircon microstructures, indicate that processes other than simply metamictization influence zircon behaviour. This chapter examines the environmental factors and considers how other processes, in addition to metamictization, may affect zircon behaviour in low temperature environments. To do this, the chemical and textural characteristics of zircon from mudstones and sandstones will be compared with their metamorphic equivalents. This chapter will also examine how sedimentary processing, fluid flow and fluid composition may affect zircon behaviour. The various factors that influence zircon behaviour will be interpreted in a model through a low temperature rock cycle. This chapter concludes by speculating as to the fate of low temperature zircon in higher grade rocks.

6.1 Metamorphic grade

6.1.1 Textural comparison

Many of the textures and microstructures found are present in zircon from both sediments and greenschist facies metasediments (compare **Table 1** & **Table 8**). Although the sets of lithologies examined are broadly equivalent, the sedimentary suite lacked a non-carbonate cemented

mudstone.

Dark BSE zircon is abundant in both suites of rocks with Group 1 dark BSE zircon the dominant form. However Group 2 dark BSE zircon is more common in sedimentary rocks with about four times as many zircons containing Group 2 dark BSE zircon in comparison to zircon in greenschist facies rocks. Group 2 dark BSE zircon in greenschist facies rocks is rare (Fig. 6m). Porous zones in zircon and more unusual textures (e.g. mosaic zircon, Fig. 9c and Fig. 62) are present in rocks from both grades.

Zircon outgrowths are found in much greater abundance, both in size and number, in greenschist facies slates compared to rock samples that have only experienced diagenesis. This suggests Zr mobility is enhanced by temperature and that dissolution rates of metamict zircon increases appreciably above 100°C (the maximum temperature of the diagenetic rocks studied). The discovery of zircon outgrowths in sedimentary rocks (Chapter 4) has not been previously reported in the literature. The zircon outgrowths in Dalradian greenschist facies metasediments observed in this study bear a very close resemblance to those outgrowths described by Rasmussen (2005) in metasediments spanning a range of temperatures (250-500°C) and localities (Australia, South Africa, UK). Yet Rasmussen found no evidence that may explain the source of Zr for these zircon outgrowths. Examination of the images published in Rasmussen (2005) however show features very similar to dark BSE zircon observed in the Dalradian metasediments (e.g. Fig. 3e&h in Rasmussen, 2005). It therefore seems likely that Zr has been mobilised from these altered areas and precipitated on the margins of unmodified zircon. Utsunomiya et al., (2007) have also identified natural, secondary low temperature alteration textures in zircon from a porphyritic granite in the Jack Hills, Australia (which they also refer to as dark BSE zircon). They observe similar textural characteristics to those in Group 2 dark BSE zircon. The chemical characterisation of the altered areas in the Jack Hills zircon reveal remarkably similar chemistries and substitution trends to those in greenschist facies dark BSE zircon from the Dalradian. Utsunomiya and co. workers also found that dark BSE zircon is enriched in Ce which we did not analyse for in our study. Energy electron loss analysis of Ce reveals it is tetravalent indicating dark BSE zircon

formed an oxidising environment.

Light and dark BSE zircon have rounded grain edges in highest grade quartzites (*c.*450°C). This suggests that at these grades, zircon may experience dissolution that is independent of metamictization as this is significantly above the annealing zone.

In greenschist facies rocks, the majority of low temperature zircon is thought likely to have formed during prograde metamorphism when permeability of fluids is enhanced. In contrast to this, dark BSE zircon in sedimentary rocks may potentially form at any stage of the burial and uplift cycle provided temperature does not exceed the annealing temperature for zircon.

6.1.2 Chemical comparison

All the low temperature zircon textures from both greenschist facies and sedimentary rocks have broadly similar chemical characteristics as all are depleted in Zr and Si, with respect to their unmodified composition, and enriched in non-formula elements (Table 12). While there is some variation in the element concentration and chemical substitution trends within each texture, mostly between individual grains, the composition of each texture follows reasonably defined chemical trends. It is apparent from these trends however that the chemistry and the substitution mechanisms between textures are not all the same (Fig. 76).

Zr substitution trends with Al, Ca and Y in sedimentary dark BSE zircon and zircon outgrowths are similar although sedimentary dark BSE zircon is typically more enriched in all. Zircons from the different environments have slightly different Zr-Ca and Zr-Al trends (Fig. 76) but both have a Ca:Al ratio of 3:1 (Fig. 76). Fe is found in similar concentrations in sedimentary dark BSE zircon and zircon outgrowths but there is significant spread in the data on Zr-Fe plots and therefore no consistent substitution trend can be identified. This spread in the data is possibly due to the inclusion-rich nature of both zircon outgrowths and sedimentary Group 1 dark BSE zircon.

	Greenschist dark BSE zircon	Sedimentary dark BSE zircon	Zircon outgrowths
Zr:Ca	1:1	5:2	3:1
Si:Ca	2:1	3:1	1:1
Zr:Y	1:1	20:3	20:3
Si:Y	1:1	10:1	10:1
Zr:Al	1:1	20:3	10:1
Si:Al	2:1	10:1	20:3
Zr:Fe	2:1	4:1	1:1-10:1
Ca:Al	1:1	3:1	3:1
Ca:Mg	10:1	5:1	n/a
Si:NFE	1:3	3:2	1:1
Zr:NFE	1:3	1:1	2:1
Total wt%	89.8(±4.3)	96.0(±2.5)	97.4(±2.5)
Total c.p.f.u.	1.93(±0.02)	1.82(±0.05)	1.89(±0.02)

Table 12 Comparison of element trends in low temperature zircon.

Metamorphic zircon outgrowths differ from sedimentary dark BSE zircon where the summed total of the non-formula elements is plotted against Zr and Si (Fig. 76). Sedimentary dark BSE zircon exhibits a 1:1 Zr:Sum of non-formula elements while substitutions in zircon outgrowths follow a 3:2 trend. Further variations between zircon outgrowths and sedimentary dark BSE zircon are observed in zircon outgrowths following a 2:3 Si:Sum of non-formula elements substitution trend, contrasting with a 3:2 of Si:Sum of non-formula elements in sedimentary dark BSE zircon. Si loss in zircon outgrowths is considerably less than in sedimentary dark BSE zircon and the result is very different Si-non-formula element substitution trends (Table 12) and zircon outgrowths having a lower Zr/Si ratio

Greenschist facies dark BSE zircon is the most non-formula element enriched low temperature zircon. Greenschist facies dark BSE zircon is particularly enriched in Y and Al with respect to

sedimentary dark BSE zircon (Fig. 76). However, Zr and Si in greenschist facies dark BSE zircon follow the same 1:1 substitution relationship as sedimentary dark BSE zircon and the latter also experiences more Zr and Si loss than greenschist facies dark BSE zircon. This is unexpected as the most non-formula element-rich phase would also be predicted to be the most depleted in Zr and Si (Fig. 76). Thus there is an imbalance between the amount of Zr and Si lost and the amount of non-formula elements gained in dark BSE zircon. The amount of non-formula elements in greenschist facies dark BSE zircon (3 units) that is greater the amount of Zr and Si lost (2 units). This means that some of the non-formula elements are probably at interstitial sites within the lattice of greenschist facies dark BSE zircon. Sedimentary dark BSE zircon and zircon outgrowths however have a considerable loss of Zr and Si (5 units) compared to only 2 units of non-formula elements (76). This suggests that sedimentary dark BSE zircon and zircon outgrowths are considerably more hydrated than greenschist dark BSE zircon. However the total weight percent of greenschist facies dark BSE zircon is considerably lower than sedimentary dark BSE zircon (89.8 ± 4.3 and 95.8 ± 2.4 respectively). A minor deficit in greenschist facies dark BSE zircon weight percent totals is potentially explained by the omission of P during EPMA analysis. The uptake of Y in zircon is often coupled to the substitution of P for Si into the lattice (Eq. (4), Chapter 1 and Hoskin and Schaltegger, 2003). As greenschist facies dark BSE zircon is significantly enriched in Y compared to sedimentary dark BSE zircon, the amount of P may be expected to be higher in Y enriched zircon. If the uptake for P is coupled to Y and a 1:1 enrichment trend is assumed, the most the amount of P associated with the most Y rich point (0.1 c.p.f.u. which correlates to *c.*4wt%) is *c.*1.4wt%. Therefore this deficit is does still not account for the loss in weight percent. What the loss in the total weight percent in greenschist facies dark BSE zircon is likely to represent is the relative amount of hydrous species present within the structure. However this is a surprising conclusion because the relatively low concentration of non-formula elements in sedimentary dark BSE zircon in relation to the large amount of Zr and Si loss would be expected to be the result of more hydrous species but this is not the case. The relative microporosity could possibly be responsible for some loss in the weight percent total however the microstructures of greenschist facies dark BSE zircon and sedimentary dark BSE zircon appear similar. As such, although microporosity may result in reduced weight percent totals, it is not thought that there is a consistent

variation between the greenschist facies and sedimentary dark BSE zircon microstructures that could account for such a low drop in weight percent totals between the two. Another possibility is that the different weight percent totals are due to where hydrous species are located in the structures. OH groups are bound into the lattice would affect the relative substitution relationships of other elements while hydrous species held along grain boundaries in the dark BSE zircon microstructure will have no affect on the substitution relationships but act to lower the total weight percent.

The substitution trends between greenschist facies and sedimentary dark BSE zircon are distinctly different. As it most likely that greenschist facies dark BSE zircon has previously experienced diagenesis and similar processes to that of sedimentary dark BSE zircon, then it is reasonable to expect some substitution trends that reflect this. Despite variation in the substitution trends within individual textures, at no point do these trends match those of the sedimentary dark BSE zircon. There would appear to be two possible answers to this problem. The first is that all the chemical alteration in sedimentary zircon is overprinted by subsequent chemical changes as a result of greenschist facies metamorphism. The second explanation may be that chemistry of the altered zircon is most strongly controlled by the bulk composition of the host rock. It would be expected that there would be considerable scatter in the greenschist facies dark BSE zircon substitution trends if metamorphism overprinted a previous sedimentary dark BSE zircon history. Instead, well-defined substitution trends are observed. Therefore, it appears more likely that bulk rock composition affects the composition of the fluids thereby affecting the availability of non-formula elements. This may also be the case with such extremely different compositions between zircon outgrowths and greenschist facies dark BSE zircon, which have been analysed from slate in comparison to more phyllosilicate-poor lithologies respectively.

It is likely that the most important factor in controlling the uptake of non-formula elements into the zircon structure is the metamict state (Geisler et al., 2003b). However, variations in the concentration of cations in the fluid are also likely to impact on the concentration of non-formula elements in dark BSE zircon and zircon outgrowths. This is probably most applicable to Y, as it

likely to be the least readily available element of the cations that substitute into the zircon structure, the rest being widely available “major” elements (Ca, Mg, Al, Fe). The strong correlation of Y and Al enrichment in greenschist facies dark BSE zircon from psammites and quartzites is not observed in zircon outgrowths from slates and probably due to the majority of available Y being incorporated into xenotime which form as outgrowths. Y in psammites and quartzites is therefore taken into the structure of dark BSE zircon possibly because there is less P available to form xenotime. It is not clear why dark BSE zircon from diagenetic rock does not follow a similar pattern to their greenschist facies equivalents but it may be that xenotime is more readily mobilised at higher temperatures than the diagenetic rocks have experienced.

It is not apparent why dark BSE zircon has a high Zr/Si signature. Based on the known substitution mechanism for non-formula elements in zircon, substitutions in the zircon structure should result in low Zr/Si ratios as Zr is preferentially substituted for by non-formula elements upto 4:1 from Si in some mechanisms. U appears to remain concentrated within Group 1 dark BSE zircon (e.g. Fig. 63) and therefore, over time, dark BSE zircon will be the area most likely to become metamict again. If the uptake of Mg, Al and Fe occurs at interstitial sites within the lattice, this is likely to strain the lattice and may facilitate the enrichment of other mineral phases, like xenotime, which is isostructural with zircon.

The chemistry of dark BSE zircon and zircon outgrowths is varied and the substitution mechanisms by which non-formula elements enter the lattice are complicated. A larger data set documenting the chemistry of low temperature zircon in a wider range of lithologies and “grades” is required. This may allow a better understanding of how zircon chemistry varies with the local environment whilst addressing how the substitution mechanisms involved in these processes operate. This has been labelled for future work.

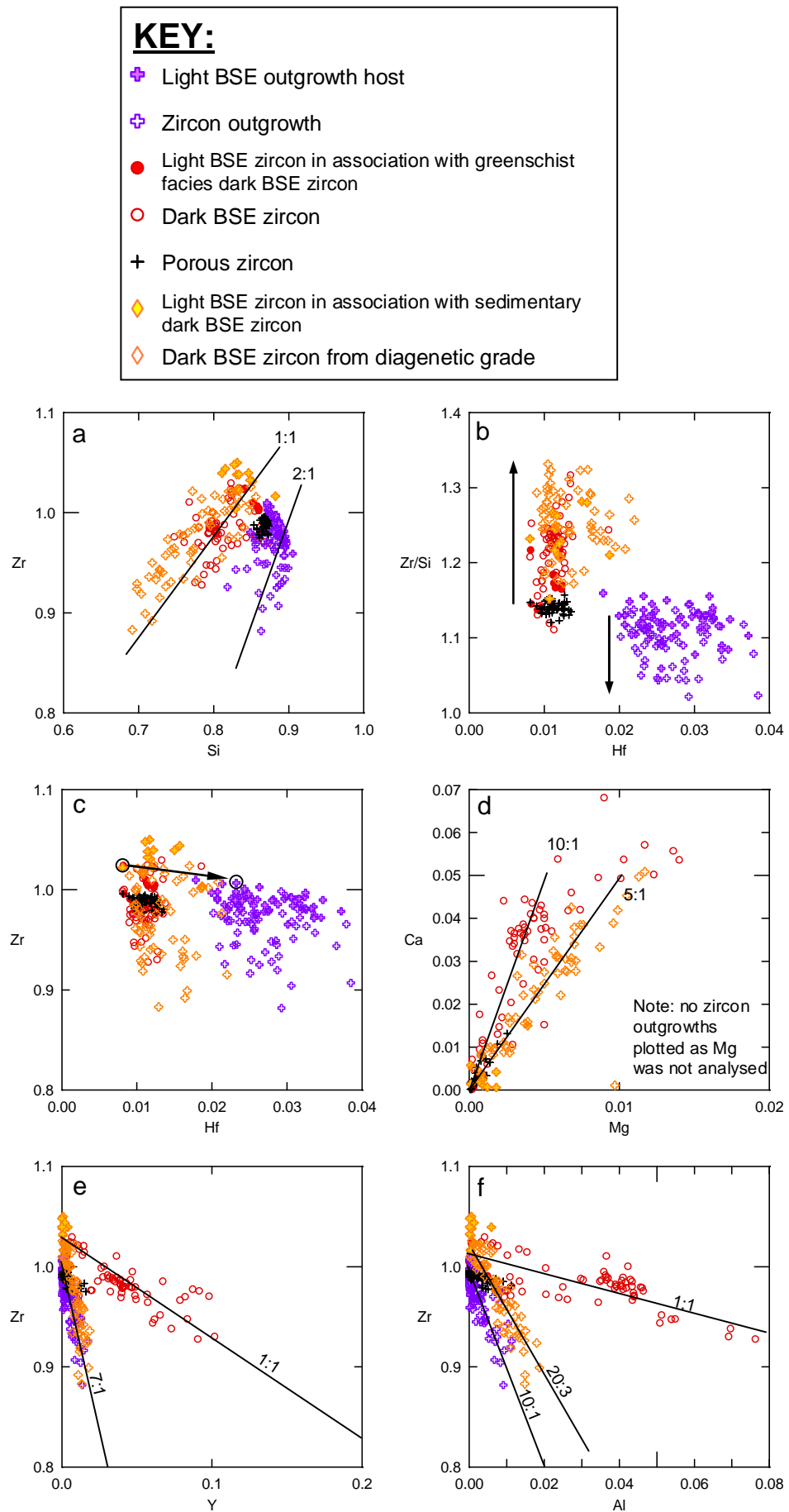


Figure 76 Element plots (units in c.p.f.u.) of zircon textures in sedimentary and greenschist facies rocks

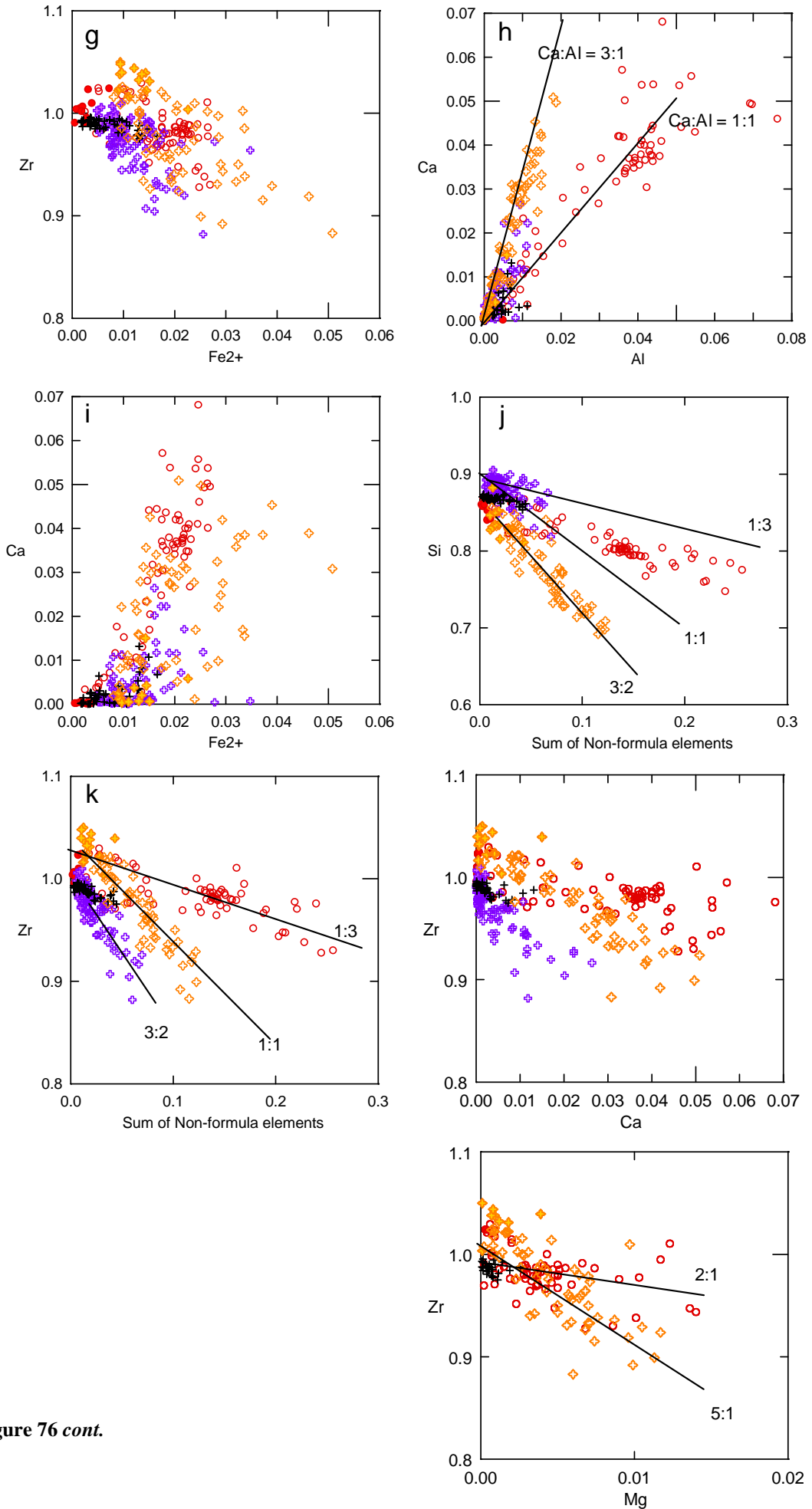
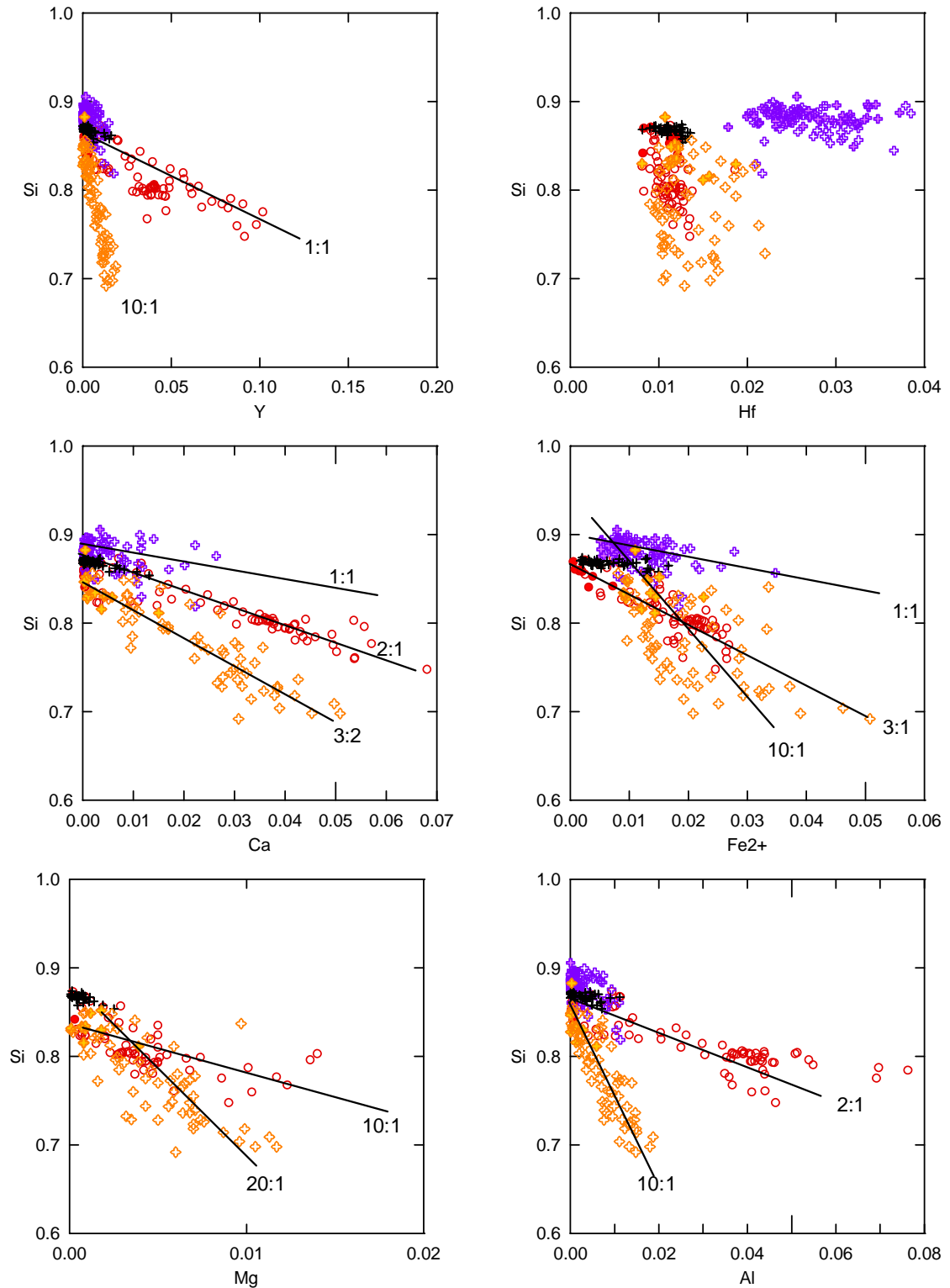


Figure 76 cont.

**Figure 76 cont.**

6.2 Depositional environment

During sedimentary transport zircon is mechanically worn down and sorted into sediments based on their durability, size and density. Crystalline zircon is extremely durable and has a remarkable ability to survive considerable amounts of sedimentary reworking. Consequently mature sediments (e.g. quartz arenite) will contain large, well-rounded detrital zircon while fragments broken off as the grain is rounded, are sorted into the fine-grained sediment (e.g. mud). However metamictization is a common cause of mechanical failure in zircon and so may play a key role in the break up of zircon during sedimentary transport (Fig. 77). Source rocks containing metamict zircon or the generation of metamict zircon whilst in a sediment, may have the metamict and crystalline fragments reworked into finer-grained sediments. The mechanical strength of metamict zircon is lower than crystalline zircon and therefore metamict fragments may break down further. As a consequence of metamictization, fine-grained sediment is a sink for U- and Th-rich, strongly radiation damaged zircon. Mature sediments will favour more pristine zircon with little radiation damage (i.e. U- and Th-poor) or young zircon, where insufficient damage has accumulated in the time elapsed. Muddy sandstones and immature sediments may contain a wide variety of zircon types and potentially lithic arenites can contain highly metamict zircon in clasts that have remained intact due to protection from sedimentary processing. Metamictization therefore creates a severe bias in the detrital zircon population in sediments.

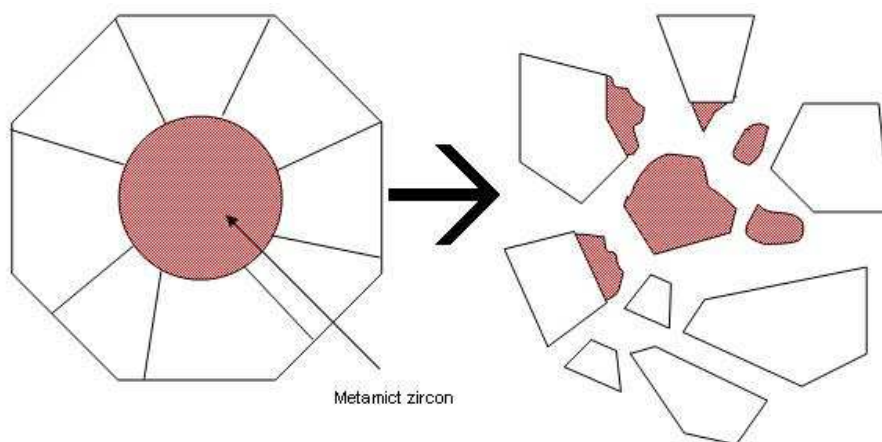


Figure 77 Schematic illustration of zircon grain breakup due to metamictization

As previously stated (Chapters 3 & 4), the necessity for nucleation points on existing crystalline zircon appears to be key to the precipitation of zircon in low temperatures. Without crystalline zircon around the site of dissolution, there is substrate for zircon to nucleate on and Zr may remain in solution. Zircon grains that are entirely metamict at both the mesoscopic and macroscopic scale will go into solution without precipitating dark BSE zircon as there are no nucleation sites onto which new zircon can grow (i.e. crystalline zircon). This implies that where no crystalline zircon is present around the area of dissolution, metamict zircon may be stripped from the rock. Without crystallisation of zircon the fluid phase will be saturated in Zr. Once Zr is mobile in the fluid, the fluid composition is likely to change due to interactions with other mineral phases. Changes in the fluid composition may lead to Zr becoming supersaturated. Supersaturated fluids will precipitate zircon on the next suitable nucleation site (i.e. crystalline zircon) as an outgrowth. However, the presence of only a small crystalline area (e.g. thin lath of crystalline zircon from the original grain) in a metamict zircon grain may be sufficient to cause virtually the whole grain to form dark BSE zircon. Once dark BSE zircon begins to crystallise, it also provides a platform on which more zircon can precipitate. Metamict zircon will mostly be absent from mature sediments for reasons discussed above. Entirely metamict zircon grains are preferentially concentrated in fine grained sediments and the removal of these grains may cause supersaturation in the Zr and is likely to be responsible for crystallisation of outgrowths. The issue of Zr supersaturation in the fluid phase will be explored further in the next section.

The great majority of zircon that displays in-situ radial fractures will be found in coarse grained lithologies. Grains with such features are likely to be relatively young with respect to the timing of deposition but where the accumulation of radiation damage has been rapid (i.e. U and Th rich). This is a further example of how sedimentary processing may affect the zircon texture that forms in the rock.

Metamictization in zircon, together with sedimentological processes, create severe biases in the detrital zircon population at the Earth surface. However, the biases created at the Earth surface may control the formation of zircon outgrowths in fine grained rocks. Therefore sedimentological

processes have a major impact on the behaviour of zircon during metamorphism.

6.3 Fluids

6.3.1 Fluid permeability

Permeability in sandstones and mudstones will be relatively low at the burial depths (2-3km) that metamict zircon may begin to experience dissolution. During diagenesis and metamorphism transient periods of increased permeability may exist due to dehydration reactions in unstable clastic and authigenic clays that alter with increasing temperature. Examples of these dehydration reactions are the formation of illite, silica and water from smectite (usually above depths of 3km and below 100°C) and kaolinite combined with K-feldspar. Significant quantities of chlorite are also usually produced during the formation of illite from smectite (Velde, 1992). These reactions are accompanied by a very strong reduction in porosity that are associated with extensive quartz cementation in rocks (Bjørlykke, 1997). During metamorphism, deformation may locally enhance permeability in metasediments, allowing fluids to interact with zircon grains causing dissolution and rounding of zircon grain edges in the highest grade rocks (c.450°C). In general, sandstones and mudstones and their metamorphic equivalents are characterised by relatively low permeability but with intermittent periods of higher permeability associated with fluid flux.

6.3.2 Fluid composition

Fluid composition continuously evolves throughout burial, diagenesis and metamorphism because of mineral reactions and associated devolatilization. The nature of the sedimentary succession has an important control over fluid composition, particularly the presence of evaporite deposits within the sedimentary sequence which can affect fluid salinity (Yardley, 1997). However there is no evidence of significant evaporite deposits in any of the sequences studied.

It has been proposed that Cl^- , Br^- but particularly F^- ions in the fluid phase may be important in the enhanced dissolution of zircon (Rasmussen, 2005b and references therein) because of the increased fluorine concentrations found associated with Zr mobility and new growth in hydrothermal

environments. Fluorine has been shown to appreciably increase the solubility of crystalline zircon in experiments conducted in melts at temperatures $>800^{\circ}\text{C}$ (Keppler, 1993; Baker et al., 2002). F^{-} may also readily substitute into the crystal structure of clays and micas (Robert et al., 1993; Boukili et al., 2001; Boukili et al., 2002; Rasmussen, 2005b) and therefore may be released from devolatilization reactions in clays and micas during diagenesis and prograde metamorphism. In muds and slates, where clays and micas are abundant, this could potentially form a fluid capable of enhancing dissolution rates of metamict zircon. The effects of this are two fold, as both F^{-} and temperature would therefore increase the rate of metamict zircon dissolution.

Experiments on the hydrothermal synthesis of zircon from fluorinated gels found zircon that crystallised from acidic solutions was heavily enriched in F^{-} and depleted in Si whereas zircon from alkali solutions had a normal composition (Valero et al., 1998). Although in our study F^{-} was not analysed during EPMA, the analysis of multiple dark BSE zircon and zircon outgrowths EDX spectra show no enhanced F^{-} -enrichment, possibly implying that dark BSE zircon and zircon outgrowths did not crystallise from an acidic fluid. Experiments by Valero et al. (1999) indicated that the morphology of synthetic zircon was strongly dependent on F^{-} concentration. The presence of F^{-} in rocks may therefore have an influence on the microstructure of dark BSE zircon and zircon outgrowths, not just the rate of dissolution. However, on the premise that F^{-} is important, the fluid that metamict zircon is exposed to in sandstones, psammities and quartzites will be less corrosive than in mudstone and slate as they lack clays and micas. Therefore it may be expected that clay- or mica- rich bands in sandstones, psammities and quartzites create locally elevated F^{-} concentrations in the fluid. On examination of zircon grains in layered rocks however, there would appear to be little correlation between enhanced dissolution within or around clay- or mica-rich bands. In such instances, maybe F^{-} concentration is too dilute to affect zircon solubility or perhaps the metamict state of zircon exerts too strong an influence on the behaviour of zircon for any appreciable affect to be observed. However dark BSE zircon has been demonstrated to form in wide variety of rock types, an indication that metamict zircon is out of equilibrium with fluids in most low-temperature environments. This suggests that metamict zircon will likely go into solution provided the fluid phase is undersaturated in Zr . F^{-} , Cl and Br , among many other elements in the fluid phase, may

affect dissolution rates of metamict zircon. However it is more likely that these elements are important in changing the level of Zr saturation in the fluid rather than directly affecting the zircon solubility. Increasing Zr saturation levels in the fluid phase will trigger more dissolution of metamict zircon until saturation is reached again. If Zr saturation levels drop, perhaps by consumption of saturation enhancing elements by other mineral phases, the fluid will become supersaturated and dark BSE zircon will precipitate providing a suitable nucleation site is available. The release of fluids from dehydration reactions and the changing mineralogy during burial, diagenesis and metamorphism may ensure that fluids are in a constant flux between states of undersaturation, saturation and supersaturation with respect to Zr. The equilibration of metamict zircon to dark BSE zircon consequently proceeds via a series of dissolution and reprecipitation microsteps.

Variations in the chemistry of dark BSE zircon between individual grains, particularly those that formed in greenschist rocks, may be a consequence of the availability of non-formula elements in the fluid phase. Therefore the concentration of non-formula elements in the fluid phase could be significant in the chemistry of dark BSE zircon.

Zircon behaviour in relation to the concentration of Zr in the fluid phase may be affected by the rock permeability. Where permeability is higher, Zr from dissolved metamict zircon can become diluted. Dilution will trigger more dissolution of metamict zircon. If dilution is rapid (i.e. when permeability is high), Zr may be more readily transported away from the dissolution site resulting a cavity-rich microstructure like those observed in zircons from sandstone, psammite and quartzite (e.g. Fig. 9 and 47). However the opportunity to create cavities in zircon is limited as both sandstone permeability quickly diminishes with burial (Bjørlykke, 1997) and the solubility of metamict zircon is low at shallow burial depths. Once reduced, permeability creates more local fluid conditions that are likely to enhance the dissolution-reprecipitation process and dark BSE zircon. The formation of Group 2 dark BSE zircon via a diffusion-driven, structural recovery, cation-exchange process is considered to be a background process to dissolution and precipitation. For Group 2 dark BSE zircon to form, the metamict zircon must be exposed to fluids saturated in

Zr for periods long enough to allow diffusion of water species into the structure. These conditions are most likely to occur where fluid flow rates are negligible. Permeability in early carbonate cemented rocks will be very low and such rocks will not experience the same volume of fluid flux as non-cemented sandstones. This creates an environment more favourable for the formation of Group 2 dark BSE zircon and the absence of a carbonate cement may explain the relative lack of Group 2 dark BSE zircon in greenschist facies rocks.

The controls that fluid composition and permeability have on zircon behaviour have been generalised greatly. This has been necessary, so that some simplified view of zircon behaviour may be obtained. Other factors that have not been taken into consideration are the lateral heterogeneities that exist within sedimentary sequences. This may affect fluid flow and hence affect how Zr is transported. Faulting is the most effective way of increasing permeability in more deeply buried rocks (Bjørlykke, 1997). Muds and mudstones usually remain ductile until the onset of extensive quartz cementing (>80-100°C (3-4km)). However, this study has found no evidence of Zr mobilisation in quartz veining on microfractures.

The great heterogeneity in the mineralogy on a thin section scale (e.g. non-cemented domains in sandstone, carbonate cement areas, mica-rich domains), and the affect mineralogy has on fluid composition make predicting zircon behaviour in natural systems difficult. This is also further complicated by the degree of metamictization in the zircon, which is the overriding factor in controlling zircon behaviour. The potential to dissolve metamict zircon and mobilise significant quantities of Zr in rocks is relatively limited due to rapid reduction in permeability with burial and the low dissolution rates of metamict zircon at shallow depths. Potentially, the textures and microstructure of zircon as a result of metamictization may provide unique information on the permeability of the rock in the shallow crust.

6.4 Modelling zircon behaviour in the crustal environment

It is the purpose of this section to synthesise the key processes that affect zircon behaviour in low

temperature environments. To illustrate this the behaviour of a population of zircon grains in mud and sand units will be considered throughout a history of sediment transport and deposition, burial and diagenesis at 100°C, further burial and diagenesis at 250°C, low temperature metamorphism at 350°C and exhumation and cooling. Zircon behaviour is extremely complex resulting in a wide variety in textures and features due to the heterogeneity of the individual grains and the variable nature of the conditions in which they form. It should therefore be emphasised that this model (Fig. 78) is simplified in order to demonstrate how the broad range of controls effect and influence zircon behaviour. To do this, the zircons that have been modelled have derived from a granite source rock, as this will contain variably zoned zircon with some metamict high U zircon. For simplicity the genesis age for all the source zircon is the same. Variable U concentrations give rise to the potential that zircon may go metamict at any stage below the annealing temperature of the modelled history and consequently “skip” earlier events. Zircon populations in the below text refer to zircons illustrated in Fig. 78.

- i) **Stage 1 - Surface processes:** Key factors – **metamictization and sedimentary processing.** Sedimentary transport will concentrate large, rounded detrital zircon in mature sediments (population B&C). Metamictization is a common cause of mechanical failure in zircon and so plays a key role in breaking up zircon during sedimentary transport (Fig.77). This results in small crystalline (zircon d) and metamict fragments (zircons E-G) being sorted into the fine-grained sediment. Therefore as a consequence of metamictization in zircon at source, fine-grained sediments (mudstone) are sinks for U- and Th-rich, strongly radiation damaged zircon and mature sediments (sandstone) favour zircon with little radiation damage (i.e. U- and Th-poor, zircon C) or young zircon where insufficient damage has accumulated in the time elapsed to cause break up. Heavily radiation damaged zircon that is protected within an inclusion (e.g. quartz) may survive to be incorporated into coarse-grained sediment (zircon A). If sediment remains passive for prolonged period of time before metamorphism, in-situ fractures may be generated as a result of metamictization (zircon B).

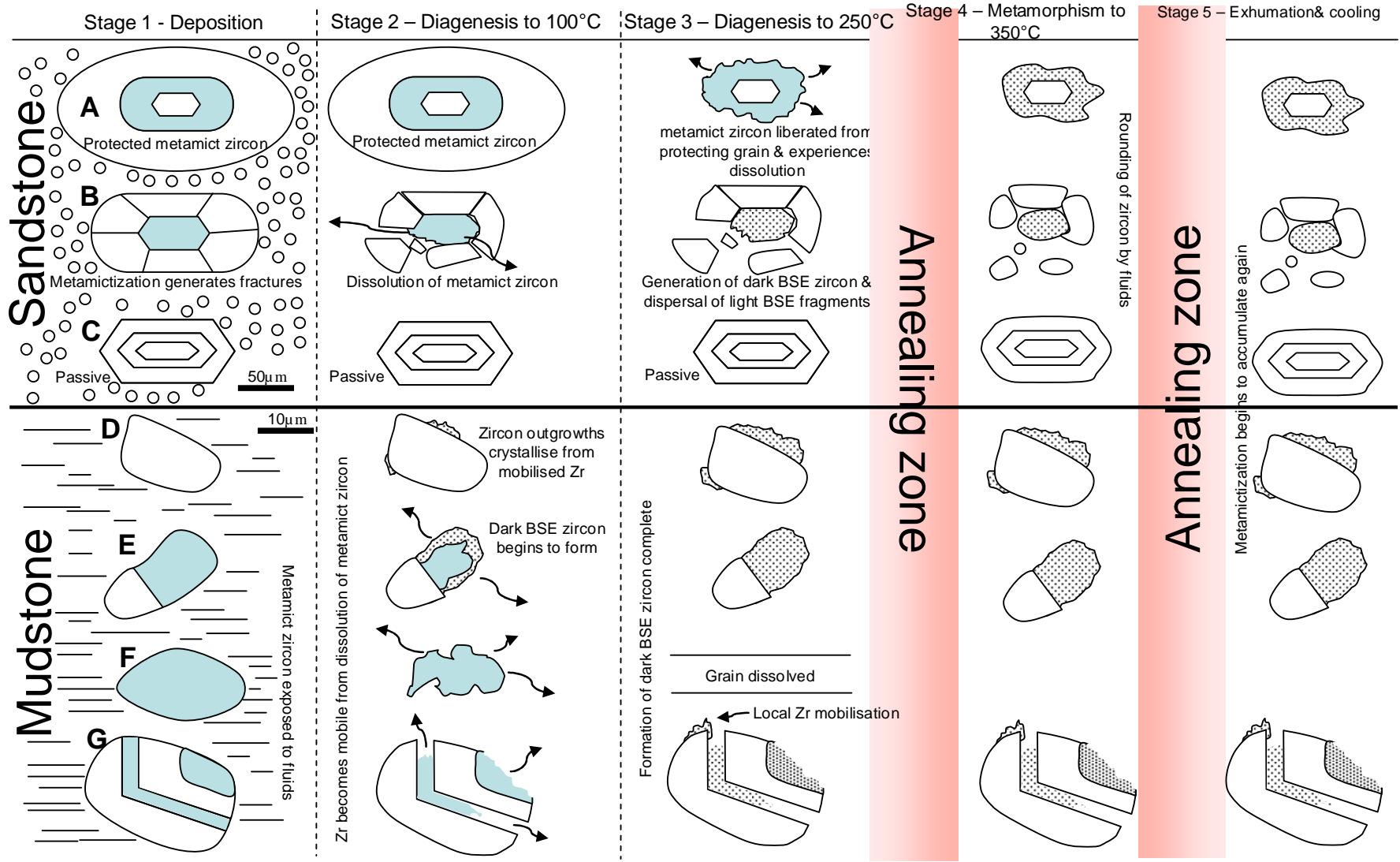


Figure 78 Modelling zircon behaviour through a metamorphic cycle.

- ii) **Stage 2 – Diagenesis to 100°C:** Key factors – **metamictization, fluids, temperature, protection.** Metamict zircon becomes more soluble with increased temperature triggering dissolution (zircon B, E-G). Permeability rapidly reduces with burial and so there is potential to locally saturate the fluid phase with Zr enhancing possible local precipitation of dark BSE zircon (zircon E). However sandstone units are still more permeable than mudstone and therefore have greater potential for Zr to be lost from the system (zircon B). Mobilisation of Zr causes small outgrowths to crystallise (zircon D). Metamict zircon may remain protected as an inclusion in a grain or by crystalline zircon (zircon A).
- iii) **Stage 3 – Diagenesis to 250°C:** Key factors – **metamictization, fluids, temperature.** Solubility of metamict zircon rises with temperature causing dark BSE zircon reactions to reach completion (zircon B, E&G). Permeability in all rocks is low and fluid flow is characterised by transient periods of increased flux due to dehydration reactions allowing Zr to be mobilised (zircon F). Zircon nucleates and crystallises as outgrowths on crystalline zircon from solutions locally supersaturated with respect to Zr (zircon D&G). Recrystallisation of quartz liberates metamict zircon from the grain that protected it as an inclusion (zircon A).
- iv) **Stage 4 – Metamorphism to 350°C:** Key factors – **fluids, temperature, deformation.** Metamictization is no longer an overriding factor above the annealing temperature (*c.*250°C) however, heavily radiation damaged zircon may not anneal until slightly higher temperatures (*c.*300°C) allowing dark BSE zircon to still form (zircon A). Dehydration reactions continue to produce fluids fluxes. These fluids may still be important but less so than at low temperatures. Fluids are likely to be undersaturated in Zr and corrode zircon in quartzites producing rounded grains through dissolution of angular margins (zircon A&B). Slates are relatively impermeable and the amount of fluid produced can only equal the amount that escapes. Therefore zircon in slates has much more closed system behaviour allowing fragile microstructures to be preserved

(zircon D, E&G).

- v) **Stage 5 – Exhumation and cooling:** Metamictization begins to accumulate again below 250°C but the lack of fluid producing reactions and sufficiently metamict zircon mean zircon is effectively stable.

In natural examples, there is a huge variation to the textures, microstructures and features formed compared with those in this model. This is due to the many variables that influence zircon behaviour. Zircon provenance is a key part in generating this heterogeneity. The sediment source for basins will probably come from a whole range of rock types. This may include reworking of sedimentary sequences, erosion of basement rock that can span a range of metamorphic grades and erosion of igneous complexes. Sediments that derive from such rocks will likely contain zircon that represent a wide range of forms, zoning types, compositions and ages. If however, the sediment source is from the erosion of lower grade metasediment basement rock, then the zircon in these rocks will have a similar record of the low-temperature processes described here. Dark BSE zircon and zircon outgrowths will be likely to be broken down due their porous and inclusion rich microstructures. Furthermore, the ability to retain actinide elements during low temperature alteration, make dark BSE zircon likely to become metamict again. Porous particles of metamict dark BSE zircon will be sorted into fine-grained sediment. These may act as source of Zr for zircon outgrowths but if dissolution and reprecipitation of metamict dark BSE zircon occurs, the result could be an extremely complex microstructure. Lithic fragments in sandstone may harbour highly metamict zircon that would otherwise break down through sedimentary processing. Conglomerates may contain a huge variety of different zircons with a wide range of characteristics.

Just as metamict zircon can be protected from fluids by encasing crystalline zircon, metamict zircon as inclusions within grains (e.g. qtz) may also remain protected. As grains containing zircon recrystallise during burial and deformation, metamict zircon may be released, exposing it to fluids. If the metamict grain is not released from the protecting grain during metamorphism, the metamict zircon may remain unaltered throughout the entire metamorphic history of the rock. The result is a

zircon population that spans from crystalline to strongly metamict states and often this variability can be replicated at grain scale.

The continual process of zircons being exposed to the fluid phase throughout the history of the rock (either by reaching metamictization at the 1st percolation point, exposed through metamict generated fractures or becoming liberated from grains it was an inclusion in) causes significant heterogeneity in the timing of formation of dark BSE zircon and Zr mobility. However, the flip side of this is the continual liberation of Zr from metamict zircon may allow fluid flow behaviour in rocks to be uniquely monitored. This may potentially give a better understanding of fluid flow in low temperature rocks, an area of research in Earth science that is rather a “grey area”.

Changes in the fluid composition may also significantly affect whether metamict zircon will go into solution (fluids undersaturated in Zr) or whether Group 2 dark BSE zircon forms (Zr saturated solution). Changes in the fluids composition with respect to elements like F may cause supersaturation resulting in precipitation of zircon. Without the presence of a suitable host (i.e. crystalline zircon) it is unlikely that zircon will crystallise and therefore Zr may be mobilised.

The many factors described have a wide ranging influence as to how zircon behaves once in the rock.

6.5 Low temperature pseudomorph

The traditional view of zircon is that crystallisation occurs in high temperature regimes (e.g. magmas and high-grade metamorphism) and that zircon is passive throughout its low temperature history (Hanchar and Hoskin, 2003). Although there are variations in trace elements and Hf, the bulk of zircon is composed of ZrO_2 , SiO_2 (c.98%) and therefore has a fairly limited composition. However this limited composition is far from surprising if most of the zircon studied is zircon that has formed in relatively similar high temperature environments. The widespread alteration of metamict zircon at low temperatures, that is associated with the uptake of non-formula elements (Speer, 1982; Geisler et al., 2007; Utsunomiya et al., 2007; this study), suggests that non-formula

element rich zircon is the preferred composition and state for zircon forming under low temperature conditions. Thus altered, non-formula element-rich zircon is a low temperature pseudomorph of “normal” zircon and may be far more common than typically appreciated. The volume of zircon that it represents in low temperature rocks is considerable. The result of this is we may have a wrongly perceived view that all zircon has the structure of that formed in magmas or in high-grade metamorphic conditions where the majority of zircon growth is typically thought to occur. Very few studies examine zircon within the context of the rock in which it is contained. Crushing and mineral separation processes destroy low temperature zircon features and therefore create a severe bias in the zircon population. This emphasises the need for a new approach to be taken when studying the behaviour of zircon.

6.6 Dark BSE zircon and zircon outgrowths in higher grade rocks

Zircon alteration and Zr mobility seems ubiquitous in low-grade metasediments where metamict zircon has developed. The widespread nature of metamict zircon in low-grade metasediments means that zircons in equivalent rocks of higher-grade should have experienced a similar low temperature history. However SEM analysis of zircon from several Scottish Dalradian lower amphibolite facies schists found low temperature zircon forms were absent (T.J.Dempster, personal communication). This prompts the obvious but crucial question, what has happened to these features?

Radiation damage in zircon will cease to accumulate above 250°C (Meldrum et al., 1999) and so metamictization cannot be a key control on zircon behaviour in amphibolite facies rocks. Zircon outgrowths are extremely fragile as they are exceptionally rare on detrital zircon in mineral separates (Dempster et al., 2004). Consequently, deformation in moderate grade regionally metamorphosed rocks is likely to mechanically breakup zircon outgrowths, dispersing nanocrystalline zircon particles into the matrix. The high surface energy of these particles and their nanocrystalline structure make them susceptible to either dissolution or recrystallisation to reduce

surface energy. Due to a similar microstructure and composition, it is predicted that dark BSE zircon will be similarly consumed or recrystallised. The discontinuous nature of the dark BSE zircon microstructure provides opportunities for fluid infiltration. The nanocrystalline structure is likely to be unstable at these higher temperatures due to the high surface energy. However, the issue as to whether dark BSE zircon is dissolved or recrystallised remains and these two possibilities will now be considered.

We will examine the evidence for dissolution of dark BSE zircon. Occasional dissolution features are observed by Dempster et al. (in prep.) in small ($<10\mu\text{m}$) light BSE zircon grains from the matrix of lower amphibolite facies rocks. If light BSE zircon can be removed from the rock, then it is likely that dark BSE zircon will undergo similar but probably more extensive dissolution. However, it would be expected that dark BSE zircon, which forms in particular growth layers or domains, is preferentially removed while light BSE zircon, that commonly encases dark BSE zircon, remains. Yet, the majority of zircon is absent from the matrix of lower amphibolite schists. Perhaps during dark BSE zircon dissolution, the encasing light BSE zircon is broken down to smaller fragments. Light BSE zircon cores may remain unmodified but the smaller surrounding light BSE fragments will be more susceptible to dissolution as they become dispersed into the matrix. The absence of zircon in the matrix implies that significant amounts of Zr may be mobilised during upper greenschist to lower amphibolite facies metamorphism and the recent discovery of “micro-zircon” grains preferentially concentrated in garnet and biotite porphyroblasts (Dempster et al., in prep.) provides good evidence that supports this hypothesis. Furthermore, the discovery of micro-zircon may indicate that new zircon readily crystallises at these metamorphic grades without the requirement of nucleation on an existing zircon host.

Despite convincing evidence that zircon experiences dissolution and recrystallisation in lower amphibolite facies conditions, some zircon must survive intact otherwise large ($>50\mu\text{m}$) zircon would not be observed in higher-grade rocks. Consequently we must consider what zircon may appear like if it is able to survive beyond lower amphibolite facies metamorphism.

Zircon recrystallising in higher temperature regimes is likely to have a “typical” zircon composition in comparison to low-temperature forms. By equilibrating to higher temperature conditions, the dark BSE zircon effectively repairs itself through recrystallisation, expelling non-formula elements. The liberation of non-formula elements during recrystallisation may imply some coupled reaction with other phases such as garnet or biotite. Zonation patterns formed in zircon grains with recrystallised dark BSE zircon may be texturally indistinguishable from many zircons that preserve other high-grade features (e.g. high-grade metamorphic overgrowths) when examined using conventional imaging techniques (BSE, CL, SE). Therefore it is possible that some of the features interpreted as forming at high temperature may well be characteristics that were established at low temperatures.

The amount of zircon grains in which dark BSE zircon have potentially recrystallised implies around 20% of the zircon population in quartzites (based on the average percentage of zircon with dark BSE zircon in greenschist facies quartzites, Table 1) and around 40% of the zircon population in pelites (based on the average percentage of zircon with dark BSE zircon in slates, Table 1) would have experienced some low temperature event in a rock that experienced a similar thermal history to that of the Dalradian rocks studied. Therefore recrystallisation of low temperature zircon may not have been previously considered when interpreting features in zircon from higher-grade rocks. The thickness of many dark BSE zircon zones is well below the minimum resolution of most quantitative analytical systems (*c.* 10-20 μ m) and therefore recrystallised zones of dark BSE zircon in zircon from higher-grade rocks should be a consideration when analysing these grains. For example, this may lead to discordance in U-Pb dating systems, or cause disruption to $\delta^{18}\text{O}$ values that may result in misinterpretation.

The fate of low temperature features in zircon at higher metamorphic grades is uncertain. Although it is outwith the scope of this thesis to study the behaviour of zircon in higher-grade metamorphic rocks, the surprising absence of low temperature features in zircon demands further assessment if reliable information is to be obtained from analysis of zircon that has experienced such conditions.

7

Conclusions, implications and further work

7.1 Conclusions

The findings from this thesis contradict the traditional view that zircon remains stable and largely refractory in the Earth's shallow crust (Hancher and Hoskin, 2003). In contrast, this study identified that secondary low temperature features are abundant in zircon from both sedimentary and metasedimentary rocks. Such features indicate that zircon is out of equilibrium in low temperature environments. This is primarily due to the accumulation of radiation damage in the zircon crystal below the annealing zone (<250°C). A summary of features observed follows and the implications they have for many aspects of earth and material science.

7.1.1 Dark BSE zircon

Radiation damaged zircon readily responds to fluids at <100°C through a dissolution-precipitation process to form Group 1 dark BSE zircon. However it may also experience “background” diffusion-driven cation exchange processes that result in structurally recovered Group 2 dark BSE zircon. The chemistry of Group 1 and Group 2 dark BSE zircon is very similar. The composition of dark BSE zircon is different when observed in rocks of different grades. The cause of this may be due to overall changes in fluid composition as a result of the bulk composition of the rocks in which dark BSE zircon formed rather than any particular factor that relates to grade.

Chemical zonation patterns as a function of their U and Th content have a strong control over the resulting grain macrostructure.

The continual accumulation of radiation damage below the annealing temperature can lead to zircon grains becoming metamict throughout various stages of the diagenetic and metamorphic cycle. How metamict zircon responds to alteration by fluids at these stages may provide a useful monitor of fluid behaviour in the shallow crust. This information would be of considerable interest to hydrogeologists, petroleum geologists and reservoir engineers who are keen to understand and predict fluid flow, particularly in sedimentary rocks.

The findings of this study may be a concern for the safe storage of nuclear waste over geological timescales in zircon ceramics proposed by Ewing et al, (1988; 1995). The findings in this thesis agree other work (Geisler et al., 2003d; Trachenko et al., 2003) that shows zircon readily undergoes recrystallisation, alteration, dissolution and that Zr may be mobilised in response to radiation damage at low temperatures. The concern is that radiation damage affected areas may significantly degrade the ceramic in which the nuclear waste is stored by both volume expansion of amorphous phase and increased susceptibility to alteration by fluids. However, dark BSE zircon's ability to retain U and Th and include actinide-bearing phases, such as xenotime and thorite, may actually provide an alternative mechanism to store nuclear waste. By recrystallising and incorporating actinide elements in response to radiation damage, dark BSE zircon may provide an effective mechanisms that "soaks up" radioactive isotopes in storage sites.

Metamictization may also be responsible for the formation of porous zircon that is observed in close association to dark BSE zircon which warrants further investigation.

7.1.2 Zircon outgrowths

Extensive Zr mobilisation and crystallisation of zircon as outgrowths on unmodified zircon in fine-grained sedimentary and metasedimentary rocks is controlled by the reworking of zircon during sedimentary processing at the Earth's surface. During such processes, radiation-damaged zircon is sorted in fine-grained sediment making mudstones and siltstones a sink for metamict zircon.

Ancient zircons (>4Ga) provide glimpses of conditions on early Earth by analysing the relative proportions of oxygen isotopes in them. As such, zircon has been used to postulate that tectonics were well established within 200Ma from the formation of the earth (Valley et al., 2005; Watson and Harrison, 2005). However some Earth scientists debate that such an explanation is necessary, arguing that this data may simply be due to early stage alteration of magmatic zircon and not a result of permanent liquid oceans (Hoskin, 2005; Nemchin et al., 2006). As the presence of zircon outgrowths can be related to surface processes, identifying zircon outgrowths in ancient rocks (>4Ga) may also provide an indicator for water on the surface of early Earth and an indication that the rock cycle of genesis, erosion, sedimentation and burial was established. Zircon outgrowths in low-temperature rocks may also potentially be a tool to date low temperature metamorphic events (see 7.1.6.2).

7.1.3 Xenotime

This study has found that xenotime can form substantial overgrowths on zircon at <100°C. The source of Y and P is considered to come from the dissolution of detrital xenotime due to the absence of such grains in the host rock. Xenotime outgrowths are observed to be far more abundant in fine-grained greenschist facies metasediments where evidence for greater volumes of Zr mobilisation is also preserved. Zircon has an intimate relationship with xenotime when forming at low temperatures where xenotime is commonly found as inclusions in Group 1 dark BSE zircon and zircon outgrowths. When growth is synchronous, zircon-xenotime complexes form.

Isotopic analysis of xenotime, together with zircon, may provide valuable insights into fluid behaviour and chemistry during diagenesis and low temperature metamorphism.

7.1.4 Zircon provenance

Metamictization causes the breakup of the zircon grain on the Earth's surface. Sedimentary processing then redistributes the resulting fragments creating a severe bias in the zircon population. Metamict zircon fragments (U- and Th-rich) will be concentrated in fine-grained sediments while mature sediments will contain young or U- and Th- poor pristine zircon.

Zircon is routinely used in provenance studies to help reconstruct the palaeogeography of past continents (e.g. Fedo et al., 2003) and has also been used to describe the palaeogeography of the Dalradian (Cawood et al., 2003; Cawood et al., 2004; Banks et al., 2007; Cawood et al., 2007). However such analysis is based on the premise that zircon is entirely refractory on the Earth's surface. Furthermore, analysis is typically carried out on mineral separates. Mineral separates create a severe bias towards sampling pristine zircons whilst removing low-temperature zircon features. Low temperature secondary features that are abundant in Dalradian metasediments would therefore be largely ignored. This may have implications in sedimentary provenance studies which will favour the analysis of U-poor zircon or young zircon. U-rich zircon or old zircon may therefore represent large populations of zircon that have not been considered as part of the provenance history. This illustrates the necessity to analyse zircon in-situ so that its relationship to the rock may be assessed.

7.1.5 Techniques

This study has revealed the huge potential in using the FIB microscope to prepare extremely accurate, site specific electron-transparent foils, a result which is highly desirable to earth scientists. LV-STEM imaging of FIB-prepared foils has also been shown to be a valuable tool in revealing the structure and components of sub-micron features that cannot be distinguished using conventional SEM technology, and may be an alternative to TEM.

This study has shown that EBSD is a powerful tool in determining the crystallinity of zircon and may be used as an alternative to RAMAN spectroscopy. Unmodified zircon often displays large variations in IQ when mapped using EBSD. This reflects significant variation in the structural state (i.e. the degree of structural breakdown due to radiation damage) of single grain zircons that were not metamict enough to alter during low temperature events. Low IQ can be mostly linked with BSE intense zones in unmodified zircon (e.g. Fig. 35). In an experiment studying BSE intensities in natural zircon, Nasdala et al., (2006) found that BSE intensity is strongly affected by the structural state of the zircon. In some cases, BSE intensity was shown to increase with the degree of radiation damage. Although the results presented in this thesis are only preliminary, it would

appear to agree with the observations made by Nasdala et al. (2006). Furthermore, Nasdala et al., (2003) used Raman spectroscopy to identify areas of structural damage in zircon, a well established technique in distinguishing the degree of radiation damage in zircon. However, the successful application of using EBSD to determine the crystal condition in zircon demonstrates that EBSD is also a powerful tool in identifying the structural condition of zircon. EBSD maps can identify varying degrees of metamictization in excellent detail in radiation damaged zircon crystals which have not experienced low-temperature alteration. EBSD maps are comparable to those produced by Raman mapping in identifying crystallinity but EBSD may provide significantly better resolution than Raman (50nm (Humphreys, 2001) compared to 1 μ m (Nasdala et al., 2003)). EBSD should therefore be considered as a viable alternative to Raman spectroscopy when determining the crystallinity of zircon.

EBSD does have limitations. When analysing the nano-crystalline domains of altered zircon (dark BSE zircon) and zircon outgrowths obtaining crystallographic information is difficult. This may be due to the random orientation of the crystals in the analysed area however until the microstructure is determined, this will remain uncertain. Another problem is that determining radiation damage in zircon using EBSD is not yet a quantitative technique. Therefore absolute comparisons cannot be made between individual grains due to small differences in the setup and operating conditions (e.g. quality of thin section polish, thickness of carbon coat, working distance).

7.1.6 Suitability of dark BSE zircon and zircon outgrowths for geochronology

There is presently a lack of suitable mineral chronometers that have a widespread distribution and an ability to retain information on the age of low-temperature events in sedimentary rocks. Zircon is widely used in geochronology because of its perceived stability in its crystalline state. The widespread occurrence of zircon outgrowths in slate (mud is the most abundant sediment on the Earth) and dark BSE zircon (found in virtually all sedimentary rocks) make them potentially valuable tools in constraining the timing of diagenesis and metamorphism. The suitability of dark BSE zircon and zircon outgrowths as a chronometer for low temperature events will now be

considered.

7.1.6.1 Dark BSE zircon

Dark BSE zircon would potentially be an attractive target for geochronologists as it can form domains large enough that can be analysed using conventional in-situ techniques, such as SIMS or LA-ICPMS. However, problems arise in obtaining meaningful U-Pb ages as dark BSE zircon is likely to contain small remnants of original structure due to the nature of metamictization. These crystalline remnants will likely remain chemically stable during alteration and retain U, Th and radiogenic Pb. In contrast, the amorphous matrix surrounding the crystalline remnants in metamict areas will readily alter, potentially losing variable amounts of Pb and modifying U and Th concentrations. The ability to retain U and Th in dark BSE zircon makes it susceptible to radiation damage again. Dark BSE zircon is therefore susceptible to subsequent alteration resulting in Pb loss and possible disruption to U and Th concentrations. This may overprint previous evidence of low temperature modification. These characteristics make dark BSE zircon unsuitable as a geochronometer.

7.1.6.2 Zircon outgrowths

Zircon outgrowths may provide better potential for age dating because they are formed from Zr mobilised by fluids and will therefore not contain relics of protolith zircon. However, the greatest problem is that few isotopic analysis techniques are capable of the spatial resolution necessary to analyse zircon outgrowths. At present, only EPMA can achieve this resolution but does not have the sensitivity required for accurate age dating. Nevertheless, recent developments in NanoSIMS technology provide the tantalising possibility of accurate isotope analysis at a spatial resolution of less than 5µm (Sano et al., 2005; Stern et al., 2005). Despite such developments, age dating of zircon outgrowths will not be straightforward and will be complicated by the likelihood of being U and Th deficient. Furthermore, a sample strategy must be determined that excludes samples containing xenotime. This is due to the strong affinity xenotime has with zircon in low temperature rocks resulting in complexes of zircon and xenotime and sub micron xenotime inclusions within the outgrowth domains. This would significantly complicate the microstructure of the zircon

outgrowth and make reliable age determination difficult.

7.2 Further work

In light of the results described before this section, the following work is proposed that may help to further assess zircons suitability as a geochronometer, container to nuclear waste but also the mechanisms by which such secondary features form and the scales and controls of Zr mobility in low temperature rocks.

- Determining the microstructure of dark BSE zircon and porous zircon using the FIB microscope to create wafers for analysis on the TEM, STEM and HR-TEM.
- The composition of the fluid phase in which low temperature zircon forms.
- Chemical analysis of low temperature zircon via SIMS to determine P, REE, actinide and other trace element concentrations. Analysis would also include the investigation of water to observe whether this is structurally bound. This may also help to reveal information regarding the composition of the fluid phase in which low temperature zircon forms.
- Gain a better understanding for the complex substitution mechanisms in low temperature zircon.
- Raman analysis of dark BSE zircon and comparative EBSD vs Raman study to reveal the advantages and limitations of both techniques.
- Assessing the alpha-decay doses from actinide contents in dark BSE zircon.
- Examine the effects that different cements in rocks have on zircon alteration and Zr mobility.
- More focused study to constrain scales of Zr mobility by investigating zircon behaviour across lithological boundaries and the effects deformation has on Zr mobility.

- Assessing zircon behaviour in a greater variety of rock types including immature sediments and low temperature metamorphosed granites.
- NanoSIMS analysis of zircon outgrowths may help constrain ages on timing of metamorphism in the Dalradian.

7.3 Summary

As stated at the very beginning of this thesis, the aim of this project was to investigate the behaviour of zircon in low temperature environments. The findings reveal an abundance of secondary low temperature features that form in zircon as a consequence of radiation damage to the mineral lattice. These include dissolution of metamict zircon and reprecipitation both in-situ and as zircon outgrowths on the margins of unmodified zircon. These features have considerable implications for the safe storage of nuclear waste and acquiring reliable U-Pb ages from zircon populations. In short, zircon is a fully fledged metamorphic mineral.

A

Thin section descriptions of metasediments

KL01 Medium grained (c.50-100 μ m) quartzite. Quartz is predominantly monocrystalline with occasional polycrystalline grains and quartz grains are angular in shape and well compacted with many grains sharing around 5 grain boundaries. Phyllosilicates constitute around 10% of the overall rock and define a weak cleavage in the rock. Biotite upto 200 μ m long (and 50% of the phyllosilicates present in the rock), muscovite upto 100 μ m (45%) are present. Chlorite upto 200 μ m long (5% of phyllosilicates in the rock) are altering to biotite.

KL02 Medium to course grained (c.100-200 μ m) quartzite composed almost entirely of quartz. Mostly polycrystalline quartz (90%) with very irregular grain margins with many grains sharing boundaries with 5 or 6 grains. Very occasional flakes of muscovite (c.100-200 μ m long) and patches of carbonate (c.500 μ m across).

KL03 Medium to course grained (c.100-300 μ m) quartzite with mm-scale banding and a well-developed cleavage defined by muscovite. Quartz is virtually all polycrystalline (90%) with angular and irregular grain boundaries, many forming grain boundaries with 5-6 other quartz grains between cleavage planes. Matrix is composed of 60% quartz and 35% muscovite. Muscovite mainly c.200 μ m long but can be upto 500 μ m long. Very occasional chlorites (c.500 μ m long) are also present as are large biotite grains (c.500-700 μ m long) within cleavage planes.

KL04 Banded fine to course grained (c.30-300 μ m) quartzite with bands c.500 μ m thick of

muscovite (70%) and biotite (30%) upto 500µm long that define a well-developed cleavage. Quartz is 50-50 mono- poly- crystalline with angular grain boundaries and grains are elongated in the direction of cleavage. Most quartz has undergone recrystallisation.

KL05-KL05light-KL05heavy Medium to course grained (c.100-300µm) quartzite with around 5% feldspar. Quartz is polycrystalline (70%) and monocrystalline (30%) and exhibit angular and highly irregular grain margins. Boundaries upto 5 grains. Also muscovite (40%) and biotite (60%) present and constitute around 10% of rock but where in enough abundance can define a cleavage. Muscovite and biotite are generally c.50µm long but some large biotites are also present (c.300µm). Large (c.300µm) occasional chlorites can also be seen altering to biotite. KL05heavy contains heavy mineral layers and also slightly more biotite than the other samples.

KL06 Banded fine to course grained (c.<50-300µm) quartzite, many layers with an abundance of phyllosilicate minerals. Muscovite (45%), biotite (35%) and chlorite (20%) constitute c.30%. Bands of phyllosilicates vary from muscovite-chlorite rich to muscovite and biotite rich. Phyllosilicates can be upto 300µm long. Calcite grains are occasionally present in course grained quartz-rich bands upto c.0.5mm in size. Occasional rounded garnets upto c.500µm across are also present in finer grained muscovite-biotite rich layers. Quartz is angular and irregular and predominantly polycrystalline.

BAL1 (a to d) Banded (at mm scale) graphite-rich slate with lenses of predominately recrystallised monocrystalline quartz (grains 30-200µm across) that follow parallel to the original bedding of the rock. Matrix composed graphite-rich phyllosilicate (10%, <5µm long), muscovite (40%, 5-10µm long) and quartz (50%, 5-20µm). Muscovite defines weakly defined cleavage. Pyrite grains form within matrix and range from c.100µm to 5mm in length with larger pyrites exhibiting a euhedral grain shape.

BAL3 Graphitic phyllite with mm-scale laminations. Bands of predominantly muscovite (70%) form a strongly defined cleavage with quartz (30%) that weave between almost pure quartz bands. Muscovite (30-400µm long) with quartz (30-100µm across) is predominantly non-undulatory and

recrystallised. Quartz bands are composed almost solely of quartz. Occasional irregularly formed pyrites have developed throughout the thin section and upto 3mm long. Occasionally associated with muscovite grains in some bands are very thin and small biotites (c.50 μ m).

E1 Course grained (30-100 μ m) finely laminated graphitic slate with matrix composed of quartz (50%), muscovite (25%) and chlorite (25%). Cleavage is relatively well-defined. Quartz has undergone recrystallisation and is elongated slightly with the cleavage. Large pyrite grains (c.3mm across) form euhedral margins and thin veins of pyrite also form cross cutting cleavage.

EAS1 Fine grain (<10 μ m) finely banded slate but with significant amounts of carbonate matrix. Seams (c.2mm thick) of course calcite (c.200 μ m, 80%) and non-undulatory recrystallised quartz (50-100 μ m, 20%) follow between weakly defined cleavage planes. Pods c.7mm long, containing slightly courser (300 μ m) carbonate (50%) and irregular shaped non-undulatory quartz (50%) with occasional irregular shaped undulatory quartz. Matrix is composed of very fine grained carbonate grains (<5 μ m across, 60%) and quartz (10 μ m across, 20%) and muscovite (10 μ m, 30%).

Dh1 Very fine grained (matrix <5 μ m), graphitic slate with finely laminated bands (<0.25mm) and a well-developed and weakly crenulated cleavage. Matrix dominated by muscovite and chlorite (c.80%) and quartz (20%) with lenses (c.1mm by 10mm) of very fine (<5 μ m) grained quartz-rich bands.

Dh2 Graphitic slate that is slightly courser grained than Dh1 (matrix grains typically c.10 μ m across) and with a strongly defined and weakly crenulated cleavage. Matrix is composed of graphite (20%), muscovite (30%) and quartz (50%). Quartz is present in the matrix as angular fragments (10-20 μ m across) but also elongate quartz grains aligned to the cleavage (upto 30 μ m in length). Some very fine grained (<5 μ m), quartz rich bands (c.1mm thick) that are discontinuous over the cm scale are also present.

Dh3 Banded chlorite-rich slate. Some very fine-grained bands contain 60% chlorite (<5 μ m across), 30% muscovite (c.10 μ m long) and <5 μ m quartz (10%) and some slightly courser bands

containing 40% chlorite (c.10 μ m long), 40% muscovite (10-30 μ m long) and 20% quartz (10-30 μ m) present as both angular fragments and elongate grains aligned to matrix. Rock contains bands (3mm thick) of recrystallised coarse (50-1000 μ m) monocrystalline quartz that follow parallel to a well developed and slightly crenulated cleavage. Also present is a 3mm thick quartz seam that cross cuts the cleavage of the rock.

Dh4 Course grained psammite composed of (0.3-3mm) polycrystalline (80%) and monocrystalline (20%) quartz and have an overall well rounded shape. Most quartz grains however have irregular margins some of which are recrystallising to finer grained quartz and micas. The rock is matrix supported and the matrix is composed of 30-50 μ m quartz (60%) that are angular with some bands in the matrix having recrystallised and muscovite (40% of matrix) (c.30-300 μ m) which forms a reasonably defined cleavage between large quartz grains. Rock also contains large (c.2mm in diameter), well-rounded felsic clasts and there are isolated patches of heavily altered carbonate cement (upto 2mm in length) that, overall, are roughly orientated to cleavage. Other clasts of well round fine grained phyllite are also observed in similar size.

B

EPMA analyses in weight percent

B1 Dark BSE zircon

Sample	Analysis No.	Mg	Al	Si	Ca	Fe	Y	Zr	Hf	O	Total
<i>Light BSE zircon</i>											
dh4zr14	2	0.00	0.00	14.62	0.01	0.04	0.04	48.61	1.17	33.95	98.44
dh4zr14	3	0.00	0.00	14.62	0.01	0.02	0.04	48.47	1.09	33.88	98.13
dh4zr14	4	0.00	0.00	14.55	0.01	0.06	0.04	48.48	1.06	33.80	97.99
dh4zr14	5	0.00	0.01	14.62	0.01	0.05	0.06	48.37	1.16	33.88	98.16
dh4zr40	68	0.00	0.00	15.09	0.00	0.09	0.03	49.08	0.80	34.59	99.67
dh4zr23	75	0.00	0.07	14.85	0.00	0.02	0.05	48.08	1.07	34.05	98.18
dh4zr32	79	0.00	0.00	15.32	0.01	0.08	0.21	49.50	0.88	35.06	101.05
kl05hxr16core	80	0.00	0.00	14.65	0.01	0.11	0.16	49.29	1.07	34.25	99.54
kl05hxr16core	81	0.00	0.01	14.32	0.01	0.09	0.15	49.54	1.14	33.98	99.23
Elzr2	102	0.00	0.01	14.61	0.01	0.22	0.07	50.49	0.79	34.60	100.80
<i>Dark BSE zircon</i>											
dh4zr14	1	0.01	0.05	14.37	0.07	0.07	0.26	47.84	1.11	33.52	97.30
dh4zr14	6	0.06	0.15	13.33	0.30	0.28	1.22	44.88	1.09	31.82	93.13
dh4zr14	9	0.11	0.49	10.71	0.95	0.65	3.40	39.14	1.04	28.10	84.59
dh4zr14	10	0.14	0.47	11.59	0.95	0.69	1.52	43.35	1.13	30.11	89.94
dh4zr14	13	0.03	0.47	12.07	0.65	0.59	1.41	42.28	0.99	30.01	88.51
dh4zr14	14	0.03	0.47	12.21	0.64	0.58	1.34	42.70	0.94	30.28	89.19
dh4zr14	15	0.03	0.51	12.02	0.66	0.52	1.63	41.72	0.95	29.83	87.88
dh4zr14	16	0.04	0.53	12.00	0.68	0.56	1.67	41.55	0.90	29.79	87.72
dh4zr14	17	0.04	0.55	12.10	0.71	0.56	1.66	41.58	0.99	29.96	88.15
dh4zr14	18	0.04	0.54	11.88	0.72	0.57	1.61	41.90	0.90	29.79	87.94
dh4zr14	19	0.05	0.51	11.77	0.76	0.63	1.51	41.67	0.86	29.56	87.33
dh4zr14	20	0.05	0.51	11.91	0.75	0.69	1.60	42.00	0.95	29.89	88.35
dh4zr14	21	0.05	0.53	11.93	0.75	0.58	1.78	41.98	0.97	29.94	88.49
dh4zr14	22	0.06	0.55	11.87	0.75	0.59	1.87	41.63	1.04	29.80	88.13
dh4zr14	23	0.06	0.58	11.80	0.76	0.59	1.93	41.40	0.91	29.67	87.69
dh4zr14	24	0.05	0.57	11.83	0.70	0.60	1.92	41.51	1.04	29.74	87.97
dh4zr14	26	0.06	0.55	12.12	0.72	0.57	1.49	42.47	0.89	30.25	89.12
dh4zr14	27	0.05	0.48	12.19	0.70	0.54	1.63	42.44	1.07	30.30	89.38
dh4zr14	28	0.04	0.47	12.26	0.65	0.53	1.62	42.80	0.99	30.45	89.80
dh4zr14	29	0.04	0.50	12.20	0.66	0.59	1.65	42.41	0.97	30.30	89.31
dh4zr14	30	0.03	0.50	12.11	0.70	0.57	1.71	42.01	1.00	30.08	88.69
dh4zr14	31	0.03	0.50	12.16	0.69	0.54	1.70	42.10	0.89	30.13	88.72
dh4zr14	32	0.04	0.52	12.12	0.72	0.50	1.75	42.07	0.93	30.12	88.75
dh4zr14	33	0.04	0.55	12.00	0.68	0.51	2.02	41.27	1.03	29.82	87.93
dh4zr14	34	0.04	0.50	12.25	0.68	0.47	1.70	42.25	1.05	30.31	89.25
dh4zr14	35	0.08	0.47	12.26	0.80	0.56	1.30	43.31	1.07	30.66	90.51
dh4zr14	36	0.09	0.46	12.33	0.81	0.54	1.46	43.27	1.18	30.78	90.91

Sample	Analysis No.	Mg	Al	Si	Ca	Fe	Y	Zr	Hf	O	Total
dh4zr26	39	0.04	0.14	14.07	0.22	0.36	0.88	45.55	0.87	32.74	94.86
dh4zr26	41	0.06	0.33	12.43	0.56	0.44	2.06	41.45	0.75	30.07	88.16
dh4zr26	42	0.05	0.26	12.31	0.53	0.39	2.36	41.51	0.82	29.96	88.19
dh4zr26	44	0.06	0.31	12.08	0.65	0.48	2.02	41.49	0.82	29.72	87.62
dh4zr26	45	0.06	0.38	11.91	0.69	0.45	1.88	41.65	0.85	29.62	87.50
dh4zr26	46	0.04	0.32	13.04	0.48	0.47	1.71	43.15	0.86	31.24	91.31
dh4zr26	47	0.03	0.19	13.44	0.34	0.42	1.43	44.14	0.81	31.77	92.57
dh4zr26	48	0.03	0.18	13.42	0.41	0.42	1.07	44.83	0.86	31.93	93.15
dh4zr26	49	0.02	0.13	14.24	0.27	0.40	0.92	46.16	0.87	33.18	96.19
dh4zr009	55	0.09	0.81	10.82	0.86	0.65	3.93	36.87	0.98	27.82	82.86
dh4zr009	56	0.07	0.91	11.12	0.82	0.61	3.56	37.36	0.91	28.26	83.64
dh4zr009	57	0.05	0.66	11.25	0.76	0.51	3.30	38.34	0.84	28.39	84.13
dh4zr009	58	0.05	0.52	11.18	0.78	0.45	3.11	39.14	0.88	28.42	84.57
dh4zr009	59	0.04	0.52	10.90	0.78	0.40	3.18	38.54	0.85	27.88	83.14
dh4zr40	64	0.05	0.42	11.24	0.76	0.44	2.68	40.30	0.96	28.70	85.61
dh4zr40	66	0.09	0.52	10.03	1.14	0.57	3.40	37.21	1.00	26.76	80.82
dh4zr40	67	0.06	0.51	10.41	0.92	0.45	3.72	37.72	0.88	27.28	82.06
dh4zr23	69	0.04	0.43	12.03	0.59	0.40	2.35	40.57	0.95	29.52	86.94
dh4zr23	72	0.00	0.13	14.71	0.15	0.21	0.45	46.42	1.05	33.60	96.73
dh4zr23	73	0.01	0.16	14.50	0.24	0.25	0.53	46.10	1.00	33.32	96.10
dh4zr23	74	0.13	0.45	11.60	1.07	0.46	1.95	42.23	1.02	29.79	88.69
dh4zr32	76	0.02	0.11	14.57	0.13	0.18	0.46	47.32	0.89	33.69	97.36
dh4zr32	78	0.01	0.17	15.44	0.08	0.15	0.44	49.60	0.90	35.50	102.28
kl05hxr16core	82	0.01	0.08	13.86	0.10	0.15	0.49	48.44	1.15	33.28	97.55
kl05hxr16core	83	0.00	0.04	13.68	0.08	0.14	0.26	47.73	1.03	32.69	95.66
kl05hxr16core	84	0.01	0.06	13.44	0.06	0.38	0.31	47.76	1.21	32.56	95.78
kl05hxr16core	85	0.01	0.18	12.95	0.21	0.27	0.50	45.43	1.03	31.34	91.92
kl05hxr16core	86	0.02	0.14	12.92	0.46	0.39	0.60	45.10	0.94	31.30	91.86
kl05hxr16core	87	0.01	0.10	13.09	0.19	0.32	0.64	46.04	0.88	31.65	92.92
kl05hxr16core	88	0.02	0.20	12.82	0.29	0.38	0.65	45.07	0.93	31.18	91.54
kl05hxr16core	89	0.02	0.38	12.46	0.51	0.61	1.32	42.95	0.87	30.51	89.63
kl05hxr16core	90	0.01	0.28	13.32	0.36	0.25	1.17	45.71	0.72	32.12	93.93

B2 Porous zircon

Sample	Analysis No.	Mg	Al	Si	Ca	Fe	Y	Zr	Hf	O	Total
dh4zr17a	1	0.00	0.00	15.12	0.00	0.11	0.14	49.28	0.79	34.73	100.17
dh4zr17a	2	0.00	0.00	15.23	0.00	0.13	0.13	49.30	0.94	34.89	100.62
dh4zr17a	3	0.00	0.00	15.21	0.00	0.10	0.13	49.35	0.87	34.86	100.53
dh4zr17a	4	0.01	0.01	15.06	0.05	0.16	0.19	49.22	1.00	34.74	100.44
dh4zr17a	5	0.00	0.00	15.08	0.01	0.14	0.12	49.06	1.15	34.67	100.23
dh4zr17a	6	0.00	0.01	15.02	0.04	0.34	0.07	48.57	1.20	34.51	99.75
dh4zr17a	7	0.00	0.01	15.19	0.01	0.19	0.02	49.23	0.97	34.82	100.43
dh4zr17a	8	0.00	0.00	15.20	0.01	0.22	0.02	49.46	1.07	34.93	100.91
dh4zr17a	9	0.00	0.00	15.13	0.01	0.25	0.01	49.11	1.08	34.74	100.33
dh4zr17a	10	0.00	0.00	15.23	0.00	0.25	0.00	49.08	0.94	34.82	100.33
dh4zr17a	11	0.00	0.00	15.18	0.01	0.28	0.02	49.56	1.08	34.96	101.09
dh4zr17a	12	0.00	0.00	15.24	0.00	0.30	0.03	49.57	1.06	35.04	101.24
dh4zr17a	13	0.00	0.00	15.29	0.00	0.32	0.05	49.66	1.11	35.14	101.57
dh4zr17b	14	0.00	0.00	15.15	0.00	0.09	0.06	48.98	0.91	34.65	99.84
dh4zr17b	15	0.00	0.00	15.12	0.00	0.06	0.03	49.04	1.06	34.65	99.97
dh4zr17b	16	0.00	0.00	15.13	0.00	0.05	0.05	48.96	1.23	34.66	100.08
dh4zr17b	17	0.00	0.01	15.12	0.00	0.06	0.05	48.88	1.13	34.61	99.86
dh4zr17b	18	0.00	0.01	15.17	0.00	0.06	0.04	48.70	1.21	34.63	99.83
dh4zr17b	19	0.00	0.01	15.03	0.01	0.07	0.05	48.83	1.18	34.51	99.68
dh4zr17b	20	0.00	0.04	14.97	0.03	0.06	0.10	48.76	1.15	34.46	99.58
dh4zr17b	21	0.01	0.13	14.86	0.07	0.16	0.24	48.04	1.00	34.22	98.72
dh4zr17b	22	0.02	0.16	14.81	0.07	0.29	0.21	47.66	0.92	34.08	98.20
dh4zr17b	23	0.00	0.08	14.94	0.04	0.19	0.19	48.02	0.98	34.23	98.66
dh4zr17b	24	0.00	0.03	14.95	0.03	0.14	0.15	48.38	1.01	34.31	99.00
dh4zr17b	25	0.00	0.03	14.89	0.02	0.13	0.15	48.30	1.03	34.21	98.77
dh4zr17b	26	0.01	0.07	14.91	0.03	0.15	0.15	48.19	1.07	34.24	98.80
dh4zr17b	27	0.01	0.09	14.87	0.04	0.13	0.13	47.82	1.01	34.07	98.17
dh4zr17b	28	0.01	0.07	14.85	0.05	0.10	0.17	47.97	1.11	34.11	98.44
dh4zr17b	29	0.01	0.05	14.73	0.05	0.11	0.17	47.89	1.17	33.95	98.14
dh4zr17b	30	0.01	0.03	14.94	0.06	0.11	0.17	48.35	1.18	34.32	99.15
dh4zr17b	31	0.01	0.05	14.84	0.05	0.11	0.22	48.24	1.21	34.20	98.92
dh4zr17b	32	0.01	0.05	14.71	0.05	0.19	0.32	47.60	1.12	33.86	97.90
dh4zr17b	33	0.01	0.05	14.59	0.08	0.27	0.56	47.05	1.27	33.66	97.53
dh4zr17b	34	0.01	0.07	14.36	0.11	0.37	0.70	46.77	1.18	33.38	96.94
dh4zr17b	35	0.01	0.10	14.32	0.15	0.38	0.74	46.05	1.15	33.14	96.05
dh4zr17b	36	0.01	0.10	14.34	0.17	0.39	0.58	46.31	1.23	33.23	96.36
dh4zr17b	37	0.01	0.07	14.54	0.14	0.49	0.34	46.70	1.24	33.53	97.06
dh4zr17b	38	0.02	0.09	14.40	0.22	0.44	0.28	46.97	1.21	33.48	97.11
dh4zr17b	39	0.03	0.10	14.29	0.28	0.38	0.28	46.97	1.18	33.37	96.87
dh4zr17b	40	0.02	0.05	14.77	0.14	0.16	0.17	48.32	1.05	34.17	98.84
dh4zr17b	41	0.00	0.01	15.00	0.03	0.11	0.09	48.95	0.97	34.51	99.67
dh4zr17b	42	0.00	0.01	15.02	0.02	0.14	0.11	48.36	1.06	34.35	99.07
dh4zr17b	43	0.01	0.03	14.86	0.05	0.26	0.15	48.03	1.01	34.13	98.53
dh4zr17b	44	0.01	0.05	14.87	0.07	0.38	0.13	47.43	1.13	34.00	98.06
dh4zr17b	45	0.00	0.06	14.82	0.07	0.38	0.15	47.16	1.03	33.84	97.51

B3 Zircon outgrowths

Sample	Analysis no.	Al	Si	Ca	Fe2+	Y	Zr	Hf	O	Total
Host zircons										
'bal1bz8a	1	<0.01	15.38	0.01	0.23	<0.03	48.22	1.18	34.82	99.86
'bal1bz8c	2	<0.01	15.36	0.01	0.21	<0.03	47.94	1.17	34.69	99.39
'bal1bz8d	3	<0.01	15.39	0.01	0.22	<0.03	48.00	1.12	34.75	99.52
'bal1bzc23a	16	<0.01	15.60	<0.007	0.30	<0.03	47.10	1.63	34.80	99.46
'bal1bzc23b	17	<0.01	15.60	0.02	0.29	<0.03	46.82	1.62	34.69	99.07
'bal1bzc23c	18	<0.01	15.55	0.02	0.25	<0.03	46.70	1.66	34.58	98.77
'bal1bz25-4a	21	0.02	15.64	0.02	0.31	0.07	47.63	1.31	35.06	100.07
'bal1bz26a	25	<0.01	15.54	0.03	0.19	<0.03	47.91	1.12	34.90	99.72
'bal1bz26b	26	<0.01	15.52	0.03	0.16	0.03	47.18	1.15	34.61	98.67
'bal1bz26c	27	<0.01	15.53	0.03	0.21	<0.03	47.73	1.13	34.83	99.48
'bal1bz28c	35	<0.01	15.94	0.07	0.24	0.08	46.77	1.25	35.11	99.48
'bal1bz30a	39	<0.01	15.53	0.01	0.26	0.16	47.51	1.08	34.89	99.43
'bal1bz32a	44	0.01	15.77	0.02	0.44	0.07	47.07	1.47	35.11	99.97
'bal1bz34a	52	<0.01	15.60	0.01	0.21	<0.03	48.28	1.01	35.06	100.20
'bal1bz34d	55	<0.01	15.45	0.02	0.20	<0.03	47.91	1.23	34.82	99.67
'bal1bz34e	56	<0.01	15.44	0.01	0.20	<0.03	47.86	1.09	34.76	99.40
'Bal1bz36a	59	<0.01	15.43	0.01	0.17	<0.03	47.79	1.26	34.74	99.43
'Bal1bz36a	60	<0.01	15.34	0.02	0.23	0.10	47.94	1.17	34.76	99.57
'bal1bz36a	61	<0.01	15.36	0.03	0.21	0.11	47.90	1.13	34.78	99.52
'bal1bz39a	65	<0.01	15.68	0.01	0.32	0.06	48.68	1.23	35.41	101.39
'bal1bz39a	66	<0.01	15.57	0.02	0.33	0.04	48.24	1.13	35.10	100.43
'bal1bz39b	67	<0.01	15.64	0.02	0.34	0.07	47.42	1.25	34.98	99.74
'bal1bz42a	71	<0.01	15.51	<0.007	0.24	0.04	47.85	1.53	34.92	100.09
'bal1bz42b	72	0.03	15.42	0.01	0.26	0.04	48.46	1.58	35.14	100.93
'bal1bz43a	79	<0.01	15.44	<0.007	0.33	0.09	48.21	1.37	35.04	100.49
'bal1bz43b	80	<0.01	15.45	<0.007	0.30	0.11	47.82	1.40	34.94	100.03
'bal1bz45a	83	<0.01	15.47	0.02	0.29	0.08	47.69	1.49	34.89	99.93
'bal1bz45b	84	<0.01	15.42	0.02	0.29	0.08	48.16	1.44	34.99	100.40
'bal1bz45c	85	<0.01	15.25	0.02	0.27	0.12	47.86	1.47	34.72	99.71
'bal1bz47a	91	<0.01	15.71	0.01	0.16	0.03	48.03	1.05	35.10	100.09
'bal1bz37a	105	0.01	15.45	0.12	0.44	0.04	47.77	1.31	34.93	100.07
'zr8-1d	109	<0.01	15.48	0.02	0.48	0.05	47.64	1.24	34.86	99.77
zr8-1e	110	0.01	15.47	0.03	0.47	0.05	47.36	1.34	34.80	99.53
'zr13-2a	117	0.01	15.33	0.02	0.31	0.08	47.34	1.62	34.68	99.40
'zr13-1a	120	0.01	15.05	0.05	0.28	0.31	48.16	1.57	35.36	100.80
'zr13-1f	125	<0.01	15.32	0.02	0.25	0.13	47.35	1.60	34.75	99.42
'zr12-1e	133	<0.01	15.34	0.02	0.46	<0.03	48.05	1.48	34.86	100.24
'zr12-1f	134	<0.01	15.35	0.01	0.46	<0.03	47.91	1.51	34.82	100.09
'zr12-1g	135	0.01	15.34	0.02	0.45	<0.03	47.71	1.50	34.74	99.80
'zr12-1h	136	0.01	15.29	0.02	0.46	<0.03	47.85	1.53	34.76	99.95
'zr11-4a	140	<0.01	15.38	<0.007	0.35	0.07	48.41	1.21	35.00	100.44
'zr11-4b	141	0.01	15.35	0.02	0.33	0.07	47.99	1.16	34.82	99.76
'easzr1-1a	147	<0.01	15.35	0.01	0.16	<0.03	48.03	1.00	34.65	99.19
'Ezr1-1b	148	<0.01	15.27	0.01	0.17	<0.03	48.56	1.03	34.76	99.80
'Ezr1-1c	149	0.02	14.97	0.05	0.14	0.04	47.66	1.25	34.22	98.35
'Ezr1-1e	151	<0.01	15.46	0.03	0.21	<0.03	48.34	0.97	34.91	99.92
'Ezr1-1f	152	0.01	15.44	0.03	0.20	<0.03	47.66	1.16	34.70	99.20
'Ezr2e	165	<0.01	15.21	0.02	0.23	0.06	47.89	1.11	34.55	99.07
'Ezr2f	166	<0.01	15.07	<0.007	0.23	0.04	48.22	1.11	34.48	99.17
'Ezr2h	167	<0.01	15.29	0.01	0.25	0.06	48.50	1.18	34.88	100.18
'Ezr4-3a	170	<0.01	15.17	0.01	0.26	0.05	47.90	1.56	34.59	99.54
'Ezr4-3b	171	<0.01	15.13	0.02	0.24	0.05	47.13	1.66	34.28	98.51
'Ezr4-3c	172	<0.01	15.41	<0.007	0.27	0.05	47.08	1.79	34.64	99.26
Ezr5	176	<0.01	15.21	0.02	0.29	<0.03	48.84	0.86	34.82	100.07
'Ezr1-5a	181	0.01	15.25	0.02	0.44	0.04	47.48	1.34	34.56	99.14

Sample	Analysis no.	Al	Si	Ca	Fe2+	Y	Zr	Hf	O	Total
Zircon outgrowths										
'bal1bz8e	4	0.03	15.43	0.14	0.24	0.13	46.41	1.06	34.49	97.93
'bal1bz10b	9	<0.01	15.46	0.02	0.29	0.24	47.32	1.17	34.86	99.35
'bal1bzr16a	13	0.01	15.44	0.01	0.41	0.19	47.10	0.97	34.72	98.86
'bal1bzr23d	19	0.06	15.60	0.04	0.39	0.05	46.30	1.63	34.83	98.89
'bal1bz26d	28	0.01	15.72	0.10	0.23	0.09	47.04	1.09	34.95	99.24
'bal1bz26e	29	0.05	15.62	0.24	0.29	0.27	45.42	1.10	34.63	97.63
'bal1bz26f	30	0.13	14.57	0.55	0.46	0.68	42.23	1.16	33.18	92.96
'bal1bz28e	37	0.01	15.61	0.11	0.24	0.32	46.27	1.13	34.81	98.51
'bal1bz30b	40	0.03	15.29	0.08	0.32	0.18	46.11	1.19	34.28	97.48
'bal1bz30c	41	0.08	15.11	0.30	0.48	0.30	43.66	1.35	33.66	94.94
'bal1bz30e	43	<0.01	15.51	0.02	0.30	0.15	47.78	1.08	34.96	99.80
'bal1bz32b	45	0.11	15.47	0.09	0.59	0.27	45.47	1.31	34.91	98.22
'bal1bz33a	48	0.02	15.49	0.02	0.38	0.10	46.60	1.26	34.58	98.44
'bal1bz34b	53	0.01	15.61	0.04	0.25	0.04	47.14	1.13	34.76	98.97
'bal1bz34c	54	0.07	14.40	0.45	0.49	0.43	41.70	1.26	32.35	91.15
'bal1bz34f	57	0.04	14.56	0.18	0.21	0.49	44.92	1.10	33.42	94.94
'bal1bz39c	68	0.10	14.55	0.24	0.58	0.44	42.17	1.20	32.82	92.09
'bal1bz39d	69	0.11	15.35	0.25	0.49	0.33	44.35	1.20	34.34	96.41
'bal1bz42g	77	0.02	15.11	0.07	0.33	0.37	45.80	1.48	34.22	97.42
'bal1bz43c	81	0.03	15.63	0.08	0.34	0.41	45.72	1.39	34.83	98.42
'bal1bz43d	92	<0.01	15.55	0.01	0.22	0.16	47.27	1.26	34.86	99.33
'bal1bz47c	93	0.01	15.55	0.02	0.24	0.18	47.35	1.23	34.93	99.50
'bal1bz47d	94	0.03	15.29	0.11	0.29	0.39	46.15	1.23	34.58	98.07
'bal1bz47e	95	0.05	15.17	0.07	0.25	0.27	45.92	1.20	34.23	97.15
'bal1bz47f	96	0.06	14.43	0.23	0.41	0.60	43.72	1.29	33.19	93.91
'bal1bz47g	97	0.06	14.59	0.17	0.41	0.55	44.03	1.32	33.39	94.53
'bal1bz47h	98	0.15	14.36	0.35	0.63	0.58	42.50	1.33	33.27	93.17
'bal1bz46a	100	0.03	15.23	0.12	0.37	0.38	46.56	1.18	34.63	98.48
'zr9-3a	112	0.04	15.44	0.01	0.85	0.08	47.23	1.54	34.97	100.17
'zr9-3b	113	0.12	14.99	0.01	1.06	0.19	46.71	1.58	34.90	99.56
'zr11-1c	115	<0.01	15.32	0.03	0.44	0.17	47.94	1.00	34.87	99.77
'zr11-1d	116	0.05	14.94	0.16	0.51	0.25	46.04	1.00	34.04	97.00
'zr13-2b	118	0.06	14.60	0.24	0.42	0.49	45.21	1.75	34.48	97.25
'zr13-1b	121	0.02	15.15	0.07	0.30	0.22	47.30	1.57	34.74	99.37
'zr13-1c	122	0.04	14.86	0.18	0.36	0.44	45.61	1.48	34.52	97.50
'zr13-1d	123	0.12	14.29	0.42	0.46	0.57	41.35	1.40	32.93	91.53
'zr12-1a	128	0.03	15.01	0.16	0.50	0.29	47.03	1.49	34.97	99.48
'zr12-1b	129	0.02	15.17	0.05	0.46	0.15	47.47	1.52	34.84	99.67
'zr12-1i	137	0.03	15.14	0.07	0.54	0.10	47.11	1.56	34.56	99.11
'zr12-1j	138	0.13	14.85	0.25	0.76	0.65	42.02	1.39	34.31	94.37
'zr11-4c	142	0.07	15.80	0.10	0.38	0.25	46.48	1.15	35.40	99.61
'zr11-4f	145	<0.01	15.16	0.01	0.32	0.29	47.72	1.34	35.12	99.96
'Ezr1-1d	150	0.11	14.21	0.22	0.23	0.27	45.06	1.36	33.23	94.69
'Ezr1-1g	153	0.04	15.15	0.03	0.25	<0.03	46.61	1.11	34.12	97.34
'Ezr3a	155	0.05	14.78	0.14	0.39	0.31	46.55	1.05	34.47	97.74
'Ezr3c	157	0.16	13.85	0.47	0.54	0.82	43.38	1.02	33.74	93.98
'Ezr3d	158	0.15	14.49	0.25	0.58	0.59	45.61	1.02	34.82	97.50
'Ezr4-3d	173	0.01	15.50	0.04	0.28	0.08	46.29	1.82	34.51	98.53
'Ezr4-3e	174	0.10	15.08	0.19	0.43	0.40	42.74	1.81	33.92	94.67
'Ezr5b	177	<0.01	15.26	0.03	0.41	<0.03	48.36	1.42	34.87	100.39
'Ezr5c	178	0.02	15.27	0.03	0.41	0.03	48.03	1.44	34.79	100.03
'Ezr5d	179	0.09	15.10	0.16	0.64	0.25	46.86	1.24	34.78	99.12

C

Thin section descriptions of sedimentary rocks

KULM 1 Pale and dark banded quartz arenite. Banding is generally on mm scale with bands of very well sorted and well-compacted *c.*100% angular quartz (30-50 μ m across). Mud-rich bands contain mud (50%), angular quartz (30%, 30-50 μ m across), blobs of bituminous material (*c.*300 μ m long, 10%) and chlorite grains (10% of band and 200-300 μ m long) aligned to banding. Quartz is dominantly monocrystalline with grains but have thick “mucky” grain boundaries. Very occasional feldspar (1%) and lithic fragments are observed (<1%).

KULM 2 Dark banded mudstone with very fine-grained bands (2-3mm thick) composed of very small (<10-30 μ m) and angular quartz (40%), very fine grained (<5 μ m) carbonate mud (40%) and very small (*c.*20 μ m) illite grains are present (20%). Coarser grained bands are 2-3mm thick with fine-grained (30-50 μ m) angular quartz (30%), very fine grained (<5 μ m) muddy carbonate (30%), illite grains (10% of band, *c.*50 μ m long), with some layers containing blobs of bituminous material (*c.*300 μ m long and around 10% of these bands) with 20% lithics and occasional feldspar grains. In coarser bands monocrystalline (60%) and polycrystalline (40%) quartz can be identified.

KULM 3 Pale banded (2-3mm thick), carbonate cemented quartz arenite. Bands typically contain 50-100 μ m monocrystalline angular quartz grains (30%), with some quartz rather elongate and

aligned to bedding, supported by a carbonate cement (50%) that is generally very fine grained (<5 μ m). Occasional illite grains (c.5%) are aligned to bedding and around 200-300 μ m long and occasional feldspar (<20 μ m across) is also present. Around 15% lithic fragments also present that range in size from <100 to 300 μ m composed of very fine grained material (too fine grained to determine). Cement does vary in places from calcitic to calcite-mud cemented and some bands also contain reworked calcitic mud flakes. Amount of carbonate also varies from matrix supported (band of c.70% carbonate cement) to grain supported (c.40% carbonate).

KULM 4 Dark and pale banded, very fine grained quartz arenite. Quartz is very well sorted (c.50 μ m) ranging from angular to sub-rounded in shape and is 70% polycrystalline, 30% monocrystalline. Quartz ranges from 30-100 μ m across and quartz-rich bands are well-compacted and composed almost entirely of quartz with occasional (2%) illite grains (c.200 μ m long) and muddy carbonate cement (10%). Banding is defined by layers of muddy very fine grained micrite cement (60%), angular quartz (20%) and illite (20% and c.200 μ m long). Occasional bituminous blobs are also found in particular layers. Micrite cement is also found in pockets throughout quartz-rich areas. Feldspar (c.3%) is also found.

KULM 5 White medium to coarse quartz arenite with quartz grains very well sorted (100-200 μ m across) and vary from sub- to well- rounded polycrystalline (80%) and monocrystalline (20%) quartz within a matrix supported calcite micritic cement (60%). Some quartz grains have very small irregularities on their margins. Thin section is relatively homogeneous throughout with no banding. Feldspar (3%) and lithics (2%) are also present as matrix grains.

L-MillG-1 White, well sorted and very compacted quartz arenite. Quartz is 95% polycrystalline, sub-angular to well rounded and 0.5-1mm in diameter and rock is grain supported with virtually no matrix. All grains heavily fractured appearing almost “shocked” and some grains display pressure dissolution. No feldspar or lithics were observed.

L-MillG-2 Dark and very fine grained organic-rich mudstone that is very finely laminated throughout. Lithics and feldspar appear absent. Bituminous blobs in the matrix (10-30 μ m across).

Too fine-grained in places to determine mineralogy. Courser bands contains a matrix of angular quartz fragments (40% and upto 30 μ m long) and illite grains (20%, 20-30 μ m long) within an matrix that is too fine grained to be identified.

L-MillG-3 Pale, very well sorted 50-100 μ m of approximately equal proportions of monocrystalline and polycrystalline quartz with most grains relatively rounded. Rock is very well compacted, grain supported with virtually no matrix and composed of almost 100% quartz. Although less common, some quartz display multiple stress fractures and some preserve small (<20 μ m) quartz overgrowths. Occasionally in patches is a matrix (*c.*1%) of course grained calcite. No lithics or feldspar.

L-MillG-4 Pale and poorly sorted quartz arenite. Quartz grain size ranges 0.1-3mm of monocrystalline (70%) and polycrystalline (30%) quartz of mostly angular grains. Quartz grains are predominantly angular and some display very small irregularities around its margins, reacting with carbonate cement. Virtually completely matrix supported (*c.*60%) although there is no particular structure or banding within the rock. The calcitic cement, although mainly micrite does contain coarser calcite in places. <1% feldspar, no lithics.

D

EPMA analyses in weight percent

D.1 Sedimentary zircon

Sample	Analysis No.	Mg	Al	Si	Ca	Fe2+	Y	Zr	Hf	O	Total
<i>Light BSE zircon</i>											
KULM3zr6	1	0.02	0.04	14.10	0.09	0.43	0.22	49.36	0.76	33.89	99.19
KULM3zr7a	11	0.00	0.02	14.10	0.12	0.67	0.09	48.47	1.76	33.71	99.04
KULM3zr10a	39	0.05	0.08	13.79	0.32	0.42	0.19	50.20	1.42	34.11	100.85
KULM3zr11	42	0.00	0.01	14.13	0.03	0.28	0.04	50.71	1.10	34.22	100.58
KULM3zr11	43	0.00	0.00	14.07	0.02	0.28	0.00	50.61	1.05	34.06	100.09
KULM3zr11	44	0.01	0.01	14.12	0.02	0.27	0.02	50.13	1.08	33.99	99.69
KULM3zr12	54	0.02	0.01	14.48	0.01	0.45	0.03	49.80	1.11	34.34	100.28
KULM3zr12	55	0.02	0.00	14.42	0.02	0.38	0.03	49.85	1.07	34.26	100.09
KULM3zr12	56	0.01	0.01	14.17	0.04	0.40	0.09	50.13	1.08	34.13	100.15
KULM3zr12	57	0.01	0.02	13.86	0.08	0.36	0.09	50.42	1.48	33.97	100.38
KULM3zr12	68	0.00	0.00	14.39	0.01	0.29	0.00	50.21	1.15	34.30	100.34
KULM3zr12	69	0.01	0.02	14.18	0.05	0.27	0.07	49.36	1.13	33.85	99.02
KULM4zr31	99	0.00	0.01	15.00	0.01	0.32	0.05	49.09	1.01	34.63	100.17
<i>Dark BSE zircon</i>											
KULM4zr19	104	0.08	0.15	13.08	0.59	0.56	0.47	46.36	1.13	32.34	95.39
KULM4zr19	105	0.09	0.15	13.22	0.64	0.57	0.50	45.04	1.04	32.06	93.97
KULM4zr19	106	0.09	0.16	13.14	0.66	0.66	0.42	46.56	1.12	32.52	95.91
KULM4zr19	107	0.08	0.13	13.79	0.58	0.57	0.40	46.13	1.10	32.98	96.29
KULM3zr7a	9	0.02	0.03	13.65	0.21	0.84	0.15	48.17	1.65	33.21	98.11
KULM3zr7a	10	0.01	0.03	13.85	0.18	0.78	0.12	48.37	1.75	33.48	98.73
KULM3zr7a	12	0.02	0.07	13.95	0.21	0.60	0.11	48.39	1.83	33.64	99.01
KULM3zr7a	13	0.13	0.21	12.20	0.89	0.87	0.51	43.07	1.55	30.64	90.79
KULM3zr7a	14	0.06	0.20	13.09	0.53	0.86	0.37	45.89	1.55	32.33	95.43
KULM3zr7a	15	0.07	0.18	12.63	0.69	0.84	0.68	44.95	1.54	31.69	94.14
KULM3zr7a	17	0.00	0.01	14.06	0.11	0.61	0.09	48.66	1.97	33.74	99.35
KULM3zr7a	18	0.03	0.09	13.53	0.36	0.71	0.36	47.67	1.24	33.09	97.54
KULM3zr7b	19	0.10	0.21	12.38	0.82	1.10	0.55	44.20	2.07	31.35	93.53
KULM3zr7b	22	0.05	0.12	12.92	0.47	0.85	0.33	47.16	2.01	32.48	96.82
KULM3zr7b	23	0.10	0.19	12.34	0.82	1.00	0.53	45.32	1.52	31.54	94.08
KULM3zr7b	24	0.04	0.06	13.48	0.36	0.98	0.17	48.40	1.76	33.30	98.77
KULM3zr7b	25	0.09	0.19	12.29	0.76	0.95	0.55	45.07	1.53	31.35	93.51
KULM3zr7b	26	0.09	0.18	12.21	0.81	0.96	0.57	45.88	1.39	31.53	94.35
KULM3zr10a	27	0.15	0.27	12.05	1.06	0.74	0.84	43.42	1.58	30.90	92.09
KULM3zr10a	31	0.09	0.16	12.83	0.72	0.48	0.47	47.26	1.37	32.46	96.46
KULM3zr10a	33	0.15	0.26	11.86	1.08	0.62	0.79	44.61	1.49	31.02	92.92
KULM3zr10a	36	0.11	0.22	12.14	0.71	0.57	0.87	45.20	1.26	31.28	93.44
KULM3zr10a	37	0.08	0.21	11.76	0.66	1.50	0.62	42.64	1.21	30.03	89.56
KULM3zr10a	38	0.05	0.10	14.29	0.33	0.99	0.21	47.58	1.31	33.95	99.13

Sample	Analysis No.	Mg	Al	Si	Ca	Fe2+	Y	Zr	Hf	O	Total
KULM3zr11	45	0.01	0.05	13.62	0.17	0.41	0.20	49.13	1.03	33.33	98.20
KULM3zr11	46	0.02	0.07	13.12	0.20	0.41	0.42	49.33	1.03	33.00	98.08
KULM3zr11	48	0.04	0.14	12.44	0.56	0.59	0.58	45.41	1.11	31.28	92.86
KULM3zr11	49	0.05	0.17	12.38	0.67	0.64	0.69	45.50	1.15	31.42	93.51
KULM3zr11	50	0.06	0.14	12.64	0.62	0.62	0.50	46.52	1.05	31.89	94.68
KULM3zr11	51	0.02	0.03	14.00	0.18	0.51	0.14	49.31	1.28	33.84	99.48
KULM3zr12	53	0.13	0.00	14.22	0.02	0.71	0.01	48.76	1.13	33.82	98.82
KULM3zr12	63	0.01	0.03	14.42	0.17	0.28	0.10	48.71	1.44	34.03	99.32
KULM3zr12	64	0.01	0.02	14.15	0.09	0.27	0.05	49.44	1.61	33.93	99.64
KULM3zr12	65	0.03	0.05	13.81	0.24	0.32	0.16	48.94	1.53	33.55	98.82
KULM3zr12	66	0.05	0.06	13.49	0.34	0.38	0.21	47.82	1.27	32.87	96.75
KULM3zr12	67	0.01	0.01	14.44	0.06	0.29	0.02	49.54	1.15	34.18	99.74
KULM3zr14a	70	0.04	0.05	13.34	0.21	0.39	0.23	48.24	0.93	32.72	96.43
KULM3zr14a	73	0.07	0.17	13.13	0.76	0.43	0.61	46.42	0.93	32.52	95.82
KULM3zr14a	74	0.09	0.21	12.51	0.90	0.45	0.81	44.73	1.01	31.49	93.21
KULM3zr14a	75	0.14	0.19	11.86	0.96	1.15	0.66	44.87	0.99	30.93	92.60
KULM3zr14a	76	0.12	0.16	11.96	0.83	1.37	0.57	44.38	1.02	30.77	91.90
KULM3zr14a	77	0.09	0.12	12.71	0.63	0.46	0.54	46.58	1.00	31.93	94.70
KULM3zr14a	78	0.09	0.11	12.56	0.59	0.70	0.49	47.00	1.00	31.93	95.07
KULM3zr14a	79	0.06	0.11	12.37	0.58	0.87	0.55	45.56	0.98	31.26	92.99
KULM3zr14a	80	0.07	0.10	12.72	0.66	0.50	0.65	46.30	0.97	31.90	94.64
KULM3zr14a	81	0.08	0.12	12.51	0.65	0.54	0.68	46.23	0.98	31.69	94.26
KULM3zr14a	85	0.04	0.09	14.12	0.18	0.54	0.16	49.05	1.03	33.98	99.43
KULM3zr14a	90	0.06	0.10	13.95	0.45	0.37	0.35	47.12	0.96	33.30	97.13
KULM3zr14a	91	0.03	0.05	14.41	0.22	0.39	0.21	48.41	0.94	34.00	98.92
KULM3zr14a	92	0.04	0.07	13.58	0.33	0.39	0.28	48.30	0.93	33.12	97.36
KULM3zr14a	93	0.06	0.10	13.17	0.50	0.43	0.38	47.55	0.91	32.58	96.12
KULM3zr14a	94	0.02	0.03	13.94	0.21	0.32	0.17	49.32	0.95	33.69	98.86
KULM3zr14a	95	0.08	0.10	13.01	0.59	0.39	0.38	47.33	0.98	32.39	95.73
KULM3zr14a	96	0.06	0.08	13.33	0.49	0.36	0.30	48.97	0.85	33.16	97.98
KULM4zr31	98	0.08	0.11	13.26	0.47	0.29	0.47	47.59	0.93	32.74	96.52

References

- Aleinikoff, J.N., Schenck, W.S., Plank, M.O., Srogi, L.A., Fanning, C.M., Kamo, S.L., and Bosbyshell, H., 2006, Deciphering igneous and metamorphic events in high-grade rocks of the Wilmington Complex, Delaware: Morphology, cathodoluminescence and backscattered electron zoning, and SHRIMP U-Pb geochronology of zircon and monazite: *Geological Society Of America Bulletin*, v. 118, p. 39-64.
- Anderton, R., 1985, Sedimentation and tectonics in the Scottish Dalradian: *Scottish Journal of Geology*, v. 21, p. 407-436.
- Baker, D.R., Conte, A.M., Freda, C., and Ottolini, L., 2002, The effect of halogens on Zr diffusion and zircon dissolution in hydrous metaluminous granitic melts: *Contributions to Mineralogy and Petrology*, v. 142, p. 666-678.
- Balan, E., Neuville, D.R., Trocellier, P., Fritsch, E., Muller, J.P., and Calas, G., 2001, Metamictization and chemical durability of detrital zircon: *American Mineralogist*, v. 86, p. 1025-1033.
- Banks, C.J., Smith, M., Winchester, J.A., Horstwood, M.S.A., Noble, S.R., and Ottley, C.J., 2007, Provenance of intra-Rodinian basin-fills: The Lower Dalradian Supergroup, Scotland: *Precambrian Research*, v. 153, p. 46-64.
- Bea, F., 1996, Residence of REE, Y, Th and U in granites and crustal protoliths; implications for the chemistry of crustal melts. : *Journal of Petrology*, v. 37, p. 521-552.
- Bjørlykke, K., 1997, Lithological control on fluid flow in sedimentary basins, *in* Jamtveit, B., and Yardley, B.W.D., eds., *Fluid Flow and Transport in Rocks - Mechanisms and effects*, p. 15-34.
- Boukili, B., Holtz, F., Beny, J.M., and Robert, J.L., 2002, "Fe-F and Al-F avoidance rule" in ferrous-aluminous (OH,F) biotites: *Schweizerische Mineralogische Und Petrographische Mitteilungen*, v. 82, p. 549-559.
- Boukili, B., Robert, J.L., Beny, J.M., and Holtz, F., 2001, Structural effects of OH double right arrow F substitution in trioctahedral micas of the system: $K_2O-FeO-Fe_2O_3-Al_2O_3-SiO_2-H_2O-HF$: *Schweizerische Mineralogische Und Petrographische Mitteilungen*, v. 81, p. 55-67.
- Brasier, M.D., and Shields, G., 2000, Neoproterozoic chemostratigraphy and correlation of the Port Askaig glaciation, Dalradian Supergroup of Scotland: *Journal Of The Geological Society*, v. 157, p. 909-914.
- Bursill, L.A., and McLaren, A.C., 1966, Transmission electron microscope study of natural radiation damage in zircon ($ZrSiO_4$): *Physical State Solids*, v. 12.
- Butterfield, J.A., 1936, Outgrowths on zircon: *Geological Magazine*, v. 73, p. 511-516.
- Caruba, R., and Iacconi, P., 1983, Les zircon des pegmatites de Narssârssuk (Groëland) - l'eau et les groupments OH dans les zircons meamictes: *Chemical Geology*, v. 38, p. 75-92.

- Cavosie, A.J., Valley, J.W., and Wilde, S.A., 2005, Magmatic delta O-18 in 4400-3900 Ma detrital zircons: A record of the alteration and recycling of crust in the Early Archean: *Earth and Planetary Science Letters*, v. 235, p. 663-681.
- Cawood, P.A., Nemchin, A.A., Smith, M., and Loewy, S., 2003, Source of the Dalradian Supergroup constrained by U-Pb dating of detrital zircon and implications for the East Laurentian margin: *Journal of the Geological Society*, v. 160, p. 231-246.
- Cawood, P.A., Nemchin, A.A., and Strachan, R., 2007, Provenance record of Laurentian passive-margin strata in the northern Caledonides: Implications for paleodrainage and paleogeography: *Geological Society of America Bulletin*, v. 119, p. 993-1003.
- Cawood, P.A., Nemchin, A.A., Strachan, R.A., Kinny, P.D., and Loewy, S., 2004, Laurentian provenance and an intracratonic tectonic setting for the Moine Supergroup, Scotland, constrained by detrital zircons from the Loch Eil and Glen Urquhart successions: *Journal of the Geological Society*, v. 161, p. 861-874.
- Chakoumakos, B.C., Oliver, W.C., Lumpkin, G.R., and Ewing, R.C., 1991, Hardness And Elastic-Modulus Of Zircon As A Function Of Heavy-Particle Irradiation Dose .1. In situ Alpha-Decay Event Damage: *Radiation Effects And Defects In Solids*, v. 118, p. 393-403.
- Cherniak, D.J., and Watson, E.B., 2001, Pb diffusion in zircon: *Chemical Geology*, v. 172, p. 5-24.
- Cherniak, D.J., and Watson, E.B., 2003, Diffusion in zircon, *in* Hanchar, J.M., and Hoskin, P.W.O., eds., *Zircon, Volume 53: Reviews in Mineralogy & Geochemistry*, p. 113-143.
- Compston, W., and Pidgeon, R.T., 1986, Jack Hills, evidence of more very old detrital zircons in Western Australia: *Nature*, v. 321, p. 766-769.
- Corfu, F., Hanchar, J.M., Hoskin, P.W.O., and Kinny, P., 2003, Atlas of zircon textures, *Zircon, Volume 53: Reviews In Mineralogy & Geochemistry*, p. 469-500.
- Coyne, E., 2004, Adapting SEMs to produce Scanning Transmission Electron Microscope Images: *Microscopy and Analysis*, v. 100, p. 13-16.
- Davis, D.W., Williams, I.S., and Krogh, T.E., 2003, Historical development of zircon geochronology, *in* Hanchar, J.M., and Hoskin, P.W.O., eds., *Zircon, Volume 53: Reviews In Mineralogy & Geochemistry*.
- Dempster, T.J., Hay, D.C., and Bluck, B.J., 2004, Zircon growth in slate: *Geology*, v. 32, p. 221-224.
- Dempster, T.J., Rogers, G., Tanner, P.W.G., Bluck, B.J., Muir, R.J., Redwood, S.D., Ireland, T.R., and Paterson, B.A., 2002, Timing of deposition, orogenesis and glaciation within the Dalradian rocks of Scotland: constraints from U-Pb zircon ages: *Journal of the Geological Society*, v. 159, p. 83-94.
- Edwards, P.R., Martin, R.W., and Lee, M.R., 2007, Combined cathodoluminescence hyperspectral imaging and wavelength dispersive X-ray analysis of minerals: *American Mineralogist*, v. 92, p. 235-242.
- Ewing, R.C., Chakoumakos, B.C., Lumpkin, G.R., Murakami, T., Gregor, R.B., and Lytle, F.W., 1988, Metamict minerals: natural analogues for radiation damage effects in ceramic nuclear waste forms: *Nuclear Instruments and Methods of Physical Research, B Beam Interactions of Materials and Atoms*, v. 32, p. 487-497.
- Ewing, R.C., Lutze, W., and Weber, W.J., 1995, Zircon: a host-phase for the disposal of weapons plutonium: *Journal of Materials Research*, v. 10, p. 243-246.
- Ewing, R.C., Meldrum, A., Wang, L.M., Weber, W.J., and Corrales, L.R., 2003, Radiation effects in zircon, *in* Hanchar, J.M., and Hoskin, P.W.O., eds., *Zircon: Reviews in Mineralogy & Geochemistry*, 53, p. 387-420.

- Farnan, I., Balan, E., Pickard, C.J., and Mauri, F., 2003, The effect of radiation damage on local structure in the crystalline fraction of ZrSiO₄: Investigating the Si-29 NMR response to pressure in zircon and reidite: *American Mineralogist*, v. 88, p. 1663-1667.
- Farnan, I., and Salje, E.K.H., 2001, The degree and nature of radiation damage in zircon observed by Si-29 nuclear magnetic resonance: *Journal of Applied Physics*, v. 89, p. 2084-2090.
- Fedo, C.M., Sircombe, K.N., and Rainbird, R.H., 2003, Detrital zircon analysis of the sedimentary record, *in* Hanchar, J.M., and Hoskin, P.W.O., eds., *Zircon*, Volume 53: Reviews In Mineralogy & Geochemistry, p. 277-303.
- Fletcher, I.R., Rasmussen, B., and McNaughton, N.J., 2000, SHRIMP U-Pb geochronology of authigenic xenotime and its potential for dating sedimentary basins: *Australian Journal Of Earth Sciences*, v. 47, p. 845-859.
- Foude, D.O., Ireland, T.R., Kinny, P.D., Williams, I.S., Compston, W., Williams, I.R., and Myers, J.S., 1983, Ion microprobe identification of 4100-4200 Myr-old terrestrial zircons: *Nature*, v. 304, p. 616-618.
- Fraser, G., Ellis, D., and Eggins, S., 1997, Zirconium abundance in granulite-facies minerals, with implications for zircon geochronology in high-grade rocks: *Geology*, v. 25, p. 607-610.
- Garver, J.I., 2002, Discussion: "Metamictisation of natural zircon: accumulation versus thermal annealing of radioactivity-induced damage" by Nasdala et al. 2001 (Contributions to Mineralogy and Petrology 141 : 125-144): *Contributions To Mineralogy And Petrology*, v. 143, p. 756-757.
- Garver, J.I., Reiners, P.W., Walker, L.J., Ramage, J.M., and Perry, S.E., 2005, Implications for timing of Andean uplift from thermal resetting of radiation-damaged zircon in the Cordillera Huayhuash, northern Peru: *Journal Of Geology*, v. 113, p. 117-138.
- Geisler, T., Pidgeon, R.T., Kurtz, R., van Bronswijk, W., and Schleicher, H., 2003a, Experimental hydrothermal alteration of partially metamict zircon: *American Mineralogist*, v. 88, p. 1496-1513.
- Geisler, T., Pidgeon, R.T., van Bronswijk, W., and Kurtz, R., 2002, Transport of uranium, thorium, and lead in metamict zircon under low-temperature hydrothermal conditions: *Chemical Geology*, v. 191, p. 141-154.
- Geisler, T., Rashwan, A.A., Rahn, M.K.W., Poller, U., Zwingmann, H., Pidgeon, R.T., Schleicher, H., and Tomaschek, F., 2003b, Low-temperature hydrothermal alteration of natural metamict zircons from the Eastern Desert, Egypt: *Mineralogical Magazine*, v. 67, p. 485-508.
- Geisler, T., Schaltegger, U., and Tomaschek, F., 2007, Re-equilibration of zircon in aqueous fluids and melts: *Elements*, v. 3, p. 43-50.
- Geisler, T., Trachenko, K., Rios, S., Dove, M.T., and Salje, E.K.H., 2003c, Impact of self-irradiation damage on the aqueous durability of zircon (ZrSiO₄): implications for its suitability as a nuclear waste form: *Journal of Physics-Condensed Matter*, v. 15, p. L597-L605.
- Geisler, T., Zhang, M., and Salje, E.K.H., 2003d, Recrystallization of almost fully amorphous zircon under hydrothermal conditions: An infrared spectroscopic study: *Journal of Nuclear Materials*, v. 320, p. 280-291.
- Glover, B.W., Key, R.M., May, F., Clark, G.C., Philips, E.R., and Chacksfield, B.C., 1995, A Neoproterozoic multiphase rift sequence: the Grampian and Appin groups of the southern Monadhliath Mountains of Scotland: *Journal of the Geological Society, London*, v. 152, p. 391-406.
- Hanchar, J.M., and Hoskin, P.W.O., 2003, *Zircon*, 500 p.

- Harley, S.L., Kelly, N.M., and Moller, A., 2007, Zircon behaviour and the thermal histories of mountain chains: *Elements*, v. 3, p. 25-30.
- Harris, A.L., Haselock, P.J., Kennedy, M.J., and Mendum, J.R., 1994, The Dalradian Supergroup in Scotland, Shetland and Ireland, *in* Gibbons, W., and Harris, A.L., eds., A revised correlation of Precambrian rocks in the British Isles, Volume 22, Geological Society [London] Special Report 22, p. 33-53.
- Heaney, P.J., Vicenzi, E.P., Giannuzzi, L.A., and Livi, K.J.T., 2001, Focused ion beam milling: A method of site-specific sample extraction for microanalysis of Earth and planetary materials: *American Mineralogist*, v. 86, p. 1094-1099.
- Hirth, G., and Tullis, J., 1992, Dislocation creep regimes in quartz aggregates: *Journal of Structural Geology*, v. 14, p. 145-159.
- Holmes, A., 1911, The association of lead with uranium in rock-minerals, and its application to the measurement of geological time: *Proceedings of the Royal Society (London)*, v. 85A, p. 248-256.
- Hoskin, P.W.O., 2005, Trace-element composition of hydrothermal zircon and the alteration of Hadean zircon from the Jack Hills, Australia: *Geochimica Et Cosmochimica Acta*, v. 69, p. 637-648.
- Hoskin, P.W.O., and Black, L.P., 2000, Metamorphic zircon formation by solid-state recrystallization of protolith igneous zircon: *Journal Of Metamorphic Geology*, v. 18, p. 423-439.
- Hoskin, P.W.O., Kinny, P.D., Wyborn, D., and Chappell, B.W., 2000, Identifying accessory mineral saturation during differentiation in granitoid magmas: an integrated approach: *Journal Of Petrology*, v. 41, p. 1365-1396.
- Hoskin, P.W.O., and Schaltegger, U., 2003, The composition of zircon and igneous and metamorphic petrogenesis, *in* Hanchar, J.M., and Hoskin, P.W.O., eds., *Zircon*, Volume 53: *Reviews In Mineralogy & Geochemistry*, p. 27-62.
- Humphreys, F.J., 2001, Review - Grain and subgrain characterisation by electron backscatter diffraction: *Journal of Materials Science*, v. 36, p. 3833-3854.
- Kelly, N.M., and Harley, S.L., 2005, An integrated microtextural and chemical approach to zircon geochronology: refining the Archaean history of the Napier Complex, east Antarctica: *Contributions To Mineralogy And Petrology*, v. 149, p. 57-84.
- Keppler, H., 1993, Influence of Fluorine on the Enrichment of High-Field Strength Trace-Elements in Granitic-Rocks: *Contributions to Mineralogy and Petrology*, v. 114, p. 479-488.
- Kositcin, N., McNaughton, N.J., Griffin, B.J., Fletcher, I.R., Groves, D.I., and Rasmussen, B., 2003, Textural and geochemical discrimination between xenotime of different origin in the Archaean Witwatersrand Basin, South Africa: *Geochimica Et Cosmochimica Acta*, v. 67, p. 709-731.
- Lee, J.K.W., and Tromp, J., 1995, Self-Induced Fracture Generation in Zircon: *Journal of Geophysical Research-Solid Earth*, v. 100, p. 17753-17770.
- Lee, M.R., Brown, D.J., Smith, C.L., Hodson, M.E., MacKenzie, M., and Hellmann, R., In press, Characterisation of mineral surfaces using FIB and TEM: A case study of naturally-weathered alkali feldspar.
- Lee, M.R., and Smith, C.L., In press, Scanning Transmission Electron Microscopy using a SEM: Applications to mineralogy and petrology: *Mineral Magazine*.
- McNaughton, N.J., Rasmussen, B., and Fletcher, I.R., 1999, SHRIMP uranium-lead dating of diagenetic xenotime in siliciclastic sedimentary rocks: *Science*, v. 285, p. 78-80.

- Meldrum, A., Boatner, L.A., Weber, W.J., and Ewing, R.C., 1998, Radiation damage in zircon and monazite: *Geochimica Et Cosmochimica Acta*, v. 62, p. 2509-2520.
- Meldrum, A., Boatner, L.A., Weber, W.J., and Ewing, R.C., 1999, Radiation damage in zircon and Monazite. (vol 62, pg 2509, 1998): *Geochimica Et Cosmochimica Acta*, v. 63, p. 2693-2693.
- Mojzsis, S.J., Harrison, T.M., and Pidgeon, R.T., 2001, Oxygen-isotope evidence from ancient zircons for liquid water at the Earth's surface 4300 Ma ago: *Nature*, v. 409, p. 178-181.
- Murakami, T., Chakoumakos, B.C., Ewing, R.C., Lumpkin, G.R., and Weber, W.J., 1991, Alpha-Decay Event Damage In Zircon: *American Mineralogist*, v. 76, p. 1510-1532.
- Nasdala, L., Hanchar, J.M., Kronz, A., and Whitehouse, M.J., 2005, Long-term stability of alpha particle damage in natural zircon: *Chemical Geology*, v. 220, p. 83-103.
- Nasdala, L., Kronz, A., Hanchar, J.M., Tichomirowa, M., Davis, D.W., and Hofmeister, W., 2006, Effects of natural radiation damage on back-scattered electron images of single crystals of minerals: *American Mineralogist*, v. 91, p. 1739-1746.
- Nasdala, L., Reiners, P.W., Garver, J.I., Kennedy, A.K., Stern, R.A., Balan, E., and Wirth, R., 2004, Incomplete retention of radiation damage in zircon from Sri Lanka: *American Mineralogist*, v. 89, p. 219-231.
- Nasdala, L., Wenzel, M., Vavra, G., Irmer, G., Wenzel, T., and Kober, B., 2001, Metamictisation of natural zircon: accumulation versus thermal annealing of radioactivity-induced damage: *Contributions To Mineralogy And Petrology*, v. 141, p. 125-144.
- Nasdala, L., Zhang, M., Kempe, U., Panczer, G., Gaft, M., Andrut, M., and Plötze, M., 2003, Spectroscopic methods applied to zircon, *in* Hanchar, J.M., and Hoskin, P.W.O., eds., *Zircon*, Volume 53: Reviews In Mineralogy & Geochemistry, p. 427-467.
- Nemchin, A.A., and Cawood, P.A., 2005, Discordance of the U-Pb system in detrital zircons: Implication for provenance studies of sedimentary rocks: *Sedimentary Geology*, v. 182, p. 143-162.
- Nemchin, A.A., Pidgeon, R.T., and Whitehouse, M.J., 2006, Re-evaluation of the origin and evolution of > 4.2 Ga zircons from the Jack Hills metasedimentary rocks: *Earth And Planetary Science Letters*, v. 244, p. 218-233.
- O'Hara, M.J., Fry, N., and Prichard, H.M., 2001, Minor phases as carriers of trace elements in non-modal crystal-liquid separation processes II: Illustrations and bearing on behaviour of REE, U, Th and the PGE in igneous processes: *Journal Of Petrology*, v. 42, p. 1887-1910.
- Palenik, C.S., Nasdala, L., and Ewing, R.C., 2003, Radiation damage in zircon: *American Mineralogist*, v. 88, p. 770-781.
- Passcheir, C.W., and Trouw, R.A.J., 2005, *Microtectonics - 2nd Edition*, Springer.
- Pidgeon, R.T., O'Neil, J.R., and Silver, L.T., 1966, Uranium and lead isotopic stability in metamict zircon under experimental hydrothermal conditions: *Science*, v. 154, p. 1538-1540.
- Putnis, A., 2002, Mineral replacement reactions: from macroscopic observations to microscopic mechanisms: *Mineral Mag*, v. 66, p. 689-708.
- Rahn, M.K., Brandon, M.T., Batt, G.E., and Garver, J.I., 2004, A zero-damage model for fission-track annealing in zircon: *American Mineralogist*, v. 89, p. 473-484.
- Rasmussen, B., 1996, Early-diagenetic REE-phosphate minerals (florencite, gorceixite, crandallite, and xenotime) in marine sandstones: A major sink for oceanic phosphorus: *American Journal of Science*, v. 296, p. 601-632.

- Rasmussen, B., 2005a, Radiometric dating of sedimentary rocks: the application of diagenetic xenotime geochronology: *Earth-Science Reviews*, v. 68, p. 197-243.
- Rasmussen, B., 2005b, Zircon growth in very low grade metasedimentary rocks: evidence for zirconium mobility at similar to 250 degrees C: *Contributions To Mineralogy And Petrology*, v. 150, p. 146-155.
- Rasmussen, B., Fletcher, I.R., and Sheppard, S., 2005, Isotopic dating of the migration of a low-grade metamorphic front during orogenesis: *Geology*, v. 33, p. 773-776.
- Rasmussen, B., and Glover, J.E., 1994, Diagenesis of Low-Mobility Elements (Ti, Rees, Th) and Solid Bitumen Envelopes in Permian Kennedy Group Sandstone, Western- Australia: *Journal of Sedimentary Research Section a-Sedimentary Petrology and Processes*, v. 64, p. 572-583.
- Raymond, A.C., and Murchison, D.G., 1991, Influence Of Exinitic Macerals On The Reflectance Of Vitrinite In Carboniferous Sediments Of The Midland Valley Of Scotland: *Fuel*, v. 70, p. 155-161.
- Read, W.A., Browne, M.A.E., Stephenson, D., and Upton, B.G.J., 2002, Carboniferous, *in* Trewin, N.H., ed., *The Geology of Scotland*, The Geological Society, London, p. 251-300.
- Robert, J.L., Beny, J.M., Dellaventura, G., and Hardy, M., 1993, Fluorine in Micas - Crystal-Chemical Control of the Oh-F Distribution between Trioctahedral and Dioctahedral Sites: *European Journal of Mineralogy*, v. 5, p. 7-18.
- Rouquerol, J., Avnir, D., Fairbridge, C.W., Everett, D.H., Haynes, J.H., Pernicone, N., Ramsay, J.D.F., Sing, K.S.W., and Unger, K.K., 1994, Recommendations For The Characterization Of Porous Solids: *Pure And Applied Chemistry*, v. 66, p. 1739-1758.
- Rubatto, D., and Gebauer, D., 2000, Use of cathodoluminescence for U-Pb zircon dating by ion microprobe: some examples from the western alps, *in* Pagel, M., Barbin, V., Blanc, P., and Ohnenstetter, D., eds., *Cathodoluminescence in Geosciences*, Springer, p. 373-400.
- Rubatto, D., Williams, I.S., and Buick, I.S., 2001, Zircon and monazite response to prograde metamorphism in the Reynolds Range, central Australia: *Contributions to Mineralogy and Petrology*, v. 140, p. 458-468.
- Rubin, J.N., Henry, C.D., and Price, J.G., 1993, The Mobility of Zirconium and Other Immobile Elements During Hydrothermal Alteration: *Chemical Geology*, v. 110, p. 29-47.
- Salje, E.K.H., Chrosch, J., and Ewing, R.C., 1999, Is "metamictization" of zircon a phase transition?: *American Mineralogist*, v. 84, p. 1107-1116.
- Sano, Y., Takahata, N., and Tsutsumi, Y., 2005, NANO-SIMS U-Pb dating of monazite: *Geochimica Et Cosmochimica Acta*, v. 69, p. A397-A397.
- Sawka, W.N., 1988, REE and trace element variation in accessory minerals and hornblende from the strongly zoned McMurry Meadows Pluton, California: *Transactions of the Royal Society of Edinburgh: Earth Science*, v. 79, p. 157-168.
- Scharer, U., Corfu, F., and Demaiffe, D., 1997, U-Pb and Lu-Hf isotopes in baddeleyite and zircon megacrysts from the Mbuji-Mayi kimberlite: constraints on the subcontinental mantle: *Chemical Geology*, v. 143, p. 1-16.
- Schmidt, C., Rickers, K., Bilderback, D.H., and Huang, R., 2007, In situ synchrotron-radiation XRF study of REE phosphate dissolution in aqueous fluids to 800 degrees C: *Lithos*, v. 95, p. 87-102.
- Schmidt, C., Rickers, K., Wirth, R., Nasdala, L., and Hancher, J.M., 2006, Low-temperature Zr mobility: An in situ synchrotron-radiation XRF study of the effect of radiation damage in

- zircon on the element release in H₂O+HCl +/- SiO₂ fluids: *American Mineralogist*, v. 91, p. 1211-1215.
- Siyانبola, W.O., Fasasi, M.K., Ogundare, F.O., and Owolabi, S.A., 2005, Effects of gamma-irradiation on the TL characteristics of pre-annealed natural ZrSiO₄: *Nuclear Instruments & Methods In Physics Research Section B-Beam Interactions With Materials And Atoms*, v. 239, p. 407-413.
- Spear, F.S., and Pyle, J.M., 2002, Apatite, Monazite and Xenotime in metamorphic rocks, *Phosphates: geochemical, geobiological & materials of importance*, Volume 48, *Reviews in mineralogy & geochemistry*, p. 293-336.
- Speer, J.A., 1982, *Zircon*, Mineralogical Society of America, 67-112 p.
- Stern, R.A., Fletcher, I.R., Rasmussen, B., McNaughton, N.J., and Griffin, B.J., 2005, Ion microprobe (NanoSIMS 50) Pb-isotope geochronology at < 5 μm scale: *International Journal Of Mass Spectrometry*, v. 244, p. 125-134.
- Stroud, R.M., Alexander, C.M.O.D., and MacPherson, G.J., 2000, A precise new method of microsampling chondritic material for transmission electron microscope analysis: preliminary application to calcium-aluminium-rich inclusions and associated matrix material in the Vigarano CV3 meteorite: *Meteoritics and Planetary Sciences Supplement*, v. 35, p. A153-154.
- Tichomirowa, M., Whitehouse, M.J., and Nasdala, L., 2005, Resorption, growth, solid state recrystallisation, and annealing of granulite facies zircon - a case study from the Central Erzgebirge, Bohemian Massif: *Lithos*, v. 82, p. 25-50.
- Tomaschek, F., Kennedy, A.K., Villa, I.M., Lagos, M., and Ballhaus, C., 2003, Zircons from Syros, Cyclades, Greece - Recrystallization and mobilization of zircon during high-pressure metamorphism: *Journal of Petrology*, v. 44, p. 1977-2002.
- Trachenko, K., Dove, M.T., Geisler, T., Todorov, I., and Smith, B., 2004, Radiation damage effects and percolation theory: *Journal Of Physics-Condensed Matter*, v. 16, p. S2623-S2627.
- Trachenko, K., Dove, M.T., and Salje, E.K.H., 2002, Structural changes in zircon under alpha-decay irradiation: *Physical Review B*, v. 65.
- Trachenko, K., Dove, M.T., and Salje, E.K.H., 2003, Large swelling and percolation in irradiated zircon: *Journal Of Physics-Condensed Matter*, v. 15, p. L1-L7.
- Trewin, N.H., and Rollin, K.E., 2002, Geological history and structure of Scotland, *in* Trewin, N.H., ed., *The Geology of Scotland*: London, The Geological Society, p. 1-26.
- Trocellier, P., and Delmas, R., 2001, Chemical durability of zircon: *Nuclear Instruments & Methods In Physics Research Section B-Beam Interactions With Materials And Atoms*, v. 181, p. 408-412.
- Utsunomiya, S., Palenik, C.S., Valley, J.W., Cavosie, A.J., Wilde, S.A., and Ewing, R.C., 2004, Nanoscale occurrence of Pb in an Archean zircon: *Geochimica Et Cosmochimica Acta*, v. 68, p. 4679-4686.
- Utsunomiya, S., Valley, J.W., Cavosie, A.J., Wilde, S.A., and Ewing, R.C., 2007, Radiation damage and alteration of zircon from a 3.3 Ga porphyritic granite from the Jack Hills, Western Australia: *Chemical Geology*, v. 236, p. 92-111.
- Valero, R., Durand, B., Guth, J.L., and Chopin, T., 1998, Mechanism of hydrothermal synthesis of zircon in a fluoride medium: *Journal of Sol-Gel Science and Technology*, v. 13, p. 119-124.
- Valero, R., Durand, B., Guth, J.L., and Chopin, T., 1999, Hydrothermal synthesis of porous zircon in basic fluorinated medium: *Microporous and Mesoporous Materials*, v. 29, p. 311-318.

- Valley, J.W., Lackey, J.S., Cavosie, A.J., Clechenko, C.C., Spicuzza, M.J., Basei, M.A.S., Bindeman, I.N., Ferreira, V.P., Sial, A.N., King, E.M., Peck, W.H., Sinha, A.K., and Wei, C.S., 2005, 4.4 billion years of crustal maturation: oxygen isotope ratios of magmatic zircon: *Contributions to Mineralogy and Petrology*, v. 150, p. 561-580.
- Vallini, D., Rasmussen, B., Krapez, B., Fletcher, I.R., and McNaughton, N.J., 2002, Obtaining diagenetic ages from metamorphosed sedimentary rocks: U-Pb dating of unusually coarse xenotime cement in phosphatic sandstone: *Geology*, v. 30, p. 1083-1086.
- Vallini, D.A., Rasmussen, B., Krapez, B., Fletcher, I.R., and McNaughton, N.J., 2005, Microtextures, geochemistry and geochronology of authigenic xenotime: constraining the cementation history of a Palaeoproterozoic metasedimentary sequence: *Sedimentology*, v. 52, p. 101-122.
- Vavra, G., Gebauer, D., Schmid, R., and Compston, W., 1996, Multiple zircon growth and recrystallization during polyphase Late Carboniferous to Triassic metamorphism in granulites of the Ivrea Zone (Southern Alps): An ion microprobe (SHRIMP) study: *Contributions to Mineralogy and Petrology*, v. 122, p. 337-358.
- Velde, B., 1992, *Introduction to clay minerals: Chemistry, origins, uses and environmental significance*, Chapman & Hall.
- Watson, E.B., Cherniak, D.J., Hanchar, J.M., Harrison, T.M., and Wark, D.A., 1997, The incorporation of Pb into zircon: *Chemical Geology*, v. 141, p. 19-31.
- Watson, E.B., and Harrison, T.M., 2005, Zircon thermometer reveals minimum melting conditions on earliest Earth: *Science*, v. 308, p. 841-844.
- Watt, G.R., Griffin, B.J., and Kinny, P.D., 2000, Charge contrast imaging of geological materials in the environmental scanning electron microscope: *American Mineralogist*, v. 85, p. 1784-1794.
- Wilde, S.A., Valley, J.W., Peck, W.H., and Graham, C.M., 2001, Evidence from detrital zircons for the existence of continental crust and ocean on the Earth 4.4 Gyr ago: *Nature*, v. 409, p. 175-177.
- Wirth, R., 2004, Focused Ion Beam (FIB): A novel technology for advanced application of micro- and nanoanalysis in geosciences and applied mineralogy: *European Journal Of Mineralogy*, v. 16, p. 863-876.
- Wirth, R., 2005, Focused ion beam (FIB): Applications in micro- and nanoanalysis in geosciences and applied mineralogy: *Praktische Metallographie-Practical Metallography*, v. 42, p. 188-205.
- Yamada, K., Tagami, T., and Shimobayashi, N., 2003, Experimental study on hydrothermal annealing of fission tracks in zircon: *Chemical Geology*, v. 201, p. 351-357.
- Yardley, B.W.D., 1997, The evolution of fluids through the metamorphic cycle, *in* Jamtveit, B., and Yardley, B.W.D., eds., *Fluid Flow and Transport in Rocks: Mechanisms and effects*, p. 99-121.
- Zhang, M., Salje, E.K.H., Capitani, G.C., Leroux, H., Clark, A.M., Schluter, J., and Ewing, R.C., 2000, Annealing of alpha-decay damage in zircon: a Raman spectroscopic study: *Journal of Physics-Condensed Matter*, v. 12, p. 3131-3148.